The molecule at the heart of migraine *p. 116*

Thermoelectric performance gets a boost *pp. 124 & 141*

Prehistoric pathogen genome *p. 162*

Science

$15
8 JANUARY 2016
sciencemag.org
AAAS

Vascular dynamics

Branching promotes stem cell expansion in the developing liver

pp. 126, 139, & 176

CONTENTS

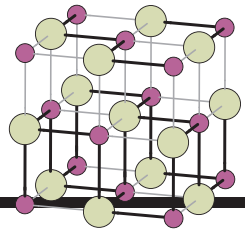

124 & 141
Powering forward thermoelectrics

8 JANUARY 2016 • VOLUME 351 • ISSUE 6269

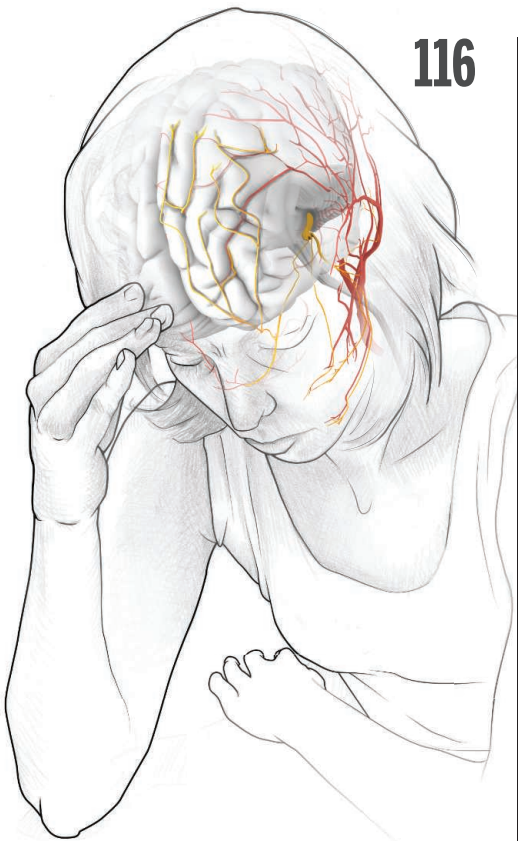

116

NEWS

IN BRIEF

108 News at a glance

IN DEPTH

110 A RACE TO EXPLAIN BRAZIL'S SPIKE IN BIRTH DEFECTS
Evidence points toward the fast-spreading Zika virus as the cause of microcephaly *By G. Vogel*

111 IRAQ CONFRONTS A NEW ENEMY—THE PERSIAN GULF
Drought and dams allow saltwater to invade, threatening people and the ancient marshes of Mesopotamia *By A. Lawler*

113 CESIUM FORTIFIES NEXT-GENERATION SOLAR CELLS
A dash of the metal could hold the key to making cheap solar cells that can withstand the elements *By R. F. Service*
▸ REPORT P. 151

114 CONSERVATION RESEARCHERS GET A NEW ROOST IN CAMBRIDGE
Renovated building aims to foster alliances between academics and advocates *By E. Stokstad*

115 DATA CHECK: FOR FEMALE SCIENTISTS, MIXED FUNDING RESULTS AT U.S. AGENCIES
Report to Congress finds a gender disparity in grant awards—and a dearth of data *By J. Mervis*

FEATURE

116 A SHOT AT MIGRAINE
Drug companies are racing to prove antibody treatments can prevent the debilitating headaches *By E. Underwood*
▸ PODCAST

INSIGHTS

PERSPECTIVES

120 ANCIENT GRASSLANDS AT RISK
Highly biodiverse tropical grasslands are at risk from forest-planting efforts *By W. J. Bond*

122 LOWER-MANTLE MATERIALS UNDER PRESSURE
Laboratory measurements provide a window into Earth's mantle dynamics *By J. Chen*
▸ REPORT P. 144

124 FINDING MERIT IN DIVIDING NEIGHBORS
The favorable thermoelectric properties of SnSe are related to its crystal symmetry *By K. Behnia*
▸ REPORT P. 141

125 DISRUPTED NUCLEAR IMPORT-EXPORT IN NEURODEGENERATION
Toxicity arises from amyloid-like protein accumulation in the cytoplasm, not the nucleus *By S. Da Cruz and D. W. Cleveland*
▸ REPORT P. 173

126 POTENCY FINDS ITS NICHES
Adult bone marrow employs a surprisingly simple hematopoietic hierarchy *By N. Cabezas-Wallscheid and A. Trumpp*
▸ RESEARCH ARTICLE P. 139; REPORT P. 176

128 BALANCING HYDROPOWER AND BIODIVERSITY IN THE AMAZON, CONGO, AND MEKONG
Basin-scale planning is needed to minimize impacts in mega-diverse rivers *By K. O. Winemiller* et al.

BOOKS *ET AL.*

130 TUNNEL VISIONS
By M. Riordan et al., *reviewed by J. Mervis*

131 A BRIEF HISTORY OF CREATION
By B. Mesler and H. J. Cleaves II, reviewed by J. Strick

LETTERS

132 CALL FOR CONSERVATION: ABANDONED PASTURE
By J. A. C. Poore

132 RECOGNIZING THERMAL PLASTICITY IN FISH
By A. P. Farrell and C. E. Franklin

133 HIV/AIDS EPIDEMIC: THE WHOLE TRUTH
By N. Nathanson

133 ERRATA

120

Published by AAAS

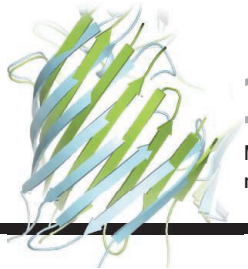

180
Machinery to insert membrane proteins

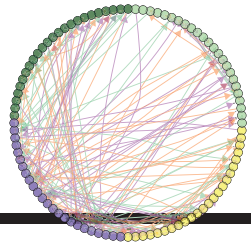

158
Life after death

RESEARCH

IN BRIEF

134 From *Science* and other journals

REVIEW

137 EARTH HISTORY
The Anthropocene is functionally and stratigraphically distinct from the Holocene *C. N. Waters* et al.
REVIEW SUMMARY; FOR FULL TEXT: dx.doi.org/10.1126/science.aad2622

RESEARCH ARTICLES

138 BRAIN CIRCUITS
Gating of hippocampal activity, plasticity, and memory by entorhinal cortex long-range inhibition *J. Basu* et al.
RESEARCH ARTICLE SUMMARY; FOR FULL TEXT: dx.doi.org/10.1126/science.aaa5694

139 HEMATOPOIESIS
Distinct routes of lineage development reshape the human blood hierarchy across ontogeny *F. Notta* et al.
RESEARCH ARTICLE SUMMARY; FOR FULL TEXT: dx.doi.org/10.1126/science.aab2116
▸ PERSPECTIVE P. 126; REPORT P. 176

140 GEOMORPHOLOGY
Geomorphic and geologic controls of geohazards induced by Nepal's 2015 Gorkha earthquake *J. S. Kargel* et al.
RESEARCH ARTICLE SUMMARY; FOR FULL TEXT: dx.doi.org/10.1126/science.aac8353
▸ REPORT P. 147

REPORTS

141 THERMOELECTRICS
Ultrahigh power factor and thermoelectric performance in hole-doped single-crystal SnSe *L.-D. Zhao* et al.
▸ PERSPECTIVE P. 124

144 GEOPHYSICS
Shear deformation of bridgmanite and magnesiowüstite aggregates at lower mantle conditions *J. Girard* et al.
▸ PERSPECTIVE P. 122

147 GEOMORPHOLOGY
Repeated catastrophic valley infill following medieval earthquakes in the Nepal Himalaya *W. Schwanghart* et al.
▸ RESEARCH ARTICLE P. 140

151 SOLAR CELLS
A mixed-cation lead mixed-halide perovskite absorber for tandem solar cells *D. P. McMeekin* et al.
▸ NEWS STORY P. 113

155 FOREST ECOLOGY
Dominance of the suppressed: Power-law size structure in tropical forests *C. E. Farrior* et al.

158 MICROBIOME
Microbial community assembly and metabolic function during mammalian corpse decomposition *J. L. Metcalf* et al.
▸ PODCAST

162 ANCIENT MICROBIOME
The 5300-year-old *Helicobacter pylori* genome of the Iceman *F. Maixner* et al.

165 PALEOCLIMATE
Reconciliation of the Devils Hole climate record with orbital forcing *G. E. Moseley* et al.

169 CELL BIOLOGY
Accurate concentration control of mitochondria and nucleoids *R. Jajoo* et al.

173 PROTEIN AGGREGATES
Cytoplasmic protein aggregates interfere with nucleocytoplasmic transport of protein and RNA *A. C. Woerner* et al.
▸ PERSPECTIVE P. 125

176 STEM CELL NICHE
Fetal liver hematopoietic stem cell niches associate with portal vessels *J. A. Khan* et al.
▸ PERSPECTIVE P. 126; RESEARCH ARTICLE P. 139

180 PROTEIN STRUCTURE
The structure of the β-barrel assembly machinery complex *J. Bakelar* et al.

186 CHEMOTAXIS
Polysialylation controls dendritic cell trafficking by regulating chemokine recognition *E. Kiermaier* et al.

DEPARTMENTS

107 EDITORIAL
Biggest opportunity of our age
By Sir David King

198 WORKING LIFE
Want a letter? You write it for me
By Roger S. Day

ON THE COVER

Tree of portal blood vessels in the murine fetal liver at embryonic days 12 (bottom left), 13 (bottom right), and 14.5 (top), reconstructed in three dimensions from serial cryosections of portal vasculature. Branch surface area is scaled according to fractal geometries, together with the number of hematopoietic stem cells (HSCs; yellow spheres), suggesting that HSC niche expansion is related to portal vessel surface area. See pages 126, 139, and 176. *Data visualization: Valerie Altounian/* Science*; base meshes created by Jalal Khan (Icahn School of Medicine at Mount Sinai) using MeshLab*

Science Staff 106
New Products 191
Science Careers 192

SCIENCE (ISSN 0036-8075) is published weekly on Friday, except the last week in December, by the American Association for the Advancement of Science, 1200 New York Avenue, NW, Washington, DC 20005. Periodicals mail postage (publication No. 484460) paid at Washington, DC, and additional mailing offices.

Copyright © 2016 by the American Association for the Advancement of Science. The title SCIENCE is a registered trademark of the AAAS.

Domestic individual membership and subscription (51 issues): $165 ($74 allocated to subscription). Domestic institutional subscription (51 issues): $1522; Foreign postage extra: Mexico, Caribbean (surface mail) $55; other countries (air assist delivery) $89. First class, airmail, student, and emeritus rates on request. Canadian rates with GST available upon request, GST #1254 88122. Publications Mail Agreement Number 1069624. **Printed in the U.S.A.**
Change of address: Allow 4 weeks, giving old and new addresses and 8-digit account number. **Postmaster:** Send change of address to AAAS, P.O. Box 96178, Washington, DC 20090–6178. **Single-copy sales:** $15.00 current issue, $20.00 back issue prepaid includes surface postage; bulk rates on request. **Authorization to photocopy** material for internal or personal use under circumstances not falling within the fair use provisions of the Copyright Act is granted by AAAS to libraries and other users registered with the Copyright Clearance Center (CCC) Transactional Reporting Service, provided that $35.00 per article is paid directly to CCC, 222 Rosewood Drive, Danvers, MA 01923. The identification code for *Science* is 0036-8075. *Science* is indexed in the *Reader's Guide to Periodical Literature* and in several specialized indexes.

Published by AAAS

Science
AAAS
1200 New York Avenue, NW, Washington, DC 20005
Bateman House, 82-88 Hills Road, Cambridge, UK CB2 1LQ

Editor-in-Chief Marcia McNutt
Executive Editor Monica M. Bradford **News Editor** Tim Appenzeller
Managing Editor, Research Journals Katrina L. Kelner
Deputy Editors Barbara R. Jasny, Andrew M. Sugden(UK), Valda J. Vinson, Jake S. Yeston

Research and Insights

SR. EDITORS Caroline Ash(UK), Gilbert J. Chin, Lisa D. Chong, Julia Fahrenkamp-Uppenbrink(UK), Pamela J. Hines, Stella M. Hurtley(UK), Paula A. Kiberstis, Marc S. Lavine(Canada), Kristen L. Mueller, Ian S. Osborne(UK), Beverly A. Purnell, L. Bryan Ray, Guy Riddihough, H. Jesse Smith, Jelena Stajic, Peter Stern(UK), Phillip D. Szuromi, Brad Wible, Nicholas S. Wigginton, Laura M. Zahn **ASSOCIATE EDITORS** Brent Grocholski, Keith T. Smith, Sacha Vignieri **ASSOCIATE BOOK REVIEW EDITOR** Valerie B. Thompson **ASSOCIATE LETTERS EDITOR** Jennifer Sills **CHIEF CONTENT PRODUCTION EDITOR** Cara Tate **SR. CONTENT PRODUCTION EDITORS** Harry Jach, Lauren Kmec **CONTENT PRODUCTION EDITORS** Jeffrey E. Cook, Chris Filiatreau, Cynthia Howe, Barbara P. Ordway, Catherine Wolner **SR. EDITORIAL COORDINATORS** Carolyn Kyle, Beverly Shields **EDITORIAL COORDINATORS** Ramatoulaye Diop, Joi S. Granger, Lisa Johnson, Anita Wynn **PUBLICATIONS ASSISTANTS** Aneera Dobbins, Jeffrey Hearn, Dona Mathieu, Le-Toya Mayne Flood, Shannon McMahon, Scott Miller, Jerry Richardson, Rachel Roberts(UK), Alice Whaley(UK), Brian White **EXECUTIVE ASSISTANT** Anna Bashkirova **ADMINISTRATIVE SUPPORT** Janet Clements(UK), Lizanne Newton(UK), Maryrose Madrid, Laura-Nadine Schuhmacher (UK, Intern), Alix Welch (Intern), John Wood(UK)

News

NEWS MANAGING EDITOR John Travis **INTERNATIONAL EDITOR** Richard Stone **DEPUTY NEWS EDITORS** Daniel Clery(UK), Robert Coontz, Elizabeth Culotta, David Grimm, David Malakoff, Leslie Roberts **CONTRIBUING EDITOR** Martin Enserink(Europe) **SR. CORRESPONDENTS** Jeffrey Mervis, Elizabeth Pennisi **NEWS WRITERS** Adrian Cho, Jon Cohen, Jennifer Couzin-Frankel, Carolyn Gramling, Eric Hand, Jocelyn Kaiser, Catherine Matacic, Kelly Servick, Robert F. Service, Erik Stokstad(Cambridge, UK), Emily Underwood **INTERNS** Hanae Armitage, Nala Rogers **CONTRIBUTING CORRESPONDENTS** Michael Balter(Paris), John Bohannon, Ann Gibbons, Mara Hvistendahl, Sam Kean, Eli Kintisch, Kai Kupferschmidt(Berlin), Andrew Lawler, Christina Larson(Beijing), Mitch Leslie, Charles C. Mann, Eliot Marshall, Virginia Morell, Dennis Normile(Shanghai), Heather Pringle, Tania Rabesandratana(London), Gretchen Vogel(Berlin), Lizzie Wade(Mexico City) **CAREERS** Donisha Adams, Rachel Bernstein(Editor) **COPY EDITORS** Julia Cole, Dorie Chevlen, Jennifer Levin (Chief) **ADMINISTRATIVE SUPPORT** Jessica Williams

Executive Publisher Rush D. Holt
Publisher Kent R. Anderson **Chief Digital Media Officer** Rob Covey

BUSINESS OPERATIONS AND PORTFOLIO MANAGEMENT DIRECTOR Sarah Whalen **BUSINESS SYSTEMS AND FINANCIAL ANALYSIS DIRECTOR** Randy Yi **MANAGER OF FULFILLMENT SYSTEMS** Neal Hawkins **SYSTEMS ANALYST** Nicole Mehmedovich **ASSISTANT DIRECTOR, BUSINESS OPERATIONS** Eric Knott **MANAGER, BUSINESS OPERATIONS** Jessica Tierney **BUSINESS ANALYSTS** Cory Lipman **FINANCIAL ANALYST** Robert Clark **RIGHTS AND PERMISSIONS ASSISTANT DIRECTOR** Emilie David **PERMISSIONS ASSOCIATE** Elizabeth Sandler **RIGHTS, CONTRACTS, AND LICENSING ASSOCIATE** Lili Kiser

MARKETING DIRECTOR Elise Swinehart **ASSOCIATE DIRECTOR OF ACQUISITION AND RETENTION** Julianne Wielga **MARKETING ASSOCIATE** Elizabeth Sattler **SR. MARKETING EXECUTIVE** Jennifer Reeves **ASSOCIATE DIRECTOR, CREATIVE SERVICES** Tzeitel Sorrosa **ART ASSOCIATE** Seil Lee **JR. ART ASSOCIATE** Kim Huynh **ASSISTANT COMMERCIAL EDITOR** Selby Frame **MARKETING PROJECT MANAGER** Angelissa McArthur **PROGRAM DIRECTOR, AAAS MEMBER CENTRAL** Peggy Mihelich **FULFILLMENT SYSTEMS AND OPERATIONS** membership@aaas.org **MANAGER, MEMBER SERVICES** Pat Butler **SPECIALISTS** Terrance Morrison, Latasha Russell **MANAGER, DATA ENTRY** Mickie Napoleoni **DATA ENTRY SPECIALISTS** Brenden Aquilino, Fiona Giblin

DIRECTOR, SITE LICENSING Tom Ryan **DIRECTOR, CORPORATE RELATIONS** Eileen Bernadette Moran **SR. PUBLISHER RELATIONS SPECIALIST** Kiki Forsythe **PUBLISHER RELATIONS MANAGER** Catherine Holland **PUBLISHER RELATIONS, EASTERN REGION** Keith Layson **PUBLISHER RELATIONS, WESTERN REGION** Ryan Rexroth **SALES RESEARCH COORDINATOR** Aiesha Marshall **MANAGER, SITE LICENSE OPERATIONS** Iquo Edim **SENIOR PRODUCTION SPECIALIST** Robert Koepke **SENIOR OPERATIONS ANALYST** Lana Guz **FULFILLMENT ANALYST** Judy Lillibridge **ASSOCIATE DIRECTOR, MARKETING** Christina Schlecht **MARKETING ASSOCIATES** Thomas Landreth, Isa Sesay-Bah

WEB TECHNOLOGIES SR. DEVELOPER Chris Coleman **DEVELOPERS** Dan Berger, Jimmy Marks, Ryan Jensen **SR. PROJECT MANAGER** Trista Smith

MULTIMEDIA DIRECTOR OF ANALYTICS Enrique Gonzales **SR. WEB PRODUCER** Sarah Crespi **WEB PRODUCER** Alison Crawford **VIDEO PRODUCER** Nguyen Nguyen **SOCIAL MEDIA PRODUCER** Brice Russ

DIRECTOR OF OPERATIONS PRINT AND ONLINE Lizabeth Harman **DIGITAL/PRINT STRATEGY MANAGER** Jason Hillman **QUALITY TECHNICAL MANAGER** Marcus Spiegler **PROJECT ACCOUNT MANAGER** Tara Kelly **DIGITAL PRODUCTION MANAGER** Lisa Stanford **ASSISTANT MANAGER DIGITAL/PRINT** Rebecca Doshi **SENIOR CONTENT SPECIALISTS** Steve Forrester, Antoinette Hodal, Lori Murphy, Anthony Rosen **CONTENT SPECIALISTS** Jacob Hedrick, Kimberley Oster

DESIGN DIRECTOR Beth Rakouskas **DESIGN EDITOR** Marcy Atarod **SENIOR DESIGNER** Garvin Grullón **DESIGNER** Chrystal Smith **GRAPHICS MANAGING EDITOR** Alberto Cuadra **SENIOR SCIENTIFIC ILLUSTRATORS** Chris Bickel, Katharine Sutliff **SCIENTIFIC ILLUSTRATOR** Valerie Altounian **SENIOR ART ASSOCIATES** Holly Bishop, Nathalie Cary, Preston Huey **SENIOR PHOTO EDITOR** William Douthitt **PHOTO EDITORS** Leslie Blizard, Christy Steele

DIRECTOR, GLOBAL COLLABORATION, CUSTOM PUBLICATIONS, ADVERTISING Bill Moran **EDITOR, CUSTOM PUBLISHING** Sean Sanders: 202-326-6430 **ASSISTANT EDITOR, CUSTOM PUBLISHING** Tianna Hicklin: 202-326-6463 **ADVERTISING MARKETING MANAGER** Justin Sawyers: 202-326-7061 science_advertising@aaas.org **ADVERTISING MARKETING ASSOCIATE** Javia Flemmings **ADVERTISING SUPPORT MANAGER** Karen Foote: 202-326-6740 **ADVERTISING PRODUCTION OPERATIONS MANAGER** Deborah Tompkins **SR. PRODUCTION SPECIALIST/GRAPHIC DESIGNER** Amy Hardcastle **SR. TRAFFIC ASSOCIATE** Christine Hall **SALES COORDINATOR** Shirley Young **ASSOCIATE DIRECTOR, COLLABORATION, CUSTOM PUBLICATIONS/CHINA/TAIWAN/KOREA/SINGAPORE** Ruolei Wu: +86-186 0082 9345, rwu@aaas.org **COLLABORATION/CUSTOM PUBLICATIONS/JAPAN** Adarsh Sandhu + 81532-81-5142 asandhu@aaas.org **EAST COAST/E. CANADA** Laurie Faraday: 508-747-9395, FAX 617-507-8189 **WEST COAST/W. CANADA** Lynne Stickrod: 415-931-9782, FAX 415-520-6940 **MIDWEST** Jeffrey Dembksi: 847-498-4520 x3005, Steven Loerch: 847-498-4520 x3006 **UK EUROPE/ASIA** Roger Goncalves: TEL/FAX +41 43 243 1358 **JAPAN** Katsuyoshi Fukamizu(Tokyo): +81-3-3219-5777 kfukamizu@aaas.org **CHINA/TAIWAN** Ruolei Wu: +86-186 0082 9345, rwu@aaas.org

WORLDWIDE ASSOCIATE DIRECTOR OF SCIENCE CAREERS Tracy Holmes: +44 (0) 1223 326525, FAX +44 (0) 1223 326532 tholmes@science-int.co.uk **CLASSIFIED** advertise@sciencecareers.org **U.S. SALES** Tina Burks: 202-326-6577, Nancy Toema: 202-326-6578 **EUROPE/ROW SALES** Sarah Lelarge **SALES ASSISTANT** Kelly Grace **JAPAN** Hiroyuki Mashiki(Kyoto): +81-75-823-1109 hmashiki@aaas.org **CHINA/TAIWAN** Ruolei Wu: +86-186 0082 9345 rwu@aaas.org **MARKETING MANAGER** Allison Pritchard **MARKETING ASSOCIATE** Aimee Aponte

AAAS BOARD OF DIRECTORS RETIRING PRESIDENT, CHAIR Gerald R. Fink **PRESIDENT** Geraldine (Geri) Richmond **PRESIDENT-ELECT** Barbara A. Schaal **TREASURER** David Evans Shaw **CHIEF EXECUTIVE OFFICER** Rush D. Holt **BOARD** Bonnie L. Bassler, May R. Berenbaum, Carlos J. Bustamante, Stephen P.A. Fodor, Claire M. Fraser, Michael S. Gazzaniga, Laura H. Greene, Elizabeth Loftus, Mercedes Pascual

SUBSCRIPTION SERVICES For change of address, missing issues, new orders and renewals, and payment questions: 866-434-AAAS (2227) or 202-326-6417, FAX 202-842-1065. Mailing addresses: AAAS, P.O. Box 96178, Washington, DC 20090-6178 or AAAS Member Services, 1200 New York Avenue, NW, Washington, DC 20005

INSTITUTIONAL SITE LICENSES 202-326-6730 **REPRINTS:** Author Inquiries 800-635-7181 **COMMERCIAL INQUIRIES** 803-359-4578 **PERMISSIONS** 202-326-6765, permissions@aaas.org **AAAS Member Services** 202-326-6417 or http://membercentral.aaas.org/discounts

Science serves as a forum for discussion of important issues related to the advancement of science by publishing material on which a consensus has been reached as well as including the presentation of minority of conflicting points of view. Accordingly, all articles published in *Science*—including editorials, news and comment, and books reviews—are signed and reflect the individual views of the authors and not official points of view adopted by AAAS or the institutions with which the authors are affiliated.

INFORMATION FOR AUTHORS See pages 678 and 679 of the 6 February 2015 issue or access www.sciencemag.org/about/authors

SENIOR EDITORIAL BOARD
Robert H. Grubbs, *California Institute of Technology,* **Gary King,** *Harvard University*
Susan M. Rosenberg, *Baylor College of Medicine,* **Ali Shilatifard,** *Northwestern University Feinberg School of Medicine,* **Michael S. Turner,** *U. of Chicago*

BOARD OF REVIEWING EDITORS (Statistics board members indicated with **(S)**)
Adriano Aguzzi, *U. Hospital Zürich*
Takuzo Aida, *U. of Tokyo*
Leslie Aiello, *Wenner-Gren Foundation*
Judith Allen, *U. of Edinburgh*
Sonia Altizer, *U. of Georgia*
Sebastian Amigorena, *Institut Curie*
Kathryn Anderson, *Memorial Sloan-Kettering Cancer Center*
Meinrat O. Andreae, *Max-Planck Inst. Mainz*
Paola Arlotta, *Harvard U.*
Johan Auwerx, *EPFL*
David Awschalom, *U. of Chicago*
Clare Baker, *University of Cambridge*
Jordi Bascompte, *University of Zurich*
Facundo Batista, *London Research Inst.*
Ray H. Baughman, *U. of Texas, Dallas*
David Baum, *U. of Wisconsin*
Carlo Beenakker, *Leiden U.*
Kamran Behnia, *ESPCI-ParisTech*
Yasmine Belkaid, *NIAID, NIH*
Philip Benfey, *Duke U.*
May Berenbaum, *U. of Illinois*
Gabriele Bergers, *U. of California, San Francisco*
Bradley Bernstein, *Massachusettes General Hospital*
Peer Bork, *EMBL*
Bernard Bourdon, *Ecole Normale Supérieure de Lyon*
Chris Bowler, *École Normale Supérieure*
Ian Boyd, *U. of St. Andrews*
Emily Brodsky, *U. of California, Santa Cruz*
Ron Brookmeyer, *U. of California Los Angeles* **(S)**
Christian Büchel, *U. Hamburg-Eppendorf*
Joseph A. Burns, *Cornell U.*
Carter Tribley Butts, *U. of California, Irvine*
Gyorgy Buzsaki, *New York U. School of Medicine*
Blanche Capel, *Duke U.*
Mats Carlsson, *U. of Oslo*
Ib Chorkendorff, *U. of Denmark*
David Clapham, *Children's Hospital Boston*
Joel Cohen, *Rockefeller U., Columbia U.*
James J. Collins, *MIT*
Robert Cook-Deegan, *Duke U.*
Lisa Coussens, *Oregon Health & Science U.*
Alan Cowman, *Walter & Eliza Hall Inst.*
Robert H. Crabtree, *Yale U.*
Roberta Croce, *Vrije Universiteit*
Janet Currie, *Princeton U.*
Jeff L. Dangl, *U. of North Carolina*
Tom Daniel, *U. of Washington*
Frans de Waal, *Emory U.*
Stanislas Dehaene, *Collège de France*
Robert Desimone, *MIT*
Claude Desplan, *New York U.*
Dennis Discher, *U. of Pennsylvania*
Gerald W. Dorn II, *Washington U. School of Medicine*
Jennifer A. Doudna, *U. of California, Berkeley*
Bruce Dunn, *U. of California, Los Angeles*
William Dunphy, *Caltech*
Christopher Dye, *WHO*
Todd Ehlers, *U. of Tuebingen*
David Ehrhardt, *Carnegie Inst. of Washington*
Tim Elston, *U. of North Carolina at Chapel Hill*
Gerhard Ertl, *Fritz-Haber-Institut, Berlin*
Barry Everitt, *U. of Cambridge*
Ernst Fehr, *U. of Zurich*
Anne C. Ferguson-Smith, *U. of Cambridge*
Michael Feuer, *The George Washington U.*
Toren Finkel, *NHLBI, NIH*
Kate Fitzgerald, *U. of Massachusetts*
Peter Fratzl, *Max-Planck Inst.*
Elaine Fuchs, *Rockefeller U.*
Daniel Geschwind, *UCLA*
Karl-Heinz Glassmeier, *TU Braunschweig*
Ramon Gonzalez, *Rice U.*
Julia R. Greer, *Caltech*
Elizabeth Grove, *U. of Chicago*
Nicolas Gruber, *ETH Zurich*
Kip Guy, *St. Jude's Children's Research Hospital*
Taekjip Ha, *U. of Illinois at Urbana-Champaign*
Christian Haass, *Ludwig Maximilians U.*
Michael Hasselmo, *Boston U.*
Martin Heimann, *Max-Planck Inst. Jena*
Yka Helariutta, *U. of Cambridge*
James A. Hendler, *Rensselaer Polytechnic Inst.*
Janet G. Hering, *Swiss Fed. Inst. of Aquatic Science & Technology*
Kai-Uwe Hinrichs, *U. of Bremen*
David Hodell, *U. of Cambridge*
David Holden, *Imperial College*
Lora Hooper, *UT Southwestern Medical Ctr. at Dallas*
Tamas Horvath, *Yale University*
Raymond Huey, *U. of Washington*
Auke Ijspeert, *EPFL Lausanne*
Steven Jacobsen, *U. of California, Los Angeles*
Stephen Jackson, *U. of Arizona*
Kai Johnsson, *EPFL Lausanne*
Peter Jonas, *Inst. of Science & Technology (IST) Austria*
Matt Kaeberlein, *U. of Washington*
William Kaelin Jr., *Dana-Farber Cancer Inst.*
Daniel Kahne, *Harvard U.*
Daniel Kammen, *U. of California, Berkeley*
Masashi Kawasaki, *U. of Tokyo*
V. Narry Kim, *Seoul National U.*
Joel Kingsolver, *U. of North Carolina at Chapel Hill*
Robert Kingston, *Harvard Medical School*
Etienne Koechlin, *Ecole Normale Supérieure*
Alexander Kolodkin, *Johns Hopkins U.*
Thomas Langer, *U. of Cologne*
Mitchell A. Lazar, *U. of Pennsylvania*
David Lazer, *Harvard U.*
Thomas Lecuit, *IBDM*
Virginia Lee, *U. of Pennsylvania*
Stanley Lemon, *U. of North Carolina at Chapel Hill*
Ottoline Leyser, *Cambridge U.*
Wendell Lim, *U.C. San Francisco*
Marcia C. Linn, *U. of California, Berkeley*
Jianguo Liu, *Michigan State U.*
Luis Liz-Marzan, *CIC biomaGUNE*
Jonathan Losos, *Harvard U.*
Ke Lu, *Chinese Acad. of Sciences*
Christian Lüscher, *U. of Geneva*
Laura Machesky, *CRUK Beatson Inst. for Cancer Research*
Anne Magurran, *U. of St. Andrews*
Oscar Marin, *CSIC & U. Miguel Hernández*
Charles Marshall, *U. of California, Berkeley*
C. Robertson McClung, *Dartmouth College*
Graham Medley, *U. of Warwick*
Tom Misteli, *NCI*
Yasushi Miyashita, *U. of Tokyo*
Mary Ann Moran, *U. of Georgia*
Richard Morris, *U. of Edinburgh*
Alison Motsinger-Reif, *NC State U.* **(S)**
Thomas Murray, *The Hastings Center*
Daniel Neumark, *U. of California, Berkeley*
Kitty Nijmeijer, *U. of Twente*
Pär Nordlund, *Karolinska Inst.*
Helga Nowotny, *European Research Advisory Board*
Ben Olken, *MIT*
Joe Orenstein, *U. of California Berkeley & Lawrence Berkeley National Lab*
Harry Orr, *U. of Minnesota*
Andrew Oswald, *U. of Warwick*
Steve Palumbi, *Stanford U.*
Jane Parker, *Max-Planck Inst. of Plant Breeding Research*
Giovanni Parmigiani, *Dana-Farber Cancer Inst.* **(S)**
John H. J. Petrini, *Memorial Sloan-Kettering Cancer Center*
Samuel Pfaff, *Salk Institute for Biological Studies*
Joshua Plotkin, *U. of Pennsylvania*
Albert Polman, *FOM Institute AMOLF*
Philippe Poulin, *CNRS*
Jonathan Pritchard, *Stanford U.*
David Randall, *Colorado State U.*
Felix Rey, *Institut Pasteur*
Trevor Robbins, *U. of Cambridge*
Jim Roberts, *Fred Hutchinson Cancer Research Ctr.*
Barbara A. Romanowicz, *U. of California,Berkeley*
Amy Rosenzweig, *Northwestern University*
Mike Ryan, *U. of Texas, Austin*
Mitinori Saitou, *Kyoto U.*
Shimon Sakaguchi, *Kyoto U.*
Miquel Salmeron, *Lawrence Berkeley National Lab*
Jürgen Sandkühler, *Medical U. of Vienna*
Alexander Schier, *Harvard U.*
Vladimir Shalaev, *Purdue U.*
Robert Siliciano, *Johns Hopkins School of Medicine*
Denis Simon, *Arizona State U.*
Uri Simonsohn, *U. of Pennsylvania*
Alison Smith, *John Innes Centre*
Richard Smith, *U. of North Carolina* **(S)**
John Speakman, *U. of Aberdeen*
Allan C. Spradling, *Carnegie Institution of Washington*
Jonathan Sprent, *Garvan Inst. of Medical Research*
Eric Steig, *U. of Washington*
Paula Stephan, *Georgia State U. and National Bureau of Economic Research*
Molly Stevens, *Imperial College London*
V. S. Subrahmanian, *U. of Maryland*
Ira Tabas, *Columbia U.*
Sarah Teichmann, *Cambridge U.*
John Thomas, *North Carolina State U.*
Shubha Tole, *Tata Institute of Fundamental Research*
Christopher Tyler-Smith, *The Wellcome Trust Sanger Inst.*
Herbert Virgin, *Washington U.*
Bert Vogelstein, *Johns Hopkins U.*
Cynthia Volkert, *U. of Göttingen*
Douglas Wallace, *Dalhousie U.*
David Wallach, *Weizmann Inst. of Science*
Ian Walmsley, *U. of Oxford*
Jane-Ling Wang, *U. of California, Davis*
David A. Wardle, *Swedish U. of Agric. Sciences*
David Waxman, *Fudan U.*
Jonathan Weissman, *U. of California, San Francisco*
Chris Wikle, *U. of Missouri* **(S)**
Ian A. Wilson, *The Scripps Res. Inst.* **(S)**
Timothy D. Wilson, *U. of Virginia*
Rosemary Wyse, *Johns Hopkins U.*
Jan Zaanen, *Leiden U.*
Kenneth Zaret, *U. of Pennsylvania School of Medicine*
Jonathan Zehr, *U. of California, Santa Cruz*
Len Zon, *Children's Hospital Boston*
Maria Zuber, *MIT*

BOOK REVIEW BOARD
David Bloom, *Harvard U.,* **Samuel Bowring,** *MIT,* **Angela Creager,** *Princeton U.,* **Richard Shweder,** *U. of Chicago,* **Ed Wasserman,** *DuPont*

Published by AAAS

EDITORIAL

Biggest opportunity of our age

Sir David King is the United Kingdom Foreign Secretary's Special Representative for Climate Change. E-mail: david.king@fco.gov.uk

The importance of the agreement reached at the Paris climate Conference of Parties (COP21) last month cannot be overstated. It is a major step toward preventing some of the worst risks that climate change presents to the global economy and security. Now is the time to seize the opportunity that this moment represents. We must transform world economies away from fossil fuels toward a more sustainable low-carbon future.

Research and innovation have a critical role in this transformation. Advances in renewable energy generation, smart energy storage, smart grids, and improved energy efficiency will help countries meet the targets they have signed up to in Paris for reducing greenhouse gas emissions. But crucially, these advances will enable countries to increase their emission reduction targets, which are set to be reviewed every 5 years under the United Nations Framework Convention on Climate Change system. Indeed, nations must increase their targets if we are to achieve a safe and stable climate in which temperature rise is limited to less than 2°C. The Paris agreement sets out a distinct long-term goal of net zero emissions in the second half of the century, showing that the world is committed to decarbonizing the economy. This sends a strong signal to industry and investors that the shift is global, irreversible, and transformational, and provides confidence that will clear a path for the private sector to drive a long-term solution.

Many companies are considering signing up to 100% renewable energy pledges. The dynamic has changed—previously, the cost-benefit analysis was more finely balanced; now, it is a higher-risk strategy not to invest in renewable energy and sustainability.

"Now is the time to...transform world economies...toward a more sustainable low-carbon future."

There is already more investment in renewable energy globally than there is in conventional energy. This trend is expected to increase to meet the enormous new demand resulting from the Paris agreement. Although there is currently a shortage of good investable green projects, an increase in finance to meet the new demands for clean energy will create more business opportunities for such projects, such as cheap and large rechargeable batteries and solar- and battery-powered airships for transport.

"Mission Innovation," the initiative announced in Paris, will see 20 countries, including the United Kingdom and the United States, double their public sector budgets for clean energy research and development. In addition, the Breakthrough Energy Coalition, a global group of private investors including Bill Gates, will provide investment flows of potentially $20 billion in its early stages, for the most promising new clean energy technologies that can be streamlined into the marketplace.

Backed by the U.S. and UK governments, the Energy Africa initiative aims to ensure that every home in Africa has clean, affordable energy by 2030. A huge challenge, indeed, but renewable clean energy is already growing faster in many developing nations than it is in richer countries because it makes economic sense and is the right choice for environmental and health reasons, too.

So the direction is set: decarbonization. The target: to reduce greenhouse gas emissions fast enough to prevent the worst impacts of climate change from hitting all of us, particularly the world's poorest and most vulnerable. The opportunity: immense. The question that remains: What part are you going to play?

– Sir David King

10.1126/science.aaf1428

PHOTOS: (RIGHT) UNITED KINGDOM FOREIGN AND COMMONWEALTH OFFICE; (INSET) © STEVE ALLEN TRAVEL PHOTOGRAPHY/ALAMY

Published by AAAS

NEWS

> “Some question whether people even care what happens to a vial of blood or bits of a tumor after they leave the doctor. But trust me, they care.”
>
> **Rebecca Skloot, author of *The Immortal Life of Henrietta Lacks***, in a *The New York Times* op-ed on proposed changes to U.S. rules governing patient consent for biospecimen research.

IN BRIEF

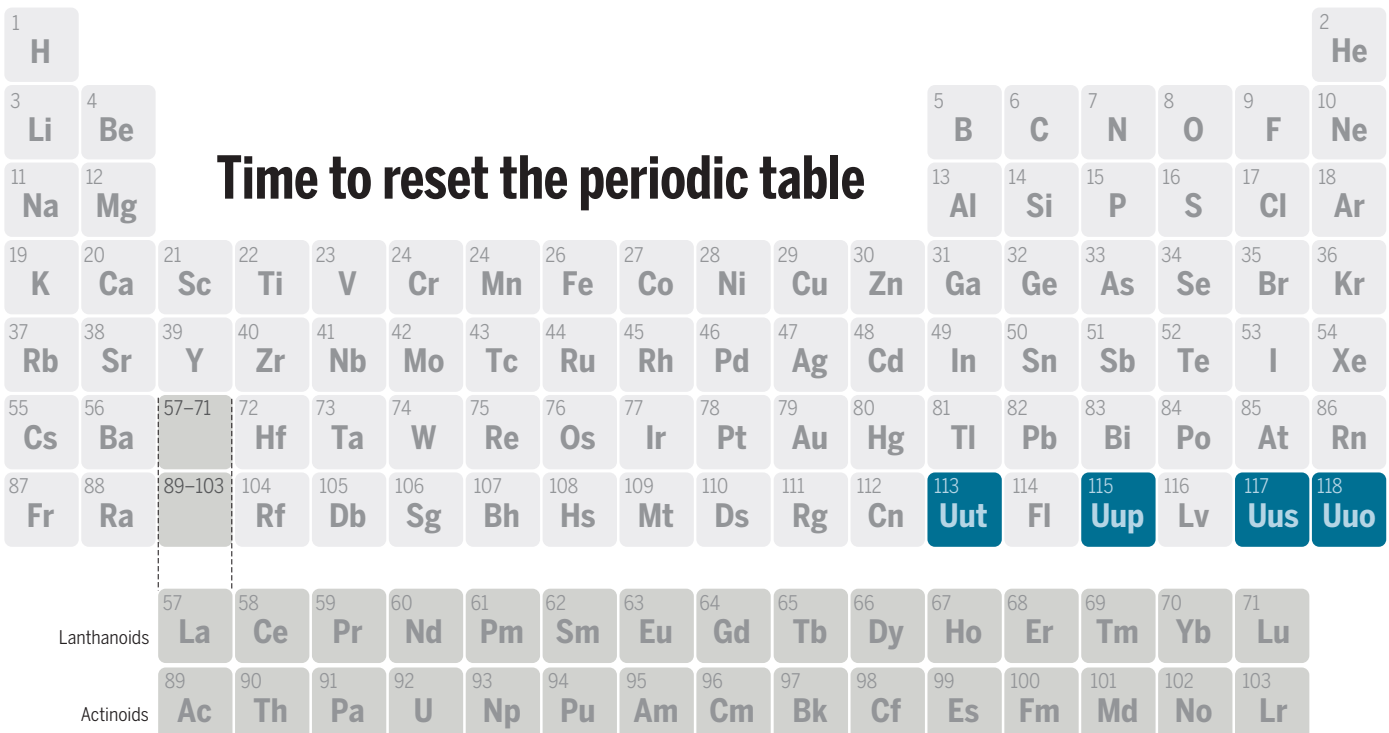

That periodic table poster on your wall is about to be out of date, thanks to four new chemical elements that just received official recognition. The newcomers, acknowledged by the International Union of Pure and Applied Chemistry last week, are some of the heaviest ever discovered, with atomic numbers of 113, 115, 117, and 118. They will be named by the two research teams that discovered them between 2002 and 2010. The researchers generated the atoms using a particle accelerator, firing beams of lighter elements at the nuclei of heavier ones until some of them fused. Studies of how these massive nuclei quickly decay have already offered insight into the forces that hold atoms together. According to these findings, even heavier elements might have conformations that are especially stable—suggesting that if scientists can ever make atoms that big, they might stick around for longer than a few microseconds.

IMAGES: (TOP TO BOTTOM) ADAPTED FROM IUPAC BY C. SMITH/*SCIENCE*; TOM JEFFERSON/GREENPEACE

AROUND THE WORLD

Coal port expansion under fire

SYDNEY, AUSTRALIA | Australian scientists have slammed the environmental impact assessment (EIA) process behind projects such as the expansion of the Abbot Point coal terminal near the Great Barrier Reef, approved last month by federal environment minister Greg Hunt. “It’s a tick-the-box exercise,” says Alana Grech, a spatial information scientist at Sydney’s Macquarie University. In a paper online in *Conservation Letters*, Grech and colleagues assert that EIAs are plagued by conflicts of interest, inconsistent methods, and a lack of independent evaluation. They suggest an independent review process using expert peer reviewers, funded by companies proposing development. The coal terminal expansion will dredge more than a million cubic meters of spoil near

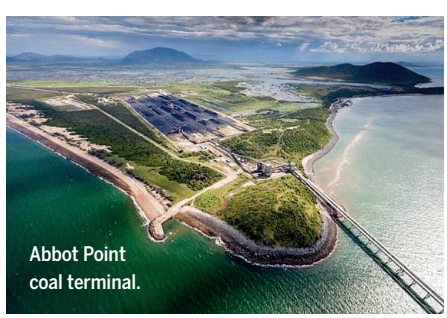
Abbot Point coal terminal.

Published by AAAS

the reef, and make Abbot Point one of the world's largest coal ports.

Iran creates 'Muslim Nobels'

TEHRAN | Iran is offering a lucrative new science prize, which it hopes will further its goal of becoming known as a research powerhouse. Late last month, two nanotechnology experts took home inaugural Mustafa Prizes, each including $500,000 in cash. Jackie Ying, executive director of the Agency for Science, Technology and Research's Institute of Bioengineering and Nanotechnology in Singapore, won the "top scientific achievement" award for a body of work including nanoparticles that deliver insulin to diabetic patients, and Omar Yaghi, co-director of the Kavli Energy NanoSciences Institute at the University of California, Berkeley, snared the prize for nanoscience. One rationale for the awards is that only three Muslims have won a Nobel Prize in science, but the award is also open to non-Muslims in Islamic nations. The "most important policy" of the new prize, explains Mehdi Safarinia, director of the Pardis Technology Park in Tehran, which manages the awards, is to make Iran "a center of excellence in the Islamic world."

FINDINGS

Predicting vaccine side effects

People who are prone to having mild side effects to vaccines may have telltale signs in their blood cells, suggests a study reported online this week in *Nature Immunology*. A team led by immunologist Adrian Hayday of King's College London analyzed which genes were turned on in blood samples taken from 178 people in the United Kingdom before and after they received a flu vaccine. About 20% of the people had side effects such as inflammation at the injection site or headaches, and the researchers found that this subset was more likely to have turned on genes affiliated with antibody-producing B cells before receiving the shot. A closer analysis of this group found high levels of a specific type of B cell—again, prevaccination—that is linked to autoimmune responses.

NEWSMAKERS

Three Q's

On 1 December 2015, archaeologist **Nicole Boivin** accepted a job as director at the Max Planck Institute for the Science of Human History in Jena, Germany. She joined archaeogeneticist Johannes Krause and linguist Russell Grey as the new institute's third director-level scientist.

Q: What is "the science of human history"?
A: It's about using new scientific methods and approaches to looking at the past. Techniques like ancient DNA and quantitative linguistics, when combined with new techniques in archaeology, are revolutionary. They are going to transform completely what we understand about the past.

Q: What sorts of new questions can you answer?
A: It's clear from ancient DNA that people have moved around a lot. Those migrations and their influence on both culture and ecology is something we have not been able to look at in deeper time. We'll be able to better understand present-day diversity.

Q: Aren't there serious tensions between your three fields?
A: The stories you get from the different disciplines in many cases don't line up. [But that has] forced geneticists and archaeologists to talk to each other and figure out why the data sets are so different. What we need is productive dialogue. Researchers need to have lunch together and seminars together. That's what is exciting about Jena. We may mix departments so linguists have their desks next to geneticists and archaeologists.

PHOTO: KILEY RIFFELL

Platanthera obtusata is pollinated by mosquitoes.

This orchid smells like humans

Orchids are masters of deception, mimicking the looks of nectar-laden flowers or the smells of rotting meat or female insects to lure potential pollinators. Now, sensory biologists have discovered that the orchid *Platanthera obtusata* emits a smell like human body odor to recruit tiger mosquitoes. The species is one of only a few flowers that rely on mosquitoes to transfer pollen. Chloé Lahondère and Jeff Riffell from the University of Washington, Seattle, and their colleagues collected chemicals emitted by several *Platanthera* species to better understand how these plants could coexist in the same bog without interbreeding. They suspected that each attracts a different set of pollinators. *P. obtusata* has some odor components common to many flowers, but it also gives off chemicals found in human body odor, they reported this week at the annual meeting of the Society for Integrative and Comparative Biology in Portland, Oregon. Although the orchid's odor is barely detectable by humans, it elicits electrical activity in mosquito antennae. Riffell suggests that the potentially mosquito-attracting chemicals could prove useful in traps and lures.

Published by AAAS

IN DEPTH

EMERGING DISEASES

A race to explain Brazil's spike in birth defects

Evidence points toward the fast-spreading Zika virus as the cause of microcephaly

By **Gretchen Vogel**

Brazilian fetal medicine specialist Manoel Sarno first noticed in July that something was seriously wrong. In just 2 weeks, he diagnosed four cases of microcephaly, a previously rare birth defect in which the baby's head is too small because the brain fails to fully develop. Sarno, who works at the Federal University of Bahia in Salvador, Brazil, says he typically sees half-a-dozen cases in a year.

It was the beginning of an avalanche. Since then, Sarno has diagnosed more than 70 fetuses with microcephaly, which can lead to seizures, developmental delays, learning disabilities, and impaired motor function. Across northeastern Brazil, doctors have reported nearly 3000 cases in the same period—more than 20 times the usual rate.

Scientists are scrambling to understand what is going on. The leading theory so far—and Sarno's initial hunch—is that the spike is caused by a little known mosquito-borne virus called Zika that surfaced in Brazil in March and is quickly spreading through Latin America (*Science*, 27 November 2015, p. 1012). But Zika has never before been linked to microcephaly. "The challenge is that this has just exploded, and we know so little about the natural history of Zika virus," says Albert Ko, a tropical disease specialist at Yale University and the Oswaldo Cruz Foundation in Salvador.

Meanwhile, pregnant women in Brazil have panicked, the government has declared a public health emergency, and some doctors are telling women not to get pregnant until more is known. The spectrum of emotions at maternity wards "would break anyone's heart," says Nikos Vasilakis, a virologist at the University of Texas Medical Branch in Galveston on assignment in Salvador to help improve Zika tests. In parents of afflicted infants, he says, "I have witnessed expressions of love but also rejection of the babies."

Zika usually causes only mild symptoms, including fever and rashes; as many as 80% of infected people may not get sick at all. That benign reputation explains why early warnings from Sarno and other obstetricians about Zika were met with disbelief. Yet to Sarno, the link seemed plausible. Infections are a known cause of microcephaly, which is thought to result from the loss of developing brain cells, especially during the key early weeks of fetal development. Almost all the mothers whose babies had microcephaly told Sarno that they'd had a mild fever or rash early in their pregnancy; mothers whose babies were healthy or had other types of birth defects rarely reported such symptoms, he says.

Circumstantial evidence for a link to Zika has continued to build. Doctors found the virus in the amniotic fluid of two fetuses diagnosed with microcephaly via ultrasound. Zika was also detected in tissues of a baby with microcephaly that died shortly after birth. And after Brazil raised the alarm, health officials in French Polynesia—which had a Zika outbreak in 2013 and 2014—said they had identified more than a dozen babies born with neural defects; tests showed that many of their mothers had been exposed to a flavivirus, the family to which Zika belongs.

Most of the Brazilian babies born with microcephaly don't test positive for Zika, however, nor do their mothers. That may be because current tests for the virus are only conclusive for a short time after symptoms appear; tests on recovered patients can't distinguish between antibodies to Zika and those to dengue, a related virus that is extremely common in Brazil. Several groups are working to develop better diagnostic tools, including one that could identify Zika antibodies in umbilical cord blood. IgM antibodies don't cross the placenta, so the presence of such antibodies to Zika would be evidence that the baby was infected in the womb,

Vasilakis says.A link between Zika and microcephaly may not have surfaced before because previous outbreaks were simply too small, says Ana Maria Bispo de Filippis, head of the flavivirus laboratory at the Oswaldo Cruz Institute in Rio de Janeiro, Brazil. But the virus may also somehow have become more pathogenic. (Some virologists suspect a recent genetic change has also allowed the virus to spread more easily.) Another possibility is that pregnant women who have antibodies to dengue might mount a less intense immune response to Zika, says Patrícia Carvalho de Sequeira, who works in Bispo's lab. That might increase the chance that the virus crosses the placenta and infects a fetus.

Dejailson Arruda holds his daughter Luiza, born with microcephaly, at their house in Pernambuco state, Brazil.

PHOTO: AP PHOTO/FELIPE DANA

Corrected 7 January 2016; see full text.

Published by AAAS

virus crosses the placenta and infects a fetus.

One way to nail down the connection would be to show that the virus causes similar brain anomalies in developing animals. But although Zika can infect mice when injected into their brains or bloodstreams, the animals aren't considered good models for the virus's behavior in humans, Vasilakis says. "Nonhuman primates are the only model that comes close."

A possible alternative is tests in cerebral organoids, tiny models of the developing human brain grown from stem cells. The organoid model has already been used to help explain how a genetic mutation causes microcephaly (*Science*, 30 August 2013, p. 946). Now, Patricia Garcez of the Federal University of Rio de Janeiro, together with colleagues at the neighboring D'Or Institute for Research and Education, has begun studies that will infect organoids to see how the virus affects them.

Slowing Zika's spread will not be easy. Controlling *Aedes* mosquitoes, the hosts to Zika, dengue, and chikungunya (another mosquito-borne virus rampant in Brazil), is notoriously difficult; for now, Brazilian health authorities simply recommend that pregnant women do what they can to avoid being bitten. That means wearing protective clothing, keeping doors and windows screened, and using insect repellant.

In the long run, a vaccine might help prevent Zika outbreaks; vaccines already exist for dengue and two other related viruses, and one for Zika could be constructed using similar strategies within a year, says Duane Gubler of the Duke-National University of Singapore Graduate Medical School. "But it would take years to test," he adds. So little is known about Zika's natural pattern of spread that clinical trials could be difficult to design.

Meanwhile, the virus is advancing fast. It surfaced in Colombia, Suriname, Guatemala, El Salvador, and Mexico in October and November; Puerto Rico reported its first cases last week. Countries across the Americas should be prepared for a similar wave of birth defects in coming months, Ko warns. In northeast Brazil, Zika infections tapered off after peaking in May, but officials are bracing for a new wave when the rainy season begins in February.

Researchers are working overtime to answer basic questions asked by patients, says epidemiologist Federico Costa of the Federal University of Bahia. If a woman has had Zika but recovered, are future pregnancies safe? How long does Zika virus remain in an infected person? Is Zika also causing other types of damage in unborn babies, which will only show up later in development? As Ko puts it, "is this really just the tip of the iceberg?" ■

WATER RESOURCES

Iraq confronts a new enemy—the Persian Gulf

Drought and dams allow saltwater to invade, threatening people and the ancient marshes of Mesopotamia

By **Andrew Lawler**, *in Basra, Iraq*

At the Huweza Station for Marsh Research in southern Iraq, Badir Albadran pulls out a Swiss Army knife, cuts a plastic soda bottle in half, and fills it with river water. Using a pocket salinity meter, the geologist at the University of Basra pegs the sample at 3.8 grams of salt per kilogram. "This was fresh until recently, but now it is brackish," he says, offering a taste. It is too bitter to drink.

As Iraqi forces consolidate their victory last week over the Islamic State (IS) group in the city of Ramadi north of Baghdad, a new and insidious enemy is marching on the south. The Persian Gulf is creeping relentlessly up rivers and canals shrunken by water diversions upstream and by years of drought. The result is a growing crisis for farmers and the 2.5 million residents of Iraq's booming southern metropolis of Basra. The rising salinity also threatens attempts to restore the region's famous marshes—the most extensive wetlands in the Middle East—which nearly disappeared during the reign of Saddam Hussein.

"If we allow nature to take its course, the gulf will move inland," says Ali Douabul, a marine chemist at the Marine Science Center at the University of Basra.

At emergency meetings last month in Baghdad and Basra, officials from the Ministry of Water Resources huddled with researchers to consider options for rescuing the marshes while assuring adequate freshwater for people, crops, and livestock in southern Iraq. But the stakeholders have yet to agree on a strategy to combat dwindling freshwater and rising salinity.

The unfolding crisis is tied to contentious Middle East politics, Douabul says. Turkey is building dozens of dams in the mountainous headwaters of the Euphrates and Tigris rivers, which flow through Iraq, while the IS group also restricts flow along the stretches of river it now controls. Water that does reach southern Iraq is mismanaged, with the government encouraging water-intensive crops such as rice. Exacerbating these human factors is a months-long dry spell that came hard on the heels of a 2006 to 2010 drought believed to have contributed to the onset of Syria's civil war.

PHOTO: JASSIM AL-ASADI

Freshwater flowing through southern Iraq's marshes, including this one, is critical to sustaining the people and animals that have lived for thousands of years in this ecosystem.

Published by AAAS

A half-century ago, the discharge at the mouth of the Shatt-al-Arab, the waterway formed from the confluence of the Tigris and Euphrates near the Persian Gulf, was 900 cubic meters of water per second. Now it is less than 50 cubic meters per second, Douabul says. (Albadran estimates the rate is closer to 20 cubic meters per second.) The flow of freshwater is no longer strong enough to hold back the gulf. As recently as a decade ago, tidal impact was limited to the mouth of the Shatt-al-Arab. In recent years, however, tidal effects have been observed 100 kilometers inland, far north of Basra. The seawater is also working its way up the beds of rivers and canals, turning groundwater brackish.

The lack of freshwater has devastated marsh ecology, says Latif Nasra, a local who works at Huweza Station. The Huweza Marsh near Basra once covered approximately 2500 square kilometers, and was home to thousands of Marsh Arabs who lived on small islands, fishing the freshwater and grazing cattle on reeds. Cinderblock houses along rough dirt roads are now appearing where reeds once grew along wide canals. Less than 10% of the marsh is left, Albadran says, and only a few dozen families still live there. The loss stems from a combination of new dams upstream, the drought, and government attempts in the 1990s to drain the marshes. Without copious freshwater, restoring the ecosystem would be difficult, experts say.

In a startling consequence of the dwindling river flow, a new coral reef has formed just a few kilometers off the Iraqi coast, a team from the University of Basra and Germany's Freiberg University of Mining and Technology found in 2014. Previously, sediment-filled freshwater gushing into the sea prevented such coral growth in this part of the Persian Gulf.

Albadran says the rising salinity is even overwhelming desalination plants constructed in recent years around Basra and downstream to supply increasingly scarce freshwater. These use membranes that tolerate only certain salinity levels and require extensive maintenance.

In a meeting last week, Douabul urged water officials to construct a barrage on the Shatt-al-Arab 30 kilometers south of Basra to restrict saltwater incursion. Such barrages have proved successful in places like Singapore but the high cost makes some of his colleagues skeptical that the government would follow through.

Last month, the water ministry agreed to divert water from the Euphrates to ensure that the Central Marsh, 100 kilometers northwest of Basra, can survive, says Jassim al-Asadi from the Chibaish office of Nature Iraq, an environmental organization that seeks to protect and restore the marshes. "This means that we can save a good part of the marsh, but not all," he says. But Douabul argues that the marshes are beyond saving and that the little freshwater still reaching southern Iraq must go to agriculture and drinking water.

In the long run, Douabul believes that an international water agreement between Iraq, Turkey, and Iran is critical to Iraq's future, along with better management of the water that crosses the Turkish border. It's a tall order for a nation facing existential challenges, but he is emphatic that the issue must be faced—and soon. "Wake up, Iraq," he says. "Think water, water, water!" ■

A water crisis deepens across Iraq

Drought, dams, irrigated crops, and growing cities like Basra mean less freshwater is flowing into the marshes and the Persian Gulf. As a result, the swamps are in crisis and the salty gulf is steadily creeping inland.

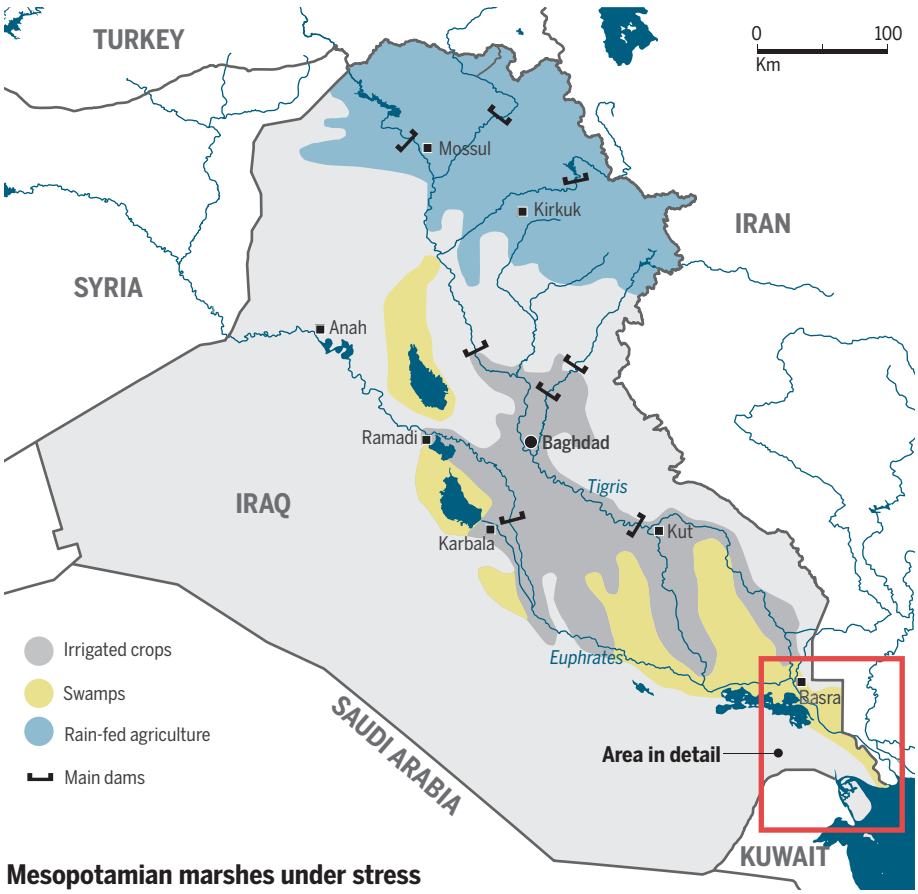

Mesopotamian marshes under stress

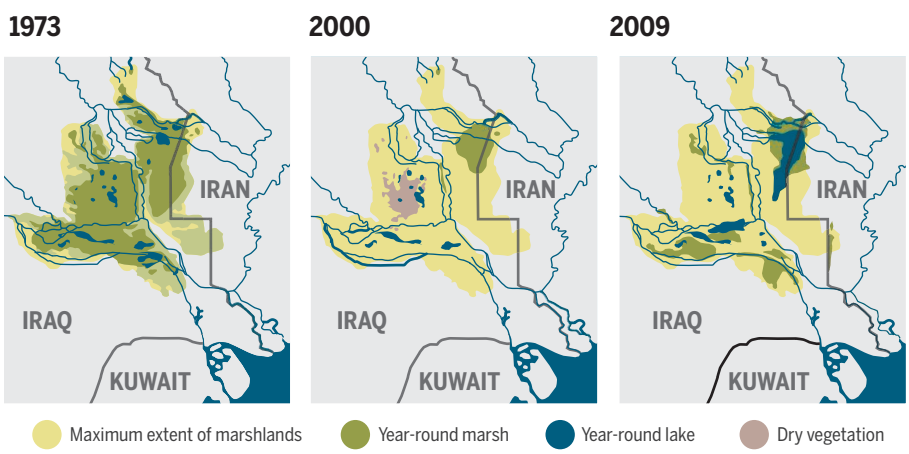

IMAGE: CIRCLE OF BLUE/KALIN WOOD; ADAPTED BY A. CUADRA/*SCIENCE*

Published by AAAS

SOLAR ENERGY

Cesium fortifies next-generation solar cells

A dash of the metal could hold the key to making cheap, durable perovskite photovoltaics

By **Robert F. Service**, *in Boston*

In a world looking for better, cheaper alternative energy, the solar cell materials called perovskites are a bright hope. Their efficiency at converting sunlight into electricity is climbing faster than that of any solar technology before them. They're cheap and easy to make, can be manufactured roll-to-roll like newsprint, and can even be layered atop conventional silicon solar cells to boost their output. But they are fragile stars: Moisture, air, heat, or even prolonged sunlight makes them fall apart.

Now, these materials are toughening up. Over the past few months, three separate teams have reported that adding a dash of cesium to their perovskite recipes produces efficient solar cells that are far more stable when exposed to the elements. It's still too early to say whether cesium-spiked perovskites will withstand years or decades on a rooftop. Even so, "this is really a breakthrough for the field," says Michael Graetzel, a chemist at the Swiss Federal Insitute of Technology in Lausanne, who leads one of the groups.

Perovskites are rapidly overcoming other shortcomings. The first perovskite-based solar cells, made 6 years ago by Japanese researchers, turned just 3.8% of the energy in sunlight into electricity, an efficiency well below that of silicon and other commercial technologies (*Science*, 15 November 2013, p. 794). But last month, at a meeting of the Materials Research Society here, researchers from South Korea reported evidence that their latest cells rival silicon, reaching a record 21.7% efficiency. Researchers are growing ever more hopeful that perovskite solar cells will soon approach 30% efficiency, rarefied territory now occupied only by costly gallium arsenide cells. "There seems to be no fundamental reason these materials won't achieve the efficiencies gallium arsenide has achieved," says Henry Snaith, a physicist at the University of Oxford in the United Kingdom.

Yet unlike gallium arsenide, perovskites are made from cheap components—typically including the inorganic elements lead and iodine, together with one of two simple organic compounds, methylammonium (MA) or formamidinium (FA)—in a layered crystalline arrangement. All the chemistry needed to make them can be done without the expensive high-temperature setups or clean room facilities needed for many other solar cell materials. "This is really quite remarkable for the perovskites," says David Mitzi, a physicist at Duke University in Durham, North Carolina.

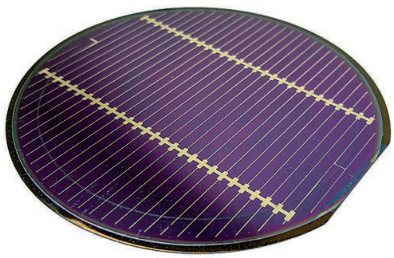

Tandem solar cells, such as this 10-centimeter disk, combine the benefits of perovskite and silicon.

Perovskites are also exceptionally good at absorbing photons. As a result, cells can be made very thin, which further lowers costs. A thinner cell can also be more efficient, because electrons energized by sunlight are less likely to get hung up on imperfections in its crystalline lattice as they travel to an electrode, which feeds them to an external circuit.

Yet "high efficiency is meaningless if the cells aren't stable," says Giles Eperon, a physicist at Oxford. So researchers around the globe are searching for more stable perovskite recipes. They've swapped out lead for tin, antimony, and bismuth: other metals nearby in the periodic table. And they've replaced iodine with bromine and chlorine. Most such changes reduce the materials' efficiency.

But one change—replacing MA with FA, a slightly larger organic molecule—actually increases it. In the 12 June 2015 issue of *Science*, for example, Sang Il Seok, a chemist at the Korea Research Institute of Chemical Technology in Daejeon, South Korea, and his colleagues reported achieving more than 20% efficiency with FA-lead iodide perovskite solar cells. Cells with FA alone or a mixture of FA and MA also appear to be somewhat more stable than pure MA-lead iodide cells. When MA cells are taken out of a protective glove box, they degrade almost immediately, turning from black to yellow—a change that shows they are absorbing a narrower band of visible light. Mixed FA-MA materials also degrade, but more slowly: in minutes rather than seconds, Snaith says.

Now, several groups have found that adding cesium to their recipe seems to further stabilize the other components and helps the mixture retain its perovskite structure and black appearance. Nam-Gyu Park, a chemical engineer at Sungkyunkwan University, Suwon, in South Korea, first described the approach. In a 21 October 2015 online paper in *Advanced Energy Materials*, he and colleagues reported that replacing 10% of the MA with cesium yielded

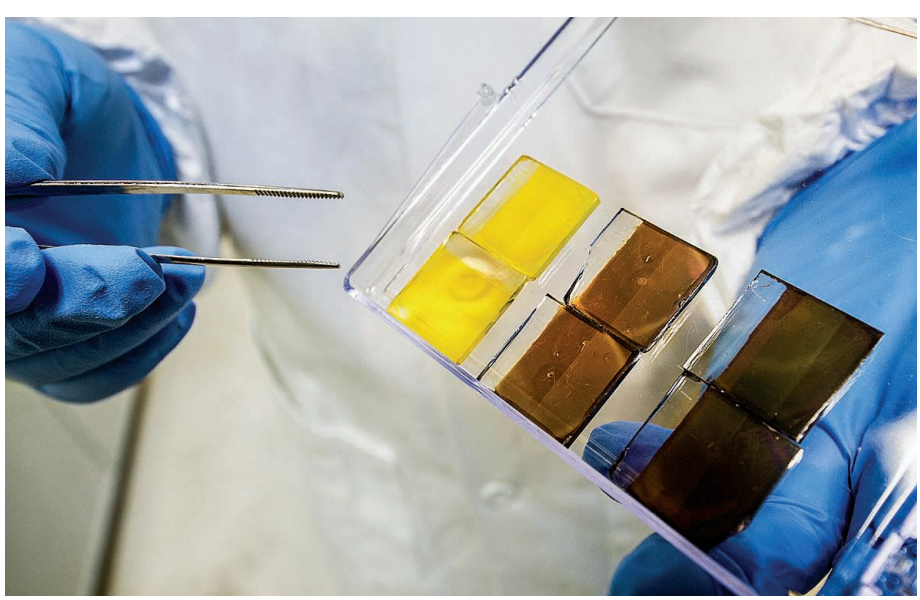

Perovskite solar cells reflect different colors depending on their composition; darker ones absorb more light.

PHOTOS: (TOP TO BOTTOM) OXFORD PV; © LEN COLLECTION/ALAMY STOCK PHOTO

Published by AAAS

solar cells that held up "significantly" better to humidity and sunlight, although they did not give specific numbers.

These cells had a top efficiency of 16.5%, a step behind the best MA-only cells. But progress has continued. In a paper published online 3 December 2015 in *Energy & Environmental Science*, Graetzel and colleagues reported perovskite cells with a mix of MA, FA, and cesium that had an efficiency of just over 21%, a result verified by an independent lab. It seems clear that cesium is a key to making cells more stable and powerful. "I'm sure this is where the field is going to go," Graetzel says.

Cesium-containing perovskites can also be coaxed to work well with silicon cells, as Snaith and colleagues report online this week in *Science*. Such combinations typically layer a perovskite cell on top of a silicon cell. The materials absorb different wavelengths of light, because they have different band gaps—the amount of extra energy they must absorb to shake electrons loose from their atoms so they travel through the material. Silicon, with a band gap of 1.1 electron volts (eV), is good at absorbing photons on the red end of the visible spectrum. Typical MA-based perovskites have a bandgap of 1.5 eV and thus absorb slightly shorter, or bluer, photons. Combining the two materials captures more of the solar spectrum—and thus more energy—than either could harvest alone.

To make tandem cells perform better, researchers want to widen their net by pushing the band gap of perovskites higher so they will absorb even bluer light. Groups led by Snaith and others have done that by replacing some or all of the iodine with bromine. But the changes made the cells more vulnerable to heat and light.

In their current study, Snaith's team replaced 17% of the FA with cesium. The resulting bromine-based perovskites could withstand exposure to prolonged light and high temperatures. The cells were also 17% efficient, and they had the wider band gap needed to work well with silicon. The researchers calculate that by layering the material atop a 19% efficient silicon cell, they could create a tandem cell with an efficiency of 25%. Snaith says silicon-perovskite tandems eventually ought to exceed 30% efficiencies.

So far, numbers like that have been the sole territory of gallium arsenide cells—devices so expensive they are used primarily in space, where it's worth paying a premium for higher efficiency. If cesium-spiked perovskites can bring high-efficiency solar cells down to Earth, the temperamental challengers' brightest days may still lie ahead. ■

ENVIRONMENTAL SCIENCE

Conservation researchers get a new roost in Cambridge

Renovated building aims to foster alliances

By **Erik Stokstad** *in Cambridge, U.K.*

Conservation and cement often don't mix. But a concrete, 1960s-era Brutalist office building here is set to become home to one of the largest concentrations of conservation scientists in the world. Five hundred researchers, conservation practitioners, and support staff are now settling into the freshly refurbished David Attenborough Building, renamed after the prominent naturalist and television host. The building is the new hub of the Cambridge Conservation Initiative (CCI), an effort to expand collaborations between the University of Cambridge, its Museum of Zoology, and the many conservation groups here.

David Attenborough visited the conservation hub when it was named for him last year.

"The scale of the ambition and vision is really remarkable," says biologist Georgina Mace of University College London, who has advised CCI but is not involved in the center. Academics will find new opportunities to apply their research, planners predict, while conservation groups will get help addressing key problems. "This building will become a flagship for conservation," predicts Peter Crane, Dean of the Yale School of Forestry & Environmental Studies.

Cambridge has long been a conservation hotbed. Organizations with nearby headquarters, the Royal Society for the Protection of Birds and the British Trust for Ornithology, were joined over the years by others including BirdLife International, the United Nations Environment Programme's World Conservation Monitoring Centre (WCMC), and the International Union for Conservation of Nature's Global Species Programme. In 2007, nine groups and the university founded CCI to strengthen ties, and have raised some £2 million for pilot projects.

Several years ago, CCI saw an opportunity to deepen such alliances after the university's mathematics and metallurgy departments left their aging downtown home: a three-story, turreted concrete fortress. CCI helped the university raise nearly one-third of the £58 million spent on the renovation, which included adding a green roof and an atrium with a 12-meter-tall wall of plants. Architects worked to avoid isolated offices, instead creating long sight lines and numerous common rooms. "I see this as an experiment," says Mike Rands, CCI's director. He notes that a team of social scientists is studying how the building affects interactions between the academics and the conservation advocates.

The offices will be occupied by up to 150 people from university departments, including zoology, plant sciences, law, and business, along with an estimated 350 from conservation organizations. Smaller groups are moving in all of their employees, whereas larger ones will rotate in staffers. "There is an incredible buzz about the place," says Matt Walpole, WCMC's director of partnerships and development.

Fostering collaboration between academics and conservation advocates will likely bring benefits, but it also has hazards, says Josh Tewksbury, a conservation biologist with the University of Colorado, Boulder, who is not involved in the project. "For a university, there's always a brand risk to the credibility of science by bringing in advocacy organizations," he says. Those groups, meanwhile, risk being distracted by basic research not relevant to their missions.

But Rands believes that by harnessing "the Cambridge brand" for conservation research, the hub will become a go-to resource for government, business, and philanthropy leaders. In November, for instance, the president of Madagascar paid a 3-hour visit. "We'll see more of this happening," Walpole predicts.

In the meantime, the new space is having a psychological impact on its occupants. "It is an impressive statement of intent," says conservation scientist Andrew Balmford of the University of Cambridge. "Everyone feels an inch taller." ■

PHOTO: CCI

Published by AAAS

BEHIND THE NUMBERS

For female scientists, mixed funding results at U.S. agencies

By **Jeffrey Mervis**

Are female scientists less likely than men to receive research grants from the U.S. government? The first cross-agency effort to answer that question suggests the answer is sometimes yes.

But the new study by the congressional Government Accountability Office (GAO) in Washington, D.C., comes with several caveats. Some agencies don't collect the data needed to reveal gender disparities in funding, which forced GAO to find a novel way to address the concerns of the three Democratic congresswomen who requested the study. In addition, discrimination may not be the reason for a disparity. Finally, some agencies aren't doing what the law requires to track the impact of their investments on gender equity at U.S. universities.

GAO intended to use grant application success rates as a marker for potential government discrimination against women. It requested data from 2009 through 2013 from six agencies that together manage 90% of the government's research investment in basic and applied research in science and engineering. And there's some good news in the report (GAO-16-14): Success rates for men and women are similar at the two biggest agencies, the National Institutes of Health (NIH) and the National Science Foundation (NSF).

But there's also bad news. The picture is less rosy at the other agencies: At the Department of Energy's (DOE's) Office of Science and the Department of Defense's (DOD's) Office of Naval Research, success rates for men are seven percentage points and six percentage points higher, respectively, than for women. And GAO couldn't even answer the question at NASA and other research units within DOD and DOE because those agencies don't systematically collect and maintain demographic information on grant applicants. The lack of data makes it impossible to know whether NASA, DOE, and DOD are fulfilling their mission to fund "the best science and the best scientists, irrespective of gender," GAO concludes.

The missing data didn't stop the GAO analysts. They turned to NSF's Survey of Doctoral Recipients (SDR), a long-running study that tracks the career paths of nearly 1 million scientists and engineers and includes self-reported data on funding sources. GAO could not use the SDR data to compute success rates directly, because the survey does not ask recipients whether they have applied for a federal grant. But the data do offer glimpses of gender differences among those who have received grants from NIH, NSF, DOE, and DOD (see table, below).

Taken as a whole, the data show that women were actually one-third more likely than men to have received NIH funding. They were only one-third as likely as men to have received DOE funding, however, and half as likely to have gotten DOD funding.

One reason for the disparities, GAO analysts note, might be variations in the pool of applicants. Women represent a larger percentage of the pool in biomedical research than in the physical science and engineering fields that DOE and DOD typically support. Taking discipline into account does bring women close to parity with men at NIH, GAO found. It also erases a significant gap at the more eclectic NSF, and improves the situation for women at DOE and DOD.

Who is more likely to get a grant?

An initial edge for women (shaded area) at the National Institutes of Health disappears after correcting for discipline and other variables. Those adjustments improve a dismal picture at the Department of Defense and the Department of Energy.

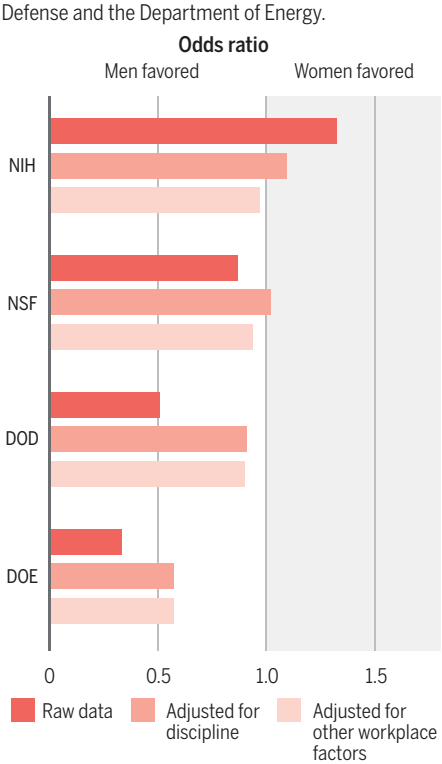

DATA: GAO-16-14

GAO also looked at other variables, such as where scientists work, their academic rank, and their years of experience. Controlling for those factors, it found almost no gender gap in success rate at NIH. But a small gap reopened at NSF, and there was no change in women's grants odds at DOD and DOE.

The ever-cautious GAO analysts note that a gender disparity in grant awards isn't necessarily due to bias in the grantsmaking process. "We can't conclude that there is discrimination," says GAO's Melissa Emrey-Arras, the lead author. "For example, you can't fault DOE for not giving half of its money to women if women make up only 15% of the pool in the disciplines they fund."

Still, the report suggests that the gender disparity is real. "Where the analysis points to unequal funding outcomes for similarly qualified men and women, more data would be needed to explain the sources of these differences," the report notes, "and it is possible that these differences would persist even with better data."

GAO also found that although NIH has been even-handed in awarding grants, it has ignored a federal requirement to monitor whether the universities it funds are complying with a provision of a 1972 law—known as Title IX—intended to prevent gender discrimination. That means NIH is not tracking the effect of the tens of billions of dollars it spends on academic opportunities for women, GAO concluded.

NIH's parent organization, the Department of Health and Human Services (HHS), doesn't dispute that finding. But HHS officials told GAO that they "had received only a few Title IX complaints" from NIH-funded institutions and that they rely on the "expertise" of the Department of Education to ensure Title IX compliance by universities.

That's not good enough, says the American Association of University Women (AAUW) in Washington, D.C. "We've suspected that there were significant gaps [in compliance reviews] based on conversations with our members," says AAUW's Erin Prangley. Conducting such reviews, she adds, "is not just a good idea, it's the law."

The analysts hope their report won't be the last word on the subject. Are the apparent gender disparities "a pipeline issue, or a lack of mentoring, or an institutional culture?" Emrey-Arras asks. "We need to try and figure out what's happening." ■

Published by AAAS

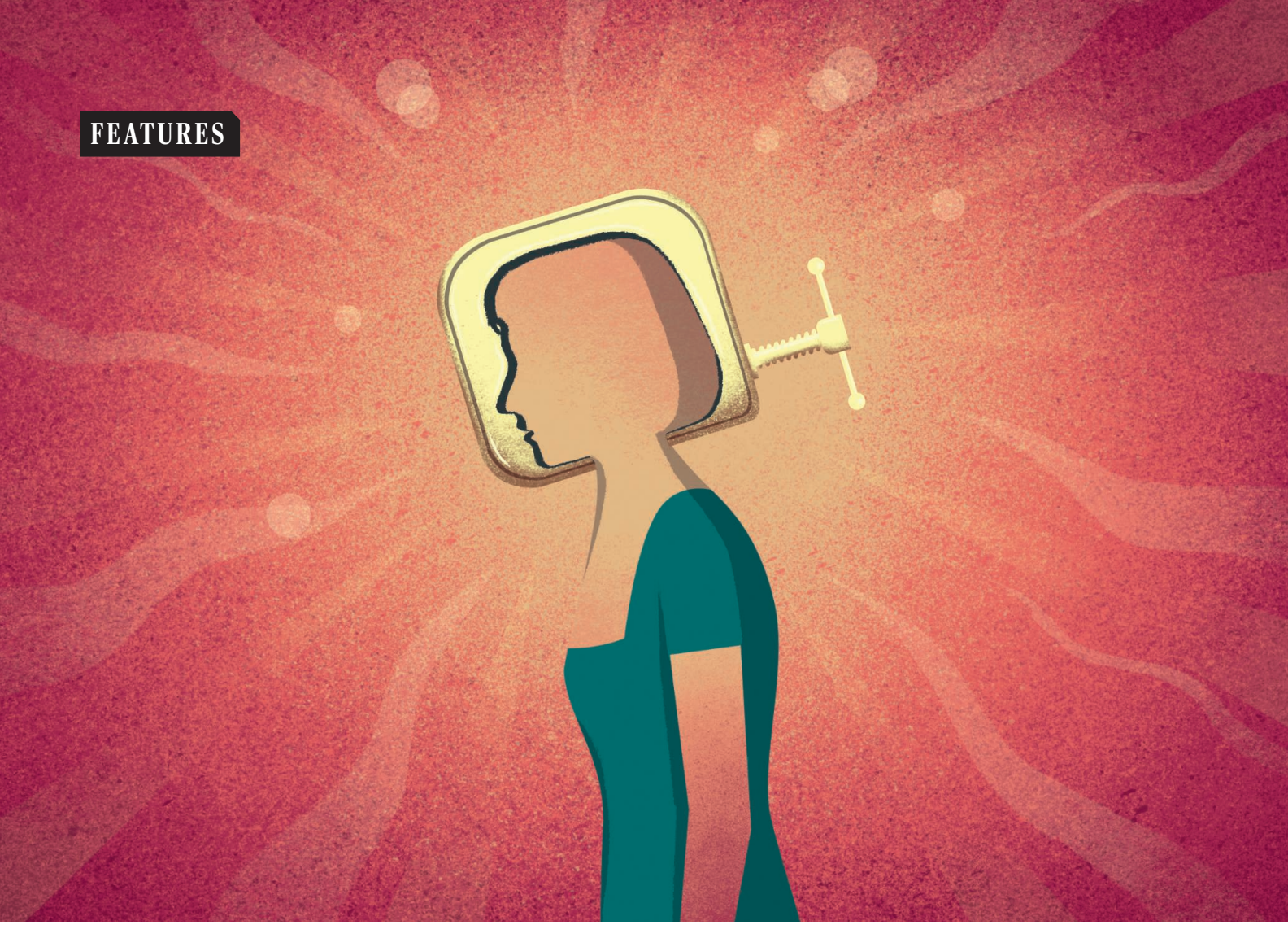

A SHOT AT MIGRAINE

Drug companies are racing to prove antibody treatments can prevent the debilitating headaches

By **Emily Underwood**

As long as she can remember, 53-year-old Rosa Sundquist has tallied the number of days per month when her head explodes with pain. The migraines started in childhood and have gotten worse as she's grown older. Since 2008, they have incapacitated her at least 15 days per month, year-round.

Head-splitting pain isn't the worst of Sundquist's symptoms. Nausea, vomiting, and an intense sensitivity to light, sound, and smell make it impossible for her to work—she used to be an office manager—or often even to leave her light-proofed home in Dumfries, Virginia. On the rare occasions when she does go out to dinner or a movie with her husband and two college-aged children, she wears sunglasses and noise-canceling headphones. A short trip to the grocery store can turn into a full-blown attack "on a dime," she says.

Every 10 weeks, Sundquist gets 32 bee sting–like injections of the nerve-numbing botulism toxin into her face and neck. She also visits a neurologist in Philadelphia, Pennsylvania, who gives her a continuous intravenous infusion of the anesthetic lidocaine over 7 days. The lidocaine makes Sundquist hallucinate, but it can reduce her attacks, she says—she recently counted 20 migraine days per month instead of 30. Sundquist can also sometimes ward off an attack with triptans, the only drugs specifically designed to interrupt migraines after they start.

Millions of others similarly dread the onset of a migraine,

PODCAST

To hear a podcast with author Emily Underwood, go to http://scim.ag/pod_6269

ILLUSTRATION: DAVIDE BONAZZI/@SALZMANART

Published by AAAS

although many are not afflicted as severely as Sundquist. Worldwide, migraines strike roughly 12% of people at least once per year, with women roughly three times as likely as men to have an attack. The Migraine Research Foundation estimates that U.S. employees take 113 million sick days per year because of migraines, creating an annual loss of $13 billion. The toll underscores how little current treatments—not just drugs, but nerve-numbing injections, behavioral therapies, and special diets—can help many people.

On the horizon, however, is a new class of drugs that many scientists believe can stop migraines at their root. The drugs block the activity of a molecule called calcitonin gene-related peptide, or CGRP, which spikes during migraine attacks. CGRP is "the best validated target for migraine, ever," says David Dodick, a neurologist at the Mayo Clinic in Phoenix. It may also help finally solve the centuries-old puzzle of what triggers the complex events of a migraine attack, which can cause brain activity to be "completely disregulated" for several days, similar to epilepsy and other recurrent, seizurelike disorders, says Michel Ferrari, a neurologist at Leiden University in the Netherlands.

Four pharmaceutical companies are racing to complete advanced clinical trials of antibodies that either neutralize CGRP by binding to it, or block its receptor. So far, Dodick says, the data suggest the drugs work faster, for longer, and better than anything currently available. Most striking, he notes, is a subset of "superresponders," whose attacks appear to cease entirely for 6 months after a single injection of a CGRP-blocking antibody. "I've been in this field now for 21 years, and this is the most exciting thing we've seen so far," says Dodick, who has consulted for several of the companies developing CGRP blockers.

Others are more restrained. Given that the frequency of migraines can wax and wane, at least some people in these initial trials may simply be getting better on their own, Ferrari says. "For me, it's still too early to judge the efficacy."

GREEK PHYSICIAN HIPPOCRATES described migraines in detail in the 5th century B.C.E., including the shining, scintillating "auras" that roughly a fifth of sufferers see a few minutes before an attack. Because vomiting seemed to relieve some migraineurs' symptoms, Hippocrates believed that the headaches resulted from an excess of "yellow bile." But by the mid-20th century, most physicians thought that dilated arteries and veins in the head were key to the disorder because many patients describe feeling those blood vessels throb during an attack. "Look at any portrait of a person having a migraine, and they are pressing their hands to their temples," says neurologist Marcelo Bigal at the Frazer, Pennsylvania, location of Israel-based Teva Pharmaceutical Industries, one of the companies developing a CGRP-blocking drug.

Many of the early remedies constricted blood vessels, adding to the misperception that abnormal blood flow was key to the disorder, Bigal says. The first such drugs, called ergotamines, were powerful vasoconstrictors derived from the ergot fungus, which grows on rye and other grains and led to mass poisonings in the Middle Ages. Large doses of the fungus can cause seizures, psychosis, and gangrene in the limbs—a syndrome some called St. Anthony's fire—but doctors found that small doses could help prevent women from hemorrhaging after childbirth, and they sometimes relieved migraines.

Yet even refined, synthetic versions of ergotamine can dangerously narrow blood vessels, so doctors and patients welcomed the triptans, which selectively constrict the blood vessels of the brain. Introduced in the 1990s and still the most widely prescribed migraine-specific drugs, triptans can head off a migraine attack in roughly 50% to 60% of people who take them. They don't work for everyone, however, and they share an unpleasant side effect with ergots and many pain medications: If a person takes them frequently, their headaches may become more frequent and severe.

Although both ergotamine and triptans act on blood vessels, studies that began in the 1990s "torpedoed" the idea that dilated vessels actually cause migraines, says neurologist Jes Olesen of the University of Copenhagen. Particularly important, he notes, have been a series of detailed functional magnetic resonance imaging (fMRI)–based blood vessel studies showing no relationship between abnormal blood flow in the brain and the pain of migraine attacks.

As the blood vessel theory of migraines unraveled, researchers looked to other potential triggers. One was a disruption of normal electrical activity in the brain: a seizurelike phenomenon called cortical spreading depression (CSD). Strongly associated with the aura many migraineurs get, this slow wave of abnormal neuronal excitation usually begins in the occipital lobe at the back of the brain, and spreads over it at a rate of roughly 2 mm to 3 mm per minute, says Michael Moskowitz, a migraine researcher at Harvard University. In its wake, neuronal activity is temporarily depressed.

Genetic studies of people with inherited forms of migraine and some animal studies suggest that CSD plays a central role in many, if not all, migraines, Moskowitz says. Of the 41 gene variants the studies have linked to migraine risk, many are in genes that modulate electrical activity in neurons and are thought to make carriers more susceptible to CSD.

Based on experiments in rodents, Moskowitz believes CSD can trigger migraines by irritating a network of neurons, the trigeminovascular system, which innervates cerebral blood vessels. Moskowitz's lab discovered the system at the Massachusetts Institute of Technology in Cambridge in the 1980s, when they traced a group of fine nerve fibers radiating from blood vessels in the meninges—delicate membranes that envelop the brain and spinal cord—to the trigeminal nerve, which innervates the face, head, and jaw. Moskowitz proposed that migraine pain arises when these fine nerves are irritated or stimulated by CSD or other factors. He also suggested that blocking the release of Substance P—the only pain-signaling neurotransmitter known at the time—in these nerves might ease migraineurs' symptoms.

14%
Americans affected by migraine or severe headache

3:1
Ratio of women to men suffering migraine

$20 billion
Estimated annual U.S. cost of migraine in treatments and lost productivity

Although many found the hypothesis compelling, multiple trials of drugs designed to block the activity of Substance P failed to head off acute attacks in migraine patients. Today, although most researchers agree that a hypersensitive trigeminovascular system is likely the source of pain in migraines, few would argue that CSD is the only or most important factor in inflaming it, Moskowitz says. For one thing, most people who get the headaches don't experience the visual aura thought to be a consequence of CSD. And only a handful of brain imaging studies have actually shown hints of CSD in human migraineurs. These experiments, however, are difficult to conduct because they require deliberately sparking a migraine right before putting a person in an fMRI scanner. In 2001, Moskowitz performed what many in the field describe as the most compelling demonstration of CSD's link to migraines, in an engineer who was able to trigger his own migraines through exercise—in this case, playing basketball for 80 minutes before Moskowitz and colleagues recorded his brain activity.

DATA: AMERICAN HEADACHE SOCIETY

Published by AAAS

THE FAILURE of the Substance P–blocking drugs opened the door for CGRP, an obscure, 37–amino acid peptide, discovered largely by accident by neuroscientists Susan Amara and Michael Rosenfeld of the University of California, San Diego. While studying a thyroid hormone called calcitonin, which helps regulate the body's sodium and calcium levels, Amara and Rosenfeld found that the same gene that encodes calcitonin in the thyroid gland produces a slightly different peptide in another part of the brain. As one of the earliest examples of alternative gene splicing, which enables a single gene to produce multiple proteins, the discovery made a splash when it was published in *Nature* in 1982.

After finding CGRP is plentiful in brain pathways that process pain and in brain regions that regulate blood flow, neurologist Lars Edvinsson, of Lund University in Sweden, wondered whether CGRP is involved in migraines. His group soon found that CGRP can trigger what was then considered a hallmark sign of migraines: When released from the trigeminovascular nerves, it is a powerful vasodilator of cerebral blood vessels. In 1990, he paired up with neurologist Peter Goadsby, now at King's College London, to further explore CGRP's role in migraine patients. After getting permission to take blood samples from the jugular veins of people who had come to the emergency room for a severe migraine, the researchers measured the amounts of a range of different peptides, including Substance P, during and after attacks. "The amazing thing was that CGRP was the only peptide that was significantly released," Edvinsson says.

At first, Edvinsson and others thought CGRP triggered migraines by expanding blood vessels in the brain. Instead, a growing pile of studies suggested that CGRP was not just a vasodilator, but a previously unknown, pain-signaling neurotransmitter. Other groups found that rising levels of CGRP in jugular blood—not patterns of abnormal blood flow—signaled a migraine attack. Then, in a pivotal 2002 study, Oleson and colleagues injected CGRP into the blood of migraineurs and found that they developed migrainelike headaches within hours, whereas nonmigraineurs got at most a mild headache. That suggested migraineurs are unusually sensitive to the peptide's effects, Oleson says.

By the early 2000s, the biology around CGRP and migraine was strong enough to inspire a few companies to attempt drug development. German pharmaceutical company Boehringer Ingelheim designed a small molecule called bibn4096bs to block CGRP's receptor. The drug could stop acute migraine attacks in some people, but produced adverse side effects. Another company, Merck, tried to block the CGRP receptor with a different small compound. It, too, seemed to work modestly well, but its trial also had to stop because it showed signs of liver toxicity. But the glimmers of efficacy were encouraging, says Jaume Pons in San Francisco, California, who was at that time head of protein engineering at Rinat, a spinoff of Genentech that specialized in antibodies to treat cancer.

Pons and others began to explore other approaches. Perhaps antibodies were worth a shot, he thought, because they can last a long time in the body and can be exceptionally specific, reducing the frequency with which people need injections. But because most researchers thought it necessary to target migraines in the brain and antibodies are generally too large to pass through the blood-brain barrier, they tended to dismiss the option, Pons says. Back then, "most people were not considering the use of antibodies for pain," but Rinat had already begun clinical trials of a different antibody pain treatment with promising initial results, he says.

In 2004, Rinat launched an antibody program targeting CGRP. If it worked, the team reasoned, it would show that it was possible to treat migraines from outside the brain, by blocking CGRP only in the peripheral nervous system. That would lower the risk of the side effects often provoked by drugs that act in the brain, Pons says. In a few months, the firm developed the peptide-blocking antibody now being tested by Teva under the name TEV-48125. The antibody faced plenty of roadblocks. The Rinat team

Migraine's tangled roots

Once considered a disorder of blood vessels, neuroscientists have pinpointed a new mechanism for migraines: the release of a substance called calcitonin gene-related peptide (CGRP, below), which sensitizes nerves (yellow) in the face, head, and jaw, and alongside blood vessels (red) surrounding the brain. Antibodies that block interactions between CGRP and its receptors on cells could become the next generation of migraine drugs.

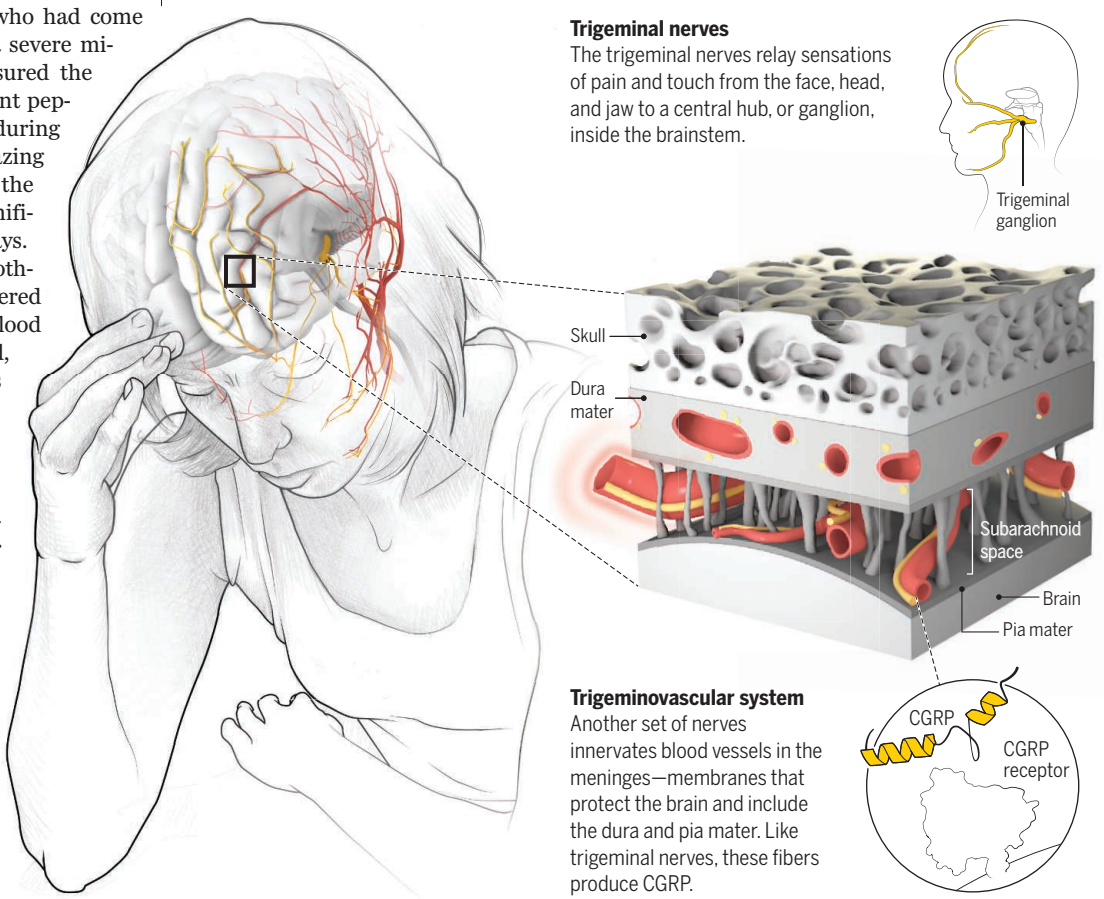

ILLUSTRATION: V. ALTOUNIAN/*SCIENCE*

Published by AAAS

managed to launch a phase I study testing TEV-48125's safety, but Pfizer acquired the company in 2006, and by 2011, the firm "decided that migraine was not an area it wanted to pursue," Pons says.

Other big companies had made similar decisions at the time, Pons says. The Food and Drug Administration (FDA) has especially stringent safety standards for pain treatments, and estimates for the market value of a new migraine drug are uncertain, ranging wildly from roughly $200 million several years ago to $5 billion, making it hard for companies to commit a large amount of money to drug development.

Despite the risk, in 2013 a venture capital company called venBio bought the rights to TEV-48125 and launched a new company called Labrys Biologics and continued the antibody's clinical development. Neuroscientist Corey Goodman, a managing partner of venBio in San Francisco, California, had until 2009 been president of the biotherapeutics division at Pfizer, where he oversaw Rinat and Pons's team. Goodman remembered TEV-48125 was a "very good antibody," and after recruiting more investors, Labrys kicked off two phase II trials in people with frequent migraines. The trials produced "the most beautiful phase II data I've ever seen," Goodman says, with significant reductions in number of headache days over placebo, even for the most severe cases.

Teva bought Labrys in 2014 and is now racing with Alder Biopharmaceuticals, Eli Lilly, and Amgen to win FDA approval for the first migraine antibody drug. So far, the four phase II clinical trials, at least one from each firm, have produced similarly encouraging results, with up to 15% of participants experiencing complete relief, Goodman says: "I don't think it's too early to start talking about a cure for some patients suffering from this debilitating disease."

One of the superresponders is 26-year-old Julia Berner, who has been getting a migraine every day since she was a little girl. Over the years, she's tried epilepsy medications, Chinese remedies, and nerve blocks, among countless other treatments, with no success. Within a few days of receiving four shots of Teva's thick, viscous, antibody-containing solution in the back of her arms and the skin around her hips, however, the migraines disappeared.

The difference was "mind-blowing," she says. Berner usually spends her days avoiding any small disturbance that could make her constant, low-grade migraines more severe. After getting the antibody injections, that burden lifted. "I hadn't realized how tired they make me," she says. "Everyone around me noticed the change in my demeanor."

DESPITE SUCH ANECDOTAL SUCCESSES, some migraine researchers don't think it's time to celebrate yet. If CGRP "really is a fundamental mechanism, you would expect a much higher proportion of patients to be completely free of attacks," Ferrari says. Safety also concerns him because of CGRP's natural role in dilating arteries and maintaining blood supply to the heart and brain. "Theoretically, if you block CGRP you could translate a minor stroke or cardiac ischemia … into a full blown stroke or heart attack," he says. So far, the companies say they haven't seen that or other significant side effects in the several thousand people who have completed phase I and II trials, but the drugs have only been administered for up to 6 months—not long enough to judge long-term effects, Bigal says.

Still, the fact that CGRP antibodies can prevent migraines in some fraction of patients is a "really cool finding" from a research perspective, says Andrew Russo, a molecular physiologist and neurologist at the University of Iowa in Iowa City, who consults for Alder.

> ***"I've been in this field now for 21 years, and this is the most exciting thing we've seen so far."***
> **David Dodick**, Mayo Clinic

The trial results confirm that CGRP is a major new player in migraines—and perhaps even the fundamental trigger—even though the chain of events remains murky. "We don't really know what's going on, but we have some ideas," Russo says. One view is that the increased amounts of CGRP released at the start of a migraine sensitize the trigeminal nerve to what are normally innocuous signals, resulting in inflammation in the nerves that is relayed to the brain as a pain signal.

In that scenario, Dodick says, a migraineur's brain is like a car with a heightened alarm system that "goes off simply because you walked close to it." In the end, the brain reaches what Sigal describes as a "permissive" state, in which normal light becomes very bright, normal sounds very loud, "and you can smell a perfume two blocks away from Bloomingdale's." CGRP-binding antibodies help turn down the volume in the trigeminal nerve, by "mopping up" excess peptide or preventing it from binding to and activating cells, Dodick proposes.

But why are migraineurs more sensitive to CGRP—or produce too much of it—in the first place? Some researchers loop back to CSD, which certain animal studies suggest can trigger a surge of CGRP, Russo says. In that case, genetic predisposition to the abnormal brain activity could lead to many migraines.

A growing number of studies point to another important factor: stress. Even minor insults, such as missing a few hours' sleep, can often "push the migraine brain over the line into having an attack," Sigal says. And experiments in rats and cultured cells show that corticotropin-releasing hormone, which the body releases in response to stress, also increases neuronal production of CGRP, Russo says. Strikingly, many migraine medications also boost CGRP in animal models, possibly explaining why people who use drugs like triptans too frequently end up with more severe migraines, he says.

That the relatively large CGRP-blocking antibodies can prevent migraines in some people have convinced most in the field that it is indeed possible to stop the headache from outside the central nervous system, even though it is clearly a brain disorder, according to Moskowitz. "The evidence is favoring that [the drugs are] working somewhere on the trigeminal connections into the brain, not in the brain itself, unless there's some massive change" in the permeability of the blood-brain barrier during an attack, he says.

Some researchers, however, still argue that the CGRP-blocking antibodies must be getting past the blood-brain barrier into the brainstem—even in trace amounts—to be effective. Goadsby favors this view, and notes that some sections of the brainstem are not very well protected by the barrier.

Whatever the resolution to that debate, the discovery of CGRP's migraine connection underscores the value of carefully dissecting the neural pathways that lead to pain and searching for a linchpin molecule, Moskowitz says. If CGRP fulfills its promise as a blockbuster pain target, that success could signal to drug developers that effective treatments for other complex and seemingly intractable pain disorders, such as fibromyalgia, are also within reach, Moskowitz says. Eli Lilly is already testing its CGRP-antibody in people with cluster headaches, which occur in regular, cyclical patterns and can be even more painful than migraines.

As for Sundquist, she's well aware of the clinical trials for the various CGRP-related drugs, and she is hopeful. But the random assortment of failed remedies that fills her closet—antidepressants, nutritional supplements, a headband that transmits painful electric zaps to her scalp and "looks like something from *Star Trek*"—makes her wary as well. "I'm just waiting for more information, and praying that I will be healthy again." ■

Published by AAAS

INSIGHTS

Probing Earth's mantle dynamics *p. 122* ▸

Hydropower threats to iconic rivers *p. 128*

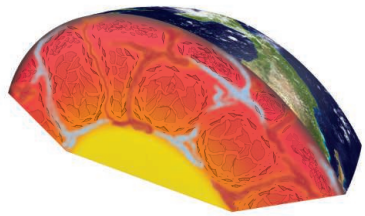

PERSPECTIVES

Ancient grasslands. Mosaics of forests and grasslands—as shown here for the southern Patanal, Brazil—are common in the tropics and subtropics. The grasslands have long been interpreted as secondary vegetation produced by deforestation, and many are targets for "reforestation" (*1*). However, they have a rich endemic ancient biota adapted to frequent fires.

ECOLOGY

Ancient grasslands at risk

Highly biodiverse tropical grasslands are at risk from forest-planting efforts

By **William J. Bond**[1,2]

Concerns over deforestation have led to attempts to identify suitable areas for reforestation around the world (*1*). The most ambitious effort to date is the World Resources Institute (WRI) Atlas of Forest and Landscape Restoration Opportunities (*1*). This map is linked to a global plan to reforest degraded lands to offset anthropogenic CO_2 emissions. The immediate target is the reforestation of 1.5 million km^2 by 2020 (*2*, *3*). Vast areas of open grassy vegetation have been identified as suitable for reforestation. But are all these grasslands secondary products of deforestations? Recent research shows that grasslands are often ancient and highly biodiverse, but it remains difficult to distinguish between primary and secondary grasslands on a large scale. Reforestation efforts thus risk converting ancient tropical grasslands to plantations.

Research on tropical grassy biomes has been remarkably neglected relative to forests (*4*, *5*). This neglect has been attributed to the widespread perception that they are human artifacts created and maintained by human-lit fires. Yet, there is evidence for a much more ancient origin of fire-maintained grassy vegetation in regions where the climate and soils can support closed forests (see the figure). Tropical grassy biomes (grasslands and savannas) include ecosystems with a rich plant and animal life entirely restricted to open habitats (*4*, *6*). They provide important ecosystem goods and services to the ~500 million people who live in them (*5*). Furthermore, the full consequences for the Earth-atmosphere system of converting grassy ecosystems to forests have not been evaluated (*7*). For example, changes in albedo can offset

PHOTO: © DANITA DELIMONT/ALAMY STOCK PHOTO

Published by AAAS

any gains in stored carbon as the reflective surface of grasslands, especially in the dry season, are converted to the dark absorptive surfaces of forests.

A key clue to the antiquity of grasslands is the presence of species unique (endemic) to open grassy habitats. The cerrado (savannas) of Brazil are ranked 12th on a list of global biodiversity hot spots with about 6000 plant species. Once considered poor in vertebrate species, cerrado is now proving to have a rich, endemic fauna of reptiles (*8*). The grassland biomes of southern Brazil and South Africa are also rich in plant species, with an estimated 3000 to 4000 in an area of 137,000 km^2 in southern Brazil and 3800 in 112,000 km^2 in South Africa (*4*, *9*). The Atlantic coastal plain of North America is also species-rich, with some 6000 plant species (nearly a third of the North American flora), of which 29% are endemic (*10*, *11*). Most of the endemic species occur in pine savannas and communities embedded within them. All these systems depend on frequent fires to maintain them and are replaced by closed forests where fires are suppressed.

The Atlantic coastal plain grasslands of North America have only recently been recognized as a significant biodiversity hot spot (*11*). Noss attributes this oversight to misconceptions and myths, such as the myth that fires can only be ignited by humans. Similar misconceptions are widespread throughout the tropics. In Madagascar, for example, unique for its remarkable endemic forest fauna and flora, the grasslands that cover most of the island were long thought to be produced by deforestation in the aftershock of human settlement a few thousand years ago (*12*). This narrative of deforestation as the source of grasslands was powerful enough to put off researchers from exploring the diversity of grasslands. Recent grass collections have revealed a remarkably rich grass flora, with some 40% of the 580 grass species endemic to the island. These levels of endemism are among the highest in the world for a grass flora (*12*). Despite clear evidence for the antiquity of Madagascar's grassland biota, it remains highly uncertain how much of the island's grasslands is a result of deforestation.

Tropical grassy ecosystems are highly flammable. They are most extensive in seasonal wet/dry climates, where high rainfall supports high productivity in the rainy season, whereas the long dry season produces highly flammable grass fuels. Humid tropical grasslands burn several times in a decade; some regularly burn twice in a year. The grassy biomes of Africa alone accounted for more than 70% of the world's burnt area from 1997 to 2009.

Plants living in these highly flammable environments survive by retreating underground, developing large underground storage organs (USOs) that resprout rapidly after a burn (*6*). Nongrassy herbs (forbs) with USOs commonly flower in the first growing season after a burn before they are smothered by grass growth. Among woody plants, thick bark, insulated buds, clonal spread, and juvenile forms with USOs are adaptations to frequent grass-fueled fires (*13*).

"Underground trees" are a peculiar growth form characteristic of frequently burnt savannas in South America and Africa (*14*). These plants have massive underground branches protected from surface fires (see the figure). The leaves are borne on short stems that resprout from the buried branches after fires. Underground trees have evolved multiple times from different lineages in South America and Africa in open grassy habitats with frequent fires and, often, poor soils (*13*, *15*).

Underground trees (geoxylic suffrutices) have close relatives that are true trees. Using a dated phylogeny, Maurin *et al.* (*15*) have shown that most underground trees in fire-maintained savannas in Africa originated between 6 and 2.5 million years ago, with peak divergence in the past 2 million years (*15*). These times of origin are remarkably similar to those obtained from phylogenetic studies of fire-adapted woody legumes in South American savannas (*13*). They are also consistent with fossil evidence for the spread of tropical grassy systems from the late Miocene and with charcoal records from marine cores that show a sharp increase in fire activity over the same period (*16*).

Thus, fire-dependent tropical grassy systems predate human deforestation by millions of years. Nevertheless, this is an intriguingly late origin from an Earth history perspective. The causes of this late spread of savannas are currently an area of intense research interest.

A distinctive feature of the flora of tropical grasslands is a marked intolerance of shade. Fire-suppression experiments have led to the elimination of long-lived forbs as a result of shading by an accumulation of dense undecomposed grass litter. Old-growth grassland plants, especially long-lived forbs with USOs, are eliminated

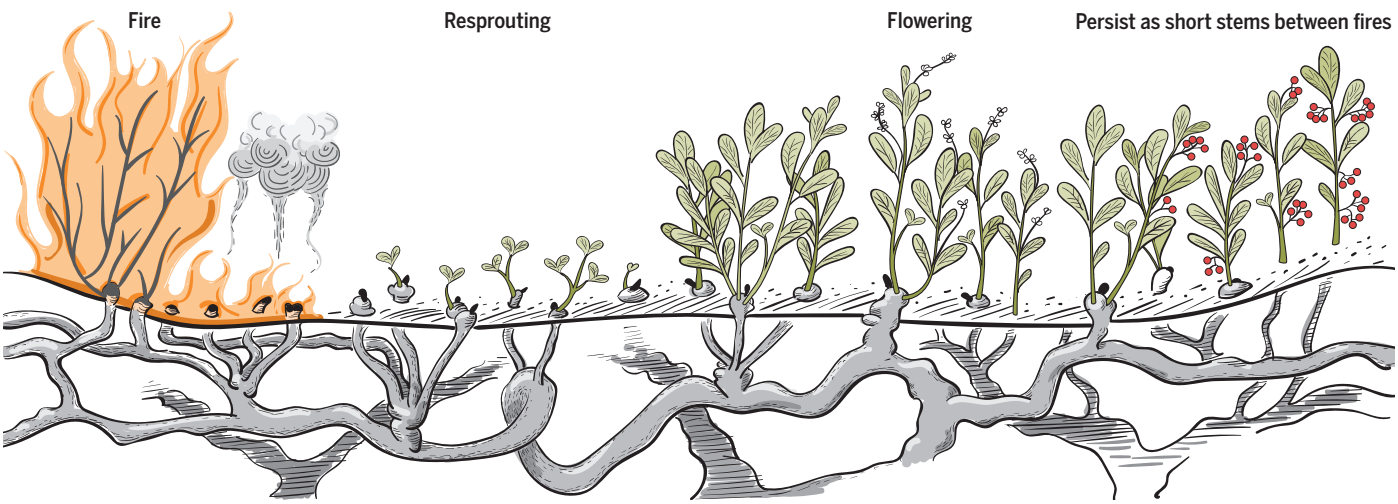

Underground trees. Many tropical grassland species have large underground storage organs that enable them to survive frequent grass-fueled fires. Some woody species with tall tree relatives form "underground trees," with massive belowground branches supporting short aboveground stems that resprout rapidly after a fire.

ILLUSTRATION: K. SUTLIFF/*SCIENCE*

[1]*South African Environmental Observation Network, National Research Foundation, Private Bag X7, Claremont, 7735, South Africa.* [2]*Department of Biological Sciences, University of Cape Town, Rondebosch 7701, South Africa.* *E-mail: william.bond@uct.ac.za*

Published by AAAS

by forest expansion or afforestation with pines and eucalypts. Secondary grasslands, formed after deforestation or removal of plantations, have completely different species compositions from primary grasslands (*4*, *6*). Forbs with USOs and underground trees are particularly vulnerable, with no recovery to old-growth conditions after decades of natural succession.

These studies are revealing striking differences in old-growth versus secondary grasslands. However, the scale of analysis does not yet permit large-scale identification of old-growth grasslands. It is not yet possible to map old-growth grasslands at the scale of the WRI Atlas of Forest and Landscape Restoration Opportunities (*1*–*3*). The Food and Agriculture Organization (FAO) uses tree cover and height to classify forest and ignores the herbaceous layer (*5*). Yet there are profound functional differences between open woodlands with a highly flammable grassy understorey and closed forests that lack fuel to burn. Ultimately, old-growth versus secondary grasslands will have to be classified by identifying characteristics of the herbaceous layer, such as grass composition, that are visible from satellites and that are also proxies for primary grasslands.

There are many fundamental unanswered questions about grassy biomes, their function, origins, and antiquity. The recent spate of papers on these fascinating systems suggests that this neglect is coming to an end. There has been considerable progress in identifying old-growth grasslands and their ecological requirements, and this bodes well for restoring forests and the services they provide while also maintaining ancient tropical grassy ecosystems. It would be a travesty if ancient grasslands are replaced by ill-conceived forest plantation projects because of misconceptions about the origins of tropical grassy systems. ■

REFERENCES

1. World Resources Institute maps; www.wri.org/resources/maps/.
2. L. Laestadius *et al.*, *Unasylva* **238**, 47 (2011).
3. J. W. Veldman *et al.*, *BioScience* **65**, 1011 (2015).
4. W. J. Bond, C. L. Parr, *Biol. Cons.* **143**, 2395 (2010).
5. C. L. Parr *et al.*, *TREE* **29**, 205 (2014).
6. J. W. Veldman *et al.*, *Front. Ecol. Env.* **13**, 154 (2015).
7. R. B. Jackson *et al.*, *Environ. Res. Lett.* **3**, 044006 (2008).
8. C. Nogueira *et al.*, *J. Biogeog.* **38**, 1907 (2011).
9. G. E. Overbeck *et al.*, *Persp. Plant Ecol. Evol. Syst.* **9**, 101 (2007).
10. R. F. Noss, *Forgotten Grasslands of the South: Natural History and Conservation* (Island Press, 2012).
11. R. F. Noss *et al.*, *Div. Distr.* **21**, 236 (2015).
12. M. S. Vorontsova, S. E. Rakotoarisoa, *Malagasy Nature* **8**, 14 (2014).
13. M. F. Simon *et al.*, *Proc. Natl. Acad. Sci.* **106**, 20359 (2009).
14. F. White, *Gardens Bull. Singapore* **24**, 57 (1976).
15. O. Maurin *et al.*, *New Phyt.* **204**, 201 (2014).
16. S. Scheiter *et al.*, *New Phyt.* **195**, 653 (2012).

10.1126/science.aad5132

GEOCHEMISTRY

Lower-mantle materials under pressure

Laboratory measurements provide a window into Earth's mantle dynamics

By **Jiuhua Chen**

Modern high-pressure experimental techniques have enabled us to achieve the pressure and temperature at the center of Earth (about 360 GPa and 6000 K) in laboratories. However, studies of rheological properties of minerals under controlled strain rate (creep experiments) have been limited to the pressure equivalent to that in Earth's transition zone, a depth only about one-tenth of Earth's radius. Determinations of rheological laws that govern the flows and viscosities of minerals in Earth's deep mantle have been far beyond our reach. In the absence of such critical data, the nature of mantle dynamics—such as whether the convection involves the entire lower mantle, yielding a chemically homogeneous deep mantle—remains controversial. Discovery of the breakdown of ringwoodite into the denser bridgmanite and magnesiowüstite phases at 24 GPa (*1*) removed the need for a major chemical discontinuity in Earth inferred from observations of a strong seismic reflector at 660 km depth. On page 144 of this issue, Girard *et al.* (*2*) report on the detailed rheological nature of this bridgmanite plus magnesiowüstite mineral aggregate, shedding more light on the mantle convection. The integration of brilliant synchrotron radiations and rotating apposed anvils enables creep experiments for large strain at pressures equivalent to that in Earth's lower mantle.

> ***"All the evidence leads us to a hybrid convection model—a mixture of layered and whole-mantle circulations."***

Center for High Pressure Science and Technology Advanced Research, Jilin University, Changchun 130015, China, and Center for the Study of Matter at Extreme Conditions, Department of Mechanical and Materials Engineering, Florida International University, Miami, FL 33199, USA. E-mail: chenj@fiu.edu

Nearly 90% of the lower mantle is occupied by the minerals bridgmanite and magnesiowüstite. Bridgmanite is believed to be the rheologically strongest phase at high pressure and high temperature among all dominant minerals in the shallower mantle (*3*), giving rise to a high viscosity of the lower mantle relative to the upper mantle and the transition zone. In their creep experiment on these two minerals directly converted from natural olivine, Girard *et al.* not only recognized that bridgmanite is substantially stronger than magnesiowüstite and that a large fraction of the strain is accommodated by magnesiowüstite, but also observed a tendency of strain weakening of bridgmanite when large strain (>40%) is applied. These observations may indicate shear localizations in the lower mantle—a result that would have an impact on the mantle dynamics.

If we assume that large enough strains occurring in deep mantle convection eventually produce interlinking of the weak magnesiowüstite phase in the microstructure of the mineral aggregate due to the shear localization, then a transition of its rheological behavior from a load-bearing framework (LBF) phase to an interconnected weak layers (IWL) phase might be expected on the basis of the semitheoretical model described by Handy (*4*). Taking 2×10^{21} Pa·s and 1×10^{19} Pa·s as the viscosities of bridgmanite and magnesiowüstite, respectively, at the top of the lower mantle (*5*), the viscosities of the mineral aggregate for the IWL and LBF regions would be 4.5×10^{19} Pa·s and 1.5×10^{21} Pa·s, respectively (assuming a bridgmanite/magnesiowüstite volume ratio of 7:2). This contrast in viscosity, as a result of shear localization, provides us with key information about the lower mantle such as long-lived geochemical reservoirs and the absence of seismic anisotropy in the majority of the lower mantle. The result may actually have much broader implications for our understanding of the lower mantle.

High viscosity of the lower mantle is considered to be the major resistance slowing down the sinking rate of a subducting slab (*6*). This is true at the early stage of convec-

Published by AAAS

tion, when the lower mantle is in the LBF state. Once the downwelling process triggers shear localization around the sinking slab, however, the lower viscosity of the IWL zone formed along the slab will promote the subduction to a much faster rate. The subduction history of the Tethyan region (*7*) reveals free sinking rates of about 3 cm/year in the upper mantle and 2 cm/year in the lower mantle, corresponding to only a factor of 5 difference in viscosity. This is remarkably consistent with the estimated weakening of the shear localization if the bulk viscosities of the upper and lower mantles differ by two orders of magnitude.

Whether mantle convection occurs through layered circulations (favored by geochemical observations) or through a whole-mantle circulation (preferred by geodynamic modeling) is unclear. Viscosity profiling derived from oceanic geoid and seismic tomography indicates a low-viscosity zone at the top of the lower mantle (*8*). A large amount of strain caused by lateral flow at the top of the lower mantle may induce such a low-viscosity layer. Joint inversion of long-wavelength mantle convection and postglacial rebound data (*9*) reveals a viscosity contrast of 1.5 orders of magnitude between the low-viscosity layer and the mantle beneath, matching that expected from the shear localization. Although stratified convections are acceptable to geodynamic modeling, the origin of the low-viscosity layer on the top of the lower mantle is unclear (*10*). The rheological property of the lower-mantle mineral assemblage lays an important foundation in terms of mineral physics for such layered convection within the lower mantle. In addition, a three-dimensional radially anisotropic model of shear velocity (*11*) indicates that the lower mantle is more anisotropic at the top and bottom, signifying flow-induced shape or lattice-preferred orientation in these regions. Nonetheless, a purely layered mantle convection model is insufficient for the heat removal from Earth's interior. High-resolution seismic imaging indicates that some subduction slabs deflect at the base of the transition zone and some reach the bottom of the lower mantle. All the evidence leads us to a hybrid convection model—a mixture of layered and whole-mantle circulations (see the figure).

The work by Girard *et al.* is a breakthrough in high-pressure creep experiment technique. The result on the rheological property of bridgmanite and magnesiowüstite aggregate offers critical experimental data of mineral physics helping us to illustrate many observations and models in geodynamics, geochemistry, and geophysics, although the consequential promoted subduction and reduced viscosity in the IWL zone along the slabs do not seem to support the cessation of earthquakes in the lower mantle. Some other facts, such as temperature sensitivity of strength required for runaway instability in the mantle-dominant minerals (*12*), may have to be considered to explain this deep seismicity phenomenon. ■

REFERENCES

1. E. Knittle, R. Jeanloz, *Science* **235**, 668 (1987).
2. J. Girard, G. Amulele, R. Farla, A. Mohiuddin, S.-i. Karato, *Science* **351**, 144 (2016).
3. J. Chen, D. J. Weidner, M. T. Vaughan, *Nature* **419**, 824 (2002).
4. M. R. Handy, *J. Struct. Geol.* **16**, 287 (1994).
5. D. Yamazaki, S.-i. Karato, *Am. Mineral.* **86**, 385 (2001).
6. G. Stadler *et al.*, *Science* **329**, 1033 (2010).
7. E. Hafkenscheid, M. J. R. Wortel, W. Spakman, *J. Geophys. Res.* **111**, B08401 (2006).
8. M. Kido, D. A. Yuen, O. Čadek, T. Nakakuki, *Phys. Earth Planet. Inter.* **107**, 307 (1998).
9. A. M. Forte, J. X. Mitrovica, *Geophys. Res. Lett.* **23**, 1147 (1996).
10. L. Wen, D. L. Anderson, *Earth Planet. Sci. Lett.* **146**, 367 (1997).
11. M. Panning, B. Romanowicz, *Geophys. J. Int.* **167**, 361 (2006).
12. J. Chen, *J. Phys. Chem. Solids* **71**, 1032 (2010).

10.1126/science.aad7813

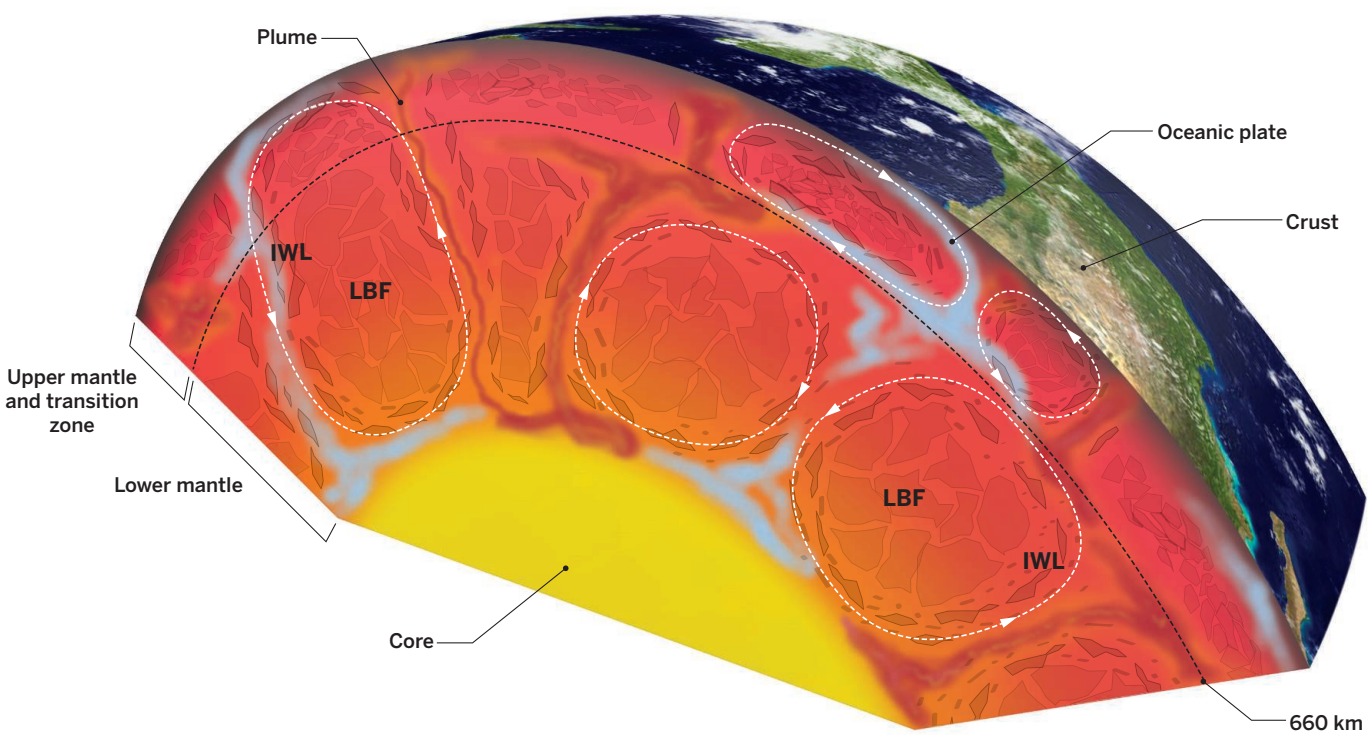

ILLUSTRATION: C. BICKEL/*SCIENCE*

Hybrid mantle convection model. Subducting slabs bring oceanic plates (blue) into the deep mantle. The slabs deflected at the 660-km discontinuity form layered convection within upper mantle and transition zone. The slabs penetrating into the lower mantle reaching the core-mantle boundary form whole-mantle convection. Plumes (red) rise from the core-mantle boundary, bringing materials that are enriched in incompatible elements relative to the expected mantle average back to the 660-km discontinuity. Some of them penetrate through the discontinuity, whereas others are deflected and may produce secondary upper-mantle plumes. Shear localization induces interconnected weak layers (IWL) along the slabs or plumes as well as the top and bottom of the lower mantle, yielding a less efficient mixing for the central LBF (load-bearing framework) part of the lower mantle (the reason for long-lived geochemical reservoirs).

Published by AAAS

THERMOELECTRICS

Finding merit in dividing neighbors

The favorable thermoelectric properties of SnSe are related to its crystal symmetry

By **Kamran Behnia**

A large fraction of energy consumed by humankind is wasted as heat. Some of this energy can be recycled with thermoelectric devices that convert a thermal gradient into electricity. However, their wide adoption will require development of materials with high thermoelectric figure of merit (*ZT*) that lack rare or harmful elements. On page 141 of this issue, Zhao *et al.* (*1*) report on p-doped tin selenide (SnSe), which helps meet these goals.

Favorable increases in *ZT* can be achieved by modifying a material (usually a semiconductor) to increase its Seebeck coefficient (a measure of the thermopower, or change in voltage induced by temperature) or electric conductivity or lower its thermal conductivity. However, this combination can be difficult to achieve—for example, good electrical conductors are often good heat conductors—and only a handful of materials meet all three requirements. Unfortunately, two of the most prominent, Bi_2Te_3 (the best near room temperature) and PbTe (the best near 800 K), contain rare tellurium or toxic lead.

Last year, this same research group identified SnSe as a thermoelectric material with a large *ZT* near 900 K, thanks to its remarkably low thermal conductivity (*2*). This latest study reports on p-doping of the SnSe single crystals (junctions require both n- and p-doped materials) and an increase in *ZT*, which, along one of the crystal axes, exceeds unity between 400 and 800 K. Thus, SnSe competes with both Bi_2T_3 and PbTe over a wide temperature window.

The newcomer to this arena is a member of a family of binary salts that contain elements of column IV and column VI of the periodic table. The IV-VI family and column V elements crystallize in one of the three varieties derived from the cubic rock-salt structure (see the figure) (*3*). Like black phosphorus, SnSe adopts the orthorhombic crystal structure, which imparts its anisotropic electrical conductivity.

LPEM-ESPCI, 10 Rue Vauquelin 75005 Paris, France.
E-mail: kamran.behnia@espci.fr

The complexity emerging in the presence of only one or two types of atoms has intrigued condensed-matter physicists for decades (*3*–*5*). Why should atoms undergoing crystallization opt for anything less symmetric than cubic? The rock-salt structure can be seen as a network of interpenetrating octahedra with an atom at the center of each octahedron and its six nearest neighbors at the vertices. What drives lower symmetry is the problem of placing 10 electrons along three perpendicular axes with six equivalent neighbors. Rhombohedral and orthorhombic distortions divide the six immediate neighbors in two distinct sets of first neighbors and second neighbors .

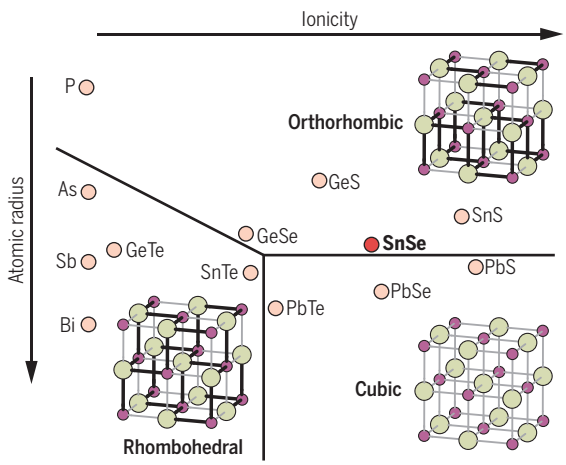

Packing matters. The IV-VI salts like SnSe and column-V elements like black phosphorus (P) crystallize in three different structures, according to their size and ionicity. Both distortions of the symmetric cubic rock-salt structure favor three out of the six nearest neighbors. Solid black lines represent bonds strengthened by the shift of neighbors toward each other. In the orthorhombic structure of SnSe, strong bonds are absent across layers (compare bonds between upper and middle layers of the inset figures), which generates substantial anisotropy (*3*, *4*).

Heavier and ionic salts in the bottom-right corner of the figure, like PbTe, avoid the distortion. Cubic symmetry is preserved in the presence of strong spin-orbit interaction and large ionicity because the six p and the four s orbitals become energetically distinct. With only p electrons to consider, it is much easier to keep six neighbors along three perpendicular axes. Moreover, ionicity, by distinguishing between partner atoms, impedes Peierels dimerization in each of the three perpendicular chains (*5*). In short, covalency favors rhombohedral distortion, whereas s-p hybridization leads to orthorhombicity and a layered anisotropic structure.

There are at least two links between this structural competition and the remarkable *ZT* in SnSe and PbTe. The first concerns the unusually low lattice thermal conductivity. Its magnitude at 800 K in both PbTe and SnSe implies that the phonon mean-free-path becomes as short as the interatomic distance (*6*), the result of strong phonon-phonon scattering caused by anharmonicity in proximity of the structural instability (*7*).

The second link is specific to SnSe in which *ZT* is large along one crystalline axis. Charge flows easily along the *b* axis, yet the Seebeck coefficient is as large as along the other axes. The anisotropy of conductivity (as in the case of black phosphorus) results from the layered structure of the orthorhombic crystal. However, the Seebeck coefficient remains almost isotropic because in a simple anisotropic Fermi liquid, the Fermi radius and the thermal fuzziness of the Fermi surface share the same anisotropy, and the Seebeck coefficient is set by the ratio of these two (*6*). Indeed, in numerous layered conductors, the Seebeck coefficient remains isotropic.

The present work of Zhao *et al.* will certainly inspire many other studies. Are other anisotropic conductors of the family as interesting? How different are the Fermi surface topologies among the family members? According to band calculations by Zhao *et al.*, at a carrier concentration of 4×10^{19} cm^{-3}, the Fermi surface of p-doped SnSe consists of several anisotropic pockets at low-symmetry points of the Brillouin zone. This structure remains to be checked by experimental study of quantum oscillations, as in the better-documented case of PbTe (*8*). ■

REFERENCES

1. L.-D. Zhao *et al.*, *Science* **351**, 141 (2016).
2. L.-D. Zhao *et al.*, *Nature* **508**, 373 (2014).
3. P. Littlewood, *J. Phys. C Solid State Phys.* **13**, 4855 (1980).
4. J. K. Burdett, T. J. McLarnan, *J. Chem. Phys.* **75**, 5764 (1981).
5. R. Peierls, *More Surprises in Theoretical Physics* (Princeton Univ. Press, Princeton, PA, 1991).
6. K. Behnia, *Fundamentals of Thermoelectricity* (Oxford Univ. Press, Oxford, UK, 2015).
7. J. An, A. Subedi D. J. Singh, *Solid State Commun.* **148**, 417 (2008).
8. J. D. Jensen, B. Houston, J. R. Burke, *Phys. Rev. B* **18**, 5567 (1978).

10.1126/science.aad8688

ILLUSTRATION: P. HUEY/*SCIENCE*

Published by AAAS

CELL BIOLOGY

Disrupted nuclear import-export in neurodegeneration

Toxicity arises from amyloid-like protein accumulation in the cytoplasm, not the nucleus

By **Sandrine Da Cruz**[1] *and* **Don W. Cleveland**[1,2]

The major human neurodegenerative diseases, including Alzheimer's, amyotrophic lateral sclerosis, Parkinson's, and Huntington's diseases, are associated with accumulation and aggregation of misfolded proteins. In most cases, the majority of aberrantly aggregated proteins are found in the cell cytoplasm. However, in disorders caused by the expansion of a trinucleotide repeat, including Huntington's disease and spinocerebellar ataxia, the corresponding aggregates of proteins containing the encoded polyglutamine expansions are predominantly nuclear. Whether differences in intracellular location matter for the toxicity generated by such proteins has not been determined. On page 173 of this issue, Woerner *et al.* (*1*) report that the location does indeed matter, with toxicity arising from the cytoplasmic accumulation of a pair of artificial proteins designed to mimic the properties of amyloid aggregates. Surprisingly, forcing the same artificial proteins into the nucleus substantially reduces their toxicity.

Woerner *et al.* established a cell culture system in which artificial β-sheet proteins, previously shown to form fibrillar amyloid aggregates (*2*), can be targeted to accumulate in the cytoplasm or nucleus by inclusion of a nuclear export sequence (NES) or nuclear localization sequence (NLS), respectively (see the figure). With this approach, they demonstrate that only the cytoplasmically targeted proteins, but not the nuclear counterparts, enhance cell death. The authors propose that the reduced toxicity of the nuclear proteins and their aggregates, despite accumulating in amounts comparable to those in the cytoplasm, may be the result of the chaperone-like activity of a highly abundant nucleolar protein called nucleophosmin-1 (NPM1), which they show interacts with nuclear but not cytoplasmic aggregates.

[1]*Ludwig Institute for Cancer Research, University of California at San Diego, La Jolla, CA 92093, USA.* [2]*Department of Cellular and Molecular Medicine, University of California at San Diego, La Jolla, CA 92093, USA. E-mail: dcleveland@ucsd.edu*

These discoveries add to other emerging evidence that compartment-enriched chaperones—which form complexes with misfolded proteins in the cytosol (*3*) or nucleus (*4*)—may play central roles in ameliorating damage, possibly by generating compartment-specific conformers of aggregated proteins with different propensities for cellular toxicity. Woerner *et al.* report that nuclear β-sheet–containing proteins produce aggregates that have reduced solubility and weaker affinity for an amyloid-specific dye compared to their cytosolic counterparts, underscoring possible differences in aggregate conformation between the two subcellular compartments. Whether any of the nuclearly enriched chaperones (*4*) contribute to these possible conformational changes or whether they shield the surfaces of the nuclear amyloid-like protein aggregates (thereby making them more innocuous) has not been established.

So why is misfolded protein accumulation and aggregation in the cytoplasm toxic? Woerner *et al.* used a proteomic approach to implicate the THOC2 subunit of a messenger RNA (mRNA) export complex that facilitates mRNA delivery to the cytoplasm. In primary neurons, THOC2 is mislocalized to the cytoplasm in cells with cytoplasmic β-sheet aggregates, although its interaction with those is unlikely to be direct as the aggregates are distinct from cytoplasmic redistributed THOC2. Components of the nuclear pore complex and nuclear import receptors are misaccumulated in the cytoplasm, strongly implicating diminished nuclear import and export in the affected cells. Not yet determined is whether nuclear proteins or nuclear pore components, and if so which ones, are trapped by the cytoplasmic amyloid aggregates, thus preventing their proper nuclear localization and function.

Using similar assays, Woerner *et al.* show that expression of disease-linked

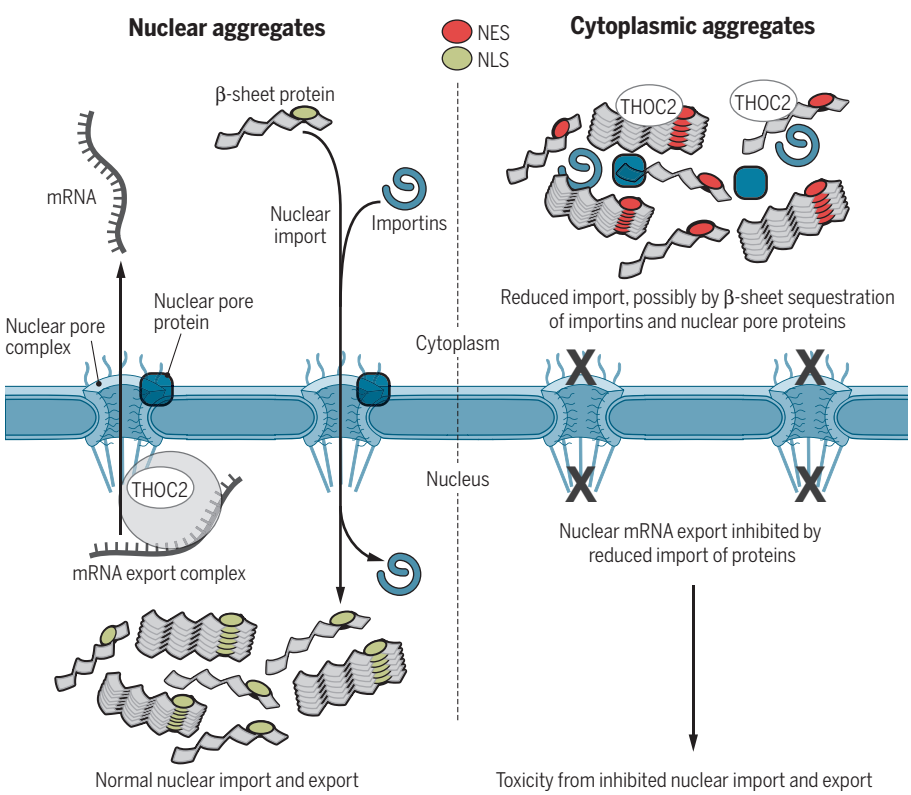

Nucleocytoplasmic transport. An artificial β-sheet protein tagged with a NLS accumulates in the nucleus and aggregates there, but is nontoxic; transport through the nuclear pore is unaffected. The same β-sheet protein tagged with a NES signal aggregates in the cytoplasm and is toxic; a component of the nuclear export machinery (THOC2) is mislocalized and transport through the nuclear pore is disrupted.

ILLUSTRATION: K. SUTLIFF/*SCIENCE*

Published by AAAS

fragments of polyglutamine-containing huntingtin protein or amyotrophic lateral sclerosis–causing mutants in the transactivation element (TAR) DNA binding protein–43 (known as TDP-43) also inhibit mRNA export when expressed in cultured cells, suggesting that errors in nucleocytoplasmic transport may be common to multiple neurological conditions. That said, expression of mutant huntingtin in primary cultures of cortical neurons led preferentially to nuclear aggregation, which did not impair nuclear mRNA export. This is consistent with evidence that intranuclear inclusions of polyglutamine-containing huntingtin fragments are not toxic per se (*5*). In the widely used R6/2 Huntington's disease mouse model in which aggregates of a mutant huntingtin fragment accumulate intranuclearly in most neurons, Woerner *et al.* report impaired RNA export in the small proportion of neurons that accumulate aggregated huntingtin in the cytoplasm. These findings, and the consensus from analyses of human samples and most mouse models, raise the question of whether the much rarer cytoplasmic aggregates are primary contributors to toxicity in Huntington's disease, rather than the more abundant intranuclear ones.

The finding by Woerner *et al.* that cytoplasmic aggregates diminish nuclear import and/or export adds to the growing recognition that diminished nucleocytoplasmic transport may be a common component of multiple human neurodegenerative diseases, including Huntington's (*6*), Alzheimer's, amyotrophic lateral sclerosis, frontotemporal dementia, and Parkinson's, where components of the import and/or export machinery are mislocalized and found to interact with disease-associated mutant proteins. Coupled with nuclear "leakiness" that dramatically accelerates during aging (*7*), altered cytoplasmic localization offers one explanation for the age-dependence of these neurodegenerative disorders.

How nuclear import-export is inhibited in the various diseases is still unclear. Recently, expression of a hexanucleotide expansion within the *C9orf72* gene, which is the most frequently inherited cause of both amyotrophic lateral sclerosis and frontotemporal dementia, has been reported to disrupt nuclear import and/or export (*8*–*10*), but how this defect arises is not firmly established. One study identified a direct interaction between the hexanucleotide repeat–containing RNAs and Ran GTPase-activating protein (Ran-GAP), a factor required for nuclear import (*10*). Other studies implicated import inhibition by repeat associated non-AUG (referred to as RAN)–dependent translation-produced polydipeptides encoded by expansion-containing RNAs (*8*, *9*).

To this controversy, Woerner *et al.* demonstrate that nuclear and/or cytoplasmic transport defects can be attributed to a proteotoxicity caused by cytoplasmic accumulation of β-sheet proteins and their aggregates. Additionally, the recent finding that RAN translation is not restricted to diseases with noncoding region repeat expansions, but also occurs across repeats located in an open reading frame such as in Huntington's disease (*11*), provides a new perspective on potential mechanisms underlying toxicity in this disorder. A critical next step will be to determine whether RAN-encoded peptides can directly provoke nucleocytoplasmic transport defects previously reported in Huntington's disease (*6*), and whether there is compartment-selective toxicity, as now demonstrated for the β-sheet proteins.

To the unresolved, key question of how cytoplasmic accumulation of aberrant proteins and/or their aggregation provokes diminished nuclear import and/or export, it must be noted that the focus in Alzheimer's disease (*12*), Huntington's disease (*5*, *13*), and most recently in inherited amyotrophic lateral sclerosis (*14*), has reversed. An initial focus was on the large aggregates seen with conventional pathology. Most investigators have refocused on oligomeric assemblies of the misfolded protein as the most important contributors to neuronal dysfunction that leads to the characteristic disease symptoms (*15*). Seen from this prospective, location definitely matters, but the β-sheet protein aggregates (and other aggregates in the various disorders) may actually be protective, with toxicity arising from oligomeric species that are hard to detect. ■

REFERENCES

1. A. C. Woerner *et al.*, *Science* **351**, 173 (2016).
2. H. Olzscha *et al.*, *Cell* **144**, 67 (2011).
3. D. Kaganovich, R. Kopito, J. Frydman, *Nature* **454**, 1088 (2008).
4. S. B. Miller *et al.*, *EMBO J.* **34**, 778 (2015).
5. F. Saudou, S. Finkbeiner, D. Devys, M. E. Greenberg, *Cell* **95**, 55 (1998).
6. J. Cornett *et al.*, *Nat. Genet.* **37**, 198 (2005).
7. M. A. D'Angelo, M. Raices, S. H. Panowski, M. W. Hetzer, *Cell* **136**, 284 (2009).
8. B. D. Freibaum *et al.*, *Nature* **525**, 129 (2015).
9. A. Jovicic *et al.*, *Nat. Neurosci.* **18**, 1226 (2015).
10. K. Zhang *et al.*, *Nature* **525**, 56 (2015).
11. M. Banez-Coronel *et al.*, *Neuron* **88**, 667 (2015).
12. E. Cohen, J. Bieschke, R. M. Perciavalle, J. W. Kelly, A. Dillin, *Science* **313**, 1604 (2006).
13. M. Arrasate, S. Mitra, E. S. Schweitzer, M. R. Segal, S. Finkbeiner, *Nature* **431**, 805 (2004).
14. P. A. Parone *et al.*, *J. Neurosci.* **33**, 4657 (2013).
15. S. Treusch, D. M. Cyr, S. Lindquist, *Cell Cycle* **8**, 1668 (2009).

10.1126/science.aad9872

STEM CELLS

Potency finds its niches

Adult bone marrow employs a surprisingly simple hematopoietic hierarchy

By **Nina Cabezas-Wallscheid**[1,2] *and* **Andreas Trumpp**[1,2]

Hematopoietic stem cells (HSCs) located atop the hematopoietic hierarchy are responsible for the lifelong production of all mature blood cells. These partly dormant, long-term self-renewing, multipotent HSCs in the bone marrow generate multipotent progenitors (MPPs) with reduced self-renewal activity before lineage determination and differentiation are initiated (*1*, *2*). For decades, it was thought that MPPs lose their multipotent capacity in a stepwise fashion, generating first a series of oligopotent and from there unipotent progenitors to finally make all hematopoietic cell types. The presence of oligopotent intermediates such as common lymphoid progenitors (CLPs) and common myeloid progenitors (CMPs) is crucial to this model because they define the path from multipotent to unipotent cells. A study by Notta *et al.* on page 139 of this issue (*3*) and another study by Paul *et al.* (*4*) provide strong evidence for the nonexistence of CMPs in human and mouse bone marrow. And on page 176 of this issue, Khan *et al.* (*5*) report a niche population in the fetal liver that maintains proliferating HSCs.

> ***"...fetal liver pericytes... promote FL-HSC cycling without differentiation..."***

In the standard textbook model, all myeloid cells (erythroid cells, megakaryocytes, granulocytes, and monocytes) are derived from oligopotent CMPs. This concept is based on the prospective isolation of CMPs by flow cytometry and their potential to generate all myeloid cell types in vitro and

[1]*Heidelberg Institute for Stem Cell Technology and Experimental Medicine (HI-STEM gGmbH), 69120 Heidelberg, Germany.* [2]*Division of Stem Cells and Cancer, Deutsches Krebsforschungszentrum (DKFZ), 69120 Heidelberg, Germany. E-mail: a.trumpp@dkfz-heidelberg.de*

Published by AAAS

in vivo (*6*). However, because these analyses were performed at the population level, it remained possible that CMPs may contain several unipotent progenitors rather than one oligopotent population.

Notta *et al.* identified 11 distinct cell populations in human fetal liver, cord blood, and adult bone marrow by fluorescence-activated cell sorting using conventional and novel markers (cMPL/BAH1 and CD71). This analysis revealed substantial heterogeneity in MPPs, CMPs, and megakaryocyte-erythroid progenitors (MEPs). The authors then used an improved functional single-cell culture assay to address the potential of each population to give rise to granulocytes, monocytes, megakaryocytes, and erythroid cells. Evaluation of nearly 3000 single cells suggests that unipotent progenitors, rather than oligopotent progenitors such as CMPs, dominate the blood hierarchy during bone marrow hematopoiesis. By assessing the reconstitution potential of the new cell populations in mice, Notta *et al.* found that megakaryocytes were derived directly from HSCs or MPPs, thereby obviating a lineage route via oligopotent CMP and MEP intermediates. This agrees with mouse data demonstrating the presence of stem cell–like megakaryocyte progenitors within the HSC compartment, which rapidly generate new platelets in response to stress (*7*, *8*).

Paul *et al.* (*4*) used single-cell transcriptomic analysis of more than 2700 mouse myeloid progenitors. They clustered each cell according to its expression of 3461 genes, revealing 19 progenitor subpopulations displaying a homogeneous expression signature. Using known lineage-specific gene networks, the authors found that each of the identified myeloid progenitor subpopulations was transcriptionally primed toward one of at least seven myeloid fates. For example, isolation of classically defined MEPs led to a homogeneous erythrocyte progenitor spectrum with no significant megakaryocyte expression signature. This agrees with the idea that these are instead derived from HSCs or MPPs (*3*). Single-cell transcriptome analysis failed to detect cells such as CMPs that express multiple lineage-specific genes or transcription factors that promote different fates (*3*, *4*), in line with recent studies (*9, 10*).

The findings of Notta *et al.* and Paul *et al.* suggest that either CMPs represent a highly transient cell state, or that such oligopotent cells do not exist, at least in mouse or human bone marrow. Instead, Notta *et al.* suggest a simpler two-tier model for the human bone marrow: a top tier containing multipotent cells such as HSCs or MPPs, and a bottom tier composed of committed unipotent progenitors. However, the progenitors identified during homeostasis appear to give rise to only one lineage on the basis of their expression signature, whereas transplanted megakaryocyte-erythroid progenitors reconstituted megakaryocytes and erythroid cells in mice (*4*). Thus, the potential of stem cells or their progenitors may be much broader in a stressed environment compared to what they actually do in the unperturbed system.

Whether an adult HSC remains dormant, self-renews, or differentiates toward a specific lineage is regulated in conjunction with its microenvironment (niche). Several distinct niches exist in the adult bone marrow, including cell types such as arteriolar pericytes [expressing Nestin and neural/glial antigen 2 (NG2)], leptin receptor–expressing pericytes, and megakaryocytes (*11, 12*). During hematopoiesis, HSCs in the fetal liver (FL-HSCs) are highly proliferative, and in contrast to the ones in the bone marrow, lineage differentiation arises from them via oligopotent progenitors (*4*). However, the niche cells that promote FL-HSC expansion during embryonic and fetal growth were unknown.

Khan *et al.* report that murine portal vessels in the fetal liver also contain Nestin- and NG2-expressing pericytes (see the figure). These cells sustain the highly proliferative FL-HSCs (*5*). The authors found that FL-HSCs are located in close proximity to the pericytes and that these niche cells, rather than other fetal liver components, are sufficient to maintain FL-HSCs in vitro. Khan *et al.* also show that deletion of NG2-expressing cells (98% of which are Nestin-expressing pericytes) in mice reduces the numbers and proliferative status of FL-HSCs.

Although Khan *et al.* demonstrate the importance of Nestin-expressing pericytes for maintaining proliferative FL-HSCs, similar cells located in the bone marrow maintain HSC quiescence (*11*). To uncover this difference, Khan *et al.* performed comparative transcriptome analysis, revealing no differential expression of stem cell–maintaining signaling molecules. Instead, there was enrichment for cell cycle processes and vessel development in fetal liver pericytes, which suggests that niche and FL-HSC expansion are linked.

Why do FL-HSCs leave this environment in the liver around the moment of birth? Khan *et al.* show in mice that ligation of the umbilical inlet at birth causes drastic hemodynamic changes in portal vessel blood flow, leading to loss of Nestin-expressing pericytes and consequent disruption of the portal vessel stem cell niche. Consequently, hematopoiesis is driven from the liver into adult bone marrow niches, which subsequently promote a dormant HSC state in the adult organism (*1*). The potential of fetal liver pericytes to promote FL-HSC cycling without differentiation may be used to develop complex niches in the culture dish for clinical applications, such as the expansion of HSCs derived from cord blood. ■

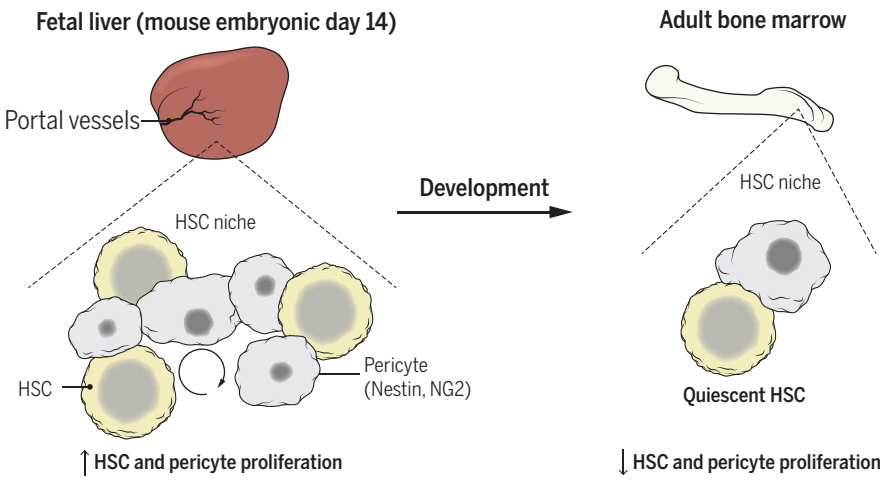

From one niche to another. HSCs and niche pericytes jointly expand in the fetal liver. At birth, the fetal liver niche collapses. HSCs then move to the bone marrow, where niche pericytes and HSCs become quiescent.

ILLUSTRATION: P. HUEY/*SCIENCE*

REFERENCES

1. A. Wilson *et al.*, *Cell* **135**, 1118 (2008).
2. N. Cabezas-Wallscheid *et al.*, *Cell Stem Cell* **15**, 507 (2014).
3. F. Notta *et al.*, *Science* **351**, aab2116 (2016)
4. F. Paul *et al.*, *Cell* **163**, 1663 (2015).
5. J. A. Khan *et al.*, *Science* **351**, 176 (2016).
6. M. Kondo *et al.*, *Annu. Rev. Immunol.* **21**, 759 (2003).
7. R. Yamamoto *et al.*, *Cell* **154**, 1112 (2013).
8. S. Haas *et al.*, *Cell Stem Cell* **17**, 422 (2015).
9. G. Guo *et al.*, *Cell Stem Cell* **13**, 492 (2013).
10. C. J. Pronk *et al.*, *Cell Stem Cell* **1**, 428 (2007).
11. A. Mendelson, P. S. Frenette, *Nat. Med.* **20**, 833 (2014).
12. S. J. Morrison, D. T. Scadden, *Nature* **505**, 327 (2014).

10.1126/science.aae0325

Published by AAAS

DEVELOPMENT AND ENVIRONMENT

Balancing hydropower and biodiversity in the Amazon, Congo, and Mekong

Basin-scale planning is needed to minimize impacts in mega-diverse rivers

By **K. O. Winemiller,* P. B. McIntyre, L. Castello, E. Fluet-Chouinard, T. Giarrizzo, S. Nam, I. G. Baird, W. Darwall, N. K. Lujan, I. Harrison, M. L. J. Stiassny, R. A. M. Silvano, D. B. Fitzgerald, F. M. Pelicice, A. A. Agostinho, L. C. Gomes, J. S. Albert, E. Baran, M. Petrere Jr., C. Zarfl, M. Mulligan, J. P. Sullivan, C. C. Arantes, L. M. Sousa, A. A. Koning, D. J. Hoeinghaus, M. Sabaj, J. G. Lundberg, J. Armbruster, M. L. Thieme, P. Petry, J. Zuanon, G. Torrente Vilara, J. Snoeks, C. Ou, W. Rainboth, C. S. Pavanelli, A. Akama, A. van Soesbergen, L. Sáenz**

The world's most biodiverse river basins—the Amazon, Congo, and Mekong—are experiencing an unprecedented boom in construction of hydropower dams. These projects address important energy needs, but advocates often overestimate economic benefits and underestimate far-reaching effects on biodiversity and critically important fisheries. Powerful new analytical tools and high-resolution environmental data can clarify trade-offs between engineering and environmental goals and can enable governments and funding institutions to compare alternative sites for dam building. Current site-specific assessment protocols largely ignore cumulative impacts on hydrology and ecosystem services as ever more dams are constructed within a watershed (*1*). To achieve true sustainability, assessments of new projects must go beyond local impacts by accounting for synergies with existing dams, as well as land cover changes and likely climatic shifts (*2*, *3*). We call for more sophisticated and holistic hydropower planning, including validation of technologies intended to mitigate environmental impacts. Should anything less be required when tampering with the world's great river ecosystems?

POLICY

ONE-THIRD OF FRESHWATER FISH AT RISK. The Amazon, Congo, and Mekong basins hold roughly one-third of the world's freshwater fish species, most of which are not found elsewhere. Each of these rivers has experienced limited hydropower development to date, largely because their vast catchments had limited infrastructure and low energy demand. Most existing dams are relatively small and located in upland tributaries, but more than 450 additional dams are planned for these three rivers alone (see the chart), with many already under construction (*4*). Dams are usually built where rapids and waterfalls boost hydropower potential. Unfortunately, these high-gradient reaches are home to many unique fishes adapted for life in fast water (fig. S1).

Although available data on geographic distributions of tropical fishes and other aquatic taxa are incomplete, recent research within these great river basins makes it clear that dam site selection matters greatly for conserving biodiversity (*5*) (see the chart). Given recent escalation of hydropower development in the tropics (*4*), planning is needed at the basin scale to minimize biodiversity loss, as well as other environmental, social, and economic effects (*3*, *6*–*9*). Large dams invariably reduce fish diversity but also block movements that connect populations and enable migratory species to complete their life cycles. This may be particularly devastating to tropical river fisheries, where many high-value species migrate hundreds of kilometers in response to seasonal flood pulses (*8*–*12*). Model simulations of proposed dams in the lower Mekong Basin predict major reductions of migratory stocks (*8*), as has been widely observed globally (*11*). Fish passages constructed to mitigate dam impacts on migratory fishes in the neotropics have proven unsuccessful (*10*) and even harmful (*12*). Yet, dam proposals continue to tout fish passages as the principal means for minimizing impacts on migratory stocks.

> *"[D]am site selection matters greatly for conserving biodiversity."*

Large dams delay and attenuate seasonal flood pulses, reducing fish access to floodplain habitats that are essential nursery areas and feeding grounds. Physical alterations bring about an ecological regime shift, whereby a dynamic system with high structural and functional complexity becomes relatively homogeneous and less productive. Tropical reservoir fisheries are often dominated by low-value species plus a few nonindigenous species introduced for recreational angling or aquaculture (*13*). Ecological effects of large dams are not limited to rivers; trapping sediment alters nutrient dynamics and other biogeochemical processes in deltas, estuaries, and marine-shelf ecosystems, which in turn impact agriculture, fisheries, and human settlements (*14*).

A lack of transparency during dam approval processes has raised questions about whether funders and the public are fully informed about risks and long-term impacts on tropical river systems that support livelihoods of millions of people (*3*). Some tropical developing countries lack protocols guiding construction of hydroelectric dams, and many countries exempt small dams (<10 MW) from any formal decision-making process. Even when environmental impact assessments are mandated, millions of dollars may be spent on studies that have no actual influence on design parameters, sometimes because they are completed after construction is under way.

Planners have generally failed to assess the true benefits and costs of large hydropower projects. Returns have usually fallen short of expectations even without adjustment for risk, and an estimated 75% of large dams suffered cost overruns that averaged 96% above the figures used to justify their creation (*15*). Economic projections frequently exclude or underestimate the costs of environmental mitigation, as in the case of the ~$26 billion spent by China to moderate ecological impacts of the Three Gorges Dam (*16*).

Hydropower accounts for more than two-thirds of Brazil's energy supply, and at least 334 new Amazon dams have been proposed (*4*). Impacts of these dams would extend well beyond direct effects on rivers to include forced relocation of human populations and expanding deforestation associated with new roads (*4*). Scheduled for completion in 2016, Brazil's Belo Monte hydropower complex was designed with installed capacity of 11,233 MW, ranking it the

See supplementary materials for author affiliations.
**Corresponding author. E-mail: k-winemiller@tamu.edu*

Published by AAAS

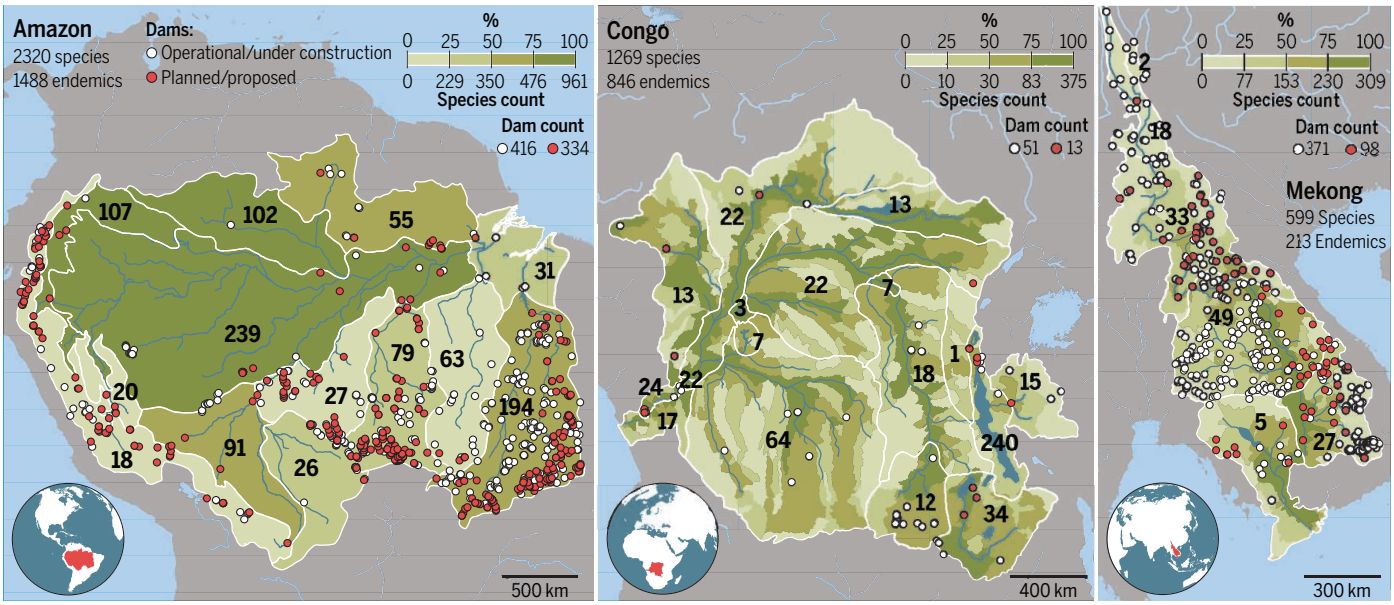

Fish diversity and dam locations in the Amazon, Congo, and Mekong basins. In addition to basin-wide biodiversity summaries (upper left in first two panels, middle in third panel), each basin can be divided into ecoregions (white boundaries). Many species are found only in a single ecoregion (black numbers), and subbasins within each river basin differ widely in their total species richness (shades of green illustrate breakpoints between quartiles in rank order within each basin). Dozens of new taxa are discovered every year in each basin; hence, actual fish diversity is underestimated, and distribution data are lacking for many species. Nonetheless, fish diversity data are now sufficient to support basin-scale impact assessments. See SM for data and methods.

world's third largest. Actual power generation, however, is expected to be much lower. Belo Monte may set a record for biodiversity loss owing to selection of a site with exceptional species endemism (*5*).

The Congo has far fewer dams than the Amazon or Mekong (see the chart), yet most power generated within the basin is from hydropower. Inga Falls, a 14.5-km stretch of the lower Congo that drops 96 m to near sea level, has greater hydropower potential than anywhere else (*6*). The Inga I and II dams, constructed in the 1970s and 1980s, currently yield 40% of the 2132-MW installed capacity (*6*). Planned additional dams (Inga III and Grand Inga) would harness as much as 83% of the Congo's annual discharge, with most of the energy to be exported (*6*). Grand Inga would divert water and substantially reduce flow for at least 20 km downstream from the falls.

Six large dams have been built on the upper Mekong since the mid-1990s, and there are plans for at least 11 more on the middle and lower reaches. Rural communities in the lower basin rely on harvesting wild fish species whose longitudinal migrations would be profoundly disrupted by dams on the mainstem or even major tributaries (*7*–*9*). For instance, damming the Mun River in Thailand has had a wide range of detrimental social and economic impacts (*7*). Maintaining regional food security in the face of projected fishery losses arising from 88 new dams planned for the basin by 2030 would require a 19 to 63% expansion of agricultural land (*9*).

RECOMMENDATIONS. Long-term ripple effects on ecosystem services and biodiversity are rarely weighed appropriately during dam planning in the tropics. We are skeptical that rural communities in the Amazon, Congo, and Mekong basins will experience benefits of energy supply and job creation that exceed costs of lost fisheries, agriculture, and property. An improved approach to dam evaluation and siting is imperative.

Integrative, strategic planning must be applied at the basin scale, with the goal of finding balance between tapping hydropower potential and sustaining key natural resources. Spatial data on biodiversity and ecosystem services are increasingly available to support sophisticated trade-off analyses [see supplementary material (SM)]. New analytical methods can account for cumulative impacts from multiple dams to hydrology, sediment dynamics, ecosystem productivity, biodiversity, fisheries, and rural livelihoods throughout watersheds (*1*, *17*–*19*). Incorporating these data and tools into assessment protocols would boost the credibility of dam siting to stakeholders.

Institutions that permit and finance hydropower development should require basin-scale analyses that account for cumulative impacts and climate change. Proposed dam sites must be evaluated within the context of sustaining a portfolio of ecosystem services and biodiversity conservation, and alternative sites should be considered explicitly. Such common-sense adjustments to assessment procedures would ensure that societal objectives for energy production are met while avoiding the most environmentally damaging projects. Without more careful planning, species extinctions and basin-wide declines in fisheries and other ecosystem services are certain to accompany new hydropower in the world's mega-diverse tropical rivers. ■

REFERENCES AND NOTES

1. G. Grill *et al.*, *Environ. Res. Lett.* **10**, 015001 (2015).
2. N. L. Poff *et al.*, *Nat. Clim. Change* 10.1038/nclimate2765 (2015).
3. L. Castello, M. Macedo, ***Glob. Change Biol.*** 10.1111/gcb.13173 (2015).
4. C. Zarfl *et al.*, *Aquat. Sci.* **77**, 161 (2015).
5. M. Sabaj Pérez, *Sci. Am.* **103**, 395 (2015).
6. K. B. Showers, in *Engineering Earth: The Impacts of Megaengineering Projects*, S. D. Brunn, Ed. (Springer, Dordrecht, Netherlands, 2011), p. 1651.
7. T. Foran, K. Manorom, in *Contested Waterscapes in the Mekong Region: Hydropower, Livelihood, and Governance*, F. Molle, T. Foran, M. Käkönen, Eds. (Earthscan, London, 2009), p. 55.
8. G. Ziv, E. Baran, S. Nam, I. Rodríguez-Iturbe, S. A. Levin, *Proc. Natl. Acad. Sci. U.S.A.* **109**, 5609 (2012).
9. S. Orr, J. Pittock, A. Chapagain, D. Dumaresq, *Glob. Environ. Change* **22**, 925 (2012).
10. P. S. Pompeu, A. A. Agostinho, F. M. Pelicice, *River Res. Appl.* **512**, 504 (2012).
11. D. C. Jackson, G. Marmulla in *Dams, Fish and Fisheries: Opportunities, Challenges and Conflict Resolution*, G. Marmulla, Ed. (United Nations Food & Agriculture Organization, Rome, 2001), p. 1.
12. F. M. Pelicice, A. A. Agostinho, *Conserv. Biol.*, **22**, 180 (2008).
13. D. J. Hoeinghaus *et al.*, *Conserv. Biol.*, **23**, 1222 (2009).
14. G. M. Kondolf, Z. K. Rubin, J. T. Minear, *Water Resour. Res.* **50**, 5158 (2014).
15. A. Ansar *et al.*, *Energy Policy* **69**, 43 (2014).
16. R. Stone, *Science* **333**, 817 (2011).
17. B. Lehner *et al.*, *Front. Ecol. Environ.* **9**, 494 (2011).
18. M. Finer, C. N. Jenkins, *PLOS ONE* **7**, e35126 (2012).
19. K. E. McCluney *et al.*, *Front. Ecol. Environ.* **12**, 48 (2014).

SUPPLEMENTARY MATERIALS

www.sciencemag.org/content/351/6269/128/suppl/DC1

10.1126/science.aac7082

IMAGE: WINEMILLER *ET AL.* ADAPTED BY P. HUEY/*SCIENCE*

Published by AAAS

PHYSICS

The supercollider that wasn't

An ambitious history of the SSC falls short on lessons for future megascience projects

By **Jeffrey Mervis**

When a multibillion-dollar physics experiment is canceled, it's tempting to look for lessons that can be applied to future megascience projects. A new book on the rise and fall of the Superconducting Supercollider (SSC) by a trio of science historians takes on that challenge. And while the authors do an excellent job of describing what occurred in the decade from its inception to its demise in 1993, they stumble when trying to assign blame.

Tunnel Visions presents a wealth of information on the internal conflicts that plagued the planning and construction of the SSC, a 40-TeV proton-proton collider that was to be built in a 70-km oval tunnel running under Waxahachie, Texas. There are loads of juicy stories for SSC aficionadas about the bad blood between the physicists and the engineers and between the lab managers and their overseers at the U.S. Department of Energy (DOE). The collider also triggered bitter internecine fights within the scientific community over its value and potential negative effect on prospects for other fields.

Equally at home in the laboratory and the halls of Congress, the authors trace the uphill—and ultimately successful—battle waged by a small group of legislators to pull the plug on the project's funding. The retelling of these events highlights the SSC's remarkably brief time in the national spotlight: Its death in October 1993 came less than 7 years after then-President Ronald Reagan endorsed the project by telling his domestic policy advisers to "throw deep" and only 11 years from the time physicists began talking about building a "desertron."

Clearly a labor of love, the book itself was three decades in the making. It draws upon extensive archival material and interviews with more than 100 people who played roles, large and small, in the SSC saga. And while some of their stories have already appeared in other accounts, putting them all together creates as complete a picture of what happened as we're ever likely to get.

The problem is attaching meaning to that narrative. The SSC is hardly the first planned science facility to be abandoned—DOE's initial $18 million investment in the SSC, ironically, came from money originally budgeted for the next iteration of Brookhaven's Isabelle accelerator, which also was never built. And the saga unfolded in a time and place that seems quite distant from the present—an era in which the hope for lasting world peace after the end of the Cold War combined with fears of an economically dominant Japan, to name just two features. So sifting through key strategic decisions in hopes of charting a path forward is a very risky business.

The book examines several "if-only" scenarios that, it argues, might have saved the collider, of which four stand out: If Cornell physicist Maury Tigner, architect of the original design, had been named lab director; if Fermilab in Illinois had been chosen as the site; if Japan had agreed to invest up to $1.5 billion in the project; and if George H. W. Bush had been reelected in 1992. Although it's hard to refute alternative history, there's little evidence that any or all of those developments would have turned the tide.

Equally dubious are some of the purported lessons to be learned—among them, that big science requires global cooperation, that the U.S. government favors applied over fundamental research, and that science is the first thing to go when Congress trims federal budgets. International partnerships certainly can ease the financial pain on individual countries. However, the troubled International Thermonuclear Experimental Reactor (ITER) currently being built in France demonstrates that global cooperation is hardly a guarantee of success. And NASA's James Webb Space Telescope—with no obvious application beyond understanding the cosmos—seems likely to be completed despite a price tag that's comparable to the SSC's.

In addition, generalizations about congressional attitudes toward "science" writ large are rarely accurate. Only a few years after the SSC was defunded, for example, Congress began a 5-year doubling of NIH's budget that added tens of billions of dollars to the U.S. research enterprise.

So what can be learned from the SSC's demise? Very little, it seems. The U.S. government wrote off its $2.5 billion investment in a project whose estimated cost had grown from $4.3 billion to north of $10 billion.

Those who wish to keep the SSC in their hearts have a very affordable option, however. In 2004, Herman Wouk, author of *The Caine Mutiny*, made the SSC the setting—and centerpiece—for a serious novel about science and global politics. The book, *A Hole in Texas*, was not a commercial hit, but you can buy it on Amazon for a penny.

10.1126/science.aad9865

Tunnel Visions
The Rise and Fall of the Superconducting Super Collider
Michael Riordan, Lillian Hoddeson, Adrienne W. Kolb
University of Chicago Press, 2015. 462 pp.

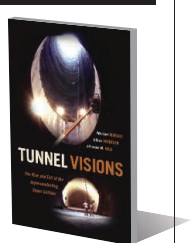

Smaller research projects would have been more defensible during the economic contraction of the 1990s, argue the authors.

PHOTO: ASSOCIATED PRESS

The reviewer is a senior correspondent for Science, *AAAS, Washington, DC 20005, USA. E-mail: jmervis@aaas.org*

Published by AAAS

HISTORY OF SCIENCE

Origin stories

Looking back at our ever-evolving understanding of what it means to be alive

By **James Strick**

A Brief History of Creation, like many popular books on ideas about the origin of life, approaches the topic with a broad sweep: digging into ancient myths, the pre-Socratics, Aristotle, and up through modern NASA-funded research. Few previous works, however, have done justice to the factual historical details. Many recycle old versions of Francesco Redi and his experiments on maggots, or Louis Pasteur and his swan-necked flasks, unaware that they are repeating inaccuracies historians have set straight.

The book under review, *A Brief History*, while clearly written for a popular audience, does what Stephen Jay Gould was so good at: taking a lot of new information from the professional history of science literature and rendering it accessible to a wide popular audience. For this reason, although the authors take the kind of yarn-spinning liberties Paul de Kruif did in his famous *Microbe Hunters*, their book is nonetheless far more accurate and up-to-date than any previous work targeted to the general public. It may thus do yeoman's service in general public science education, as well as making the public aware of the utility of the history of science.

In one of the book's early chapters, the authors set out to place Francesco Redi, the 17th-century Italian physician who was the first to refute the idea of the spontaneous generation of living organisms, in historical context. Redi is described as an Early Modern courtier in the service of the Grand Duke of Tuscany. Rather than presenting his work as a set of controlled, scholarly studies, as typically comes across in biology textbooks, Mesler and Cleaves show how these experiments were conducted as a form of court entertainment and a display of the Grand Duke's support for natural philosophy.

Similarly, Buffon and Needham's 18th-century experiments, which are normally mentioned in passing as flawed attempts to demonstrate spontaneous generation, are presented with great nuance in this book. Their methods, although imperfect, were conducted using high-quality single-lens microscopes, and their analysis insightfully stretched the envelope of biological thought in ways Darwin would later find worth his study. In addition, their debates with the Italian scientist Lazzaro Spallanzani, who ultimately disproved their work, are clearly shown to be as much about how such work threatened religious and philosophical understandings of the origin of life as they were about experimental evidence.

Louis Pasteur, a chemist by training, had tackled few biological questions prior to taking on the theory of spontaneous generation.

IMAGE: ALBERT EDELFELT, *LOUIS PASTEUR*, EN 1885

As with Gould, some historians may take exception to the lack of primary sources and academic citation style (only verbatim quotes are cited fully). Further, when the authors cite anecdotes from recent scientists' research—for instance, Cleaves's graduate adviser, the chemist Stanley Miller, in chapter 9—they treat this material as an unproblematic source. Particularly if they are recalled or told many years after the fact, anecdotes (such as Darwin's in his *Autobiography*) are often reshaped in the telling over the years. Unless they can be corroborated by period correspondence or other primary source records from when events were unfolding, anecdotes must be treated with considerable skepticism.

Occasionally, important items get overlooked. For example, while discussing historian Loren Graham's studies of Soviet biochemist Alexander Oparin, whose book on the origin of life was regarded as a seminal work on the subject for much of the 20th century, the authors repeat Graham's story about how Oparin supported Soviet biologist and agronomist T. D. Lysenko, whose rejection of Mendelian genetics had a destructive influence on Soviet biology. However, they fail to remark on Graham's more important finding: that the Marxist philosophy of science, dialectical materialism, did provide Oparin with some useful scientific insights into the origin-of-life problem—insights that had practical consequences in Oparin's experiments. Because many Western scholars resisted this new finding at the height of the Cold War, its importance deserves to be emphasized.

Regrettably, a few factual errors did slip into this book. In chapter 10, for example, the authors mistakenly claim that Avery, MacLeod, and McCarty's 1944 landmark study that ushered in the era of modern DNA research was performed in viruses. This paragraph seems to conflate the famous 1944 Avery *et al.* paper with the later work of Alfred Hershey and Martha Chase.

However, these are relatively minor criticisms compared to the service the book will perform. If in many ways this book aims to be a modern version of *Microbe Hunters*, it is to be hoped that it will do as much to excite the public about science as did that venerable earlier work.

A Brief History of Creation
Science and the Search for the Origin of Life
Bill Mesler and H. James Cleaves II
Norton, 2015. 332 pp.

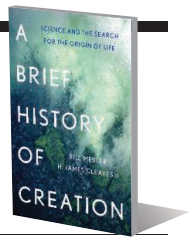

The reviewer is professor and chair, Program in Science, Technology, and Society, Franklin and Marshall College, Lancaster, PA 17604-3003, USA. E-mail: james.strick@fandm.edu

10.1126/science.aad4347

Published by AAAS

LETTERS

Edited by **Jennifer Sills**

Call for conservation: Abandoned pasture

THE STATISTICS DIVISION of the Food and Agriculture Organization (FAO) has recently released its national land distribution data for the year 2013 (*1*), which is currently the only annual cross-country time series on agricultural land use. According to these data, over the past 15 years, total global pasture area has declined by 62 million hectares (–2%), the first significant decrease on record. In the 65 countries where pasture has shrunk, only 15 have shown an increase in total agricultural land, and across all 65, total agricultural area declined by 109 million hectares. This implies that pasture land is not being used for different agricultural purposes, and instead suggests that an area approximately the size of South Africa may have recently been abandoned. All of this is despite a production increase from ruminants (meat, milk, hides, and wool) of 35% over the same period (*1*).

Where pasture has declined, most reductions have been annually persistent; a one-off methodology change is an unlikely explanation. Rather, these striking data could be due to a range of factors making grazing more intensive and less mobile, coupled with changing economic and environmental conditions. For example, in Australia, which represents a large part of the decline, 25 years of low wool prices (*1*) have affected stock numbers, and desertification and woody encroachment have reduced productive pasture area (*2*). In Iran, Mongolia, Turkmenistan, and Uzbekistan (also countries of substantial decline), land and livestock privatization, urbanization, and changing management practices have spatially concentrated production (*3*), reducing total land use.

If the data are accurate, we may be able to benefit from a sizeable land-sparing conservation opportunity (*4*) and restore vast areas of natural habitat through reforestation or reestablishment of natural grasslands. In doing so, we will confront a number of questions: Will the land become wild again naturally, meaning no action is required? Is it most productive to build relationships with landowners to facilitate conservation goals? Given that land values are likely low, is this a chance for opportunistic and targeted land acquisitions that could serve as foundations for new protected areas? Whatever the case, conservationists need to move quickly, as other actors are already laying out their ambitions for using pasture (*5*).

Joseph A. C. Poore*[1]

Park Cottage, Lee, Devon, EX34 8LN, UK.
E-mail: josephpoore@gmail.com

REFERENCES

1. Food and Agriculture Organization of the United Nations, FAOSTAT (Database) (2015); http://faostat3.fao.org/.
2. G. P. Asner, A. J. Elmore, L. P. Olander, R. E. Martin, A. T. Harris, *Annu. Rev. Environ. Resour.* **29**, 261 (2004).
3. D. Ojima, T. Chuluun, in *Fragmentation in Semi-Arid and Arid Landscapes*, K. A. Galvin *et al.*, Eds. (Springer, Dordrecht, 2008), pp. 179–193.
4. B. Phalan, M. Onial, A. Balmford, R. E. Green, *Science* **333**, 1289 (2011).
5. J. Smyth, L. Hornby, "Chinese companies eye Australia's vast land sale," *Financial Times*, 7 October 2015.

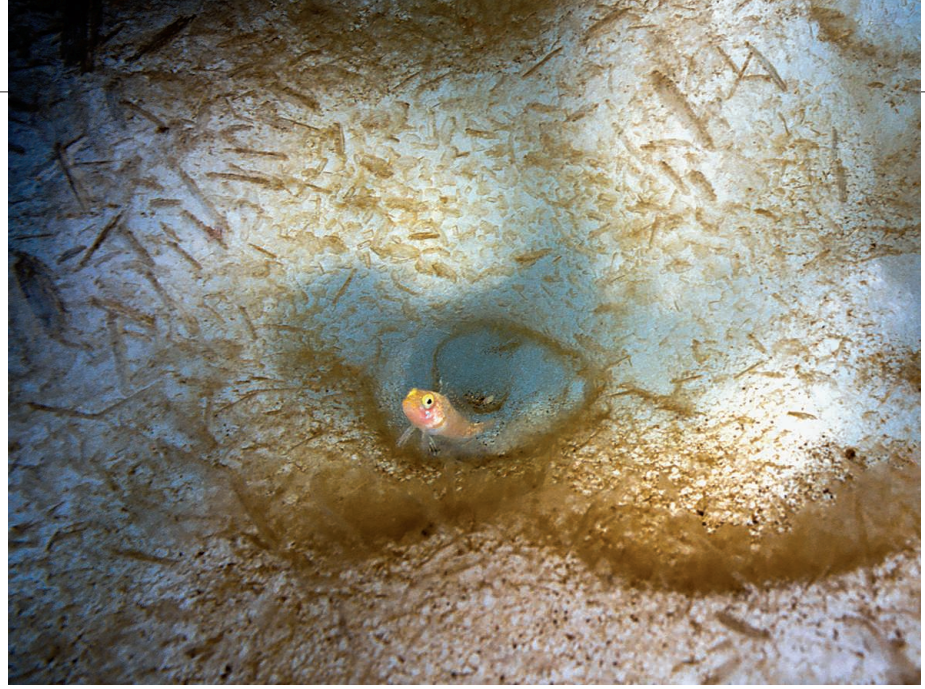

Evidence indicates that the Antarctic *Pagothenia borchgrevinki* can adapt to a range of temperatures.

Recognizing thermal plasticity in fish

IN THEIR REVIEW "Climate change and marine vertebrates" (13 November 2015, p. 772), W. J. Sydeman *et al.* acknowledge but understate the significance of phenotypic plasticity in modulating population responses to climate change and in mitigating the direct effects of increasing temperature. Indeed, a meta-analysis of thermal phenotypic plasticity found that some species of fish possess a substantial capacity to compensate for increases in temperature, potentially making them more resilient to global warming (*1*). Thus, prognostications for the future of certain fish species may not be as dire.

For example, stenothermal polar fishes such as the Antarctic *Pagothenia borchgrevinki* can thermally compensate, producing a new phenotype that functions well at 4°C (*2*, *3*), much warmer than their usual –1.8°C. Similarly, the Arctic cod (*Boreogadus saida*), a key prey species in the Arctic food web (*1*) that spends most of the year under ice, grows better at 5°C and 9°C than at 0°C (*4*) and maintains a rhythmic heartbeat up to 10°C (*5*). Native Pacific northwest rainbow trout (*Oncorhynchus mykiss*) have been introduced in every continent except Antarctica, have been selectively bred to physiologically tolerate temperature extremes in Western Australia (*6*), and have a subspecies (redband trout, *O. mykiss gairdnerii*) naturally adapted to the thermal extremes of a desert environment (*7*). Populations of northwest Pacific adult sockeye salmon (*O. nerka*) show a range of thermal reaction norms (*8*, *9*). That said, not all sockeye populations would flourish in warmer temperatures; one population's once-in-a-lifetime river migration has already been largely prevented by an unusually warm temperature event (*10*).

Reducing model uncertainty is an urgent matter (*11*), but it will require a better understanding of phenotypic plasticity and genotypic diversity within a species, as well as the key mechanistic features that enable certain individuals to perform better at warmer temperatures and be subjected to natural selection.

***Anthony P. Farrell*[1]* and Craig E. Franklin*[2]**

[1]Department of Zoology, University of British Columbia, Vancouver, BC V6T1Z4, Canada. [2]School of Biological Sciences, The University of Queensland, St. Lucia, QLD 4072, Australia.

*Corresponding author. E-mail: farrellt@mail.ubc.ca

REFERENCES

1. F. Seebacher, C. R. White, C. E. Franklin, *Nat. Clim. Change* **5**, 61 (2015).
2. C. E. Franklin, W. Davison, F. Seebacher, *J. Exp. Biol.* **210**, 3068 (2007).

PHOTO: © NORBERT WU/SCIENCE FACTION/CORBIS

Published by AAAS

3. C. E. Franklin, F. Seebacher, *Science* **323**, 876 (2009).
4. B. J. Laurel, M. Spencer, P. Iseri, L. A. Copeman, *Polar Biol.* 10.1007/s00300-015-1761-5 (2015).
5. H. E. Drost, E. C. Carmack, A. P. Farrell, *J. Fish Biol.* **84**, 1781 (2014).
6. K. J. Rodnick *et al.*, *J. Fish Biol.* **64**, 310 (2004).
7. Z. Chen *et al.*, *J. Exp. Biol.* **218**, 803 (2015).
8. H. O. Pörtner, A. P. Farrell, *Science* **322**, 690 (2008).
9. E. J. Eliason *et al.*, *Science* **332**, 109 (2011).
10. A. P. Farrell *et al.*, *Physiol. Biochem. Zool.* **81**, 697 (2008).
11. H. M. Pereira *et al.*, *Science* **330**, 1496 (2010); published online 26 October 2010.

HIV/AIDS epidemic: The whole truth

THE NEWS FEATURE "What does a disease deserve?" (J. Kaiser, 20 November 2015, p. 900) asserts that "AIDS death rates began dropping dramatically" about 2 decades ago. This is only part of the truth. According to the Centers for Disease Control and Prevention (CDC) (*1*), the number of people living with HIV has been rapidly increasing. The number of new infections has been steady in the United States (~45,000 annually) for at least 20 years, and the afflicted populations are underpowered and marginalized. For a country with our resources, this is a national disgrace. The leadership of the CDC has made a similar case (*2*).

Many of us seem to have forgotten that—in contrast to many noncommunicable diseases—HIV is an infectious disease that can be controlled by reducing transmission. So what's needed? Even absent an AIDS vaccine, we have the tools needed to reduce transmission and control this epidemic. To do so, the Office of AIDS Research and the National Institutes of Health must make a major investment in implementation science (with the participation of social, political, and economics experts) and coordinate these initiatives with the CDC. This is no time to turn our back on the research required to end the epidemic of HIV/AIDS in the United States.

Neal Nathanson

Emeritus Professor, Department of Microbiology, University of Pennsylvania, Philadelphia, PA 19104, USA. E-mail: nathansn@upenn.edu

REFERENCES

1. CDC, "CDC fact sheet: New HIV infections in the United States" (2012); www.cdc.gov/nchhstp/newsroom/docs/2012/hiv-infections-2007-2010.pdf.
2. T. R. Frieden, K. E. Foti, J. Mermin, *N. Engl. J. Med.* **373**, 2281 (2015).

ERRATA

Erratum for the Report "Polariton superfluids reveal quantum hydrodynamic solitons" by A. Amo *et al.*, *Science* **350**, aad9363 (2015). Published online 11 December 2015; 10.1126/science.aad9363

Erratum for the Report "14-Step synthesis of (+)-ingenol from (+)-3-carene" by L. Jørgensen *et al.*, *Science* **350**, aad8935 (2015). Published online 27 November 2015; 10.1126/science.aad8935

Erratum for the Report "Genomic correlates of response to CTLA-4 blockade in metastatic melanoma" by E. M. Van Allen *et al.*, *Science* **350**, aad8366 (2015). Published online 13 November 2015; 10.1126/science.aad8366

Erratum for the Report "Base triplet stepping by the Rad51/RecA family of recombinases" by J. Y. Lee *et al.*, *Science* **350**, aad6940 (2015). Published online 30 October 2015; 10.1126/science.aad6940

Erratum for the Research Article "The protein LEM promotes $CD8^+$ T cell immunity through effects on mitochondrial respiration" by I. Okoye *et al.*, *Science* **350**, aad6462 (2015). Published online 23 October 2015; 10.1126/science.aad6462

RESEARCH

Mapping the lineage potential of stem and progenitor cells

Notta et al., *p. 139*

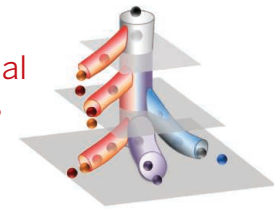

IN *SCIENCE* JOURNALS

Edited by **Nick Wigginton**

The 5000-year-old remains of the "Iceman" hold clues to deciphering the mummy's microbiome

ANCIENT MICROBIOME

Stomach ache for a European mummy

Five thousand years ago in the European Alps, a man was shot by an arrow, then clubbed to death. His body was subsequently mummified by ice until glacier retreat exhumed him in 1991. Subsequently, this ancient corpse has provided a trove of intriguing information about copper-age Europeans. Now, Maixner *et al*. have identified the human pathogen *Helicobacter pylori* within the mummy's stomach contents. The strain the "Iceman" hosted appears to most closely resemble pathogenic Asian strains found today in Central and Southern Asia. — CA

Science, this issue p. 162

SOLAR CELLS

Perovskites for tandem solar cells

Improving the performance of conventional single-crystalline silicon solar cells will help increase their adoption. The absorption of bluer light by an inexpensive overlying solar cell in a tandem arrangement would provide a step in the right direction by improving overall efficiency. Inorganic-organic perovskite cells can be tuned to have an appropriate band gap, but these compositions are prone to decomposition. McMeekin *et al*. show that using cesium ions along with formamidinium cations in lead bromide–iodide cells improved thermal and photostability. These improvements lead to high efficiency in single and tandem cells. — PDS

Science, this issue p. 151

STEM CELL NICHE

How HSCs populate the fetal liver

Hematopoietic stem cells (HSCs) undergo dramatic expansion in the fetal liver before migrating to their definitive site in the bone marrow. Khan *et al*. identify portal vessel–associated Nestin$^+$NG2$^+$ pericytes as critical HSC niche components (see the Perspective by Cabezas-Wallscheid and Trumpp). The portal vessel niche and HSCs expand according to fractal geometries, suggesting that niche cells—rather than factors expressed by the niche—drive HSC proliferation. After birth, arterial portal vessels transform into portal veins, and lose Nestin$^+$NG2$^+$ pericytes. When this happens, the niche is lost and HSCs migrate away from the neonatal liver. — BAP

Science, this issue p. 176; see also p. 126

PALEOCLIMATE

The difference is all in the water

Glacial cycles are in part controlled by the pattern of incident solar energy determined by the geometry of Earth's orbit around the Sun. The classic record of the penultimate deglaciation from Devils Hole, Nevada, did not reconcile the presumption of so-called orbital forcing, however, suggesting that deglaciation began ~10,000 years too early. Moseley *et al*. present analyses of a new set of data from Devils Hole that show that the deglaciation indeed occurred at the time expected on the basis of orbital forcing. The age offset displayed by the older samples apparently was caused by interaction with groundwater, which preferentially affected the deeper original samples but not the new shallower samples. — HJS

Science, this issue p. 165

HIV TRANSMISSION

The ART of HIV prevention

Despite the relative success of antiretroviral therapy (ART) for individuals infected with human immunodeficiency virus (HIV), the rate of new diagnoses has remained fairly constant. Now, Ratmann *et al.* examined probable sources of transmission in the Netherlands for men who have sex with men. They found that neither ineffective ART nor inadequate retention in care contributed to new infections.

PHOTO: ©EURAC/MARION LAFOGLER

Published by AAAS

Rather, many of these cases could have been averted with available ART had there been more comprehensive testing coverage among men at risk of transmission. These findings support broader, more frequent testing followed by immediate ART as a strategy to decrease transmission rates. — ACC

Sci. Transl. Med. **8**, 320ra2 (2016)

PROTEIN AGGREGATES

Location, location, location

Aggregates of certain disease-associated proteins are involved in neurodegeneration. Woerner *et al*. now show that the exact location of these aggregates in the cell may be the key to their pathology (see the Perspective by Da Cruz and Cleveland). An artificial aggregate-prone protein caused problems when expressed in the cytoplasm but not when expressed in the nucleus. Cytoplasmic aggregates interfered with nucleocytoplasmic import and export. Perhaps if we can shunt pathological aggregates to the nucleus in the future, we will be able to ameliorate some forms of degenerative disease. — SMH

Science, this issue p. 173; see also p. 125

FOREST ECOLOGY

Size distributions of tropical trees

The distribution of tree size in tropical forests follows a power-law regardless of location. This pattern has largely eluded mechanistic explanation. Using 30 years of tree demography and growth data from a forest plot in Panama, Farrior *et al*. show that the power-law size structure emerges after natural local disturbances such as the gaps formed by falling trees. A model of forest dynamics identifies the structural parameter governing the power-law distribution. A mechanistic understanding of tropical forest structural dynamics will benefit forest carbon cycling studies. — AMS

Science, this issue p. 155

Tropical rainforest in Panama with a fresh treefall gap

PHOTO: (FROM LEFT) ©DANITA DELIMONT/ALAMY STOCK PHOTO; JOHN SHAW/SCIENCE SOURCE

QUORUM SENSING

Plants send out a bacterial mimic

Bacteria use the quorum-sensing pathway to regulate community-level interactions, such as the formation of biofilms. Corral-Lugo *et al.* determined that a common plant compound mimics a quorum-sensing signal. Rosmarinic acid stimulated the activity of a transcriptional regulator in the quorum-sensing pathway of the plant and human pathogen *Pseudomonas aeruginosa*, increasing biofilm formation. Because rosmarinic acid could stimulate a premature quorum-sensing response, this compound may strategically disrupt bacterial communication. — NRG

Sci. Signal. **9**, ra1 (2016).

THERMOELECTRICS

Heat conversion gets a power boost

Thermoelectric materials convert waste heat into electricity, but often achieve high conversion efficiencies only at high temperatures. Zhao *et al*. tackle this problem by introducing small amounts of sodium to the thermoelectric SnSe (see the Perspective by Behnia). This boosts the power factor, allowing the material to generate more energy while maintaining good conversion efficiency. The effect holds across a wide temperature range, which is attractive for developing new applications. — BG

Science, this issue p. 141; see also p. 124

IN OTHER JOURNALS

Edited by **Sacha Vignieri** *and* **Jesse Smith**

Lake Powell, seen from Alstrom Point in Arizona, USA.

BIOGEOCHEMISTRY

A global census of lake nutrients

Lakes of all sizes are sensitive to local water and pollution management strategies. Excess nutrients in lakes can induce a series of unexpected consequences for water quality or greenhouse gas emissions. Based on previously collected data from over 8000 lakes across six continents, Chen *et al.* compiled a global estimate of carbon, nitrogen, and phosphorus in lakes. These trace nutrients have intertwined fates in lakes, often related to morphological and climatic factors that change over time. Perturbations of climate or land use by humans will therefore have wide-ranging effects on biogeochemical cycling of nutrients within lakes across the globe. — NW

Sci. Rep. 10.1038/srep15043 (2015).

Published by AAAS

Seven progenitor cells lead to a variety of blood cells

IMMUNOGENOMICS

Following the bloodline downstream

There are many different types of blood cells that originate from a single progenitor cell, but their developmental pathways are not well understood. Applying single-cell sequencing to mouse bone marrow cell populations, Paul *et al.* identify seven myeloid progenitor states indicating developmental heterogeneity among these cells. Characterizing cellular in vivo functions, they find clusters of cells that express previously well-characterized transcriptional profiles in both rare and common cell types, as well as novel profiles helping demarcate different cellular lineages. — LMZ

Cell **163,** 1663 (2015).

GEOPHYSICS

Setting the table for a new plate

A new and surprising discovery on the floor of the Indian Ocean could help determine the age of the Himalayan Mountains. Matthews *et al.* suggest that the India-Eurasia collision responsible for the great mountain range also explains an unexpected extinct tectonic plate. The formation of a previously unknown "Mammericx Microplate" was created at the beginning of plate convergence. The microplate is about 50 million years old, providing an independent estimate for the continent-continent collision. — BG

Earth Planet. Sci. Lett. 10.1016/j.epsl.2015.10.040 (2015).

DNA REPAIR

Breaking DNA for gene expression

DNA breaks are potentially highly mutagenic, and the cell has an array of DNA damage response systems to rapidly repair such damage. Curiously, DNA repair factors have been found associated with transcriptionally paused, inducible genes. Bunch *et al.* show that the activation of paused and inducible genes in human tissue culture cells triggers DNA breaks at the RNA polymerase pause site. The subsequent recruitment and signaling activity of DNA repair factors is critical for DNA repair, release of the RNA polymerase, and the transition to the transcription elongation phase of gene expression. — GR

Nat. Commun. **6**, 10191 (2015).

GRAPHENE ELECTRONICS

Tuning graphene at a stretch

Graphene is often described as the superlative material, collectively possessing electronic, thermal, and mechanical properties that exceed those of most other materials. The ability to tune these properties is, however, challenging. Stretching graphene alters the lattice structure, causing a change in the electronic properties as if there was a large magnetic field locally applied to the electrons. Zhu *et al.* exploit this electromechanical property to demonstrate that, by patterning the geometry of the graphene layer in just the right way, they can design-in the desired strain that then gives rise to uniform pseudomagnetic fields. The engineered stretching technique should offer a route toward enhanced and tunable functionality of graphene. — ISO

Phys. Rev. Lett. **115**, 245501 (2015).

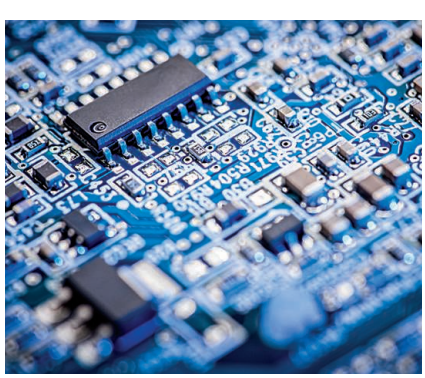

Testing cell circuits like an engineer

SIGNAL TRANSDUCTION

Testing a cell signaling circuit

It remains a challenge to understand how a limited number of signaling mechanisms encode a broad range of cellular responses. Ryu *et al.* explored signaling by the mitogen-activated protein kinase pathway activated by various growth factors in single PC-12 rat pheochromocytoma cells. As Blüthgen explains in a commentary, the authors tested the circuit much as an electrical engineer might test an electrical circuit. They compared effects of pulses or sustained doses of growth factor. Sustained growth factor stimulus caused a heterogeneous response of single cells—some transiently and some sustaining pathway activation. Mathematical modeling and evaluation of pulsed growth factor stimulation in cells showed that different frequencies of stimulation enabled the same growth factor to cause different cell fate decisions. — LBR

Mol. Syst. Biol. 10.15252/msb.20156458 (2015).

Mol. Syst. Biol. 10.15252/msb.20156642 (2015).

DRUG DELIVERY

A protein assist for brain border crossings

Getting therapies into the brain represents a major challenge to drug developers. A layer of brain endothelial cells (BECs) acts as a barrier by preventing large molecules in the blood from accessing the brain. One promising way to overcome this is by using protein receptors on BECs to transfer large molecules like antibodies across the barrier. Zuchero *et al.* used proteomics to identify candidate proteins expressed highly on mouse BECs. They found that BECs expressed high amounts of CD98hc and then created antibodies to target it. These antibodies could access the brain after systemic dosing of mice and showed substantial pharmacodynamic activity after being engineered so that one antibody arm recognized a potential drug target for Alzheimer's disease. — KLM

Neuron 10.1016/j.neuron.2015.11.024 (2016).

PHOTO: (FROM TOP) ANDREW SYRED/SCIENCE SOURCE; KRYSTIAN NAWROCKI/ISTOCK PHOTO

Published by AAAS

ALSO IN *SCIENCE* JOURNALS

Edited by **Nick Wigginton**

EARTH HISTORY

Evidence of an Anthropocene epoch

Humans are undoubtedly altering many geological processes on Earth—and have been for some time. But what is the stratigraphic evidence for officially distinguishing this new human-dominated time period, termed the "Anthropocene," from the preceding Holocene epoch? Waters *et al.* review climatic, biological, and geochemical signatures of human activity in sediments and ice cores. Combined with deposits of new materials and radionuclides, as well as human-caused modification of sedimentary processes, the Anthropocene stands alone stratigraphically as a new epoch beginning sometime in the mid–20th century. — NW

Science, this issue p. 137

ECOLOGY

Reforest with care

Grasslands throughout the tropics are targeted for forest planting. In his Perspective, Bond argues that such efforts put ancient, highly biodiverse ecosystems at risk. Although some grasslands are the result of deforestation, wide areas have supported mosaics of grassland and forest for millions of years. Examples include grasslands in southern Brazil, South Africa, and Madagascar. Many of these grasslands require frequent fires to maintain them. Plants have evolved to survive fires, for example, by developing extensive root systems. It is crucial that efforts are made to protect these ancient tropical grassy ecosystems. — JFU

Science, this issue p. 120

BRAIN CIRCUITS

Fine-tuned information flow in the brain

In addition to providing well-characterized excitatory inputs, the entorhinal cortex also sends long-range inhibitory projections to the hippocampus. Basu *et al*. described this input in detail and characterized its role for learning and memory. Multimodal sensory stimuli activate long-range inhibitory input in vivo. This input enables precisely timed information transfer within the cortico-hippocampal circuit. In this way, long-range inhibitory projections play an important role in providing specificity of fear conditioning, and thus help prevent overgeneralization. — PRS

Science, this issue p. 138

HEMATOPOIESIS

Adjusting hematopoietic hierarchy

In adults, more than 300 billion blood cells are replenished daily. This output arises from a cellular hierarchy where stem cells differentiate into a series of multilineage progenitors, culminating in unilineage progenitors that generate over 10 different mature blood cell types. Notta *et al*. mapped the lineage potential of nearly 3000 single cells from 33 different cell populations of stem and progenitor cells from fetal liver, cord blood, and adult bone marrow (see the Perspective by Cabezas-Wallscheid and Trumpp). Prenatally, stem cell and progenitor populations were multilineage with few unilineage progenitors. In adults, multilineage cell potential was only seen in stem cell populations. — BAP

Science, this issue p. 139; see also p. 126

GEOMORPHOLOGY

Nepal's quake-driven landslide hazards

Large earthquakes can trigger dangerous landslides across a wide geographic region. The 2015 M_w 7.8 Gorhka earthquake near Kathmandu, Nepal, was no exception. Kargal *et al*. used remote observations to compile a massive catalog of triggered debris flows. The satellite-based observations came from a rapid response team assisting the disaster relief effort. Schwanghart *et al*. show that Kathmandu escaped the historically catastrophic landslides associated with earthquakes in 1100, 1255, and 1344 C.E. near Nepal's second largest city, Pokhara. These two studies underscore the importance of determining slope stability in mountainous, earthquake-prone regions. — BG

Science, this issue p. 140; see also p. 147

MICROBIOME

Decomposition spawns a microbial zoo

The death of a large animal represents a food bonanza for microorganisms. Metcalf *et al*. monitored microbial activity during the decomposition of mouse and human cadavers. Regardless of soil type, season, or species, the microbial succession during decomposition was a predictable measure of time since death. An overlying corpse leaches nutrients that allow soil- and insect-associated fungi and bacteria to grow. These microorganisms are metabolic specialists that convert proteins and lipids into foul-smelling compounds such as cadaverine, putrescine, and ammonia, whose signature may persist in the soil long after a corpse has been removed. — CA

Science, this issue p. 158

CELL BIOLOGY

Mitochondria migration during mitosis

Every time a cell divides, it is faced with the problem of ensuring adequate distribution of all components to the daughter cells. This includes components that are present in relatively small numbers, like the mitochondria and their DNA-containing nucleoids. Jajoo *et al*. used quantitative time-lapse fluorescence microscopy of single yeast cells to explore how this works. Unlike chromosomes or macromolecules, mitochondria and nucleoids are distributed in proportion to the volume of cytoplasm received by each daughter cell. Partitioning errors are kept low by even distribution of the mitochondrial volume and roughly equal spacing of the nucleoids before they are distributed. — LBR

Science, this issue p. 169

GEOPHYSICS

Mantle minerals won't share the strain

The deformation of a mixed block of material depends on the strength of the components of which it is made. Weak materials will deform more than the strong ones in a mixture that is squished or stretched. Girard *et al*. find a large difference in strength between the two primary minerals making up Earth's lower mantle (see the Perspective by Chen). Deformation in the convecting mantle may occur only near boundary layers as a result, leaving large regions potentially unaffected. This could explain long-lived chemical reservoirs in Earth's interior and the lack of seismic anisotropy in the lower mantle. — BG

Science, this issue p. 144; see also p. 122

Published by AAAS

CHEMOTAXIS

A chemokine's sugary release

As immune cells survey the body for pathogens, they circulate through the blood and migrate through the lymphatic system. The latter route allows for tissues and lymph nodes—the central hubs of the immune system—to communicate. Kiermaier *et al*. reveal the importance of the monosaccharide sialic acid in keeping immune cells in motion. Multiple sialic acids decorate the surface CCR7 on immune cells. CCR7 recognizes proteins called chemokines, which direct where cells move in the body. Sialic acids on CCR7 release one such chemokine present on lymph node endothelial cells from an inhibited state, allowing immune cells to enter lymph nodes. — KLM

Science, this issue p. 186

PROTEIN STRUCTURE

Going in with a BAM

Integral membrane proteins in bacterial outer membranes play roles in nutrient import and infectivity. These proteins are folded into a barrel shape composed of β-strands and inserted into the outer membrane by the β-barrel assembly machinery (BAM) complex. Bakelar *et al*. determined the crystal structure of a four-component BAM subcomplex. The structure of a central β barrel in BAM changes in the presence of the accessory components to create a lateral opening that may be involved in how BAM inserts proteins into the outer membrane. — VV

Science, this issue p. 180

Published by AAAS

REVIEW SUMMARY

EARTH HISTORY

The Anthropocene is functionally and stratigraphically distinct from the Holocene

Colin N. Waters,* Jan Zalasiewicz, Colin Summerhayes, Anthony D. Barnosky, Clément Poirier, Agnieszka Gałuszka, Alejandro Cearreta, Matt Edgeworth, Erle C. Ellis, Michael Ellis, Catherine Jeandel, Reinhold Leinfelder, J. R. McNeill, Daniel deB. Richter, Will Steffen, James Syvitski, Davor Vidas, Michael Wagreich, Mark Williams, An Zhisheng, Jacques Grinevald, Eric Odada, Naomi Oreskes, Alexander P. Wolfe

BACKGROUND: Humans are altering the planet, including long-term global geologic processes, at an increasing rate. Any formal recognition of an Anthropocene epoch in the geological time scale hinges on whether humans have changed the Earth system sufficiently to produce a stratigraphic signature in sediments and ice that is distinct from that of the Holocene epoch. Proposals for marking the start of the Anthropocene include an "early Anthropocene" beginning with the spread of agriculture and deforestation; the Columbian Exchange of Old World and New World species; the Industrial Revolution at ~1800 CE; and the mid-20th century "Great Acceleration" of population growth and industrialization.

ADVANCES: Recent anthropogenic deposits contain new minerals and rock types, reflecting rapid global dissemination of novel materials including elemental aluminum, concrete, and plastics that form abundant, rapidly evolving "technofossils." Fossil fuel combustion has disseminated black carbon, inorganic ash spheres, and spherical carbonaceous particles worldwide, with a near-synchronous global increase around 1950. Anthropogenic sedimentary fluxes have intensified, including enhanced erosion caused by deforestation and road construction. Widespread sediment retention behind dams has amplified delta subsidence.

Geochemical signatures include elevated levels of polyaromatic hydrocarbons, polychlorinated biphenyls, and pesticide residues, as well as increased $^{207/206}$Pb ratios from leaded gasoline, starting between ~1945 and 1950. Soil nitrogen and phosphorus inventories have doubled in the past century because of increased fertilizer use, generating widespread signatures in lake strata and nitrate levels in Greenland ice that are higher than at any time during the previous 100,000 years.

Detonation of the Trinity atomic device at Alamogordo, New Mexico, on 16 July 1945 initiated local nuclear fallout from 1945 to 1951, whereas thermonuclear weapons tests generated a clear global signal from 1952 to 1980, the so-called "bomb spike" of excess ^{14}C, ^{239}Pu, and other artificial radionuclides that peaks in 1964.

Atmospheric CO_2 and CH_4 concentrations depart from Holocene and even Quaternary patterns starting at ~1850, and more markedly at ~1950, with an associated steep fall in δ^{13}C that is captured by tree rings and calcareous fossils. An average global temperature increase of 0.6° to 0.9°C from 1900 to the present, occurring predominantly in the past 50 years, is now rising beyond the Holocene variation of the past 14,000 years, accompanied by a modest enrichment of δ^{18}O in Greenland ice starting at ~1900. Global sea levels increased at 3.2 ± 0.4 mm/year from 1993 to 2010 and are now rising above Late Holocene rates. Depending on the trajectory of future anthropogenic forcing, these trends may reach or exceed the envelope of Quaternary interglacial conditions.

Biologic changes also have been pronounced. Extinction rates have been far above background rates since 1500 and increased further in the 19th century and later; in addition, species assemblages have been altered worldwide by geologically unprecedented transglobal species invasions and changes associated with farming and fishing, permanently reconfiguring Earth's biological trajectory.

OUTLOOK: These novel stratigraphic signatures support the formalization of the Anthropocene at the epoch level, with a lower boundary (still to be formally identified) suitably placed in the mid-20th century. Formalization is a complex question because, unlike with prior subdivisions of geological time, the potential utility of a formal Anthropocene reaches well beyond the geological community. It also expresses the extent to which humanity is driving rapid and widespread changes to the Earth system that will variously persist and potentially intensify into the future. ■

ON OUR WEB SITE

Read the full article at http://dx.doi.org/10.1126/science.aad2622

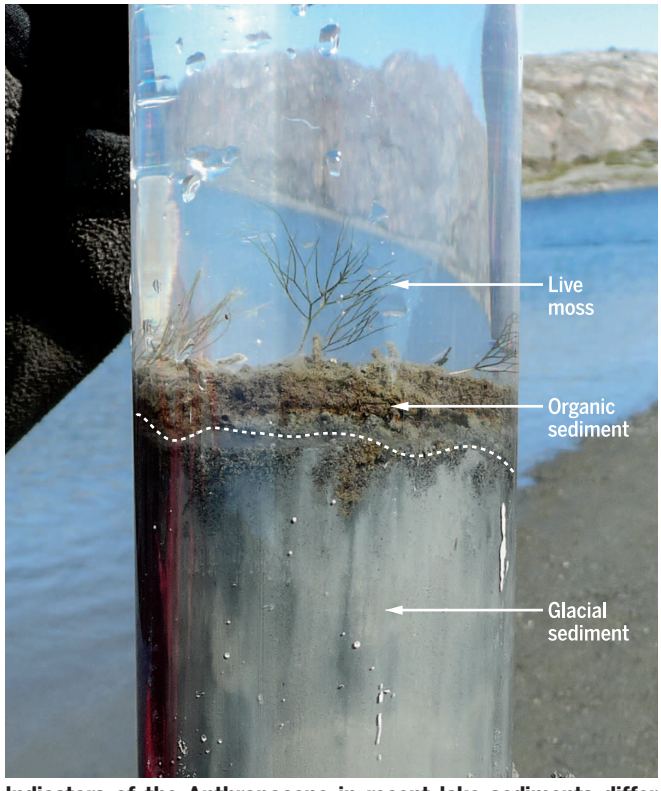

Indicators of the Anthropocene in recent lake sediments differ markedly from Holocene signatures. These include unprecedented combinations of plastics, fly ash, radionuclides, metals, pesticides, reactive nitrogen, and consequences of increasing greenhouse gas concentrations. In this sediment core from west Greenland (69°03'N, 49°54'W), glacier retreat due to climate warming has resulted in an abrupt stratigraphic transition from proglacial sediments to nonglacial organic matter, effectively demarcating the onset of the Anthropocene. [Photo credit: J. P. Briner]

The list of author affiliations is available in the full article online.
*Corresponding author. E-mail: cnw@bgs.ac.uk
Cite this article as C. N. Waters *et al.*, *Science* 351, aad2622 (2016). DOI: 10.1126/science.aad2622

REVIEW

EARTH HISTORY

The Anthropocene is functionally and stratigraphically distinct from the Holocene

Colin N. Waters,[1]* Jan Zalasiewicz,[2] Colin Summerhayes,[3] Anthony D. Barnosky,[4] Clément Poirier,[5] Agnieszka Gałuszka,[6] Alejandro Cearreta,[7] Matt Edgeworth,[8] Erle C. Ellis,[9] Michael Ellis,[1] Catherine Jeandel,[10] Reinhold Leinfelder,[11] J. R. McNeill,[12] Daniel deB. Richter,[13] Will Steffen,[14] James Syvitski,[15] Davor Vidas,[16] Michael Wagreich,[17] Mark Williams,[2] An Zhisheng,[18] Jacques Grinevald,[19] Eric Odada,[20] Naomi Oreskes,[21] Alexander P. Wolfe[22]

Human activity is leaving a pervasive and persistent signature on Earth. Vigorous debate continues about whether this warrants recognition as a new geologic time unit known as the Anthropocene. We review anthropogenic markers of functional changes in the Earth system through the stratigraphic record. The appearance of manufactured materials in sediments, including aluminum, plastics, and concrete, coincides with global spikes in fallout radionuclides and particulates from fossil fuel combustion. Carbon, nitrogen, and phosphorus cycles have been substantially modified over the past century. Rates of sea-level rise and the extent of human perturbation of the climate system exceed Late Holocene changes. Biotic changes include species invasions worldwide and accelerating rates of extinction. These combined signals render the Anthropocene stratigraphically distinct from the Holocene and earlier epochs.

The term "Anthropocene" is currently used informally to encompass different geological, ecological, sociological, and anthropological changes in recent Earth history. The origins of the concept of the Anthropocene, its terminology, and its sociopolitical implications are widely discussed (*1*, *2*). When considering the stratigraphic definition of the Anthropocene, there are two basic questions: Have humans changed the Earth system to such an extent that recent and currently forming geological deposits include a signature that is distinct from those of the Holocene and earlier epochs, which will remain in the geological record? If so, when did this stratigraphic signal (not necessarily the first detectable anthropogenic change) become recognizable worldwide? These questions are considered here in the context of how stratigraphic units have been formally recognized earlier in the Quaternary period.

Proposals for marking the start of the Anthropocene have included (i) an "early Anthropocene" associated with the advent of agriculture, animal domestication, extensive deforestation, and gradual increases in atmospheric carbon dioxide (CO_2) and methane (CH_4) levels thousands of years ago (*3*, *4*); (ii) the Columbian Exchange of Old World and New World species associated with colonization of the Americas (*5*); (iii) the beginning of the Industrial Revolution at ~1800 CE (*6*, *7*); and (iv) the mid-20th century "Great Acceleration" of population growth, industrialization, and mineral and energy use (*8*–*10*).

Here we review several lines of evidence suggesting that the Anthropocene's stratigraphic signatures distinguish it from the Holocene (Fig. 1). We find that criteria available to recognize the Anthropocene are consistent with those used to define other Quaternary stratigraphic units. Earlier Quaternary time-unit subdivisions are defined by signals from cyclical forcings of climate change, such as variation in Earth's orbit or solar irradiance, and irregular events such as volcanic eruptions. Although these forcings continue, the Anthropocene markers reflect an additional key driver, that of human modification of global environments at unprecedented rates. This driver has produced a wide range of anthropogenic stratigraphic signals (Fig. 1), including examples that are novel in Earth history, that are global in extent, and that offer fine temporal resolution. The signals vary in their development: Some are already advanced, and others are at early stages. We describe these signals and suggest how they may be used in the stratigraphic characterization and correlation of a formalized Anthropocene epoch with a lower boundary (still to be identified) potentially placed in the mid-20th century.

How are Quaternary stratigraphic units defined?

The Quaternary period, which began 2.6 million years ago (Ma), is subdivided into geochronological time units (epochs and ages) with boundaries that are linked at least in part to climate change events (expressed as marine isotope stages), in association with paleomagnetic reversals (*11*). This contrasts with the subdivision of most of the Phanerozoic eon (the past ~541 ± 1 Ma), for which the first or last appearance of key fossil taxa is typically used to define time units. Fossil-based boundaries represent change at rates too slow and time-transgressive for the geologically recent past, in which the time units are of comparatively short duration (about 12,000 years for the Holocene versus 2 million years or more for earlier epochs). These time intervals are recognizable in the geologic record as chronostratigraphic units (series and stages), which, in contrast to the time units, are physical entities, including rocks, sediments, and glacier ice. Ideally, a chronostratigraphic unit is exemplified, and its lower boundary defined, at a single locality termed the Global Boundary Stratotype Section and Point (GSSP), which is typically in marine strata for pre-Holocene series (*12*).

The start of the Holocene epoch (or series) is based on the termination of the transition from the last glacial phase into an interval of warming accompanied by ~120 m of sea-level rise. The warming took place over about 1600 years and is recorded by a variety of stratigraphic signals that are not all globally synchronous. In the Northern Hemisphere, the signal for the Holocene's beginning

[1]British Geological Survey, Keyworth, Nottingham NG12 5GG, UK. [2]Department of Geology, University of Leicester, University Road, Leicester LE1 7RH, UK. [3]Scott Polar Research Institute, Cambridge University, Lensfield Road, Cambridge CB2 1ER, UK. [4]Department of Integrative Biology, Museum of Paleontology, and Museum of Vertebrate Zoology, University of California–Berkeley, Berkeley, CA 94720, USA. [5]Morphodynamique Continentale et Côtière, Université de Caen Normandie, Centre National de la Recherche Scientifique (CNRS), 24 Rue des Tilleuls, F-14000 Caen, France. [6]Geochemistry and the Environment Division, Institute of Chemistry, Jan Kochanowski University, 15G Świętokrzyska Street, 25-406 Kielce, Poland. [7]Departamento de Estratigrafía y Paleontología, Facultad de Ciencia y Tecnología, Universidad del País Vasco/Euskal Herriko Unibertsitatea, Apartado 644, 48080 Bilbao, Spain. [8]School of Archaeology and Ancient History, University of Leicester, University Road, Leicester LE1 7RH, UK. [9]Department of Geography and Environmental Systems, University of Maryland–Baltimore County, Baltimore, MD 21250, USA. [10]Laboratoire d'Etudes en Géophysique et Océanographie Spatiales (CNRS, Centre National d'Études Spatiales, Institut de Recherche pour le Développement, Université Paul Sabatier), 14 Avenue Edouard Belin, 31400 Toulouse, France. [11]Department of Geological Sciences, Freie Universität Berlin, Malteserstraße 74-100/D, 12249 Berlin, Germany. [12]Georgetown University, Washington, DC, USA. [13]Nicholas School of the Environment, Duke University, Box 90233, Durham, NC 27516, USA. [14]The Australian National University, Canberra, Australian Capital Territory 0200, Australia. [15]Department of Geological Sciences, University of Colorado–Boulder, Box 545, Boulder, CO 80309-0545, USA. [16]Marine Affairs and Law of the Sea Programme, The Fridtjof Nansen Institute, Lysaker, Norway. [17]Department of Geodynamics and Sedimentology, University of Vienna, A-1090 Vienna, Austria. [18]State Key Laboratory of Loess and Quaternary Geology, Institute of Earth Environment, Chinese Academy of Sciences, Xi'an 710061, Beijing Normal University, Beijing 100875, China. [19]Institut de Hautes Études Internationales et du Développement, Chemin Eugène Rigot 2, 1211 Genève 11, Switzerland. [20]Department of Geology, University of Nairobi, Nairobi, Kenya. [21]Department of the History of Science, Harvard University, Cambridge, MA 02138, USA. [22]Department of Biological Sciences, University of Alberta, Edmonton, Alberta T6G 2E9, Canada.
***Corresponding author. E-mail: cnw@bgs.ac.uk**

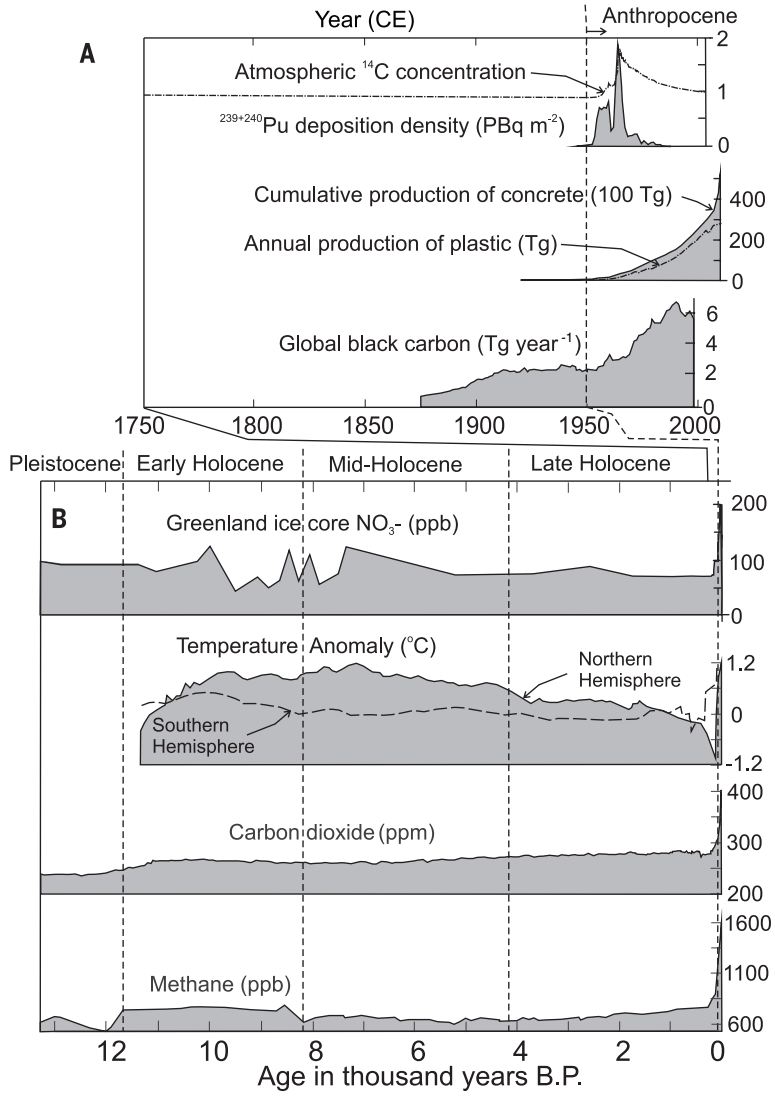

Fig. 1. Summary of the magnitude of key markers of anthropogenic change that are indicative of the Anthropocene. (**A**) Novel markers, such as concrete, plastics, global black carbon, and plutonium (Pu) fallout, shown with radiocarbon (^{14}C) concentration. (**B**) Long-ranging signals such as nitrates (NO_3^-), CO_2, CH_4, and global temperatures, which remain at relatively low values before 1950, rapidly rise during the mid-20th century and, by the late 20th century, exceed Holocene ranges.

was taken as the abrupt end of the Younger Dryas cooling event. The GSSP chosen to define the base of the Holocene was agreed to lie within the NGRIP2 ice core from central Greenland (NGRIP, North Greenland Ice Core Project) (*13*). The core contains a detailed archive of environmental change, preserved in the composition of air bubbles trapped in the ice and in the chemical and physical characteristics of the ice. The GSSP lies within a multidecade warming and moistening trend, which is inferred from oxygen isotopes showing rising $\delta^{18}O$, associated with a reduction in dust content. About midway through this trend, the sharpest change is a decrease in excess deuterium, which is interpreted as representing a reorganization of North Atlantic ocean-atmosphere circulation at 11,700 years before the year 2000 CE, ± 99 years at 2σ (*13*). This distinctive change is used to define the base of the Holocene series (the material chronostratigraphic unit). Thus, by definition, the Holocene epoch (the abstract time unit) began ~11,700 years ago.

The Holocene epoch (and corresponding series) is being considered for subdivision into three component sub-epochs (subseries), again using climatic signatures to guide the positioning of their bases. The base of the Lower Holocene, by default, would be the base of the Holocene series, as described above. The base of the Middle Holocene has been proposed to lie within a short-lived (150 ± 30 years) cooling event at 8200 years before the present (yr B.P.), where there is a marked shift to lower $^{18}O/^{16}O$ values (more negative $\delta^{18}O$ values) within the NGRIP1 ice core in the Greenland Ice Sheet (*13*). Within the same narrow interval of time, Greenland ice cores show low deuterium/hydrogen (D/H) ratios, a decline in annual layer thickness, an atmospheric CH_4 minimum, and a volcanic marker characterized by high fluoride content. Such signals have led to the proposal that a Greenland ice core should be used to define the Middle Holocene GSSP (*13*). Although such signals are most strongly evident at localities adjacent to the North Atlantic, they probably make up part of a global signature, because correlative signals are evident in lake sediments as changes in pollen assemblages and oxygen isotopes; in cave speleothems as isotopic signals reflecting changes in the intensity of the South American monsoon; in marine foraminiferal assemblages (species compositions); and in increased aridification around the Mediterranean that broadly coincides with the Mesolithic-Neolithic transition (*13*).

The base of the Upper Holocene has been proposed to lie at a mid- and low-latitude aridification event at 4200 yr B.P. (*13*). This event appears to have coincided with cooling of the North Atlantic and tropical Pacific, the arrival of cooler and wetter conditions in Europe, and a weakening of the Asian monsoon (*13*). The proposed stratotype is in a speleothem record from Mawmluh Cave in northeast India, at the midpoint of a two-stage shift of $\delta^{18}O$ values in calcite from more positive, starting at 4300 yr B.P., to more negative, starting at 4100 yr B.P. (*13*). Although there is no doubt that marked environmental perturbations occurred at both 8200 and 4200 yr B.P., most proxies indicate subsequent recovery in a matter of centuries, implying that these were temporally discrete paleoclimatic events as opposed to truly novel states within the Earth system.

Human drivers of stratigraphic signatures

The driving human forces responsible for many of the anthropogenic signatures are a product of the three linked force multipliers: accelerated technological development, rapid growth of the human population, and increased consumption of resources. These have combined to result in increased use of metals and minerals, fossil fuels, and agricultural fertilizers and increased transformation of land and nearshore marine ecosystems for human use. The net effect has been a loss of natural biomes to agriculture, cities, roads, and other human constructs and the replacement of wild animals and plants by domesticated species to meet growing demands for food. This increase in consumption of natural resources is closely linked to the growth of the human population. Anatomically modern *Homo sapiens* emerged ~200,000 years ago (*14*). By 12,000 yr B.P., around the start of the Holocene, humans had colonized all of the continents except Antarctica and the South Pacific islands and had reached a total population estimated at 2 million (*15*, *16*). Up to this point, human influence on the Earth system was small relative to what has happened since the mid-20th century; even so, human impacts contributed to the extinction of Pleistocene megafauna (*17*). However, the key signals used to recognize the start of the Holocene epoch were not directly influenced by human forcing, which is a major distinction from the proposed Anthropocene epoch.

Humans had a growing stratigraphic influence throughout the Holocene epoch as the global population gradually increased. It has been argued that ~8000 years ago, with a global population estimated at less than 18 million (*15*, *16*), the initiation of agricultural practices and forest clearances began to gradually increase atmospheric CO_2 levels (*3*). But it was not until ~1800 CE that the global population first reached 1 billion (*16*). Increased mechanization and the drive to urbanization during the Industrial Revolution, initially in Western Europe and eventually worldwide (*18*), then facilitated a more rapid population increase. Although this population growth is commonly thought to have increased exponentially through the 19th and 20th centuries (*8*, *9*), recent analyses (*15*, *16*) suggest that it can be differentiated into a period of relatively slower growth from 1750 to 1940 CE and one of more rapid growth from 1950 to 2010 CE. The inflection point at ~1950 CE coincides with the Great Acceleration (*8*, *9*), a prominent rise in economic activity and resource consumption that accounts for the marked mid-20th century upturns in or inceptions of the anthropogenic signals detailed below.

New anthropogenic materials

Recent anthropogenic deposits, which are the products of mining, waste disposal (landfill), construction, and urbanization (*19*), contain the greatest expansion of new minerals since the Great Oxygenation Event at 2400 Ma (*20*) and are accompanied by many new forms of "rock," in the broad sense of geological materials with the potential for long-term persistence. Over many millennia, humans have manufactured materials previously unknown on Earth, such as pottery, glass, bricks, and copper alloys. Remains of these materials are present as a persistent and widespread geological signal that is markedly time-transgressive, reflecting the migration of peoples (*21*). In contrast, elemental aluminum, which was almost unknown in native form before the 19th century, has seen 98% of its cumulative global production of ~500 Tg since 1950 CE (Fig. 2A) (*20*, *22*). Concrete, which was invented by the Romans, became the primary building material from World War II (1939–1945 CE) onward. The past 20 years (1995–2015) account for more than half of the 50,000 Tg of concrete ever produced (*22*, *23*) (Fig. 2A), equivalent to ~1 kg m^{-2} of the planet surface. Concrete and aluminum are widely disseminated across terrestrial, particularly urban, settings.

Similarly, the manufacture of new organic polymers (plastics), which were initially developed in the early 1900s, rapidly grew from the 1950s to an annual production of about ~300 Tg in 2013 (*24*) (Fig. 2A), comparable to the present human biomass. Plastics spread rapidly via rivers into lakes, and they are now also widespread in both shallow- and deep-water marine sediments as macroscopic fragments and as virtually ubiquitous microplastic particles (microbeads, "nurdles," and fibers) (Fig. 2A) (*25*–*27*), which are dispersed by both physical and biological processes. The decay resistance and chemistry of most plastics suggest that they will leave identifiable fossil and geochemical records.

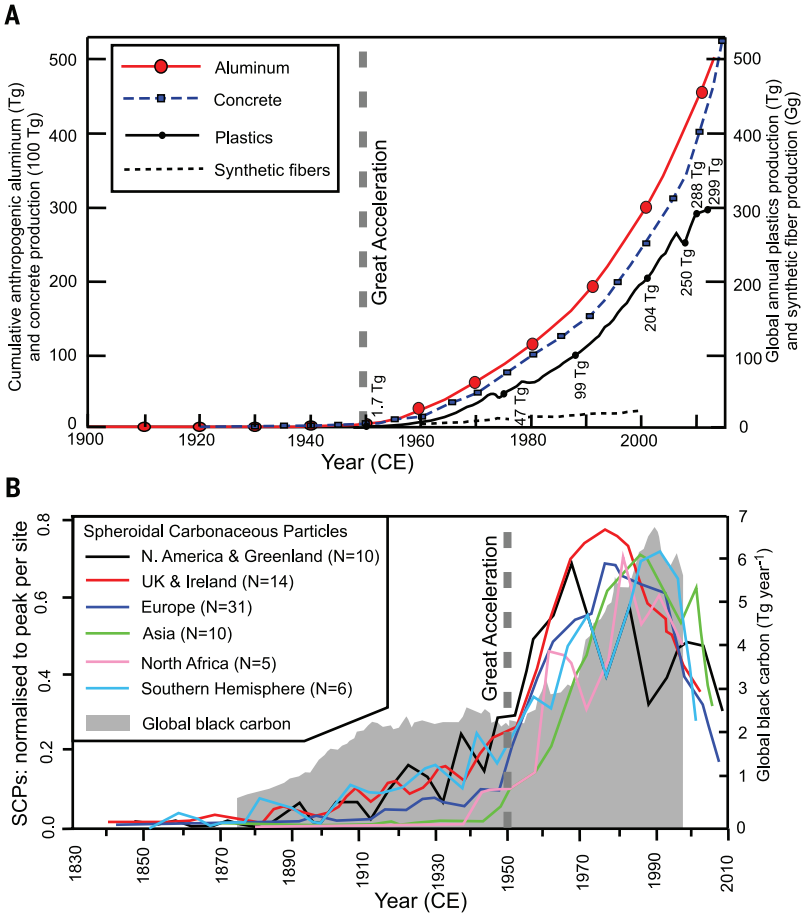

Fig. 2. The production of selected new anthropogenic materials. (**A**) Cumulative growth of manufactured aluminum in the surface environment [adapted from data in (*23*), assuming a recycling rate of 50%]; cumulative growth of production of concrete, assuming that most cement goes into concrete and that ~15% of average concrete mass is cement [from (*22*), derived from U.S. Geological Survey global cement production statistics]; annual growth of plastics production [from (*24*)]; and synthetic fibers production [from (*26*)]. (**B**) Global mid–20th century rise and late–20th century spike in SPCs, normalized to the peak value in each lake core [modified from (*32*)], and global black carbon from available annual fossil fuel consumption data for 1875–1999 CE (*30*). Numbers of lake cores for each region are indicated.

These and other new materials are commonly shaped into abundant artifacts with the capacity to be preserved in and to help date future geological deposits. Analogous to biotic fossil remains, these so-called technofossils (*28*) provide annual to decadal stratigraphic resolution (*19*, *22*)—far greater than what can be obtained from the first and last appearances of fossil taxa, which have traditionally been the most common means of correlating stratal sections (*29*).

Fossil fuel combustion disseminates unburned particles as black carbon, inorganic ash spheres (IASs), and spherical carbonaceous particles (SCPs). Black carbon increased markedly toward the end of the 19th century, and especially after ~1970 CE, with a peak at 6.7 Tg $year^{-1}$ in ~1990 CE (Fig. 2B) (*30*). IASs, which are locally detectable in the stratigraphic record starting in the 16th century, increased across Britain, Scandinavia, and North America from ~1835 to 1960 CE (*31*). SCPs, which were first recorded at various sites in the UK from 1830 to 1860 CE, show a near-synchronous global increase around 1950 CE, with peak signatures from the 1960s to the 1990s (Fig. 2B) (*32*, *33*). Black carbon, IASs, and SCPs, being airborne particulates, leave a permanent marker within both sediments and glacial ice. An ancient analog is the marker horizon of carbon impact spherules at the Cretaceous-Paleogene boundary, which was created by the Chicxulub bolide impact (*34*). These low-temperature natural spherules, which are readily distinguishable from high-temperature industrial SCPs, demonstrate the likely persistence of SCPs as a stratigraphic marker (*32*).

Modification of sedimentary processes

The transformation of more than 50% of Earth's land surface for human use (*35*) has generated anthropogenically modified materials that extend across multiple terrestrial settings. They are most ubiquitous in anthropogenic (artificial) deposits such as landfills, urban structures, and mine tailings,

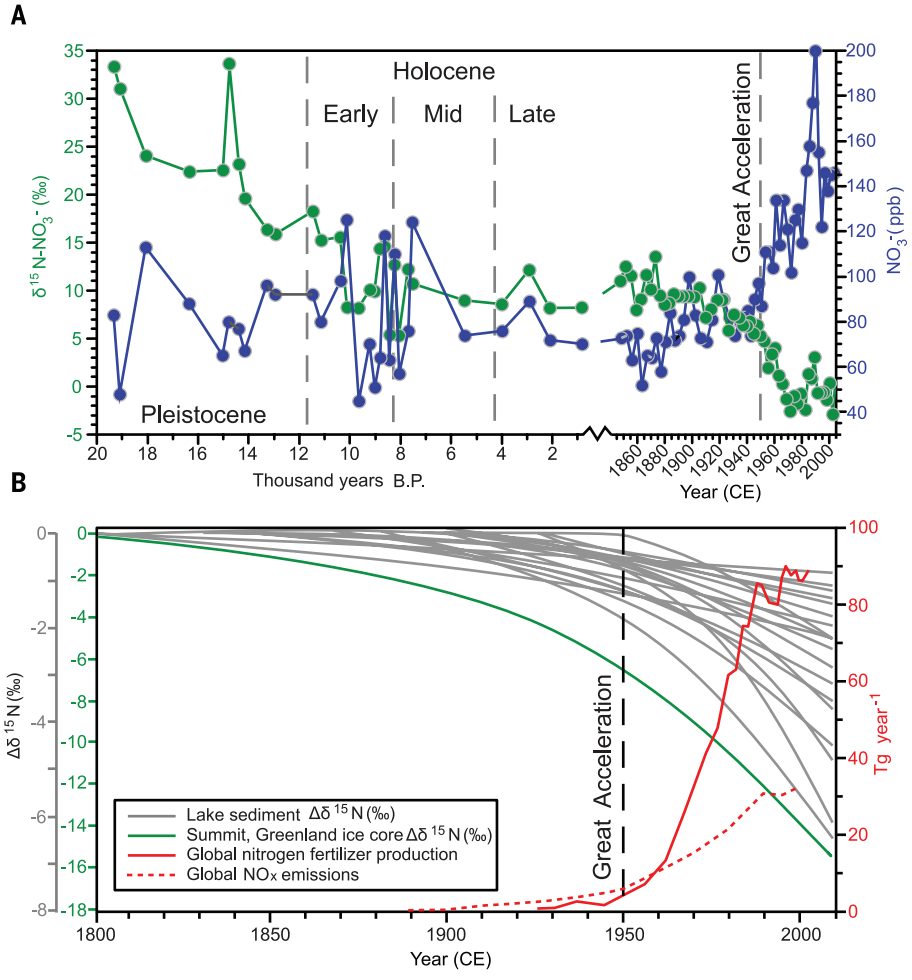

Fig. 3. Perturbations of the nitrogen cycle since the start of the Late Pleistocene. (**A**) Coevolution of ice core NO_3^- (blue) and $\delta^{15}N$ for NO_3^- (green) from the Late Pleistocene to the present, obtained by splicing data from two cores from Summit, Greenland (72.5°N, 38.4°W, 3200 m above sea level) (*55*–*57*). (**B**) Power functions fitted to $\delta^{15}N$ data from lake sediments (gray lines, representing 25 remote Northern Hemisphere sites) and ice cores (green line), expressed as departures ($\Delta\delta^{15}N$) from preindustrial baseline values (*53*, *54*). These isotopic trends are shown alongside annual rates of reactive N production from agricultural fertilizer (solid red line) and NO_x emissions from fossil fuel combustion (dashed red line) (*51*).

in addition to soils associated with cultivation. This influence is increasingly extending into the oceans, both directly, through coastal reclamation works, sediment reworking by trawler fishing, and the extraction of sand and gravel; and indirectly, through changes in coastal sedimentary facies in response to rising sea levels, the eutrophication of coastal environments, and coral bleaching events (*36*). Human land alteration also increasingly extends into the subsurface via drilling into Earth's crust to extract minerals, to store wastes, or to host utilities (*37*). Mineral extraction alone accounts for the displacement of ~57,000 Tg $year^{-1}$ of sediments, exceeding the current rate of riverborne sediment transport by almost a factor of 3 (*38*).

Human activities have also modified sedimentary processes sufficiently to leave clear expressions in river, lake, windblown, and glacial deposits that are often far removed from direct point sources (*36*). Sediment fluxes in many fluvial systems increased historically because of greater deforestation, livestock grazing, and cropland development. Clearing of primary forests for agriculture, usually by burning, began in Early to Mid-Holocene times, especially in temperate woodland biomes; this shifted diverse primary forest communities toward domesticates and early successional species and left widespread, time-transgressive geological traces that include profound shifts in plant and animal remains, charcoal, and sediment deposits from soil erosion (*39*, *40*). In recent decades, secondary forests have recovered across much of the temperate zone, and forest clearing has shifted toward tropical regions; for example, periods of rapid deforestation have occurred in Amazonia, Indonesia, and other regions in Asia and Africa in response to economic and governance dynamics (*41*). The construction of mountain roads in these tropical regions is resulting in substantial surface erosion and landslides (*42*).

Extensive sediment retention behind dams constructed across major river systems has created a global signal more rapidly. Most dams were built in the past 60 years, at an average rate of more than one large dam per day (*8*, *9*), and each will last 50 to 200 years, interrupting sediment transport to the oceans. The reduced sediment flux to major deltas, combined with increasing extraction of groundwater, hydrocarbons, and sediments (for aggregates), has caused many large deltas to subside more quickly, a process beginning in the 1930s (*43*) at rates faster than modern eustatic sea-level rise. Coastal retreat is an inevitable result. These various signals, which are abrupt on geological time scales, are diachronous at the decadal scale.

Changed geochemical signatures in recent sediments and ice

Anthropogenic materials and the human influence on sedimentary environments have a near-global expression, but geochemical signatures, particularly those with airborne transport pathways, reach all global environments, including the ~12% of Earth's surface that is permanently covered by ice. Among the many distinct geochemical signatures that human activities have introduced into the sedimentary record are elevated concentrations of polyaromatic hydrocarbons, polychlorinated biphenyls, and diverse pesticide residues, each beginning at ~1945 to 1950 CE (*44*–*47*). Lead smelting during Roman times resulted in a distinctive local marker of increased $^{207/206}Pb$ ratios, a signal that changed globally in the early 20th century as a result of vehicles powered by leaded gasoline (*47*). This illustrates that some anthropogenic geochemical signatures may vary geographically in their first appearance but nevertheless become useful as global markers when they rapidly spread as the result of new technologies in the mid-20th century.

Nitrogen (N) and phosphorus (P) in soils have doubled in the past century because of increased fertilizer use (*8*, *9*, *48*). Production of P by mining, now at ~23.5 Tg $year^{-1}$, is twice the background weathering rate of P released during the Holocene (*49*). Human processes are argued to have had the largest impact on the nitrogen cycle for some 2.5 billion years (*48*). The use of the Haber-Bosch process from 1913 CE onward has increased the amount of reactive N in the Earth system by 120% relative to the Holocene baseline (*50*), accompanied by an increased flux of nitrogen oxides (NO_x) from the combustion of fossil fuels (Fig. 3) (*51*).

These changes have stratigraphic consequences. The influx of excess reactive N and P to lakes and seas has led to seasonal oxygen deficiency, affecting local microbiota and, in extreme cases, increasing mortality in macrobiota (*52*). Northern Hemisphere lakes show increasingly depleted $\delta^{15}N$ values (*53*, *54*) beginning at ~1895 CE (Fig. 3B) and accelerating over the past 60 years. In Greenland ice, $\delta^{15}N$ values during the Late Pleistocene glaciation show a gradual marked decline to a preindustrial Holocene norm [mean, 9.7 per mil (‰) in the GISP2 (Greenland Ice Sheet Project 2) ice core; (*55*)]; they decline again and more rapidly starting at ~1850 CE, with the greatest decline occurring between 1950 and 1980 CE (Fig. 3A) (*47*, *56*). The main phase of the increase in nitrate

levels also occurred between 1950 and 1980 CE (Fig. 3, A and B), culminating in values higher than any recorded for the previous 100,000 years (*57*). These markers are distinct from Holocene and Late Pleistocene background levels.

Industrial metals such as cadmium, chromium, copper, mercury, nickel, lead, and zinc have been widely and rapidly dispersed since the mid-20th century, although many show much earlier and markedly diachronous signals associated with the expansion of mineral extraction and processing (*47*, *58*). An acceleration in the use of trace metals and rare earth elements (REEs) began after World War II, resulting in an increase in the amounts mined, a global pattern of dispersion in the environment, and novel stoichiometric ratios. Metals and their derivatives are spread through inadequate processing, a lack of recycling and reuse, or loss during everyday use. For example, platinum, rhodium, and palladium lost from automotive catalytic converters accumulate preferentially in soils adjacent to highways (*59*).

Radiogenic signatures and radionuclides in sediments and ice

Potentially the most widespread and globally synchronous anthropogenic signal is the fallout from nuclear weapons testing. The start of the Anthropocene may thus be defined by a Global Standard Stratigraphic Age (GSSA) coinciding with detonation of the Trinity atomic device at Alamogordo, New Mexico, on 16 July 1945 CE (*10*). However, fallout from 1945 to 1951 CE came from fission devices and resulted in only localized deposition of radionuclides. Aggregate yields from thermonuclear weapon tests that began in 1952 CE and peaked in 1961–1962 CE left a clear and global signature, concentrated in the mid-latitudes and highest in the Northern Hemisphere, where most of the testing occurred (Fig. 4B) (*47*, *60*, *61*). Useful potential markers include excess ^{14}C, an isotope common in nature, and ^{239}Pu, a naturally rare isotope. The Holocene segment of the IntCal13 $\Delta^{14}C$ curve, corrected for radiogenic decay ($F^{14}C$), shows past natural fluctuations and a linear normalized decrease from 1.2 to ~1.0 during the Holocene, related to changes in the ^{14}C production rate and global carbon cycling (*62*) (Fig. 4A). An excess of ^{14}C forms a sharp bomb spike, starting in 1954 (*10*) and peaking in 1964 CE (*5*), both of which years have been suggested as potential markers for the start of the Anthropocene. However, the peak is diachronous between hemispheres (Fig. 4B) (*63*). ^{239}Pu, with its long half-life (24,110 years), low solubility, and high particle reactivity, particularly in marine sediments, may be the most suitable radioisotope for marking the start of the Anthropocene (*61*, *64*). The appearance of a ^{239}Pu fallout signature in 1951 CE, peaking in 1963–1964 CE (Fig. 4B), will be identifiable in sediments and ice for the next 100,000 years (*61*, *64*); it will decay to a layer enriched in ^{235}U and, ultimately, stable ^{207}Pb.

Carbon cycle evidence from ice cores

Atmospheric CO_2, now above 400 parts per million (ppm), was emitted into the atmosphere

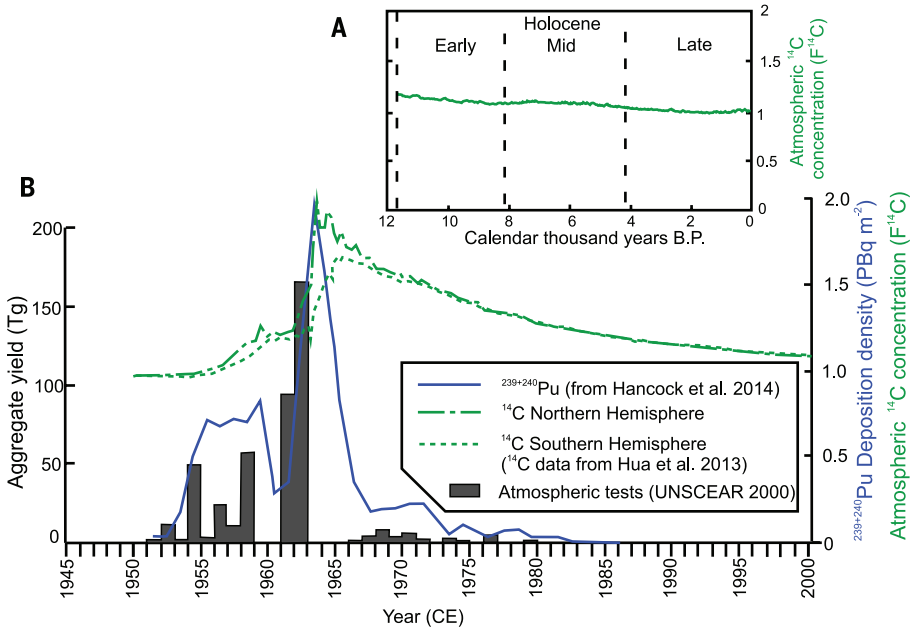

Fig. 4. Radiogenic fallout signals as a marker of the Anthropocene. (**A**) Age-corrected atmospheric ^{14}C concentration ($F^{14}C$) based on the IntCal13 curve, before nuclear testing (*62*). (**B**) The atmospheric concentration of ^{14}C ($F^{14}C$) (*63*) and $^{239+240}Pu$ (*64*) radiogenic fallout from nuclear weapons testing (PBq, petabecquerel), plotted against annual aggregate atmospheric weapons test yields (*60*).

from 1999 to 2010 CE ~100 times as fast as the most rapid emission during the last glacial termination (*65*), and concentrations have exceeded Holocene levels since at least 1850 CE (Fig. 5). During the Late Pleistocene to Early Holocene, atmospheric CO_2 preserved in air bubbles in Antarctic glacial ice underwent a stepped 70-ppm rise over 6000 years (*66*, *67*), or an average rise of 1 ppm per ~85 years. Subsequent Holocene CO_2 concentrations remained approximately stable (Fig. 5A). CO_2 concentrations showed a slightly decreasing trend from ~11,000 to 8000 yr B.P. This changed to a slightly rising trend, with a very slow rise of 260 to 285 ppm from ~7000 yr B.P. to the start of the Industrial Revolution (Fig. 5A), a change which has been ascribed to early human agriculture by some (*3*), albeit controversially (*66*). Thus, the putative anthropogenic impact on atmospheric CO_2 at this time was both gradual and much less than subsequent changes over the past 200 years. The events at 8200 and 4200 yr B.P. that mark the proposed Mid- and Late Holocene sub-epochs, respectively (*13*), are not associated with any major change in CO_2 concentrations. In sharp contrast, modern rates of atmospheric C emission (~9 Pg year^{-1}) are probably the highest of the Cenozoic era (the past 65 Ma), likely surpassing even those of the Paleocene-Eocene Thermal Maximum (*68*).

The Antarctic ice core record shows steady enrichment in $\delta^{13}C$ values from the Late Pleistocene to the Mid-Holocene time (*66*, *67*), reflecting carbon uptake by the terrestrial biosphere and carbon release from oceans (Fig. 5A) (*66*), but it shows no changes at the proposed Mid- and Late Holocene sub-epoch boundaries. The Antarctic ice record shows approximately constant CO_2 and $\delta^{13}C$ values continuing from 1200 to 1600 CE (Fig. 5B) (*69*). A short-lived dip at ~1610 CE of about 10 ppm in the CO_2 curve, with a synchronous minor enrichment in $\delta^{13}C$, has been proposed as a marker for the start of the Anthropocene (*5*), although these fluctuations do not exceed natural Holocene variability (Fig. 5A) (*70*). The most pronounced change in atmospheric CO_2 concentrations is the ~120-ppm increase since ~1850 CE (Fig. 5, B and C) (*69*), including a rise of ~2 ppm year^{-1} over the past 50 years. This coincides with a steep fall (>2‰) in $\delta^{13}C$ atmospheric CO_2 to ~−8.5‰ (Fig. 5C) (*69*), due to an increase in ^{12}C from burning fossil hydrocarbons. This isotopic signature also forms part of the permanent record, because it is inscribed in archives such as tree rings, limestones, and calcareous fossils.

Ice core records show atmospheric methane (CH_4) concentrations ranging from 590 to 760 parts per billion (ppb) through much of the Holocene (*71*–*75*), up to 1700 CE. This is followed by an unprecedented increase to 1700 ppb by 2004 CE (*72*), some 900 ppb higher than what has been recorded in Antarctic ice cores at any time in the past 800,000 years (*76*), with levels rising above Mid- to Late Pleistocene and Holocene maxima by ~1875 CE (Fig. 5D). The $\delta^{13}C$ curve for CH_4 shows a marked decrease of ~1.5‰ from ~1500 to 1700 CE, perhaps in response to reduced biomass burning (*72*), and a subsequent abrupt rise from ~1875 CE to the present of ~2.5‰, reflecting increasing pyrogenic emissions.

Climate change and rates of sea-level change since the end of the last Ice Age

The proposed subdivision of the Holocene epoch into sub-epochs is based on proxy signals for

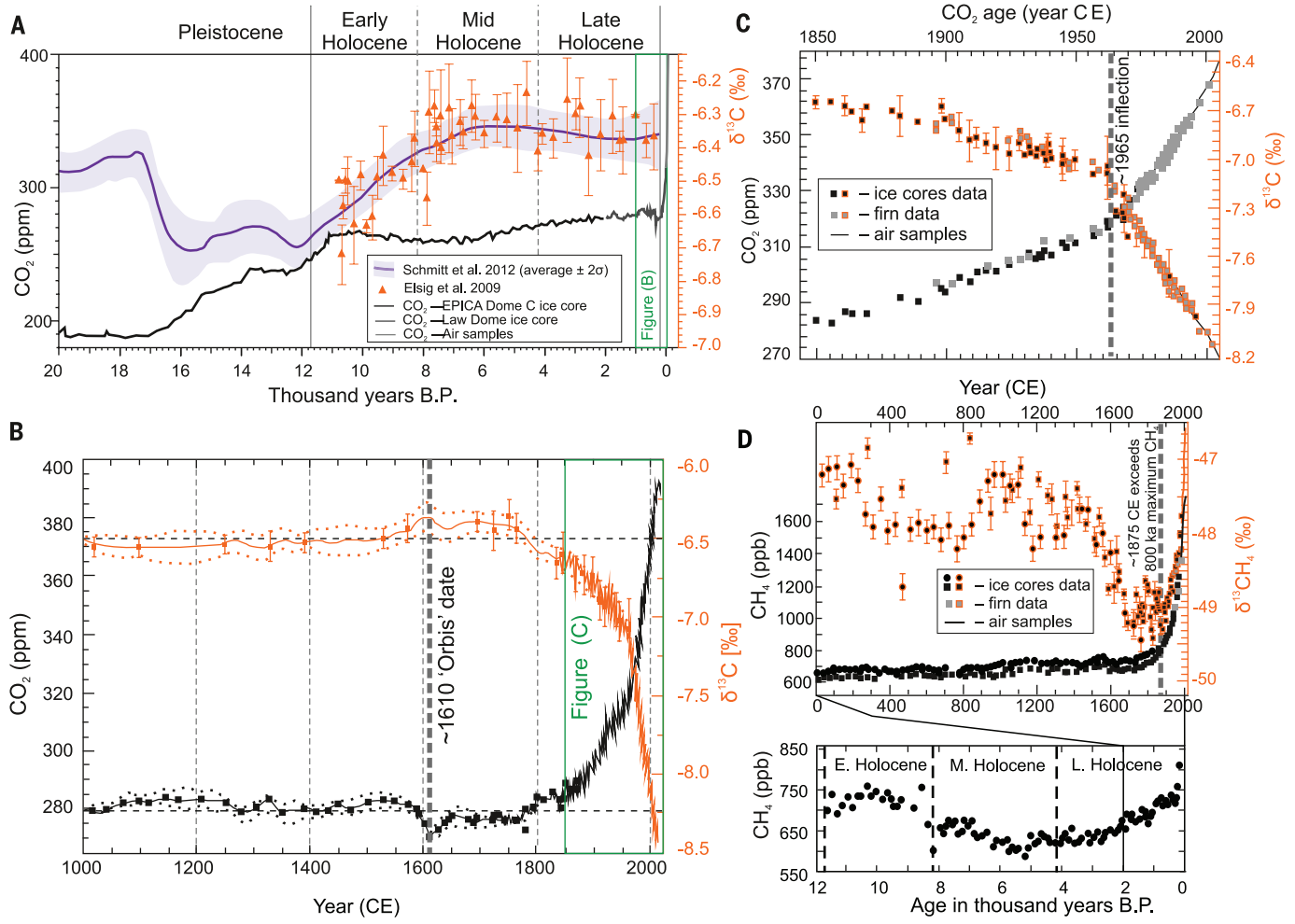

Fig. 5. Perturbations of the carbon cycle evidenced by glaciochemical CO_2 and CH_4 concentrations and carbon isotopic ratios. (**A**) Atmospheric CO_2 from the Antarctic Law Dome and EPICA (European Project for Ice Coring in Antarctica) Dome C ice cores, with observational data [from (*69*) and references therein] and $\delta^{13}C$ from atmospheric CO_2 (*66*, *67*). (**B**) CO_2 concentration and $\delta^{13}C$ from atmospheric CO_2 from the Law Dome ice cores (*69*) for the time interval indicated by the green rectangle in (A), showing a 10-ppm dip in CO_2 recognized as the Orbis event (*5*). (**C**) CO_2 concentration and $\delta^{13}C$ from atmospheric CO_2 from the Law Dome ice core, firn data, and air samples (*69*) for the time period indicated by the green rectangle in (B), showing inflections at ~1965 CE. (**D**) Antarctic (squares) and Greenland (circles) ice core and firn records for CH_4 concentration and $\delta^{13}C$ for atmospheric CH_4 for the past two millennia (*72*–*75*) (top), with Greenland ice core CH_4 data for the Holocene (bottom) (*71*).

climate change (*13*). Greenland ice cores show abrupt brief cooling events, expressed as decreases in $\delta^{18}O$ values, at 11,400, 9300, and 8200 yr B.P. (Fig. 6A) (*77*), the lattermost of which would define the start of the proposed Middle Holocene (*13*). These events are less apparent in equivalent Antarctic ice cores (Fig. 6A) (*78*). A 4200–yr B.P. climate shift, which would mark the start of the proposed Upper Holocene (*13*), is not expressed in these curves. The overall trend during the Mid- to Late Holocene was of gradual cooling (Fig. 6B), which culminated in the Little Ice Age from 1250 to 1800 CE (Fig. 6C). The cooling followed an orbitally related insolation decline, with small fluctuations representing changes in solar intensity, which are controlled by modulators such as the 208-year Suess cycle (*79*). Given that the orbital trend is continuing, Earth should still be cooling. However, increased anthropogenic emissions of greenhouse gases have instead caused the planet to warm abnormally fast, overriding the orbitally induced climate cycle.

The shift to climate warming (Fig. 6C) (*80*, *81*) is first indicated by a slight change toward less negative $\delta^{18}O$ in Greenland ice starting at ~1900 CE (Fig. 6A). This shift is well outside the natural envelope of declining temperature change for the past 1400 years (Fig. 6C), mainly due to greenhouse gases released from burning of fossil fuels and deforestation (*79*, *81*, *82*). An average global temperature increase of 0.6° to 0.9°C between 1906 and 2005 CE, with a doubling of the rate of warming over the past 50 years (*83*), is beginning to exceed Holocene natural variability (Figs. 6, B and C) in the Northern Hemisphere and is already above Holocene maxima in the tropics and Southern Hemisphere. The change in $\delta^{18}O$ since 1900 CE in Greenland ice cores (Fig. 6A) is of a smaller magnitude than that of the 8200–yr B.P. cooling event marking the base of the proposed Middle Holocene, but it is larger than that at the base of the proposed Upper Holocene.

Average global sea levels are currently higher than at any point within the past ~115,000 years (*84*), since the termination of the last interglacial of the Pleistocene epoch. The physical expression of sea-level change in the geological record is the displacement of sedimentary facies, for which the rate of change of sea level relative to rates of sediment accumulation and subsidence due to compaction is crucial. For example, rapid sea-level rise can cause delta tops to flood, producing sharp transitions into overlying relatively deep marine and anoxic muds, marking a flooding surface. By the time of peak sea level, the rate of rise is slower, and fluvial systems can resupply sediment to reestablish deltas as progradational successions building up and out from the coast.

Very high rates of sea-level change (>40 mm $year^{-1}$) occurred at about 14,000 to 14,300 yr B.P.

during the Bølling warming event, associated with rapid ice sheet disintegration during the transition between the last glacial phase and the current interglacial phase (*85*). The high rate of rise caused widespread inundation of coastal areas, and sedimentary facies back-stepped (retrograded landward).

The past 7000 years of the Holocene epoch, when ice volumes stabilized near present-day values, provide the baseline for discussion of anthropogenic contributions. Relative sea-level records indicate that from ~7000 to 3000 yr B.P., global mean sea level rose ~2 to 3 m to nearly present-day levels (*84*). Based on local sea-level records spanning the past 2000 years, there is medium confidence that fluctuations in global mean sea level during this interval have not exceeded ~0.25 m on time scales of a few hundred years. As a consequence, coastlines have been more or less fixed, and sediment accumulation within beaches, tidal flats, and deltas has been progradational.

The most robust signal, captured in salt marsh records from both the Northern and Southern Hemispheres, supports a transition from relatively low rates of change during the Late Holocene (<1 mm year^{-1}) to modern rates of 3.2 ± 0.4 mm year^{-1} from 1993 to 2010 CE (*84*). By combining paleo–sea-level records with tide gauge records at the same localities, it is clear that sea level began to rise above the Late Holocene background rate between 1905 and 1945 CE (*86*); if continued, this trend will lead to a return to dominantly retrogradational shifts in sedimentary facies along coastal zones. However, reconstructions from the U.S. Atlantic coast suggest that the rate of sea-level rise is not linear (*87*). A rate of 0.06 to 0.39 mm year^{-1} during the 18th century shows a change between 1827 and 1860 CE to a late–19th century rate of 1.22 to 1.53 mm year^{-1}, and a secondary and less pronounced change from 1924 to 1943 CE to a subsequent late 20th century rate of 1.9 to 2.22 mm year^{-1} (*87*). The timing of the inflections in this rising sea-level curve matches, with a delay of about a decade, the stepped changes in CO_2 concentrations (Fig. 5C).

Compared with other stratigraphic changes described above, the climate and sea-level signals of the Anthropocene are not yet as strongly expressed, in part because they reflect the combined effects of fast and slow climate feedback mechanisms. However, given that anthropogenic forcing is driving these changes, they are likely to exceed the envelope of not only Holocene but Quaternary baseline conditions (*79*). Projections of continued warming due to greenhouse gases (*82*), even with reductions below current emissions levels, suggest that by 2070, Earth will be at its hottest since the last interglacial period ~125,000 years ago [Figure 5.3 in (*82*)]—and hence hotter than it has been for most, if not all, of the time since modern humans emerged as a species 200,000 years ago.

Changes in global average surface temperature and increases in sea level are manifestations of changes in the surface energy balance. Perhaps a more fundamental measure of human perturbation of the climate system is the human-driven change to the planetary energy balance at Earth's surface, as measured by changes in radiative forcing. Human activities, primarily the burning of fossil hydrocarbons, have increased the radiative forcing by 2.29 (1.13 to 3.33) W m^{-2} relative to 1750 CE, with a more rapid increase since 1970 CE than during prior decades. Overwhelming the natural changes in radiative forcing during the Late Holocene (solar irradiance and volcanic aerosols), which are estimated to be 0.05 (0.00 to 0.10) W m^{-2} (*82*), the anthropogenic energy imbalance is poised to amplify stratigraphic signals associated with warming and sea-level rise.

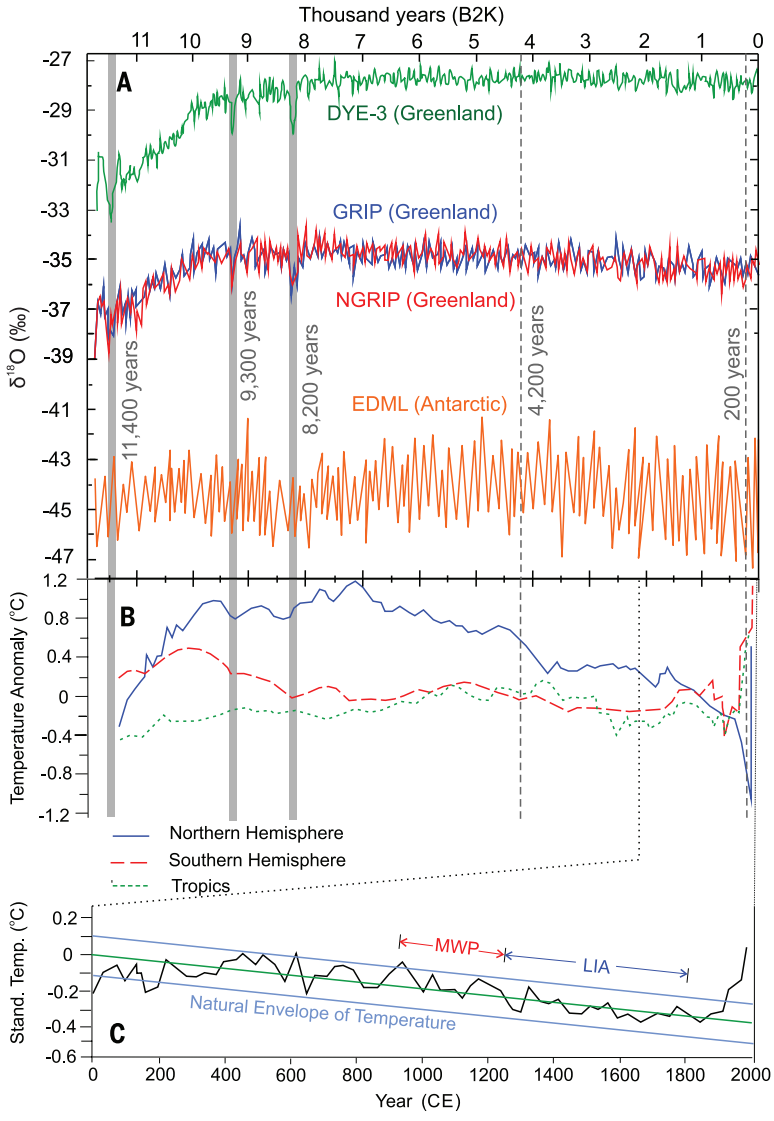

Fig. 6. Climate variations during the Holocene, indicated by oxygen isotopic ratios and modeled temperature variations. (**A**) Holocene profiles of $\delta^{18}O$ from three Greenland ice cores, with three short-duration cooling events indicated by shading (*77*), shown with an Antarctic ice core profile for comparison (EDML, EPICA Dronning Maud Land Ice Core) (*78*). (**B**) Temperature reconstructions for the Holocene and global temperatures for the past 2000 years [B2K, before 2000 CE (*81*)]. (**C**) Standardized global mean temperature for the past 2000 years, represented by 30-year means (*80*, *81*), showing the natural temperature envelope for the past 2000 years [based on (*79*)]. The Little Ice Age (LIA) and the Medieval Warm Period (MWP, also known as the Medieval Climatic Anomaly) of the Northern Hemisphere are indicated.

Biotic change as an indicator of the Anthropocene

Most Phanerozoic time intervals are defined using either the first or last appearance of key fossils (*29*). Evolution and extinction rates are mostly too slow and diachronous to provide an obvious biological marker for the start of the Anthropocene, but important biotic change has taken place recently (*88*). Although Earth still retains most of the species that were present at the start

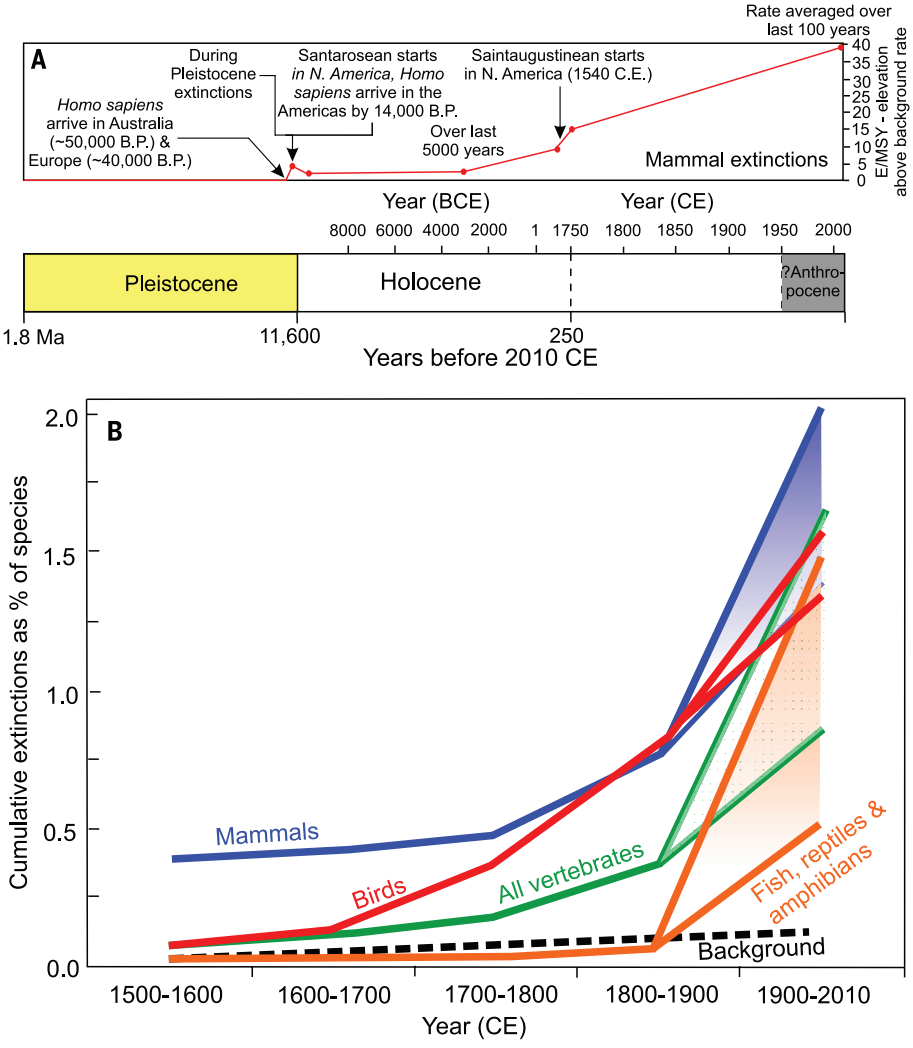

Fig. 7. Increased rates of vertebrate extinctions. (**A**) The approximate rise in mammal extinction rates calculated over varying time intervals, as extended backward from 2010 CE (Ma, millions of years ago). Lines indicate the amount by which extinction rates exceed 1.8 extinctions per million species years (E/MSY) [see (*89*); sourced from (*22*)]. (**B**) Cumulative vertebrate species extinctions as a percentage of total species, with ranges (shaded) between conservative rates (including extinctions, extinctions in the wild, and possible extinctions) and lower highly conservative rates (verified extinctions only). A background rate of 2.0 E/MSY is shown for comparison [after (*89*)].

of the Holocene, even conservative estimates of extinction rates since 1500 CE are far above mean per-million-year background rates (Fig. 7A), with a notable increase from the 19th century onward (*89*) (Fig. 7B). Current trends of habitat loss and overexploitation, if maintained, would push Earth into the sixth mass extinction event (with ~75% of species extinct) in the next few centuries (*90*), a process that is probably already underway (*89*).

Irrespective of the number of extinctions, species assemblages and relative abundances have been altered worldwide. This is especially true in recent decades because of geologically unprecedented transglobal species invasions and biological assemblage changes associated with agriculture on land and fishing in the sea (*91*). The terrestrial biosphere has undergone a dramatic modification from 1700 CE, when almost 50% of the global ice-free land area was wild and only ~5% was intensively used by humans, to 2000 CE, when the respective percentages were 25% and 55% (*92*). The paleontological expression of these assemblages will markedly differ from the typical Holocene fossil record as recognizable, novel biostratigraphic zones (*93*), and the new assemblages of species have already permanently reconfigured Earth's biological trajectory. These biotic changes are not synchronous, but they accelerated after 1500 CE on land (*94*) and in the seas, affecting both micro- and macrobiota (*52*).

The case for a new epoch

The stratigraphic signatures described above (Fig. 1) are either entirely novel with respect to those found in the Holocene and preexisting epochs or quantitatively outside the range of variation of the proposed Holocene subdivisions. Furthermore, most proximate forcings of these signatures are currently accelerating. These distinctive attributes of the recent geological record support the formalization of the Anthropocene as a stratigraphic entity equivalent to other formally defined geological epochs. The boundary should therefore be placed following the procedures of the International Commission on Stratigraphy.

If such formalization is to be achieved, however, further work is required. First, it needs to be determined how the Anthropocene is to be defined, whether by GSSA (calendar age), GSSP [reference point in a stratal section (*10*)], or a combination of both. Whichever is ultimately chosen, the location and comparative analyses of candidate stratotype sections are necessary, not least to explore how effectively any chosen levels may be traced and correlated within stratal archives. This is linked to the question of when exactly the Anthropocene may be determined to begin. Our analysis is more consistent with a beginning in the mid-20th century, and a number of options have already been suggested within that interval, ranging from 1945 to 1964 CE (*5*, *10*). There is also the question, which is still under debate, of whether it is helpful to formalize the Anthropocene or better to leave it as an informal, albeit solidly founded, geological time term, as the Precambrian and Tertiary currently are (*95*). This is a complex question, in part because, quite unlike other subdivisions of geological time, the implications of formalizing the Anthropocene reach well beyond the geological community. Not only would this represent the first instance of a new epoch having been witnessed firsthand by advanced human societies, it would be one stemming from the consequences of their own doing.

REFERENCES AND NOTES

1. W. Steffen, J. Grinevald, P. Crutzen, J. McNeill, The Anthropocene: Conceptual and historical perspectives. *Philos. Trans. R. Soc. London Ser. A* **369**, 842–867 (2011). doi: 10.1098/rsta.2010.0327; pmid: 21282150
2. A. Malm, A. Hornborg, The geology of mankind? A critique of the Anthropocene narrative. *Anthropocene Rev.* **1**, 62–69 (2014). doi: 10.1177/2053019613516291
3. W. F. Ruddiman, The anthropogenic greenhouse era began thousands of years ago. *Clim. Change* **61**, 261–293 (2003). doi: 10.1023/B:CLIM.0000004577.17928.fa
4. W. F. Ruddiman, The Anthropocene. *Annu. Rev. Earth Planet. Sci.* **41**, 45–68 (2013). doi: 10.1146/annurev-earth-050212-123944
5. S. L. Lewis, M. A. Maslin, Defining the Anthropocene. *Nature* **519**, 171–180 (2015). doi: 10.1038/nature14258; pmid: 25762280
6. P. J. Crutzen, Geology of mankind. *Nature* **415**, 23 (2002). doi: 10.1038/415023a; pmid: 11780095
7. J. Zalasiewicz *et al.*, Are we now living in the Anthropocene? *GSA Today* **18**, 4–8 (2008). doi: 10.1130/GSAT01802A.1
8. W. Steffen, J. Crutzen, J. R. McNeill, The Anthropocene: Are humans now overwhelming the great forces of nature? *Ambio* **36**, 614–621 (2007). doi: 10.1579/0044-7447(2007)36[614:TAAHNO]2.0.CO;2; pmid: 18240674
9. W. Steffen, W. Broadgate, L. Deutsch, O. Gaffney, C. Ludwig, The trajectory of the Anthropocene: The Great Acceleration. *Anthropocene Rev.* **2**, 81–98 (2015). doi: 10.1177/2053019614564785
10. J. Zalasiewicz *et al.*, When did the Anthropocene begin? A mid-twentieth century boundary level is stratigraphically optimal. *Quat. Int.* **383**, 196–203 (2015). doi: 10.1016/j.quaint.2014.11.045
11. B. Pillans, P. Gibbard, "The Quaternary Period," in *The Geologic Time Scale*, F. M. Gradstein, J. Ogg, M. Schmitz, G. Ogg, Eds. (Elsevier B.V., 2012), pp. 979–1010.
12. J. Remane *et al.*, Guidelines for the establishment of global chronostratigraphic standards by the International Commission on Stratigraphy (ICS). *Episodes* **19**, 77–81 (1996).

13. M. J. C. Walker *et al*., Formal subdivision of the Holocene Series/Epoch: A discussion paper by a Working Group of INTIMATE (Integration of ice-core, marine and terrestrial records) and the Subcommission on Quaternary Stratigraphy (International Commission on Stratigraphy). *J. Quat. Sci.* **27**, 649–659 (2012).
14. I. McDougall, F. H. Brown, J. G. Fleagle, Stratigraphic placement and age of modern humans from Kibish, Ethiopia. *Nature* **433**, 733–736 (2005). doi: 10.1038/nature03258; pmid: 15716951
15. "Population," *History Database of the Global Environment* (Netherlands Environmental Assessment Agency, Bilthoven, Netherlands, 2013); http://themasites.pbl.nl/tridion/en/themasites/hyde/basicdrivingfactors/population/index-2.html.
16. K. Klein Goldewijk, A. Beusen, P. Janssen, Long-term dynamic modeling of global population and built-up area in a spatially explicit way: HYDE 3.1. *Holocene* **20**, 565–573 (2010). doi: 10.1177/0959683609356587
17. A. D. Barnosky *et al*., Prelude to the Anthropocene: Two new North American Land Mammal Ages (NALMAs). *Anthropocene Rev.* **1**, 225–242 (2014). doi: 10.1177/2053019614547433
18. C. N. Waters, J. A. Zalasiewicz, M. Williams, M. A. Ellis, A. M. Snelling, "A stratigraphical basis for the Anthropocene?," in *A Stratigraphical Basis for the Anthropocene*, C. N. Waters, J. A. Zalasiewicz, M. Williams, M. A. Ellis, A. M. Snelling, Eds. (Geological Society, London, 2014), pp. 1–21.
19. J. R. Ford, S. J. Price, A. H. Cooper, C. N. Waters, "An assessment of lithostratigraphy for anthropogenic deposits," in *A Stratigraphical Basis for the Anthropocene*, C. N. Waters, J. A. Zalasiewicz, M. Williams, M. A. Ellis, A. M. Snelling, Eds. (Geological Society, London, 2014), pp. 55–89.
20. J. Zalasiewicz, R. Kryza, M. Williams, "The mineral signature of the Anthropocene," in *A Stratigraphical Basis for the Anthropocene*, C. N. Waters, J. A. Zalasiewicz, M. Williams, M. A. Ellis, A. M. Snelling, Eds. (Geological Society, London, 2014), pp. 109–117.
21. M. Edgeworth *et al*., Diachronous beginnings of the Anthropocene: The lower bounding surface of anthropogenic deposits. *Anthropocene Rev.* **2**, 33–58 (2015). doi: 10.1177/2053019614565394
22. J. Zalasiewicz, M. Williams, C. N. Waters, A. D. Barnosky, P. Haff, "Anthropocene," in *Origins*, O. Seberg, D. A. Harper, Eds. (Cambridge Univ. Press, in press).
23. U.S. Geological Survey, in *Historical Statistics for Mineral and Material Commodities in the United States*, T. D. Kelly, G. R. Matos, Eds. (U.S. Geological Survey Data Series 140, U.S. Geological Survey, 2010); http://minerals.usgs.gov/minerals/pubs/historical-statistics/cement-use.pdf.
24. *Plastics – the Facts 2013. An Analysis of European Latest Plastics Production, Demand and Waste Data* (PlasticsEurope, 2013); www.plasticseurope.org/documents/document/20131014095824-final_plastics_the_facts_2013_published_october2013.pdf.
25. P. L. Corcoran, Benthic plastic debris in marine and fresh water environments. *Environ. Sci. Processes Impacts* **17**, 1363–1369 (2015). doi: 10.1039/C5EM00188A; pmid: 26129903
26. R. C. Thompson *et al*., Lost at sea: Where is all the plastic? *Science* **304**, 838 (2004). doi: 10.1126/science.1094559; pmid: 15131299
27. J. R. Jambeck *et al*., Plastic waste inputs from land into the ocean. *Science* **347**, 768–771 (2015). doi: 10.1126/science.1260352; pmid: 25678662
28. J. Zalasiewicz, M. Williams, C. N. Waters, A. D. Barnosky, P. Haff, The technofossil record of humans. *Anthropocene Rev.* **1**, 34–43 (2014). doi: 10.1177/2053019613514953
29. A. G. Smith, T. Barry, P. Bown, J. Cope, A. Gale, P. L. Gibbard, J. Gregory, M. Hounslow, D. Kemp, R. Knox, J. Marshall, M. Oates, P. Rawson, J. Powell, C. Waters, "GSSPs, global stratigraphy and correlation," in *Strata and Time: Probing the Gaps in Our Understanding*, D. G. Smith, R. J. Bailey, P. M. Burgess, A. J. Fraser, Eds. (Special Publication 404, Geological Society, London, 2014), pp. 37–67.
30. T. Novakov *et al*., Large historical changes of fossil-fuel black carbon aerosols. *Geophys. Res. Lett.* **30**, 1324 (2003). doi: 10.1029/2002GL016345
31. F. Oldfield, Can the magnetic signatures from inorganic fly ash be used to mark the onset of the Anthropocene? *Anthropocene Rev.* **2**, 3–13 (2015). doi: 10.1177/2053019614534402
32. N. L. Rose, Spheroidal carbonaceous fly ash particles provide a globally synchronous stratigraphic marker for the Anthropocene. *Environ. Sci. Technol.* **49**, 4155–4162 (2015). doi: 10.1021/acs.est.5b00543; pmid: 25790111
33. G. T. Swindles *et al*., Spheroidal carbonaceous particles are a defining stratigraphic marker for the Anthropocene. *Sci. Rep.* **5**, 10264 (2015). doi: 10.1038/srep10264; pmid: 26020614
34. M. C. Harvey, S. C. Brassell, C. M. Belcher, A. Montanari, Combustion of fossil organic matter at the Cretaceous-Paleogene (K-P) boundary. *Geology* **36**, 355–358 (2008). doi: 10.1130/G24646A.1
35. R. LeB. Hooke, J. F. Martín-Duque, Land transformation by humans: A review. *GSA Today* **22**, 4–10 (2012).
36. J. Zalasiewicz, M. Williams, C. N. Waters "Can an Anthropocene Series be defined and recognized?," in *A Stratigraphical Basis for the Anthropocene*, C. N. Waters, J. A. Zalasiewicz, M. Williams, M. A. Ellis, A. M. Snelling, Eds. (Geological Society, London, 2014), pp. 39–53.
37. J. Zalasiewicz, C. N. Waters, M. Williams, Human bioturbation, and the subterranean landscape of the Anthropocene. *Anthropocene* **6**, 3–9 (2014). doi: 10.1016/j.ancene.2014.07.002
38. I. Douglas, N. Lawson, The human dimensions of geomorphological work in Britain. *J. Ind. Ecol.* **4**, 9–33 (2000). doi: 10.1162/108819800569771
39. E. C. Ellis, Anthropogenic transformation of the terrestrial biosphere. *Philos. Trans. R. Soc. London Ser. A* **369**, 1010–1035 (2011). doi: 10.1098/rsta.2010.0331; pmid: 21282158
40. A. Brown, P. Toms, C. Carey, E. Rhodes, Geomorphology of the Anthropocene: Time-transgressive discontinuities of human-induced alluviation. *Anthropocene* **1**, 3–13 (2013). doi: 10.1016/j.ancene.2013.06.002
41. P. Meyfroidt, E. F. Lambin, Global forest transition: Prospects for an end to deforestation. *Annu. Rev. Environ. Resour.* **36**, 343–371 (2011). doi: 10.1146/annurev-environ-090710-143732
42. R. C. Sidle, A. D. Ziegler, The dilemma of mountain roads. *Nat. Geosci.* **5**, 437–438 (2012). doi: 10.1038/ngeo1512
43. J. P. M. Syvitski, A. Kettner, Sediment flux and the Anthropocene. *Philos. Trans. R. Soc. London Ser. A* **369**, 957–975 (2011). doi: 10.1098/rsta.2010.0329; pmid: 21282156
44. C. K. Paull, W. Ussler III, P. J. Mitts, D. W. Caress, G. J. West, Discordant ^{14}C-stratigraphies in upper Monterey Canyon: A signal of anthropogenic disturbance. *Mar. Geol.* **233**, 21–36 (2006). doi: 10.1016/j.margeo.2006.07.008
45. C. H. Vane *et al*., Chemical signatures of the Anthropocene in the Clyde estuary, UK: Sediment-hosted Pb, $^{207/206}$Pb, total petroleum hydrocarbon, polyaromatic hydrocarbon and polychlorinated biphenyl pollution records. *Philos. Trans. R. Soc. London Ser. A* **369**, 1085–1111 (2011). doi: 10.1098/rsta.2010.0298; pmid: 21282161
46. D. C. G. Muir, N. L. Rose, "Persistent organic pollutants in the sediments of Lochnagar," in *Lochnagar: The Natural History of a Mountain Lake*, N. L. Rose, Ed. (Springer, Dordrecht, Germany, 2007), pp. 375–402.
47. J. R. Dean, M. J. Leng, A. W. Mackay, Is there an isotopic signature of the Anthropocene? *Anthropocene Rev.* **1**, 276–287 (2014). doi: 10.1177/2053019614541631
48. D. E. Canfield, A. N. Glazer, P. G. Falkowski, The evolution and future of Earth's nitrogen cycle. *Science* **330**, 192–196 (2010). doi: 10.1126/science.1186120; pmid: 20929768
49. S. R. Carpenter, E. M. Bennett, Reconsideration of the planetary boundary for phosphorus. *Environ. Res. Lett.* **6**, 014009 (2011). doi: 10.1088/1748-9326/6/1/014009
50. J. N. Galloway *et al*., Transformation of the nitrogen cycle: Recent trends, questions, and potential solutions. *Science* **320**, 889–892 (2008). doi: 10.1126/science.1136674; pmid: 18487183
51. E. A. Holland, J. Lee-Taylor, C. Nevison, J. Sulzman, *Global N Cycle: Fluxes and N_2O Mixing Ratios Originating from Human Activity. Data Set* (Oak Ridge National Laboratory Distributed Active Archive Center, Oak Ridge, TN, 2005); http://daac.ornl.gov/cgi-bin/dsviewer.pl?ds_id=797.
52. I. P. Wilkinson, C. Poirier, M. J. Head, C. D. Sayer, J. Tibby, "Microbiotic signatures of the Anthropocene in marginal marine and freshwater palaeoenvironments," in *A Stratigraphical Basis for the Anthropocene*, C. N. Waters, J. A. Zalasiewicz, M. Williams, M. A. Ellis, A. M. Snelling, Eds. (Geological Society, London, 2014), pp. 185–219.
53. G. W. Holtgrieve *et al*., A coherent signature of anthropogenic nitrogen deposition to remote watersheds of the Northern Hemisphere. *Science* **334**, 1545–1548 (2011). doi: 10.1126/science.1212267; pmid: 22174250
54. A. P. Wolfe *et al*., Stratigraphic expressions of the Holocene–Anthropocene transition revealed in sediments from remote lakes. *Earth Sci. Rev.* **116**, 17–34 (2013). doi: 10.1016/j.earscirev.2012.11.001
55. M. G. Hastings, D. M. Sigman, E. J. Steig, Glacial/interglacial changes in the isotopes of nitrate from the Greenland Ice Sheet Project 2 (GISP2) ice core. *Global Biogeochem. Cycles* **19**, GB4024 (2005). doi: 10.1029/2005GB002502
56. M. G. Hastings, J. C. Jarvis, E. J. Steig, Anthropogenic impacts on nitrogen isotopes of ice-core nitrate. *Science* **324**, 1288 (2009). doi: 10.1126/science.1170510; pmid: 19498161
57. E. W. Wolff, "Ice sheets and the Anthropocene," in *A Stratigraphical Basis for the Anthropocene*, C. N. Waters, J. A. Zalasiewicz, M. Williams, M. A. Ellis, A. M. Snelling, Eds. (Geological Society, London, 2014), pp. 255–263.
58. A. Gałuszka, Z. M. Migaszewski, J. Zalasiewicz, "Assessing the Anthropocene with geochemical methods," in *A Stratigraphical Basis for the Anthropocene*, C. N. Waters, J. A. Zalasiewicz, M. Williams, M. A. Ellis, A. M. Snelling, Eds. (Geological Society, London, 2014), pp. 221–238.
59. K. E. Jarvis, S. J. Parry, J. M. Piper, Temporal and spatial studies of autocatalyst-derived platinum, rhodium, and palladium and selected vehicle-derived trace elements in the environment. *Environ. Sci. Technol.* **35**, 1031–1036 (2001). doi: 10.1021/es0001512; pmid: 11347910
60. UNSCEAR-United Nations Scientific Committee on the Effects of Atomic Radiation, *Sources and Effects of Ionizing Radiation* (United Nations, New York, 2000).
61. C. N. Waters *et al*., Can nuclear weapons fallout mark the beginning of the Anthropocene Epoch? *Bull. Atom. Sci.* **71**, 46–57 (2015). doi: 10.1177/0096340215581357
62. P. J. Reimer *et al*., IntCal13 and Marine13 radiocarbon age calibration curves 0–50,000 years cal BP. *Radiocarbon* **55**, 1869–1887 (2013). doi: 10.2458/azu_js_rc.55.16947
63. Q. Hua, M. Barbetti, A. Z. Rakowski, Atmospheric radiocarbon for the period 1950–2010. *Radiocarbon* **55**, 2059–2072 (2013). doi: 10.2458/azu_js_rc.v55i2.16177
64. G. J. Hancock, S. G. Tims, L. K. Fifield, I. T. Webster, "The release and persistence of radioactive anthropogenic nuclides," in *A Stratigraphical Basis for the Anthropocene*, C. N. Waters, J. A. Zalasiewicz, M. Williams, M. A. Ellis, A. M. Snelling, Eds. (Geological Society, London, 2014), pp. 265–281.
65. E. W. Wolff, Greenhouse gases in the Earth system: A palaeoclimate perspective. *Philos. Trans. R. Soc. London Ser. A* **369**, 2133–2147 (2011). doi: 10.1098/rsta.2010.0225; pmid: 21502180
66. J. Elsig *et al*., Stable isotope constraints on Holocene carbon cycle changes from an Antarctic ice core. *Nature* **461**, 507–510 (2009). doi: 10.1038/nature08393; pmid: 19779448
67. J. Schmitt *et al*., Carbon isotope constraints on the deglacial CO_2 rise from ice cores. *Science* **336**, 711–714 (2012). doi: 10.1126/science.1217161; pmid: 22461496
68. Y. Cui *et al*., Slow release of fossil carbon during the Palaeocene–Eocene Thermal Maximum. *Nat. Geosci.* **4**, 481–485 (2011). doi: 10.1038/ngeo1179
69. M. Rubino *et al*., A revised 1000 year atmospheric δ^{13}C-CO_2 record from Law Dome and South Pole, Antarctica. *J. Geophys. Res.* **118**, 8482–8499 (2013).
70. J. Zalasiewicz *et al*., Colonization of the Americas, 'Little Ice Age' climate, and bomb-produced carbon: Their role in defining the Anthropocene. *Anthropocene Rev.* **2**, 117–127 (2015). doi: 10.1177/2053019615587056
71. T. Blunier, J. Chappellaz, J. Schwander, B. Stauffer, D. Raynaud, Variations in atmospheric methane concentration during the Holocene epoch. *Nature* **374**, 46–49 (1995). doi: 10.1038/374046a0
72. D. F. Ferretti *et al*., Unexpected changes to the global methane budget over the past 2000 years. *Science* **309**, 1714–1717 (2005). doi: 10.1126/science.1115193; pmid: 16151008
73. C. MacFarling Meure *et al*., Law Dome CO_2, CH_4 and N_2O ice core records extended to 2000 years BP. *Geophys. Res. Lett.* **33**, L14810 (2006). doi: 10.1029/2006GL026152
74. C. J. Sapart *et al*., Natural and anthropogenic variations in methane sources during the past two millennia. *Nature* **490**, 85–88 (2012). doi: 10.1038/nature11461; pmid: 23038470
75. L. Mitchell, E. Brook, J. E. Lee, C. Buizert, T. Sowers, Constraints on the late Holocene anthropogenic contribution to the atmospheric methane budget. *Science* **342**, 964–966 (2013). doi: 10.1126/science.1238920; pmid: 24264988
76. L. Loulergue *et al*., *EPICA Dome C Ice Core, 800 KYyr Methane Data. IGBP PAGES, World Data Center for Paleoclimatology, Data Contribution Series #2008-054* (National Oceanic and Atmospheric Administration/National Climatic Data Center Paleoclimatology Program, Boulder, CO, 2008); http://cdiac.ornl.gov/trends/atm_meth/ice_core_methane.html.
77. B. M. Vinther *et al*., A synchronized dating of three Greenland ice cores throughout the Holocene. *J. Geophys. Res.* **111**, D13102 (2006). doi: 10.1029/2005JD006921
78. T. Felis *et al*., Pronounced interannual variability in tropical South Pacific temperatures during Heinrich Stadial 1. *Nat. Commun.* **3**, 965 (2012). pmid: 22828625
79. C. P. Summerhayes, *Earth's Climate Evolution* (Wiley-Blackwell, 2015).

80. M. Ahmed *et al*., Continental-scale temperature variability during the past two millennia. *Nat. Geosci.* **6**, 339–346 (2013). doi: 10.1038/ngeo1797
81. H. Wanner, L. Mercolli, M. Grosjean, S. P. Ritz, Holocene climate variability and change; a data-based review. *J. Geol. Soc. London* **172**, 254–263 (2015). doi: 10.1144/jgs2013-101
82. IPCC, *Climate Change 2013: The Physical Science Basis. Contribution of Working Group I to the Fifth Assessment Report of the Intergovernmental Panel on Climate Change*, T. F. Stocker *et al*., Eds. (Cambridge Univ. Press, 2013).
83. J. R. Hansen, R. Ruedy, M. Sato, K. Lo, Global surface temperature change. *Rev. Geophys.* **48**, RG4004 (2010). doi: 10.1029/2010RG000345
84. J. A. Church, P. U. Clark, A. Cazenave, J. M. Gregory, S. Jevrejeva, A. Levermann, M. A. Merrifield, G. A. Milne, R. S. Nerem, P. D. Nunn, A. J. Payne, W. T. Pfeffer, D. Stammer, A. S. Unnikrishnan, "Sea level change," in *Climate Change 2013: The Physical Science Basis. Contribution of Working Group I to the Fifth Assessment Report of the Intergovernmental Panel on Climate Change*, T. F. Stocker *et al*., Eds. (Cambridge Univ. Press, 2013), pp. 1137–1216.
85. P. Deschamps *et al*., Ice-sheet collapse and sea-level rise at the Bølling warming 14,600 years ago. *Nature* **483**, 559–564 (2012). doi: 10.1038/nature10902; pmid: 22460900
86. R. Gehrels, P. L. Woodworth, When did modern rates of sea-level rise start? *Global Planet. Change* **100**, 263–277 (2013). doi: 10.1016/j.gloplacha.2012.10.020
87. A. C. Kemp *et al*., Relative sea-level change in Connecticut (USA) during the last 2200 yrs. *Earth Planet. Sci. Lett.* **428**, 217–229 (2015). doi: 10.1016/j.epsl.2015.07.034
88. A. D. Barnosky, "Palaeontological evidence for defining the Anthropocene," in *A Stratigraphical Basis for the Anthropocene*, C. N. Waters, J. A. Zalasiewicz, M. Williams, M. A. Ellis, A. M. Snelling, Eds. (Geological Society, London, 2014), pp. 149–165.
89. G. Ceballos *et al*., Accelerated modern human-induced species losses: Entering the sixth mass extinction. *Sci. Adv.* **1**, e1400253 (2015). doi: 10.1126/sciadv.1400253; pmid: 26601195
90. A. D. Barnosky, N. Matzke, S. Tomiya, G. O. U. Wogan, B. Swartz, T. B. Quental, C. Marshall, J. L. McGuire, E. L. Lindsey, K. C. Maguire, B. Mersey, E. A. Ferrer, Has the Earth's sixth mass extinction already arrived? *Nature* **471**, 51–57 (2011). doi: 10.1038/nature09678
91. M. Williams *et al*., The Anthropocene biosphere. *Anthropocene Rev.* **2**, 196–219 (2015). doi: 10.1177/2053019615591020
92. E. C. Ellis, K. K. Goldewijk, S. Siebert, D. Lightman, N. Ramankutty, Anthropogenic transformation of the biomes, 1700 to 2000. *Glob. Ecol. Biogeogr.* **19**, 589–606 (2010).
93. S. M. Kidwell, Biology in the Anthropocene: Challenges and insights from young fossil records. *Proc. Natl. Acad. Sci. U.S.A.* **112**, 4922–4929 (2015). doi: 10.1073/pnas.1403660112; pmid: 25901315
94. J. R. McNeill, "Biological exchanges in world history," in *The Oxford Handbook of World History*, J. Bentley, Ed. (Oxford Univ. Press, 2011), pp. 325–342.
95. W. F. Ruddiman, E. C. Ellis, J. O. Kaplan, D. Q. Fuller, Defining the epoch we live in. *Science* **348**, 38–39 (2015). doi: 10.1126/science.aaa7297; pmid: 25838365

ACKNOWLEDGMENTS

C.W. and M.E. publish with the permission of the Executive Director, British Geological Survey, Natural Environment Research Council; the former is funded by the British Geological Survey's Engineering Geology program. We thank three referees, along with I. Fairchild, I. Hajdas, and S. Price, for their comments. This paper is a contribution of the Anthropocene Working Group (AWG), part of the Subcommission on Quaternary Stratigraphy of the International Commission on Stratigraphy. The AWG receives no direct funding to carry out its research, and the authors declare no competing financial interests.

10.1126/science.aad2622

RESEARCH ARTICLE SUMMARY

BRAIN CIRCUITS

Gating of hippocampal activity, plasticity, and memory by entorhinal cortex long-range inhibition

Jayeeta Basu,* Jeffrey D. Zaremba, Stephanie K. Cheung, Frederick L. Hitti, Boris V. Zemelman, Attila Losonczy, Steven A. Siegelbaum*

INTRODUCTION: The precise association of contextual cues with a behavioral experience enables an animal to discriminate between salient (harmful or rewarding) versus neutral environments. What signaling mechanisms during learning help select specific contextual signals to be stored as long-term memories? Hippocampal CA1 pyramidal neurons integrate direct multisensory excitatory input from entorhinal cortex (EC) with indirect, mnemonic excitatory input from the upstream hippocampal CA3 area, and both pathways have been implicated in memory storage. Paired activation of the direct and indirect inputs at a precise timing interval that matches the dynamics of the cortico-hippocampal circuit induces a long-term enhancement of the activation of CA1 neurons by their CA3 inputs (input timing–dependent plasticity or ITDP). However, EC additionally sends long-range inhibitory projections (LRIPs) to CA1, the function of which is largely unknown. Here, we explore the role of the LRIPs in regulating hippocampal synaptic activity and memory.

RATIONALE: GABAergic neurons in medial entorhinal cortex (MEC) were recently found to send to hippocampus LRIPs that form relatively weak and sparse synapses on CA1 GABAergic interneurons, those that are potentiated by γ-aminobutyric acid (GABA). As lateral entorhinal cortex (LEC) conveys important contextual and object-related information to hippocampus, we examined whether this region also sends LRIPs to CA1. We expressed channelrhodopsin-2 (ChR2) selectively in LEC inhibitory neurons and examined the synaptic effects of LRIP photostimulation. The behavioral impact of the LRIPs was determined by selectively silencing these inputs locally in CA1 during contextual fear conditioning (CFC) and novel object recognition (NOR) tasks. We also used in vivo Ca^{2+} imaging to assess how different sensory and behavioral stimuli that typically make up a contextual experience activate the LEC LRIPs. Finally, we examined how the LRIPs influence information flow through the cortico-hippocampal circuit and contribute to ITDP.

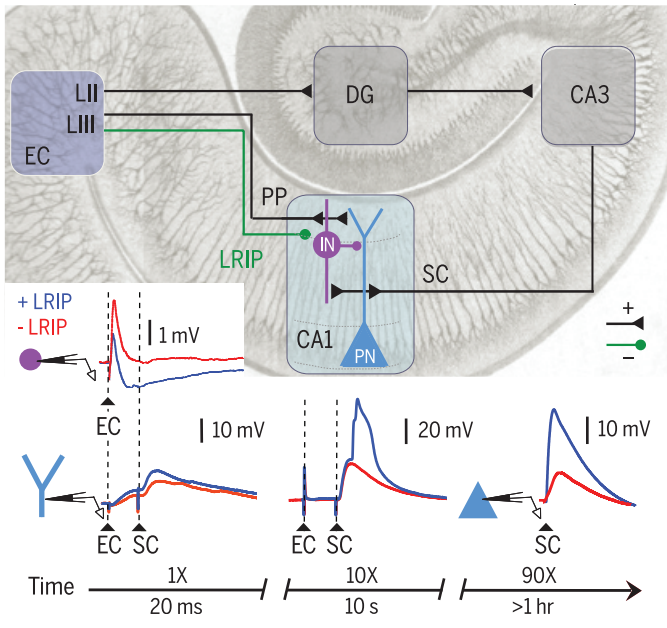

Long-range inhibitory projections gate cortico-hippocampal information flow in the short and long term. (**Top**) The cortico-hippocampal circuit. Inputs from EC arrive at CA1 directly through excitatory perforant path (PP) and LRIPs and indirectly through SCs of the trisynaptic path [dentate gyrus (DG)→CA3→CA1]. (**Bottom**) Recordings from different EC LRIP→CA1 circuit elements. (Top left) A CA1 IN that normally inhibits the pyramidal neuron (PN) dendrite is inhibited maximally by LRIP (blue, LRIP intact) 20 ms after EC stimulation (dotted guide lines). (Bottom left) This disinhibits the PN dendritic depolarization evoked by a SC input arriving 20 ms after EC input. Multiple EC-SC pairings result in more disinhibition (middle), which triggers dendritic Ca^{2+} spikes (10× pairings for 10 s) and (right) induces somatic long-term plasticity (90× pairings for 90 s) in the CA1 PN, where SC responses are potentiated for >1 hour. LRIP silencing (red) decreases dendritic depolarization and spike probability and blocks somatic plasticity. [Background from a plate by C. Golgi *et al.*, 1886; text translated and republished with plates in *Brain Res. Bull.* **54**, 461–483 (2001)]

ON OUR WEB SITE

Read the full article at http://dx.doi.org/10.1126/science.aaa5694

RESULTS: LRIPs from LEC produced strong inhibitory postsynaptic potentials in a large fraction of CA1 interneurons located in the region of the EC inputs. Although pharmacogenetic silencing of LRIPs in hippocampus did not prevent CFC or NOR memory, it caused mice to show an inappropriate fear response to a neutral context and a diminished ability to distinguish a novel object from a familiar object. Calcium imaging revealed that the LRIP axons and presynaptic terminals responded to various sensory stimuli. Moreover, pairing such signals with appetitive or aversive stimuli increased LRIP activity, consistent with a role of the LRIPs in memory specificity.

Intracellular recordings demonstrated that the LRIPs powerfully suppressed the activity of a subclass of cholecystokinin-expressing interneurons (CCK^+ INs). These interneurons were normally strongly excited by the CA3 inputs, which results in pronounced feedforward inhibition (FFI) of CA1 pyramidal neuron dendrites. By transiently and maximally suppressing the INs in a 15- to 20-ms temporal window, the LRIPs enhanced CA3 inputs onto CA1 pyramidal neurons that arrived within that timing interval. This disinhibition enabled temporally precise, paired activation of EC–Schaffer collateral (EC-SC) inputs (15 to 20 ms apart) to trigger dendritic spikes in the distal dendrites of CA1 PNs and to induce ITDP.

CONCLUSION: LRIPs from EC act as a powerful, temporally precise disinhibitory gate of intrahippocampal information flow and enable the induction of plasticity when cortical and hippocampal inputs arrive onto CA1 PNs at a precise 20-ms interval. We propose that the LRIPs increase the specificity of hippocampal-based long-term memory by assessing the salience of mnemonic information relayed by CA3 to the immediate sensory context conveyed by direct excitatory EC inputs. ■

The list of author affiliations is available in the full article online.
*Corresponding author. E-mail: jayeeta.basu@nyumc.org (J.B.); sas8@columbia.edu (S.A.S.)
Cite this article as J. Basu *et al.*, *Science* 351, aaa5694 (2016). DOI: 10.1126/science.aaa5694

RESEARCH ARTICLE

BRAIN CIRCUITS

Gating of hippocampal activity, plasticity, and memory by entorhinal cortex long-range inhibition

Jayeeta Basu,[1]†‡ Jeffrey D. Zaremba,[1]* Stephanie K. Cheung,[1]*† Frederick L. Hitti,[1] Boris V. Zemelman,[2] Attila Losonczy,[1] Steven A. Siegelbaum[1]‡

The cortico-hippocampal circuit is critical for storage of associational memories. Most studies have focused on the role in memory storage of the excitatory projections from entorhinal cortex to hippocampus. However, entorhinal cortex also sends inhibitory projections, whose role in memory storage and cortico-hippocampal activity remains largely unexplored. We found that these long-range inhibitory projections enhance the specificity of contextual and object memory encoding. At the circuit level, these γ-aminobutyric acid (GABA)–releasing projections target hippocampal inhibitory neurons and thus act as a disinhibitory gate that transiently promotes the excitation of hippocampal CA1 pyramidal neurons by suppressing feedforward inhibition. This enhances the ability of CA1 pyramidal neurons to fire synaptically evoked dendritic spikes and to generate a temporally precise form of heterosynaptic plasticity. Long-range inhibition from entorhinal cortex may thus increase the precision of hippocampal-based long-term memory associations by assessing the salience of mnemonormation to the immediate sensory input.

The cortico-hippocampal circuit mediates the encoding and storage of specific associative memories, in part, through long-term plastic changes at neural circuit synapses. Most studies to date have focused on the importance of excitatory projections from entorhinal cortex (EC) to hippocampal CA1 pyramidal neurons, which provide the principal output of hippocampus (*1*–*3*). However, EC also sends long-range inhibitory projections (LRIPs) to the CA1 region of the hippocampus (*4*). At present, little is known about the role of these LRIPs in regulating hippocampal circuit operations, synaptic plasticity, or memory storage.

Excitatory glutamatergic input to the CA1 region arrives from EC through both a direct and an indirect pathway (*5*). In the indirect, or trisynaptic, path, EC LII stellate cells excite dentate gyrus granule cells, which excite CA3 pyramidal neurons. The Schaffer collateral (SC) axons of CA3 pyramidal neurons provide strong excitatory drive onto CA1 pyramidal neurons by forming synapses on CA1 apical dendrites in stratum radiatum (SR), relatively close to the soma. EC LII (*3*) and LIII (*6*) pyramidal neuron axons provide direct, but weak, excitatory drive by forming synapses on regions of the CA1 pyramidal neuron apical dendrites located in stratum lacunosum moleculare (SLM), very far from the soma. Both indirect and direct inputs also recruit strong feedforward inhibition (FFI) that normally limits CA1 excitation (*7*).

Previous studies have demonstrated that coordinated activation of the direct and trisynaptic inputs to CA1 pyramidal neurons enhances the propagation of excitatory postsynaptic potentials (EPSPs) along the pyramidal neuron apical dendrites (*8*), enables the firing of dendritic spikes and bursts of action potential output (*9*), induces a robust and temporally precise form of heterosynaptic plasticity (termed input timing–dependent plasticity or ITDP) (*10*, *11*), and leads to de novo place-cell firing (*12*). However, the contribution of the LRIPs to cortico-hippocampal activity has not been previously investigated. Here, we have characterized the activity of the LRIPs in vivo, analyzed their role in long-term memory storage, and investigated their function in regulating the effects of paired EC and CA3 input, in particular CA1 pyramidal neuron synaptic activation, dendritic spike firing, and the induction of heterosynaptic plasticity.

Lateral EC provides direct GABAergic inhibition to local CA1 interneurons

LRIPs from superficial layers of medial entorhinal cortex (MEC), an area that encodes spatial information (*13*, *14*), form synapses with inhibitory neurons (INs) located near the SR-SLM border of the CA1 region (*4*). However, the LRIPs from MEC are sparse and generate relatively weak inhibitory postsynaptic currents (IPSCs) in the CA1 INs (*4*). To determine whether lateral entorhinal cortex (LEC), which conveys multimodal nonspatial sensory information to hippocampus (*15*), sends a more potent inhibitory projection to CA1 INs, we injected recombinant Cre-dependent adeno-associated viral vectors (rAAV^{Cre}) into LEC or MEC to label the LRIPs and to achieve optogenetic control of their activity. To restrict expression to INs, viral injections were performed by using a pan γ-aminobutyric acid (GABA)–releasing or GABAergic Cre-driver mouse line [GAD2-Cre mice (*16*)] (Fig. 1A and fig. S1).

Injections of two separate rAAV^{Cre} vectors were used to express tdTomato in LEC and green fluorescent protein (GFP) in MEC. In contrast to the relatively weak and sparse inhibitory projections from MEC (*4*), LEC sent dense projections to CA1 (Fig. 1, B to E, and fig. S1) that covered twice the area in CA1 (82.05 ± 3.64%) as do the LRIPs from MEC (37.79 ± 2.35%; $P < 0.0001$, two-tailed t test, $n = 5$ mice) (fig. S2). Similar to their glutamatergic counterparts, LRIPs from MEC differentially targeted CA1 along its transverse, proximal-distal axis, with denser projections to proximal regions of CA1 (i.e., those closer to CA2) (fig. S2). In contrast to the preferential targeting of LEC excitatory inputs to distal CA1 (closer to subiculum), LRIPs from LEC were distributed fairly uniformly along the proximal-distal axis of CA1 with also a small, but significant, bias toward the proximal side (figs. S2 and S6).

To examine the functional impact of these inputs, we injected an rAAV^{Cre} vector in LEC or MEC of GAD2-Cre mice, which enabled us to express light-sensitive cation channel channelrhodopsin-2 fused with enhanced yellow fluorescent protein (ChR2-EYFP) (*17*) selectively in GABAergic neurons in either region. Photostimulation of ChR2-EYFP$^+$ GABAergic axons from LEC in the CA1 SLM region in hippocampal slices (Fig. 1C) evoked large inhibitory postsynaptic currents (IPSCs) in CA1 interneurons located in the SR/SLM border region voltage-clamped to +10 mV (139 ± 24.8 pA, n = 17 responsive cells) (Fig. 1, F and G, and fig. S3). In contrast, the amplitude of IPSCs evoked by photostimulation of ChR2-EYFP$^+$ MEC LRIPs was only one-fourth as large (37.7 ± 4.5 pA, n = 11 responsive cells; $P < 0.005$, t test) (Fig. 1, F and G). Moreover, a greater fraction of SR-SLM border INs responded to photostimulation of LEC LRIPs (53.4%) compared with MEC LRIPs (32.4%) (fig. S3B).

These synaptic currents were eliminated by GABA, types A and B ($GABA_A$ and $GABA_B$) receptor blockers 6-imino-3-(4-methoxyphenyl)-1(6*H*)-pyridazinebutanoic acid hydrobromide, SR 95531 (2 μM), and [*S*-(*R**,*R**)]-[3-[[1-(3,4-dichlorophenyl) ethyl]amino]-2-hydroxypropyl](cyclohexylmethyl) phosphinic acid, CGP 54626 hydrochloride (1 μM) [hereafter, CGP 54626], respectively, but were unaltered by blockade of α-amino-3-hydroxy-5-methyl-4-isoxazolepropionic acid AMPA-type glutamate receptors with [2,3-dioxo-6-nitro-1,2,3,4-tetrahydrobenzo [f]quinoxaline-7-sulfonamide, NBQX (10 μM)], which indicated that the responses represented direct IPSCs generated by GABA release from the LRIPs (Fig. 1F and fig. S3C). We failed to detect any EPSPs in CA1 SR-SLM INs when we photostimulated ChR2-YFP$^+$ LEC axons under current clamp conditions with the INs held at an initial membrane potential of −68 mV (fig. S3D), which indicated that the rAAV^{Cre} vector resulted in the selective expression of ChR2 in LEC GABAergic neurons.

[1]Department of Neuroscience, Kavli Brain Institute, Columbia University Medical Center, 1051 Riverside Drive, New York, NY 10032, USA. [2]University of Texas at Austin, Austin, TX 78712, USA. *These authors contributed equally to this work. †Present address: Department of Neuroscience and Physiology, NYU Neuroscience Institute, New York University School of Medicine, 450 East 29th Street, New York, NY 10016, USA. ‡Corresponding author. E-mail: jayeeta.basu@nyumc.org (J.B.); sas8@columbia.edu (S.A.S.)

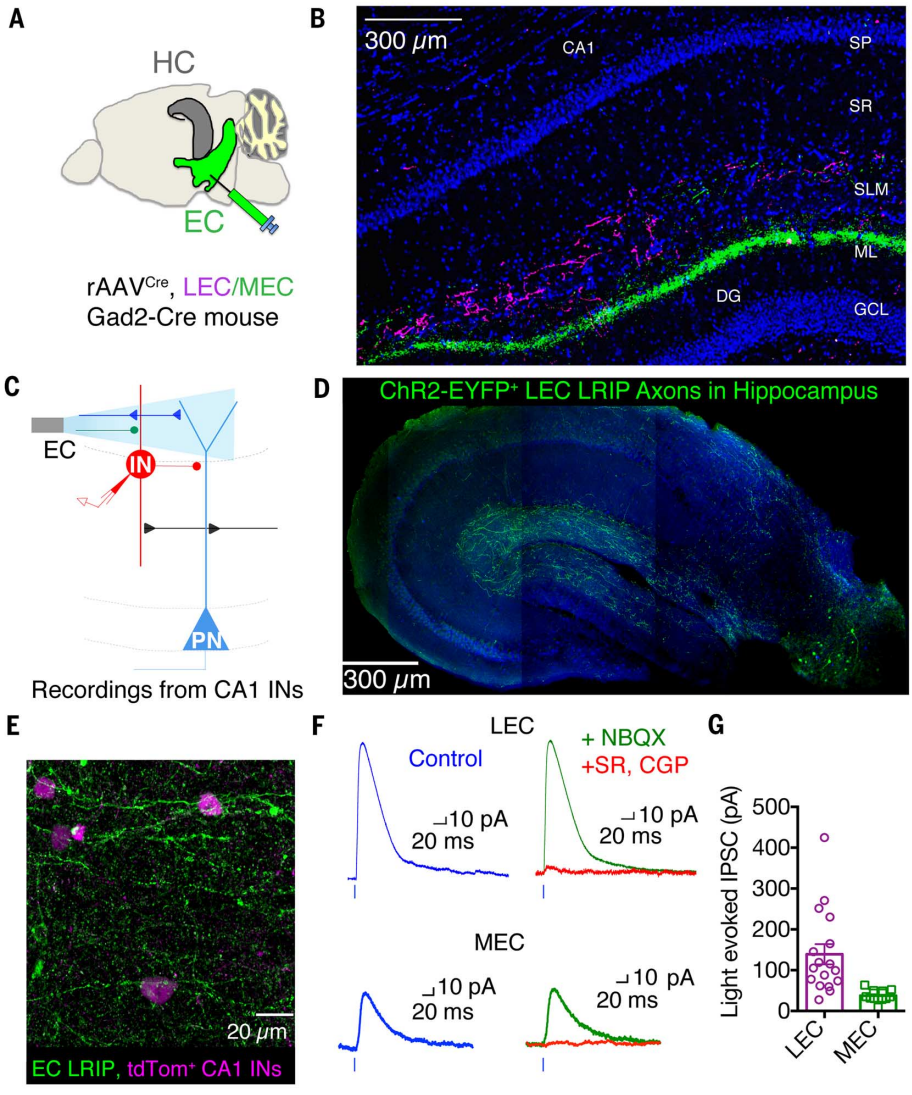

Fig. 1. LEC provides strong long-range GABAergic inputs to local CA1 inhibitory neurons. (**A**) LEC and MEC viral injection sites (in green) and their hippocampal target (HC, in gray). (**B**) TdTomato-labeled (magenta) and GFP-labeled (green) axons in SLM of CA1 from LEC and MEC Gad2-Cre^{+} LRIPs, respectively. 4′,6-diamidino-2-phenylindole (DAPI) stain in blue. The strata of hippocampal CA1 and dentate gyrus (DG): SP, stratum pyramidalis signifies pyramidal neuron (PN) cell body layer; SR, stratum radiatum where SC inputs arrive; SLM, stratum lacunosum moleculare where EC inputs arrive; and in DG, ML, molecular layer, and GCL, granule cell layer. (**C**) Scheme of experiment to functionally map impact of LRIPs from LEC or MEC on CA1 INs at SR-SLM border. ChR2-EYFP was virally expressed in GABAergic neurons in the LEC or MEC by using rAAV^{Cre} injections in *Gad2-Cre* mice. Patch-clamp recordings obtained from a CA1 IN (red) at the border of SR-SLM that targets the CA1 PN dendrite (light blue). A 470-nm laser light focused on SLM photostimulated ChR2^{+} LRIPs (green). (**D**) A 20× confocal image of ChR2-EYFP^{+} LRIP axons from LEC (green) in hippocampus from *Gad2-Cre* mouse. DAPI staining in blue. (**E**) These 63× confocal images show ChR2-EYFP^{+} LRIP axons from LEC (green) in CA1 SLM region impinging upon tdTomato^{+} IN soma (magenta). (**F**) Light-evoked IPSCs recorded from CA1 SR-SLM INs in normal extracellular solution (control, blue) and in the presence of AMPA-type glutamate receptor blocker (10 μM NBQX, green trace) or GABA receptor antagonists (2 μM SR95531 and 1 μM CGP 55845, red trace); see fig. S1 for statistics. (**G**) Bar (mean ± SEM) and scatter (individual cells) plot of the light-evoked IPSCs (pA, V_m = +10 mV) from responsive CA1 SR-SLM INs with ChR2 expressed in LEC (magenta, 139 ± 24.8 pA, n = 17) or MEC (green, 37.7 ± 4.5 pA, n = 11; P < 0.005, t test, LEC LRIP versus MEC LRIP).

LRIPs regulate the precision of memory storage

As LEC conveys nonspatial contextual information, we reasoned that the LRIP inputs may be important for nonspatial forms of learning, including contextual fear conditioning (CFC) (*18*), a hippocampus-dependent form of memory. We therefore examined the effect of silencing the LRIPs on CFC using the engineered ligand-gated glycine receptor (GlyR), PSAM (pharmacogenetically selective actuator module), which powerfully inhibits neural activity upon binding its cognate synthetic ligand PSEM^{308} (pharmacogenetically selective effector module) (*11*, *19*). To selectively silence the LEC LRIPs in CA1 without altering inhibition in EC, we implanted bilateral cannulae to locally infuse PSEM (15 μM, PSEM^{308}) in dorsal CA1 of Gad2-Cre mice expressing either GFP (control) or PSAM (test) as a result of rAAV^{Cre} injections in LEC (Fig. 2, A and B, and figs. S4 and S5). We verified that the local drug infusion selectively targeted LRIPs in hippocampus and spared EC by examining the distribution of the dye miniRuby (5%), which was present in the PSEM infusate (fig. S4, S5). PSEM^{308} infusion did not alter locomotor activity or cause anxiety-like behavior, which indicated that the drug infusion did not have significant adverse effects (fig. S7).

To test if the LRIPs were required for CFC, we infused PSEM just before the training phase on day 1 of the CFC task, in which the mice were placed in a novel context A for 2.5 min, followed by a brief, aversive foot shock (Fig. 2C) (see Materials and Methods below) (*20*). When placed in the training environment (context A) 24 hours after training (day 2, no PSEM present), the control (GFP-expressing) group demonstrated fear learning, as assessed by increased freezing behavior (Fig. 2D). However, rather than inhibiting CFC, silencing of the LEC LRIPs during training on day 1 significantly increased freezing on day 2 in context A [37.7 ± 2.3%, GFP, n = 9; 53.23 ± 2.7%, PSAM, n = 7; P < 0.0001, two-way analysis of variance (ANOVA); P < 0.001, t test, two-tailed paired by time) (Fig. 2D), which demonstrated that the LRIPs were not necessary for contextual learning.

However, when we exposed the mice on day 3 of the task to a novel context B, designed to be readily distinguishable from context A, the two groups of mice showed a revealing difference. Whereas the control mice did not freeze in the novel context, reflecting the normal specificity of CFC to the training context, the PSAM-expressing test group (where the LRIPs were only silenced during training in context A on day 1) exhibited a significant level of inappropriate freezing to the novel context (GFP: 5.1 ± 3.9%, n = 9; PSAM: 21.1 ± 7.9%, n = 7; P < 0.02, two-way ANOVA; P < 0.05, two-tailed t test paired by time) (Fig. 2D). The freezing to the novel context B in the test group was also significantly greater than the amount of freezing in context A before training (P < 0.0002), which suggested that the freezing represented an inappropriately learned response that caused an overgeneralization of fear memory. In contrast, the control group showed similar, low levels of freezing to context A on day 1 and context B on day 3 (P > 0.5). Finally, the difference in fear learning was specific for hippocampus-dependent CFC and did not reflect a general increase in fear or anxiety because the two groups of mice displayed similar extents of amygdala-dependent cued fear conditioning to a tone paired with the foot shock (Fig. 2D).

We next tested the importance of the LRIPs in a second nonspatial memory task, novel object recognition, using a version of the task that is

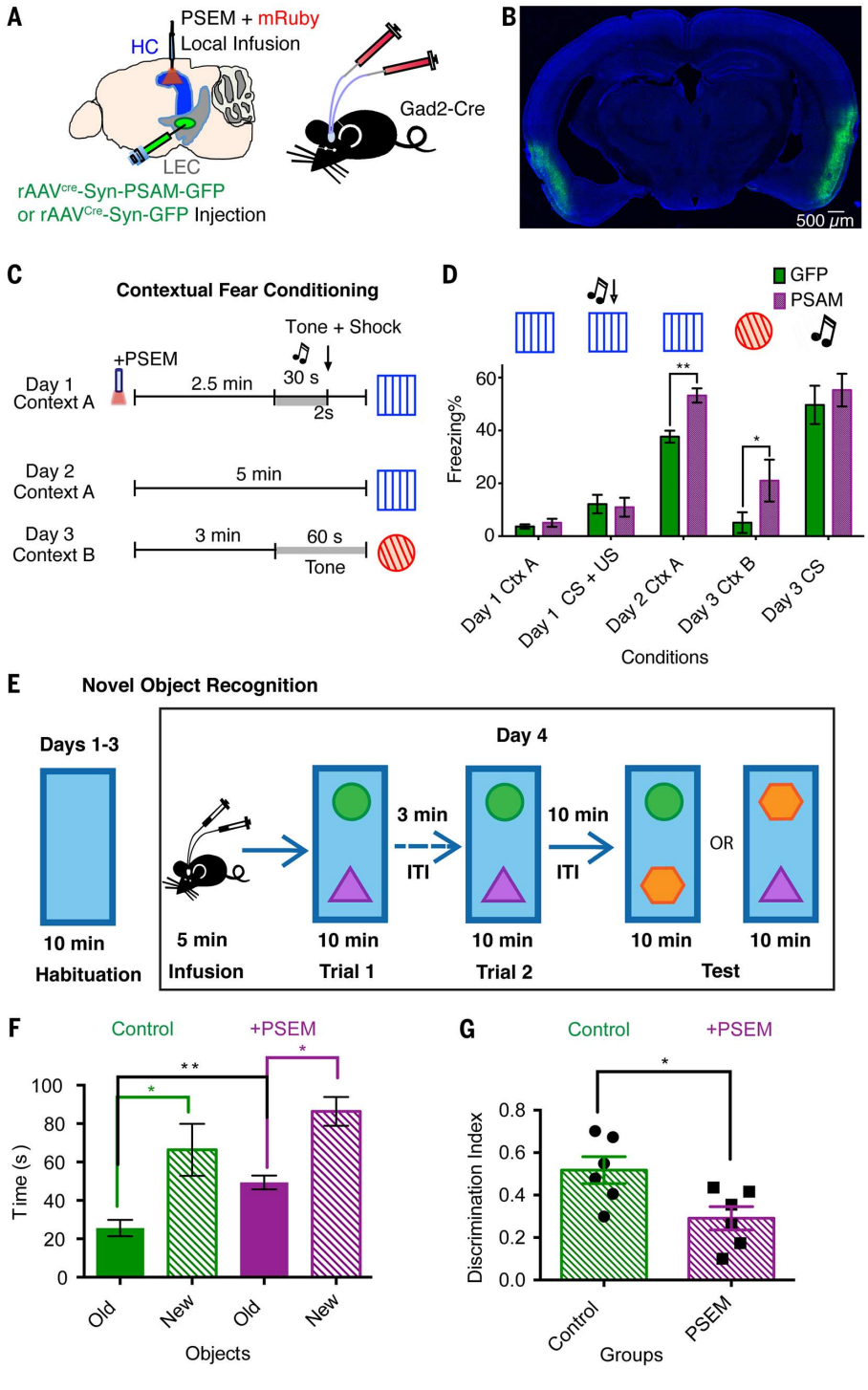

Fig. 2. Silencing LEC LRIPs in CA1 alters both context and object recognition memory. (**A**) Diagram of the experimental design. *Gad2-Cre* mice were injected with AAV^{Cre} to express GFP or PSAM in LEC. PSEM and the dye mini Ruby (mRuby) were delivered bilaterally to the CA1 region just before the training phase of memory tasks. (**B**) Confocal image (5×) of coronal section from a *Gad2-Cre* mouse injected in LEC with an AAV^{Cre}-expressing PSAM-2A-GFP, showing expression of GFP (green) in LEC (DAPI in blue). (**C**) Scheme of CFC (see Materials and Methods). On day 1, mice were exposed to context A, then given a tone followed by footshock. On day 2, mice were reexposed to context A. On day 3, mice were exposed to novel context B, followed by a tone. PSEM was delivered just before training in mice expressing GFP (control) or PSAM in LRIPs. (**D**) Bar plot (mean ± SEM) of time spent freezing (GFP, green; PSAM, purple): day 1, in context A before (Ctx A) and after (CS+US) footshock; day 2, during recall testing in context A; day 3, in novel context B before (Ctx B) and after cued tone (day 3 CS). Two-way repeated-measures ANOVA revealed no significant difference between groups in freezing on day 1 in context A (treatment × time $F_{6,105} = 0.8055$, $P = 0.5679$; treatment $F_{1,105} = 3.655$, $P = 0.0586$; time $F_{6,105} = 8.583$, $P < 0.0001$). There was significantly greater freezing in PSAM versus GFP groups in context A on day 2 (treatment × time $F_{4,48} = 0.8918$, $P = 0.4761$; treatment $F_{12,48} = 5.069$, $P < 0.0001$; time $F_{4,48} = 11.75$, $P < 0.0001$) and in context B (no tone) on day 3 (treatment × time $F_{3,45} = 1.230$, $P = 0.3069$; treatment $F_{15,45} = 2.246$, $P < 0.02$; time $F_{3,45} = 53.01$, $P < 0.0001$). The PSAM group also showed significantly greater freezing on day 3 in context B versus context A on day 1 before footshock (treatment $F_{12,24} = 5.332$; time $F_{2,24} = 19.76$; $P < 0.0002$). The GFP control group showed no significant difference in freezing in context A on day 1 versus context B on day 3 [treatment $F_{18,18} = 0.4932$; time $F_{2,18} = 12.84$; $P = 0.928$, not significant (n.s.)]. (**E**) Schematic of experiment to test effect of silencing LEC LRIPs on NOR. Mice were exposed to two objects in training trials 1 and 2, followed by a test trial in which one (now familiar or "old") object was replaced by a novel ("new") object. Before training, mice were infused with 0.5 μl of either 15 μM PSEM^{308} plus miniRuby (silenced group, + PSEM) or miniRuby alone (control). Both groups expressed PSAM in LEC. (**F**) Bar plots of time spent with familiar (old) versus novel (new) object in test trial. The PSEM-treated group explored the old object for 49.4 ± 3.6 s ($P < 0.005$ versus control) and the new object for 86.4 ± 7.5 s ($n = 6$; $P < 0.05$, new versus old object, paired t test). (**G**) The discrimination index, calculated as [(time spent exploring the new object) − (time spent exploring old object)]/(total exploration time), was significantly greater in control versus PSEM-treated mice ($P < 0.05$, paired t test).

hippocampus-dependent (*21*–*25*) (Fig. 2E). Mice were exposed to two objects during two 10-min training trials. After a 10-min delay, one of the now-familiar objects was substituted with a novel object, and the time spent exploring the novel versus familiar object was determined. The control group explored the old object for 25.6 ± 4.3 s and the new object for 66.3 ± 13.5 s ($n = 6$; $P < 0.05$, paired t test), which indicated object recognition memory. Similar to CFC, the LRIPs were not required for object memory storage as mice treated with PSEM during the training trials explored the novel object for a significantly longer time (86.4 ± 7.5 s) than they explored the familiar object (49.4 ± 3.6 s; $n = 6$; $P < 0.05$, paired t test) (Fig. 2F). However, the LRIPs were required for optimal memory storage, as the degree of memory performance, measured by the discrimination index for the two objects (Fig. 2G, see legend), was significantly greater for control (0.52 ± 0.06; $n = 6$) than for PSEM-treated mice (0.29 ± 0.06; $n = 6$; $P < 0.05$, paired t test). PSEM treatment also decreased the habituation that mice normally show to the objects during the

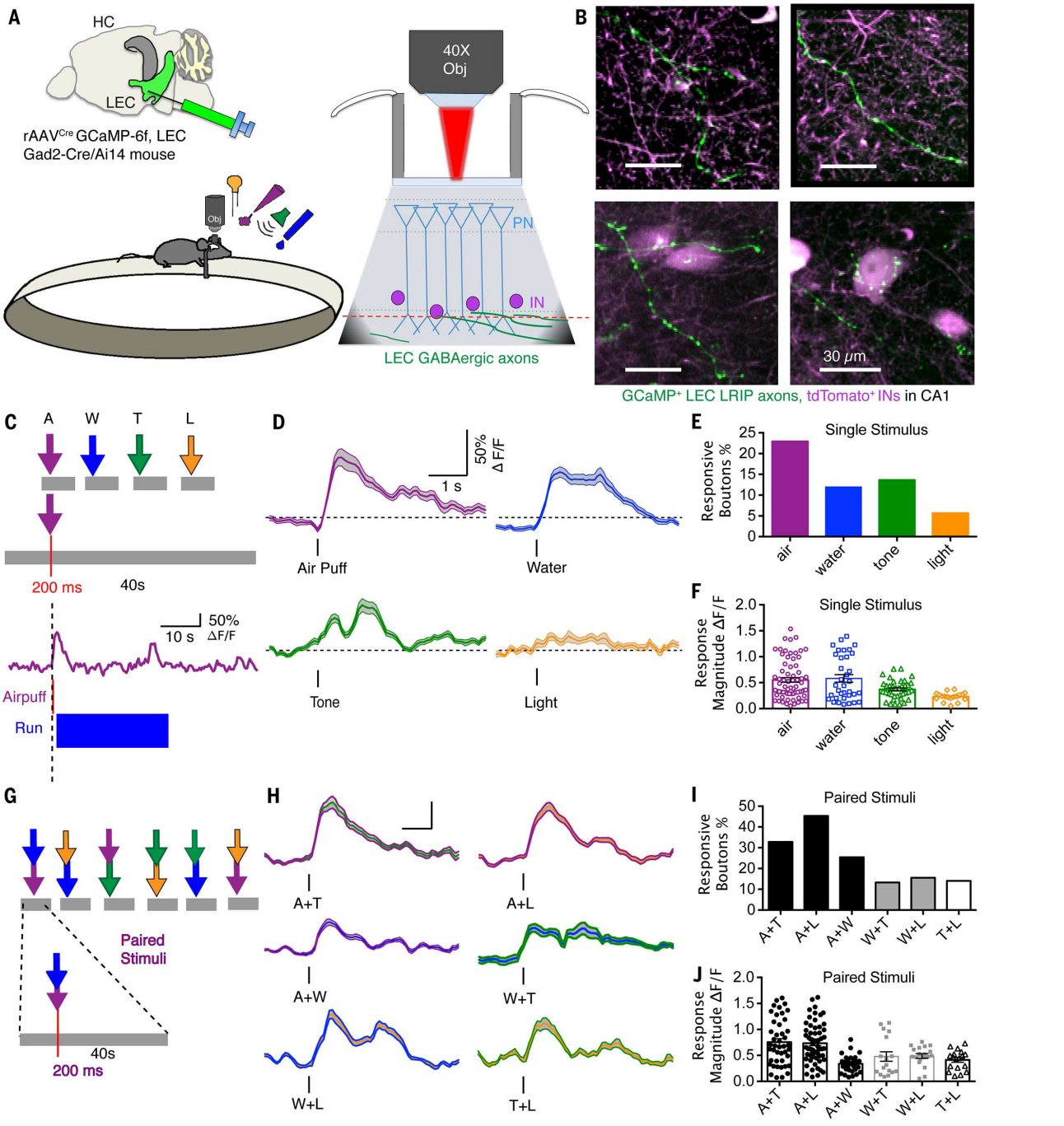

Fig. 3. Functional imaging of sensory coding in LEC LRIPs present in SLM of CA1. (**A**) Diagram of in vivo imaging experiment. GCaMP6f was expressed in dorsal LEC, by injecting Cre-dependent rAAV in *Gad2-Cre/Ai 14* mice that also expressed tdTomato in all GABAergic neurons. A 40× water immersion objective was used for two-photon imaging through a cranial window over CA1 in head-fixed awake mice during multimodal sensory and behavioral stimuli presentation. (**B**) Four examples of time-averaged images of GCaMP6f fluorescence in LEC LRIP axons in SLM (green) with tdTomato labeling CA1 interneurons (magenta). (**C**) Experimental design of single-stimulus protocol. Imaging was performed in blocks of four trials, each 40 s in duration. After a 10 ± 3 s baseline, one of four types of stimuli—aversive air puff (A), water drop (W), tone (T), or light (L)—was presented in random order for 200 ms, except the water drop was limited to 50 ms to prevent satiation. Each block was repeated to obtain at least five trials per stimulus. The animal's behavioral response (running and licking) was monitored. $\Delta F/F$ traces showing increased Ca^{2+} signal in a single bouton on an LRIP axon in response to air puff. (**D**) Mean (± SEM) $\Delta F/F$ Ca^{2+} signal (PSTH) from responsive ROIs to indicated stimuli. (**E**) Percentage of responsive boutons to the stimuli (air = 22.92%, water = 11.96%, tone = 13.64%, and light = 5.65%). (**F**) Scatter and mean (± SEM) plots of $\Delta F/F$ signals from individual responsive boutons (air = 0.55 ± 0.05, n = 68; water = 0.58 ± 0.07, n = 35; tone = 0.37 ± 0.03, n = 37; light = 0.23 ± 0.02, n = 18). (**G**) Experimental protocol: Imaging was performed as described above, but in response to pairs of stimuli, presented in blocks of 10 trials, each 40 s long. Stimuli were randomized and paired stimuli were interleaved with single stimulus presentations. (**H**) Mean (± SEM) $\Delta F/F$ Ca^{2+} signal (PSTH) from responsive ROIs to paired stimuli. (**I**) Percentage of responsive boutons for paired stimuli (A+T = 32.8%; A+L = 45.3%; A+W = 25.4%; W+T = 13.3%; W+L = 15.6%; T+L = 14.1%). (**J**) Scatter and mean (± SEM) plots of $\Delta F/F$ signals to paired stimuli from individual responsive boutons (A+T = 0.76 ± 0.07, n = 44; A+L = 0.74 ± 0.05, n = 58; A+W = 0.34 ± 0.03, n = 31; W+T = 0.48 ± 0.09, n = 17; W+L = 0.49 ± 0.04; T+L = 0.41 ± 0.045, n = 18).

second of the two training trials (fig. S7) ($P < 0.005$). Thus, although the LRIPs were not necessary for memory storage in two separate hippocampus-dependent nonspatial memory tasks, these inputs were important for enhancing the specificity of memory associations in performance of the two tasks.

LEC GABAergic inputs to CA1 are activated by sensory, motivational, and aversive stimuli in vivo

To explore how the LRIPs encode signals that might contribute to performance of nonspatial memory tasks, we used Ca^{2+} imaging to examine the responses of these inputs to a variety of sensory cues. We injected $rAAV^{Cre}$ in LEC of GAD2-Cre mice to express the genetically encoded Ca^{2+} indicator GCaMP6f (*26*) in GABAergic neurons. In vivo two-photon microscopy was then used to image Ca^{2+} signals in LRIP axons and axon terminals in the CA1 SLM region in response to a light stimulus, tone, aversive air puff, or water reward (Fig. 3, A to C) as described (*27*, *28*).

The sensory and behaviorally relevant stimuli elicited transient Ca^{2+} signals in LRIP axons and presynaptic boutons (Fig. 3, D to F), with the aversive air puff eliciting the largest increase in fluorescence intensity relative to the resting fluorescence intensity ($\Delta F/F = 0.55 \pm 0.05$) and greatest percentage of responsive boutons (22.9%). This result is of interest, as the aversive air puff is capable of serving as the unconditioned stimulus in a head-fixed CFC protocol (*28*). Water reward elicited a comparable Ca^{2+} signal in responsive boutons ($\Delta F/F = 0.58 \pm 0.07$) (movie S1), but only half as many boutons responded (11.9%) as compared with the response to the air puff.

As environmental contexts are composed of multisensory modalities, we also examined LRIP responses to pairs of stimuli (Fig. 3G). Paired stimuli tended to evoke larger Ca^{2+} responses in a greater fraction of boutons than did single stimuli. Pairing tone or light with air puff led to a 1.4-, 2.0-, and 3.2-fold greater Ca^{2+} response than when air puff, tone, or light were presented alone, respectively, with a 2- to 8-fold increase in the fraction of active boutons (Fig. 3, H to J). Whereas individual boutons usually responded to at most one or two of the four individual stimuli, collectively the LRIPs were able to represent the four sensory modalities examined (fig. S8D).

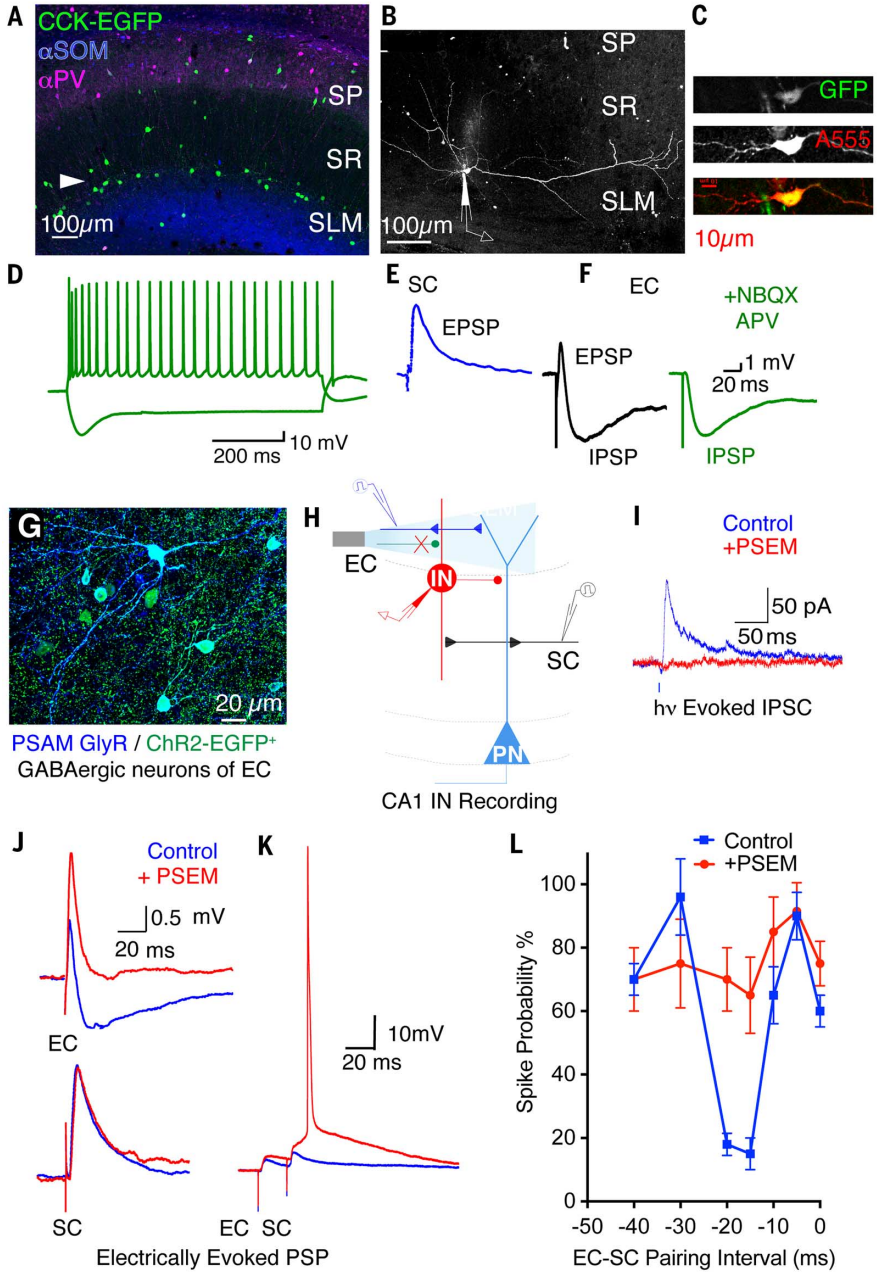

Fig. 4. CCK IN excitation and spike firing is suppressed 15 to 20 ms after LRIP activation. (**A**) Confocal projection image (left) showing CCK^+ (GFP, green), PV^+ (immunostained, magenta), and SOM^+ (immunostained, blue) IN soma in a hippocampal section from a *CCK-Cre/DLX-Flpe/RCE* dual-reporter mouse. Note abundant GFP^+ CCK IN soma at the SR-SLM border (arrowhead). (**B**) *Z*-axis projection image (right) of a GFP^+ CCK IN at SR-SLM border filled with neurobiotin-Alexa 555 (white). (**C**) Zoomed in image of IN in (B), showing GFP (top) and Alexa 555-neurobiotin (middle) colabeling (bottom, yellow). Scale bar, 10 μm. (**D** to **F**) Whole-cell voltage recordings from IN in (B) and (C). (D) Spike firing and voltage sag in response to 700-ms, 200 pA depolarizing and hyperpolarizing current steps, respectively. (E) Depolarizing PSP evoked by SC stimulation. (F) Mixed depolarizing and hyperpolarizing PSP evoked by EC stimulation (black). Bath application of NBQX (10 μM) and D-APV (100 μM) blocked the depolarization but not the hyperpolarization (green trace). (**G**) A 63× projection image of PSAM (α-bungarotoxin Alexa 647, blue) and ChR2-EGFP (green) showing coexpression in ~75% of EC INs in horizontal brain section from a *Gad2-Cre* mouse injected in LEC and MEC with $rAAV^{Cre}$. (**H**) Experimental scheme showing whole-cell recording from a CA1 SR-SLM IN with photostimulation of LRIPs or electrical activation of EC inputs. (**I**) Voltage-clamped IPSCs (at +10 mV) from CCK^+ IN (verified by post hoc staining) evoked by photostimulation of LRIPs in the absence (blue trace) or presence (red trace) of PSEM (3 μM). (**J**) Voltage responses in CA1 IN evoked by electrical stimulation of EC (top) or SC (bottom) inputs in the absence (control, blue trace) or presence (red trace) of PSEM. (**K**) Voltage responses of CA1 SR-SLM IN to paired electrical stimulation of EC and SC inputs (20-ms delay) in the absence (blue trace) or presence (red trace) of PSEM. (**L**) Mean probability of SR-SLM IN spike firing (percent of stimuli eliciting a spike ±SEM) in response to paired EC-SC stimulation as a function of pairing interval in the absence and presence of PSEM (spike probability with −20-ms EC-SC pairing: control = 18 ± 4%; PSEM = 70 ± 10%; $P < 0.005$, $n = 7$).

Moreover, the probability that a single bouton responded to three distinct pairs of stimuli was higher than predicted from a random, independent distribution of boutons based on the measured response to individual pairs of stimuli. Thus, a subpopulation of LRIPs may be specifically tuned to encode multimodal sensory cues, similar to what constitutes a behavioral context.

Spontaneous motor behaviors, such as spontaneous running and licking, also elicited Ca^{2+} responses in the LRIPs (fig. S8E). Although the aversive air puff typically elicited a running response, the air puff recruited a greater fraction of boutons and evoked a larger Ca^{2+} signal compared with that seen with spontaneous running. This indicates a specific sensory contribution to the air-puff response. Furthermore, LRIP boutons that made apparent contacts on dendrites had larger Ca^{2+} responses than did boutons that targeted SR-SLM interneuron somata (fig. S8, F and G).

We wondered why different boutons showed such diverse responses to different stimuli. One clue came from the finding that boutons along a single axon responded more uniformly to a set of sensory cues than did neighboring boutons from different axonal fibers (fig. S8, H and I). This indicated that the variability in bouton response was likely not caused by random trial-to-trial variability but rather resulted from the specific tuning of individual LRIP axons to distinct combinations of sensory and behavioral cues. This finding is consistent with the idea that these inputs are important for regulating nonspatial contextual and object memory.

LRIPs from LEC transiently inhibit spike output of local CA1 dendrite-targeting feedforward inhibitory neurons

How do the long-range GABAergic projections influence information flow through the cortico-hippocampal circuit to regulate memory storage? We began to investigate this question by performing whole-cell recordings from cholecystokinin-positive (CCK^+) SR-SLM interneurons, which represent a large fraction of the SR-SLM border INs targeted by the LRIPs (fig. S9). Moreover, the CCK^+ INs receive strong excitatory drive from the SCs and send strong inhibitory output to CA1 pyramidal neuron dendrites (*11*, *29*, *30*).

To determine how the CCK^+ INs integrate their cortical and hippocampal inputs, we electrically stimulated the SC axons (using an electrode in SR) or a mixed population of excitatory and inhibitory EC axons (using an electrode in SLM). We then recorded the synaptic responses in genetically defined CCK^+ SR-SLM INs tagged with GFP (*11*, *16*) (Fig. 4, A to C). These neurons displayed a large voltage sag in response to hyperpolarization and an intermediate firing pattern, characteristic of CCK^+ INs (*29*, *31*–*33*) (Fig. 4D).

SC stimulation elicited a strongly depolarizing PSP in the CCK^+ INs, with a peak amplitude of 9.83 ± 0.17 mV at 50% maximal stimulation strength (Fig. 4E). In contrast, EC stimulation evoked a mixed EPSP-IPSP (inhibitory postsynaptic potential peak depolarization of 0.79 ± 0.34 mV) that was dominated by a large hyperpolarization, which reached its peak negative value (–5.59 ± 0.17 mV, n = 7) ~20 ms after the stimulus (Fig. 4F). As we show below, the time course of the hyperpolarization imposes a precise timing dependence for disinhibition, which regulates the timing of the induction of ITDP and the generation of dendritic spikes in response to paired stimulation of the EC and SC inputs. The EC-evoked IPSP was unaffected by blockers of glutamatergic transmission NBQX 10 μM and 2-amino-5-phosphonovaleric acid (APV) 100 μM, which demonstrated that it resulted from direct activation of GABAergic axons rather than disynaptic FFI (Fig. 4F).

To determine whether the electrically evoked IPSP in CA1 INs was caused by GABA release from the EC LRIPs, we silenced these projections using the PSAM-PSEM approach (Fig. 4, G and H). Two independent $rAAV^{Cre}$ vectors expressing ChR2 and PSAM were injected into LEC and MEC of Gad2-Cre mice (Fig. 4G). The light-evoked IPSC recorded from SR-SLM INs was fully blocked by local bath application of 3 to 5 μM $PSEM^{308}$ (IPSC = 0.013 ± 0.04 pA, n = 11), which verified

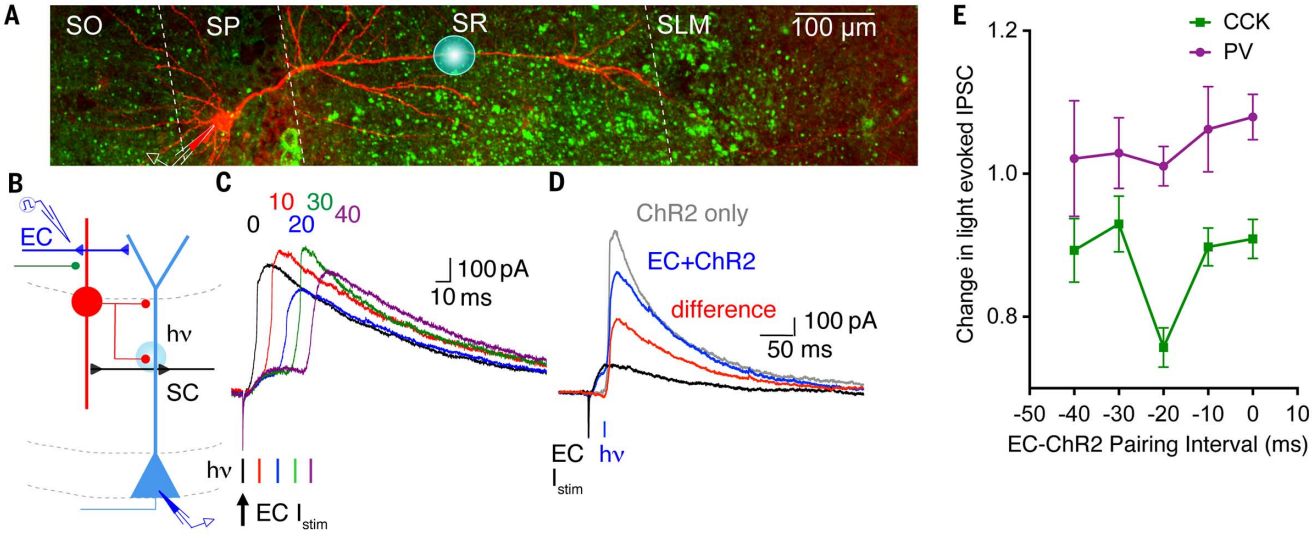

Fig. 5. LRIPs suppress SC-evoked FFI from CCK^+ SR-SLM INs. (**A**) Confocal projection image of a CA1 PN filled with Alexa 594 (red) in a slice where CCK^+ INs expressed ChR2-EGFP (green). Blue circle represents the perimeter of 470-nm light stimulus. (**B**) Experimental scheme depicting somatic recording from a CA1 PN (red); electrical stimulation of EC inputs in SLM was paired at variable delays with photostimulation of CCK^+ INs. (**C**) IPSCs evoked by photostimulation of CCK^+ INs (*hv*) recorded from soma of a voltage-clamped CA1 PN (+10 mv) during paired electrical stimulation of EC inputs (arrow) at 0, 10-, 20-, 30-, and 40-ms delays. (**D**) IPSCs in CA1 PNs evoked by electrical stimulation of EC inputs and photostimulation of CCK^+ INs. Gray trace (ChR2 only), CA1 PN IPSC evoked by photostimulation of CCK^+ IN. Black trace (EC), CA1 PN IPSC evoked by electrical stimulation of EC input. Blue trace (EC+ChR2), net IPSC evoked by pairing EC electrical stimulation with photostimulation of CCK^+ IN (20-ms delay). Red trace (difference), inferred CCK^+ IN IPSC evoked when EC electrical stimulation preceded photostimulation of CCK^+ IN by 20 ms. Trace obtained by subtracting EC-evoked IPSC (black trace) from IPSC evoked during paired stimulation (blue trace). (**E**) Effect of pairing interval on EC-dependent suppression of IPSC evoked by photostimulation of CCK^+ INs or PV^+ INs. Mean (±SEM) amplitude of photostimulation-evoked IPSC during pairing with EC stimulation [measured as in (D)] normalized by photostimulated IPSC amplitude in the absence of EC stimulation, plotted versus pairing interval. ChR2-EGFP expressed in either PV^+ INs (magenta, 1.01 ± 0.03-fold change at –20-ms pairing interval, P = 0.3319, paired two-tailed t test, n = 5) or CCK^+ INs (green, 0.76 ± 0.03-fold decrease in IPSC at –20-ms pairing interval, $P < 0.001$ paired two-tailed t test, n = 9).

the efficacy of this method (Fig. 4I). Silencing the LRIPs nearly abolished the hyperpolarizing component of the mixed PSP evoked by electrical stimulation (peak negative value reduced to –0.29 ± 0.21 mV, n = 7), whereas it increased the peak depolarization during the PSP (to 4.79 ± 0.79 mV), which demonstrated the importance of this projection. PSEM caused no change in the PSP evoked by electrical stimulation of the SC axons in SR (Fig. 4J), which indicated the specificity of the approach.

Does LRIP activation affect action potential output of the SR-SLM INs in response to paired stimulation of their EC and SC inputs? Electrical stimulation of the EC pathway alone failed to trigger spike firing (Fig. 4K), consistent with the weak depolarizing phase of the mixed EPSP-IPSP response (Fig. 4F). In contrast, moderately strong stimulation of the SC pathway alone (50 μA stimulus current injection) elicited a large depolarizing PSP that triggered a spike in SR-SLM INs with >50% probability (Fig. 4L). However, when the SC stimulus was preceded by a stimulus to the EC inputs that occurred 15 to 20 ms before stimulation of the SC inputs, the ability of the SC inputs to trigger action potentials in the SR-SLM INs was suppressed (Fig. 4, K and L). The timing dependence of spike suppression (Fig. 4L) coincided with the maximal hyperpolarization of the SR-SLM INs in response to EC stimulation, which suggested that the suppression of spike firing was mediated by the activation of the LRIP inputs. Consistent with this idea, silencing the LRIPs with PSAM-PSEM prevented the suppression of spike firing upon electrical stimulation of the EC inputs (Fig. 4, K and L).

LRIPs provide a temporally precise gate of hippocampal input to CA1 pyramidal neurons

What are the consequences of the LRIP-mediated suppression of SR-SLM IN firing for the activity of CA1 pyramidal neurons? To examine this question, we virally expressed ChR2 in CCK$^+$ INs in the CA1 SR/SLM region and measured the light-evoked IPSC in CA1 pyramidal neurons voltage-clamped at +10 mV (Fig. 5, A and B). Photostimulation of the CCK$^+$ INs with a light pulse focused in SR produced a robust IPSC in the

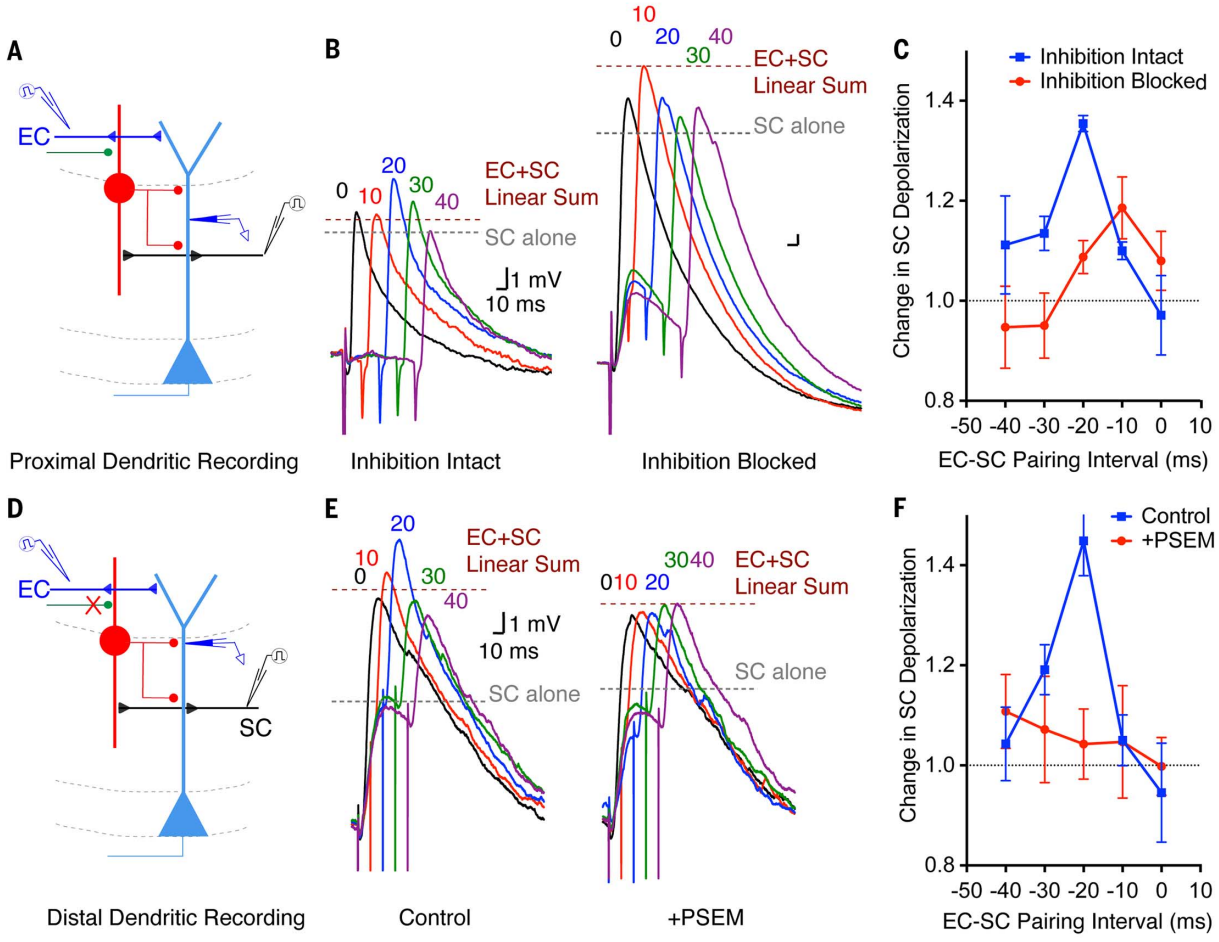

Fig. 6. LRIPs enhance CA1 pyramidal neuron dendritic depolarization in response to SC stimulation through disinhibition. (**A**) Experimental scheme for assessing the synaptic response in CA1 PN dendrites to paired EC-SC electrical stimulation. Horizontal lines show approximate locations of EC and SC stimulation electrodes and dendritic recording pipette. (**B**) Dendritic voltage responses to paired EC-SC electrical stimulation at indicated delays (SC after EC), in the absence (left) or presence (right) of GABAR antagonists SR 95531 (2 μM) and CGP 55845 (1 μM). Gray dashed line, amplitude of PSP evoked by SC stimulation alone. Red dashed line, predicted linear sum of PSPs evoked by EC and SC paired stimulation. (**C**) Summary plot (mean ± SEM) of paired EC-SC peak PSP normalized by PSP evoked by SC stimulation alone recorded in CA1 PN proximal dendrites. PSPs measured in the absence (blue squares) and presence (red circles) of GABAR blockers (EC-SC –20-ms pairing: with inhibition intact, fold change = 1.35 ± 0.02; with inhibition blocked, fold change = 1.08 ± 0.03; P = 0.001, two-way ANOVA with Sidak multiple comparisons test, n = 5). (**D**) Experimental scheme to determine how silencing LRIPs (denoted by X) affects PSP in CA1 PN distal dendrites during paired EC-SC stimulation. PSAM expressed in LEC GABAergic neurons in *GAD2-Cre* mouse with AAV^{Cre}. (**E**) CA1 PN distal dendrite PSPs evoked by paired stimulation of EC-SC inputs at indicated intervals, first in the absence (left) and then the presence (right) of PSEM. (**F**) Mean (± SEM) PSP amplitude recorded in CA1 PN distal dendrites evoked by paired EC-SC stimulation normalized by PSP evoked by SC stimulation alone, in the absence (blue squares) and presence (red circles) of PSEM. PSEM significantly reduced the effect of paired EC-SC stimulation at –20-ms delay to increase PSP size (control, 1.45 ± 0.07-fold increase; PSEM, 1.04 ± 0.07-fold increase; P < 0.001, two-way ANOVA with Sidak multiple comparisons test, n = 8).

CA1 pyramidal neuron soma (~250 μm from the light spot). Electrical stimulation of the EC inputs 20 ms before photostimulation significantly suppressed the light-evoked IPSC (to 75.6 ± 2.7% of the unpaired light-evoked IPSC, n = 9; P < 0.0001, two-way ANOVA) (Fig. 5, C to E), with little change at other pairing intervals. Electrical stimulation did not alter the light-evoked IPSC when ChR2-EYFP was expressed in PV^+ INs, regardless of pairing interval, which indicated the specificity of the effect. As ChR2 photostimulation provides an unusually strong excitatory drive compared with an action potential, the LRIPs are likely to produce an even greater suppression of the CCK^+ IN–mediated IPSP evoked by excitatory synaptic input.

Does the suppression of CCK^+ IN firing by the LRIPs influence the ability of the EC or SC inputs to excite CA1 pyramidal neurons? As the SR-SLM INs are known to target CA1 pyramidal neuron apical dendrites, we addressed this question using whole-cell recordings from CA1 pyramidal neuron dendrites 150–300 μm from the soma in SR during single or paired stimulation of the EC and SC inputs (Fig. 6).

Stimulation of the SC input alone evoked a large depolarizing PSP in the proximal dendrite ~150 μm from the soma (4.48 ± 0.57 mV, n = 5) (fig. S10). Stimulation of the EC input alone evoked only a very small dendritic depolarization (1.00 ± 0.24 mV) (fig. S10). However, when we stimulated the EC input 20 ms before the SC input, we observed a supralinear boosting of dendritic depolarization (Fig. 6, B and C), which resulted in a net PSP that was 1.35 ± 0.02 times the PSP evoked by stimulation of the SC pathway alone. This boost was significantly greater than the predicted linear sum of 1.13 ± 0.024-fold for the SC response alone (P < 0.05, t test; n = 5). Paired EC-SC stimulation at the −20-ms interval was associated with an even greater 2.2-fold increase in the postsynaptic Ca^{2+} transient evoked by SC stimulation in CA1 pyramidal neuron dendritic spines in SR, relative to the Ca^{2+} transient elicited by SC input alone (fig. S10) (P < 0.001, t test, n = 5).

It was striking that the supralinear boosting was sharply tuned to the −20-ms pairing interval. Paired activation of EC and SC inputs at other intervals resulted in linear or sublinear summation (Fig. 6, B and C). Moreover, pairing at the −10-ms interval produced a significantly lower boosting in spine Ca^{2+} compared with the −20-ms interval (1.3-fold, P < 0.0001, t test, n = 5).

The timing dependence of the supralinear boosting of the CA1 pyramidal neuron PSP suggested to us that it might result from a disinhibitory action of the LRIPs to suppress SC-evoked FFI through the SR-SLM INs (Fig. 6D). We therefore compared the effect of paired EC-SC stimulation before and after application of GABA receptor channel antagonists (Fig. 6, B and C). Blockade of inhibition greatly increased the peak depolarization during the PSP evoked by stimulation of the EC and/or SC inputs, reflecting the removal of FFI (Fig. 6B and fig. S10, B and C). Of note, paired EC-SC stimulation produced only a linear or sublinear summation at all pairing intervals in the presence of the antagonists, consistent with the view that supralinear summation was caused by disinhibition. For example, pairing at a −10-ms interval resulted in a net PSP 1.19 ± 0.06 times that of the SC PSP alone and not significantly different from the linear sum of the EC+SC PSPs when stimulated independently (P = 0.238). In addition, the peak of the paired response was shifted to the −10-ms pairing interval, which corresponds to the expected peak of temporal summation of the individual EC and SC EPSPs.

Next, we tested directly whether the LRIPs were responsible for the supralinear boosting by recording PSPs in distal CA1 pyramidal neuron dendrites (300 μm from the soma) in response to paired EC-SC stimulation, before and after silencing the LRIPs (Fig. 6, D to F). We found that application of $PSEM^{308}$ (3 μM) to slices in which the LRIPs expressed PSAM fully prevented the supralinear boosting (Fig. 6, E and F). Thus, we propose that the EC LRIPs potentiate the ability of the SC inputs to excite CA1 pyramidal neuron dendrites by suppressing SC-evoked feedforward inhibition mediated by the SR-SLM interneurons.

Disinhibition through LEC LRIPs enables input timing–dependent plasticity and dendritic spike firing

Given the behavioral role of the LRIPs in memory storage, we asked whether these inputs may also contribute to more robust, longer-lasting forms of SC input gating than the transient boosting of dendritic depolarization and spine Ca^{2+} levels seen above. Paired EC-SC stimulation at 1 Hz for 90 s induces a long-lasting form of heterosynaptic plasticity, termed input timing–dependent plasticity (ITDP) which strongly enhances SC-evoked excitation of the CA1 pyramidal neuron through combined long-term potentiation of the SC EPSP and long-term depression of inhibition mediated by somatic-targeting CCK^+ basket cells (which are distinct from the CCK^+ SR/SLM INs) (*10*, *11*). As the induction of ITDP is finely tuned to the same −20-ms pairing interval optimal for LRIP-mediated disinhibition, we hypothesized that the LRIPs from EC may be required for this plasticity. In support of this view, we found that silencing of PSAM-expressing LRIPs, either from LEC alone or from both LEC and MEC, with $PSEM^{308}$ fully blocked the induction of ITDP (Fig. 7, A and B).

The above results suggest that the induction of ITDP is normally suppressed by FFI evoked by SC stimulation and, thus, requires LRIP activation to suppress this inhibition. This model would also explain how the induction of ITDP is finely tuned to the −20-ms pairing interval. This scenario predicts that robust ITDP may be induced over a broader range of intervals when EC-SC paired stimulation is given in the presence of GABAR antagonists, which would eliminate FFI at all pairing intervals. Consistent with this model, we found that the presence of GABAR blockers

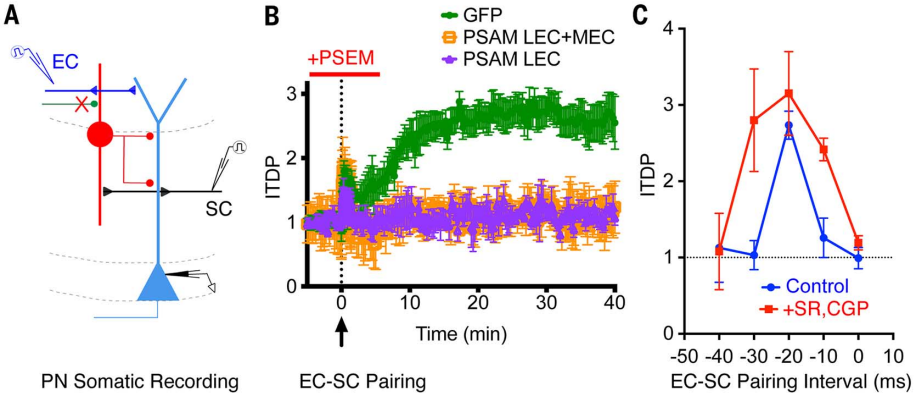

Fig. 7. LEC LRIPs enable induction of ITDP in CA1 PNs. (**A**) Experimental scheme to assess role of LRIPs in ITDP. PSAM or GFP was expressed in GABAergic neurons in LEC alone or in both LEC and MEC. ITDP was induced by pairing EC-SC stimulation at 1 Hz for 90 s with a −20-ms delay. (**B**) Pairing protocol induces a 2.65 ± 0.23-fold increase in the SC-evoked depolarization in the CA1 PN soma (ITDP relative to baseline PSP) when PSEM is applied to slices expressing GFP in LEC GABAergic neurons (green, n = 5, P < 0.0001, two-tailed t test, before versus after ITDP pairing). ITDP is absent when the pairing protocol is applied with PSEM present in slices expressing PSAM in GABAergic neurons in LEC alone (purple triangles, 1.09 ± 0.12-fold potentiation, n =4, P = 0.114, two-tailed t test before versus after ITDP pairing; P < 0.0001, two-tailed t test for ITDP with GFP versus PSAM in LEC). ITDP is also absent in the presence of PSEM when PSAM was expressed in both LEC and MEC (orange squares, 1.10 ± 0.31-fold potentiation, n = 4, P = 0.189, two-tailed t test pre versus post ITDP pairing; P < 0.0001, two-tailed t test for ITDP with GFP versus PSAM in LEC+MEC). Peak PSP value normalized to value 5 min before ITDP induction. Mean fold potentiation obtained by averaging normalized PSP values during the 25- to 30-min period after ITDP induction. (**C**) ITDP tuning curve showing potentiation (mean ± SEM) as a function of EC-SC pairing interval. Blue circles, with inhibition intact (−10-ms interval, 1.25 ± 0.26-fold change, n = 4; −20-ms interval, 2.74 ± 0.18-fold change, n = 5; −30-ms interval, 1.03 ± 0.19-fold change, n = 4). Red squares, ITDP with GABAR antagonists applied only during induction protocol (−10 ms, 2.41 ± 0.15-fold change, n = 5; −20 ms, 3.15 ± 0.55-fold change, n = 7; −30 ms, 2.8 ± 0.67-fold change, n = 4). Inhibition blocked versus intact, no significant difference, P = 0.105 two way ANOVA −20, −10, and −30 ms comparison.

during the ITDP induction protocol alone enabled the induction of robust ITDP over a broader range of pairing intervals, from –10 to –30 ms (Fig. 7I). This ITDP tuning curve now matched the expected time course of temporal summation of the EC and SC EPSPs (*10*).

How could the relatively modest boosting by the LRIPs of the EC-SC synaptic depolarization lead to such a robust form of plasticity? Many forms of long-term synaptic plasticity that do not depend on somatic action potentials [such as ITDP (*10*, *11*)] require the firing of dendritic spikes, which can enhance Ca^{2+} influx into the postsynaptic cell (*34*, *35*). Thus, we next examined whether more prolonged EC-SC pairing, as used to induce ITDP, promoted dendritic spiking, using whole-cell recordings from distal CA1 pyramidal neuron dendrites (≥300 μm from the soma) (Fig. 8A).

Although single paired–EC-SC stimulation failed to elicit a dendritic spike, large regenerative spikes began to appear when we delivered 10 or more paired EC-SC stimuli at 1 Hz using a –20-ms interval (Fig. 8B). Event amplitude frequency histograms (Fig. 8C) showed three peaks, corresponding to subthreshold PSPs (~20 mV amplitude); small, brief action potentials (~40 mV) resembling dendritic Na^+ spikes (*34*, *36*); and longer, larger events (~60 mV) resembling dendritic Ca^{2+} spikes (*34*, *36*, *37*). Both types of spikes were preferentially generated at the –20-ms pairing interval compared with a –10-ms pairing interval. Both types of spikes also required LRIP input as spike probability greatly decreased when the LEC LRIPs were silenced with PSAM-PSEM (Fig. 8, D to F).

Experiments using two-photon Ca^{2+} imaging in CA1 pyramidal neurons supported the view that the dendritic spikes may contribute to the induction of ITDP. Repetitive stimulation of EC-SC inputs at 1 Hz using a –20-ms pairing interval led to long-lasting Ca^{2+} signals in the apical dendrites that propagated to the soma (fig. S10, F and G). These dendritic signals provide a likely source for the intracellular Ca^{2+} required for the induction of ITDP (*10*, *11*). Pairing-induced dendritic spikes gated by the LRIPs may thus provide a powerful nonlinear mechanism for the long-term enhancement of SC-mediated excitation in response to temporally precise, coordinated cortico-hippocampal dendritic activity.

Discussion

The importance of excitatory projections from LEC and MEC to hippocampus for memory storage and spatial encoding is well established (*38*). MEC also sends LRIPs to hippocampus that form synapses on CA1 SR-SLM GABAergic interneurons (*4*), although the in vivo function of these inputs was not determined. Here, we report that LEC sends LRIPs to CA1 that exert an even stronger inhibitory drive on CA1 SR-SLM INs than the LRIPs from MEC. We also found that LRIPs from LEC convey multimodal sensory information that helps fine-tune the specificity of hippocampus-dependent contextual memory storage and enhances the ability to distinguish novel from familiar objects. Finally, the LRIPs provide a temporally precise disinhibitory gating mechanism for enhancing information flow within the hippocampal circuit at both short and long time scales.

Within the context of the cortico-hippocampal circuit, the LRIPs transiently suppress dendritic FFI to enhance excitatory signals from the trisynaptic path that arrive at CA1 pyramidal neurons precisely 20 ms after LRIP activation. The effect of this disinhibitory gating has ramifications across widely different time scales. Activation of the LRIPs with a single pairing of EC-SC stimulation at a –20-ms interval causes a transient supralinear boost in local dendritic depolarization and proximal spine Ca^2. Repetitive paired stimulation of EC and SC inputs at the same interval leads to further amplification of synaptic input by promoting the firing of dendritic spikes (*8*, *9*) and the induction of ITDP, a robust Ca^{2+}-dependent form of long-term heterosynaptic plasticity (*10*, *11*). Given that dendritic spikes are normally suppressed by strong FFI (*9*), the ability of the LRIPs to enhance dendritic spiking during a precise temporal window may contribute to the dendritic spike firing in vivo observed during behaviorally relevant cooperative activity (*39*). The LRIP-dependent

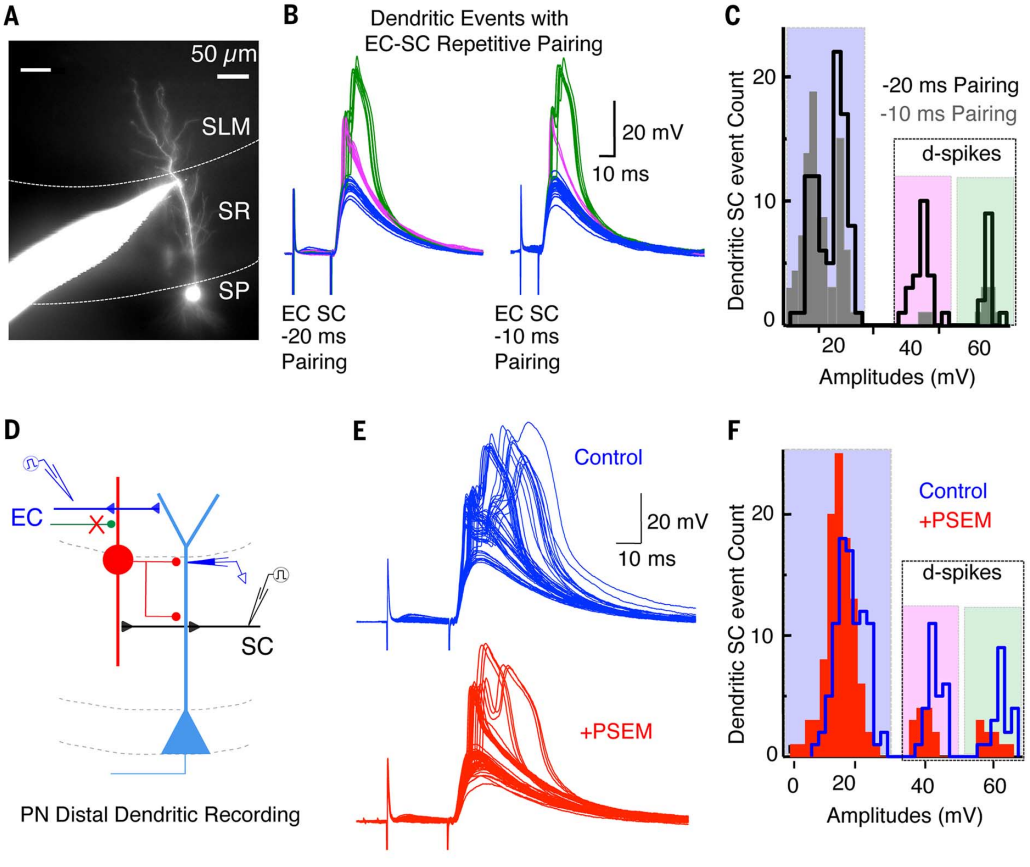

Fig. 8. EC-SC pairing at –20-ms interval induces dendritic spikes. (**A**) Image showing CA1 PN filled with Alexa 594 during a distal dendritic recording. (**B**) Dendritic PSPs (blue), brief spikes (magenta), and long spikes (green) evoked by 10- to 30-s repetitive pairing of EC-SC inputs at 1 Hz with –20- or –10-ms pairing intervals. During the first 5 to 10 paired stimuli, only subthreshold PSPs (blue) were observed. Subthreshold PSPs, brief spikes, and long spikes were then observed interspersed with subsequent paired stimuli. (**C**) Histograms of the peak dendritic voltage response evoked by a train of 30 paired EC-SC stimuli at 1 Hz, by using a –20-ms (black open bars) or –10-ms (gray filled bars) pairing interval ($P < 0.005$, t test within cell comparisons for –20 ms vs –10 ms; $n = 3$). Responses were classified on the basis of amplitude and duration as subthreshold PSPs (blue) or dendritic spikes (magenta, brief spikes; green, long spikes. (**D**) Experimental scheme to assess the role of LRIPs in dendritic spike firing. PSAM was virally expressed in LEC of Gad2-Cre mice. (**E** and **F**) Distal dendritic responses (E) and event amplitude histograms (F) to paired EC-SC stimulation at 1 Hz by using a –20-ms delay interval in the absence (blue) and then presence (red) of PSEM ($P < 0.0001$, t test within cell comparisons, control vs. +PSEM; $n = 3$).

dendritic spikes are likely to participate in the induction of ITDP and the fine-tuning of learning and memory; this likelihood is based on the role of such spikes in both other forms of Ca^{2+}-dependent synaptic plasticity (*34*, *35*, *40*) and nonlinear gain modulation during associative learning (*35*) and sensory tuning (*41*).

Our findings, together with previous results (*28*, *42*–*45*), further demonstrate how distinct populations of local interneurons play well-defined roles in hippocampus-dependent behaviors and circuit function. We found that CCK^+ INs located near the SR-SLM border exert strong FFI onto CA1 pyramidal neuron dendrites; LRIP-mediated transient suppression of these INs enables temporally precise supralinear dendritic excitation. The GABAR kinetics, CA1 pyramidal neuron membrane time constant (*29*, *46*), and in vivo firing patterns (*47*) of the CCK^+ INs are all likely to participate in ensuring that the kinetics of the LRIP-mediated IPSP are appropriately tuned to implement the 20-ms gating of information flow from the SC inputs to CA1 pyramidal neurons. Of note, mice have been found to display an overgeneralized contextual learning phenotype when signaling in CA1 CCK^+ INs is perturbed (*48*), similar to our behavioral findings when the LRIPs that target these INs are silenced.

The role of the CCK^+ SR-SLM border INs in implementing the ITDP timing rule contrasts with the role in ITDP of a separate subclass of CCK^+ INs, the perisomatic-targeting basket cells located in and around the CA1 pyramidal neuron cell body layer (*11*). Previously, we found that the expression of ITDP results from the combined effects of long-term potentiation of the SC excitatory synapses on CA1 pyramidal neurons and the long-term depression of FFI from a population of perisomatic-targeting CCK^+ basket cell INs onto the same CA1 pyramidal cells (*11*). Thus, anatomically distinct subpopulations of the same genetically defined class of CCK^+ INs are specifically involved in the induction versus the expression of ITDP. Yet another class of CA1 INs, the somatostatin-positive (SOM^+) dendrite targeting INs, has been found to be required for CFC (*28*). These INs serve to suppress EC input to CA1 pyramidal neuron dendrites during aversive stimuli, thereby ensuring that the unconditioned stimulus is not encoded as part of the contextual representation. Thus, distinct populations of GABAergic INs participate in distinct microcircuits to regulate separate phases of memory encoding.

What is the significance of the precise 20-ms temporal window for LRIP-dependent disinhibitory gating? One interesting possibility is suggested by the fact that this interval is matched to the dynamics of the delay-line architecture of the cortico-hippocampal circuit, where signals propagating through the trisynaptic path arrive at CA1 pyramidal neurons about 15 to 20 ms after the arrival of signals through the direct path (*49*). Thus, the temporal dynamics of LRIP-mediated disinhibition will enhance the propagation to a given CA1 pyramidal neuron of those signals arriving through the trisynaptic path that were initiated by activity in EC LII stellate cells (which project to dentate gyrus) simultaneously with activity in the subset of EC LII (*3*) and LIII pyramidal neurons (*6*) that directly project to the same CA1 pyramidal neuron. This timing rule for disinhibitory gating may therefore serve as a filter to assess the salience of processed associations arriving from CA3 inputs on the basis of their temporal relation to the direct multimodal sensory inputs arriving from EC.

Because our studies of the effects of LRIP activation on CA1 pyramidal neuron function were carried out in ex vivo hippocampal slices, a key question is whether the 20-ms timing interval between cortical and SC input that is required for the boosting of SC excitation is implemented by in vivo patterns of cortico-hippocampal activity. Studies of the temporal relation of oscillatory activity in entorhinal cortex and hippocampus in vivo suggest that the disinhibitory gating mechanism may indeed be engaged during spatial behavior (*50*, *51*) and associational learning (*52*). For example, during running and memory tasks, fast gamma oscillations (100 Hz) arising from EC LIII are observed in SLM of CA1 and precede the slow gamma oscillations (50 Hz) in SR of CA1, which are thought to reflect CA3 pyramidal neuron input (*50*). Notably, EC LIII–CA1 gamma activity and CA3-CA1 gamma activity display a 90° phase offset during theta frequency oscillations (8 to 9 Hz) (*50*) that is consistent with a ~20- to 25-ms time delay.

Learning is a critical adaptive behavior, and the precision of memory storage normally enables an animal to discriminate between harmful (salient) versus safe (neutral) environments. Failure to do so can lead to overgeneralization of fear memories, a characteristic feature of posttraumatic stress and other anxiety disorders. How might the effect of the LRIPs to enhance cortico-hippocampal information flow contribute to their behavioral role to enhance learning specificity? The increased freezing in the conditioned and novel contexts upon silencing the LRIPs indicates that the disinhibitory circuit, and by implication ITDP, is not required for generalized fear learning, which may be implemented by other intrahippocampal circuits (*28*, *53*) or other forms of plasticity, such as SC Hebbian LTP. Similarly, the LRIPs are not needed for basic object recognition memory. Rather, we suggest that the LRIPs may enhance contextual and object memory storage and may improve memory specificity by creating a sparse, high-contrast ensemble of potentiated SC synapses whose dynamics conform to the temporal window of paired EC-SC associative inputs that enables the induction of ITDP.

Materials and Methods

All experiments were conducted in accordance with the National Institutes of Health guidelines and with the approval of the Columbia University and New York State Psychiatry Institute (NYSPI) Institutional Animal Care and Use Committee.

Mice

Gad2-IRES-Cre (*16*), PV-IRES-Cre (*54*), and Ai14-tdTomato (*55*) mouse lines were obtained from the Jackson Laboratory (JAX); IRES refers to internal ribosomal entry site. The CCK IN-specific enhanced green fluorescent protein (EGFP)–labeled line was generated as described in references (*11*, *16*). Briefly, CCK-IRES-Cre driver mice (generous gift of Z. J. Huang, Cold Spring Harbor Laboratory) (*11*, *16*) were crossed with the Dlx5/6-Flpe driver mice [generous gift from G. Fishell, New York University (*56*)] and a Cre- and Flp-dependent EGFP reporter strain, R26NZG [JAX (*57*)].

Viruses

For anatomy and slice electrophysiology experiments in Fig. 1, we used the following: (i) rAAV2/1 EF1α-DIO-ChR2-EYFP (K. Deisseroth, Stanford University), (ii) AAV2/9 CAG-Flex-EGFP, and (iii) rAAV2/9 CAG-Flex-tdTomato [all prepared by University of Pennsylvania (UPenn) Vector Core]. Behavioral experiments in Fig. 2 utilized: (i) for the PSAM-silencing group rAAV2/9 Syn-Flex-PSAM (L141F)GlyR-IRES-GFP (plasmid generous gift from S. Sternson, Janelia Farm; prepared by UPenn Vector Core); and (ii) for the GFP control group rAAV2/9 Syn-Flex-EGFP (B. Roth, University of North Carolina; prepared by UNC Vector Core). Imaging experiments in Fig. 4 used rAAV2/1 Syn-Flex-GCaMP6f (L. Looger, Janelia Farm; prepared by UPenn Vector Core). The following custom-prepared viruses were used for the LRIP activation and silencing experiments in Fig. 5, G to L and I to K, and Fig. 6, D to H: (i) rAAV2/7 Syn-Flex-Chr2-sfGFP; and (ii) rAAV2/7 Syn-Flex-PSAM-IRES-GFP [B. Zemelman, University of Texas at Austin (UT Austin), both custom-prepared]. Experiments in Fig. 6, A to E, involving (i) photostimulation of GABAergic CCK-Cre^+ INs used an rAAV2/7 Gad65-$(Chr2\text{-}sfGFP)^{Cre}$ (B. Zemelman, UT Austin, custom-prepared); (ii) photostimulation of PV-Cre^+ INs used rAAV2/5 EF1α-DIO-ChR2-EYFP [K. Deisseroth, Stanford University, commercially derived from UPenn (*58*)].

Surgery

Stereotaxic virus injection

The viral injection procedure is as previously described (*11*, *59*). Virus was injected into the brains of mice under stereotactic control by using thin glass pipettes pulled by using a micropipette puller and fire-polished with a microforge to have a long taper ending with a 10-μm tip diameter. Pipettes were first back-filled with light mineral oil, then front-filled with the virus by using a Nanoject II injector. Adult mice (5 to 10 weeks old) were injected with 50 μl buprenorphine (0.3 mg/ml), subsequently anesthetized with 3.5% isofluorane for 3 min (1.5 ml/min flow rate) in an induction chamber, head-fixed in a stereotaxic frame, and maintained under anesthesia with 1.5 to 2.5% isofluorane (1 ml/min) with a facemask. The hair on the head was clipped, the scalp sterilized with ethanol and betadine, and a 5- to 7-mm incision made to expose the skull.

The skull was then cleaned with hydrogen peroxide (0.1%), and the level adjusted to align bregma and lambda in the z axis. Small craniotomies were made bilaterally to target the dorsal hippocampal CA1 subfield [anteroposterior (A/P), −2.3 ± 0.2 from bregma; mediolateral

(M/L), 1.5 ± 0.2 from bregma, dorsoventral (D/V), −1.2 ± 0.2 mm from surface of the brain]; LEC (A/P, −3.2 ± 0.2 from bregma; M/L, 4.5 ± 0.2 from bregma, D/V, −2.5 ± 0.2 mm); and MEC (A/P 0.2 ± 0.2 from lamboid sinus at a 9° angle, M/L 3.1 ± 0.2 from lambda, D/V 0.9 ± 0.1 from surface of the brain). The pipette was lowered to penetrate the dura and a total of ~92 to 115 nl of virus was injected at each stereotactic coordinate (23 nl at a time with a 30-s interval between injections) by using the Nanoject II auto injector under slow mode. The pipette was retracted from the brain after a 5-min waiting period after the final injection per site. The scalp was disinfected with betadine, treated with triple antibiotic and the topical anesthetic Marcaine (0.5%), and sutured. Mice were allowed to recover for 2 to 4 weeks postinjection before the electrophysiology experiments.

Hippocampal cannula guide implantation

To selectively silence the long-range inhibitory projections from the entorhinal cortex to the hippocampus, we used local infusion of the cognate synthetic ligand PSEM in CA1 using a cannula. The presurgical and craniotomy procedures were identical to that of the stereotaxic viral injection. The skull surface was dried completely and coated with a thin layer of Vetbond and then lightly scratched with a scalpel blade to form crevices for the cement mix to seep in. A sterilized custom-designed bilateral cannula guide with a dummy cannula was inserted in the skull over dorsal hippocampal CA1 (A/P, −2.2; M/L, 1.5, D/V, −1.7 from bregma) along with two stainless steel anchoring screws inserted partially into the skull, one over the prefrontal cortex and the other over the cerebellum. The implant was secured to the animal's skull with dental cement (grip cement or dental acrylic) and two bone screws. The cement was allowed to dry for 20 min, and the wound was sutured around the implant. Marcaine was applied locally to decrease postoperative pain.

Hippocampal cranial window implantation

The cranial window implantation method used here is as described previously (*27*, *28*). The presurgical anesthesia and exposed skull preparation procedures were identical to that described above. A 3-mm-diameter circle was drilled in the skull over left dorsal CA1, to match the size of the cannula window implant. The bone and dura were gently removed, and the cortex covering the hippocampus was slowly aspirated while constant irrigation with chilled artificial cerebrospinal fluid (ACSF) was maintained until the external capsule was exposed. A sterilized stainless steel cannula implant with a glass cover slip window was inserted into the craniotomy. The top of the cannula and a titanium head post were secured to the skull with grip cement. The cement was allowed to dry for 20 min before mice were returned to the home cage.

Postsurgical care

The animals recovered from anesthesia and were mobile within 5 to 15 min postsurgery. Mice were monitored every 12 hours for 3 days after surgery, and buprenorphine was administered to minimize any signs of discomfort.

Freely moving behavior

The contextual fear conditioning and open-field behavioral tests were performed as described previously (*20*). The novel object recognition behavior task was a modified version of the paradigm described in (*25*) to ensure hippocampal dependence.

Subjects and habituation

Male mice (n = 4 or 5) were housed per cage with ad libitum access to food and water, kept on a 12-hour (6 a.m. to 6 p.m.) light-dark cycle with the ambient temperature maintained at 21°C. Tests were conducted during the light cycle. Half of the littermate mice in each cage were injected with the control GFP virus bilaterally in LEC, whereas the other half were injected with the PSAM virus. For 5 days before the start of behavioral testing, the mice were habituated to handling, transport from the postprocedural housing room to the behavioral testing room, and momentary head restraint for connecting the cannula guide with dummy tubing. During these habituation sessions, mice were allowed to move around with the tubing attached to simulate the PSEM infusion conditions. The experimenter was blind to the group identities, which were revealed after testing was completed.

Microinfusion of PSEM

An internal injection cannula was connected to a 10-μl Hamilton syringe via thin tubing. The tubing was prefilled with sterifiltered PSEM 308 (15 μM) in oxygen-enriched ACSF, and the syringe was mounted in a syringe pump. The animal was gently restrained in its home cage by hand, and the injection cannula was slowly introduced into the previously implanted guide cannula. The cannula was fixed to the head implant via a screw-top connector, and the animal was released in an empty cage. Next 0.5 μl of PSEM was injected over the course of 5 min with the syringe pump, followed by a 2-min rest period with the tubing connected to the animal. The animal was gently restrained once again by hand, the connector detached, the internal cannula removed, and the dummy internal cannula restored to the guide cannula. The animal was then placed in the open field, CFC chamber, or object recognition arena for testing in the behavioral tasks.

During all microinfusion experiments, the dye miniRuby (5% in water) was included in the cannula solution to gauge post hoc the accuracy of cannula targeting and spread of substances during the microinfusion. At the end of the experiments, the animals were infused with miniRuby again 10 min before perfusion with paraformaldehyde, and the brains were examined for miniRuby fluorescence. These experiments provide an overestimate of the likely extent of PSEM diffusion during its application, as the brains were analyzed 1 to 24 hours after the first miniRuby infusion and subjected to more than one miniRuby infusion, whereas PSEM is only active for 20 min after application (*19*)

Open field

Mice were placed in an open field (45 cm L by 45 cm W by 30.5 cm) for 30 min. The testing chambers were cleaned with 70% isopropanol wipes between animals to eliminate any odor-related cues. Locomotor and rearing activity was monitored via motion-sensitive infrared (IR) beam breaks and recorded by the Med Associates Activity Monitor software. The entire apparatus was enclosed in a soundproof box.

Contextual and cued fear conditioning

Hippocampus-dependent contextual fear memory and amygdala-dependent auditory fear memory were tested by using a 3-day-delay fear conditioning protocol. A sound-attenuating chamber equipped with a FireWire camera for tracking, a light, and a speaker for delivering contextual and conditioning cues was used. Mice were placed in an enclosure (17 cm by 17 cm by 25 cm) housed within the sound-attenuated chamber. The flooring, wall patterns, dominant odors, and light conditions of the enclosure could be changed to provide different contexts. Context A on day 1 consisted of an enclosure with a steel grid floor, three Plexiglas walls and one opaque wall with black and white stripes, 1% acetic acid as the dominant odor, and the house fan turned on. The enclosure was cleaned with 70% isopropanol between animals. Mice were moved from their home cage to a transfer cage with no bedding for the PSEM microinfusion as detailed above. After 2-min post-infusion of PSEM, the mice were placed in the fear conditioning chamber (context A). The mice explored the environment for 150 s, following which a tone (30 s, 2.8 kHz, 85 dB) was presented that coterminated with a shock (2 s, 0.7 mA). Mice were removed from the chamber 30 s after the shock. On day 2, the mice were placed back in context A for 300 s and contextual fear memory was assayed by scoring percent time spent freezing (defined as the absence of all movement except for respiration). No shock or tone was presented on day 2.

On day 3, the mice were exposed to novel context B: The testing room was dimly illuminated with red light, and the enclosure was cleaned between animals with Vimoba; the enclosure had an opaque white-colored plastic floor, with three solid gray-colored walls, one Plexiglas wall with a circular door, and a red, flat plastic roof and 0.25% benzaldehyde as the dominant odor. Mice were first moved from their home cage to a circular bucket and then a cage with paper towel bedding during PSEM infusion before moving them to the testing chamber. Mice were exposed to context B for 180 s, and then the tone from day 1 was played for 60 s to assess cued fear conditioning by using percentage of time spent freezing. Freezing during fear conditioning was analyzed automated with ANY-maze and parsed into the different behavioral task phases.

Novel object recognition

Twelve male mice were injected with AAV9-Syn-FLEX-PSAM L141F:GlyR-IRES-GFP (Penn)

and kept on a 12-hour reversed light-dark cycle in a room maintained at 21°C. All trials of the novel object recognition (NOR) task were conducted during the dark cycle and in dim lighting. White plastic transport boxes (55 by 40 by 15 cm^3) were used as testing arenas. Three different objects were used: (i) a blue ceramic shoe (diameter 9.5 cm, maximal height 6 cm), (ii) a black plastic slide box (8 by 3 by 9.5 cm^3), and (iii) a semiclear plastic funnel (diameter 8.5 cm, maximal height 8.5 cm). Pilot experiments found that these objects elicited equal exploration time. Mice were habituated to handling and transported from the holding room to the behavioral room and were given 1 hour in the behavioral room each day to habituate before any tasks began. Mice were habituated to the infusion set-up and empty testing arena for 10 min each day for three consecutive days. On the fourth day, mice were infused over a duration of 5 min with either miniRuby + ACSF + PSEM or a control solution of miniRuby + ACSF. The solutions were kept in coded tubes to ensure that the experimenter was blinded and to randomize the treatment groups. In trial 1, mice were exposed to object A and object B for 10 min. After a 3-min intertrial interval, mice were again exposed to the same pair of objects for trial 2. The mice were then tested for object recognition memory after a 10-min interval by replacing either object A or object B with object C, the novel object. Objects and arenas were cleaned with 30% ethanol between all trials. Mice were recorded with an overhead FireWire camera and their movements tracked by using ANY-maze software. Exploration time was determined by using ANY-maze by measuring time spent with the animal's head within a region-of-interest (ROI) that extended 2 cm around each object.

In vivo imaging with head-fixed behavioral cues

Imaging experiments in head-fixed, awake behaving mice were performed as described previously (*27*, *28*). Briefly, Gad2-Cre: Ai14 tdTomato mice were injected in the left LEC with Cre-dependent rAAV to express the genetically encoded calcium indicator GCaMP6f (*26*) selectively in Cre^+ GABAergic neurons within the LEC. Two weeks postinjection, a glass-bottomed stainless steel cannula was implanted directly over the left hippocampus to allow for optical access to the long-range GABAergic axons projecting from LEC to SLM. After 1 week of recovery, water-deprived mice were head-fixed on a treadmill belt under a two-photon laser-scanning microscope within a custom-built behavioral apparatus that allows for simultaneous imaging and recording of behavior in response to four sensory stimuli: an aversive air puff to the snout, an appetitive water reward, a flash of light, and pure tones. Each experiment contained three to five blocks of stimuli presented either singularly or in pairs. Locomotion was monitored while imaging during each trial, which consisted of a 5- to 10-s pretrial interval, a randomly chosen stimulus or pair of stimuli, and a 10- to 30-s posttrial recording interval. Imaging was performed with an ultra fast pulsed laser beam (920-nm wavelength; 20 to 40 mW average power at the back focal plane of the objective) through a 40× objective. Green (GCaMP) and red (tdTomato) fluorescence was separated with an emission filter cube set (green, HQ525/70m-2p; red, HQ607/45m-2p; and 575dcxr) and was detected with photomultiplier tubes (PMTs) (green: GaAsP PMTs; red: multialkali PMTs) at either 256 × 128 pixels (75 × 75 μm; 0.295 μm/pixel in X; 0.588 μm/pixel in Y), 4× optical zoom, at 5.3 Hz or 128 × 128 pixels (105 × 105 μm), 2.8× optical zoon, at 6.1 Hz.

Acute-slice electrophysiology

Solutions

Recordings were performed with ACSF (pH 7.3, osmolarity 305 to 320 mOsm and saturated with 95% O_2 and 5% CO_2) for the extracellular solution. The ACSF consisted of (in mM) NaCl (125), $NaHCO_3$ (25), KCl (2.5), NaH_2PO_4 (1.25), $MgCl_2$ (1), $CaCl_2$ (2), glucose (22.5), Na-pyruvate (3), and ascorbate (1). Hippocampal slices were prepared and incubated in sucrose-enriched modified ACSF containing (in mM) NaCl (10), NaH_2PO_4 (1.2), KCl (2.5), $NaHCO_3$ (25), glucose (25), $CaCl_2$ (0.5), $MgCl_2$ (7), sucrose (190), and pyruvate (2). The intracellular current-clamp recording solution contained (in mM) $KMeSO_4$ (135), KCl (5), NaCl (2), EGTA (0.2), Hepes (10), phosphocreatine Na_2 (10), MgATP (5), Na_2GTP (0.4), Alexa Fluor 594 cadaverine (0.1), and biocytin (0.2%). The intracellular solution for voltage-clamp recordings contained $CsMeSO_4$ (135), KCl (5), NaCl (2), EGTA (0.2), Hepes (10), phosphocreatine Na_2 (10), MgATP (5), Na_2GTP (0.4), Alexa Fluor 594 (0.1), and biocytin (0.2%). In a subset of experiments, the following drugs were applied via bath application (in μM): SR95531 (2), CGP 55845 (1), NBQX (10), D-APV (100), and $PSEM^{308}$ (3 to 5). PSEM was generously provided by S. Sternson, Janelia Farm.

Slice preparation

We prepared 400-μm-thick horizontal hippocampal sections using a vibrating microtome from brains of mice that were transcardially perfused with ice-cold dissection ACSF. For the horizontal sections, hemisected brains were blocked ventromedially at an angle of 10° before sectioning. For the transverse sections, the hippocampi were dissected out, embedded in agar (4%), and then sliced. Slices were allowed to recover for at least 20 min at 34°C and then stored at room temperature in a 50% dissection: 50% standard ACSF solution before transfer to the recording chamber.

Electrophysiology setup

For IR-guided patch recordings, slices were visualized with a microscope equipped with Dodt-gradient-contrast optics and a 2× to 4× zoom module, IR filter, 60 × 1.0 nA water immersion objective, and a camera using image acquisition software. We performed fluorescence-guided targeted patch-clamp recordings using an epifluorescence illumination system equipped with a metal-halide lamp, ET-GFP and mCherry filter sets, Uniblitz shutter VCM-D1, and Orca R2 charge-coupled device camera controlled by μ-Manager (*60*). Photostimulation of ChR2 was achieved with an optical fiber coupled to a solid-state blue laser (470 nm) to illuminate SLM. In some experiments, the light was routed through a set of pinholes to produce a 50-μm focal-beam spot over SR.

Two-photon imaging and electrophysiology setup

Two-photon imaging of proximal dendritic spine Ca^{2+} used a custom-designed system with dual X-Y scanning galvanometers, coupled to a pulsed Ti:Sapphire MaiTai DeepSee femtosecond laser. Fluorescence was detected using high-sensitivity GaAsP PMTs. The scanning system was mounted on a microscope equipped with a 60 × 0.9 numerical aperture (NA) water immersion objective, and infrared Dodt-gradient-contrast optics coupled to a multialkali detector. Recording and stimulating electrodes were positioned using three junior micromanipulators on a movable motorized base plate connected to a MultiClamp 700B amplifier, Digidata 1440, and two constant-current stimulators for patch-clamp electrophysiology during imaging.

Electrophysiology recordings

Whole-cell patch-clamp recordings were performed at 34°C in standard ACSF using borosilicate glass pipettes with tip resistances of 3.5 to 4.5 MΩ for somatic and 9 to 16 MΩ for dendritic recordings. A MultiClamp 700B amplifier, pClamp 9 software, and a personal computer were used for data acquisition. Pipette capacitance (Cp), series resistance (Rs), and whole-cell capacitance (Cm) were compensated under voltage clamp initially with maximal allowable prediction and correction (75 to 85%). The average series resistance for whole-cell voltage-clamp recordings was kept between 9 and 15 MΩ. These values were used as a guide to estimate the pipette capacitance compensation and bridge balance under current clamp. The average access resistances for the current-clamp recordings ranged from 10 to 20 MΩ for soma and 10 to 40 MΩ for dendrite recordings. The membrane potential (V_m) of IN and pyramidal neuron soma was held at +10 mV under voltage clamp to measure IPSCs, whereas current clamp recordings were performed from soma and dendrites at the cell's resting membrane potential.

Synaptic responses were evoked by electrical stimulation of the EC inputs or SCs, with focal glass pipette stimulating electrodes coupled to constant current stimulators placed in SLM or SR, respectively. Stimulus strengths were adjusted to evoke EC and SC PSPs <50% of their maximal amplitude. Basal transmission was monitored every 15 s with EC and SC electrical stimuli spaced 2 s apart. Laser pulses delivered during episodes involving optical stimulation were also spaced 15 s apart. Cells were intracellularly filled for 10 to 15 min with the Ca^{2+} indicator Fluo-5F (500 μM) and the structural dye Alexa Fluor 594 (25 μM). Random-access line scans (256 lines per frame, 5.6× optical zoom, 25.709 × 17.504 μm field of vision, 2.8-μs dwell time, 1.28-ms scan-line period) and two-dimensional scan (512 × 512 pixels, 1× optical zoom, 198.45 × 198.45 μm field of vision,

1.6-μs dwell time, 1.4-ms scan-line period) image series were acquired using the PrairieView software in both the green and red channel. The image *t*-series acquisition on PrairieView was synchronized and used transistor-transistor logic triggered by the electrophysiology acquisition software Axograph. Line scans were acquired after each EC-SC stimulus pair simultaneously with the SC stimulus trigger once every 15 s for the single pairings at variable timing intervals (0 to 40 ms). For multiple pairings at 10- or 20-ms intervals, images were acquired at a 1 Hz frequency up to 90 times, identical to the ITDP induction protocol.

Immunohistochemistry, confocal imaging, and neuronal tracing

Immunohistochemistry

Adult animals were deeply anesthetized with ketamine-xylazine and perfused with 1× phosphate-buffered saline (PBS) followed by 4% parformaldehyde in PBS. The brains were removed and postfixed overnight in 4% paraformaldehyde at 4°C. The brains were sectioned in the coronal plane for hippocampal sections or sagittal plane for entorhinal sections at 50-μm thickness by using a vibrating microtome. For experiments involving the expression of GFP alone, GCaMP, and TdTomato, the signal was bright enough and did not require further immuno-enhancement. For immunostaining, slices were permeabilized in 1× PBS + 0.3% Triton, blocked in 3% normal goat serum, and then incubated with primary (overnight) and secondary (2 to 4 hours) antibodies in blocking solution (1× PBS, 0.2% Triton and 3% normal goat serum), unless otherwise stated. ChR2-EYFP– and ChR2-GFP–labeled neurons and their projections were stained by using a rabbit polyclonal antibody against GFP primary antibody (1:1000; Invitrogen) with a secondary goat antibody against primary rabbit immunoglobulin G (IgG) antibody conjugated with Alexa Fluor 488 dye (1:1000; Invitrogen). For the GFP-tagged CCK, PV, and SOM interneuron triple staining, we used a similar procedure for washing, permeabilization, and blocking as described above but substituted PBS with Tris-buffer solution (TBS, TB 0.1 M; NaCl 0.9%; pH 7.4). The primary antibodies we used were chicken polyclonal anti-GFP (1:1000, Abcam), rabbit polyclonal anti-parvalbumin (1:500, Synaptic Systems—SYSY), and rat monoclonal antibody against somatostatin (1:200, Millipore, clone YC7). The secondary antibodies for these stains included secondary goat antibody against chicken IgG antibody conjugated with Alexa Fluor 488 dye (1:1000, Invitrogen), goat anti-rabbit IgG antibody conjugated with Alexa Fluor 555 dye (1:1000, Invitrogen), and minimal cross reactivity goat anti-rat IgG conjugated with Alexa Fluor 647 dye (1:1000, Jackson Laboratories).

For experiments involving PSAM and CCK after electrophysiology recordings, 400-μm slices were drop-fixed overnight in 4% paraformaladhyde, embedded in agar, and resectioned to 50 μm. For the α-bungarotoxin staining of PSAM-GlyR, we followed the procedure previously described (*11*). Resliced sections were permeabilized with 0.5% Triton by using a Tris-buffered saline (TBS) at a pH of 7.4. The slices were blocked in 10% normal goat serum in TBS with 0.5% Triton for 4 hours at room temperature and then incubated with Alexa Fluor 647 α-bungarotoxin (1:3000; Invitrogen) in TBS + 0.1% Triton, first at room temperature for 1 hour, then at 4°C for 48 hours to stain for nicotinic α7 receptor–containing PSAM(L141F)-GlyR. In sections that coexpressed ChR2-GFP or GFP alone with the PSAM, primary antibody for GFP (rabbit polyclonal anti-GFP primary antibody, 1:1000; Invitrogen) was added for the last 12 hours of overnight incubation at 4°C. After TBS washes (4 × 15 min), the slices were incubated at room temperature for 4 hours with secondary antibody for GFP (goat antirabbit Alexa Fluor 488, 1:1000; Invitrogen) along with fresh Alexa Fluor 647 α-bungarotoxin (1:3000; Invitrogen) in TBS + 0.1% Triton to counterstain for GFP and PSAM. For the CCK staining, we followed a previously described procedure (*61*).

Briefly, slices were put through antigen retrieval by being placed in a citrate buffer at pH 8.6 for 70 min at 90°C. Then, slices were washed three times for 5 min each time in PBS. Slices were permeabilized with blocking solution (1% BSA and 0.5% Triton in PBS) with 10% normal goat serum for 4 hours at room temperature. Slices were then incubated with primary antibodies against cholecystokinin (mouse monoclonal; 1:1000; generous gift of G. Ohning, CURE center, UCLA) or GFP (rabbit polyclonal; 1:1000; Invitrogen) in blocking solution for 48 hours at 4°C. Slices were then washed 4 × 15 min each time with carrier solution (1% BSA, 0.1% Triton, and 1% normal goat serum in PBS) at room temperature. After this, slices were incubated with a Biotin-SP–conjugated AffiniPure $F(ab')_2$ fragment goat anti-mouse IgG (1:250; Jackson) and goat anti-rabbit Alexa Fluor 488 dye–conjugated IgG antibody (1:1000; Invitrogen) in carrier solution for 4 hours at room temperature. After PBS washes (4 × 15 min), the slices were incubated in ABC complex for 1 hour. Then slices were washed with PBS (4 × 15 min) and incubated with TSA-tyramide-tetramethylrhodamine amplification kit plus buffer solution for 3 to 10 min at room temperature. PBS washed slices were next incubated with Alexa Fluor 555 streptavidin (1:500; Invitrogen), Alexa Fluor 488 dye–conjugated anti-rabbit IgG secondary antibody (1:1000; Invitrogen), and Alexa Fluor 555 dye–conjugated anti-mouse IgG secondary antibody (1:1000; Invitrogen) in carrier solution for 4 hours at room temperature. Finally, the slices were washed in PBS (4 × 15 min) and mounted.

Stained slices were mounted with Prolong Gold or Vectashield hard-set mounting medium with 4′,6-diamidino-2-phenylindole (DAPI) for the GFP, CCK, PV, and somatostatin stains or Aqua-Mount aqueous mounting medium for the bungarotoxin staining.

Confocal imaging

An inverted laser-scanning confocal microscope was used to acquire tile scan and *Z*-stack images of multichannel fluorescent signals from fixed tissue sections by using 5×, 10×, or 20× air objectives, as well as a high NA 63× oil immersion objective. Maximum intensity projections were created using Image J.

Neuronal reconstruction

During the electrophysiology recordings, all cells were intracellularly filled with Alexa Fluor 594 for online visualization and 0.2% neurobiotin to allow for enhanced visualization and post hoc reconstruction with a streptavidin-bound fluorophore (Streptavidin Alexa Fluor 555). Immediately after recording, the acute brain slice was drop-fixed overnight at 4°C in 4% paraformaldehyde solution. The tissue was then thoroughly rinsed with PBS-glycine (1 × 15 min) and PBS (3 × 15 min) and processed for immunohistochemistry. The 20× high-resolution (1024 × 1024, 16-bit depth) fluorescent confocal *Z*-stack images of the fluorophore-labeled filled neurons were used to trace the soma, axons, and dendrites by using Neurolucida reconstruction software.

Data analysis

Behavior data

For the behavioral experiments, we analyzed the open-field data using Activity Monitor, and an automated analysis was used for calculating freezing during fear conditioning with ANY-maze. The data were exported in tab-delimited format into Prism for further statistical analysis. The red fluorescent signal of miniRuby infused along with PSEM during the behavioral tasks served as an indicator of accurate cannula targeting and drug spread. One animal from the control cohort (total of 10 animals) and test cohort (total of 8 animals) each was removed from the data analysis because of mistargeting. Statistical significance was assessed by two-tailed unpaired Student's *t* tests, two-way ANOVA, or two-way repeated-measures ANOVA where appropriate. Significant main effects or interactions were followed up with multiple comparison testing by using Sidak's correction. Results were considered significant when $P < 0.05$. α was set equal to 0.05 for multiple comparison tests. Sample sizes were chosen based on previous studies.

In vivo imaging data

Sequential Image Analysis (SIMA) toolkit (*62*) was used to correct motion artifacts in the raw imaging data, to identify and tag regions of interest (ROIs), and to extract fluorescence traces from each ROI. Extracted signals were synchronized to the recorded running signal and presented stimuli, and peristimulus time histograms (PSTHs) were calculated. For each ROI-stimulus pair, the response magnitude was calculated as the mean of the PSTH in the 3 s preceding the stimulus subtracted from the mean of the 3 s after the stimulus. Significantly responding ROIs were determined by randomly shuffling the stimulus times across all trials 10,000 times, calculating the response magnitude for each shuffle, and then selecting any ROIs with a response magnitude

above the 95th percentile of the distribution of shuffled values.

Electrophysiology data

Axograph X was used for electrophysiology data analysis. A 7pA amplitude threshold was set for sorting failures and successes for the light-evoked IPSCs to map the LEC and MEC LRIP connectivity. All IPSCs above this cutoff were included in calculating the mean response amplitude and percentage of responsive INs for the two groups. For calculating amplitude changes in the EC-SC and EC-ChR2 single pairing, the responses to SC electrical stimulation or ChR2 photostimulation alone were averaged for 3 min before pairing, and the mean was used to normalize the responses paired with EC stimulation. For comparing the effect of application of NBQX, APV, SR 95531, CGP 55845, or PSEM, the predrug baseline synaptic-response amplitude for the "control" condition was obtained by averaging the responses recorded for the 5 min preceding drug application. The postdrug synaptic-response amplitudes were obtained by averaging responses recorded for 5 min in the presence of the drug, once a steady-state response was reached, typically 7 to 10 min after starting bath application of the drug. For sorting and generating the histograms of the dendritic PSPs and spikes, an event-detection algorithm in Axograph was used. Time-course plots for ITDP were generated by using a boxcar average of every four responses (1-min period), as previously described (*11*). All statistical errors are standard errors of the population mean or boxcar mean (SEM); all P values (significance level set at $P < 0.05$) for t tests are two-tailed; and all ANOVAs were corrected for multiple comparisons using post hoc tests as indicated.

KaleidaGraph 4 and Prism 6 were used for plotting all data and statistical analysis. Figures were generated with Adobe Illustrator.

REFERENCES AND NOTES

1. V. H. Brun *et al*., Impaired spatial representation in CA1 after lesion of direct input from entorhinal cortex. *Neuron* **57**, 290–302 (2008). doi: 10.1016/j.neuron.2007.11.034; pmid: 18215625
2. J. Suh, A. J. Rivest, T. Nakashiba, T. Tominaga, S. Tonegawa, Entorhinal cortex layer III input to the hippocampus is crucial for temporal association memory. *Science* **334**, 1415–1420 (2011). doi: 10.1126/science.1210125; pmid: 22052975
3. T. Kitamura *et al*., Island cells control temporal association memory. *Science* **343**, 896–901 (2014). doi: 10.1126/science.1244634; pmid: 24457215
4. S. Melzer *et al*., Long-range-projecting GABAergic neurons modulate inhibition in hippocampus and entorhinal cortex. *Science* **335**, 1506–1510 (2012). doi: 10.1126/science.1217139; pmid: 22442486
5. D. G. Amaral, M. P. Witter, The three-dimensional organization of the hippocampal formation: A review of anatomical data. *Neuroscience* **31**, 571–591 (1989). doi: 10.1016/0306-4522(89)90424-7; pmid: 2687721
6. M. P. Witter, D. G. Amaral, Entorhinal cortex of the monkey: V. Projections to the dentate gyrus, hippocampus, and subicular complex. *J. Comp. Neurol.* **307**, 437–459 (1991). doi: 10.1002/cne.903070308; pmid: 1713237
7. G. Buzsáki, Feed-forward inhibition in the hippocampal formation. *Prog. Neurobiol.* **22**, 131–153 (1984). doi: 10.1016/0301-0082(84)90023-6; pmid: 6433403
8. T. Jarsky, A. Roxin, W. L. Kath, N. Spruston, Conditional dendritic spike propagation following distal synaptic activation of hippocampal CA1 pyramidal neurons. *Nat. Neurosci.* **8**, 1667–1676 (2005). doi: 10.1038/nn1599; pmid: 16299501
9. H. Takahashi, J. C. Magee, Pathway interactions and synaptic plasticity in the dendritic tuft regions of CA1 pyramidal neurons. *Neuron* **62**, 102–111 (2009). doi: 10.1016/j.neuron.2009.03.007; pmid: 19376070
10. J. T. Dudman, D. Tsay, S. A. Siegelbaum, A role for synaptic inputs at distal dendrites: Instructive signals for hippocampal long-term plasticity. *Neuron* **56**, 866–879 (2007). doi: 10.1016/j.neuron.2007.10.020; pmid: 18054862
11. J. Basu *et al*., A cortico-hippocampal learning rule shapes inhibitory microcircuit activity to enhance hippocampal information flow. *Neuron* **79**, 1208–1221 (2013). doi: 10.1016/j.neuron.2013.07.001; pmid: 24050406
12. K. C. Bittner *et al*., Conjunctive input processing drives feature selectivity in hippocampal CA1 neurons. *Nat. Neurosci.* **18**, 1133–1142 (2015). doi: 10.1038/nn.4062; pmid: 26167906
13. V. H. Brun *et al*., Place cells and place recognition maintained by direct entorhinal-hippocampal circuitry. *Science* **296**, 2243–2246 (2002). doi: 10.1126/science.1071089 pmid: 12077421
14. M. Fyhn, S. Molden, M. P. Witter, E. I. Moser, M. B. Moser, Spatial representation in the entorhinal cortex. *Science* **305**, 1258–1264 (2004). doi: 10.1126/science.1099901; pmid: 15333832
15. E. L. Hargreaves, G. Rao, I. Lee, J. J. Knierim, Major dissociation between medial and lateral entorhinal input to dorsal hippocampus. *Science* **308**, 1792–1794 (2005). doi: 10.1126/science.1110449; pmid: 15961670
16. H. Taniguchi *et al*., A resource of Cre driver lines for genetic targeting of GABAergic neurons in cerebral cortex. *Neuron* **71**, 995–1013 (2011). doi: 10.1016/j.neuron.2011.07.026; pmid: 21943598
17. E. S. Boyden, F. Zhang, E. Bamberg, G. Nagel, K. Deisseroth, Millisecond-timescale, genetically targeted optical control of neural activity. *Nat. Neurosci.* **8**, 1263–1268 (2005). doi: 10.1038/nn1525; pmid: 16116447
18. S. Maren, K. L. Phan, I. Liberzon, The contextual brain: Implications for fear conditioning, extinction and psychopathology. *Nat. Rev. Neurosci.* **14**, 417–428 (2013). doi: 10.1038/nrn3492; pmid: 23635870
19. C. J. Magnus *et al*., Chemical and genetic engineering of selective ion channel-ligand interactions. *Science* **333**, 1292–1296 (2011). doi: 10.1126/science.1206606; pmid: 21885782
20. F. L. Hitti, S. A. Siegelbaum, The hippocampal CA2 region is essential for social memory. *Nature* **508**, 88–92 (2014). doi: 10.1038/nature13028; pmid: 24572357
21. S. J. Cohen, R. W. Stackman Jr., Assessing rodent hippocampal involvement in the novel object recognition task. A review. *Behav. Brain Res.* **285**, 105–117 (2015). doi: 10.1016/j.bbr.2014.08.002; pmid: 25169255
22. R. E. Clark, S. M. Zola, L. R. Squire, Impaired recognition memory in rats after damage to the hippocampus. *J. Neurosci.* **20**, 8853–8860 (2000). pmid: 11102494
23. J. A. Ainge *et al*., The role of the hippocampus in object recognition in rats: Examination of the influence of task parameters and lesion size. *Behav. Brain Res.* **167**, 183–195 (2006). doi: 10.1016/j.bbr.2005.09.005; pmid: 16214239
24. S. J. Cohen *et al*., The rodent hippocampus is essential for nonspatial object memory. *Curr. Biol.* **23**, 1685–1690 (2013). doi: 10.1016/j.cub.2013.07.002; pmid: 23954431
25. C. A. Denny, N. S. Burghardt, D. M. Schachter, R. Hen, M. R. Drew, 4- to 6-week-old adult-born hippocampal neurons influence novelty-evoked exploration and contextual fear conditioning. *Hippocampus* **22**, 1188–1201 (2012). doi: 10.1002/hipo.20964; pmid: 21739523
26. T. W. Chen *et al*., Ultrasensitive fluorescent proteins for imaging neuronal activity. *Nature* **499**, 295–300 (2013). doi: 10.1038/nature12354; pmid: 23868258
27. P. Kaifosh, M. Lovett-Barron, G. F. Turi, T. R. Reardon, A. Losonczy, Septo-hippocampal GABAergic signaling across multiple modalities in awake mice. *Nat. Neurosci.* **16**, 1182–1184 (2013). doi: 10.1038/nn.3482; pmid: 23912949
28. M. Lovett-Barron *et al*., Dendritic inhibition in the hippocampus supports fear learning. *Science* **343**, 857–863 (2014). doi: 10.1126/science.1247485; pmid: 24558155
29. D. W. Cope *et al*., Cholecystokinin-immunopositive basket and Schaffer collateral-associated interneurones target different domains of pyramidal cells in the CA1 area of the rat hippocampus. *Neuroscience* **109**, 63–80 (2002). doi: 10.1016/S0306-4522(01)00440-7; pmid: 11784700
30. T. Klausberger, P. Somogyi, Neuronal diversity and temporal dynamics: The unity of hippocampal circuit operations. *Science* **321**, 53–57 (2008). doi: 10.1126/science.1149381; pmid: 18599766
31. H. Pawelzik, D. I. Hughes, A. M. Thomson, Physiological and morphological diversity of immunocytochemically defined parvalbumin- and cholecystokinin-positive interneurones in CA1 of the adult rat hippocampus. *J. Comp. Neurol.* **443**, 346–367 (2002). doi: 10.1002/cne.10118; pmid: 11807843
32. S. H. Lee, I. Soltesz, Requirement for CB1 but not GABAB receptors in the cholecystokinin mediated inhibition of GABA release from cholecystokinin expressing basket cells. *J. Physiol.* **589**, 891–902 (2011). doi: 10.1113/jphysiol.2010.198499; pmid: 21173082
33. M. I. Daw, L. Tricoire, F. Erdelyi, G. Szabo, C. J. McBain, Asynchronous transmitter release from cholecystokinin-containing inhibitory interneurons is widespread and target-cell independent. *J. Neurosci.* **29**, 11112–11122 (2009). doi: 10.1523/JNEUROSCI.5760-08.2009; pmid: 19741117
34. N. L. Golding, N. P. Staff, N. Spruston, Dendritic spikes as a mechanism for cooperative long-term potentiation. *Nature* **418**, 326–331 (2002). doi: 10.1038/nature00854; pmid: 12124625
35. F. Gambino *et al*., Sensory-evoked LTP driven by dendritic plateau potentials in vivo. *Nature* **515**, 116–119 (2014). doi: 10.1038/nature13664; pmid: 25174710
36. N. L. Golding, N. Spruston, Dendritic sodium spikes are variable triggers of axonal action potentials in hippocampal CA1 pyramidal neurons. *Neuron* **21**, 1189–1200 (1998). doi: 10.1016/S0896-6273(00)80635-2; pmid: 9856473
37. M. E. Larkum, J. J. Zhu, B. Sakmann, A new cellular mechanism for coupling inputs arriving at different cortical layers. *Nature* **398**, 338–341 (1999). doi: 10.1038/18686; pmid: 10192334
38. G. Buzsáki, E. I. Moser, Memory, navigation and theta rhythm in the hippocampal-entorhinal system. *Nat. Neurosci.* **16**, 130–138 (2013). doi: 10.1038/nn.3304; pmid: 23354386
39. A. Kamondi, L. Acsády, G. Buzsáki, Dendritic spikes are enhanced by cooperative network activity in the intact hippocampus. *J. Neurosci.* **18**, 3919–3928 (1998). pmid: 9570819
40. A. Losonczy, J. K. Makara, J. C. Magee, Compartmentalized dendritic plasticity and input feature storage in neurons. *Nature* **452**, 436–441 (2008). doi: 10.1038/nature06725; pmid: 18368112
41. M. E. Sheffield, D. A. Dombeck, Calcium transient prevalence across the dendritic arbour predicts place field properties. *Nature* **517**, 200–204 (2015). doi: 10.1038/nature13871; pmid: 25363782
42. S. Royer *et al*., Control of timing, rate and bursts of hippocampal place cells by dendritic and somatic inhibition. *Nat. Neurosci.* **15**, 769–775 (2012). doi: 10.1038/nn.3077; pmid: 22446878
43. L. Roux, G. Buzsáki, Tasks for inhibitory interneurons in intact brain circuits. *Neuropharmacology* **88**, 10–23 (2015). doi: 10.1016/j.neuropharm.2014.09.011; pmid: 25239808
44. A. J. Murray *et al*., Parvalbumin-positive CA1 interneurons are required for spatial working but not for reference memory. *Nat. Neurosci.* **14**, 297–299 (2011). doi: 10.1038/nn.2751; pmid: 21278730
45. F. Donato, S. B. Rompani, P. Caroni, Parvalbumin-expressing basket-cell network plasticity induced by experience regulates adult learning. *Nature* **504**, 272–276 (2013). doi: 10.1038/nature12866; pmid: 24336286
46. S. Hefft, P. Jonas, Asynchronous GABA release generates long-lasting inhibition at a hippocampal interneuron-principal neuron synapse. *Nat. Neurosci.* **8**, 1319–1328 (2005). doi: 10.1038/nn1542; pmid: 16158066
47. T. Klausberger *et al*., Complementary roles of cholecystokinin- and parvalbumin-expressing GABAergic neurons in hippocampal network oscillations. *J. Neurosci.* **25**, 9782–9793 (2005). doi: 10.1523/JNEUROSCI.3269-05.2005 pmid: 16237182
48. W. Jacob, R. Marsch, G. Marsicano, B. Lutz, C. T. Wotjak, Cannabinoid CB1 receptor deficiency increases contextual fear memory under highly aversive conditions and long-term potentiation in vivo. *Neurobiol. Learn. Mem.* **98**, 47–55 (2012). doi: 10.1016/j.nlm.2012.04.008; pmid: 22579951
49. M. F. Yeckel, T. W. Berger, Feedforward excitation of the hippocampus by afferents from the entorhinal cortex: Redefinition of the role of the trisynaptic pathway. *Proc. Natl. Acad. Sci. U.S.A.* **87**, 5832–5836 (1990). doi: 10.1073/pnas.87.15.5832; pmid: 2377621
50. E. W. Schomburg *et al*., Theta phase segregation of input-specific gamma patterns in entorhinal-hippocampal networks. *Neuron* **84**, 470–485 (2014). doi: 10.1016/j.neuron.2014.08.051; pmid: 25263753
51. J. J. Chrobak, A. Lörincz, G. Buzsáki, Physiological patterns in the hippocampo-entorhinal cortex system. *Hippocampus* **10**, 457–465 (2000). doi: 10.1002/1098-1063(2000)10:4<457::AID-HIPO12>3.0.CO;2-Z; pmid: 10985285

52. K. M. Igarashi, L. Lu, L. L. Colgin, M. B. Moser, E. I. Moser, Coordination of entorhinal-hippocampal ensemble activity during associative learning. *Nature* **510**, 143–147 (2014). doi: 10.1038/nature13162; pmid: 24739966
53. T. Nakashiba, J. Z. Young, T. J. McHugh, D. L. Buhl, S. Tonegawa, Transgenic inhibition of synaptic transmission reveals role of CA3 output in hippocampal learning. *Science* **319**, 1260–1264 (2008). doi: 10.1126/science.1151120; pmid: 18218862
54. S. Hippenmeyer *et al*., A developmental switch in the response of DRG neurons to ETS transcription factor signaling. *PLOS Biol.* **3**, e159 (2005). doi: 10.1371/journal.pbio.0030159; pmid: 15836427
55. L. Madisen *et al*., A robust and high-throughput Cre reporting and characterization system for the whole mouse brain. *Nat. Neurosci.* **13**, 133–140 (2010). doi: 10.1038/nn.2467; pmid: 20023653
56. G. Miyoshi *et al*., Genetic fate mapping reveals that the caudal ganglionic eminence produces a large and diverse population of superficial cortical interneurons. *J. Neurosci.* **30**, 1582–1594 (2010). doi: 10.1523/JNEUROSCI.4515-09.2010; pmid: 20130169
57. M. Yamamoto *et al*., A multifunctional reporter mouse line for Cre- and FLP-dependent lineage analysis. *Genesis* **47**, 107–114 (2009). doi: 10.1002/dvg.20474; pmid: 19165827
58. F. Zhang *et al*., Optogenetic interrogation of neural circuits: Technology for probing mammalian brain structures. *Nat. Protoc.* **5**, 439–456 (2010). doi: 10.1038/nprot.2009.226; pmid: 20203662
59. J. V. Kupferman *et al*., Reelin signaling specifies the molecular identity of the pyramidal neuron distal dendritic compartment. *Cell* **158**, 1335–1347 (2014). doi: 10.1016/j.cell.2014.07.035; pmid: 25201528
60. A. Edelstein, N. Amodaj, K. Hoover, R. Vale, N. Stuurman, Computer control of microscopes using μManager. *Curr. Protoc. Mol. Biol.* Chap.: Unit 14.20 (2010). pmid: 20890901
61. L. Tricoire *et al*., A blueprint for the spatiotemporal origins of mouse hippocampal interneuron diversity. *J. Neurosci.* **31**, 10948–10970 (2011). doi: 10.1523/JNEUROSCI.0323-11.2011; pmid: 21795545
62. P. Kaifosh, J. D. Zaremba, N. B. Danielson, A. Losonczy, SIMA: Python software for analysis of dynamic fluorescence imaging data. *Front. Neuroinform.* **8**, 80 (2014). doi: 10.3389/fninf.2014.00080

ACKNOWLEDGMENTS

We thank K. Deisseroth, S. Sternson, Z. J. Huang, and G. Fishell for generously sharing reagents and transgenic mice. We thank V. Jayaraman, R. A. Kerr, D. S. Kim, L. L. Looger, and K. Svoboda from the GENIE Project, Janelia Farm Research Campus, Howard Hughes Medical Institute, for the use of the GCaMP6f-encoding virus. We are grateful to G. Buzsaki, R. Tsien, R. Hen, Al. Dranovsky, C. Kellendonk, S. Fusi, R. Bruno, and A. Das for invaluable discussions on the study and C. Magnus, S. Sternson, C. Denny, A. Katzman, and M. Russo for critical technical advice. We are also indebted to J. Kupferman, Z. Rosen, A. Masurkar, Q. Sun, and T. Bock for helpful comments on previous versions of the manuscript. This work was supported by a NARSAD Young Investigator grant to J.B.; a Ruth L. Kirschstein F30 National Research Service Award from the National Institute of Mental Health (NIMH), NIH, to F.L.H.; a Human Frontier Science Program grant and a grant (1R01MH100510) from NIMH to B.V.Z.; a grant (1R01MH100631) from NIMH and support from the Searle Scholars Program, Human Frontier Science Program, and the McKnight Memory and Cognitive Disorders Award to A.L.; and a grant (R01NS036658) from National Institute of Neurological Disorders and Stroke, NIH, and support from the Howard Hughes Medical Institute to S.A.S.

SUPPLEMENTARY MATERIALS

www.sciencemag.org/content/351/6269/aaa5694/suppl/DC1
Figs. S1 to S10
References (*63*–*67*)
Movie S1

24 December 2014; accepted 17 November 2015
10.1126/science.aaa5694

RESEARCH ARTICLE SUMMARY

HEMATOPOIESIS

Distinct routes of lineage development reshape the human blood hierarchy across ontogeny

Faiyaz Notta,* Sasan Zandi,* Naoya Takayama, Stephanie Dobson, Olga I. Gan, Gavin Wilson, Kerstin B. Kaufmann, Jessica McLeod, Elisa Laurenti, Cyrille F. Dunant, John D. McPherson, Lincoln D. Stein, Yigal Dror, John E. Dick†

INTRODUCTION: The hematopoietic road map is a compilation of the various lineage differentiation routes that a stem cell takes to make blood. This program produces greater than 10 blood cell fates and is responsible for generating more than 300 billion cells daily. On several occasions over the past six decades, the murine road map has been reconceived due to new information overturning dogma. However, the human road map has changed little. In the human model, blood differentiation initiates at the level of multipotent stem cells and passes through a series of increasingly lineage-restricted oligopotent and, finally, unipotent progenitor intermediates. One critical oligopotent intermediate is the common myeloid progenitor (CMP), believed to be the origin of all myeloid (My), erythroid (Er), and megakaryocyte (Mk) cells. Although murine studies challenge the existence of oligopotent progenitors, a comprehensive analysis of human My-Er-Mk differentiation is lacking. Moreover, whether the pool of oligopotent intermediates is fixed across human development (fetal to adult) is unknown.

RATIONALE: The differentiation road map taken by human hematopoietic stem cells (HSCs) is fundamental to our understanding of blood homeostasis, hematopoietic malignancies, and regenerative medicine.

RESULTS: We mapped the cellular origins of My, Er, and Mk lineages across three time points in human blood development: fetal liver (FL), neonatal cord blood (CB), and adult bone marrow (BM). Using a cell-sorting scheme based on markers linked to Er and Mk lineage specification (CD71 and CD110), we found that previously described populations of multipotent progenitors (MPPs), CMPs, and megakaryocyte-erythroid progenitors (MEPs) were heterogeneous and could be further purified. Nearly 3000 single cells from 11 cellular subsets from the $CD34^+$ compartment of FL, CB, and BM (33 subsets in total) were evaluated for their My, Er, and Mk lineage potential using an optimized single-cell assay.

In FL, the ratio of cells with multilineage versus unilineage potential remained constant in both the stem cell ($CD34^+CD38^-$) and progenitor cell ($CD34^+CD38^+$) enriched compartments. By contrast, in BM, nearly all multipotent cells were restricted to the stem cell compartment, whereas unilineage progenitors dominated the progenitor cell compartment. Oligopotent progenitors were only a negligible component of the human blood hierarchy in BM, leading to the inference that multipotent cells differentiate into unipotent cells directly by adulthood.

Mk/Er activity predominantly originated from the stem cell compartment at all developmental time points. In CB and BM, most Mks emerged as part of mixed clones from HSCs/MPPs, indicating that Mks directly branch from a multipotent cell and not from oligopotent progenitors like CMP. In FL, an almost pure Mk/Er progenitor was identified in the stem cell compartment, although less potent Mk/Er progenitors were also present in the progenitor compartment. In a hematological condition of HSC loss (aplastic anemia), Mk/Er but not My progenitors were more severely depleted, pinpointing a close physiological connection between HSC and the Mk/Er lineage.

ON OUR WEB SITE

Read the full article at http://dx.doi.org/10.1126/science.aab2116

CONCLUSION: Our data indicate that there are distinct road maps of blood differentiation across human development. Prenatally, Mk/Er lineage branching occurs throughout the cellular hierarchy. By adulthood, both Mk/Er activity and multipotency are restricted to the stem cell compartment, whereas the progenitor compartment is composed of unilineage progenitors forming a "two-tier" system, with few intervening oligopotent intermediates. ■

The list of author affiliations is available in the full article online.
*These authors contributed equally to this work.
†Corresponding author. E-mail: jdick@uhnres.utoronto.ca
Cite this article as F. Notta *et al.*, *Science* **351**, aab2116 (2016). DOI: 10.1126/science.aab2116

Road maps of human blood stem cell differentiation. The classical model envisions that oligopotent progenitors such as CMP are an essential intermediate stage from which My/Er/Mk differentiation originates. The redefined model proposes a developmental shift in the progenitor cell architecture from the fetus, where many stem and progenitor cell types are multipotent, to the adult, where the stem cell compartment is multipotent but the progenitors are unipotent. The grayed planes represent theoretical tiers of differentiation.

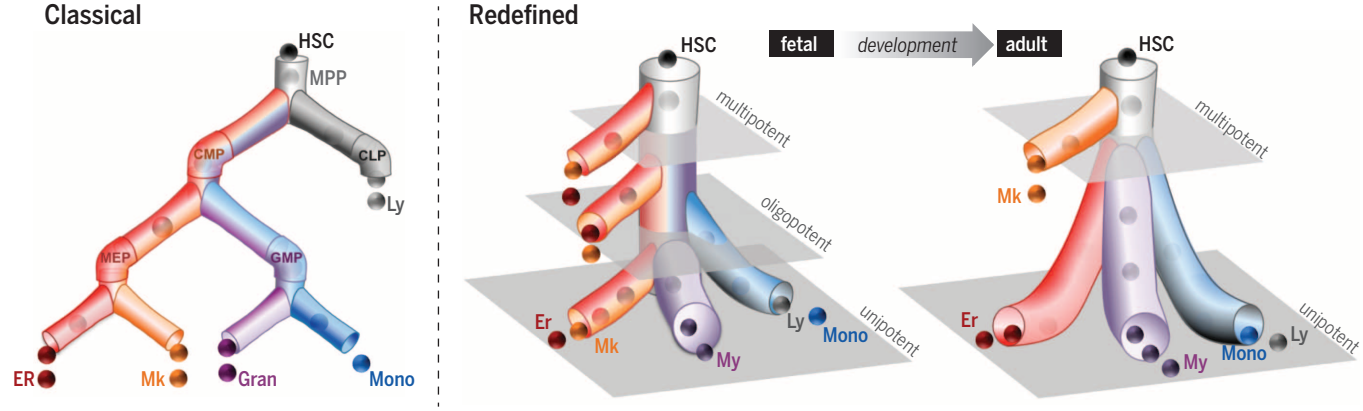

RESEARCH ARTICLE

HEMATOPOIESIS

Distinct routes of lineage development reshape the human blood hierarchy across ontogeny

Faiyaz Notta,[1,2]*† Sasan Zandi,[1,2]* Naoya Takayama,[1,2] Stephanie Dobson,[1,2] Olga I. Gan,[1] Gavin Wilson,[2,4] Kerstin B. Kaufmann,[1,2] Jessica McLeod,[1] Elisa Laurenti,[6] Cyrille F. Dunant,[7] John D. McPherson,[3,4] Lincoln D. Stein,[2,4] Yigal Dror,[5] John E. Dick[1,2]‡

In a classical view of hematopoiesis, the various blood cell lineages arise via a hierarchical scheme starting with multipotent stem cells that become increasingly restricted in their differentiation potential through oligopotent and then unipotent progenitors. We developed a cell-sorting scheme to resolve myeloid (My), erythroid (Er), and megakaryocytic (Mk) fates from single CD34$^+$ cells and then mapped the progenitor hierarchy across human development. Fetal liver contained large numbers of distinct oligopotent progenitors with intermingled My, Er, and Mk fates. However, few oligopotent progenitor intermediates were present in the adult bone marrow. Instead, only two progenitor classes predominate, multipotent and unipotent, with Er-Mk lineages emerging from multipotent cells. The developmental shift to an adult "two-tier" hierarchy challenges current dogma and provides a revised framework to understand normal and disease states of human hematopoiesis.

For decades, both human and mouse hematopoiesis has been described as a cellular hierarchy maintained by self-renewing hematopoietic stem cells (HSCs) that reside at the apex of its pyramidal structure of differentiating cells (*1*, *2*). This differentiation scheme highlights key features of the blood hierarchy that has been critical to our understanding of how stem cells manage lifelong blood production. In general, self-renewing cell types with extended life span like long-term HSCs (LT-HSCs), as well as short-term HSCs (ST-HSCs) and multipotent progenitors (MPPs), are rare and remain closer to the conceptual peak of the hierarchy; oligopotent and unipotent progenitors farther down the scheme have shorter life spans, increase numerically, and ultimately differentiate into more than 10 functional blood cell types. In the standard model of hematopoiesis, hierarchical differentiation commences from HSCs with the production of stem cell intermediates with less durable self-renewal potential that culminate with the generation of MPPs, the penultimate step before lineage specification. From MPPs, the common lineages for myelopoiesis [common myeloid progenitor (CMP)] and lymphopoiesis [common lymphoid progenitor (CLP)] are segregated (*3*, *4*). In myeloid (My) (defined herein as granulocyte/monocyte) differentiation, oligopotent CMPs undergo further restriction into bivalent granulocyte-monocyte progenitor (GMPs) that go on to make granulocytes and monocytes, and megakaryocyte-erythroid progenitors (MEPs) that go on to make platelets and red blood cells (RBCs). Thus, CMPs represent the critical oligopotent progenitor from which all My, erythroid (Er), and megakaryocyte (Mk) cells arise. Although the standard model is still used extensively as an operational paradigm, further cell purification and functional clonal assays have led to key revisions to the model. In mouse, the identification of lymphoid-primed multipotent progenitors (LMPPs) argued that Mk-Er potential must be the first lineage branch lost in lymphomyeloid specification of HSCs (*5*, *6*). Recently, paired-daughter analysis monitoring of mouse HSC cell divisions have demonstrated that Mk-Er progenitors can be derived from HSC directly without progressing through conventional MPPs and CMPs (*7*). Although these data challenge the standard model, clear consensus on a revised model of hematopoiesis is still lacking. Human hematopoiesis is widely regarded as following the same differentiation scheme as mouse hematopoiesis [reviewed in (*8*)]. Early work involving cell purification and methylcellulose (MC) colony-forming cell (CFC) assays identified CMPs and CLPs (*9*, *10*). However, purification schemes to resolve My, Er, Mk, and lymphoid (Ly) fates remained poor. Through the development of more efficient assays to monitor Ly fates in single-cell stromal assays and an improved sorting scheme, we identified human multilymphoid progenitors (MLPs) as the earliest lymphoid differentiation precursor with concomitant lymphoid (T, B, and natural killer) and myelomonocytic potential (*11*, *12*). Considerable uncertainty remains concerning the myelo-erythro-megakaryocytic branch of human hematopoiesis because clonogenic CFC assays do not read out My, Er, and Mk fates efficiently or contemporaneously, making it difficult to account for all cells within phenotypically pure populations of CMPs and MEPs. A comprehensive analysis of human myelo-erythro-megakaryocytic development has not been undertaken, so it is really only by default that the standard model applies.

Much of our understanding of the molecular basis of cellular differentiation and lineage commitment is derived from the assumptions implicit in the standard model. For example, simultaneous expression of molecular factors associated with My-Er-Mk lineages at low levels is considered to maintain CMPs as the origin of the common lineage for myelopoiesis (*3*). During lineage restriction to GMPs and MEPs, progressive upregulation of particular lineage factors initiates feedforward and feedback molecular controls that lock in a granulocyte/monocyte or a Mk-Er differentiation program. An important axiom that arises from this molecular view of the standard model is that cellular differentiation is gradual. However, transcriptional studies of highly purified or single-cell murine HSC has established that molecular programs corresponding to My-Er-Mk fates can directly emerge in multipotent cells, arguing that cellular differentiation is not gradual and that myeloid differentiation can occur without progressing through an intermediate CMP stage (*6*, *7*, *13*–*17*). Naik *et al.* have demonstrated that nearly half of the LMPP compartment is biased toward dendritic cell commitment, a lineage previously thought to come from the CMP-to-GMP route (*15*). Molecular factors associated with Mk-Er differentiation have been shown to be active in LT-HSCs (*13*, *14*), and prospective isolation of platelet-biased LT-HSCs strongly supports that this lineage is not derived from the CMP to MEP route (*16*). Whether molecular programs that regulate My-Er-Mk fates arise at the level of HSCs in humans is not known. It is important to understand where Er and Mk lineage branching occurs in the human hematopoietic hierarchy because these lineages comprise 99% of the cellular component of blood and represent the bulk of the 300 billion blood cells that turn over daily in humans. Mapping the cellular origins of Er and Mk lineages in the human blood hierarchy represents a critical step to define the molecular basis of their fate commitment.

The cellular road map describing the blood hierarchy has been built on two core experimental pillars: cell purification and clonal assays. Human

[1]Princess Margaret Cancer Centre, University Health Network, University of Toronto, Toronto, Ontario, Canada. [2]Department of Molecular Genetics, University of Toronto, Toronto, Ontario, Canada. [3]Medical Biophysics, University of Toronto, Toronto, Ontario, Canada. [4]Ontario Institute for Cancer Research, Toronto, Ontario, Canada. [5]The Hospital for Sick Children Research Institute, University of Toronto, Ontario, Canada. [6]Wellcome Trust, Medical Research Council Cambridge Stem Cell Institute, Department of Haematology, University of Cambridge, Cambridge, UK. [7]Ecole Polytechnique Fédérale de Lausanne, LMC, Station 12, Lausanne, CH-1015, Switzerland.
*These authors contributed equally to this work. †Present address: Ontario Institute for Cancer Research, Toronto, Ontario, Canada.
‡Corresponding author. E-mail: jdick@uhnres.utoronto.ca

studies reporting on sorting schemes for the myelo-erythroid progenitor hierarchy (CMPs, GMPs, and MEPs) have often assumed that "marker-pure" subsets are synonymous with "functionally pure" subsets (*9*). In other words, each cell within the purified subset possesses the same differentiation potential (Fig. 1A, 1). This interpretation is primarily derived from clonogenic assessment of human CMPs, GMPs, and MEPs using standard CFC assays. In CFC assays, purified CMPs typically generate My, Er, or Mk colonies; GMPs give rise to My colonies only; and MEPs give rise to Er and/or Mks (*9*). Because CMPs displayed all lineage readouts, whereas GMPs and MEPs did not, CMPs were interpreted as both marker-pure and functionally pure on the basis that the CFC assay was inefficient in being able to read out mixed differentiation potential. This reasoning underpins the basic bifurcating scheme of human CMPs to GMPs and MEPs. However, an alternate interpretation exists if we assume that the CFC assay is actually efficient. In this case, human CMPs are phenotypically homogenous (e.g., marker-pure) but are functionally heterogeneous, consisting of diverse unipotent progenitors (Fig. 1A, 2). This contention could only be proven if a new sorting strategy is able to isolate, in functionally pure form, each type of the unilineage progenitor from the starting CMP population. To distinguish between the two alternatives, we need (i) a new sorting strategy for human myelo-erythroid progenitors, and (ii) a more sensitive assay to assess mixed cell potential. Until both scenarios can be experimentally resolved, there is considerable uncertainty that clouds the classical view of the human hematopoietic hierarchy. We attempted to address both of these issues by developing a cell-sorting scheme and an optimized single-cell assay to efficiently read out My, Er, and Mk fates from putative multilineage cell types.

Results

Previously defined human MPPs, CMPs, and MEPs are heterogeneous

We developed a cell-sorting scheme to examine the cellular heterogeneity within the CD34$^+$ compartment of human blood. To a previous seven-parameter design (CD34, CD38, CD7, CD10, FLT3, CD45RA, and Thy1) (*11*), we distinguished HSCs from MPPs by adding CD49f (*18*); identified Er-Mk progenitors by adding cMPL (CD110) (*19*, *20*) (designated here as BAH1 to be consistent with the antibody clone used to detect this antigen) (*21*, *22*) and CD71 (transferrin receptor); and distinguished B-lymphoid–committed progenitors from My progenitors, such as GMPs in the CD45RA$^+$ fraction, by adding CD19. Upon evaluation in human fetal liver (FL), neonatal cord blood (CB), and adult bone marrow (BM), this 11-parameter cell-sorting layout provided a high-resolution view of the phenotypic heterogeneity that exists within CD34$^+$ cells across all developmental stages (Fig. 1B and fig. S1).

Many distinct cell types, such as HSCs, MPPs, and MLPs, reside within the CD34$^+$CD38$^-$/lo (simplified as CD34$^+$CD38$^-$ herein) stem cell–enriched compartment of human blood. We investigated whether CD71 or BAH1 expression corresponded to a known cell type within this compartment in the FL. About 10% of the FL CD34$^+$CD38$^-$ expressed CD71, and half of these CD71$^+$ cells also expressed BAH1 (fig. S1A, 2). Neither CD71 nor BAH1 was expressed on Thy1$^+$ HSCs (fig. S2A) or on CD45RA$^+$ MLPs (fig. S2B), which suggests that these markers identify a different cell type within the MPP compartment. We redefined the current MPP compartment into three fractions (F1, F2, and F3) on the basis of CD71 and BAH1 expression: MPP F1 cells were CD71$^-$BAH1$^-$, MPP F2 cells were CD71$^+$BAH1$^-$, and MPP F3 cells were CD71$^+$BAH1$^+$ (Fig. 1B, vii). The expression of these molecules in the CD34$^+$CD38$^-$ compartment was unexpected because the onset of Mk-Er lineage commitment according to the standard model occurs at the level of CMPs and MEPs that are found in the progenitor-enriched CD34$^+$CD38$^+$ compartment. These data suggest that the detection of functional Er and Mk differentiation molecules on a subset of CD34$^+$CD38$^-$ cells represents a unique Mk-Er branch point within the multilineage compartment.

We next analyzed CD71 and BAH1 expression in the CD34$^+$CD38$^+$ progenitor compartment. Co-expression of FLT3 and the lymphoid antigen CD7 in FL CD34$^+$CD38$^+$ cells (fig. S2C) indicated that CD7 expression is not exclusive to lymphoid progenitors as reported previously in CB (*23*). Thus, CD7-expressing cells were not excluded in our sorting layout. In lieu of CD7, we used CD10 expression to exclude Ly progenitors (Fig. 1B, i; fig. S1, 6). In the FL CD34$^+$CD38$^+$CD10$^-$ cell compartment, FLT3 and CD45RA expression

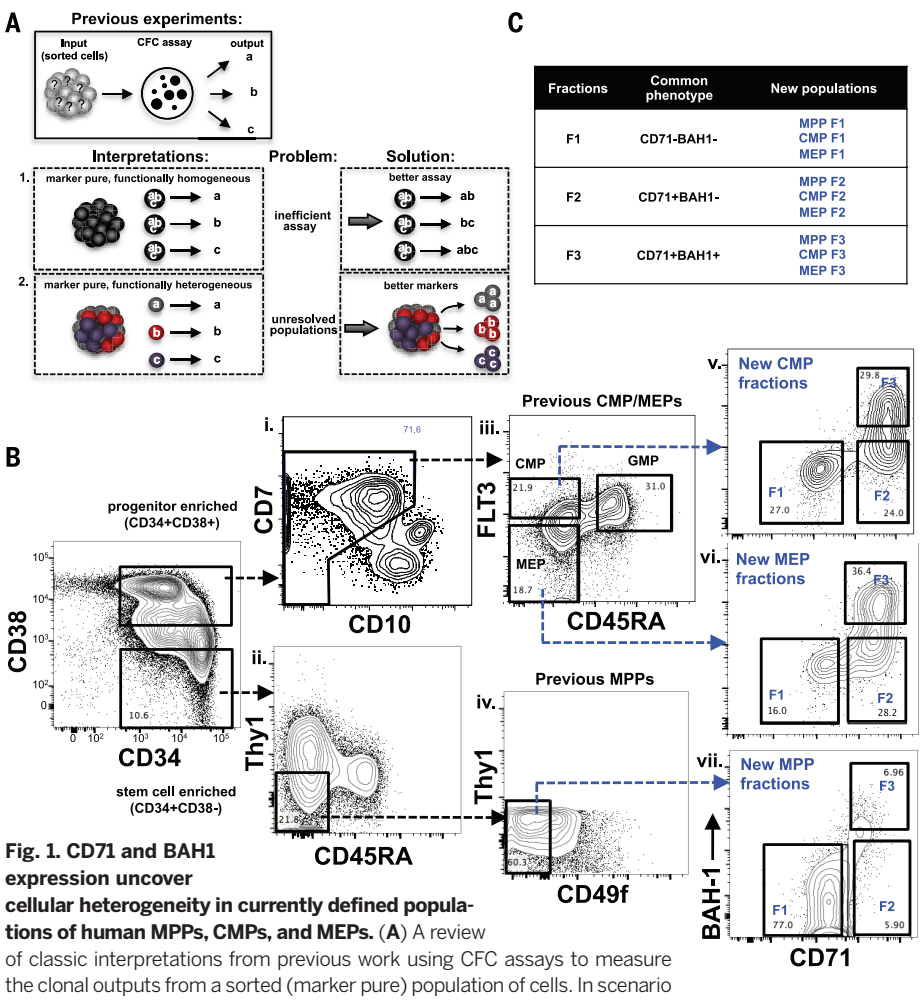

Fig. 1. CD71 and BAH1 expression uncover cellular heterogeneity in currently defined populations of human MPPs, CMPs, and MEPs. (**A**) A review of classic interpretations from previous work using CFC assays to measure the clonal outputs from a sorted (marker pure) population of cells. In scenario 1, each cell within a marker-pure population has the potential to give rise to three functional outputs (a, b, and c) but only gives rise to one of them in the assay. Under this condition, diverse functional outputs from a marker-pure population are interpreted to be derived from a functionally homogeneous population of multilineage cells. In the alternate scenario 2, a marker-pure population is composed of three distinct unipotent cell types that give rise to lineages a, b, and c independently. Both of these scenarios can be reconciled with a better assay (right top) or better markers (right bottom). (**B**) The gating scheme of defining MPPs (CD34$^+$CD38$^-$Thy1$^-$CD45RA$^-$CD49f$^-$), CMPs (CD34$^+$CD38$^+$CD10$^-$FLT3$^+$CD45RA$^-$), and MEPs (CD34$^+$CD38$^+$CD10$^-$FLT3CD45RA$^-$) from a representative human FL sample is shown (black dashed arrows). MPPs, CMPs, and MEPs were further divided into F1 (CD71$^-$BAH1$^-$), F2 (CD71$^+$BAH1$^-$), and F3 (CD71$^+$BAH1$^+$) (blue dashed arrows). Full gating scheme for FL, CB, and BM CD34$^+$ cells is presented in fig. S1. (**C**) Summary of the new subsets used in this study.

was used to identify commonly defined CMPs ($FLT3^+CD45RA^-$), GMPs ($FLT3^+CD45RA^+$), and MEPs ($FLT3^-CD45RA^-$) (Fig. 1B, iii; fig. S1, 7). Addition of CD71 and BAH1 to CMP and MEP populations uncovered phenotypic heterogeneity within these populations previously considered to be homogeneous. In line with the nomenclature we used for the redefined MPP compartment described above, CMP and MEP compartments were also subdivided into three fractions with CD71 and BAH1 (F1, $CD71^-BAH1^-$; F2, $CD71^+BAH1^-$; F3, $CD71^+BAH1^+$) (Fig. 1B, v to vii, and fig. S1, panels 8 and 10). We repeated the same analysis in CB and adult BM to determine whether CB and adult BM samples were similarly heterogeneous. All the major cell populations identified in the FL were also observed in CB and BM, albeit to different degrees (table S1), indicating that the cellular heterogeneity uncovered by CD71 and BAH1 existed across all developmental stages (fig. S1, B and C). Thus, previously defined human CMPs and MEPs that were considered homogeneous are in fact phenotypically heterogeneous when Er and Mk markers are applied.

In summary, previously defined MPPs, CMPs, and MEPs contain three distinct cellular fractions: F1, lacking CD71 and BAH1; F2, expressing CD71 but lacking BAH1; and F3, expressing both molecules. A total of 33 distinct cellular classes from FL, CB, and BM (11 per developmental stage) were functionally interrogated to evaluate their lineage fate potential. To facilitate the review of the results below, a legend and complete phenotype is provided in Fig. 1C and table S1.

An optimized single-cell assay for human My-Er-Mk progenitors

To evaluate the functional potential of the cellular subsets identified above, we developed a single-cell in vitro assay that overcame the shortcomings of previous approaches to characterize human myeloid progenitors. An ideal assay would support the ability of single cells to simultaneously commit along My, Er, and/or Mk fates, as well as to provide the conditions for their differentiated progeny to survive, propagate, and expand to permit detection. Standard MC assays do not strictly fulfill these criteria. For example, $CD49f^+$ HSCs exclusively generated CFU-My in MC (fig. S3A and supplementary text), yet single HSCs sustain multilineage hematopoiesis in vivo (*18*). Also, the limited self-renewal potential of downstream progenitors makes them difficult to read out in vivo at clonal resolution, further highlighting the need to develop more sensitive in vitro methodology to assess the lineage potential of progenitors. We found that serum-free conditions supplemented with growth factors (SCF, FLT3, TPO, EPO, IL-6, IL-3, IL-11, GM-CSF, and LDL) and stroma were highly efficient at assaying My, Er, and Mk lineage potential from single $CD34^+$ cells. Single-cell–derived clones were analyzed by flow cytometry after a 2- to 3-week culture period for Mk (CD41 and CD42b), Er (GlyA), and My (CD14, CD15, and CD33) cells. One example of the efficiency of this new assay comes from the analysis of the $CD49f^+$ HSC subset, which previously could not be read out in vitro as single cells (*11*). Under these new conditions, 77% of FL, 72% of CB, and 48% of BM single $CD49f^+$ HSCs were able to produce a clone (fig. S5A, left). Whereas only CFU-My were produced from HSC in MC, mixed clonogenic potential was now readily detectable with this assay. We used this assay to functionally map the lineage potential of all the newly defined $CD34^+$ subsets from all three developmental time points.

Unipotent progenitors dominate the blood hierarchy by adulthood

To gain a global perspective of the functional differences in the blood hierarchy across ontogeny, we first combined all 11 $CD34^+$ subsets from each developmental time point into one analysis of nearly 3000 single cells. Cloning efficiency was highest for FL and decreased gradually in CB and BM (FL, 74%; CB, 69%; BM, 55%) (Fig. 2A). A simple stratification based on whether a single cell gave rise to one (unilineage) or more (multilineage) cell lineages revealed that 40% of FL $CD34^+$ cells were multilineage compared with 27% of CB ($P < 10^{-3}$, Fisher's exact test) and 18% of BM ($P < 10^{-3}$, Fisher's exact test) $CD34^+$ cells (Fig. 2B). Thus, the ratio of multilineage to unilineage progenitors changes en bloc in development within the $CD34^+$ population, a result that is independent of the complex marker scheme that we used.

To continue exploring the organizational relationships of progenitors across developmental time points, we investigated the proportion of multilineage to unilineage cells in the stem-cell–enriched ($CD34^+CD38^-$) and the progenitor-enriched ($CD34^+CD38^+$) subsets. Within $CD34^+CD38^-$ cells, FL and CB had a significantly higher proportion of multilineage cells compared with BM (FL versus BM: 48.6% versus 32.9%, $P = 0.0016$; CB versus BM: 46.1% versus 32.9%, $P = 0.011$; Fisher's exact test). These proportional differences were more pronounced in the $CD34^+CD38^+$ progenitor compartment. In $CD34^+CD38^+$ cells, BM displayed a factor of 3 fewer multilineage cells compared with FL (FL, 28.8%; CB, 17.3%; BM, 9.6%; $P < 0.0001$, Fisher's exact test) (Fig. 2, C and D). Thus, both the stem and progenitor compartments from each developmental stage exhibited a proportional

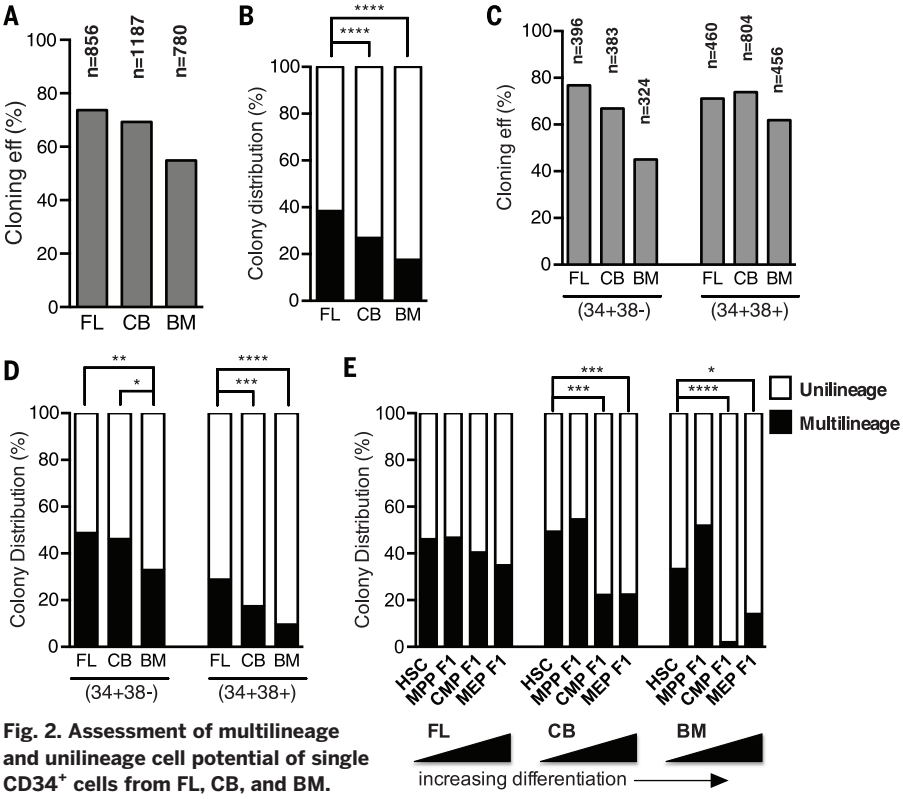

Fig. 2. Assessment of multilineage and unilineage cell potential of single $CD34^+$ cells from FL, CB, and BM. (**A** to **D**) Single cells from subsets defined in Fig. 1C were deposited by fluorescence-activated cell sorting (FACS) and cultured for several weeks. Emergent clones were analyzed by flow cytometry for My, Er, and Mk lineages (Fig. 3A). To gain a global perspective of the functional differences between FL, CB, and BM, subsets were combined into one analysis of $CD34^+$ cells [(A) and (B)] or stem ($CD34^+CD38^-$) and progenitor ($CD34^+CD38^+$) cell compartments [(C) and (D)]. A single cell was defined as multilineage (black) when it gave rise to more than one lineage (any two of My, Er, or Mk) and unipotent when it gave rise to one lineage (My or Er or Mk) [(B) and (D)]. Overall cloning efficiency is shown in gray [(A) and (C)]. (**E**) Distribution of multilineage and unilineage cell potential from populations that lack CD71 and BAH-1 (F1) expression (shown by increasing differentiation: HSC > MPP F1 > CMP F1 > MEP F1). Asterisks indicate significance based on Fisher's exact test (*$P < 0.05$, **$P < 0.01$, ***$P < 0.001$, ****$P < 0.0001$).

change in the percentage of multilineage cell types.

Next, we localized the differentiation stages most affected by the loss of multilineage progenitors. We reasoned that HSCs and subsets that lack differentiation markers CD71 and BAH1 (MPP F1, CMP F1, and MEP F1) would be enriched for cells with multilineage cell potential. Notably, in FL, the ratio of multilineage to unilineage progenitors remained nearly constant across these subsets (Fig. 2E). By contrast, only HSC and MPP F1 subsets from CB and BM were highly enriched for multilineage cells, whereas their corresponding CMP/MEP F1s were composed mostly of unilineage cell types (Fig. 2E; $P < 0.05$, Fisher's exact test). In BM, virtually all multilineage cells were restricted to the $CD34^+CD38^-$ stem cell compartment (Fig. 2E; $P < 0.05$, Fisher's exact test). Hence, multilineage cell potential extends into the progenitor compartment in FL, but in BM, this potential is restricted to the $CD34^+CD38^-$ stem cell compartment. In parallel, the progenitor compartment in BM is dominated by unilineage cell types.

Mk-Er lineage branching in the blood hierarchy is developmentally defined

To gain a detailed understanding of the differentiation potential of each progenitor subset identified by our sorting scheme applied to FL, CB, and BM, we classified the functional potential of each single cell in our data set. Five distinct clonal outputs were classified: Mk only, Er only, My only, Mk/Er, and mixed (bipotent, Er/My or Mk/My; tripotent, Er/Mk/My) (Fig. 3A). The cloning efficiency of all subsets was high in MPP, CMP, and MEP fractions (50 to 80%) (Fig. 3B and fig. S5A).

The highest percentage of mixed clones was found among the HSC subsets (FL, 46.1%; CB, 49.3; BM, 33.3%) (fig. S5A), except in BM, where MPP F1 harbored higher mixed clone potential than HSC (51.9%), although this was not significant (BM HSC versus MPP F1: $P = 0.1$, Fisher's exact test) (Fig. 2E). FL HSC and MPP F1 subsets had a statistically higher distribution of tripotent versus bipotent mixed clones compared with CB and BM HSC and MPP F1 (fig. S5B). In FL and CB, Mk-Er-only clones appeared at the MPP F1 stage (FL, 29% of total; CB, 18% of total) (Fig. 3B, column 1, row 1). In BM, Mk-Er clones from MPP F1 were rare (~2%); rather, 15% of all clones from this subset were Er-only. Mk activity from BM MPP F1 was detected as a component of mixed clones that also contained My cells (further discussed below).

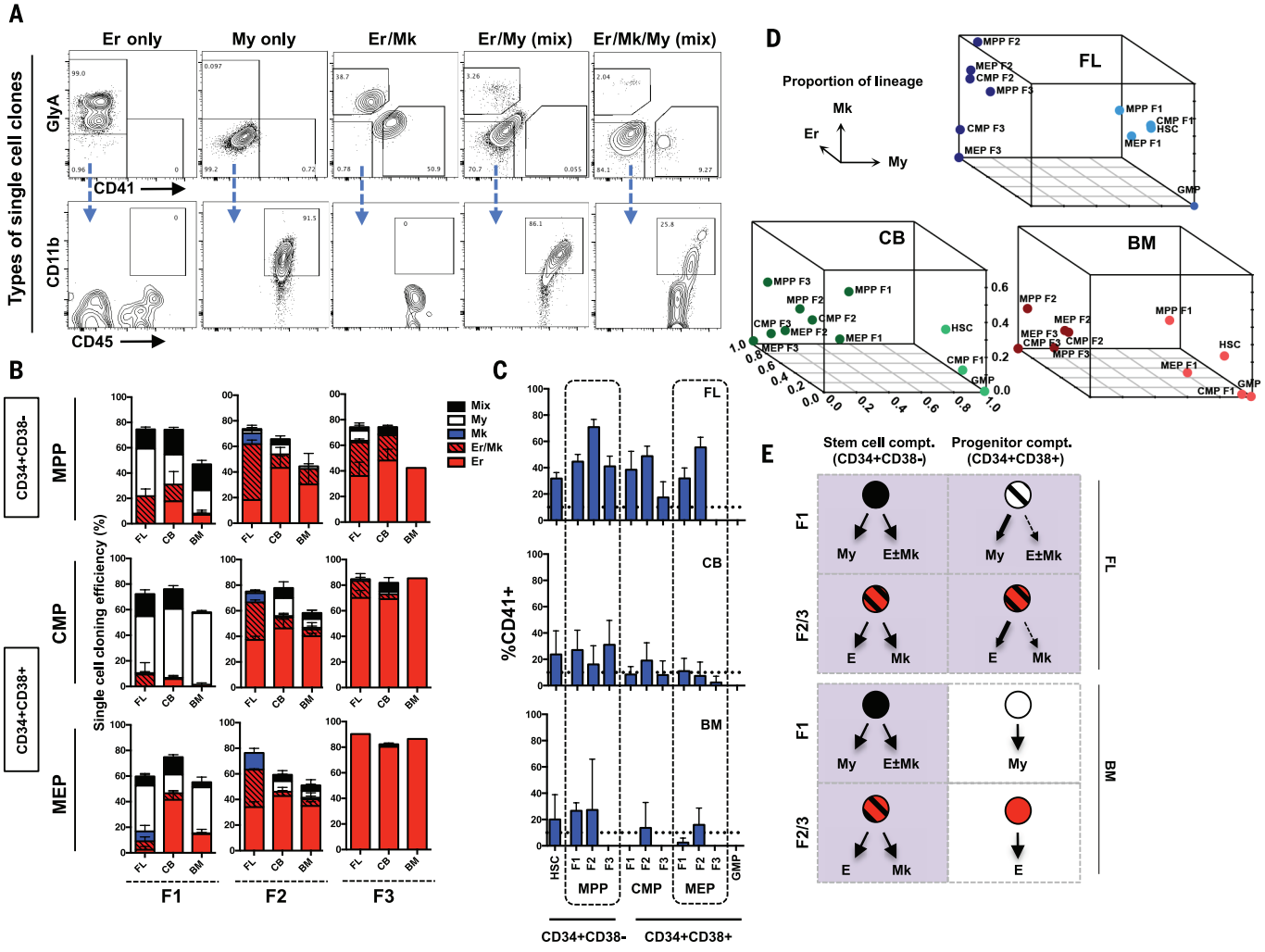

Fig. 3. Lineage analysis of single-cell clones from subfractions of MPP, CMP, and MEP populations. (**A**) Single-cell clones were analyzed by flow cytometry and binned into five distinct lineage outcomes. Erythroid clones were defined as $GlyA^+$ only (Er only). Myeloid clones were identified as $GlyA^-CD41^-$ but $CD45^+CD11b^+$ (My only). Erythroid-megakaryocyte clones were defined as $GlyA^+$ and $CD41^+$ but negative for CD11b (Er/Mk). Mix clones were defined My and Er or Mk (column 4) or My, Er, and Mk (column 5). (**B**) Cloning efficiency and lineage outcomes of single cells from newly defined MPP, CMP, and MEP fractions (F1, F2, and F3) from FL, CB, and BM. (**C**) Total Mk output ($CD41^+$) from all newly defined subsets from FL, CB, and BM. Bars indicate mean ± SE. Total number of independent experiments: $n = 3$, 6, and 4 for FL, CB, and BM, respectively. The dotted line defines the threshold for detecting positive Mk lineage potential from a sorted fraction due to analytical noise that arises from single clone flow cytometry. (**D**) Three-dimensional summary of lineage outputs (My, Er, and Mk) from all cellular subsets in FL, CB, and BM presented in (B). (**E**) Pictorial depiction of the predominant lineage outcomes from stem ($CD34^+CD38^-$) and progenitor ($CD34^+CD38^+$) cell compartments in FL and BM data.

We next interrogated the $CD34^+CD38^+$ compartment. Based on the classical view of the blood hierarchy, we would expect that true CMPs reside in a subset that lacks expression of differentiation markers such as CD71 and BAH1 (CMP F1). Only 15% of FL and CB CMP F1 clones were mixed, and no mixed clones from this subset were detected in BM (Fig. 3B, column 1, row 2). Thus, we conclude that previously defined BM CMPs are not homogeneous for cells with multilineage My-Er-Mk potential; rather, they are heterogeneous and composed of subpopulations of unilineage My, Er, and Mk progenitors (Fig. 3B, row 2). To determine whether the small percentage of mixed clones from FL and CB CMPs F1 population were derived from bona fide CMPs, we evaluated their My-Er-Mk potential. More than 80% of the mixed clones from FL and CB were bipotent (either Er/My or Mk/My) without concurrent Mk-Er-My potential (fig. S5C). These data demonstrate that bona fide CMPs are a rare component of the human hematopoietic tree, irrespective of developmental stage.

MC and megacult colony assays indicated that subsets defined by CD71 and BAH1 expression (F2 and F3) were highly enriched for Mk and Er activity (fig. S3, A to D, and supplementary text). However, these assays cannot formally rule out that Er and Mk potential was derived from independent unilineage progenitors. We first tracked Mk-Er activity from single cells within the MEP subsets (MEP F1 through F3) (Fig. 3B, row 3). MEP F1 was highly heterogeneous across developmental time points and composed mostly of My progenitors in FL and BM (60% or more) (Fig. 3B, column 1, row 3) that functionally resemble other F1 subsets from MPPs and CMPs. In CB and BM, ~70% of clones from MEP F2 were Er-only, and 10% or less were Mk-Er clones (Fig. 3B, column 2, row 3). MEP F2 is likely the subset within classical MEPs that gave rise to low-level Mk colonies in previous studies. MEP F3, the numerically dominant cell population within the classical MEPs, uniformly produced Er-only clones in FL, CB, and BM (Fig. 3B, column 3, row 3). Thus, classically defined MEPs are principally composed of Er-only progenitors when analyzed at single-cell resolution and are not Mk-Er progenitors as previously thought.

As only rare cells within the MEP fractions give rise to Mks, Mk potential must lie elsewhere in the blood hierarchy. We found that most Mk-Er activity came from the $CD34^+CD38^-$ stem cell compartment (fig. S3C) and was particularly enriched within one of our newly defined MPP subsets (Fig. 3B, column 2, row 1). In FL, 60% of clones from MPP F2 were of Mk-Er type, and the remainder of this subset was composed of Mk-only or Er-only clones (Fig. 3B, column 2, row 1). Notably, Mk activity was enriched but not restricted to the stem cell compartment in the FL. Because we did not find strong evidence for FL CMPs, we expect that FL Mk-Er progenitors arise from the stem cell compartment, specifically from MPP F2. In CB and BM, Mk-Er clones represented one-quarter of the total clonal output from this subset (Fig. 3B, column 2, row 1), and the rest were Er-only clones. In CB—and more evident in BM—Mks predominantly emerged as part of mixed clones from HSCs and MPP F1, supporting the hypothesis that Mk branching occurs directly from a multipotent cell, as predicted by the murine studies (7). These data suggest that both Mk-Er and multilineage potential are restricted to the stem cell compartment by adulthood, whereas unilineage fates predominate the progenitor compartment, forming a simple "two-tier" hierarchy, with few intervening oligopotent intermediates (Fig. 3, D and E).

In vivo analysis establishes hierarchical relationships between progenitor subsets

In the blood hierarchy, cell types near the peak of the hierarchy, such as HSCs and MPPs, are rarer but possess higher proliferative potential. Lineage differentiation typically correlates with loss of proliferative potential. Although HSC and MPP subsets (F1 to F3) are minor populations, they yielded 5 to 10 times as many cells compared with more abundant populations from the CMP and MEP subsets in vitro (fig. S6A).

We then transplanted our cellular subsets in vivo and measured graft durability and size, as well as its lineage composition, to establish the hierarchical relationships of our newly defined progenitor subsets. Due to tissue availability, only CB was used. Because there are limited data on the engraftment capacity of human progenitors in the NOD-*Scid-Il2rg*^{null} (NSG) model, we first scrutinized the repopulation kinetics of human blood cells in this model. Using HSCs, we observed low-level lymphomyeloid as well as erythro-megakaryocytic engraftment as early as 2 weeks after transplant (fig. S6, B and C), consistent with previous studies using NOD-*Scid* mice (24). We used 2 weeks as the standpoint from which to assess progenitor cell engraftment in vivo. One thousand CMP F1 cells and 3000 MEP F1 cells generated a myelo-erythroid restricted graft that did not persist beyond 2 weeks (Fig. 4A, column 3 and 5, and fig. S6E). By contrast, 200 MPP F1 cells were able to sustain a robust and systemic multilineage graft (My-Er-Ly) beyond 2 weeks, consistent with the functional potential of true MPPs (Fig. 4A, column 1; Fig. 4B; and fig. S6E) (18).

To gather enough cell numbers for in vivo detection of Er-enriched subsets, we combined the F2 and F3 subsets from MPPs, CMPs, and MEPs for transplantation because they shared similar functional potential in vitro. The combined F2/F3 subsets from MPPs, CMPs, and MEPs all gave rise to prominent Er grafts in vivo, concordant with their in vitro potential (Fig. 4A, columns 2, 4, and 6; and fig. S6D, top panels). MPP F2/F3 cells were highly proliferative and generated a robust Er graft with only 400 transplanted cells

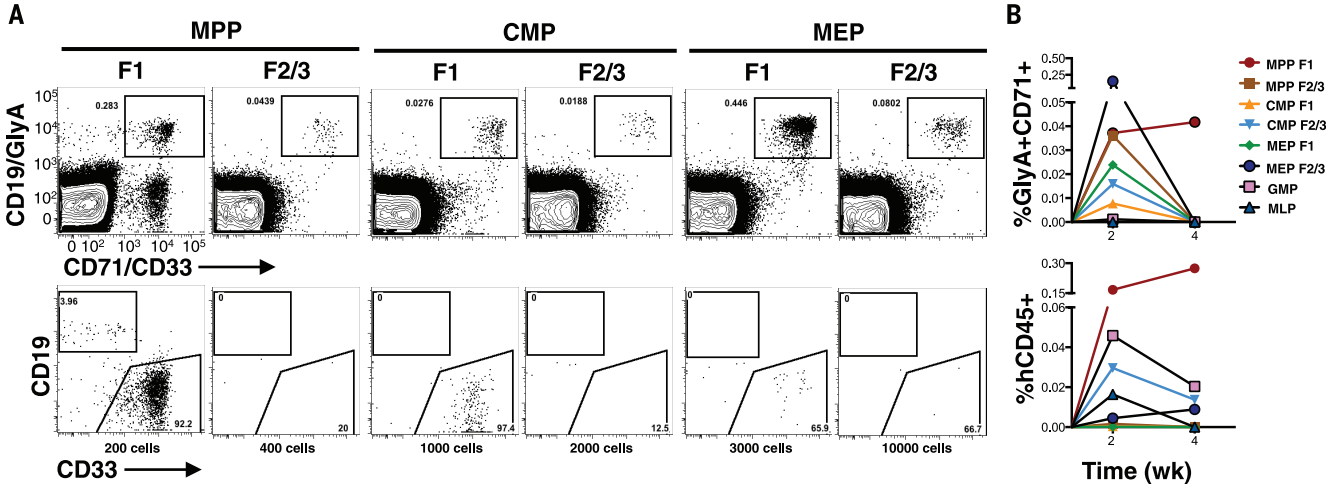

Fig. 4. In vivo potential of progenitor subsets. (**A**) Freshly sorted populations from CB were intrafemorally transplanted into sublethally irradiated NSG mice. Bone marrow from injected femur and noninjected bones were analyzed by flow cytometry 2 weeks after transplant. The average transplanted cell dose is shown at the bottom of the flow plot. Top row indicates Er engraftment ($GlyA^+CD71^+$). Bottom row indicates total human leukocyte engraftment ($CD45^+$). B-lymphoid cells and My cells were detected using CD19 and CD33, respectively. (**B**) Kinetic analysis of engraftment from progenitor subsets. Mean levels of Er ($GlyA^+CD71^+$) and total human cell engraftment ($CD45^+$) are shown.

(Fig. 4A, column 2), whereas CMP F2/F3 and MEP F2/F3 required cell doses higher by a factor of 5 to 25 to generate an in vivo graft (Fig. 4A, columns 4 and 6). Although platelets were difficult to detect in vivo from progenitor subsets, we did observe them in rare mice engrafted with either MPP F1 or MPP F2/3 cells (fig. S6C). Only MPP F2/F3, but not CMP F2/3 and MEP F2/3, were able to migrate systemically to nontransplanted bones and resemble the proliferative potential of MPP F1 (fig. S6E). When combined with the in vitro analyses of these subsets, these in vivo experiments support that Mk-Er-enriched MPP F2/F3 are derived from HSCs or MPPs directly without invoking a lineage route via a CMP intermediate.

A transcriptionally defined erythroid progenitor subnetwork in the CD34 hierarchy

Lineage commitment coincides with the expression of key molecules that aid to "lock in" a differentiation program (*25*). Using low-cell-input RNA-sequencing methodology (*26*), we first analyzed the expression profile of canonical lineage factors in bulk CB subsets. Genes associated with My specification, such as *MPO* and *CSF2RA* (*GM-CSFR*), were highly expressed in GMPs, whereas genes associated with the Er lineage, such as *GATA-1* and *EPOR*, were highly expressed in F2/F3 subsets from MPP, CMP, and MEP populations (fig. S7A). Mk differentiation markers, *CD41* (*ITGA2B*) and *CD42b* (*GP1BA*), were highly expressed in MPP F2, in line with the functional potential of this subset. These data provide an independent line of evidence that committed Mk progenitors reside within the stem cell compartment. Low-level expression of *CD41* and *CD42b* was also detected in MPP F3 and MEP F2, consistent with the residual Mk activity from these CB subsets (fig. S7A).

Unsupervised hierarchical clustering and principal component analysis of the entire data set revealed two major molecular subgroups: those with Er-enriched potential (MPP, CMP, and MEP F2/F3), and another with multilineage (HSC or MPP F1) or My-enriched potential (CMP F1 or MEP F1) (fig. S7B). F2 and F3 subsets within MPP, CMP, and MEP populations clustered together, suggesting that these pairs are more closely related within each broader compartment (fig. S7Bi). Due to their close transcriptional and functional relationship, we merged F2 and F3 subsets from MPP, CMP, and MEP subsets to compare global transcriptional differences among these Er-enriched subsets. We found that 230 genes were differentially expressed between MPP (F2/F3) versus CMP (F2/F3), and 52 genes between CMP (F2/F3) versus MEP (F2/F3). These differentially expressed genes were highly enriched in the cell cycle and DNA replication and metabolic processes, and coincide with the extensive proliferation that Er progenitors undergo during specification (fig. S7C). These data reinforce the idea that the close functional relationship between Mk-Er and Er enriched subsets is likely due to shared molecular programs.

Molecular heterogeneity among single cells within a purified subset is commonly lost in a population-level analysis. We tracked the expression of key lineage factors among single cells in our progenitor subsets. Only FL and BM were used in this experiment because they represent the two ends of the development time points used in this study. In both FL and BM, single cells from F2 and F3 from MPPs, CMPs, and MEPs displayed a dominant Er gene expression program, often co-expressing both *GATA1* and *EPOR* genes in the same cell (Fig. 5A and fig. S7D). Our sorting method

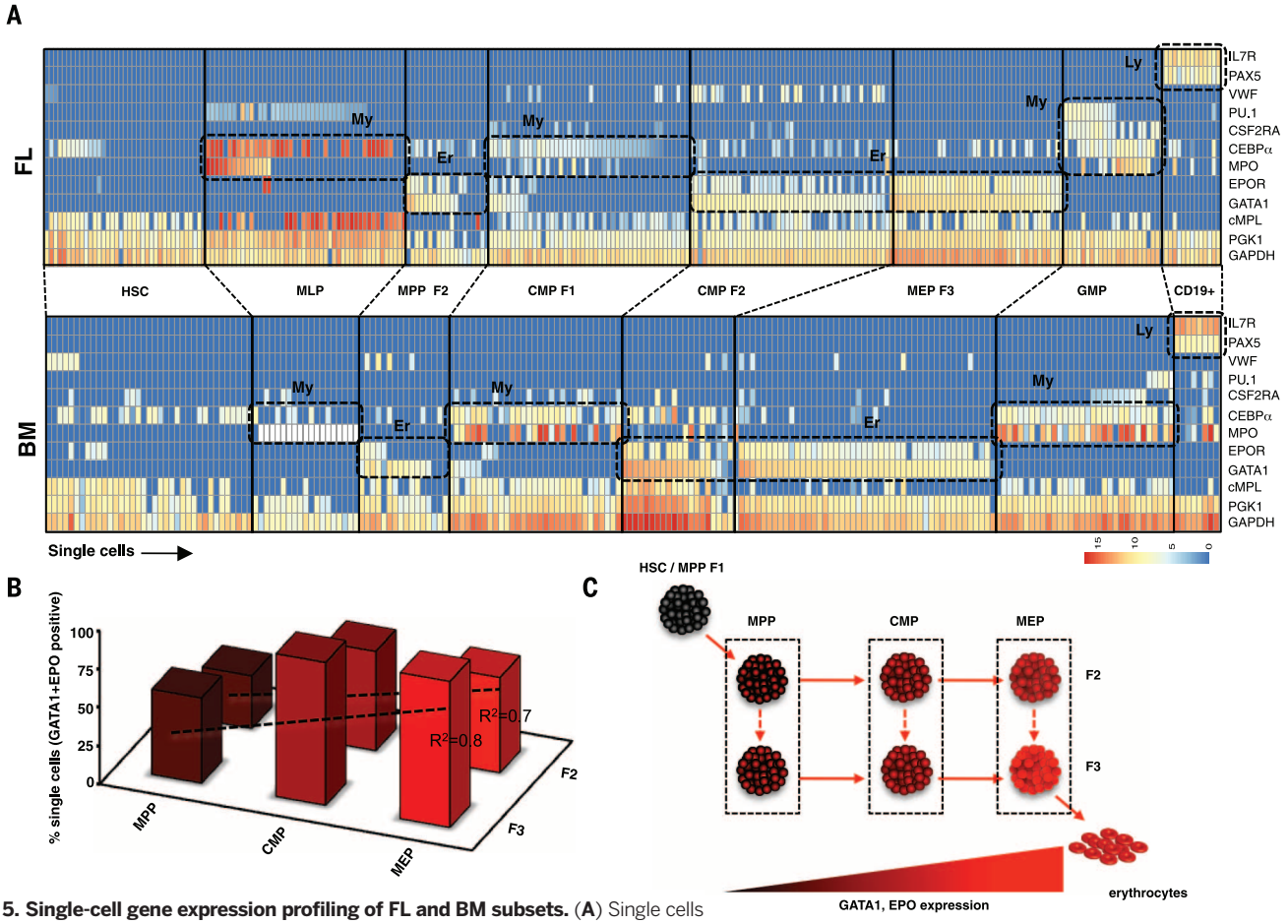

Fig. 5. Single-cell gene expression profiling of FL and BM subsets. (**A**) Single cells from FL (top) and BM (bottom) subsets were sorted and analyzed for expression of genes associated with My, Er, and Ly lineages (shown on right) on the Fluidigm platform. My, Er, or Ly gene clusters are shown as dashed boxes. (**B**) Percentage of single cells that coexpress *GATA1* and *EPOR* in F2 and F3 from MPP, CMP, and MEP subsets. BM and FL F2 and F3 subsets were combined in this analysis. (**C**) A theoretical subnetwork of Er progenitors within the $CD34^+$ compartment.

can essentially resolve the Er-committed progenitors within the CD34$^+$ hierarchy. We observed that *GATA1* expression was present among most single cells in MPP F2 and MPP F3, but *EPOR* expression was only present in a subset of *GATA1*-positive cells (Fig. 5, A and B). Because *GATA1* precedes *EPOR* expression in Er differentiation, MPP F2/F3 cells represent the earliest erythroid differentiation precursor in the human blood hierarchy. The percentage of single cells that co-expressed *GATA1* and *EPOR* increased in proportion among F2 and F3 subsets from MPPs, CMPs, and MEPs in both FL and BM (Fig. 5B). These molecular factors are considered a surrogate of the degree of Er differentiation (Fig. 5B). When considered jointly with our in vitro and in vivo analyses, these subsets are already Er-specified but vary mostly in their proliferative potential. We hypothesize that these subsets compose a hierarchical subnetwork of Er progenitors within the CD34$^+$ compartment (Fig. 5C). A candidate network map is shown in Fig. 5C. Because erythrocytes comprise nearly 99% of all blood cells, this network may offer a high degree of flexibility to synthesize erythrocytes under homeostatic and emergency erythropoiesis without HSC input.

Dramatic loss of Er progenitors compared with My progenitors in a hematologic condition of HSC deficiency

Recent HSC fate-mapping analyses in mice have provocatively shown that progenitors, but not HSCs, are fundamental for ongoing hematopoiesis under homeostatic conditions (*27*, *28*). Physiological studies to experimentally test this question are not possible in normal human subjects. However, certain disease states permit a glimpse into the consequences of HSC loss on progenitors and may shed light on the role of HSCs in human blood synthesis under nontransplant conditions. In aplastic anemia (AA), HSCs are damaged, likely due to an autoimmune response, and are unable to contribute to ongoing hematopoiesis (*29*, *30*). This effect seems to be specific to HSCs, because all mature blood lineages are depressed in AA (*31*–*33*). We examined the progenitor hierarchy in three cases of AA by applying our sorting scheme (Fig. 6). Consistent with previous reports, the proportion of CD34$^+$ cells within the overall mononuclear cell (MNC) pool was significantly lower in AA compared with normal BM (0.1% versus 4.2%, $P < 0.0001$, t test) (Fig. 6B) (*31*, *32*). The CD34$^+$CD38$^-$ stem cell compartment in AA patients was more significantly depleted compared with the CD34$^+$CD38$^+$ progenitor compartment (Fig. 6A, left column, and Fig. 6, C and D). Moreover, HSCs and MPPs were virtually undetectable in the residual CD34$^+$CD38$^-$ compartment, confirming that HSCs are specifically lost in this clinical condition (Fig. 6A, column 2), at least at the phenotypic level. Despite the loss of phenotypic HSCs, the CD34$^+$CD38$^+$ compartment was detectable in all cases. We quantified the subsets within the CD34$^+$CD38$^+$ compartment to determine whether all cell types are indiscriminately affected. Based on our single-cell functional readouts, we grouped progenitors enriched for myeloid (CMP F1, MEP F1, and GMP) and erythroid (CMP F2/F3 and MEP F2/F3) differentiation potential to increase the power of the analysis due to relative loss of CD34$^+$ cells in AA. Despite significant depletion of HSCs, the percentage of myeloid progenitors was stable compared with normal BM (Fig. 6E). In contrast, erythroid progenitors were significantly lost, like HSCs, in all three patients analyzed (Fig. 6F, $P < 0.0001$, t test). These results suggest that ongoing erythropoiesis is more reliant on HSC input compared with myelopoiesis. Although we cannot rule out a specific Er lineage defect in AA, the pan-lineage deficiencies observed in AA likely rule out this possibility and support the idea that the Er progenitor loss is most likely a repercussion of HSC depletion. Because all HSC types and MPPs seem to be broadly lost in AA, our results cannot distinguish which type of HSC is crucial to maintain erythropoiesis. Recognizing that hematopoiesis in AA is not normal, the revised hierarchy model predicted from our experimental data does appear to have physiological relevance in the human setting.

Discussion

Our study challenges the current view that human blood development occurs progressively through a series of multipotent, oligopotent, and then unilineage progenitor stages. By subjecting the classically defined progenitor subsets to a sorting scheme that efficiently resolved My, Er, and Mk lineage fates, combined with single-cell functional analysis, we made two findings. First, we found that the cellular hierarchy of human blood is not identical across development. In FL, oligopotent progenitors with My-Er-Mk and Er-Mk activity were a prominent component of the hierarchy. By contrast, the BM was dominated by unilineage progenitors with primarily My or Er potential. This shift in progenitor classes demarcates a fundamental readjustment in the blood hierarchy during in utero to adulthood time points. The absence of oligopotent intermediates that become gradually restricted to unilineage progenitors in BM cannot be reconciled under the standard model of blood differentiation. Instead, our data support a hierarchy composed mainly of two tiers in adults: a top tier that contains multipotent cells such as HSCs and MPPs, and a bottom tier composed of committed unipotent progenitors (Fig. 7). We cannot formally rule out the presence of a highly transient adult CMP-like progenitor stage that exists when multipotent cells differentiate into unipotent progenitors; however, our in vitro and in vivo assays surveyed large cell numbers (~3000), and such a progenitor was not detected. If lineage-restricted cell types able to generate a subset or full spectrum of myeloid cells do exist in the stem cell compartment of adult marrow, they most probably represent the murine counterparts of myeloid-biased or myeloid-restricted HSC subtypes (*7*, *34*). Second, we found the origins

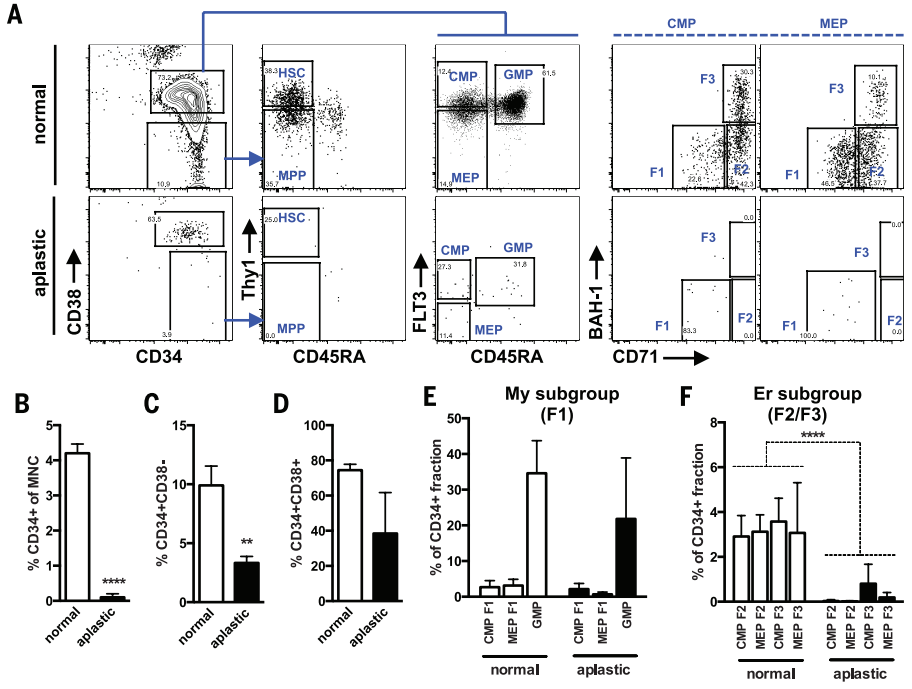

Fig. 6. Analysis of My and Er progenitors in patients with AA. (**A**) To examine the consequences of HSC loss on progenitor subsets, BM cells from three AA patients and normal controls were subjected to the new sorting design shown in Fig. 1B. Representative flow plots from a single AA case and a control are shown. (**B**) Quantification of total CD34$^+$ cells as a fraction of MNC pool from controls (empty bars) versus AA (filled bars). (**C** and **D**) The CD34$^+$ subset from controls and AA was further subdivided into the stem (CD34$^+$CD38$^-$) and progenitor (CD34$^+$CD38$^+$) cell compartments. (**E**) Analysis of My-enriched subsets (CMP F1, MEP F1, and GMP) in controls and in AA. (**F**) Analysis of Er-enriched subsets (CMP F2/F3 and MEP F2/F3) in controls and in AA. Bars indicate mean ± SE from three controls and three cases of AA. Asterisks indicate significance based on t test (**$P < 0.01$, ****$P < 0.0001$).

of the Mk lineage branch change from FL to BM. In FL, Mk progenitors were enriched but not restricted to the stem cell compartment, whereas in BM, the Mk lineage was closely tied to the fate of multipotent cells. These data are not consistent with the principal tenet of the standard model that My, Er, and Mk lineages originate from a common lineage progenitor such as CMP.

Historically, the first major lineage bifurcation step in the blood hierarchy was considered to be the segregation of myeloid (My-Er-Mk) and lymphoid fates (B, T, or Nk), with CMPs occupying the lineage fork that gives rise to the entire myeloid arm. The coemergence of My, Er, and Mk lineages was central to the description of CMPs. Our results reveal that the originally defined CMPs are highly heterogeneous, primarily composed of unipotent My or Er progenitors, with little Mk activity. In the absence of CMPs, how can the origins of lineage-restricted progenitors such as GMPs and MEPs be reconciled? Our previous clonal analysis suggested that myelomonocytic lineages originate from MLPs, which we suspect are the most probable precursor of GMPs, owing to their shared functional and transcriptional profiles (*11*, *12*, *35*). In this study, we found that *GATA-1*–positive Mk-Er–committed progenitors exist in the stem cell compartment, suggesting that MEPs are derived from multipotent cells. In the murine bone marrow niche, up to a quarter of LT-HSCs lie directly adjacent to Mks (*36*–*38*). Mks play a dual role in HSC regulation. Under normal conditions, Mk-HSC contact is essential to preserve the quiescent nature of adult LT-HSCs. After myeloablation, this effect is temporarily abrogated and Mks secrete growth factors that permit HSCs to expand (*37*). Thus, direct differentiation of Mks from HSCs may represent a physical mechanism to regulate blood stem cell functionality in the niche. Overall, the first major bifurcation step in blood differentiation is far more complex than a simple segregation of myeloid and lymphoid lineages. In humans, we suspect that this first step splits the Mk-Er lineage from the myelomonocytic lineage that cosegregates with the lymphoid fate (*11*). Why the myelomonocytic lineage, but not the granulocytic lineage, is tied to the lymphoid fate will be a critical area of future investigation (*39*, *40*). The ability to isolate developmental populations reported here provides a critical experimental framework to facilitate such studies in humans.

Our data may also have implications for our understanding of lineage specification at the molecular level. *vWF*, a key molecular marker strongly associated with Mk differentiation, was expressed in a subset of BM HSCs and may identify an HSC subtype primed for platelet production as shown in mouse (*16*). Molecular factors involved in Mk (*vWF*), Er (*EPOR*), and My (*CSF2RA*) differentiation were expressed in small pockets of single cells from undifferentiated cells, like BM HSCs, in a near mutually exclusive manner. This is consistent with the notion that transcription factors (TFs) associated with myeloid lineage specification are individually but not simultaneously primed at the level of stem cells. It is difficult to preclude that this type of molecular heterogeneity reflects impurities in human HSC isolation. However, analysis of purer murine HSC compartments supports that molecular factors associated with lineage commitment are stochastically activated at the level of HSCs (*16*, *17*). Maintenance of a multipotent state is thought to occur via low-level lineage priming, where TFs of different lineages are coexpressed in the same cell. In this model, commitment toward a particular lineage occurs by the mutual antagonism of these TFs, where one TF eventually wins, locking in a differentiation program. However, the near mutually exclusive expression of *vWF*, *CSFR2A*, and *EPOR* in BM HSCs does not agree with this logic. The hypothesis that lineage commitment occurs in the absence of a coordinated differentiation program (*17*, *25*, *41*) is more consistent with our data.

Ultimately, a better understanding of normal blood differentiation programs will be critical to deciphering how such programs go awry in disease. Indeed, in AA, we observed that Mk-Er progenitors are lost alongside HSC, but the My progenitor pool can continue to persist. Recent evidence from murine in situ tracking expriments showed that My progenitors can be sustained long term without contribution from HSCs (*27*, *28*). If human My progenitors are similarly long-lived, they would have a higher probability of acquiring mutations that could lead to clonal expansion and eventual My lineage leukemias. The short-lived nature of Mk-Er progenitors and their dependency on HSC input reduce their probability of accumulating enough mutations leading to leukemia. Clinical evidence that acute leukemia of the Mk and Er lineages is extremely rare compared with My leukemia is consistent with this idea. Our work on AA highlights one example of the clinical utility of a high-resolution developmental road map of normal hematopoiesis. The adaptable nature of our new sorting scheme should similarly inform on other hematological conditions.

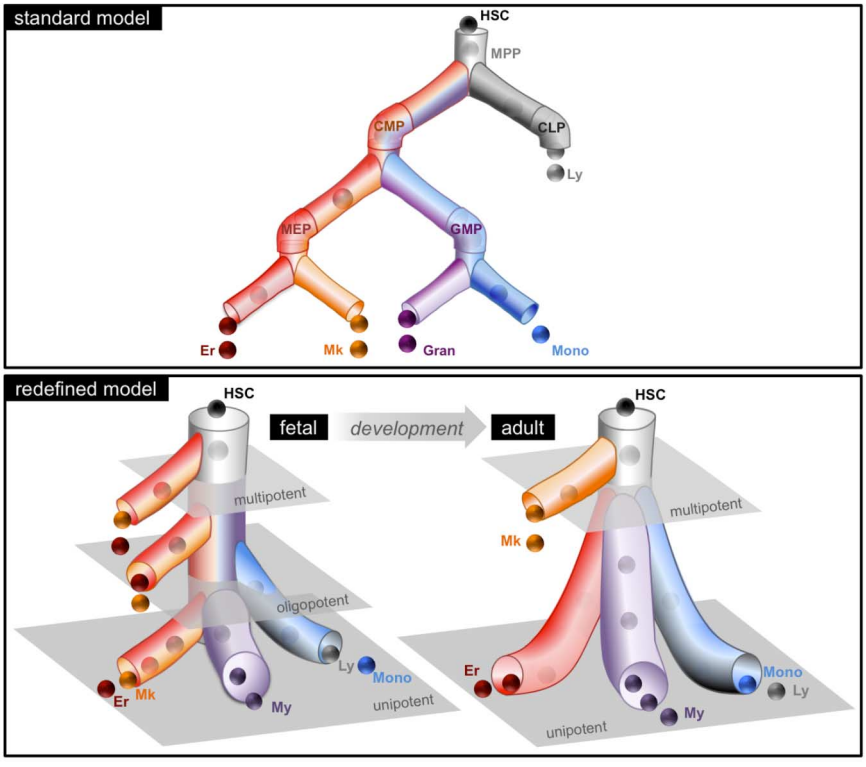

Fig. 7. A model of the changes in human My-Er-Mk differentiation that occur across developmental time points. Graphical depiction of My-Er-Mk cell differentiation that encompasses the predominant lineage potential of progenitor subsets; the standard model is shown for comparison. The redefined model proposes a developmental shift in the progenitor cell architecture from the fetus, where many stem and progenitor cell types are multipotent, to the adult, where the stem cell compartment is multipotent but the progenitors are unipotent. The grayed planes represent theoretical tiers of differentiation.

REFERENCES AND NOTES

1. J. E. Till, E. A. McCulloch, Hemopoietic stem cell differentiation. *Biochim. Biophys. Acta* **605**, 431–459 (1980). pmid: 7006701
2. G. J. Spangrude *et al.*, Mouse hematopoietic stem cells. *Blood* **78**, 1395–1402 (1991). pmid: 1884012
3. K. Akashi, D. Traver, T. Miyamoto, I. L. Weissman, A clonogenic common myeloid progenitor that gives rise to all myeloid lineages. *Nature* **404**, 193–197 (2000). doi: 10.1038/35004599; pmid: 10724173
4. M. Kondo, I. L. Weissman, K. Akashi, Identification of clonogenic common lymphoid progenitors in mouse bone marrow. *Cell* **91**, 661–672 (1997). doi: 10.1016/S0092-8674(00)80453-5; pmid: 9393859
5. J. Adolfsson *et al.*, Identification of Flt3$^+$ lympho-myeloid stem cells lacking erythro-megakaryocytic potential a revised road map for adult blood lineage commitment. *Cell* **121**, 295–306 (2005). doi: 10.1016/j.cell.2005.02.013; pmid: 15851035
6. R. Månsson *et al.*, Molecular evidence for hierarchical transcriptional lineage priming in fetal and adult stem cells and

multipotent progenitors. *Immunity* **26**, 407–419 (2007). doi: 10.1016/j.immuni.2007.02.013; pmid: 17433729
7. R. Yamamoto *et al*., Clonal analysis unveils self-renewing lineage-restricted progenitors generated directly from hematopoietic stem cells. *Cell* **154**, 1112–1126 (2013). doi: 10.1016/j.cell.2013.08.007; pmid: 23993099
8. S. Doulatov, F. Notta, E. Laurenti, J. E. Dick, Hematopoiesis: A human perspective. *Cell Stem Cell* **10**, 120–136 (2012). doi: 10.1016/j.stem.2012.01.006; pmid: 22305562
9. M. G. Manz, T. Miyamoto, K. Akashi, I. L. Weissman, Prospective isolation of human clonogenic common myeloid progenitors. *Proc. Natl. Acad. Sci. U.S.A.* **99**, 11872–11877 (2002). doi: 10.1073/pnas.172384399; pmid: 12193648
10. A. Galy, M. Travis, D. Cen, B. Chen, Human T, B, Natural killer, and dendritic cells arise from a common bone marrow progenitor cell subset. *Immunity* **3**, 459–473 (1995). doi: 10.1016/1074-7613(95)90175-2; pmid: 7584137
11. S. Doulatov *et al*., Revised map of the human progenitor hierarchy shows the origin of macrophages and dendritic cells in early lymphoid development. *Nat. Immunol.* **11**, 585–593 (2010). doi: 10.1038/ni.1889; pmid: 20543838
12. E. Laurenti *et al*., The transcriptional architecture of early human hematopoiesis identifies multilevel control of lymphoid commitment. *Nat. Immunol.* **14**, 756–763 (2013). doi: 10.1038/ni.2615; pmid: 23708252
13. C. J. H. Pronk *et al*., Elucidation of the phenotypic, functional, and molecular topography of a myeloerythroid progenitor cell hierarchy. *Cell Stem Cell* **1**, 428–442 (2007). doi: 10.1016/j.stem.2007.07.005; pmid: 18371379
14. G. Guo *et al*., Mapping cellular hierarchy by single-cell analysis of the cell surface repertoire. *Cell Stem Cell* **13**, 492–505 (2013). doi: 10.1016/j.stem.2013.07.017; pmid: 24035353
15. S. H. Naik *et al*., Diverse and heritable lineage imprinting of early haematopoietic progenitors. *Nature* **496**, 229–232 (2013). doi: 10.1038/nature12013; pmid: 23552896
16. A. Sanjuan-Pla *et al*., Platelet-biased stem cells reside at the apex of the haematopoietic stem-cell hierarchy. *Nature* **502**, 232–236 (2013). doi: 10.1038/nature12495; pmid: 23934107
17. C. Pina *et al*., Inferring rules of lineage commitment in haematopoiesis. *Nat. Cell Biol.* **14**, 287–294 (2012). doi: 10.1038/ncb2442; pmid: 22344032
18. F. Notta *et al*., Isolation of single human hematopoietic stem cells capable of long-term multilineage engraftment. *Science* **333**, 218–221 (2011). doi: 10.1126/science.1201219; pmid: 21737740
19. H. Qian *et al*., Critical role of thrombopoietin in maintaining adult quiescent hematopoietic stem cells. *Cell Stem Cell* **1**, 671–684 (2007). doi: 10.1016/j.stem.2007.10.008; pmid: 18371408
20. G. P. Solar *et al*., Role of c-mpl in early hematopoiesis. *Blood* **92**, 4–10 (1998). pmid: 9639492
21. B. Deng *et al*., An agonist murine monoclonal antibody to the human c-Mpl receptor stimulates megakaryocytopoiesis. *Blood* **92**, 1981–1988 (1998). pmid: 9731056
22. L. Edvardsson, J. Dykes, T. Olofsson, Isolation and characterization of human myeloid progenitor populations—TpoR as discriminator between common myeloid and megakaryocyte/erythroid progenitors. *Exp. Hematol.* **34**, 599–609 (2006). doi: 10.1016/j.exphem.2006.01.017; pmid: 16647566
23. L. A. Kohn *et al*., Lymphoid priming in human bone marrow begins before expression of CD10 with upregulation of L-selectin. *Nat. Immunol.* **13**, 963–971 (2012). doi: 10.1038/ni.2405; pmid: 22941246
24. F. Mazurier, M. Doedens, O. I. Gan, J. E. Dick, Rapid myeloerythroid repopulation after intrafemoral transplantation of NOD-SCID mice reveals a new class of human stem cells. *Nat. Med.* **9**, 959–963 (2003). doi: 10.1038/nm886; pmid: 12796774
25. T. Enver, M. Pera, C. Peterson, P. W. Andrews, Stem cell states, fates, and the rules of attraction. *Cell Stem Cell* **4**, 387–397 (2009). doi: 10.1016/j.stem.2009.04.011; pmid: 19427289
26. D. Ramsköld *et al*., Full-length mRNA-Seq from single-cell levels of RNA and individual circulating tumor cells. *Nat. Biotechnol.* **30**, 777–782 (2012). doi: 10.1038/nbt.2282; pmid: 22820318
27. J. Sun *et al*., Clonal dynamics of native haematopoiesis. *Nature* **514**, 322–327 (2014). doi: 10.1038/nature13824; pmid: 25296256
28. K. Busch *et al*., Fundamental properties of unperturbed haematopoiesis from stem cells in vivo. *Nature* **518**, 542–546 (2015). doi: 10.1038/nature14242; pmid: 25686605
29. V. G. Sankaran, M. J. Weiss, Anemia: Progress in molecular mechanisms and therapies. *Nat. Med.* **21**, 221–230 (2015). doi: 10.1038/nm.3814; pmid: 25742458
30. J. P. Maciejewski, A. Risitano, Hematopoietic stem cells in aplastic anemia. *Arch. Med. Res.* **34**, 520–527 (2003). doi: 10.1016/j.arcmed.2003.09.009; pmid: 14734092
31. J. C. Marsh, J. Chang, N. G. Testa, J. M. Hows, T. M. Dexter, The hematopoietic defect in aplastic anemia assessed by long-term marrow culture. *Blood* **76**, 1748–1757 (1990). pmid: 2224124
32. S. Rizzo *et al*., Stem cell defect in aplastic anemia: Reduced long term culture-initiating cells (LTC-IC) in $CD34^+$ cells isolated from aplastic anemia patient bone marrow. *Hematol. J.* **3**, 230–236 (2002). doi: 10.1038/sj.thj.6200187; pmid: 12391540
33. W. H. Matsui, R. A. Brodsky, B. D. Smith, M. J. Borowitz, R. J. Jones, Quantitative analysis of bone marrow CD34 cells in aplastic anemia and hypoplastic myelodysplastic syndromes. *Leukemia* **20**, 458–462 (2006). doi: 10.1038/sj.leu.2404119; pmid: 16437138
34. C. Benz *et al*., Hematopoietic stem cell subtypes expand differentially during development and display distinct lymphopoietic programs. *Cell Stem Cell* **10**, 273–283 (2012). doi: 10.1016/j.stem.2012.02.007; pmid: 22385655
35. T. Yoshida, S. Y.-M. Ng, J.-C. Zuñiga-Pflucker, K. Georgopoulos, Early hematopoietic lineage restrictions directed by Ikaros. *Nat. Immunol.* **7**, 382–391 (2006). doi: 10.1038/ni1314; pmid: 16518393
36. S. Y. Heazlewood *et al*., Megakaryocytes co-localise with hemopoietic stem cells and release cytokines that up-regulate stem cell proliferation. *Stem Cell Res.* **11**, 782–792 (2013). doi: 10.1016/j.scr.2013.05.007; pmid: 23792434
37. M. Zhao *et al*., Megakaryocytes maintain homeostatic quiescence and promote post-injury regeneration of hematopoietic stem cells. *Nat. Med.* **20**, 1321–1326 (2014). doi: 10.1038/nm.3706; pmid: 25326798
38. I. Bruns *et al*., Megakaryocytes regulate hematopoietic stem cell quiescence through CXCL4 secretion. *Nat. Med.* **20**, 1315–1320 (2014). doi: 10.1038/nm.3707; pmid: 25326802
39. A. Görgens *et al*., Revision of the human hematopoietic tree: Granulocyte subtypes derive from distinct hematopoietic lineages. *Cell Reports* **3**, 1539–1552 (2013). doi: 10.1016/j.celrep.2013.04.025; pmid: 23707063
40. Y. Mori *et al*., Identification of the human eosinophil lineage-committed progenitor: Revision of phenotypic definition of the human common myeloid progenitor. *J. Exp. Med.* **206**, 183–193 (2009). doi: 10.1084/jem.20081756; pmid: 19114669
41. M. A. Rieger, P. S. Hoppe, B. M. Smejkal, A. C. Eitelhuber, T. Schroeder, Hematopoietic cytokines can instruct lineage choice. *Science* **325**, 217–218 (2009). doi: 10.1126/science.1171461; pmid: 19590005

ACKNOWLEDGMENTS

We thank all members of the Dick laboratory for critical review of the manuscript, especially J. C. Y. Wang, E. Lechman, and M. Cooper; and N. Simard and S. Zhao and members of the Sickkids-UHN Flow Cytometry facility for technical support. We thank K. Moore and the obstetrics unit of Trillium Hospital (Mississauga, Ontario) for providing cord blood. We thank J. Rohrer from BD Biosciences (La Jolla, CA) for supplying BAH-1 clone. This work was supported by postdoctoral fellowship awards from the Canadian Institute of Health Research (CIHR) to F.N. and S.Z. S.Z. is supported by the Aplastic Anemia and Myelodysplasia Association of Canada. F.N. is a recipient of a scholar's research award from the Ontario Institute of Cancer Research (OICR), through generous support from the Ontario Ministry of Research and Innovation. Research in E.L.'s laboratory is supported by a Wellcome Trust Sir Henry Dale Fellowship and a core support grant from the Wellcome Trust and the Medical Research Council to the Wellcome Trust–Medical Research Council Cambridge Stem Cell Institute. Work in the Dick laboratory is supported by grants from CIHR, Canadian Cancer Society, Terry Fox Foundation, Genome Canada through the Ontario Genomics Institute, OICR with funds from the province of Ontario, a Canada Research Chair, and the Ontario Ministry of Health and Long-Term Care (OMOHLTC). Author Contributions: F.N., S.Z., and J.E.D. designed the study; F.N. and S.Z. analyzed and interpreted data; F.N., S.Z., N.T., S.D., O.I.G., and J.M. performed experiments; G.W., J.D.M., and L.D.S. performed RNA sequencing and analysis. K.B.K., S.Z., F.N., and J.E.D. generated the model; Y.D. provided clinical samples from aplastic anemia and matched controls for the study. F.N., S.Z., and J.E.D. wrote the manuscript; all authors reviewed and approved the manuscript; J.E.D. supervised the study. Aplastic anemia samples are available from Y.D. under a material transfer agreement with Toronto Sickkids Hospital. Gene expression data have been submitted to the Gene Expression Omnibus (no. GSE76234).

SUPPLEMENTARY MATERIALS

www.sciencemag.org/content/351/6269/aab2116/suppl/DC1
Materials and Methods
Supplementary Text
Figs. S1 to S7
Table S1
References (*42*–*44*)

26 March 2015; accepted 23 October 2015
Published online 5 November 2015
10.1126/science.aab2116

RESEARCH ARTICLE SUMMARY

GEOMORPHOLOGY

Geomorphic and geologic controls of geohazards induced by Nepal's 2015 Gorkha earthquake

J. S. Kargel,*† G. J. Leonard,* D. H. Shugar,*† U. K. Haritashya,*† A. Bevington, E. J. Fielding, K. Fujita, M. Geertsema, E. S. Miles, J. Steiner, E. Anderson, S. Bajracharya, G. W. Bawden, D. F. Breashears, A. Byers, B. Collins, M. R. Dhital, A. Donnellan, T. L. Evans, M. L. Geai, M. T. Glasscoe, D. Green, D. R. Gurung, R. Heijenk, A. Hilborn, K. Hudnut, C. Huyck, W. W. Immerzeel, Jiang Liming, R. Jibson, A. Kääb, N. R. Khanal, D. Kirschbaum, P. D. A. Kraaijenbrink, D. Lamsal, Liu Shiyin, Lv Mingyang, D. McKinney, N. K. Nahirnick, Nan Zhuotong, S. Ojha, J. Olsenholler, T.H. Painter, M. Pleasants, K. C. Pratima, Q. I. Yuan, B. H. Raup, D. Regmi, D. R. Rounce, A. Sakai, Shangguan Donghui, J. M. Shea, A. B. Shrestha, A. Shukla, D. Stumm, M. van der Kooij, K. Voss, Wang Xin, B. Weihs, D. Wolfe, Wu Lizong, Yao Xiaojun, M. R. Yoder, N. Young

INTRODUCTION: On 25 April 2015, the Gorkha earthquake [magnitude (*M*) 7.8] struck Nepal, followed by five aftershocks of ≥*M* 6.0 until 10 June 2015. The earthquakes killed ~9000 people and severely damaged a 550 by 200 km region in Nepal and neighboring countries. Some mountain villages were completely destroyed, and the remote locations, blocked roads, and landslide-dammed rivers prevented ground access to many areas.

RATIONALE: Our "Volunteer Group" of scientists from nine nations, motivated by humanitarian needs, focused on satellite-based systematic mapping and analysis of earthquake-induced geohazards. We provided information to relief and recovery officials as emergency operations were occurring, while supported by one of the largest-ever NASA-led campaigns of responsive satellite data acquisitions over a vast disaster zone. Our analysis of geohazards distribution allowed evaluation of geomorphic, tectonic, and lithologic controls on earthquake-induced landsliding, process mechanisms, and hazard process chains, particularly where they affected local populations.

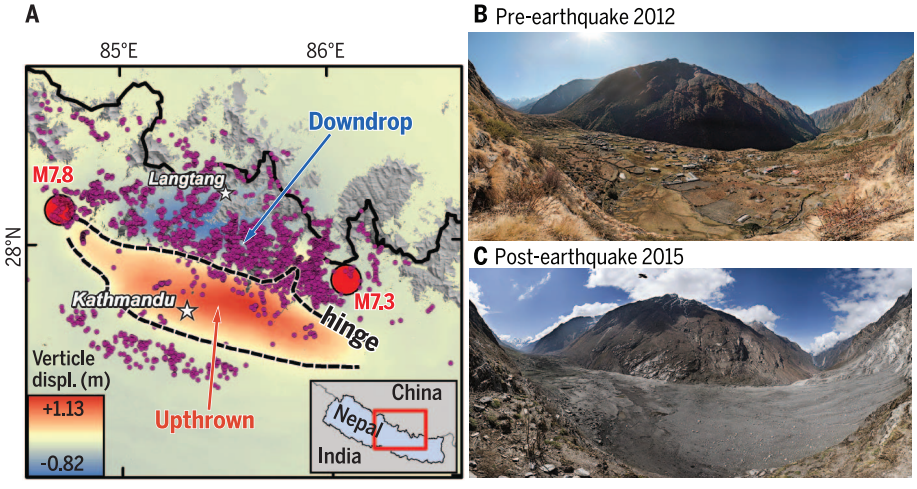

Landslide distribution and effects of a huge landslide. (**A**) Landslides (purple dots) are concentrated mostly north of the tectonic hinge-line. Also shown are the epicenters of the main shock and largest aftershock. Displacements are from the JAXA ALOS-2 ScanSAR interferogram (21 Feb and 2 May 2015 acquisitions). (**B** and **C**) Before-and-after photographs obtained by D. Breashears in Langtang Valley showing complete destruction of a large part of Langtang village by a huge landslide.

RESULTS: We mapped 4312 coseismic and postseismic landslides. Their distribution shows positive associations with slope and shaking intensity. The highest areal densities of landslides are developed on the downdropped northern tectonic block, which is likely explained by momentary reduction of the normal stress along planes of weakness during downward acceleration. The two largest shocks bracket the high-density landslide distribution, the largest magnitudes of the surface displacement field, and highest peak ground accelerations (PGAs). Landslides are heavily concentrated where PGA was >0.6*g* and slope is >30°. Additional controls on landslide occurrence are indicated by their clustering near earthquake epicenters and within specific lithologic units. The product of PGA and the sine of surface slope (defined as the landslide susceptibility index) is a good indicator of where most landslides occurred. A tail of the statistical distributions of landslides extends to low values of the landslide susceptibility index. Slight earthquake shaking affected vulnerable materials hanging on steep slopes—such as ice, snow, and glacial debris—and moderate to strong shaking affected poorly consolidated sediments deposited in low-sloping river valleys, which were already poised near a failure threshold. In the remote Langtang Valley, some of the most concentrated destruction and losses of life outside the Kathmandu Valley were directly due to earthquake-induced landslides and air blasts. Complex seismic wave interactions and wave focusing may have caused ridgetop shattering and landslides near Langtang but reduced direct shaking damage on valley floors and at glacial lakes.

ON OUR WEB SITE

Read the full article at http://dx.doi.org/10.1126/science.aac8353

CONCLUSION: The Gorkha earthquake took a tremendous, tragic toll on human lives and culture. However, fortunately no damaging earthquake-caused glacier lake outburst floods were observed by our satellite analysis. The total number of landslides was far fewer than those generated by comparable earthquakes elsewhere, probably because of a lack of surface ruptures, the concentration of deformation along the subsurface thrust fault at 10 to 15 km depth, and the regional dominance of competent high-grade metamorphic and intrusive igneous rock types. ■

The list of author affiliations is available in the full article online.
*These authors contributed equally to this work.
†Corresponding author. E-mail: kargel@hwr.arizona.edu (J.S.K.); dshugar@uw.edu (D.H.S.); uharitashya1@udayton.edu (U.K.H.)
Cite this article as J. S. Kargel *et al.*, *Science* **351**, aac8353 (2016). DOI: 10.1126/science.aac8353

RESEARCH ARTICLE

GEOMORPHOLOGY

Geomorphic and geologic controls of geohazards induced by Nepal's 2015 Gorkha earthquake

J. S. Kargel,[1]*† G. J. Leonard,[1]* D. H. Shugar,[2]*† U. K. Haritashya,[3]*† A. Bevington,[4] E. J. Fielding,[5] K. Fujita,[6] M. Geertsema,[4] E. S. Miles,[7] J. Steiner,[8] E. Anderson,[9] S. Bajracharya,[10] G. W. Bawden,[11] D. F. Breashears,[12] A. Byers,[13] B. Collins,[14] M. R. Dhital,[15] A. Donnellan,[5] T. L. Evans,[16] M. L. Geai,[17] M. T. Glasscoe,[5] D. Green,[11] D. R. Gurung,[10] R. Heijenk,[4] A. Hilborn,[16] K. Hudnut,[18] C. Huyck,[19] W. W. Immerzeel,[20] Jiang Liming,[21] R. Jibson,[22] A. Kääb,[23] N. R. Khanal,[10] D. Kirschbaum,[24] P. D. A. Kraaijenbrink,[20] D. Lamsal,[5] Liu Shiyin,[25] Lv Mingyang,[26] D. McKinney,[27] N. K. Nahirnick,[16] Nan Zhuotong,[28] S. Ojha,[5] J. Olsenholler,[29] T. H. Painter,[5] M. Pleasants,[3] K. C. Pratima,[30] Q. I. Yuan,[25] B. H. Raup,[31] D. Regmi,[32] D. R. Rounce,[33] A. Sakai,[6] Shangguan Donghui,[25] J. M. Shea,[10] A. B. Shrestha,[10] A. Shukla,[34] D. Stumm,[10] M. van der Kooij,[35] K. Voss,[36] Wang Xin,[37] B. Weihs,[38] D. Wolfe,[39] Wu Lizong,[26] Yao Xiaojun,[40] M. R. Yoder,[41] N. Young[42]

The Gorkha earthquake (magnitude 7.8) on 25 April 2015 and later aftershocks struck South Asia, killing ~9000 people and damaging a large region. Supported by a large campaign of responsive satellite data acquisitions over the earthquake disaster zone, our team undertook a satellite image survey of the earthquakes' induced geohazards in Nepal and China and an assessment of the geomorphic, tectonic, and lithologic controls on quake-induced landslides. Timely analysis and communication aided response and recovery and informed decision-makers. We mapped 4312 coseismic and postseismic landslides. We also surveyed 491 glacier lakes for earthquake damage but found only nine landslide-impacted lakes and no visible satellite evidence of outbursts. Landslide densities correlate with slope, peak ground acceleration, surface downdrop, and specific metamorphic lithologies and large plutonic intrusions.

On 25 April 2015 and over the next several weeks, a major series of displacements occurred ~15 km deep along the buried Main Himalayan Thrust without breaking the surface (*1*–*3*). The main shock of the Gorkha earthquake [magnitude (*M*) 7.8, U.S. Geological Survey (USGS); epicenter 28.147°N, 84.708°E] was followed by ~257 aftershocks of >*M* 3.0, including five ≥*M* 6.0 between 25 April and 10 June 2015. On 12 May, a *M* 7.3 aftershock struck ~150 km ENE of the main shock. The largest earthquakes caused a wide swath of casualties and destruction in Nepal and adjacent India, China, and Bangladesh. Some mountain villages were shaken to complete destruction (*4*), buried by avalanches and landslides, or destroyed by powerful avalanche and landslide air blasts. The remote locations and blocked roads and rivers meant that ground crews could not immediately access many Himalayan valleys.

We adopted a satellite-based approach to examine the vast damaged region. Satellite imagery was provided by NASA, DigitalGlobe, the Japan Aerospace Exploration Agency (JAXA), MacDonald Dettwiler and Associates (MDA), Planet Labs, Spot Image, and the China National Space Administration, including imagery triggered by the International Charter: Space and Major Disasters (www.disasterscharter.org). A "Volunteer Group" of analysts from nine nations was organized by the University of Arizona under the auspices of Global Land Ice Measurements from Space (GLIMS) (*5*) initially to assess priority hazard situations and then to build a landslide inventory (*6*). The group contributed their input of mapped geohazards to a broad ad hoc NASA-led interagency "Response Team." We scrutinized optical imagery, ranging from 15 to <1 m resolution, from Landsats 7 and 8; the Advanced Spaceborne and Thermal Emission and Reflection Radiometer (ASTER) onboard Terra; Advanced Land Imager on EO-1; WorldView-1, -2, and -3; GeoEye-1; Pleiades; and Gaofen-1 (table S1) and used radar data from ALOS-2 and RADARSAT-2 and topography from the Shuttle Radar Topography Mission (SRTM). Landslides not detectable at these scales would generally have lesser human consequences than would larger landslides.

The Response Team, including the Volunteer Group, undertook one of the broadest and fastest international emergency remote sensing and data analysis campaigns ever led by NASA for any earthquake-affected region (*7*–*9*). Parallel, but independent, landslide-mapping efforts have been undertaken by a joint British Geological Survey–Durham University group (*10*) and other groups.

During previous earthquake emergencies in mountainous terrain (such as Wenchuan, China and Denali, Alaska), landslides were numerous (*9*, *11*–*17*), sometimes initiating a process chain of secondary and tertiary geomorphic processes over time spans ranging from minutes to years after the earthquake (*18*, *19*). Landslide-initiated process chains may involve gains in mobilized mass and destructive power through energy and mass transfer cascades. Many documented or inferred examples exist, including rock/ice fall–generated debris avalanches that transformed into debris flows (*20*, *21*) or caused large impoundment lakes and upstream flooding (*22*), landslide-generated displacement waves and glacier lake

[1]Department of Hydrology and Water Resources, University of Arizona, Tucson, AZ, USA. [2]School of Interdisciplinary Arts and Sciences, University of Washington Tacoma, Tacoma, WA, USA. [3]Department of Geology, University of Dayton, Dayton, OH, USA. [4]Ministry of Forests, Lands and Natural Resource Operations, Prince George, BC, Canada. [5]Jet Propulsion Laboratory, California Institute of Technology, Pasadena, CA, USA. [6]Graduate School of Environmental Studies, Nagoya University, Nagoya, Japan. [7]Scott Polar Research Institute, University of Cambridge, Cambridge, UK. [8]Institute of Environmental Engineering, Federal Institute of Technology–ETH, Zurich, Switzerland. [9]NASA Marshall Space Flight Center, Huntsville, AL, USA. [10]International Centre for Integrated Mountain Development, Kathmandu, Nepal. [11]NASA Headquarters, Washington, DC, USA. [12]GlacierWorks, Marblehead, MA, USA. [13]The Mountain Institute, Elkins, WV, USA. [14]U.S. Geological Survey, Menlo Park, CA, USA. [15]Central Department of Geology, Tribhuvan University, Kirtipur, Kathmandu, Nepal. [16]Department of Geography, University of Victoria, Victoria, BC, Canada. [17]CVA Engineering, Suresnes, France. [18]Earthquake Science Center, U.S. Geological Survey, Pasadena, CA, USA. [19]ImageCat, Long Beach, CA, USA. [20]Faculty of Geosciences, Utrecht University, Utrecht, Netherlands. [21]State Key Laboratory of Geodesy and Earth's Dynamics, Institute of Geodesy and Geophysics, Chinese Academy of Sciences, Wuhan, Hubei Province, China. [22]U.S. Geological Survey, Golden, CO, USA. [23]Department of Geosciences, University of Oslo, Blindern, Oslo, Norway. [24]Hydrological Sciences Laboratory, NASA Goddard Space Flight Center, Greenbelt, MD, USA. [25]Cold and Arid Regions of Environmental and Engineering Research Institute, Chinese Academy of Sciences, Lanzhou, China. [26]School of Earth Sciences and Engineering, Nanjing University, Nanjing, China. [27]Department of Civil, Architectural and Environmental Engineering, University of Texas at Austin, Austin, TX, USA. [28]School of Geography Science, Nanjing Normal University, Nanjing, China. [29]Department of Geography, Texas A&M University, College Station, TX, USA. [30]Arizona Remote Sensing Center, School of Natural Resources and the Environment, University of Arizona, Tucson, AZ, USA. [31]National Snow and Ice Data Center, University of Colorado, Boulder, CO, USA. [32]Himalayan Research Center, Kathmandu, Nepal. [33]Environmental and Water Resources Engineering, University of Texas at Austin, Austin, TX, USA. [34]Wadia Institute of Himalayan Geology, Dehradun, India. [35]MacDonald Dettwiler and Associates–GSI, Ottawa, Ontario, Canada. [36]Department of Geography, University of California, Santa Barbara, Santa Barbara, CA, USA. [37]College of Architecture and Urban Planning, Hunan University of Science and Technology, Xiangtan, China. [38]Geography Department, Kansas State University, Manhattan, KS, USA. [39]**Global Land Ice Measurements from Space** (GLIMS) Steward, Alaska Region, Anchorage, AK, USA. [40]College of Geographical Science and Environment, Northwest Normal University, China. [41]Department of Physics, University of California, Davis, Davis, CA, USA. [42]Antarctic Climate and Ecosystems Cooperative Research Centre, University of Tasmania, Hobart, TAS, Australia.

*These authors contributed equally to this work. **†Corresponding author. E-mail: kargel@hwr.arizona.edu (J.S.K.); dshugar@uw.edu (D.H.S.); uharitashya1@udayton.edu (U.K.H.)**

outburst floods (GLOFs) (23, 24), and landslide-dammed lake outbursts (25, 26). As debris, ice, and lake and stream water are ingested into an outburst flood, a debris flow or hyper-concentrated slurry flood may result (21). Each geomorphic process in the chain may trigger a subsequent geohazard and extend the damaging reach of the event (27, 28). Process chains involving GLOFs are particularly worrisome.

The Volunteer Group's work focused on systematic mapping of quake-induced geohazards, understanding the geomorphic, lithologic, and tectonic control of their distribution and the identification of communities and infrastructure that might be affected. We analyzed the distribution and character of the geohazards induced by the Gorkha earthquake in Nepal and Tibet using mainly satellite-based findings, supplemented with media reports, eyewitness photography, helicopter-borne field assessments, and modeling of lake outburst flood processes. This paper considers earthquake-related landslides formed before 10 June 2015, when the monsoon arrived in eastern Nepal.

Landslide mapping and assessment

We mapped the distribution of 4312 earthquake-induced (coseismic and postseismic) landslides (Fig. 1). We identified six Areas of Interest (AOIs) that include Annapurna, Manaslu, Ganesh Himal, Langtang, Cho Oyu, and Everest (fig. S1) from west to east. The AOIs together cover 375 by 155 km, with divisions set along major valleys. Each AOI team had remote sensing and landslide expertise and was assigned an experienced lead analyst.

Multispectral satellite images from many government and commercial sensors (table S1) were made available through a number of portals, including the DigitalGlobe website, the USGS Hazards Data Distribution System (HDDS), and USGS Global Visualization Viewer (GLOVIS). Additionally, NASA provided access to expedited post-earthquake targeted ASTER imagery within the affected region. Not all locations were surveyed repetitively. We compiled a database and detailed descriptions of each AOI (29).

The highest densities of earthquake-related landslides are distributed in a broad swath between the two largest shocks, where many aftershocks also occurred. Clusters of landslides also exist outside of this zone (Fig. 1). The high landslide densities also lie between three >M 7.0 earthquakes that occurred on 26 August 1833, 25 April 2015, and 12 May 2015, thus highlighting the possible long-term effects of historic quakes. However, we assessed the landslide occurrences only within the context of the Gorkha earthquake and aftershocks and the terrain characteristics, broadly organized according to (i) surface slopes and the earthquakes' seismic peak ground accelerations (PGAs), (ii) broad-field deformation due to the earthquakes, and (iii) the distribution of underlying landcover, lithology, and tectonic structure.

Among the shaking parameters, PGA is just one factor that may control whether landslides occur in response to an earthquake. The specific frequency content, shake duration, PGA direction, and recurrent shocks also may be important (30). Furthermore, the landslides caused by the Gorkha earthquake and aftershocks appear to be far fewer than expected when compared with those of other mountainous regions with similar-magnitude earthquakes (31, 32). This might be due to the lack of surface ruptures induced by the earthquakes and the concentration of deformation along the subsurface thrust fault at 10 to 15 km depth (2).

Landslide distribution

Control by shaking and slope

The locations of the Gorkha earthquake-induced landslides are plotted with landscape physiography and the epicenters of the six largest shocks

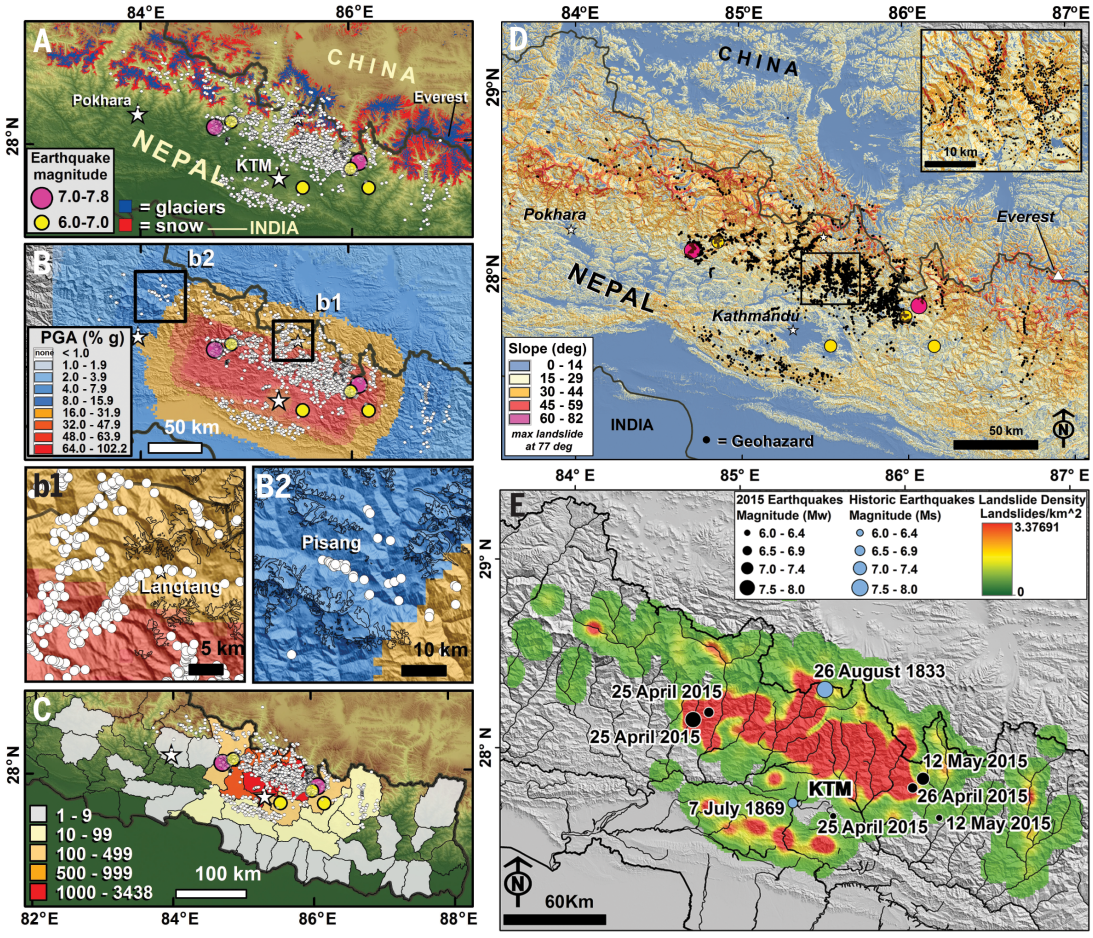

Fig. 1. Location of 4312 earthquake-related geohazards. (**A**) Distribution of glaciers (blue), late-season snowfields (red), landslides (white dots), and main shock and largest aftershock epicenters. The base topography is from the SRTM 90-m gap-filled digital elevation model (33). Glacier extents are from the Randolph Glacier Inventory (RGI) (61). Snowfields were derived from pre-event Landsat-8 visible and near-infrared (VNIR) to short-wave infrared (SWIR) band ratios and topographic masks. (**B**) (Top) Landslides plotted with local peak ground accelerations induced by the main Gorkha shock or M >6 aftershocks. PGAs are from the USGS–National Earthquake Information Center ShakeMap (62). (Bottom) Boxes b1 and b2 are enlarged to show details near Langtang and Pisang. (**C**) Landslides plotted with reported deaths per Nepal district are from the Government of Nepal, Nepal Disaster Risk Reduction Project. (**D**) Hazard occurrences (black dots) on calculated slopes. (Inset) Detail of hazard-dense region. (**E**) Smoothed area density (log scale) of earthquake-induced landslides determined by using a neighborhood 1/8° by 1/8° search window (~14 by 12 km) in relation to major (M ≥6) epicenters of historic earthquakes and the Gorkha quakes (62). Densities range between 0.01 and 3.37 landslides/km^2. Higher landslide densities occur locally on scales finer than 1/8°.

(Fig. 1A), PGA (Fig. 1B), reported deaths (Fig. 1C), and slope (Fig. 1D). We also mapped the smoothed landslide density distribution (Fig. 1E) and computed and mapped the susceptibilities of the landscape to earthquake-induced mass movements of ice, snow, or rock (Fig. 2). The computed susceptibilities depend on the product of the sine of slope (*33*) and the PGA (from the USGS ShakeMap PGA) (Fig. 1B).

Integration of slope and shaking (represented by PGA) within the susceptibility index partly accounts for where landslides occurred (Fig. 2), especially where collapse of high-elevation snow and ice may have been involved (Fig. 2, B and C). The landslide distribution shows the strongest associations with slopes of >30° (Fig. 1C and fig. S2A), PGA of >0.32*g* (Fig. 2A and fig. S2B), and shake-induced landslide susceptibility index of >0.16*g* (Fig. 2A). We infer that many of these landslides probably would not have occurred anytime soon without earthquake shaking. The control of landslide occurrences by the steep Himalayan slopes and seismic shaking is unsurprising and similar to other well-documented earthquakes (*34*). However, landslide susceptibilities differ from quake to quake. These new results detail the relationships of this Himalayan earthquake to seismic and geologic/terrain parameters. As PGA attains several tenths of *g*, entire mountainsides can collapse as shake-induced coseismic failures are not restricted to materials and terrains that were already poised near failure. Whereas landsliding on steep, strongly shaken slopes is easily understood, the tail of the landslide distribution to low shaking values, to low slopes, and low (but nonzero) shaking-induced landslide susceptibilities (fig. S2) requires further explanation.

Under any of the following conditions, low seismic PGAs at a few percent of *g* may cause failures that lead to a landslide or avalanche if the materials are already near failure.

(i) Granular materials may accumulate near the angle of repose, making them susceptible to coseismic failure owing to an acceleration that would increase shear stress along incipient planes of failure or related to rapid coseismic vibration-induced creep (*35*).

(ii) Seismic vibrations may cause liquefaction of water-saturated sediment, disturbances to the local hydrology, and coseismic or postseismic flow or rotational slumping (*36*).

(iii) At the beds of polythermal glaciers, the frictional resisting force may be carried by small frozen domains (*37*). Sharp accelerations may fracture the bed's frozen attachments, suddenly reducing the frictional force and initiating sliding.

(iv) Motion of rock or ice on fracture planes is resisted by the frictional force at the slip plane (*38*). Reduction in the normal stress because of downward acceleration, or increase in the downslope driving shear stress because of slip-plane parallel acceleration, may initiate coseismically triggered slip on steeply sloping slip planes.

(v) Upward acceleration increases the normal stress and may induce transient pressure melting of basal polythermal ice, reducing the frictional force. The subsequent downward seismic acceleration suddenly relieves the normal stress, so that newly produced basal meltwater (which might not refreeze) may initiate sliding (*39*).

The mechanisms outlined above may produce landslides or avalanches at low but nonzero shaking in granular materials occurring on steep slopes, in water-saturated sediments, and on steeply sloping glaciers. The deadly Mount Everest ice/snow avalanches on 25 April 2015 exemplify this point, where shaking was a low 0.09*g* (table S3). Glacier ice and snow are commonly poised near failure as indicated by Everest's history of ice avalanches off steep slopes, including back-to-back years in which there were a record 16 avalanche deaths in April 2014 (triggered by spring melting) and a new record 22 deaths in April 2015 (earthquake-triggered). Many Himalayan glaciers are substantially avalanche-fed, and snow or ice avalanches may occur upon a slight prompt, whether because of heavy winter or monsoon snowfall, spring melting, or slight shaking. The Gorkha earthquake struck soon after another season of spring melting began, increasing the vulnerability to shaking of ice and snow in the Everest area. Landslides in the upper Marsyangdi Valley (described below) also experienced relatively weak shaking (0.11 to 0.13*g*) but involved unconsolidated fluvial gravels and lacustrine silts (*40*).

Seismic reactivation of preseismic landslides, or hydrological reactivation of earthquake-triggered landslides, may be common where landsliding already is present. Hydrological reactivations may be caused by precipitation runoff, spring discharge, or erosional undercutting of river banks. Image time series indicate that many mapped landslides, such as in the Marsyangdi Valley, happened after the main shock. In general, these might be attributable to a host of factors such as aftershocks, failure of earthquake-disturbed hanging glaciers or debuttressed slopes (*41*, *42*), degradation of mountain permafrost and glacier-permafrost interactions (*41*), extreme precipitation, and stream undercutting of poorly consolidated sediment banks that were already disturbed by the earthquake. These mechanisms involve changes to the

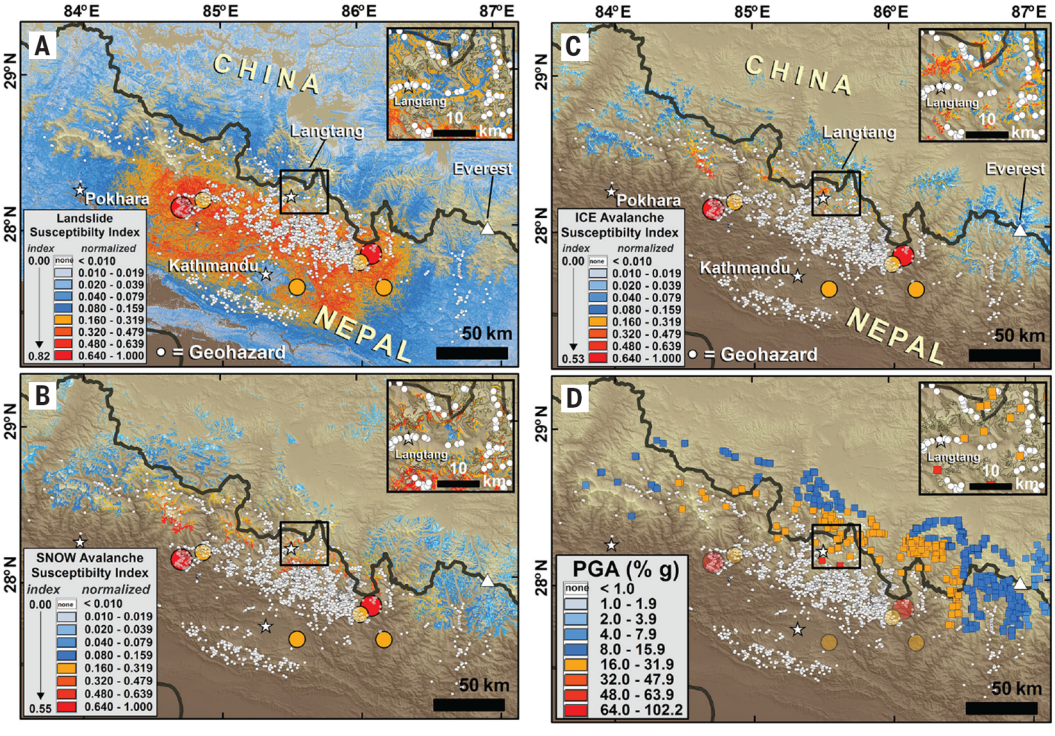

Fig. 2. Debris landslide susceptibility with mapped hazards. (**A**) Susceptibility in units of acceleration divided by *g* (9.81 m s^{-2}). (**B**) Snow avalanche susceptibility with mapped hazards. Susceptibility is in *g*. (**C**) Ice avalanche susceptibility with mapped hazards. Susceptibility is in *g*. (**D**) Maximum PGA experienced by 491 glacier lakes. Mapped hazards are shown as white dots. Maximum PGA for glacier lakes was 0.57*g*. (Insets) Detail in Langtang Valley.

supply of groundwater or rates of glacial erosion or ice melt, which have at least indirect links to climate change.

Control by the broad-field seismic deformation

Another key earthquake phenomenon is the wide-field land surface deformation pattern, which appears to have influenced the distribution of landslides (Fig. 3). The mapped surface deformation was derived from Interferometric Synthetic Aperture Radar (InSAR) (Fig. 3A) (*43*). While the ALOS-2 InSAR measurement is in the radar line-of-sight, GPS measurements show that the horizontal motion is almost in the along-track direction, so the InSAR displacements in Fig. 3A are almost purely vertical (*3*). The highest densities of landslides are correlated with the down-dropped block, which is on the back-limb of the hanging wall of the thrust and counterintuitively correlates with the higher Himalaya. Within this block, landslide densities increase southward and then abruptly decrease near the tectonic hinge line, which separates the downdropped and upthrown blocks (and also approximates the zone of maximum slip on the fault). RADARSAT-2 data provide the horizontal displacement field over part of the earthquake-affected region and confirm that the largest horizontal displacements (Fig. 3B) are near the hinge line and in the uplifted block, as defined by vertical deformation (Fig. 3A).

We do not fully understand the distinctive concentration of earthquake-induced landslides in the tectonic downdropped block of the Gorkha earthquake. The steep slopes within the downdropped block no doubt contributed to the pattern of landslide densities, but steep slopes are also present in some areas where landslides are few. The net downward acceleration implied by the downdrop possibly caused a momentary reduction in lithostatic stress, hence a reduction of normal stress along inclined planes of weakness. Relief of normal stress could have allowed non-lithostatic shear stress, including lateral seismic acceleration, to initiate motion along landslide failure planes. Because the coefficient of sliding friction is normally less than that of static friction, motion may then continue and drive a landslide. The same mechanism may apply to shaking, and hence, the broad-field deformation may modulate the shaking-induced perturbation of normal stress, again suggesting some integration of multiple causative trigger mechanisms.

The Gorkha earthquake caused fewer landslides than expected on the basis of its magnitude (*12*, *32*), mirroring the unexpected paucity of dwelling destruction (*2*). The peculiar distribution of the Gorkha earthquake landslides on the downdropped block (Fig. 3) placed them mainly north of the major population centers, reducing the death toll. For strike-slip events such as the 2010 M 7.0 Haiti earthquake (*44*), landslides were not similarly distributed systematically with respect to the fault plane. For comparison, landslides in the 1994 M 6.7 Northridge and 2008 M 7.9 Wenchuan earthquakes (*11*, *12*, *45*) were concentrated on the higher mountainous areas of the upthrown block. Both earthquakes were oblique thrust events, like the Gorkha quake. The Wenchuan earthquake induced far more landslides than did the Gorkha earthquake, despite similar steep terrain. These differences might relate to the Gorkha quake's shallow dipping fault and lack of surface rupture (a blind thrust).

The Northridge earthquake was also a blind thrust, and despite being smaller than the Gorkha quake, it produced 11,000 documented landslides (*45*). Some, mapped by an airborne survey, were smaller than the detection limit in the imagery used for our survey, in which Digital Globe data were unavailable. The numerous slides caused by the Northridge earthquake may be primarily attributed to uncemented clastic sedimentary compositions dominating the regional lithology, versus more competent high-grade metamorphic and igneous rocks dominating the higher Himalaya. The differing types and densities of vegetation and root binding might also be a factor. In general, differences in earthquake-induced landslide densities can also be related to the number and magnitude of strong high-frequency ground motions, although the paucity of strong-motion

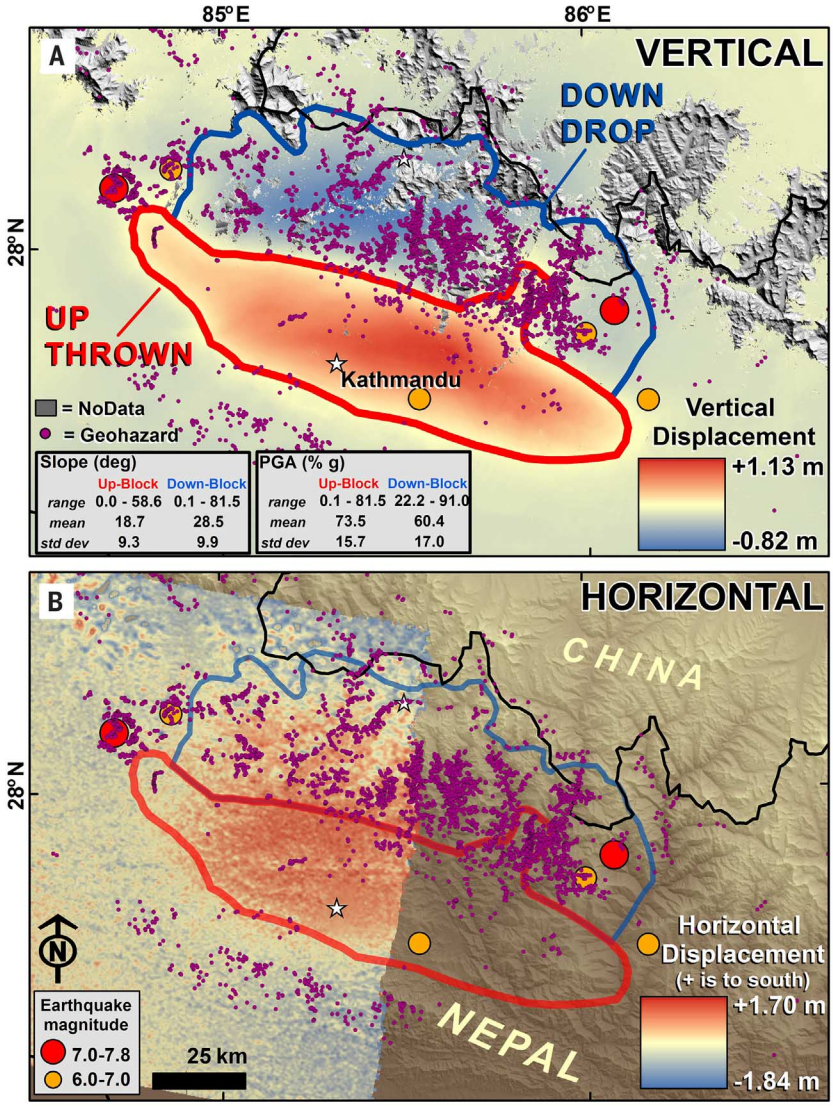

Fig. 3. Landslide distribution relative to the Earth surface deformation field. (**A**) 4312 landslides (purple dots) are concentrated mostly north of the hinge line between the downdropped block and uplifted block. Also shown are the epicenters of the main shock and five largest aftershocks. Vertical displacements are from the JAXA ALOS-2 ScanSAR interferogram (21 Feb and 2 May 2015 scenes), which represent almost entirely vertical motion. ALOS-2 interferometry of the Gorkha earthquake and largest aftershock was recently described by Lindsey *et al*. (*3*). (**B**) Horizontal motion map based on azimuth shift measurements of the RADARSAT-2 XF acquisitions of 5 April and 29 April 2015. Scale shows motion excluding outliers outside the mean ± 3σ. Values are positive for SSW azimuths >100 degrees relative to east (>S10W). Hence, both the upthrown and downdropped blocks shifted southward. The areal coverage for the RADARSAT-2 scene is not identical to that of ALOS-2; areas on the eastern side of the scene have no data.

recordings in the cases of both the Gorkha and Wenchuan quakes hampers direct comparison.

Control by lithology and major fault structure

The local clustering indicates additional controls on landslide occurrence. Lithologic variations, sediment thickness, bedding dip direction relative to slope aspect, extent of physical and chemical weathering including extent of bedrock fracturing, and vegetation cover may be important controlling factors. Lithology affects the occurrence of some landslides. For instance, the Langtang Valley slides involved the failure or ingestion of ice and unconsolidated glacial debris. Another example is the poorly consolidated sediment driving the Marsyangdi Valley landslides.

Fault structures exert indirect control of the clustering of landslides and organization of clusters (Fig. 4). High concentrations of landslides occur within particular Proterozoic metamorphic units and intrusive complexes and also near the surface of several major tectonic features, mainly low-angle thrust faults including the South Tibetan Detachment System (STDS), the Main Central Thrust (MCT), the Main Boundary Thrust (MBT), and the Main Frontal Thrust (MFT). The latter three faults splay off the subsurface Main Himalayan Thrust, which is thought to have slipped during these earthquakes (*1*). However, because none of the Gorkha earthquake fault displacements (main shock or aftershocks) are known to have pierced the surface, the association with the thrust faults might indicate underlying lithological control, in which the faults juxtapose rocks of differing compositions at the surface. Lithologic properties influenced the topographic character of the landscape and how seismic energy is transmitted, particularly through (i) elastic and brittle/elastic properties of the rock, (ii) chemical weathering and its control of erosion and slope, (iii) fracture development and fault displacement, and (iv) seismic wave interactions with topography and lithological structures. Each factor likely contributes, where lithology is a common denominator. A high density of landslides occurs within the upper Lesser Himalaya near to and east from the epicenter of the primary earthquake. Whereas this cluster's proximity to the largest shock's epicenter is evident, the pattern defined by the cluster is closely correlated with the outcrop of the upper Lesser Himalaya, which is composed of low- to medium-grade metamorphosed Proterozoic argillic-calcareous (clay and sand) units and also of higher-grade metamorphic Proterozoic rocks. The upper Lesser Himalaya here is bounded on the north by the Main Central Thrust, where the overthrusted rocks are dominated by Precambrian gneisses, but only near the thrusted contact do the latter underlie many landslides.

Many landslides occur south and west of Kathmandu (Fig. 4) near the southern edge of the Kathmandu Nappe [a thrust sheet of Precambrian/Lower Paleozoic metasedimentary rocks, as mapped by Stöcklin (*46*)]. In these areas, landslides are especially concentrated where Ordovician granitoids have intruded Proterozoic metasediments, suggesting lithological contrast as a controlling feature. Further, there is a notable absence of landslides south of the MBT-MCT south of Kathmandu.

Proterozoic slate, shale, siltstone, sandstone, graphitic schist (Fig. 4, combined as purple) and gneiss (Fig. 4, red)—all layered rock types—host relatively few landslides. Instead, the vast majority of earthquake-triggered landslides occur in the Proterozoic phyllite, amphibolite, metasandstone, and schist rock sequences of the Lesser and High Himalaya (Fig. 4, green and pink) north of Kathmandu. These occur on either side of the MCT. The landslide hotspots (Fig. 1E) comprise a small fraction of the area of this widespread rock unit; steep-sided, high-elevation ridgetops generated some of the landslide hotspots. For example, the Langtang Valley landslides largely originated high on the ridges and near the summits in places where glaciers, glacial debris, and bedrock failed. The lithological controls may manifest through rock mechanics and rock weathering and slope.

Topographic effects, along with different rock types' contrasting *S*, *P*, and surface waves affect landsliding through wave scattering, interference, and heterogeneous energy dissipation. During helicopter overflights, authors B. Collins and R. Jibson (*47*) observed pervasive ridgetop shattering through much of the near-epicentral landsliding region. Constructive wave interference and the focusing of seismic energy to shatter ridgetops was observed in the Northridge (*48*) and 1971 San Fernando (*49*) earthquakes and modeled for the 2005 I-Lan earthquake in Taiwan (*50*). Last, damage related to wave resonance occurred in the Kathmandu Basin during the Gorkha earthquake (*2*), and similar resonant effects may have occurred elsewhere at damaging frequencies affected by the spatial scales and geometry of various lithologic units. Human-built structures of different sizes and construction, having distinctive resonant vibrational frequencies, were selectively destroyed (*2*).

Some major river valleys also have high landslide densities, including along the Marsyangdi and Trishuli rivers. In the Marsyangdi Valley, a high landslide density correlates with relatively gently sloping areas of the valley floor that are covered by poorly consolidated sedimentary deposits.

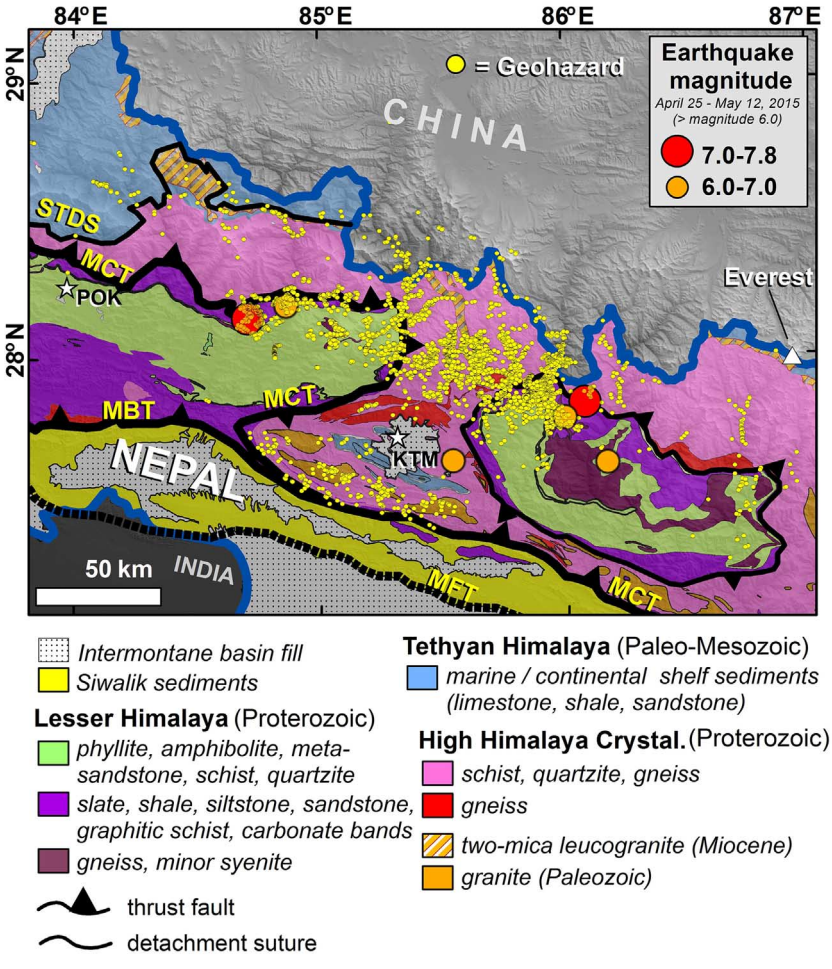

Fig. 4. Landslide occurrence on mapped geologic units. Geology is from simplified geologic map by (*46*, *63*) and major faults (*64*).

Langtang mass movements

The earthquake-induced landslides of the Langtang Valley (Fig. 5 and figs. S3 to S6) were exceptional

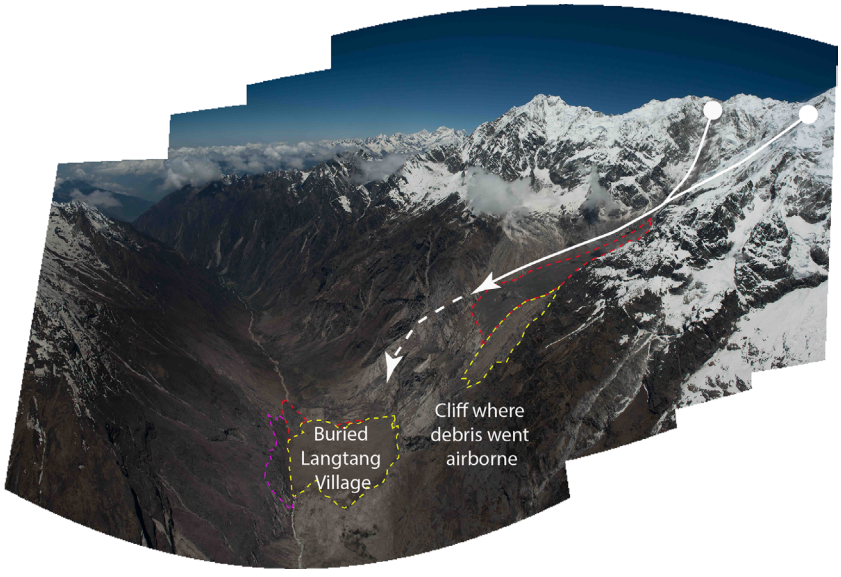

Fig. 5. Langtang's landslide flowpaths. The source areas and flow paths of the two Langtang mass movements (white arrow, dashed where airborne). The red dashed line indicates the extent of the first slide, the yellow dashed line indicates extent of second slide, and the purple dashed line indicates extent of debris run-up. The image is west-facing. [Stitched panorama from 10 May 2015; photos by D. F. Breashears/GlacierWorks]

in their tragic results (more than 350 people killed) and are also among the Gorkha earthquake's best-documented landslides from field- and space-based analysis. Langtang Valley, 70 km north of Kathmandu, is one of Nepal's major trekking regions and hosts benchmark glaciology, hydrology, and meteorology research (*51*–*53*). The valley experienced moderate shaking (up to ~0.26*g* above Langtang village) (Fig. 1B). An analysis of post-event satellite imagery and oblique aerial photographs suggests that coseismic snow and ice avalanches and rockfalls and their powerful concurrent air blasts contributed to the destruction in Langtang Valley (Fig. 5 and figs. S3 to S6) that killed or left missing at least 350 people (*54*). Panoramic photos of Langtang taken in 2012 and those taken after the earthquake on 12 May 2015 illustrate the magnitude and destruction of the Langtang events (figs. S3 and S4). Further indicating the vast scale of these events, annotated helicopter-borne photos and satellite imagery taken of the valley (Fig. 5 and figs. S5 and S6) illustrate our interpretation of this disaster-within-a-disaster.

Debris from the initial coseismic event covered 7.51×10^5 m^2 at Langtang alone, including a ~1-km stretch of the Langtang River. We did not observe stream impoundment in the days after the earthquake, indicating that meltwater and runoff tunneled rapidly through the icy deposit. Photos (D. Breashears) showed that the deposit contained abundant snow and ice. Brightness temperatures modeled from thermal band 10 of Landsat 8 on 30 April 2015 showed lower landslide surface temperatures (270 to 280 K) as compared with those of surrounding terrain (280 to 300 K). The temperature anomalies, pond formation, and moisture of debris resulted from melting.

The primary coseismic event at Langtang village was a combined ice-snow avalanche that initiated near 7000 m. Subsequently, ice and snow entrained rockfall material and descended a low-gradient part of the glacier down to ~4500 m. The rock-ice mass then became airborne as it fell off a cliff below 4500 m (Fig. 5). After the material reached the riverbed at ~3250 m, it ran up the opposing slope ~200 m (fig. S5). The air blasts propagated farther, 400 m up the mountain (fig. S3). From the impact point on the valley floor, devastation extended ~1 km up- and downvalley. From the 200-m-high surge of debris on the opposing slope, we estimate a debris speed (v) of 63 m s^{-1} (227 km h^{-1}) following Eq. 1

$$v = (2gh)^{0.5} \quad (1)$$

where g is gravitational acceleration (9.8 m s^{-2}) and h is the runup. Air blasts leveled what was not buried in Langtang, including some buildings constructed of stone slab. Wind also completely flattened a small forest, suggesting wind speeds comparable with an EF5 tornado (>322 km hour^{-1} wind speed), which is consistent with freefall drop of the landslide and heavily debris-laden wind over the cliff.

Satellite images provided by Digital Globe (fig. S6) indicate a second large post–main shock mass movement near Langtang village between 8 and 10 May 2015. The source of this landslide may have been a rock detachment from the summit ridge of Langtang-Lirung, ~6700 m elevation. The second landslide slightly increased the debris area from 7.51×10^5 to 7.61×10^5 m^2.

Nearby settlements of Singdum and Mundu (fig. S6) were also damaged by air blasts from the Langtang Valley mass movements. The larger settlement of Kyangjin was also badly damaged by an air blast created by another avalanche that originated from the eastern ridge of Langtang-Lirung. Devastation in the air-blasted zones, as captured in several photos (fig. S3), is indicative of the huge energy involved. The first Langtang landslide mass may be ~3.3×10^9 kg (area ~750,000 m^2, assumed mean thickness ≥2 m, density 2200 kg m^{-3}). With a direct fall of ~1 km, the release of gravitational potential energy was ≥3.2×10^{13} J (7.6-kiloton TNT equivalent). During freefall and impact, the main transfer of energy could only have been to the atmosphere and directly on the surface, the effects of which we sadly observed.

Landslide blockages of rivers: Marsyangdi and Tom rivers (Nepal) and Gyirong Zangbo/Trishuli River (Tibet)

We identified recurrent landslides along the upper Marsyangdi River in the Annapurna region. These are a different type of landslide than those in Langtang Valley. At least 20 mass movements intersected the river in the 10 days after the main shock (Fig. 6). The rapid sequence of similar failures demonstrates that the quakes in some way disturbed the unconsolidated sediments (*40*) along the river, perhaps by altering the hydrology or opening soft-sediment fractures, which then were exploited by spring seepage and erosion and rotational failures.

The Marsyangdi Valley experienced relatively weak shaking (to ~0.13*g*) (Fig. 1B and table S3), which triggered nine small landslides along a 16-km stretch of the upper Marsyangdi River between Humde and Bratang (Fig. 6). The landslides were identified from a WorldView-2 satellite image 27 April 2015, 2 days after the earthquake, but were not present in a Landsat 8 image 4 days prequake. Thus, we considered them primary effects of the main shock. Some slumps constricted but did not greatly obstruct the river. One landslide (Fig. 6), ~2.2 km upstream of Lower Pisang village, caused a small impoundment (135 m long, ~2×10^3 m^2).

Five more landslides reached the river between 27 April and 2 May 2015, including one ~200 m wide, which caused a complete blockage ~1.9 km upstream of Lower Pisang. The impoundment grew to ~550 m long and 30 to 40 m wide (~1.4×10^4 m^2) (Fig. 6). Six new landslides occurred by 4 May, and the lake increased to ~2.5×10^4 m^2 and 1100 m long, the same as measured again on 28 May 2015. Upstream, several smaller impoundments indicated a further hazardous situation in which a dam breach could initiate a succession of lower dam breaches and the inundation of Lower Pisang village.

Ground photographs (Fig. 6B) show a predominantly fine-grained landslide (*47*), likely composed of fluvial and lacustrine sediments from former dammed lakes (*40*). The steep headwall, back-tilted trees, and a sharp detachment at the head of the landslide indicate that the slide is a rotational slump, a common failure mode in poorly supported, unconsolidated sediments.

The appearance of eleven post–main shock landslides and growth of the impoundment lake represent secondary and tertiary effects of the earthquake and indicate that the region is susceptible to long-term slope instability and future landslides.

We observed many other earthquake-induced landslide blockages of rivers. In one case, a 450-m-wide landslide blocked the lower Tom River near Ghap, Manaslu Conservation Area, Nepal, creating an impoundment lake that stirred urgent humanitarian concerns. Satellite imagery from 3, 5, 7, and 8 May has allowed monitoring of the dammed lake. Between 3 and 8 May, the lake grew from ~5.7×10^4 to ~6.6×10^4 m^2. The nearby village of Ghap, located downstream of the confluence of the Tom and Budhi Gandaki rivers, fortunately showed no flood damage by 16 May, indicating that even though the lake was draining through a narrow outlet, the dam erosion was gradual. A satellite image from 8 June and subsequent media coverage shows that most of the lake had drained without severe consequences.

The Gorkha earthquake and its many aftershocks also triggered dozens of landslides into the south-flowing Gyirong River, China (Trishuli River downstream in Nepal). One landslide dammed the river ~1.5 km south of Chongsecun, a few kilometers north of the Nepalese border, causing development of a 450 by 50 m impoundment lake (28.363N, 85.360E, ~2600 m above sea level). The landslide destroyed ~200 m of the road connecting Chongsecun to the China-Nepal border crossing at Resuo. Boulders and debris were displaced downslope, forming a landslide scar ~700 m long and a deposit 250 by 300 m. Several landslides and a landslide-dammed lake also developed south of the Chongsecun slide at or near the Resuo border crossing in Nepal (28.275N, 85.379E, ~1,810 m above sea level) and blocked the road near the Resuo bridge. Fortunately, the dam was incised by the river, and with mitigation efforts by engineers, there was no further damage. Another landslide on the same river near Resuo was triggered by a rainstorm on 28 April 2015, with the terrain conditioned by the M 7.8 Gorkha earthquake. The landslide dammed the Trishuli River and blocked the road from Gyirong County to Resuo Port. These features near Chongsecun and Resuo exemplify the transboundary process chains of some induced hazards. The interruption of cross-border commerce is a major tangible earthquake impact in addition to the damage to infrastructure and the loss of life.

Glacier lakes stability

Many GLOFs have been recorded in the Himalaya since the mid-20th century (*55*). The lakes' moraine dams, commonly situated at the angle of repose, are fragile and prone to outburst because of either sudden collapse or piping erosion, or to gradual degradation due to climatic warming and thaw. Avalanche and landslide-generated displacement waves in the lake are thought to be a common trigger for moraine dam failure (*56*). Thus, when the largest earthquakes happened,

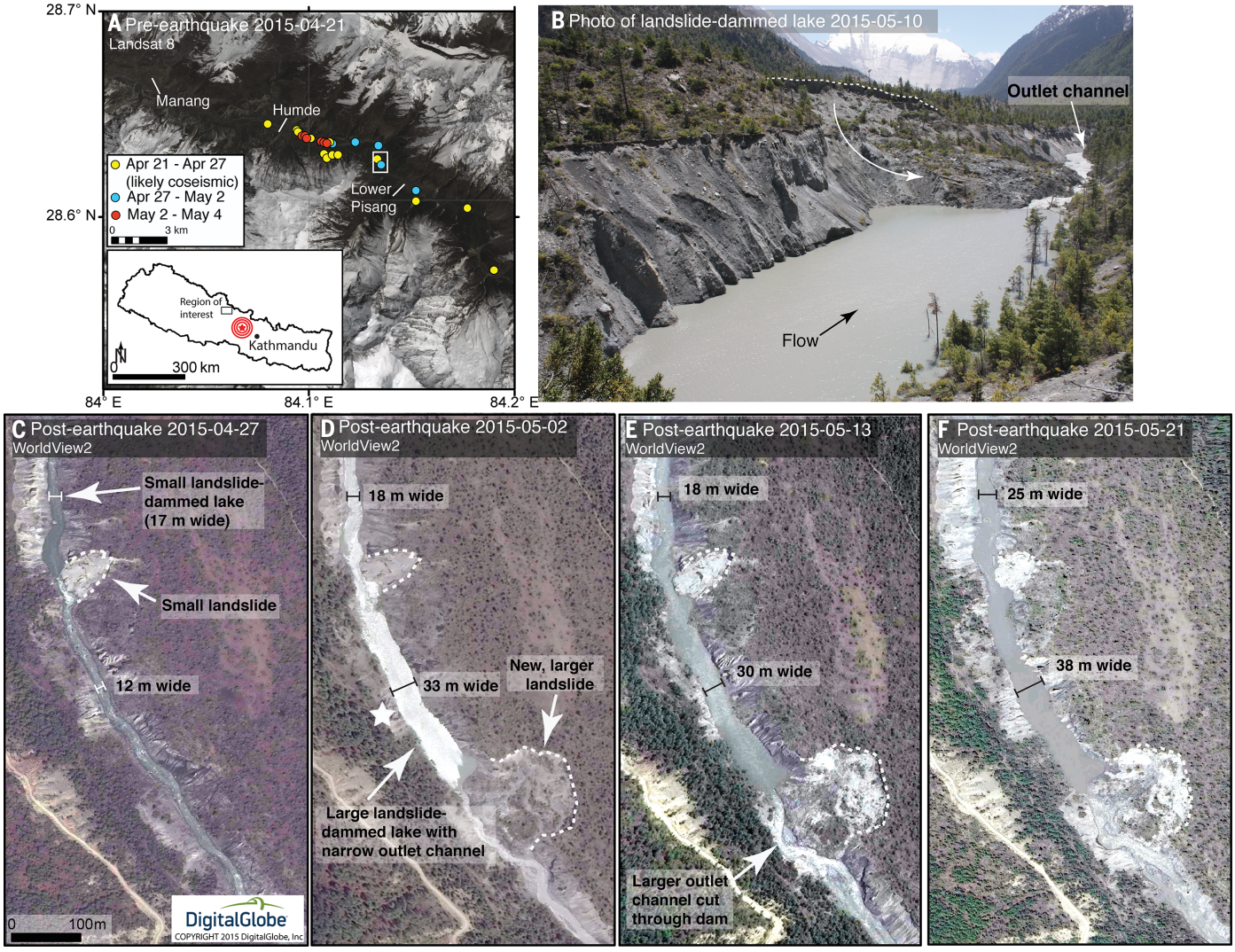

Fig. 6. Landslide-dammed lake on the Marsyangdi River. Map and satellite imagery and ground photographs of landslides and landslide-dammed lakes on upper Marsyangdi River. (**A**) Map. White box locates (C), (D), (E), and (F). (**B**) Ground photograph (courtesy M. Gotame, Manang villager) from 10 May 2015, showing the landslide-dammed lake looking south. The white dashed line is the head scarp (visible is the steep headwall), and the curved arrow shows the inferred flow path of the rotational slump. (**C**, **D**, **E**, and **F**) High-resolution WorldView-2 images of the river, showing delayed occurrence of the large landslide and lake formation. The white star in (D) locates (B). River widths are given at two locations.

many experts were concerned that shaking may have weakened or collapsed unconsolidated moraine dams of glacial lakes, or may have triggered large displacement waves and GLOFs.

Fortunately, we identified few earthquake effects on glacier lakes. We examined pre- and postquake satellite images of 491 lakes [locations drawn mainly from the inventory of Fujita *et al.* (*57*)]. The visibility of 15 lakes in our database was unclear (partially shadowed or poor resolution image), but their downstream drainages showed no signs of GLOFs. Only nine of 491 were physically hit by landslides or avalanches. Of these, ice avalanches may have ejected water from two small ponds near Everest, and debris fell onto the frozen surfaces of other lakes without further effect. No lakes in the current satellite survey produced a GLOF as a result of the earthquake. GLOFs generally do not trigger at modeled PGAs up to 0.57*g* (Fig. 2D). This unexpected result may relate to seismic wave interactions with the topography, where for shallow hypocenters, PGAs (i) are reduced on valley floors and (ii) are rapidly reduced by shielding across mountain ranges caused by wave scattering on the topography and petrologic structure (*50*, *58*).

Furthermore, we closely examined three large moraine-dammed glacial lakes (Thulagi, Rolpa, and Imja) (Fig. 7), which have been extensively surveyed, studied, and monitored because of their GLOF risk (*55*). At Thulagi Lake in the Manaslu region (just west of the Tom River blockage described above) and Imja Lake in the Everest region, no damage was immediately evident in postquake satellite imagery. However, a small glacial lake on Lhotse Glacier (south of Everest) drained on 25 May 2015, which resulted in an anomalous rise in stream level (*59*). Small supraglacial ponds commonly drain suddenly because of ice fracturing or other glacier dynamics, and it is unclear whether this event was earthquake-related.

We were especially concerned about Tsho Rolpa, located at the terminus of Trakarding Glacier in the Rolwaling Valley, because of its location near the giant aftershock's (*M* 7.3 on 12 May) epicenter. We found no evidence of damage to Tsho Rolpa's damming moraine from examination of WorldView 1 satellite images taken 9 days after the initial earthquake, on 4 May 2015, and the NASA's EO-1 satellite image taken 5 days after the *M* 7.3 aftershock on 17 May. Postquake field photographs taken by USGS on 27 May show that the moraine was intact, and the lake was nearly brim-full (Fig. 8A). Another USGS photograph (Fig. 8B) shows fractures on the moraine dam, but because no ice exists in this part of the moraine, these tension cracks appear to have been caused by slumping of moraine material toward the lake (1 to 1.5 m horizontal and ~0.5 m vertical), probably because of an earthquake but not likely to be a problem. The satellite imagery and field photographs do not demonstrate any big new additional concerns about the lake. We would not observe small GLOFs and minor damage to moraines in satellite images because of limitations in resolution. Furthermore, neither satellite and ground nor helicopter-borne inspections can easily detect interior (subsurface) structural damage that make the metastable lakes even more subject to outburst.

Summary and conclusions

Rapid, systematic mapping allowed us to investigate earthquake-induced geohazard processes and provide information to relief and recovery officials on the same timeframe as those operations were occurring. This work thus contributed to effective, timely guidance to in-country authorities responsible for response and recovery. Key findings were relayed through NASA, USGS, and the U.S. Agency for International Development (USAID), to Nepal-based experts at ICIMOD (International Centre for Integrated Mountain Development) and DHM (Department of Hydrology and Meteorology, Government of Nepal) and to the Prime Minister of Nepal.

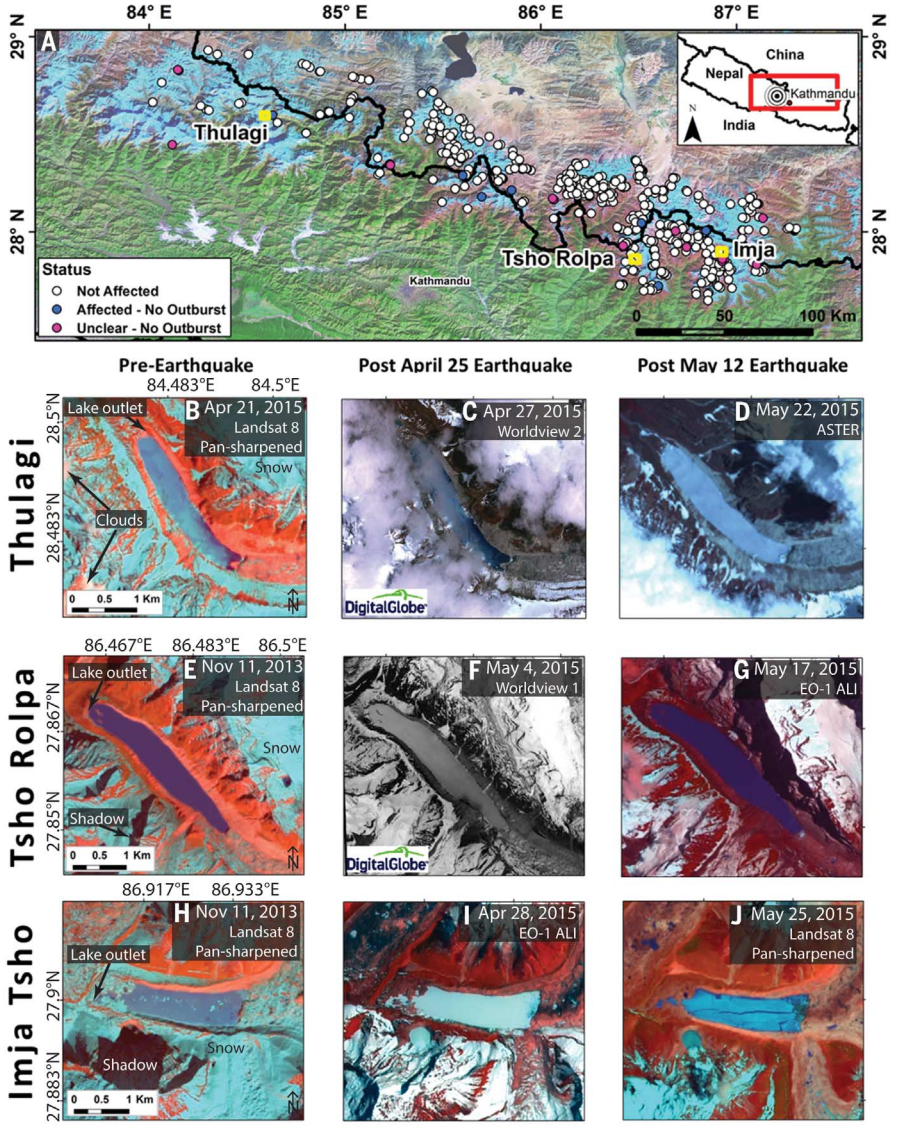

Fig. 7. Lake survey for earthquake damage. (**A**) Overview of study area, showing location of 491 surveyed lakes. (**B** to **J**) Pre-earthquake images (right column), post–main shock images (center column), and post–12 May aftershock images (left column) for the largest glacial lakes in Nepal, (B) to (D), Thulagi Lake, (E) to (G) Tsho (Lake) Rolpa, and (H) to (J) Imja Tsho. (B) Landsat 8 image of Thulagi Lake, 21 April 2015. (C) Worldview 2 image of Thulagi Lake, 27 April 2015. (D) ASTER image of Thulagi Lake, 22 May 2015. (E) Landsat 8 image of Tsho Rolpa, 11 November 2013. (F) Worldview 1 image of Tsho Rolpa, 4 May 2015. (G) EO-1 ALI image of Tsho Rolpa 17 May 2015. (H) Landsat 8 image of Imja Tsho, 11 November 2013. (I) EO-1 ALI image of Imja Tsho, 28 April 2015. (J) Landsat 8 image of Imja Tsho, 25 May 2015. A large crack developed in the lake ice on Imja Tsho, although such cracks are normal with spring thaw. Landsat 8 scenes are panchromatic band 8 sharpened images (resolution 15 m) using band combinations [7,5,3] (SWIR, NIR, Green). WorldView 2 false color composite scene uses band combination [7, 5, 3] (NIR, Red, Green). WorldView 1 image is the panchromatic band. ASTER image (resolution 15 m) uses bands [3N, 2, 1] (NIR, Red, Green). EO-1 ALI scenes use pan-sharpened band 1 (resolution 10 m) and band combination [8, 6, 4] (SWIR, NIR, Green).

The mapped features document the large geographic extent of the Gorkha earthquake's effect on hazardous Earth surface processes and constrain their geophysical limits and geomorphic, tectonic, and lithologic controls. The distribution of induced landslides shows positive associations with slope and shaking intensity. More broadly, the highest areal densities of landslides are developed primarily on the downdropped northern tectonic block. This is likely explained by momentary reduction during downward acceleration of the normal stress along planes of weakness. The largest two shocks bracket the landslide distribution because they are within the displacement field and highest PGAs. Additional controls of landslide distribution are indicated by their clustering within specific bedrock and surficial lithologies, including Proterozoic metamorphic rocks and Ordovician granitoids, in proximity to earthquake epicenters, with high PGAs, and perhaps with seismic wave scattering and interferences.

In the remote valleys of the higher Himalaya, the most concentrated losses were directly due to the induced mass movements and air blasts rather than shaking. Seismic wave interactions may have contributed to destruction in Langtang Valley and other locations because of wave focusing and ridgetop shattering but may have reduced direct shaking damage in valley floors and at glacial lakes.

The distribution of Gorkha earthquake–related landslides and the terrain susceptibilities to earthquake-induced mass movements provide a basis from which to predict future patterns of landsliding of earthquake-weakened ice, rock, and unconsolidated sediments, especially as aftershocks, precipitation, and snowmelt events continue over the next few years. Hydrological processes such as frost shattering and rockfalls at high elevations and riverbank undercutting and rotational slumping in valleys may exploit earthquake-induced damage and trigger more landslides. Conversely, high-magnitude shaking-related landslides, such as ridgetop failures that affected Langtang Valley, may be less common going forward, unless additional strong aftershocks or high-elevation melting affect seismically shattered rocks. However, earthquake-related landsliding may fade below the regional background frequency of landslide activity in the next one to several years.

The Gorkha earthquake caused fewer landslides than comparable earthquakes elsewhere, although some of Nepal's largest mass movements in recent millennia may have been triggered by earthquakes (*60*). Details of earthquake location relative to geology and topographic relief appear to be crucial in determining the magnitude of earthquake-induced hazards.

Although the Gorkha earthquake's tragic toll on human lives and culture cannot be understated, some fortunate facts are that not a single large GLOF was unleashed and the total number of landslides was far fewer than generated by comparable earthquakes (*56*). Whether the same will hold for a hypothetical future large Himalayan earthquake is uncertain. However, future earthquakes generated on the shallow Main Himalayan Thrust are not apt to generate many or any GLOFs unless the magnitude is greater than the Gorkha earthquake's or the hypocenter and zone of maximum slip is closer to the lakes, thus circumventing the shielding by Himalayan relief. The potential exists for immense landslides and river blockages, which may pose the greatest mountain hazard.

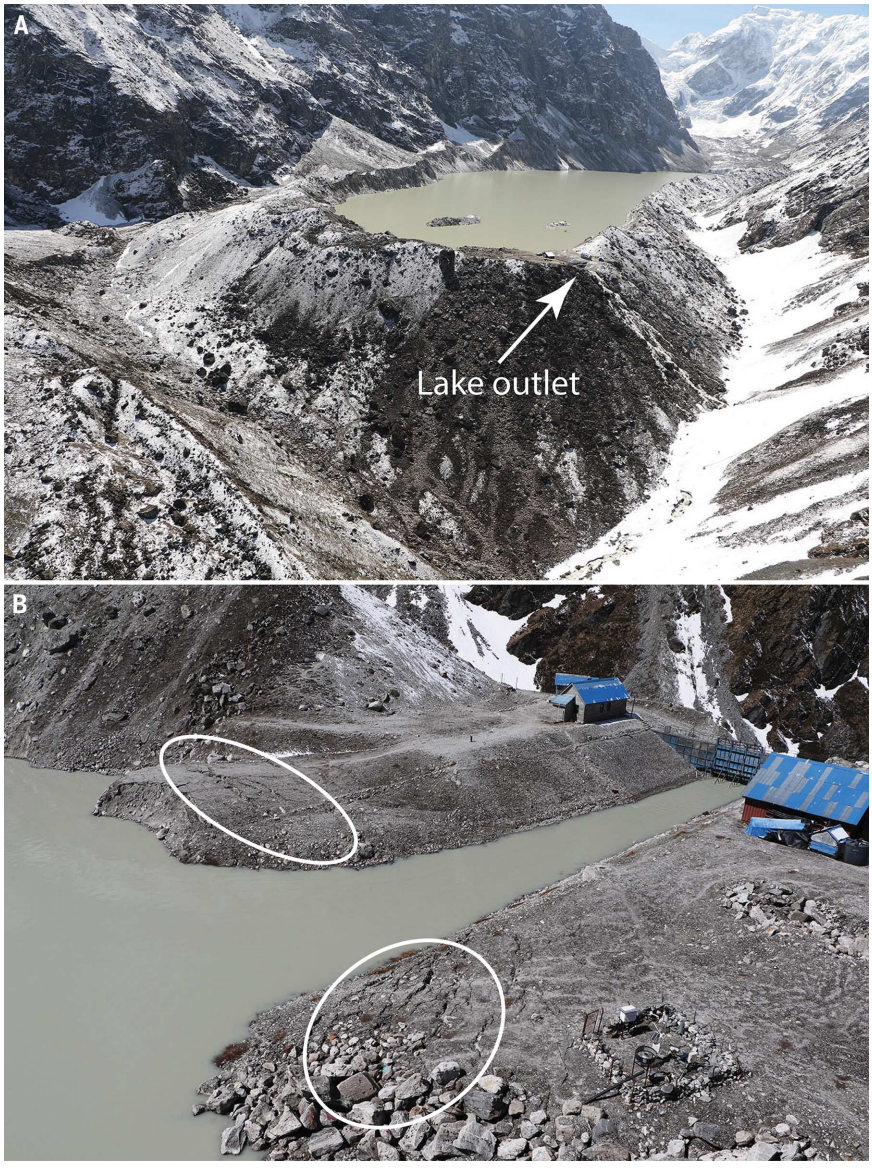

Fig. 8. Field visit identifies light damage at Tsho (lake) Rolpa. (**A**) Post-earthquake image of Tsho Rolpa appears identical to its appearance shortly before the earthquake. (**B**) Two areas of fractures (outlined in white)—believed formed by the 12 May 2015 aftershock—were observed from a helicopter on the engineered part of the end moraine during an inspection undertaken by USGS at Tsho Rolpa. Photos are from 27 May by B. Collins (USGS), courtesy of USAID–Office of Foreign Disaster Aid.

Materials and methods

We mapped 4312 landslides from high- and medium-resolution satellite imagery (Landsat 8, WorldView, and others) in the weeks after the M 7.8 main shock. Landslide locations were mapped as points, with attributes including nearest village, dates of imagery used to constrain timing, and whether the mass movement produced or could produce a secondary hazard (for example, a dammed lake). Using a previously published database and the multispectral satellite data, we also assessed damages to glacial lakes. The distribution of landslides was examined in the context of the geology (structure and lithology), the distribution of snow and ice, topographic slopes, and peak ground accelerations modeled for the Gorkha earthquake and its largest aftershock. Seismic and shake intensity data combined with slope were used to model geohazard susceptibility indices. All data, including previously published InSAR-measured ground displacements, were analyzed within a geographic information system.

REFERENCES AND NOTES

1. R. M. Parameswaran *et al*., Seismotectonics of the April–May 2015 Nepal earthquakes: An assessment based on the aftershock patterns, surface effects and deformational characteristics. *J. Asian Earth Sci.* **111**, 161–174 (2015). doi: 10.1016/j.jseaes.2015.07.030
2. J. Galetzka *et al*., Slip pulse and resonance of the Kathmandu basin during the 2015 Gorkha earthquake, Nepal. *Science* **349**, 1091–1095 (2015). doi: 10.1126/science.aac6383; pmid: 26249228
3. E. O. Lindsey *et al*., Line-of-sight displacement from ALOS-2 interferometry: M_w7.8 Gorkha Earthquake and M_w 7.3 aftershock. *Geophys. Res. Lett.* **42**, 6655–6661 (2015). doi: 10.1002/2015GL065385
4. K. Jaiswal, D. Wald, D. D'Ayala, Developing empirical collapse fragility functions for global building types. *Earthq. Spectra* **27**, 775–795 (2011). doi: 10.1193/1.3606398
5. J. S. Kargel, G. J. Leonard, M. P. Bishop, A. Kääb, B. H. Raup, *Global Land Ice Measurements from Space* (Springer-Verlag, Berlin Heidelberg, 2014).
6. E. L. Harp, D. K. Keefer, H. P. Sato, H. Yagi, Landslide inventories: The essential part of seismic landslide hazard analyses. *Eng. Geol.* **122**, 9–21 (2011). doi: 10.1016/j.enggeo.2010.06.013
7. J. A. N. van Aardt *et al*., Geospatial disaster response during the Haiti earthquake: A case study spanning airborne deployment, data collection, transfer, processing, and dissemination. *Photogramm. Eng. Remote Sensing* **77**, 943–952 (2011).
8. G. Cecchine *et al*., "The U.S. Military Response to the 2010 Haita Earthquake - Considerations for Army Leaders" (RAND Corporation, 2013).
9. H. P. Sato, E. L. Harp, Interpretation of earthquake-induced landslides triggered by the 12 May 2008, *M*7.9 Wenchuan earthquake in the Beichuan area, Sichuan Province, China using satellite imagery and Google Earth. *Landslides* **6**, 153–159 (2009). doi: 10.1007/s10346-009-0147-6
10. British Geological Survey, Nepal earthquake response 2015 (2015); available at www.bgs.ac.uk/research/earthHazards/epom/NepalEarthquakeResponse.html.
11. R. N. Parker *et al*., Mass wasting triggered by the 2008 Wenchuan earthquake is greater than orogenic growth. *Nat. Geosci.* **4**, 449–452 (2011). doi: 10.1038/ngeo1154
12. C. Xu, X. Xu, X. Yao, F. Dai, Three (nearly) complete inventories of landslides triggered by the May 12, 2008 Wenchuan M_w 7.9 earthquake of China and their spatial distribution statistical analysis. *Landslides* **11**, 441–461 (2014). doi: 10.1007/s10346-013-0404-6
13. R. M. Yuan *et al*., Density distribution of landslides triggered by the 2008 Wenchuan earthquake and their relationships to peak ground acceleration. *Bull. Seismol. Soc. Am.* **103**, 2344–2355 (2013). doi: 10.1785/0120110233
14. E. L. Harp *et al*., Landslides and liquefaction triggered by the M 7.9 Denali Fault earthquake of 3 November 2002. *GSA Today* **13**, 4–10 (2003). doi: 10.1130/1052-5173(2003)013<0004:LALTBT>2.0.CO;2
15. R. W. Jibson, E. L. Harp, W. Schulz, D. K. Keefer, Landslides triggered by the 2002 Denali fault, Alaska, earthquake and the inferred nature of the strong shaking. *Earthq. Spectra* **20**, 669–691 (2004). doi: 10.1193/1.1778173
16. D. H. Shugar, J. J. Clague, The sedimentology and geomorphology of rock avalanche deposits on glaciers. *Sedimentology* **58**, 1762–1783 (2011). doi: 10.1111/j.1365-3091.2011.01238.x
17. F. C. Dai *et al*., Spatial distribution of landslides triggered by the 2008 M_s 8.0 Wenchuan earthquake, China. *J. Asian Earth Sci.* **40**, 883–895 (2011). doi: 10.1016/j.jseaes.2010.04.010
18. D. H. Shugar, B. T. Rabus, J. J. Clague, D. M. Capps, The response of Black Rapids Glacier, Alaska, to the Denali earthquake rock avalanches. *J. Geophys. Res.* **117** (F1), F01006 (2012). doi: 10.1029/2011JF002011
19. R. N. Parker *et al*., Spatial distributions of earthquake-induced landslides and hillslope preconditioning in the northwest South Island, New Zealand. *Earth Surf. Dynamics* **3**, 501–525 (2015). doi: 10.5194/esurf-3-501-2015
20. S. G. Evans *et al*., Catastrophic detachment and high-velocity long-runout flow of Kolka Glacier, Caucasus Mountains, Russia in 2002. *Geomorphology* **105**, 314–321 (2009). doi: 10.1016/j.geomorph.2008.10.008
21. W. Haeberli *et al*., The Kolka-Karmadon rock/ice slide of 20 September 2002: An extraordinary event of historical dimensions in North Ossetia, Russian Caucasus. *J. Glaciol.* **50**, 533–546 (2004). doi: 10.3189/172756504781829710
22. J. S. Kargel *et al*., Satellite monitoring of Pakistan's rockslide-dammed Lake Gojal. *Eos Trans. AGU* **91**, 394–395 (2010). doi: 10.1029/2010EO430002
23. V. Vilímek, M. L. Zapata, J. Klimes, Z. Patzelt, N. Santillán, Influence of glacial retreat on natural hazards of the Palcacocha Lake area, Peru. *Landslides* **2**, 107–115 (2005). doi: 10.1007/s10346-005-0052-6
24. M. Carey, Living and dying with glaciers: People's historical vulnerability to avalanches and outburst floods in Peru. *Glob. Planet. Change* **47**, 122–134 (2005). doi: 10.1016/j.gloplacha.2004.10.007
25. S. A. Dunning, N. J. Rosser, D. N. Petley, C. R. Massey, Formation and failure of the Tsatichhu landslide dam, Bhutan. *Landslides* **3**, 107–113 (2006). doi: 10.1007/s10346-005-0032-x
26. J. T. Weidinger, in *Natural and Artificial Rockslide Dams*, S. G. Evans, R. L. Hermanns, A. Strom, G. Scarascia-Mugnozza, Eds. (Springer, Berlin Heidelberg, 2011), pp. 243–277.
27. M. Geertsema, J. J. Clague, Pipeline routing in landslide-prone terrain. *Innovations* **15**, 17–21 (2011).
28. K. Hewitt, Disturbance regime landscapes: Mountain drainage systems interrupted by large rockslides. *Prog. Phys. Geogr.* **30**, 365–393 (2006). doi: 10.1191/0309133306pp486ra
29. Materials and methods are available as supplementary materials on *Science* Online.
30. Y. Ogata, Statistical models for earthquake occurrences and residual analysis for point processes. *J. Am. Stat. Assoc.* **83**, 9–27 (1988). doi: 10.1080/01621459.1988.10478560
31. D. K. Keefer, Investigating landslides caused by earthquakes—A historical review. *Surv. Geophys.* **23**, 473–510 (2002). doi: 10.1023/A:1021274710840
32. C. Xu, X. Xu, J. B. H. Shyu, Database and spatial distribution of landslides triggered by the Lushan, China Mw 6.6 earthquake of 20 April 2013. *Geomorphology* **248**, 77–92 (2015). doi: 10.1016/j.geomorph.2015.07.002
33. A. Jarvis, H. I. Reuter, A. Nelson, E. Guevara, Hole-filled seamless SRTM data v4 [International Centre for Tropical Agriculture (CIAT), 2008]; available at http://srtm.csi.cgiar.org.
34. P. Meunier, N. Hovius, J. A. Haines, Topographic site effects and the location of earthquake induced landslides. *Earth Planet. Sci. Lett.* **275**, 221–232 (2008). doi: 10.1016/j.epsl.2008.07.020
35. H. T. Chou, C. F. Lee, S. C. Chen, in *Earthquake-Induced Landslides: Proceedings of the International Symposium on Earthquake-Induced Landslides*, K. Ugai, H. Yagi, A. Wakai, Eds. (2013), pp. 45–57.
36. L. Chen *et al*., Liquefaction macrophenomena in the great Wenchuan earthquake. *Earthq. Eng. Eng. Vib.* **8**, 219–229 (2009). doi: 10.1007/s11803-009-9033-4
37. P. L. Moore, N. R. Iverson, D. Cohen, Ice flow across a warm-based/cold-based transition at a glacier margin. *Ann. Glaciol.* **50**, 1–8 (2009). doi: 10.3189/172756409789624319
38. H. Blatter, G. K. C. Clarke, J. Colinge, Stress and velocity fields in glaciers: Part II. Sliding and basal stress distribution. *J. Glaciol.* **44**, 457–466 (1998).
39. N. Bo, J. Persson, in *Sliding on Ice and Snow: Physical Principles and Applications* (Springer, Berlin, 1998), p. 391.
40. J. T. Weidinger, Predesign, failure and displacement mechanisms of large rockslides in the Annapurna Himalayas, Nepal. *Eng. Geol.* **83**, 201–216 (2006). doi: 10.1016/j.enggeo.2005.06.032
41. P. Deline *et al*., in *Snow and Ice-Related Hazards, Risks and Disasters*, W. Haeberli, C. Whiteman, J. F. Shroder, Eds. (Elsevier, Amsterdam, 2015), pp. 521–561.
42. M. Geertsema, M. Chiarle, in *Treatise on Geomorphology*, J. F. Shroder, M. Stoffel, R. A. Marston, Eds. (Elsevier, Amsterdam, 2013), vol. 7, pp. 217–222.
43. C. Liang, "Interferogram for ALOS2-track 48-swath ScanSARNominal14MHz; Feb 22, 2015 to May 3, 2015," UNAVCO InSAR Product, (2015).doi: 10.7283/S2KW2R
44. R. W. Jibson, E. L. Harp, "Field reconnaissance report of landslides triggered by the January 12, 2010, Haiti earthquake" (U.S. Geological Survey Open-File Report 2011-1023, Reston, VA, 2011).
45. E. L. Harp, R. W. Jibson, Landslides triggered by the 1994 Northridge, California earthquake. *Bull. Seismol. Soc. Am.* **86**, S319–S332 (1996).
46. J. Stöcklin, Geology of Nepal and its regional frame: Thirty-third William Smith Lecture. *J. Geol. Soc. London* **137**, 1–34 (1980). doi: 10.1144/gsjgs.137.1.0001
47. B. D. Collins, R. W. Jibson, "Assessment of existing and potential landslide hazards resulting from the April 25, 2015 Gorkha, Nepal earthquake sequence" (U.S. Geological Survey Open-File Report 2015-1142, Reston, VA, 2015).
48. J. P. McCalpin, E. W. Hart, "Ridge-top spreading features and relationship to earthquakes, San Gabriel Mountains region, Southern California - Part B: Paleoseismic investigations of ridge-top depressions," *Final Technical Report, Contract 1434-HQ-GR-1026, National Earthquake Hazards Reduction Program* (U.S. Geological Survey, 2002).
49. R. D. Nason, in *The San Fernando, California, earthquake of February 9, 1971, U.S. Geological Survey Professional Paper 733* (U.S. Geological Survey, Washington, DC, 1971), pp. 97–98.
50. S.-J. Lee, D. Komatitsch, B.-S. Huang, J. Tromp, Effects of topography on seismic-wave propagation: An example from northern Taiwan. *Bull. Seismol. Soc. Am.* **99**, 314–325 (2009). doi: 10.1785/0120080020
51. W. W. Immerzeel, L. Petersen, S. Ragettli, F. Pellicciotti, The importance of observed gradients of air temperature and precipitation for modeling runoff from a glacierized watershed in the Nepalese Himalayas. *Water Resour. Res.* **50**, 2212–2226 (2014). doi: 10.1002/2013WR014506
52. K. Fujita, T. Nuimura, Spatially heterogeneous wastage of Himalayan glaciers. *Proc. Natl. Acad. Sci. U.S.A.* **108**, 14011–14014 (2011). doi: 10.1073/pnas.1106242108; pmid: 21808042
53. S. Ragettli *et al*., Unraveling the hydrology of a Himalayan catchment through integration of high resolution in situ data and remote sensing with an advanced simulation model. *Adv. Water Resour.* **78**, 94–111 (2015). doi: 10.1016/j.advwatres.2015.01.013
54. C. Cadwalladr, "Nepal earthquake: The village wiped off the map in a few terrifying seconds," *The Guardian*, 16 May 2015.
55. ICIMOD, *Glacial Lakes and Glacial Lake Outburst Floods in Nepal* (International Centre for Integrated Mountain Development, Kathmandu, Nepal, 2011), pp. 99.
56. J. J. Clague, S. G. Evans, A review of catastrophic drainage of moraine-dammed lakes in British Columbia. *Quat. Sci. Rev.* **19**, 1763–1783 (2000). doi: 10.1016/S0277-3791(00)00090-1
57. K. Fujita *et al*., Potential flood volume of Himalayan glacial lakes. *Nat. Hazards Earth Syst. Sci.* **13**, 1827–1839 (2013). doi: 10.5194/nhess-13-1827-2013
58. S. Ma, R. J. Archuleta, M. T. Page, Effects of large-scale topography on ground motions as demonstrated by a study of the San Gabriel Mountains, Los Angeles, California. *Bull. Seismol. Soc. Am.* **97**, 2066–2079 (2007). doi: 10.1785/0120070040
59. A. C. Byers, D. C. McKinney, E. A. Byers, "Post-earthquake assessment: Imja, Tsho Rolpa, and Thulagi glacial lakes in Nepal" (U.S. Agency for International Development, 2015).
60. W. Schwanghart *et al*., Repeated catastrophic valley infill following medieval earthquakes in the Nepal Himalaya. *Science* **351**, 147–150 (2015).
61. A. Arendt *et al*., "Randolph Glacier Inventory—A dataset of global glacier outlines: version 4.0" (Global Land Ice Measurements from Space, Boulder, CO, 2014).
62. U.S. Geological Survey, Earthquake Hazards Program (2015); available at http://earthquake.usgs.gov.
63. M. R. Dhital, *Geology of the Nepal Himalaya—Regional Geology Reviews* (Springer, 2015).
64. L. S. Walsh, A. J. Martin, T. P. Ojha, T. Fedenczuk, Correlations of fluvial knickzones with landslide dams, lithologic contacts, and faults in the southwestern Annapurna Range, central Nepalese Himalaya. *J. Geophys. Res.* **117**, F01012 (2012). doi: 10.1029/2011JF001984

ACKNOWLEDGMENTS

J.S.K., G.J.L., and U.K.H. thank the NASA SERVIR Applied Science Team and NASA Cryosphere Program for support. D.H.S. thanks the Hakai Institute for support. Part of this research was sponsored by the NASA Earth Surface and Interior focus area and performed at the Jet Propulsion Laboratory, California Institute of Technology. We gratefully acknowledge support from several "citizen scientists" who provided key observations and reports from various locations in Nepal: D. Rai, J. B. Rai, N. Sapkota, M. Dhan Rai, and M. Gotame, who made on-site inspections and photo documentation of Thulagi (Dona) Lake, Rolpa Lake, Kali Gandaki, and "Lower Pisang" landslide dammed lake. ASTER data are courtesy of NASA/GSFC/METI/Japan Space Systems, the U.S./Japan ASTER Science Team, and GLIMS. We especially laud DigitalGlobe's decision to acquire and make available a vast volume of data for analysis related to Gorkha earthquake response. We thank C. Liang for processing the ALOS-2 wide-swath interferogram. Original ALOS-2 data are copyright 2015 JAXA. This study was partially supported by core funds of ICIMOD contributed by the governments of Afghanistan, Australia, Austria, Bangladesh, Bhutan, China, India, Myanmar, Nepal, Norway, Pakistan, Switzerland, and the United Kingdom. This study was partially supported by the Hundred Talents Program of the Chinese Academy of Sciences (grant 784) and the National Natural Science Foundation of China (grants 41431070 and 41321063). The two chief databases produced by this work are available at ICIMOD (landslides, http://rds.icimod.org/Home/DataDetail?metadataId=24055; and glacial lakes, http://rds.icimod.org/Home/DataDetail?metadataId=24065).

SUPPLEMENTARY MATERIALS

www.sciencemag.org/content/351/6269/aac8353/suppl/DC1
Materials and Methods
Figs. S1 to S6
Tables S1 to S3

20 June 2015; accepted 27 November 2015
Published online 17 December 2015
10.1126/science.aac8353

REPORTS

THERMOELECTRICS

Ultrahigh power factor and thermoelectric performance in hole-doped single-crystal SnSe

Li-Dong Zhao,[1,2]* Gangjian Tan,[2] Shiqiang Hao,[3] Jiaqing He,[4] Yanling Pei,[1] Hang Chi,[5] Heng Wang,[6] Shengkai Gong,[1] Huibin Xu,[1] Vinayak P. Dravid,[3] Ctirad Uher,[5] G. Jeffrey Snyder,[3] Chris Wolverton,[3] Mercouri G. Kanatzidis[2]*

Thermoelectric technology, harvesting electric power directly from heat, is a promising environmentally friendly means of energy savings and power generation. The thermoelectric efficiency is determined by the device dimensionless figure of merit ZT_{dev}, and optimizing this efficiency requires maximizing ZT values over a broad temperature range. Here, we report a record high ZT_{dev} ~1.34, with ZT ranging from 0.7 to 2.0 at 300 to 773 kelvin, realized in hole-doped tin selenide (SnSe) crystals. The exceptional performance arises from the ultrahigh power factor, which comes from a high electrical conductivity and a strongly enhanced Seebeck coefficient enabled by the contribution of multiple electronic valence bands present in SnSe. SnSe is a robust thermoelectric candidate for energy conversion applications in the low and moderate temperature range.

With more than 60% of the world's produced energy being lost as waste heat in the low and moderate temperature range, a compelling need exists for high-performance thermoelectric materials that can directly convert this heat to electrical power (*1*–*5*). The thermoelectric conversion efficiency is characterized by the temperature-dependent quantity $ZT = S^2\sigma T/\kappa$, where S is the Seebeck coefficient, σ is the electrical conductivity, κ is the total thermal conductivity, T is the temperature, and the product ($S^2\sigma$) is the power factor (*PF*). The conversion efficiency of heat to electricity for a large number of potential applications requires enhancing ZT over a wide range of temperatures. However, many previous advances have focused on improving the maximum ZT (ZT_{max}) as a function of temperature (*6*–*16*). Many such improvements in ZT_{max} came from strategies such as hierarchical architecturing, band structure engineering, and intrinsically low thermal conductivity, which enabled huge reductions in lattice thermal conductivity (e.g., nanostructuring) (*6*–*8*). Materials that incorporate one or more of these strategies include the systems $AgPb_mSbTe_{m+2}$ (LAST) (*6*, *8*), PbTe-SrTe (*9*), $NaPb_mSbTe_{m+2}$ (SALT) (*10*), PbTe-Tl (*11*), PbTe-PbSe (*12*), $Mg_2(Si,Sn)$ (*13*), MgAgSb (*14*), PbSe-CdS (*15*), and triple filled Skutterudites (*16*). Many of these thermoelectrics are heavy-metal–based materials, which include rare-earth metals and elements with low abundance. Therefore, developing thermoelectrics requires not only a high maximum ZT, but a high ZT value over a wide range of temperatures, and materials made from relatively nontoxic and more earth-abundant elements.

A surprising choice for a promising thermoelectric candidate is SnSe single crystal, because its two-dimensional (2D) anisotropic and low-symmetry crystal structure would not have been expected to exhibit high carrier mobility (*17*). Recently, we showed that SnSe exhibits one of the lowest lattice thermal conductivities known for crystalline materials (<0.4 W m^{-1} K^{-1} at 923 K) (*18*) and without any doping exhibits record high ZTs along the b and c crystallographic directions at 723 to 973 K (fig. S1). Unlike the facile doping behavior of Pb-based rock-salt chalcogenides (*5*, *19*), doping SnSe is challenging because of the layered anisotropic structure, where each SnSe layer is two atoms thin, and the locally distorted bonding around the Sn and Se atoms. Here, we demonstrate successful hole doping in single crystals of SnSe using sodium as an effective acceptor and find a vast increase in ZT from 0.1 (undoped) to 0.7 (doped) along the b axis at 300 K while obtaining the ZT_{max} of 2.0 at 773 K (Fig. 1A). The hole-doped SnSe (b axis) outperforms most of current state-of-the-art p-type materials at 300 to 773 K (*9*, *10*, *14*, *18*, *20*, *21*) (Fig. 1B). The high *PF* and ZT give the highest device ZT (ZT_{dev}) from 300 to 773 K known in the field of thermoelectric materials of ~1.34. The ZT_{dev} over the entire working temperature range is important, as it determines the thermoelectric conversion efficiency (η). The thermoelectric efficiency of a material between a hot temperature T_h and cold side temperature T_c can be calculated from the Seebeck coefficient, electrical conductivity, and thermal conductivity as a function of T (*22*)

$$\eta = \frac{T_h - T_c}{T_h}\frac{\sqrt{1+ZT_{dev}}-1}{\sqrt{1+ZT_{dev}}+T_c/T_h} \quad (1)$$

The ZT_{dev} of hole-doped SnSe is much higher than that of typical high-performance thermoelectrics (*9*, *18*, *23*) from 300 to 773 K (Fig. 1C). Although the extremely low thermal conductivity enables the high ZT of undoped SnSe crystals from 723 to 973 K, we attribute the large ZT_{dev} enhancement in hole-doped SnSe to the enormous boost in *PF* in the temperature range from 300 to 773 K. The projected conversion efficiency of hole-doped SnSe for T_c = 300 K and T_h = 773 K is ~ 16.7%, which is higher than that of other high-performance thermoelectrics (*9*, *18*, *23*) (Fig. 1D).

The origins of the high performance come from various different contributions. We increased the electrical conductivity of SnSe from ~12 S cm^{-1} to >1500 S cm^{-1} (Fig. 2A) by hole doping the material, changing the temperature dependence from semiconductor-like to metal-like. With rising temperature, the electrical conductivity of hole-doped SnSe (b axis) decreases from 1486 S cm^{-1} at 300 K to 148 S cm^{-1} at 773 K. We estimated the carrier density at 300 K using Hall data as ~4 × 10^{19} cm^{-3}. The Seebeck coefficient is ~+160 μV K^{-1} at 300 K, close to that of commercial $Bi_{2-x}Sb_xTe_3$ with similar hole concentrations (*24*), and increases to ~+300 μV K^{-1} at 773 K. The combination of increased electrical conductivity and high Seebeck coefficient results in a *PF* of ~40 μW cm^{-1} K^{-2} for hole-doped SnSe (b axis) at 300 K (Fig. 2C). This value rivals that of optimized p-type $Bi_{2-x}Sb_xTe_3$ along its ab crystallographic plane direction (*24*). The *PF*s remain at a high value of ~14 μW cm^{-1} K^{-2} around 773 K for hole-doped SnSe (b axis), which is twice as high as the value of ~6.4 μW cm^{-1} K^{-2} at 773 K for the undoped SnSe (b axis) (Fig. 2C, inset). Therefore, the main contribution to the huge enhancement of ZT from 300 to 773 K is the superior *PF* afforded by doping.

The total thermal conductivity (κ_{tot}) of hole-doped SnSe is low and shows a decreasing trend with rising temperature (Fig. 2D). κ_{tot} of hole-doped SnSe (b axis) decreases from ~1.65 W m^{-1} K^{-1} at 300 K to ~0.55 W m^{-1} K^{-1} at 773 K. The lattice thermal conductivity (κ_{lat}) of hole-doped SnSe is as low as that of undoped SnSe. We previously explained this low thermal conductivity in terms of density functional theory (DFT)–calculated large Grüneisen parameters of SnSe caused by strong anharmonic bonding (*18*). This anharmonicity has recently been experimentally confirmed by inelastic neutron scattering measurements (*25*). The κ_{lat} values of hole-doped SnSe are still as low as that (0.2 to 0.3 W m^{-1} K^{-1}) of undoped SnSe at 773 K (fig. S2D). We note that the intrinsically

[1]School of Materials Science and Engineering, Beihang University, Beijing 100191, China. [2]Department of Chemistry, Northwestern University, Evanston, IL 60208, USA. [3]Department of Materials Science and Engineering, Northwestern University, Evanston, IL 60208, USA. [4]Department of Physics, South University of Science and Technology of China, Shenzhen 518055, China. [5]Department of Physics, University of Michigan, Ann Arbor, MI 48109, USA. [6]Materials Science, California Institute of Technology, Pasadena, CA 91125, USA.
*Corresponding author. E-mail: zhaolidong@buaa.edu.cn (L.-D.Z.); m-kanatzidis@northwestern.edu (M.G.K.)

low thermal conductivity of SnSe is sensitive to the stoichiometric ratio (*26*) and the sample processing conditions (*27*). A recent neutron powder diffraction analysis demonstrated a nearly ideal stoichiometry and an exceptionally high anharmonicity of the chemical bonds of SnSe and reported an ultralow thermal conductivity value close to 0.1 W m^{-1} K^{-1} at room temperature for polycrystalline SnSe (*26*). By strictly eliminating exposure to the atmosphere during sample preparation, Zhang *et al.* (*27*) observed lattice thermal conductivities of polycrystalline SnSe as low as those of the SnSe single crystals (*18*).

The *PF*s achieved in hole-doped SnSe are much higher than those in the rock-salt lead and tin chalcogenides (*19*, *28*–*30*), especially in the 300 to 500 K range. These high *PF*s derive from the much larger Seebeck coefficient, because the electrical conductivity of hole-doped SnSe (*b* axis) is comparable to those of rock-salt chalcogenides. To obtain insight into the enhanced Seebeck coefficients and PFs, we plotted (similar to a Pisarenko plot) the room-temperature Seebeck coefficients of rock-salt chalcogenides with similar carrier density of ~4 × 10^{19} cm^{-3} (Fig. 3A). The Seebeck coefficient for hole-doped SnSe at ~+160 μV K^{-1} is clearly much higher than ~+70 μV K^{-1} for PbTe (*19*), ~ +60 μV K^{-1} for PbSe (*28*), ~+50 μV K^{-1} for PbS (*29*), and ~+25 μV K^{-1} for SnTe (*30*).

For heavily hole-doped PbTe and PbSe, the Fermi level is pushed downward toward the heavy valence band (*19*), enhancing the Seebeck coefficient because of the contribution of this second valence band to transport. This enhancement, however, only appears at high temperatures, as the extra contribution of the heavy valence band requires a carrier density of (~4 to 5) × 10^{19} cm^{-3} and (1 to 2) × 10^{20} cm^{-3} at 300 K because the energy difference between the two valence bands in PbTe (0.15 eV) (*15*) and PbSe (0.25 eV) (*19*) decreases at high temperatures. The energy difference for PbS and SnTe between the two bands is even larger (>0.3 eV) (*29*, *30*), resulting in decreasing Seebeck coefficients from PbTe, to PbSe, to PbS, to SnTe (Fig. 3A). We observed a much larger Seebeck coefficient of ~+160 μV K^{-1} (at 300 K) for the hole-doped SnSe than expected from a single-band contribution (~+30 μV K^{-1}), which is well supported by the Pisarenko plot (Fig. 3B). The large Seebeck coefficient suggests the contribution of more than one valence band. This conclusion is supported by Hall data and DFT calculations of the band structure.

The Hall coefficient (R_H) is consistent with multivalley transport, as it shows a continuous increase with temperature in the range 10 to 773 K (fig. S3A). The values of R_H in hole-doped SnSe are temperature dependent, thus ruling out the single-band model of transport. The Hall data imply that the convergence of multiple band maxima of hole-doped SnSe is in effect already at very low temperatures; i.e., the energy difference between the competing valence bands is much lower than in other chalcogenide materials. To estimate the energy gap (ΔE) between the first two bands, we used a well-developed model for a typical two-band compound to analyze the Hall data. In this model, the temperature-dependent $R_H(T)$ can be expressed as (*19*)

$$\frac{R_H(T) - R_H(0)}{R_H(0)} = \left(1 - \frac{\mu_2}{\mu_1}\right)^2 \left(\frac{m_2}{m_1}\right)^{3/2} e^{-\frac{\Delta E}{k_B T}} \quad (2)$$

where $R_H(0)$ represents the Hall coefficient at 0 K; μ_1, μ_2, and m_1, m_2 denote the carrier mobilities and density-of-states (DOS) effective masses of the first and the second valence band, respectively; k_B is the Boltzmann constant; and ΔE is the energy separation between the two valence band maxima. The slope ($-\Delta E/k_B$) of $\ln[R_H(T) - R_H(0)]/R_H(0)$ versus $1/T$ yields ΔE ~ 0.02 eV at 0 K, assuming that ΔE varies linearly with temperature (fig. S4). This energy gap between the first two valence bands of SnSe is much smaller than that in PbTe, PbSe, PbS, and SnTe (*19*, *28*–*31*). The ΔE ~ 0.02 eV value is comparable to k_BT at room temperature, suggesting that the valence bands are nearly equal in energy. This near-degeneracy is consistent with the much higher Seebeck coefficients and *PF*s observed at room temperature. As the temperature increases, the carriers are thermally distributed over several bands of similar energy, resulting in the enhanced Seebeck coefficient of ~+160 μV K^{-1} at 300 K.

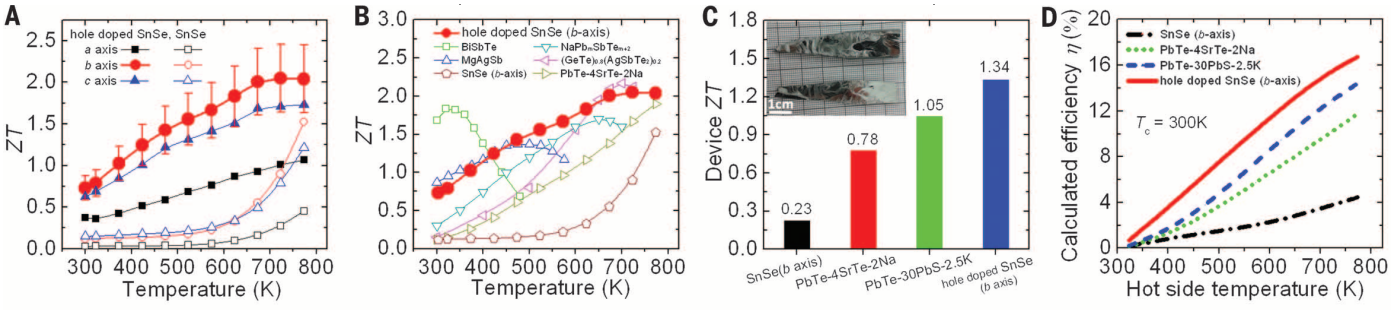

Fig. 1. *ZT* values of hole-doped SnSe crystals and projected efficiency. (**A**) *ZT* values along different axial directions of hole-doped SnSe and undoped SnSe crystals (*18*); the *ZT* measurement uncertainty is about 20%. (**B**) *ZT* values of hole-doped SnSe (*b* axis) and the current state-of-the-art p-type thermoelectrics, BiSbTe (*20*), MgAgSb (*14*), $(GeTe)_{0.8}(AgSbTe_2)_{0.2}$ (*21*), $NaPb_mSbTe_{m+2}$ (SALT) (*10*), PbTe-4SrTe-2Na (*9*), and SnSe (*b* axis) (*18*). (**C**) Device *ZT* values of hole-doped SnSe (*b* axis), undoped SnSe (*b* axis) (*18*), PbTe-4SrTe-2Na (*9*), and PbTe-30PbS-2.5K (*23*); inset shows typical hole-doped SnSe crystals. The temperature range for these values is from 300 to 773 K. (**D**) The calculated efficiency as a function of hot side temperature (cold side temperature is 300 K) of hole-doped SnSe (*b* axis), undoped SnSe (*b* axis) (*18*), PbTe-4SrTe-2Na (*9*), and PbTe-30PbS-2.5K (*23*).

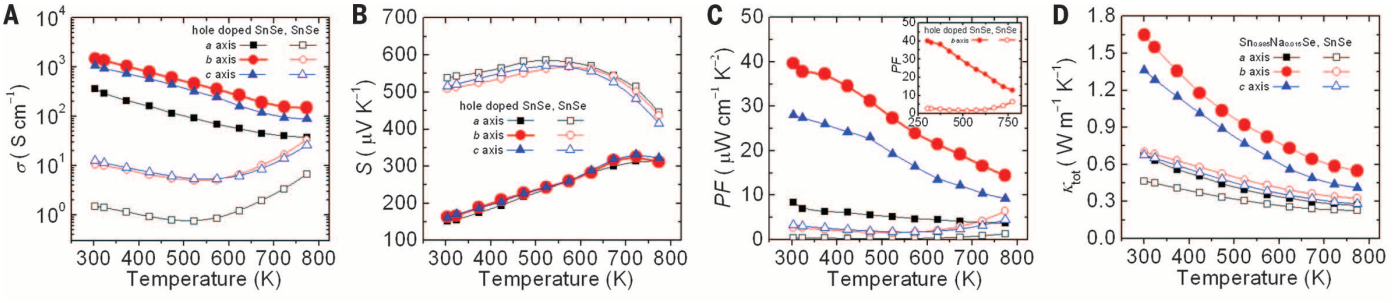

Fig. 2. Thermoelectric properties as a function of temperature for hole-doped SnSe crystals. (**A**) Electrical conductivity. (**B**) Seebeck coefficient. (**C**) Power factor (*PF*); the inset shows the *PF*s of hole-doped SnSe and undoped SnSe along the *b* axis. (**D**) Total thermal conductivity.

We analyzed the electronic structure and thermoelectric properties of hole-doped SnSe using DFT calculations of the low-temperature *Pnma* phase (Fig. 3C). The DFT valence band maximum (VBM) lies in the Γ-*Z* direction (band 1 in Fig. 3C), but another valence band is located just below the VBM (band 2). A third band also exists with its band maximum along the *U*-*X* direction (band 3). The calculation shows a very small energy gap between the first two valence bands in the Γ-*Z* direction of ~0.06 eV, consistent with the very small value experimentally estimated above (0.02 eV). We found this slight energy difference between calculation and experiment to be reasonable given the approximations underlying the DFT calculations. Such a small energy gap is easily crossed by the Fermi level as the hole doping approaches (~4 to 5) × 10^{19} cm^{-3}. In addition, the energy gap between the first and the third band (i.e., maximum of *U*-*X* to the maximum Γ-*Z*) is only 0.13 eV. This value is smaller than the 0.15 eV between the first and the second valence bands of PbTe, in which the heavy hole band contribution becomes considerable as the carrier density exceeds ~(4 to 5) × 10^{19} cm^{-3} (*19*, *31*). Interestingly, the electronic valence bands of SnSe are much more complex than those of PbTe, and the Fermi level of SnSe even approaches the fourth, fifth, and sixth valence bands for doping levels as high as 5 × 10^{20} cm^{-3} (Fig. 3C). Another illustration of the complex band structure is shown in the Fermi surface, which has multiple types of pockets (or valleys) coming from the numerous valence bands, all within a small energy window (Fig. 3, C to F). The multitude of valence band maxima is a distinctive feature of SnSe and is absent in the rock-salt chalcogenides.

The SnSe effective masses at each valence-band extremum are also anisotropic, in agreement with previous calculations (*32*). Because of the 2D nature of the material, the effective mass has a larger value along the k_x direction (*a* axis) than along either of the in-plane directions k_y and k_z (*b* and *c* axes). For the first valence maximum along Γ-*Z*, the effective masses are $m_{kx}^* = 0.76\ m_0$, $m_{ky}^* = 0.33\ m_0$, and $m_{kz}^* = 0.14\ m_0$. For the second maximum along Γ-*Z*, the $m_{kx}^* = 2.49\ m_0$, $m_{ky}^* = 0.18\ m_0$, and $m_{kz}^* = 0.19\ m_0$ are heavier than for the first band. These heavy holes play an important role in enhancing the Seebeck coefficients. We also performed Seebeck coefficient calculations as a function of hole concentration at 300 K using both a single-band model and a calculation that includes multivalley effects (*33*). We calculated the Seebeck coefficients by taking into account multiple valleys (considering all bands within ±2 eV of the Fermi level) and using a single parabolic band model with three different effective masses: $m_d^* = 0.47\ m_0$, $m_d^* = 0.75\ m_0$, and $m_d^* = 1.20\ m_0$ (Fig. 3B). The Seebeck coefficient calculated with the full, multivalley DFT band structure is +168 μV K^{-1} at 4 × 10^{19} cm^{-3}, which is very close to the experimentally observed value for this carrier concentration, +160 μV K^{-1}. In contrast, using a single-band model, we cannot reproduce the experimental Seebeck coefficient, even with a range of possible effective masses: A single-band model with our calculated DOS effective mass (0.47 m_0) from the first VBM yields a Seebeck coefficient of only +84 μV K^{-1} at 4 × 10^{19} cm^{-3}. An estimated effective mass of 0.75 m_0, obtained by fitting experimental Seebeck coefficients in polycrystalline SnSe (*34*, *35*), gives a single-band model Seebeck coefficient of ~+110 μV K^{-1} at 4 × 10^{19} cm^{-3}. The effective mass $m_d^* = 1.20\ m_0$ is an extreme value that we obtained by fitting the single-band Seebeck coefficients at extremely low concentrations (e.g., <1 × 10^{17} cm^{-3}) to the full multivalley calculated Seebeck coefficients. Even with this very heavy effective mass, the Seebeck coefficients (Fig. 3B, black dashed line) are still lower than those of the multivalley model at higher hole concentrations. We cannot explain the observed Seebeck coefficient enhancements with a single-band model, even with a wide range of possible effective masses. In SnSe, the experimental Seebeck coefficients exhibit isotropic values (Fig. 2B) along all three crystallographic directions. The electrical conductivity values, however, along these directions

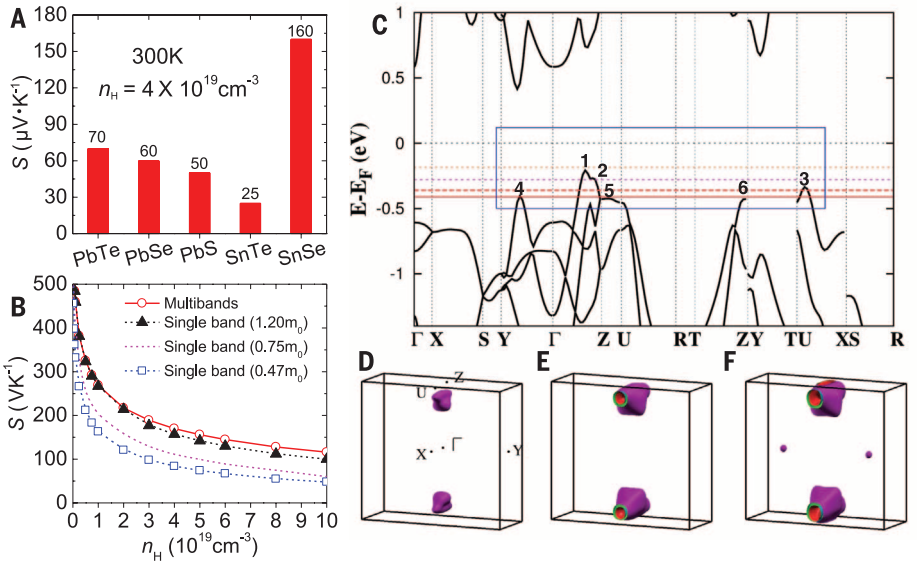

Fig. 3. Comparison of Seebeck coefficients of lead and tin chalcogenides, Pisarenko line, and DFT electronic band structure (*Pnma*). (**A**) Room-temperature Seebeck coefficients for lead and tin chalcogenides (*19*, *28*–*30*) with a similar carrier density of ~4 × 10^{19} cm^{-3}. (**B**) Calculated Seebeck coefficients as a function of carrier density at 300 K. The line connecting the red circles is calculated from the full multivalley DFT band structure. Single-band calculations yield lower Seebeck coefficients, even for a range of effective masses, and cannot reproduce the measured values. (**C**) Electronic band structure of hole-doped SnSe indicates nonparabolic, complex multiband valence states. The red dotted lines (from top to bottom) represent the Fermi levels with carrier densities of 5 × 10^{17}, 5 × 10^{19}, 2 × 10^{20}, and 5 × 10^{20} cm^{-3}, respectively, indicating that heavy doping pushes the Fermi level deep into the multivalence band structure. (**D** to **F**) The Fermi surfaces of SnSe (*Pnma*) at 5 × 10^{19}, 2 × 10^{20}, and 5 × 10^{20} cm^{-3}, respectively. The Fermi surface also illustrates the multiple types of pockets (or valleys) coming from the numerous valence bands, all within a small energy window.

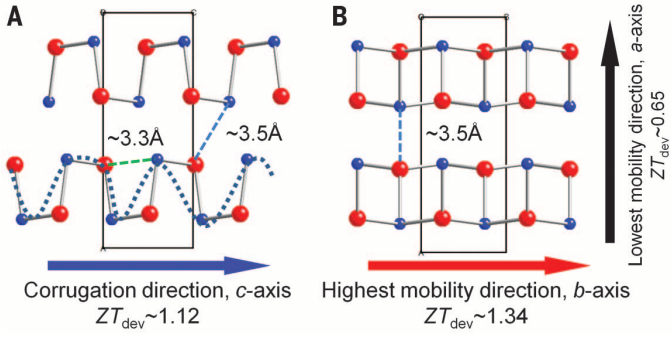

Fig. 4. Crystal structure of SnSe. The structure is shown along (**A**) the *c*-axis direction and (**B**) the *b*-axis direction. Blue atoms are Sn, red atoms are Se. The dashed wavy line is shown as a rough guide to the corrugation motif in the 2D slab. The closest Sn···Se interactions between the slabs are indicated with the blue dashed lines. The corrugation spacing within a single SnSe slab is also indicated with the green dashed line. The arrows indicate the directions along which the ZT_{dev} is marked.

are different and reflect the respective mobilities, with the highest being along the *b* and *c* axes, in agreement with the calculated lighter effective masses along these axes. The distinctive crystal structure of SnSe, therefore, plays a key role in the exceptional electronic band structure characteristics that result in an ultrahigh *PF* and *ZT*. The 2D sheets in SnSe have strong, accordion-like corrugation and are well separated from one another, with long intersheet Sn···Se bonding interactions of ~3.5 Å (Fig. 4). Longer Sn-Se bonding interactions of ~3.3 Å are also present along the corrugation direction (*c* axis). Along the *c* and *b* directions, the Sn-Se bonding is shorter, at 3.3 and 2.8 Å, respectively. As a result, the width of the valence bands along these in-plane directions is wider (and the effective hole masses lower) than along the *a* direction (lower carrier mobilities and larger effective hole masses).

We demonstrate that hole doping SnSe pushes its Fermi level deep into the band structure, activating multiple valence band maxima that lie close together in energy, enabling enhanced Seebeck coefficients and power factors (*PF*s). Therefore, the unique electronic band structure of SnSe is key to the high power factor and thermoelectric performance of the doped samples over a wide temperature plateau, from 300 to 773 K. The high conversion efficiency improves the prospects of realizing very efficient thermoelectric devices with hole-doped SnSe crystals as a p-type leg.

REFERENCES AND NOTES

1. L. E. Bell, *Science* **321**, 1457–1461 (2008).
2. J. P. Heremans, M. S. Dresselhaus, L. E. Bell, D. T. Morelli, *Nat. Nanotechnol.* **8**, 471–473 (2013).
3. X. Zhang, L. D. Zhao, *J. Materiomics* **1**, 92–105 (2015).
4. M. S. Dresselhaus *et al.*, *Adv. Mater.* **19**, 1043–1053 (2007).
5. L. D. Zhao, V. P. Dravid, M. G. Kanatzidis, *Energy Environ. Sci.* **7**, 251–268 (2014).
6. K. F. Hsu *et al.*, *Science* **303**, 818–821 (2004).
7. B. Poudel *et al.*, *Science* **320**, 634–638 (2008).
8. M. Zhou, J. F. Li, T. Kita, *J. Am. Chem. Soc.* **130**, 4527–4532 (2008).
9. K. Biswas *et al.*, *Nature* **489**, 414–418 (2012).
10. P. F. R. Poudeu *et al.*, *Angew. Chem. Int. Ed.* **45**, 3835–3839 (2006).
11. J. P. Heremans *et al.*, *Science* **321**, 554–557 (2008).
12. Y. Pei *et al.*, *Nature* **473**, 66–69 (2011).
13. W. Liu *et al.*, *Phys. Rev. Lett.* **108**, 166601 (2012).
14. H. Z. Zhao *et al.*, *Nano Energy* **7**, 97–103 (2014).
15. L. D. Zhao *et al.*, *J. Am. Chem. Soc.* **135**, 7364–7370 (2013).
16. X. Shi *et al.*, *J. Am. Chem. Soc.* **133**, 7837–7846 (2011).
17. M. M. Nassary, *Turk. J. Phys.* **33**, 201–208 (2009).
18. L. D. Zhao *et al.*, *Nature* **508**, 373–377 (2014).
19. Y. I. Ravich, B. A. Efimova, I. A. Smirnov, *Semiconducting Lead Chalcogenides* (Plenum, New York, 1970), vol. 5.
20. S. I. Kim *et al.*, *Science* **348**, 109–114 (2015).
21. S. K. Placheova, *Phys. Status Solidi (a)* **83**, 349–355 (1984).
22. G. J. Snyder, in *Thermoelectrics Handbook: Macro to Nano*, D. M. Rowe, Ed. (CRC/Taylor and Francis, Boca Raton, FL, 2006), chap. 9.
23. H. J. Wu *et al.*, *Nat. Commun.* **5**, 4515 (2014).
24. D. M. Rowe, *CRC Handbook of Thermoelectrics* (CRC Press, London, 1995).
25. C. W. Li *et al.*, *Nat. Phys.* **11**, 1063–1069 (2015).
26. F. Serrano-Sánchez *et al.*, *Appl. Phys. Lett.* **106**, 083902 (2015).
27. Q. Zhang *et al.*, *Adv. Energy Mater.* **5**, 1500360 (2015).
28. H. Wang, Y. Pei, A. D. LaLonde, G. J. Snyder, *Adv. Mater.* **23**, 1366–1370 (2011).
29. L. D. Zhao *et al.*, *J. Am. Chem. Soc.* **134**, 7902–7912 (2012).
30. G. Tan *et al.*, *J. Am. Chem. Soc.* **136**, 7006–7017 (2014).
31. Y. Pei, H. Wang, G. J. Snyder, *Adv. Mater.* **24**, 6125–6135 (2012).
32. G. Shi, E. Kioupakis, *J. Appl. Phys.* **117**, 065103 (2015).
33. Details of the calculations are available as supplementary materials on *Science* Online.
34. C. L. Chen, H. Wang, Y. Y. Chen, T. Day, G. J. Snyder, *J. Mater. Chem. A* **2**, 11171–11176 (2014).
35. S. Sassi *et al.*, *Appl. Phys. Lett.* **104**, 212105 (2014).

ACKNOWLEDGMENTS

This work was supported in part by the U.S. Department of Energy, Office of Science and Office of Basic Energy Sciences, under award DE-SC0014520 (G.T., H.C., V.P.D., S.H., C.W., and M.G.K.); and S3TEC-EFRC grant DE-SC0001299 (G.J.S.). This work was also supported by the "Zhuoyue" Program from Beihang University and the Recruitment Program for Young Professionals and the National Natural Science Foundation of China under grant 51571007 (L.-D.Z., Y.P., S.G., and H.X.). and by the Science, Technology and Innovation Commission of Shenzhen Municipality under grant no. ZDSYS20141118160434515 and Guangdong Science and Technology Fund under grant no. 2015A030308001 (J.H.). The synthesis, characterization, transport measurements, and DFT calculations were supported by DE-SC0014520. The validation measurements were supported by DE-SC0001299. Measurements at University of Michigan (C.U.) were supported by Energy Frontier Research Centers (EFRC) grant DE-SC0001054. All data in the main text and the supplementary materials are available online at www.sciencemag.org.

SUPPLEMENTARY MATERIALS

www.sciencemag.org/content/351/6269/141/suppl/DC1
Materials and Methods
Supplementary Text
Figs. S1 to S13
References (*36*–*47*)

3 September 2015; accepted 12 November 2015
Published online 26 November 2015
10.1126/science.aad3749

GEOPHYSICS

Shear deformation of bridgmanite and magnesiowüstite aggregates at lower mantle conditions

Jennifer Girard, George Amulele,* Robert Farla,† Anwar Mohiuddin, Shun-ichiro Karato‡

Rheological properties of the lower mantle have strong influence on the dynamics and evolution of Earth. By using the improved methods of quantitative deformation experiments at high pressures and temperatures, we deformed a mixture of bridgmanite and magnesiowüstite under the shallow lower mantle conditions. We conducted experiments up to about 100% strain at a strain rate of about 3×10^{-5} second^{-1}. We found that bridgmanite is substantially stronger than magnesiowüstite and that magnesiowüstite largely accommodates the strain. Our results suggest that strain weakening and resultant shear localization likely occur in the lower mantle. This would explain the preservation of long-lived geochemical reservoirs and the lack of seismic anisotropy in the majority of the lower mantle except the boundary layers.

Earth's large, rocky lower mantle is mostly composed of $(Mg,Fe)SiO_3$ bridgmanite (~70%) and (Mg,Fe)O magnesiowüstite (~20%) (and a few percent of calcium perovskite $CaSiO_3$) [e.g., (*1*)]. Many of Earth's geochemical and geophysical questions depend strongly on the rheological properties of materials in this region. For instance, geochemical observations suggest that the lower mantle hosts a large amount of incompatible elements working as a reservoir of these elements (*2*, *3*). The degree of preservation of these reservoirs is controlled by the nature of mixing or stirring of materials (*4*, *5*), which strongly depends on the rheological properties of materials in this region. However, very little is currently known about the rheological properties of materials in the lower mantle because of the difficulties in quantitative experimental studies of deformation under the conditions of the lower mantle.

Department of Geology and Geophysics, Yale University, New Haven, CT, USA.
*Present address: Department of Earth and Planetary Sciences, Macquarie University, Sydney, NSW, Australia. †Present address: Bayerisches Geoinstitut, Universität Bayreuth, Bayreuth, Germany.
‡Corresponding author. E-mail: shun-ichiro.karato@yale.edu

The main difficulties include the controlled generation of stress (or strain rate) and reliable measurements of stress and strain under the high-pressure and -temperature conditions [e.g., (*6*)]. Consequently, previous studies on plastic deformation of lower mantle minerals were either performed at high pressures and low temperatures (*7*–*10*), at high pressures and high temperatures without stress-strain rate control (*11*), or on analog materials at low pressures (*12*–*14*). Applying low-temperature experiments to Earth's interior is difficult because rheological properties are highly sensitive to temperature. Also the mechanisms by which deformation occurs are sensitive to temperature and strain rate, creating extrapolation issues for both low-temperature and poorly controlled strain-rate (stress) measurements [e.g., (*15*)]. Furthermore, microstructural evolution often leads to strain-dependent rheological behavior, which is particularly important for a sample containing two materials with a large strength contrast (*16*). The lower mantle approximates a two-phase mixture (bridgmanite and magnesiowüstite) with presumably a large strength contrast [e.g., (*13*, *17*, *18*)], and therefore large strain (>30%) experiments are essential to

are different and reflect the respective mobilities, with the highest being along the *b* and *c* axes, in agreement with the calculated lighter effective masses along these axes. The distinctive crystal structure of SnSe, therefore, plays a key role in the exceptional electronic band structure characteristics that result in an ultrahigh *PF* and *ZT*. The 2D sheets in SnSe have strong, accordion-like corrugation and are well separated from one another, with long intersheet Sn···Se bonding interactions of ~3.5 Å (Fig. 4). Longer Sn-Se bonding interactions of ~3.3 Å are also present along the corrugation direction (*c* axis). Along the *c* and *b* directions, the Sn-Se bonding is shorter, at 3.3 and 2.8 Å, respectively. As a result, the width of the valence bands along these in-plane directions is wider (and the effective hole masses lower) than along the *a* direction (lower carrier mobilities and larger effective hole masses).

We demonstrate that hole doping SnSe pushes its Fermi level deep into the band structure, activating multiple valence band maxima that lie close together in energy, enabling enhanced Seebeck coefficients and power factors (*PF*s). Therefore, the unique electronic band structure of SnSe is key to the high power factor and thermoelectric performance of the doped samples over a wide temperature plateau, from 300 to 773 K. The high conversion efficiency improves the prospects of realizing very efficient thermoelectric devices with hole-doped SnSe crystals as a p-type leg.

REFERENCES AND NOTES

1. L. E. Bell, *Science* **321**, 1457–1461 (2008).
2. J. P. Heremans, M. S. Dresselhaus, L. E. Bell, D. T. Morelli, *Nat. Nanotechnol.* **8**, 471–473 (2013).
3. X. Zhang, L. D. Zhao, *J. Materiomics* **1**, 92–105 (2015).
4. M. S. Dresselhaus *et al.*, *Adv. Mater.* **19**, 1043–1053 (2007).
5. L. D. Zhao, V. P. Dravid, M. G. Kanatzidis, *Energy Environ. Sci.* **7**, 251–268 (2014).
6. K. F. Hsu *et al.*, *Science* **303**, 818–821 (2004).
7. B. Poudel *et al.*, *Science* **320**, 634–638 (2008).
8. M. Zhou, J. F. Li, T. Kita, *J. Am. Chem. Soc.* **130**, 4527–4532 (2008).
9. K. Biswas *et al.*, *Nature* **489**, 414–418 (2012).
10. P. F. R. Poudeu *et al.*, *Angew. Chem. Int. Ed.* **45**, 3835–3839 (2006).
11. J. P. Heremans *et al.*, *Science* **321**, 554–557 (2008).
12. Y. Pei *et al.*, *Nature* **473**, 66–69 (2011).
13. W. Liu *et al.*, *Phys. Rev. Lett.* **108**, 166601 (2012).
14. H. Z. Zhao *et al.*, *Nano Energy* **7**, 97–103 (2014).
15. L. D. Zhao *et al.*, *J. Am. Chem. Soc.* **135**, 7364–7370 (2013).
16. X. Shi *et al.*, *J. Am. Chem. Soc.* **133**, 7837–7846 (2011).
17. M. M. Nassary, *Turk. J. Phys.* **33**, 201–208 (2009).
18. L. D. Zhao *et al.*, *Nature* **508**, 373–377 (2014).
19. Y. I. Ravich, B. A. Efimova, I. A. Smirnov, *Semiconducting Lead Chalcogenides* (Plenum, New York, 1970), vol. 5.
20. S. I. Kim *et al.*, *Science* **348**, 109–114 (2015).
21. S. K. Placheova, *Phys. Status Solidi (a)* **83**, 349–355 (1984).
22. G. J. Snyder, in *Thermoelectrics Handbook: Macro to Nano*, D. M. Rowe, Ed. (CRC/Taylor and Francis, Boca Raton, FL, 2006), chap. 9.
23. H. J. Wu *et al.*, *Nat. Commun.* **5**, 4515 (2014).
24. D. M. Rowe, *CRC Handbook of Thermoelectrics* (CRC Press, London, 1995).
25. C. W. Li *et al.*, *Nat. Phys.* **11**, 1063–1069 (2015).
26. F. Serrano-Sánchez *et al.*, *Appl. Phys. Lett.* **106**, 083902 (2015).
27. Q. Zhang *et al.*, *Adv. Energy Mater.* **5**, 1500360 (2015).
28. H. Wang, Y. Pei, A. D. LaLonde, G. J. Snyder, *Adv. Mater.* **23**, 1366–1370 (2011).
29. L. D. Zhao *et al.*, *J. Am. Chem. Soc.* **134**, 7902–7912 (2012).
30. G. Tan *et al.*, *J. Am. Chem. Soc.* **136**, 7006–7017 (2014).
31. Y. Pei, H. Wang, G. J. Snyder, *Adv. Mater.* **24**, 6125–6135 (2012).
32. G. Shi, E. Kioupakis, *J. Appl. Phys.* **117**, 065103 (2015).
33. Details of the calculations are available as supplementary materials on *Science* Online.
34. C. L. Chen, H. Wang, Y. Y. Chen, T. Day, G. J. Snyder, *J. Mater. Chem. A* **2**, 11171–11176 (2014).
35. S. Sassi *et al.*, *Appl. Phys. Lett.* **104**, 212105 (2014).

ACKNOWLEDGMENTS

This work was supported in part by the U.S. Department of Energy, Office of Science and Office of Basic Energy Sciences, under award DE-SC0014520 (G.T., H.C., V.P.D., S.H., C.W., and M.G.K.); and S3TEC-EFRC grant DE-SC0001299 (G.J.S.). This work was also supported by the "Zhuoyue" Program from Beihang University and the Recruitment Program for Young Professionals and the National Natural Science Foundation of China under grant 51571007 (L.-D.Z., Y.P., S.G., and H.X.). and by the Science, Technology and Innovation Commission of Shenzhen Municipality under grant no. ZDSYS20141118160434515 and Guangdong Science and Technology Fund under grant no. 2015A030308001 (J.H.). The synthesis, characterization, transport measurements, and DFT calculations were supported by DE-SC0014520. The validation measurements were supported by DE-SC0001299. Measurements at University of Michigan (C.U.) were supported by Energy Frontier Research Centers (EFRC) grant DE-SC0001054. All data in the main text and the supplementary materials are available online at www.sciencemag.org.

SUPPLEMENTARY MATERIALS

www.sciencemag.org/content/351/6269/141/suppl/DC1
Materials and Methods
Supplementary Text
Figs. S1 to S13
References (*36*–*47*)

3 September 2015; accepted 12 November 2015
Published online 26 November 2015
10.1126/science.aad3749

GEOPHYSICS

Shear deformation of bridgmanite and magnesiowüstite aggregates at lower mantle conditions

Jennifer Girard, George Amulele,* Robert Farla,† Anwar Mohiuddin, Shun-ichiro Karato‡

Rheological properties of the lower mantle have strong influence on the dynamics and evolution of Earth. By using the improved methods of quantitative deformation experiments at high pressures and temperatures, we deformed a mixture of bridgmanite and magnesiowüstite under the shallow lower mantle conditions. We conducted experiments up to about 100% strain at a strain rate of about 3×10^{-5} second^{-1}. We found that bridgmanite is substantially stronger than magnesiowüstite and that magnesiowüstite largely accommodates the strain. Our results suggest that strain weakening and resultant shear localization likely occur in the lower mantle. This would explain the preservation of long-lived geochemical reservoirs and the lack of seismic anisotropy in the majority of the lower mantle except the boundary layers.

Earth's large, rocky lower mantle is mostly composed of $(Mg,Fe)SiO_3$ bridgmanite (~70%) and (Mg,Fe)O magnesiowüstite (~20%) (and a few percent of calcium perovskite $CaSiO_3$) [e.g., (*1*)]. Many of Earth's geochemical and geophysical questions depend strongly on the rheological properties of materials in this region. For instance, geochemical observations suggest that the lower mantle hosts a large amount of incompatible elements working as a reservoir of these elements (*2*, *3*). The degree of preservation of these reservoirs is controlled by the nature of mixing or stirring of materials (*4*, *5*), which strongly depends on the rheological properties of materials in this region. However, very little is currently known about the rheological properties of materials in the lower mantle because of the difficulties in quantitative experimental studies of deformation under the conditions of the lower mantle.

Department of Geology and Geophysics, Yale University, New Haven, CT, USA.
*Present address: Department of Earth and Planetary Sciences, Macquarie University, Sydney, NSW, Australia. †Present address: Bayerisches Geoinstitut, Universität Bayreuth, Bayreuth, Germany.
‡Corresponding author. E-mail: shun-ichiro.karato@yale.edu

The main difficulties include the controlled generation of stress (or strain rate) and reliable measurements of stress and strain under the high-pressure and -temperature conditions [e.g., (*6*)]. Consequently, previous studies on plastic deformation of lower mantle minerals were either performed at high pressures and low temperatures (*7*–*10*), at high pressures and high temperatures without stress-strain rate control (*11*), or on analog materials at low pressures (*12*–*14*). Applying low-temperature experiments to Earth's interior is difficult because rheological properties are highly sensitive to temperature. Also the mechanisms by which deformation occurs are sensitive to temperature and strain rate, creating extrapolation issues for both low-temperature and poorly controlled strain-rate (stress) measurements [e.g., (*15*)]. Furthermore, microstructural evolution often leads to strain-dependent rheological behavior, which is particularly important for a sample containing two materials with a large strength contrast (*16*). The lower mantle approximates a two-phase mixture (bridgmanite and magnesiowüstite) with presumably a large strength contrast [e.g., (*13*, *17*, *18*)], and therefore large strain (>30%) experiments are essential to

characterize the evolution of rheological behavior of the lower mantle.

We performed large strain deformation experiments on a mixture of bridgmanite and magnesiowüstite by using the rotational Drickamer apparatus (*19*) at the synchrotron x-ray radiation facility (fig. S1). We have made several technical developments on the cell assembly (Fig. 1) and anvil design to increase the maximum pressure and to improve the quality of x-ray signals and performed quantitative deformation experiments under the conditions of the shallow lower mantle of Earth.

We prepared starting materials (ringwoodite or bridgmanite and magnesiowüstite) from San Carlos olivine by using the Kawai-type multianvil press. We carried out in situ deformation experiments at the shear strain rate of ~3×10^{-5} s^{-1} on lower mantle mineral mixtures at pressures at 24 to 27.5 GPa and temperatures up to 2000 to 2150 K (Table 1). All the deformed samples are a mixture of bridgmanite and magnesiowüstite with 1:1 mole ratio (~70:30 volume ratio). We estimated the pressure and temperature conditions by in situ x-ray diffraction data using the equations of state of bridgmanite and magnesiowüstite. We also estimated stress from radial x-ray diffraction and strain from x-ray image analysis of a Pt strain marker sandwiched vertically between two half rings of the sample (Fig. 1).

Stress increases with strain, initially achieving nearly steady state at strains higher than ~40%, with some hint of strain weakening for bridgmanite (Fig. 2). Because of a small sample size, the intensity of diffraction peaks is relatively weak, and we were able to determine the stress only from a limited number of diffraction planes. We used (110) and (112) planes for bridgmanite and (220) and (200) planes for magnesiowüstite. We took an arithmetic average of stress values from different planes to estimate the strength of each material. This is a crude way to estimate the strength of a polycrystalline material, but the precise relation between the strength of various slip systems and the average strength of an aggregate is not known [e.g., (*20*)]. Although the errors in the estimated stress are large, the results show that bridgmanite is likely substantially stronger than magnesiowüstite.

The microstructures of the deformed samples show evidence of substantial plastic deformation in both bridgmanite and magnesiowüstite (Fig. 3). Magnesiowüstite is isolated in most cases, whereas we infer bridgmanite to be interconnected on the basis of two-dimensional cross-sectional images. A large amount of strain accommodation by magnesiowüstite is evident from Fig. 3B, because magnesiowüstite is deformed more than the bulk strain. This is consistent with the conclusion drawn from the strength determination (Fig. 2). Our observations provide direct experimental verification that bridgmanite is substantially stronger than magnesiowüstite (*13*, *17*, *18*).

An obvious consequence of such a large rheological contrast is the evolution of strain partitioning with increasing strain, which may lead to shear localization [e.g., (*16*, *21*)]. Shear localization would limit substantial deformation to only in or near the boundary layers. Hence, stirring and mixing would occur selectively in these regions, with the rest of the lower mantle deforming very little. Relatively undeformed regions in the lower mantle, where little mass transport takes place, may act as long-lived geochemical reservoirs suggested by geochemical studies [e.g., (*2*, *5*)]. The possible localized deformation would also provide an alternative explanation for the absence of seismic anisotropy in the majority of the lower mantle other than the model proposed by Karato *et al.* (*22*), in which they attributed the absence of anisotropy in the majority of the lower mantle to the operation of diffusion creep.

Our conclusions are somewhat different from those by Wang *et al.* (*14*) on the $CaGeO_3$ perovskite and MgO analog system. They deformed their samples to less than 20% strain and found that $CaGeO_3$ perovskite is stronger than MgO by a factor of ~2. They concluded that the stronger phase $CaGeO_3$ perovskite controls the strength of the two-phase aggregate by comparing the results with the strength of pure $CaGeO_3$ perovskite.

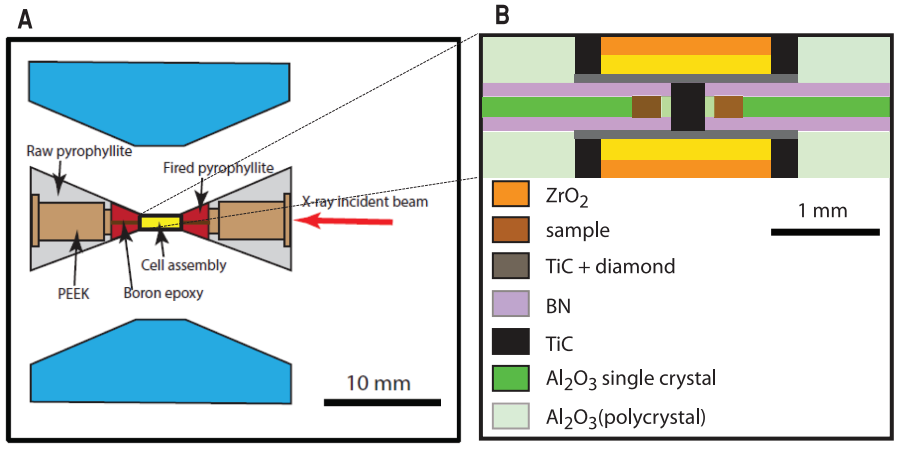

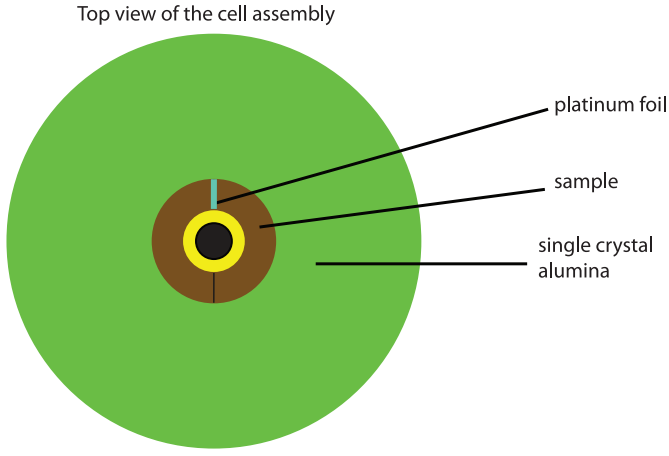

Fig. 1. The rotational Drickamer apparatus (RDA) cell assembly used to reach the shallow lower mantle conditions. (**A**) The anvils, gaskets, and cell assembly for the RDA deformation experiment; (**B**) a side view of the cell assembly; and (**C**) a top view of the cell assembly. Diffracted x-ray comes mostly from one side of a sample closer to the x-ray detectors.

Table 1. Summary of run conditions. The total strain is the equivalent strain, ε_E, including both axial compression strain (ε_U) and shear strain (ε_S) as $\varepsilon_E = \sqrt{\varepsilon_U^2 + \frac{4}{3}\varepsilon_S^2}$.

Run number	Temperature (K)	Pressure (GPa)	Total strain (%)	Strain rate ($\times 10^{-5}$ s^{-1})
beta 74*	2000 ± 100	24.1 ± 0.5	52	4.3
gamma 21*	2130 ± 100	27.0 ± 0.5	100	3.0
gamma 22	2130 ± 100	27.0 ± 0.5	55 ± 17	3.0 ± 0.9
gamma 23**	2140 ± 100	27.4 ± 0.5	0	0
gamma 24	2150 ± 100	27.5 ± 0.5	23 ± 7	3.2 ± 1.0
gamma 25	2150 ± 100	27.5 ± 0.5	48 ± 15	3.6 ± 1.1

*Strain marker was not visible in these runs. Strain was estimated from the angle of rotation of the anvil and the relationship between the angle of rotation and shear strain based on previous results. **After annealing, the furnace failed. No strain after annealing.

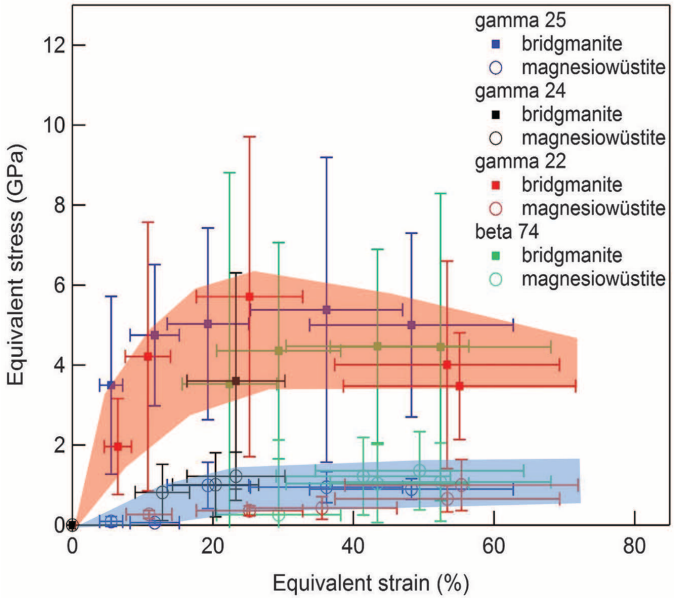

Fig. 2. A plot of the equivalent stress in bridgmanite and magnesiowüstite as a function of strain. Run conditions are given in Table 1. Stress in bridgmanite was estimated by using diffraction peaks (110) and (112). Stress in magnesiowüstite was estimated by using diffraction peaks (200) and (220). In both cases, the stresses shown here are the arithmetic average of stresses estimated from these planes. Some hint of strain weakening can be seen, particularly for bridgmanite (hatched regions are drawn to guide the eyes). Results from beta 74 are based on estimated strain (strain marker was not visible). Also, the pressure and temperature conditions for beta 74 are different from all others. Bars represent the errors. Errors are given for one standard deviation and are due to the uncertainties in the peak shift and the fitting errors to equation S1 (supplementary materials).

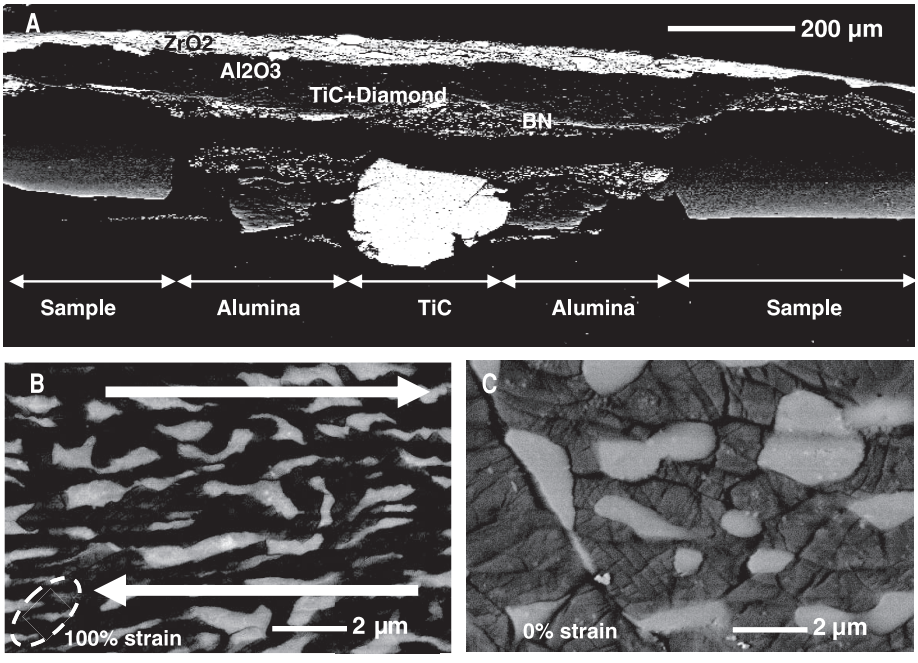

Fig. 3. SEM (scanning electron microscope) back-scattering images of the recovered sample from the run gamma 21. (**A**) A back-scattered electron image of the RDA cell assembly cut along the diameter. The sample position, alumina ring, and TiC central electrode are labeled for clarity. The layers of material above the sample are also identified (ZrO_2, Al_2O_3, TiC+Diamond, BN). (**B**) A back-scattered electron image of the recovered sample from the run gamma 21, deformed up to 100% strain. The light gray grains are mangesiowüstite, and the dark gray grains are bridgmanite. An oblate shape shows a strain ellipsoid corresponding to the bulk strain of 100%. Arrows indicate the sense of shear. (**C**) A back-scattered electron image of an undeformed sample from the run gamma 23. This sample was annealed at 27.4 GPa and 2140 K and quenched after 1.5 hours.

Although their observations on the strength contrast are similar to ours, we suggest that the larger strength contrast we observed for the lower mantle aggregate could promote shear localization more than an analog material where the strength contrast is less. Also, the difference in the strain magnitude may be responsible for the somewhat different results. Wang *et al.* (*14*) did not observe strain weakening but rather strain hardening at strain less than 20%. In that small strain regime, we also observed strain hardening. In contrast, we observed the hint of strain weakening at ~30% strain (Fig. 2). This suggests that the strength of the lower mantle aggregate could be controlled by a weaker phase at large strain. Similarly, a numerical study of deformation of a mixture of bridgmanite and magnesiowüstite by Madi *et al.* (*23*) showed no large strain partitioning to magnesiowüstite, but this study was made to very small strain (~10^{-4}).

We must examine the validity of the necessary extrapolation in strain rate (or stress level) from laboratory data to deformation in Earth. We conclude that dislocation creep dominates under the present experimental conditions on the basis of the large variation in stress estimated for different diffraction planes (*24*). Seismological observations of distribution of anisotropy suggest that dislocation creep may dominate in the boundary layers in the lower mantle (*25*). The stress dependence of strain rate in dislocation creep regime is similar between orthorhombic perovskite and magnesiowüstite (*26*, *27*). Consequently, the strength contrast between the two minerals deformed at geological strain rate would be similar to the contrast observed at laboratory strain rate in the boundary layer, where much of deformation occurs.

However, our current results contain major limitations, including (i) deformation mechanisms are not clearly identified, and the flow law was not determined in any detail; and (ii) the maximum strain is still low, and therefore the degree to which strain weakening could occur is unclear. In addition to well-characterized experimental studies to larger strains, characterization of strain weakening (and shear localization) may require numerical modeling, because small sample size might limit the full development of shear localization. The demonstration of significant stress-strain partitioning (and evolution) between the two major phases in the lower mantle, potentially resulting in shear localization, highlights the importance of experimental studies of deformation in interpreting geochemical and geodynamical observations.

REFERENCES AND NOTES

1. A. E. Ringwood, *Geochim. Cosmochim. Acta* **55**, 2083–2110 (1991).
2. A. W. Hofmann, *Nature* **385**, 219–229 (1997).
3. B. Marty, *Earth Planet. Sci. Lett.* **313-314**, 56–66 (2012).
4. U. R. Christensen, A. W. Hofmann, *J. Geophys. Res.* **99**, 19867–19884 (1994).
5. P. E. van Keken, E. H. Hauri, C. J. Ballentine, *Annu. Rev. Earth Planet. Sci.* **30**, 493–525 (2002).
6. S. Karato, D. J. Weidner, *Elements* **4**, 191–196 (2008).

7. H. Marquardt, L. Miyagi, *Nat. Geosci.* **8**, 311–314 (2015).
8. S. Merkel *et al.*, *Earth Planet. Sci. Lett.* **209**, 351–360 (2003).
9. S. Merkel *et al.*, *J. Geophys. Res.* **107**, 002002 (2002).
10. J. Chen, D. J. Weidner, M. T. Vaughan, *Nature* **419**, 824–826 (2002).
11. P. Cordier, T. Ungár, L. Zsoldos, G. Tichy, *Nature* **428**, 837–840 (2004).
12. S. Beauchesne, J.-P. Poirier, *Phys. Earth Planet. Inter.* **61**, 182–198 (1990).
13. S. Karato, *Phys. Earth Planet. Inter.* **55**, 234–240 (1989).
14. Y. Wang *et al.*, *Geochem. Geophys. Geosyst.* **14**, 3389–3408 (2013).
15. S. Karato, *Deformation of Earth Materials: Introduction to the Rheology of the Solid Earth* (Cambridge Univ. Press, Cambridge, 2008).
16. J. P. Bloomfield, S. J. Covey-Crump, *J. Struct. Geol.* **15**, 1007–1019 (1993).
17. S. Karato, *Phys. Earth Planet. Inter.* **24**, 1–14 (1981).
18. J. P. Poirier, J. Peyronneau, M. Madon, F. Guyot, A. Revcoleshi, *Nature* **321**, 603–605 (1986).
19. D. Yamazaki, S. Karato, *Rev. Sci. Instrum.* **72**, 4207–4211 (2001).
20. U. F. Kocks, *Metall. Trans.* **1**, 1121–1143 (1970).
21. M. R. Handy, *J. Struct. Geol.* **16**, 287–301 (1994).
22. S. Karato, S. Zhang, H.-R. Wenk, *Science* **270**, 458–461 (1995).
23. K. Madi, S. Forest, P. Cordier, M. Boussuge, *Earth Planet. Sci. Lett.* **237**, 223–238 (2005).
24. S. Karato, *Phys. Rev. B* **79**, 214106 (2009).
25. S. Karato, *Pure Appl. Geophys.* **151**, 565–587 (1998).
26. Z. Wang, C. Dupas-Bruzek, S. Karato, *Phys. Earth Planet. Inter.* **110**, 51–69 (1999).
27. T. G. Langdon, J. A. Pask, *Acta Metall.* **18**, 505–510 (1970).

ACKNOWLEDGMENTS

This study was supported by a grant from NSF. The experimental facilities at the Brookhaven National Laboratory are supported by the Department of Energy and COMPRES (Consortium for Materials Properties Research in Earth Sciences). We thank D. Weidner and H. Chen for the support at the synchrotron facility at Brookhaven National Laboratory. Z. Jiang provided technical support for the microstructural analyses. All data presented in this paper are available in the supplementary materials.

SUPPLEMENTARY MATERIALS

www.sciencemag.org/content/351/6269/144/suppl/DC1
Materials and Methods
Figs. S1 to S5
References (*28*–*41*)
Database S1

26 August 2015; accepted 12 November 2015
10.1126/science.aad3113

GEOMORPHOLOGY

Repeated catastrophic valley infill following medieval earthquakes in the Nepal Himalaya

Wolfgang Schwanghart,[1]* Anne Bernhardt,[1] Amelie Stolle,[1] Philipp Hoelzmann,[2] Basanta R. Adhikari,[3] Christoff Andermann,[4] Stefanie Tofelde,[1] Silke Merchel,[5] Georg Rugel,[5] Monique Fort,[6] Oliver Korup[1]

Geomorphic footprints of past large Himalayan earthquakes are elusive, although they are urgently needed for gauging and predicting recovery times of seismically perturbed mountain landscapes. We present evidence of catastrophic valley infill following at least three medieval earthquakes in the Nepal Himalaya. Radiocarbon dates from peat beds, plant macrofossils, and humic silts in fine-grained tributary sediments near Pokhara, Nepal's second-largest city, match the timing of nearby $M > 8$ earthquakes in ~1100, 1255, and 1344 C.E. The upstream dip of tributary valley fills and x-ray fluorescence spectrometry of their provenance rule out local sources. Instead, geomorphic and sedimentary evidence is consistent with catastrophic fluvial aggradation and debris flows that had plugged several tributaries with tens of meters of calcareous sediment from a Higher Himalayan source >60 kilometers away.

The M_w 7.8 Gorkha earthquake that struck Nepal in April 2015 confirmed high seismic risk projections for the Himalayas (*1*, *2*), inferred mostly from paleoseismological proxies of past events (*3*–*6*). Strong ground shaking caused the collapse of more than half a million homes, killing more than 8500 people and injuring more than 20,000. Landslides buried villages, roads, and river channels, consistent with coseismic impacts reported from other active mountain belts (*7*). Detailed sediment budgets show that landslides triggered by strong seismic ground shaking may rapidly detach millions to billions of cubic meters of rock, soil, and biomass, providing this material for subsequent entrainment by surface runoff and river flows (*8*). The resulting sediment pulses may fill even rapidly incising bedrock rivers by up to several tens of meters (*9*), thereby causing protracted channel instability, impeding access to emergency areas, destroying hydropower facilities, and compromising post-disaster rehabilitation efforts. Detailed mass balances of recent large earthquakes in China (*10*), Taiwan (*11*), Japan (*12*), and New Zealand (*13*) offer blueprints of how river networks recover from sudden input of excess sediment over several years to centuries. The high sediment transport rates in many mountain rivers, however, rarely sustain evidence of prehistoric earthquake-induced sedimentation pulses. In these cases, depositional records of catastrophic aggradation in forelands are more instructive (*14*). Both of these lines of evidence for understanding river network recovery have remained elusive in the Himalayas. We present exceptionally well-preserved sedimentary archives that connect landscape-scale disturbance around Pokhara, Nepal, to at least three documented medieval megathrust earthquakes (*3*).

The city of Pokhara (28°13′N, 83°59′E, 870 m above sea level) is located at the foot of the >8000-m peaks of the Annapurna Massif in the Seti Khola valley (Fig. 1). This steep orographic gradient receives monsoonal rainfall of ~4000 mm year^{-1} (*15*). Pokhara's geology features primarily Precambrian metamorphic sandstones, shales, and dolomites. Other rocks include Paleozoic phyllites and schists of the Lesser Himalayan Series (LHS). Higher Himalayan Crystalline (HHC) rocks north of the Main Central Thrust (MCT) are Precambrian high-grade metamorphic quartzites, schists, and gneisses (*16*, *17*). Marine calcareous metasediments of the Tethyan Sedimentary Series (TSS) prevail north of the South Tibetan Detachment Zone (*18*, *19*). Pokhara sits on a large sediment fan built by the upper Seti Khola that drains the partly glaciated and debris-filled Sabche Cirque in the Annapurna Massif. The fanhead near the MCT grades into a ~60-km-long flight of prominent terraces downstream that rise up to 140 m above the river bed and envelop several LHS bedrock hills (*20*). The fan has three stratigraphic units called the Tallakot, Ghachok, and Pokhara Formations. We focus on the youngest Pokhara Formation composed of extensive coarse gravel sheets, numerous boulders >10 m in diameter, and thick debris flow deposits. Digital topographic data (*21*) confirm damming of the more than a dozen tributaries along Seti Khola's course of >60 km by Pokhara Formation sediments (*20*). These deposits dip upstream into tributary valleys for >1 km and up to 7 km along the Magdi and Saraudi Khola featuring several meters of intercalated gravel, sand, and silt beds. We sampled enclosed peat beds, charcoal lenses, and plant macrofossils (figs. S1 and S2) for radiocarbon (^{14}C) dating and for any earthquake-related sedimentation in eight different tributaries (table S1).

Bayesian calibration of 26 ^{14}C ages with a prior informed by stratigraphic relationships between the samples (*22*) returned a pooled posterior distribution with three distinct peaks that match, within error, the timing of three large medieval earthquakes in ~1100, 1255, and 1344 C.E. (*3*–*5*) (Fig. 2, figs. S3 to S5, and table S2). Our oldest ^{14}C dates offer support for the timing of the ~1100 C.E. earthquake, which has so far been inferred from

[1]Institute of Earth and Environmental Science, University of Potsdam, Potsdam, Germany. [2]Institute of Geographical Sciences, Freie Universität Berlin, Berlin, Germany. [3]Institute of Engineering, Tribhuvan University, Kathmandu, Nepal. [4]Helmholtz-Zentrum Potsdam, German Centre for Geosciences GFZ, Germany. [5]Helmholtz-Zentrum Dresden-Rossendorf, Helmholtz Institute Freiberg for Resource Technology, Dresden, Germany. [6]CNRS UMR 8586 Prodig, Département de Géographie, Université Paris-Diderot-SPC, Paris, France.
*Corresponding author. E-mail: w.schwanghart@geo.uni-potsdam.de

7. H. Marquardt, L. Miyagi, *Nat. Geosci.* **8**, 311–314 (2015).
8. S. Merkel *et al.*, *Earth Planet. Sci. Lett.* **209**, 351–360 (2003).
9. S. Merkel *et al.*, *J. Geophys. Res.* **107**, 002002 (2002).
10. J. Chen, D. J. Weidner, M. T. Vaughan, *Nature* **419**, 824–826 (2002).
11. P. Cordier, T. Ungár, L. Zsoldos, G. Tichy, *Nature* **428**, 837–840 (2004).
12. S. Beauchesne, J.-P. Poirier, *Phys. Earth Planet. Inter.* **61**, 182–198 (1990).
13. S. Karato, *Phys. Earth Planet. Inter.* **55**, 234–240 (1989).
14. Y. Wang *et al.*, *Geochem. Geophys. Geosyst.* **14**, 3389–3408 (2013).
15. S. Karato, *Deformation of Earth Materials: Introduction to the Rheology of the Solid Earth* (Cambridge Univ. Press, Cambridge, 2008).
16. J. P. Bloomfield, S. J. Covey-Crump, *J. Struct. Geol.* **15**, 1007–1019 (1993).
17. S. Karato, *Phys. Earth Planet. Inter.* **24**, 1–14 (1981).
18. J. P. Poirier, J. Peyronneau, M. Madon, F. Guyot, A. Revcoleshi, *Nature* **321**, 603–605 (1986).
19. D. Yamazaki, S. Karato, *Rev. Sci. Instrum.* **72**, 4207–4211 (2001).
20. U. F. Kocks, *Metall. Trans.* **1**, 1121–1143 (1970).
21. M. R. Handy, *J. Struct. Geol.* **16**, 287–301 (1994).
22. S. Karato, S. Zhang, H.-R. Wenk, *Science* **270**, 458–461 (1995).
23. K. Madi, S. Forest, P. Cordier, M. Boussuge, *Earth Planet. Sci. Lett.* **237**, 223–238 (2005).
24. S. Karato, *Phys. Rev. B* **79**, 214106 (2009).
25. S. Karato, *Pure Appl. Geophys.* **151**, 565–587 (1998).
26. Z. Wang, C. Dupas-Bruzek, S. Karato, *Phys. Earth Planet. Inter.* **110**, 51–69 (1999).
27. T. G. Langdon, J. A. Pask, *Acta Metall.* **18**, 505–510 (1970).

ACKNOWLEDGMENTS

This study was supported by a grant from NSF. The experimental facilities at the Brookhaven National Laboratory are supported by the Department of Energy and COMPRES (Consortium for Materials Properties Research in Earth Sciences). We thank D. Weidner and H. Chen for the support at the synchrotron facility at Brookhaven National Laboratory. Z. Jiang provided technical support for the microstructural analyses. All data presented in this paper are available in the supplementary materials.

SUPPLEMENTARY MATERIALS

www.sciencemag.org/content/351/6269/144/suppl/DC1
Materials and Methods
Figs. S1 to S5
References (*28*–*41*)
Database S1

26 August 2015; accepted 12 November 2015
10.1126/science.aad3113

GEOMORPHOLOGY

Repeated catastrophic valley infill following medieval earthquakes in the Nepal Himalaya

Wolfgang Schwanghart,[1]* Anne Bernhardt,[1] Amelie Stolle,[1] Philipp Hoelzmann,[2] Basanta R. Adhikari,[3] Christoff Andermann,[4] Stefanie Tofelde,[1] Silke Merchel,[5] Georg Rugel,[5] Monique Fort,[6] Oliver Korup[1]

Geomorphic footprints of past large Himalayan earthquakes are elusive, although they are urgently needed for gauging and predicting recovery times of seismically perturbed mountain landscapes. We present evidence of catastrophic valley infill following at least three medieval earthquakes in the Nepal Himalaya. Radiocarbon dates from peat beds, plant macrofossils, and humic silts in fine-grained tributary sediments near Pokhara, Nepal's second-largest city, match the timing of nearby $M > 8$ earthquakes in ~1100, 1255, and 1344 C.E. The upstream dip of tributary valley fills and x-ray fluorescence spectrometry of their provenance rule out local sources. Instead, geomorphic and sedimentary evidence is consistent with catastrophic fluvial aggradation and debris flows that had plugged several tributaries with tens of meters of calcareous sediment from a Higher Himalayan source >60 kilometers away.

The M_w 7.8 Gorkha earthquake that struck Nepal in April 2015 confirmed high seismic risk projections for the Himalayas (*1*, *2*), inferred mostly from paleoseismological proxies of past events (*3*–*6*). Strong ground shaking caused the collapse of more than half a million homes, killing more than 8500 people and injuring more than 20,000. Landslides buried villages, roads, and river channels, consistent with coseismic impacts reported from other active mountain belts (*7*). Detailed sediment budgets show that landslides triggered by strong seismic ground shaking may rapidly detach millions to billions of cubic meters of rock, soil, and biomass, providing this material for subsequent entrainment by surface runoff and river flows (*8*). The resulting sediment pulses may fill even rapidly incising bedrock rivers by up to several tens of meters (*9*), thereby causing protracted channel instability, impeding access to emergency areas, destroying hydropower facilities, and compromising post-disaster rehabilitation efforts. Detailed mass balances of recent large earthquakes in China (*10*), Taiwan (*11*), Japan (*12*), and New Zealand (*13*) offer blueprints of how river networks recover from sudden input of excess sediment over several years to centuries. The high sediment transport rates in many mountain rivers, however, rarely sustain evidence of prehistoric earthquake-induced sedimentation pulses. In these cases, depositional records of catastrophic aggradation in forelands are more instructive (*14*). Both of these lines of evidence for understanding river network recovery have remained elusive in the Himalayas. We present exceptionally well-preserved sedimentary archives that connect landscape-scale disturbance around Pokhara, Nepal, to at least three documented medieval megathrust earthquakes (*3*).

The city of Pokhara (28°13′N, 83°59′E, 870 m above sea level) is located at the foot of the >8000-m peaks of the Annapurna Massif in the Seti Khola valley (Fig. 1). This steep orographic gradient receives monsoonal rainfall of ~4000 mm year^{-1} (*15*). Pokhara's geology features primarily Precambrian metamorphic sandstones, shales, and dolomites. Other rocks include Paleozoic phyllites and schists of the Lesser Himalayan Series (LHS). Higher Himalayan Crystalline (HHC) rocks north of the Main Central Thrust (MCT) are Precambrian high-grade metamorphic quartzites, schists, and gneisses (*16*, *17*). Marine calcareous metasediments of the Tethyan Sedimentary Series (TSS) prevail north of the South Tibetan Detachment Zone (*18*, *19*). Pokhara sits on a large sediment fan built by the upper Seti Khola that drains the partly glaciated and debris-filled Sabche Cirque in the Annapurna Massif. The fanhead near the MCT grades into a ~60-km-long flight of prominent terraces downstream that rise up to 140 m above the river bed and envelop several LHS bedrock hills (*20*). The fan has three stratigraphic units called the Tallakot, Ghachok, and Pokhara Formations. We focus on the youngest Pokhara Formation composed of extensive coarse gravel sheets, numerous boulders >10 m in diameter, and thick debris flow deposits. Digital topographic data (*21*) confirm damming of the more than a dozen tributaries along Seti Khola's course of >60 km by Pokhara Formation sediments (*20*). These deposits dip upstream into tributary valleys for >1 km and up to 7 km along the Magdi and Saraudi Khola featuring several meters of intercalated gravel, sand, and silt beds. We sampled enclosed peat beds, charcoal lenses, and plant macrofossils (figs. S1 and S2) for radiocarbon (^{14}C) dating and for any earthquake-related sedimentation in eight different tributaries (table S1).

Bayesian calibration of 26 ^{14}C ages with a prior informed by stratigraphic relationships between the samples (*22*) returned a pooled posterior distribution with three distinct peaks that match, within error, the timing of three large medieval earthquakes in ~1100, 1255, and 1344 C.E. (*3*–*5*) (Fig. 2, figs. S3 to S5, and table S2). Our oldest ^{14}C dates offer support for the timing of the ~1100 C.E. earthquake, which has so far been inferred from

[1]Institute of Earth and Environmental Science, University of Potsdam, Potsdam, Germany. [2]Institute of Geographical Sciences, Freie Universität Berlin, Berlin, Germany. [3]Institute of Engineering, Tribhuvan University, Kathmandu, Nepal. [4]Helmholtz-Zentrum Potsdam, German Centre for Geosciences GFZ, Germany. [5]Helmholtz-Zentrum Dresden-Rossendorf, Helmholtz Institute Freiberg for Resource Technology, Dresden, Germany. [6]CNRS UMR 8586 Prodig, Département de Géographie, Université Paris-Diderot-SPC, Paris, France.
*Corresponding author. E-mail: w.schwanghart@geo.uni-potsdam.de

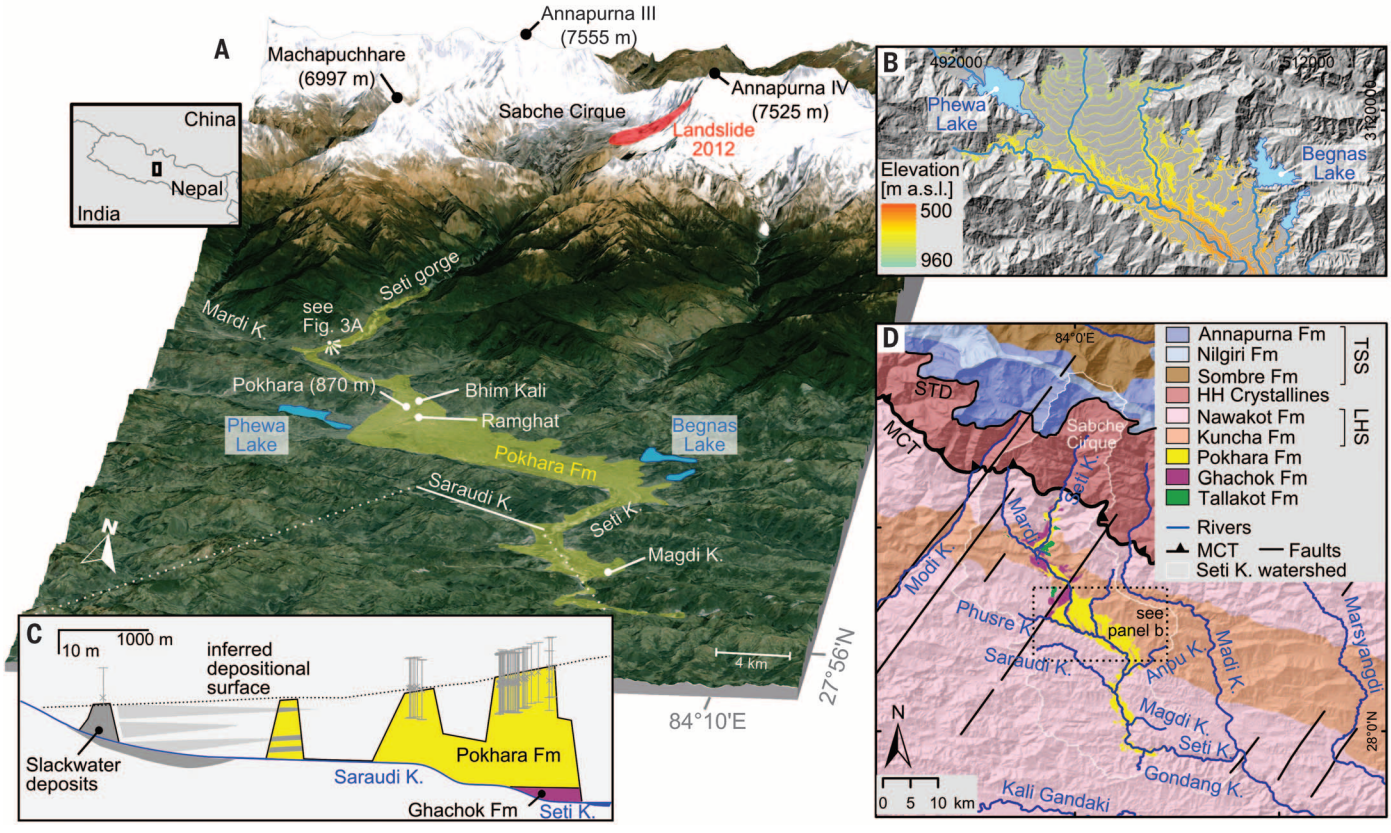

Fig. 1. Topographic and geological setting of the Pokhara Valley. The valley is covered by fan deposits of 4 to 5 km^3 that attest to massive aggradation from the Annapurna Massif. (**A**) Oblique view of the Pokhara region, Nepal Himalaya, with the fan-shaped Pokhara Formation (yellow) ponding several lakes (light blue) and tributaries [K. = Khola (river)], and 2012 rock-ice avalanche. (**B**) Shaded relief map from 15-m digital elevation model (a.s.l., above sea level). Concentric color-coded contours define the large sediment fan formed by the Seti Khola issuing from the Higher Himalayan Annapurna Massif. (**C**) Example of a longitudinal profile of small tributary backfilled by slackwater deposits (gray) of the Pokhara Formation (yellow). Error bars (±2σ) refer to GPS-derived elevation measurements of the former aggradation surface. (**D**) Simplified geological map (*16*) highlights the extent of the catastrophically emplaced Pokhara Formation (see text for abbreviations).

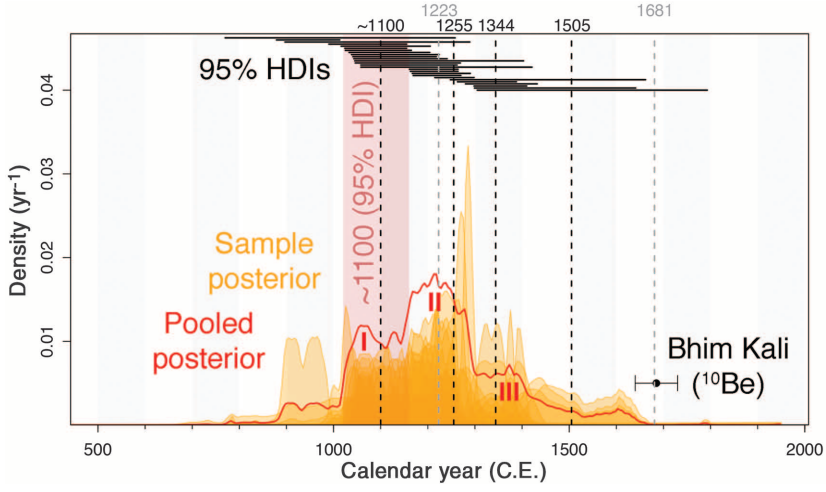

Fig. 2. Bayesian calibration of ^{14}C ages of the Pokhara Formation. Posterior probability densities (orange) of 26 ^{14}C dates from the Pokhara Formation and cosmogenic ^{10}Be exposure age of Bhim Kali boulder are shown (whiskers are ±1σ error). Horizontal lines are 95% highest density intervals (HDIs). Pooled posterior (red) has three distinct sedimentation peaks (I to III) tied to dates of $M > 8$ medieval earthquakes in ~1100, 1255, and 1344 C.E. (black dashed lines; gray dashed lines are other large earthquakes with little information on rupture extent; the 1505 C.E. earthquake is not reflected in our ^{14}C dates). Shaded red box is 95% HDI for the ~1100 C.E. earthquake based on recalibrated ^{14}C ages (*5*).

fault trenches (*5*). Each of the three medieval earthquake dates lies within the 95% highest density intervals of at least five ^{14}C dates. Our dates form a highly credible cluster that may match with another historically documented large event in 1223. The size and impact of this earthquake are unclear (*4*), however, when compared to studies on the 1255 C.E. earthquake. Four statistically indistinguishable ^{14}C dates spanning an 8-m-thick section of the trimmed fan toe in the Phusre Khola mark rapid aggradation tied to these earthquakes (fig. S6). A prominent and partly rounded 3000-ton HHC boulder (fig. S2), located on top of the Pokhara Formation and stranded ~50 m above the channel bed of the Seti Khola, has a cosmogenic ^{10}Be exposure age coeval with another major earthquake in 1681 C.E. (*3*). Regardless of whether this boulder was moved by sediment-laden flows, etched from the underlying deposits, or simply toppled, it provides a minimum age for the Pokhara Formation and attests to a sudden disturbance of its surface about 330 years ago.

We found numerous outcrops of the Pokhara Formation that illustrate its catastrophic origin. Two main facies of conglomeratic sediments are exposed within the trunk valley of the Seti Khola

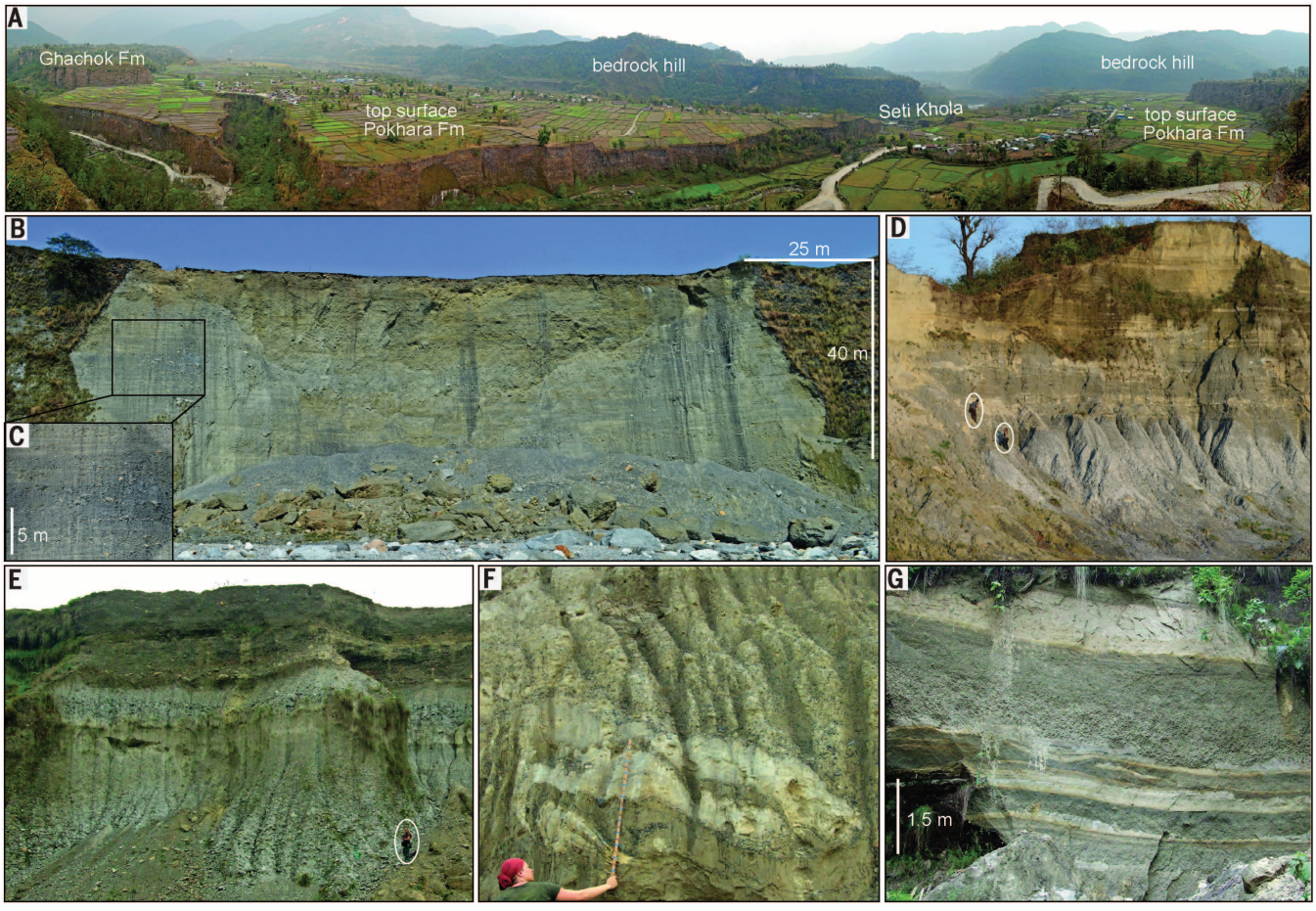

Fig. 3. Sediments of the Pokhara Formation. Fluvial processes and debris flows deposited extensive horizontal layers of poorly sorted conglomerate. (**A**) Panorama of the Pokhara sediment fan surface dissected by the Seti Khola and its tributaries (see Fig. 1A for location). (**B** and **C**) Poorly sorted, gravel-to-boulder, clast-supported conglomerate lacking erosional features and current structures. (**D**) Slackwater deposits in Saraudi Khola with cohesive debris flow deposits (light gray) topped by intercalated massive mud (dark gray), sands, and silts (light brown); white ellipses show persons for scale. (**E**) Mud matrix–supported, fining-upward conglomerate interpreted as long-runout debris flow deposits >40 km from their source. (**F**) Rip-up clasts in basal debris flow unit. (**G**) Massive dark gray, clast-supported, fining-upward pebble-to-granule layers with interbedded sands (light brown) indicate rapid settling from sediment-laden flow.

and form continuous layers for tens to hundreds of meters that dip at shallow angles (~0.5° to 1.2° measured by a tachymeter) in the direction of paleoflow. The first facies comprises >10-m-thick beds of a massive, matrix-supported, very poorly sorted, and locally fining-upward conglomerate of HHC gravels, boulders, and rip-up clasts that indicate emplacement by cohesive debris flows (Fig. 3 and fig. S7). At least three fining-upward cycles point to large debris flows, but they may equally well represent surges within one large event. The second conglomerate facies forms clast-supported units up to 40 m thick. The lack of current structures and erosive contacts, together with fining-upward massive pebble- to granule-bearing sheets, indicates rapid fallout from high concentrations of solids (Fig. 3). We interpret these clast-supported conglomerates to reflect rapid aggradation during turbulent, sediment-laden flows. The massive, structureless clay and silt layers in tributary valleys indicate rapid suspension fallout that we attribute to a waning flow velocity and possibly ponding. The dominance of dark limestone together with occasional HHC kyanite-sillimanite gneiss, pyroxenic marble, and augen gneiss excludes local LHS sediment sources.

Using x-ray fluorescence spectrometry of the fine-grained fraction of the Pokhara Formation, we confirmed an elemental composition different from the phyllitic bedrock in these LHS tributaries (Fig. 4). We found instead with x-ray diffraction a mineral composition rich in calcium carbonates, dolomite, muscovite, and traces of pyrite (table S3) characteristic of TSS rocks, particularly Nilgiri Limestone (*19*), from Sabche Cirque. We infer a catastrophic sediment transport over >60 km that culminated in deposits invading for several kilometers the lower reaches of several tributaries.

Catastrophic outbursts from natural dams and large rock-ice avalanches are two possible mechanisms for producing the long-runout debris flows. The clustered ^{14}C dates, the confined sediment provenance, and the dammed tributary mouths are consistent with one or several dam-break flows (*23*). We interpret the thick stacks of fine-grained sediments as slackwater deposits trapped in tributary valleys during backwater flooding (*24*). The Seti bedrock gorge upstream of the MCT had previously accommodated temporary lakes, judging from at least three dissected landslide dams up to 300 m in height (fig. S8). Dam-break modeling (*22*) shows that sudden failure of a 300-m-high dam could release up to 1 km^3 of water at a peak discharge of 45,000 to 600,000 $m^3 s^{-1}$ in the lower Seti gorge. Although exceeding the largest historic lake outbursts in the Himalaya (*25*), several such major events would be needed to deliver the 4 to 5 km^3 of sediments in the Pokhara Formation downstream (*20*), assuming a solids concentration of 80% by volume that is characteristic of cohesive debris flows. Some 10 to 15 km^3 of debris and lake sediments lining the Sabche Cirque floor (*20*) could feed lake outbursts and provide the necessary geochemical fingerprint for repeated catastrophic aggradation in the Pokhara basin.

Catastrophic rock-ice avalanches from the Annapurna Massif (*20*) represent an alternative initiation process for long-runout debris flows. Historic case studies from Peru (*26*), Tibet (*27*), and the

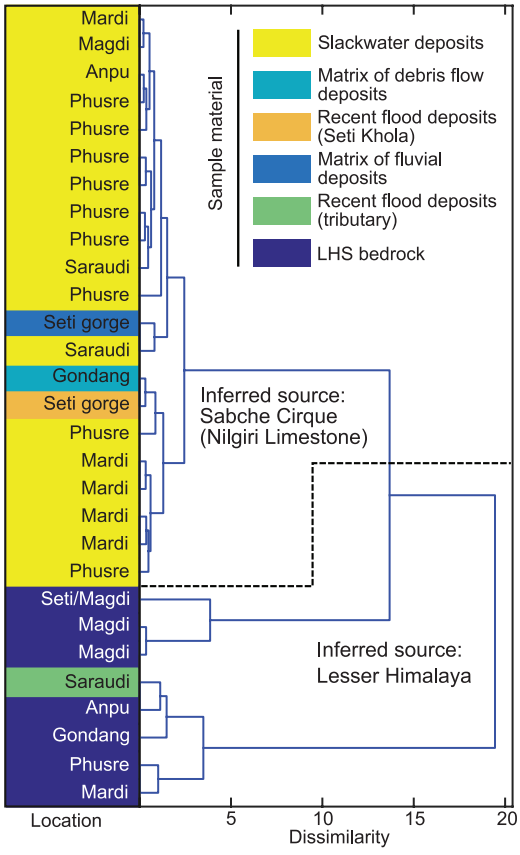

Fig. 4. Provenance of slackwater deposits from x-ray fluorescence spectrometry indicating highly localized High Himalayan source of the Pokhara Formation. Hierarchical cluster analysis yields three major classes of elemental compositions of LHS bedrock, slackwater deposits, fine-grained flood and debris flow deposits of the Pokhara Formation, and recent flood sediments of the Seti Khola and its tributaries. The three classes indicate sediment sources. Elemental compositions of the sedimentary fills in tributary mouths are highly similar, indistinguishable from load transported by the Seti Khola, and attest to a common source in the Sabche Cirque. Compositional variation of LHS bedrock reflects locally occurring limestone at the Seti and Magdi Khola confluence.

Caucasus (*28*) showed how rock avalanches detaching >10^7 m^3 from >4000-m-high mountains entrained glacier ice and transformed into debris flows and sediment-laden flows, which traveled as far as 130 km at average velocities of >30 km $hour^{-1}$ (*26*). The case of the earthquake-triggered rock-ice avalanche from the Andean peak of Nevados Huascarán (6654 m) that buried the town of Yungay beneath a large debris flow fan (*26*) in 1970 is strikingly similar to that of Pokhara in terms of topographic relief contrasts and far-reaching geomorphic impact, although much smaller in size. Some of the debris mounds in Sabche Cirque may partly derive from catastrophic rock slope failures, possibly larger than the recent one that detached ~59 Mt of rock and ice from the flanks of Annapurna IV and evolved into a flash flood that killed more than 70 people in the lower Seti gorge in May 2012 (*29*).

Our findings substantiate previous hypotheses of a catastrophic origin of the Pokhara Formation (*30*), merging several lines of evidence that point consistently to highly mobile mass movements from the upper Seti catchment triggered by medieval earthquakes. This geomorphic legacy of multiple earthquake-driven sedimentation pulses is unique in the Himalayas, recording episodic plugging of tributaries by rapid fluvial aggradation and long-runout debris flows from a single HHC source rather than aggradation in response to local coseismic landsliding. The large medieval sediment pulse(s) from the confined source area of the upper Seti Khola would have been accompanied by thousands of smaller landslide point sources, judging from the patterns of historic earthquakes including the 2015 Gorkha events (*7*). Yet evidence of repeated catastrophic valley infill following the cluster of medieval earthquakes so far remains limited to the Pokhara region. We cannot discount the remote probability that our ^{14}C dates might have no causal connection with the timing of large medieval earthquakes; at least, our ^{14}C dates show no conclusive correlation with temperature and monsoon proxies for the region (fig. S9). Contemporary rates of river incision into the Pokhara Formation remain high, triggering widespread bank erosion, terrace slumps, local ground subsidence, and high sediment yields. Thus, geomorphic adjustment to several medieval catastrophic aggradation pulses has been ongoing for at least three centuries and clearly outweighs previously documented periods of postseismic river recovery in the Himalayas or elsewhere (*8*–*13*). We conclude that Pokhara's current earthquake vulnerability profile (*31*) should consider in more detail the potential impacts and consequences of postseismic sediment pulses.

REFERENCES AND NOTES

1. R. Bilham, V. K. Gaur, P. Molnar, *Science* **293**, 1442–1444 (2001).
2. J. Galetzka *et al.*, *Science* **349**, 1091–1095 (2015).
3. J.-L. Mugnier *et al.*, *Earth Sci. Rev.* **127**, 30–47 (2013).
4. L. Bollinger *et al.*, *J. Geophys. Res.* **119**, 7123–7163 (2014).
5. J. Lavé *et al.*, *Science* **307**, 1302–1305 (2005).
6. S. N. Sapkota *et al.*, *Nat. Geosci.* **6**, 71–76 (2013).
7. J. S. Kargel *et al.*, *Science* 10.1126/science.aac8353 (2015).
8. D. K. Keefer, *Surv. Geophys.* **23**, 473–510 (2002).
9. B. J. Yanites, G. E. Tucker, K. J. Mueller, Y.-G. Chen, *Geology* **38**, 639–642 (2010).
10. G. Li *et al.*, *Geochem. Geophys. Geosyst.* **15**, 833–844 (2014).
11. N. Hovius *et al.*, *Earth Planet. Sci. Lett.* **304**, 347–355 (2011).
12. T. Koi *et al.*, *Geomorphology* **101**, 692–702 (2008).
13. A. J. Pearce, A. J. Watson, *Geology* **14**, 52–55 (1986).
14. K. R. Berryman *et al.*, *Science* **336**, 1690–1693 (2012).
15. E. J. Gabet, D. W. Burbank, J. K. Putkonen, B. A. Pratt-Sitaula, T. Ojha, *Geomorphology* **63**, 131–143 (2004).
16. D. M. Robinson, A. J. Martin, *Tectonics* **33**, 2143–2168 (2014).
17. A. J. Parsons, R. D. Law, M. P. Searle, R. J. Phillips, G. E. Lloyd, *J. Maps* **12**, 100–110 (2016).
18. L. Bollinger *et al.*, *Tectonics* **23**, TC5015 (2004).
19. A. C. Waltham, *Geol. Mag.* **109**, 205–214 (1972).
20. M. Fort, *Z. Geomorphol. N.F.* **63** (suppl.), 9–36 (1987).
21. Survey Department, Government of Nepal, Topographical map of the Pokhara area (1996).
22. See supplementary materials on *Science* Online.
23. P. A. Carling, *Earth Sci. Rev.* **125**, 87–113 (2013).
24. V. R. Baker, R. C. Kochel, P. C. Patton, G. Pickup, in *Modern and Ancient Fluvial Systems*, J. D. Collinson, J. Lewin, Eds. (Blackwell, 1983), pp. 229–239.
25. O. Korup, F. Tweed, *Quat. Sci. Rev.* **26**, 3406–3422 (2007).
26. S. G. Evans *et al.*, *Eng. Geol.* **108**, 96–118 (2009).
27. Y. Shang *et al.*, *Geomorphology* **54**, 225–243 (2003).
28. S. G. Evans *et al.*, *Geomorphology* **105**, 314–321 (2009).
29. G. Ekström, C. P. Stark, *Science* **339**, 1416–1419 (2013).
30. M. Fort, in *Geomorphological Landscapes of the World*, P. Migon, Ed. (Springer, 2009), pp. 265–274.
31. Earthquake risk reduction and recovery preparedness programme for Nepal, Earthquake vulnerability profile and preparedness plan, Pokhara Sub-Metropolitan City, UNDP/ERRRP Project Nep/07/010, final revised report (2010); http://errrp.org.np/document/study_report/Pokhara%20Vulnerability%20Profile.pdf.

ACKNOWLEDGMENTS

Funded by the German Research Foundation (KO 3937/9) and the Potsdam Research Cluster for Georisk Analysis (PROGRESS). We thank B. Situala for arranging logistical support; Alpine Consultancy Pvt. Ltd. Nepal and the Department of Survey, Nepal, for digital topographic data; J. Jansen, M. Roschlaub, E. Schönfeldt, J. Seidemann, and J. T. Weidinger for help with fieldwork; and H. Wittmann-Oelze for processing the Bhim Kali sample at GFZ-HELGES, Potsdam. C.A. acknowledges support from the Helmholtz Postdoc Program (PD-039) of the German Helmholtz Association. Author contributions: O.K. designed and drafted the project; W.S., A.B., A.S., B.R.A., C.A., M.F., and O.K. carried out the fieldwork; W.S., A.B., and A.S. analyzed the digital topographic and sedimentary data; P.H. assisted with the XRF and XRD analyses; S.T. prepared samples for ^{10}Be exposure dating; S.M., G.R., and C.A. ran the ^{10}Be AMS analysis; and W.S., A.B., A.S., and O.K. wrote the manuscript with inputs from all co-authors. Supporting data are available in the supplementary materials.

SUPPLEMENTARY MATERIALS

www.sciencemag.org/content/351/6269/147/suppl/DC1
Materials and Methods
Figs. S1 to S9
Tables S1 to S5
Database S1
References (*32*–*54*)

10 July 2015; accepted 25 November 2015
Published online 17 December 2015
10.1126/science.aac9865

SOLAR CELLS

A mixed-cation lead mixed-halide perovskite absorber for tandem solar cells

David P. McMeekin,[1] Golnaz Sadoughi,[1] Waqaas Rehman,[1] Giles E. Eperon,[1] Michael Saliba,[1] Maximilian T. Hörantner,[1] Amir Haghighirad,[1] Nobuya Sakai,[1] Lars Korte,[2] Bernd Rech,[2] Michael B. Johnston,[1] Laura M. Herz,[1] Henry J. Snaith[1]*

Metal halide perovskite photovoltaic cells could potentially boost the efficiency of commercial silicon photovoltaic modules from ~20 toward 30% when used in tandem architectures. An optimum perovskite cell optical band gap of ~1.75 electron volts (eV) can be achieved by varying halide composition, but to date, such materials have had poor photostability and thermal stability. Here we present a highly crystalline and compositionally photostable material, $[HC(NH_2)_2]_{0.83}Cs_{0.17}Pb(I_{0.6}Br_{0.4})_3$, with an optical band gap of ~1.74 eV, and we fabricated perovskite cells that reached open-circuit voltages of 1.2 volts and power conversion efficiency of over 17% on small areas and 14.7% on 0.715 cm^2 cells. By combining these perovskite cells with a 19%-efficient silicon cell, we demonstrated the feasibility of achieving >25%-efficient four-terminal tandem cells.

One concept for improving the efficiency of photovoltaics (PVs) is to create a "tandem junction"; for example, by placing a wide–band-gap "top cell" above a silicon (Si) "bottom cell." This approach could realistically increase the efficiency of the Si cell from 25.6 to beyond 30% (*1*, *2*). Given the crystalline Si band gap of 1.1 eV, the top cell material requires a band gap of ~1.75 eV in order to current-match both junctions (*3*). However, suitable wide–band-gap top-cell materials for Si or thin-film technologies that offer stability, high performance, and low cost have been lacking. In recent years, metal halide perovskite–based PVs have gained attention because of their high power conversion efficiencies (PCEs) and low processing cost (*4*–*11*). An attractive feature of this material is the ability to tune its band gap from 1.48 to 2.3 eV (*12*, *13*), implying that we could potentially fabricate an ideal material for tandem cell applications.

Perovskite-based PVs are generally fabricated with organic-inorganic trihalide perovskites with the formulation ABX_3, where A is the methylammonium (CH_3NH_3) (MA) or formamidinium ($HC(NH_2)_2$) (FA) cation, B is commonly lead (Pb), and X is a halide (Cl, Br, or I). Although these perovskite structures offer high PCEs, reaching >20% PCE with band gaps of around 1.55 eV (*14*), fundamental issues have been discovered when attempting to tune their band gaps to the optimum 1.7- to 1.8-eV range. In the case of $MAPb[I_{(1-x)}Br_x]_3$, Hoke *et al.* reported that soaking it with light induces a halide segregation within the perovskite (*15*). The formation of iodide-rich domains with a lower band gap results in an increase in sub-gap absorption and a red shift of photoluminescence (PL). The lower–band-gap regions limit the voltage attainable with such a material, so this band-gap "photoinstability" limits the use of $MAPb[I_{(1-x)}Br_x]_3$ in tandem devices (*15*). In addition, when considering real-world applications, $MAPbI_3$ is inherently thermally unstable at temperatures above 85°C, even in aninert atmosphere (international regulations require a commercial PV product to withstand this temperature) (*16*).

Concerning the more thermally stable $FAPbX_3$ perovskite, an increase in optical band gap has

[1]Clarendon Laboratory, University of Oxford, Parks Road, Oxford OX1 3PU, UK. [2]Helmholtz-Zentrum Berlin für Materialien und Energie, Institute for Silicon Photovoltaics, Kekuléstrasse 5, 12489 Berlin, Germany.
*Corresponding author. E-mail: henry.snaith@physics.ox.ac.uk

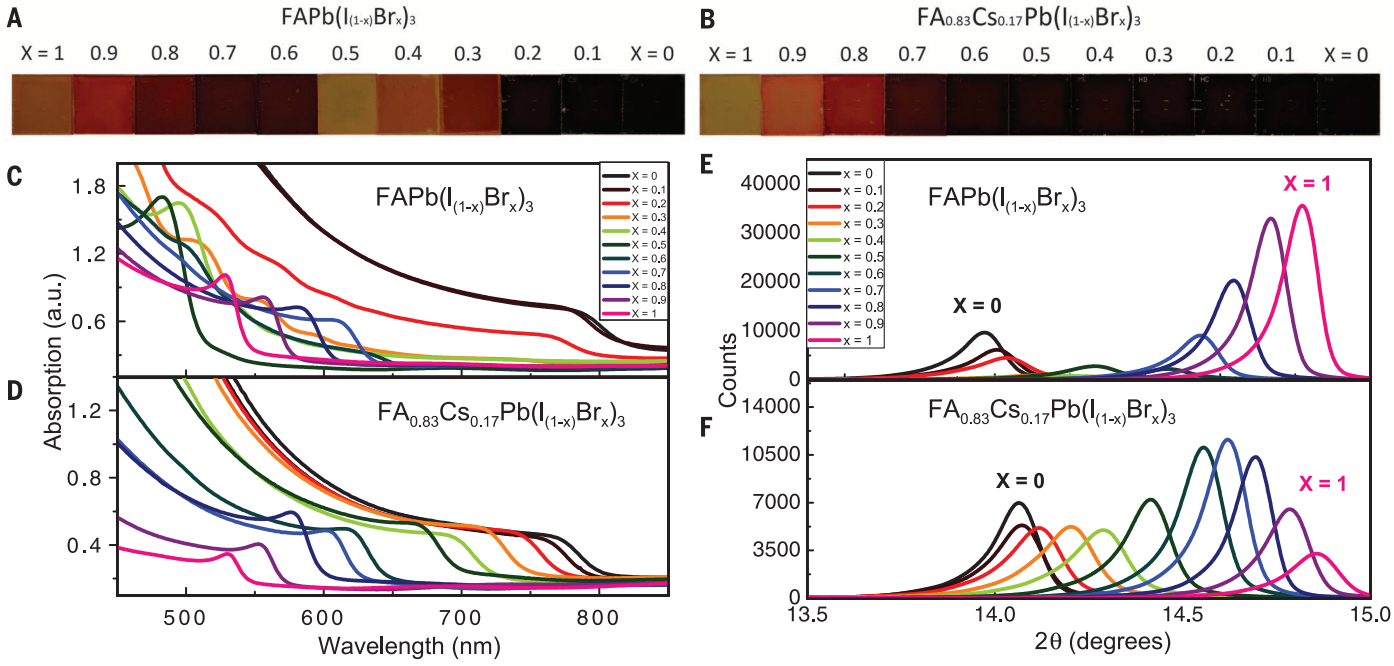

Fig. 1. Tuning the band gap. Photographs of perovskite films with Br composition increasing from $x = 0$ to 1 for (**A**) $FAPb[I_{(1-x)}Br_x]_3$ and (**B**) $FA_{0.83}Cs_{0.17}Pb[I_{(1-x)}Br_x]_3$. (**C**) Ultraviolet-visible absorbance spectra of films of $FAPb[I_{(1-x)}Br_x]_3$ and (**D**) $FA_{0.83}Cs_{0.17}Pb[I_{(1-x)}Br_x]_3$. a.u., arbitrary units. (**E**) XRD pattern of $FAPb[I_{(1-x)}Br_x]_3$ and (**F**) $FA_{0.83}Cs_{0.17}Pb[I_{(1-x)}Br_x]_3$. The stated compositions are the fractional compositions of the ions in the starting solution, and the actual composition of the crystallized films may vary slightly.

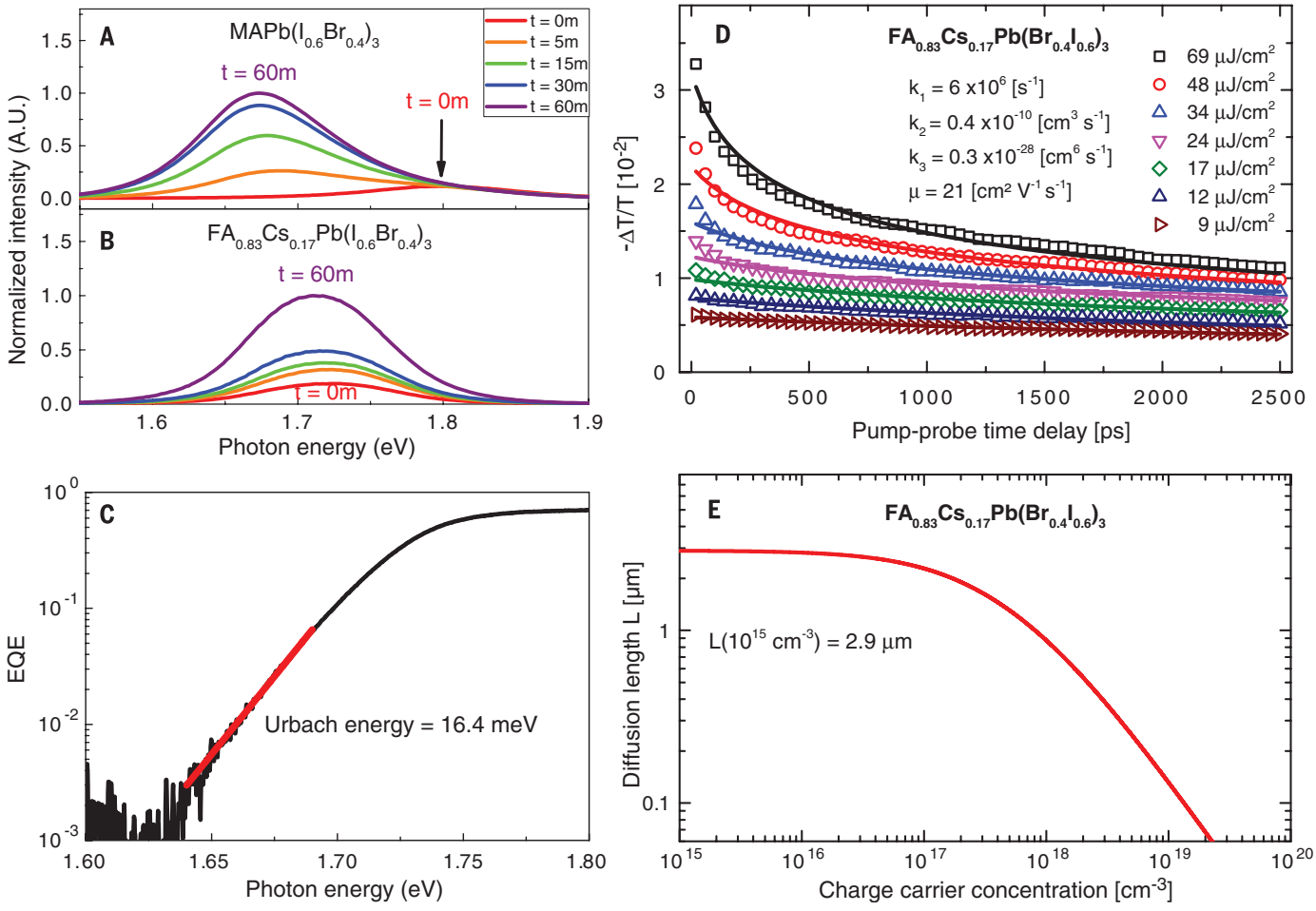

Fig. 2. Material characteristics of $FA_{0.83}Cs_{0.17}Pb(I_{0.6}Br_{0.4})_3$ perovskite. Normalized PL measurement measured after 0, 5, 15, 30, and 60 min of light exposure of the (**A**) $MAPb(I_{0.6}Br_{0.4})_3$ and (**B**) $FA_{0.83}Cs_{0.17}Pb(I_{0.6}Br_{0.4})_3$ thin films. (**C**) Semi-log plot of EQE at the absorption onset for a $FA_{0.83}Cs_{0.17}Pb(I_{0.6}Br_{0.4})_3$ PV cell, measured using FTPS at short-circuit (J_{SC}). (**D**) OPTP transients for a $FA_{0.83}Cs_{0.17}Pb(I_{0.6}Br_{0.4})_3$ thin film, measured after excitation with a 35-fs light pulse of wavelength 400 nm with different fluences. (**E**) Charge-carrier diffusion length L as a function of charge-carrier concentration.

not resulted in an expected increase in open-circuit voltage (V_{OC}) (*13*). Furthermore, as iodide is substituted with bromide, a crystal phase transition occurs from a trigonal to a cubic structure; in compositions near the transition, the material is unable to crystallize, resulting in an apparently "amorphous" phase with high levels of energetic disorder and unexpectedly low absorption. These compositions additionally have much lower charge-carrier mobilities in the range of 1 $cm^2 V^{-1} s^{-1}$, in comparison to >20 $cm^2 V^{-1} s^{-1}$ in the neat iodide perovskite (*17*). For tandem applications, these problems arise at the Br composition needed to form the desired top-cell band gap of ~1.7 to 1.8 eV.

Nevertheless, perovskite/Si tandem PVs have already been reported in four-terminal (*18*, *19*) and two-terminal (*20*) architectures. However, their reported efficiencies have yet to surpass the optimized single-junction efficiencies, in part because of non-ideal absorber band gaps. It is possible to form a lower–band-gap triiodide perovskite material and current-match the top and bottom junctions in a monolithic architecture by simply reducing the thickness of the top cell. However, this method results in non-ideal efficiency.

Here we address the issues of forming a photostable FA-based perovskite with the ideal band gap for tandem PVs. We partially substituted the formamidinium cation with Cs and observed that the phase instability region was entirely eliminated in the iodide-to-bromide compositional range, delivering complete tunability of the band gap around 1.75 eV. We fabricated planar heterojunction perovskite PVs, demonstrating PCE of >17% and stabilized power output (SPO) of 16%. To demonstrate the potential impact of this new perovskite material in tandem solar cells, we created a semi-transparent perovskite device and measured the performance of a silicon PV after "filtering" the sunlight through the perovskite top cell. The Si cells delivered an efficiency boost of 7.3%, indicating the feasibility of achieving >25%-efficient perovskite/Si tandem cells.

The A-site cations that could be used with lead halides to form suitable perovskites for PVs are Cs, MA, and FA. $CsPbI_3$ does form a "black phase" perovskite with a band gap of 1.73 eV, but this appropriate phase is only stable at temperatures above 200° to 300°C, and the most stable phase at room temperature is a nonperovskite orthorhombic "yellow" phase. MA-based perovskites are thermally unstable and suffer from halide segregation instabilities, and are thus likely to be unsuitable (*16*). FA-based perovskites are the most likely to deliver the best balance between structural and thermal stability (*13*, *21*–*25*). However, in Fig. 1A, we show photographs of a series of $FAPb[I_{(1-x)}Br_x]_3$ films; we observed a "yellowing" of the films for compositions of x between 0.3 and 0.6, which is consistent with the previously reported phase instability caused by a transition from a trigonal ($x < 0.3$) to a cubic ($x > 0.5$) structure (*13*).

We have previously observed that the band gap changes from 1.48 eV for $FAPbI_3$ to 1.73 eV for $CsPbI_3$ (*13*). Recently it has been shown that mixing Cs with FA or MA results in a slight widening of the band gap (*26*, *27*). We considered the possibility that if we partially substituted FA for Cs, we could push this region of structural instability in the Br-to-I phase space to higher energies, and thus potentially achieve a structurally stable mixed-halide perovskite with a band gap of 1.75 eV. In Fig. 1B, we show photographs of thin films fabricated from mixed-cation lead mixed-halide $FA_{0.83}Cs_{0.17}Pb[I_{(1-x)}Br_x]_3$ compositions.

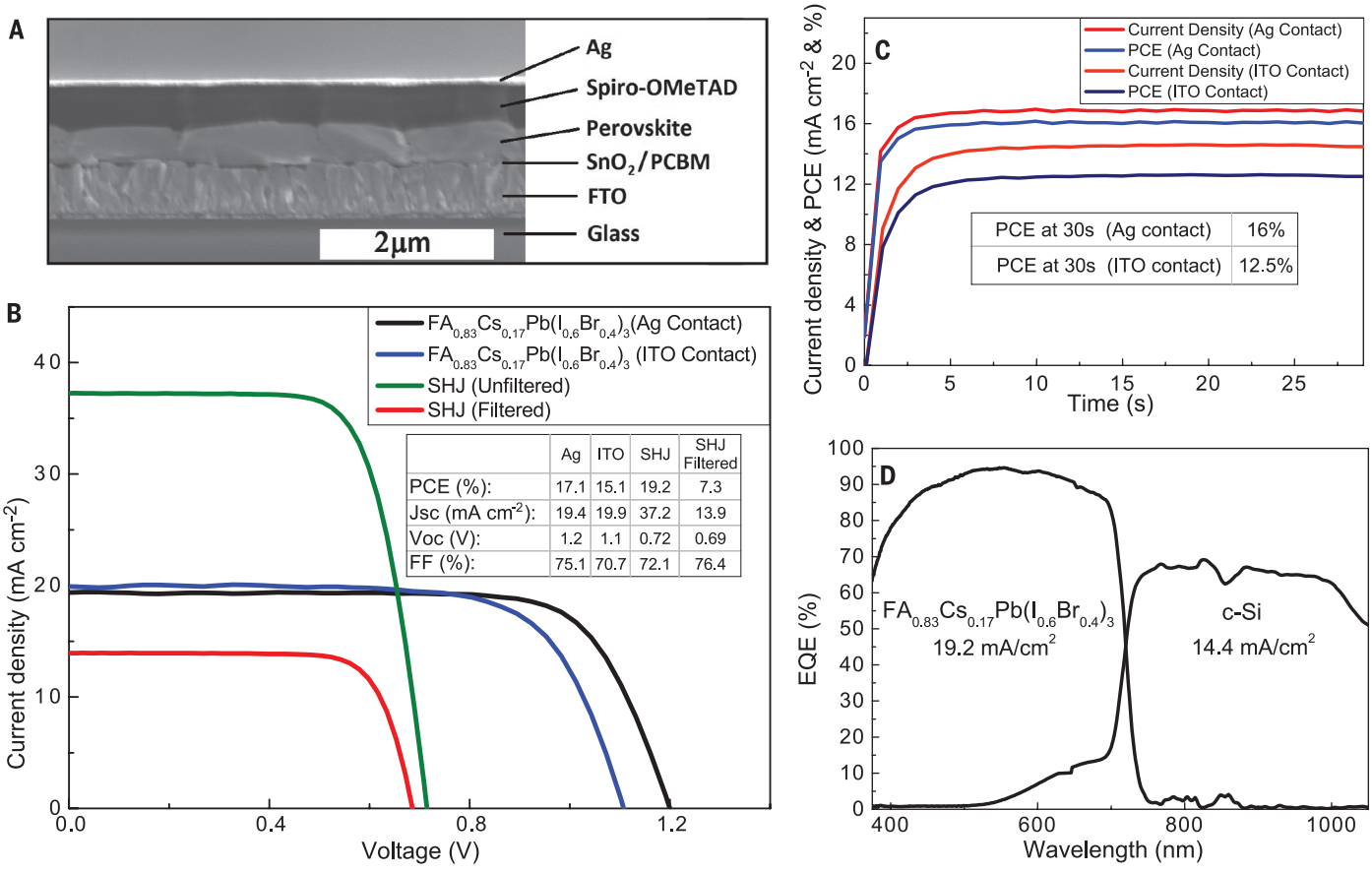

Fig. 3. Device architecture and *I-V* characteristics for $FA_{0.83}Cs_{0.17}Pb(I_{0.6}Br_{0.4})_3$ perovskite and Si PV cells. (**A**) Scanning electron microscope image of a cross-section of a planar heterojunction solar cell. PCBM, phenyl-C60-butyric acid methyl ester. (**B**) Forward bias to short-circuit *I-V* curve for the best perovskite devices fabricated, using either a Ag metal or semi-transparent ITO top electrode, measured at a 0.38 V/s scan rate. FF, fill factor. We also show the *I-V* curve of a SHJ cell, measured with direct light or with the simulated sunlight filtered through the semi-transparent perovskite solar cell (*37*). The SHJ cells were measured at the Centre For Renewable Energy Technologies, Loughborough, UK, under an extremely well-calibrated solar simulator. (**C**) Photocurrent density and power conversion efficiency measured at the maximum power point for a 30-s time span. (**D**) EQE spectrum measured in short-circuit (J_{SC}) configuration for the highest-efficiency perovskite cell and the SHJ cell measured with the incident light filtered through the semi-transparent perovskite cell.

Unexpectedly, we did not simply shift the region of structural instability to higher energy, but we observed a continuous series of dark films throughout this entire compositional range. To confirm these observations, we also performed ultraviolet-visible absorption measurements. We obtained a sharp optical band edge for all compositions of the $FA_{0.83}Cs_{0.17}Pb[I_{(1-x)}Br_x]_3$ material (Fig. 1, C and D), in contrast to $FAPb[I_{(1-x)}Br_x]_3$, which shows weak absorption in the intermediate range.

In order to understand the impact of adding Cs upon the crystallization of the perovskite, we performed x-ray diffraction (XRD) on the series of films covering the I-to-Br compositional range. In Fig. 1E, we show the XRD patterns for $FAPb[I_{(1-x)}Br_x]_3$, zoomed in to the peak around 2θ ~ 14° [the complete diffraction pattern is shown in fig. S1, along with more details on fitting these data (*28*)]. For the $FA_{0.83}Cs_{0.17}Pb[I_{(1-x)}Br_x]_3$ perovskite, the material is in a single phase throughout the entire composition range. The monotonic shift of the (100) reflection that we observed from 2θ ~ 14.2° to 14.9° is consistent with a shift of the cubic lattice constant from 6.306 to 5.955 Å as the material incorporates a larger fraction of the smaller halide, Br [in fig. S2, we show the complete diffraction pattern (*28*)]. Thus, for the $FA_{0.83}Cs_{0.17}Pb[I_{(1-x)}Br_x]_3$ perovskite, we have removed the structural phase transition and instability over the entire compositional range [in figs. S3 to S5 we show details of varying the Cs concentration and the Br-to-I concentration (*28*)]. Over the entire Br-to-I range, and for a large fraction of the Cs-FA range, the variation in lattice constant, composition, and optical band gap precisely follows Vegard's law [fig. S6 (*28*)], so we have total flexibility and predictability in tuning the composition and its impact on the band gap. For the results that follow below, we used the precise composition $FA_{0.83}Cs_{0.17}Pb(I_{0.6}Br_{0.4})_3$, which has an optical band gap of 1.74 eV as determined by a Tauc plot [fig. S7 (*28*)].

Photoinduced halide segregation has been reported in methylammonium lead mixed-halide perovskites (*15*). A red shift in PL upon light illumination, for intensities ranging from 10 to 100 mW cm^{-2} occurs, with the shift to lower energies resulting from the formation of iodine-rich domains that have lower band gaps. This limits the achievable open-circuit voltage of the solar cell device by introducing a large degree of electronic disorder. In Fig. 2, we show the PL from films of $MAPb(I_{0.6}Br_{0.4})_3$ perovskite and the mixed-cation mixed-halide material $FA_{0.83}Cs_{0.17}Pb(I_{0.6}Br_{0.4})_3$, immediately after prolonged periods of light exposure, using a power density of ~3 mW cm^{-2} and a wavelength of 550 nm as an excitation source. We confirmed the results observed by Hoke *et al.*; that is, we saw a time-dependent red shift in PL for the $MAPb(I_{0.6}Br_{0.4})_3$ film, which exhibited a 130-meV PL red shift after only 1 hour of illumination. We also show the time evolution of the PL from $MAPb(I_{0.8}Br_{0.2})_3$, a composition previously reported in other devices (*29*), which shifts from 1.72 to 1.69 eV [fig. S8 (*28*)]. In contrast, although we saw a rise in PL intensity, we observed no significant red shift in PL emission for the $FA_{0.83}Cs_{0.17}Pb(I_{0.6}Br_{0.4})_3$ precursor after 1 hour of identical light illumination (which we show in Fig. 2B). Furthermore, we exposed a similar $FA_{0.83}Cs_{0.17}Pb(I_{0.6}Br_{0.4})_3$ film to monochromatic irradiance of much higher irradiance of 5 W cm^{-2} and observed no red shift after 240 s of illumination [fig. S9, (*28*)]. Under these identical conditions, we did observe a red shift in the PL for the single-cation

$FAPb(I_{0.6}Br_{0.4})_3$ perovskite, as we have previously reported (*17*). In addition, under thermal stressing at 130°C, we observed that the optical band gap and the crystal lattice of $FA_{0.83}Cs_{0.17}Pb(I_{0.6}Br_{0.4})$ were stable, in contrast to those of $MAPb(I_{0.6}Br_{0.4})_3$ (fig. S10).

Beyond halide segregation, a further deleterious observation previously made for mixed-halide perovskites has been that the energetic disorder in the material is greatly increased in comparison to the neat iodide perovskites. The ultimate open-circuit voltage that a solar cell material can generate is intimately linked to the steepness of the absorption onset just below the band edge, which can be quantified by the Urbach energy (E_u) (*30*, *31*). This E_u reported by De Wolf *et al.* and Sadhanala *et al.* for $MAPbI_3$ was 15 meV (*31*), where small values of E_u indicate low levels of electronic disorder. In contrast, the E_u for $MAPb(I_{0.6}Br_{0.4})_3$ perovskite increased to 49.5 meV (*32*). We determined E_u by performing Fourier-transform photocurrent spectroscopy (FTPS) on complete planar heterojunction solar cells (details of the solar cells are discussed below), and in Fig. 2C we show the semi-log plot of external quantum efficiency (EQE) absorption edge of a device fabricated with the optimized precursor solution and annealing procedure. We calculated an E_u of 16.5 meV, which is near the values reported for the neat iodide perovskites.

In order to further assess the electronic quantity of $FA_{0.83}Cs_{0.17}Pb(I_{0.6}Br_{0.4})_3$, we performed optical pump terahertz-probe (OPTP) spectroscopy, which is a noncontact method of probing the photo-induced conductivity and effective charge-carrier mobility in the material. In Fig. 2D, we show the fluence dependence of the OPTP transients, which exhibit accelerated decay dynamics at higher initial photoinjected charge-carrier densities, as the result of enhanced contributions from bimolecular and Auger recombination. We extract the rate constants associated with different recombination mechanisms by global fits to these transient of the solutions to the rate equation

$$\frac{dn(t)}{dt} = -k_3 n^3 - k_2 n^2 - k_1 n \qquad (1)$$

which we show in Fig. 2D. In addition, we found that $FA_{0.83}Cs_{0.17}Pb(I_{0.6}Br_{0.4})_3$ exhibits an excellent charge-carrier mobility of 21 $cm^2\ V^{-1}\ s^{-1}$. For comparison, the corresponding neat FA perovskite $FAPb(I_{0.6}Br_{0.4})_3$ only sustains charge-carrier mobilities <1 $cm^2\ V^{-1}\ s^{-1}$ that are related to the amorphous and energetically disordered nature of these materials (*17*). Conversely, $FA_{0.83}Cs_{0.17}Pb(I_{0.6}Br_{0.4})_3$ displays a mobility value intermediate to those we previously determined (*17*) for $FAPbI_3$ (27 $cm^2\ V^{-1}\ s^{-1}$) and $FAPbBr_3$ (14 $cm^2\ V^{-1}\ s^{-1}$), which suggests that it is no longer limited by structural disorder.

We further assessed the potential of $FA_{0.83}Cs_{0.17}Pb(I_{0.6}Br_{0.4})_3$ for incorporation into planar heterojunction PV architectures by deriving the charge-carrier diffusion length $L = [\mu k_B T/(eR)]^{0.5}$ as function of the charge-carrier density n, where $R = k_1 + nk_2 + n^2k_3$ is the total recombination rate, k_B is the Boltzmann constant, T is temperature, and e is the elementary charge. In Fig. 2E, we show that for charge-carrier densities typical under solar illumination ($n \sim 10^{15}$ cm^{-3}) a value of $L \sim 2.9$ μm is reached, which is comparable to values reported for high-quality thin films of neat lead iodide perovskites (*17*, *33*). The high charge-carrier mobility, slow recombination kinetics, and the long charge carrier diffusion length imply that this mixed-cation, mixed-halide perovskite should be just as effective as a high-quality solar cell absorber material as the neat halide perovskite $FAPbI_3$.

We fabricated a series of planar heterojunction solar cells to assess the overall solar cell performance [in fig. S11 we describe in more detail and show data for solar cells fabricated with a range of compositional and processing parameters (*28*)]. We show the device architecture in Fig. 3A, which is composed of a SnO_2/phenyl-C_{60}-butyric acid methyl ester ($PC_{60}BM$) electron-selective layer, a solid $FA_{0.83}Cs_{0.17}Pb(I_{0.6}Br_{0.4})_3$ perovskite absorber layer, and Li-TFSI–doped [TFSI, bis(trifluoromethanesulfonyl)imide] spiro-OMeTAD [2,2′,7,7′-tetrakis(*N*,*N*-di-p-methoxyphenylamine)-9,9′-spirobifluorene] with 4-tert-butylpyridine (TBP) additive as the hole-collection layer, capped with an Ag electrode. We measured current-voltage (*I-V*) characteristics of such devices under a simulated air mass (AM) 1.5, under 100 mW cm^{-2} of sunlight, and show the *I-V* characteristics of one of the highest-performing devices in Fig. 3B. It delivered a short-circuit current density of 19.4 mA cm^{-2}, a V_{OC} of 1.2 V, and a PCE of 17.1%. By holding the cell at a fixed maximum power point forward-bias voltage of 0.95 V, we measured the power output over time, reaching a stabilized efficiency of 16% (Fig. 3C). The highest *I-V* scanned efficiency we measured was 17.9% [fig. S12 (*28*), along with a histogram of performance parameters for a large batch of devices in fig. S13 (*28*)]. To demonstrate that these cells can also operate with larger area, we fabricated 0.715-cm^2 active layers in which the cells reach a stabilized power output of >14% [fig. S14 (*28*)]. In Fig. 3D, we show the spectral response of the solar cell, which confirms the wider band gap of the solar cell and also integrates over the AM 1.5 solar spectrum to give 19.2 mA cm^{-2}, in close agreement to the measured short-circuit current density (J_{SC}).

This performance is very competitive with that of the best reported single-junction perovskite solar cell reported so far (*30*, *34*), especially considering the wider band gap of our material, which should result in a few percentage points of absolute efficiency drop with respect to a 1.55-eV material (*35*). Importantly for tandem solar cells, this 1.74-eV material appears to be capable of generating a higher V_{OC} than the 1.55-eV triiodide perovskites in planar heterojunction solar cells. Following Rau *et al.* (*36*), from the integration of the EQE over the blackbody radiation spectrum, we estimate the maximum attainable V_{OC} for our $FA_{0.83}Cs_{0.17}Pb(I_{0.6}Br_{0.4})_3$ device to be 1.42 V (details shown in fig. S15), which is 100 mV higher than that estimated for $MAPbI_3$ devices by Tvingstedt *et al.* and Tress *et al.* (*30*, *34*).

In order to demonstrate the potential impact of using this new perovskite composition in a tandem architecture, we fabricated semitransparent perovskite solar cells by sputter-coating indium tin oxide (ITO) on top of the perovskite cells, with the additional inclusion of a thin "buffer layer" of solution-processed ITO nanoparticles between the spiro-OMeTAD and the ITO. The efficiency of the semi-transparent $FA_{0.83}Cs_{0.17}Pb(I_{0.6}Br_{0.4})_3$ solar cells is 15.1%, as determined by the *I-V* curve, with a stabilized power output of 12.5%. Because the J_{SC} is similar to that of the cell with the Ag electrode, we expect that the slight drop in V_{OC} and SPO will be surmountable by better optimization of the ITO sputter-deposition procedure and buffer layer. We measured a Si heterojunction (SHJ) cell, with and without a semi-transparent perovskite cell held in front of it, and determined an efficiency of 7.3% filtered and 19.2% when uncovered. These results demonstrate the feasibility of obtaining a combined tandem solar cell efficiency ranging from 19.8%, if we combine with the stabilized power output of the semi-transparent cell, to 25.2% if we combine with the highest current density–voltage (*J-V*) measured efficiency of the $FA_{0.83}Cs_{0.17}Pb(I_{0.6}Br_{0.4})_3$ cell. Considering further minor improvements in the perovskite, optical management and integration, and choice of Si rear cell, it is feasible that this system could deliver up to 30% efficiency. In addition, this monotonic tunability of the band gap across the visible spectrum, without the complications of a structural phase transition will have direct impact on the color tunability and optimization of perovskites for light-emitting applications.

REFERENCES AND NOTES

1. V. Sivaram, S. D. Stranks, H. J. Snaith, *Sci. Am.* **313**, 54–59 (2015).
2. M. A. Green, K. Emery, Y. Hishikawa, W. Warta, E. D. Dunlop, *Prog. Photovolt. Res. Appl.* **23**, 805–812 (2015).
3. A. Shah, P. Torres, R. Tscharner, N. Wyrsch, H. Keppner, *Science* **285**, 692–698 (1999).
4. C. R. Kagan, D. B. Mitzi, C. D. Dimitrakopoulos, *Science* **286**, 945–947 (1999).
5. A. Kojima, K. Teshima, Y. Shirai, T. Miyasaka, *Priv. Commun.* **1**, 1 (2009).
6. M. M. Lee, J. Teuscher, T. Miyasaka, T. N. Murakami, H. J. Snaith, *Science* **338**, 643–647 (2012).
7. M. Liu, M. B. Johnston, H. J. Snaith, *Nature* **501**, 395–398 (2013).
8. J. Burschka *et al.*, *Nature* **499**, 316–319 (2013).
9. M. Green, A. Ho-Baillie, H. J. Snaith, *Nat. Photonics* **8**, 506–514 (2014).
10. N. J. Jeon *et al.*, *Nat. Mater.* **13**, 897–903 (2014).
11. N. J. Jeon *et al.*, *Nature* **517**, 476–480 (2015).
12. J. H. Noh, S. H. Im, J. H. Heo, T. N. Mandal, S. I. Seok, *Nano Lett.* **13**, 1764–1769 (2013).
13. G. E. Eperon *et al.*, *Energy Environ. Sci.* **7**, 982 (2014).
14. W. S. Yang *et al.*, *Science* **348**, 1234–1237 (2015).
15. E. T. Hoke *et al.*, *Chem. Sci.* **6**, 613–617 (2015).
16. B. Conings *et al.*, *Adv. Energy Mater.* 10.1002/aenm.201500477 (2015).
17. W. Rehman *et al.*, *Adv. Mater.* **27**, 7938–7944 (2015).
18. C. D. Bailie *et al.*, *Energy Environ. Sci.* **8**, 956–963 (2015).
19. P. Löper *et al.*, *Phys. Chem. Chem. Phys.* **17**, 1619–1629 (2015).
20. S. Albrecht *et al.*, *Energy Environ. Sci.* 10.1039/C5EE02965A (2015).
21. A. Binek, F. C. Hanusch, P. Docampo, T. Bein, *J. Phys. Chem. Lett.* **6**, 1249–1253 (2015).
22. S. Pang *et al.*, *Chem. Mater.* **26**, 1485–1491 (2014).
23. C. C. Stoumpos, C. D. Malliakas, M. G. Kanatzidis, *Inorg. Chem.* **52**, 9019–9038 (2013).
24. N. Pellet *et al.*, *Angew. Chem. Int. Ed. Engl.* **53**, 3151–3157 (2014).
25. S. D. Stranks, H. J. Snaith, *Nat. Nanotechnol.* **10**, 391–402 (2015).
26. J.-W. Lee *et al.*, *Adv. Energy Mater.* 10.1002/aenm.201501310 (2015).
27. H. Choi *et al.*, *Nano Energy* **7**, 80–85 (2014).

28. See the supplementary materials on *Science* Online.
29. C. Bi, Y. Yuan, Y. Fang, J. Huang, *Adv. Energy Mater.* 10.1002/aenm.201401616 (2014).
30. K. Tvingstedt *et al.*, *Sci. Rep.* **4**, 6071 (2014).
31. S. De Wolf *et al.*, *J. Phys. Chem. Lett.* **5**, 1035–1039 (2014).
32. A. Sadhanala *et al.*, *J. Phys. Chem. Lett.* **5**, 2501–2505 (2014).
33. R. L. Milot, G. E. Eperon, H. J. Snaith, M. B. Johnston, L. M. Herz, *Adv. Funct. Mater.* **25**, 6218–6227 (2015).
34. W. Tress *et al.*, *Adv. Energy Mater.* 10.1002/aenm.201400812 (2014).
35. H. J. Snaith, *Adv. Funct. Mater.* **20**, 13–19 (2010).
36. U. Rau, *Phys. Rev. B* **76**, 085303 (2007).
37. L. Mazzarella *et al.*, *Appl. Phys. Lett.* **106**, 023902 (2015).

ACKNOWLEDGMENTS

This project was funded in part by the Engineering and Physical Sciences Research Council through the Supergen Solar Energy Hub SuperSolar (EP/M024881/1, EP/M014797/1) and the European Research Council through the Stg-2011 Hybrid Photovoltaic Energy Relays and the European Union Seventh Framework Programme (FP7/2007-2013) under grant agreement 604032 of the MESO project, and the U.S. Office of Naval Research. M.H. is funded by Oxford PV Ltd. W.R. is supported by the Hans-Boeckler-Foundation. We thank our colleagues from the Centre For Renewable Energy Technologies Photovoltaic Measurement and Testing Laboratory, Loughborough University, for their contributions to the measurements of the semi-transparent devices. We also thank K. Jacob and M. Wittig [Helmholtz-Zentrum Berlin (HZB), Institute for Silicon Photovoltaics], L. Mazzarella, and S. Kirner (HZB, Institute PVcomB) for their contributions to fabricating the SHJ cell. The University of Oxford has filed a patent related to this work. The project was designed and conceptualized by D.M. and H.J.S. D.M. performed experiments, analyzed data, and wrote the first draft of the paper. G.S. fabricated and measured devices with semi-transparent electrodes. W.R. characterized the material using THz spectroscopy. G.E. helped with the experimental work and provided technical feedback on the writing of the paper. M.S. provided input and technical direction on the FA/Cs cation mixture. M.H. performed simulations for the optical modeling and calculated the maximum achievable V_{OC}. A.H. analyzed XRD data. N.S. provided input on the preparation of thin films using chemical bath depositions. L.K. and B.R. designed and supervised the fabrication of the SHJ cells. M.J. performed and analyzed EQE measurements. L.H. supervised and analyzed the THz spectroscopy measurements. H.J.S. supervised the overall conception and design of this project. All authors contributed to the writing of the paper.

SUPPLEMENTARY MATERIALS

www.sciencemag.org/content/351/6269/151/suppl/DC1
Materials and Methods
Supplementary Text
Figs. S1 to S15
References (*38*–*42*)

5 October 2015; accepted 3 December 2015
10.1126/science.aad5845

FOREST ECOLOGY

Dominance of the suppressed: Power-law size structure in tropical forests

C. E. Farrior,[1,2]* S. A. Bohlman,[3,4] S. Hubbell,[4,5] S. W. Pacala[6]

Tropical tree size distributions are remarkably consistent despite differences in the environments that support them. With data analysis and theory, we found a simple and biologically intuitive hypothesis to explain this property, which is the foundation of forest dynamics modeling and carbon storage estimates. After a disturbance, new individuals in the forest gap grow quickly in full sun until they begin to overtop one another. The two-dimensional space-filling of the growing crowns of the tallest individuals relegates a group of losing, slow-growing individuals to the understory. Those left in the understory follow a power-law size distribution, the scaling of which depends on only the crown area–to–diameter allometry exponent: a well-conserved value across tropical forests.

Tree size distributions—the frequency of trees by size—are important emergent properties of forests. Tree size distributions signal community-level interactions, are a critical diagnostic of the accuracy of scaling in mechanistic models, and are the basis of many aboveground forest carbon estimates (*1*–*3*). Despite differences in the tree vital rates that determine them, tropical forests worldwide have tree size distributions that follow tight power functions with very similar scaling for a wide range of diameters and commonly have deviations in the tails (*4*, *5*) (Fig. 1). Such a consistent emergent pattern begs an explanation, one that is likely to provide an important key to understanding the mechanisms governing tropical forest dynamics (*6*).

Current theories explaining the consistency of tropical forest size structure are controversial. Explanations based on scaling up individual metabolic rates (*4*, *7*, *8*) are criticized for ignoring the importance of asymmetric competition for light in causing variation in dynamic rates (*9*–*11*). Other theories, which embrace competition and scale individual tree vital rates through an assumption of demographic equilibrium (*5*, *10*, *12*, *13*), are criticized for lacking parsimony, because predictions rely on site-level, size-specific parameterizations (*14*). Despite their differences, common to these theories is the notion that the predicted size structure is a property of steady-state forests far removed from the influence of disturbance. We tested this prediction. We explored the size structure within a well-studied tropical forest and, with theoretical corroboration, present a parsimonious and biologically intuitive explanation for the power-function size structure, observed deviations, and the consistency of the scaling across forests.

[1]National Institute for Mathematical and Biological Synthesis, Knoxville, TN 37996, USA. [2]Department of Integrative Biology, University of Texas at Austin, Austin, TX 78712, USA. [3]School of Forest Resources and Conservation, University of Florida, Gainesville, FL 32611, USA. [4]Smithsonian Tropical Research Institute, Apartado 0843–03092, Balboa, Ancon, Republic of Panama. [5]Department of Ecology and Evolutionary Biology, University of California, Los Angeles, CA 90095, USA. [6]Department of Ecology and Evolutionary Biology, Princeton University, Princeton, NJ 08544, USA.
***Corresponding author. E-mail: cfarrior@nimbios.org**

We explored temporal and spatial patterns in tropical forest size structure in 50 ha and 30 years of data from Barro Colorado Island, Panama (BCI) (*15*–*17*). Forest patches in the early stages of recovery from small-scale disturbances (*18*) develop a power function that extends through a greater range of diameters as time progresses (Fig. 2). At 25 to 30 years after disturbance, the power function extends through the full range of diameters present, and unlike in younger patches, a power law is a likely model of the data [(*18*), criteria following (*19*)]. However, the power-law fit is again lost in patches with more than 30 years since the last disturbance.

Having reached the limit of our temporal analyses, we examined forest patches as grouped by forest size. We used the metric D^*_{est} as an estimate of the size threshold for tree canopy status in a patch (*18*). For each range of D^*_{est}, we fit a power function (with the same scaling as Fig. 1, fit to all data) that transitions at a single size class to an exponential distribution (Fig. 3A) (*18*). This best-fit size class of transition increases with D^*_{est} (Fig. 3B, $P = 0.005$, t test, R-squared = 0.76,

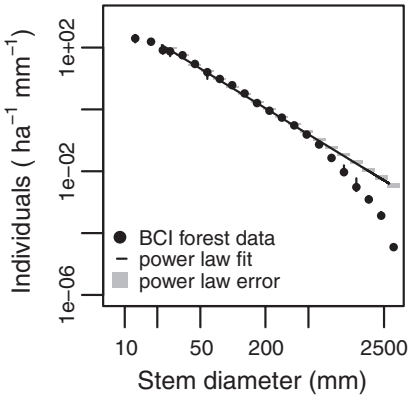

Fig. 1. Size distribution of the 50-ha tropical forest dynamics plot on BCI. The average (points) and range (bars) by size class among all seven censuses are shown. The best-fit power law distribution to all diameters from censuses 3 to 7 (*18*) is drawn (black line). The expected range of variation for that power law, given the average census sample size by size class, is in gray [95% range (*18*)].

N = 6 ranges of D^*_{est} slope = 1.23 mm mm^{-1}). Trees that are likely in the understory, with diameters less than their patch's D^*_{est}, are well characterized by the power function, whereas those that are likely in the canopy are not.

We have three main empirical results: (i) Power-function size structure emerges progressively after likely gap-generating disturbances (Figs. 1 and 2); (ii) understory trees, but not canopy trees, generally follow power-function structure (Fig. 3); and (iii) forest patches far in time from the last local disturbance are responsible for the deviations in the high tail of the landscape-level distribution (Fig. 2). Together these pieces of evidence point to a new hypothesis: Small-scale, gap-generating disturbances maintain power-function size structure whereas later-successional forest patches are responsible for deviations in the high tail. To explore and test this hypothesis, we turned to a model.

In a small, gap-sized patch of forest (1000 m^2), the simulation started from bare ground. Individuals were characterized by their diameter (d) and crown area (ϕd^{θ}). Crown area is the projected two-dimensional area of a tree's canopy. We assumed that the allometric exponent θ was a constant, following theoretical predictions at the individual-plant level (*20*, *21*). Seedlings recruit at a constant rate and grow in diameter in full sun at a constant rate with a constant probability of mortality until the canopy closes. Assuming phototropic growth (*22*), when the sum of the crown areas of all trees exceeds the patch area, the canopy closes. At this point, the largest individuals whose summed crown area is less than the patch size remain in full sun, maintaining canopy growth and mortality rates. All other individuals are overtopped and grow in the understory at a single slower rate and have a single higher probability of mortality. At each time step, the patch has a probability of a gap-generating disturbance, setting the patch back to bare ground. A forest landscape is assembled by compiling snapshots of the simulation (*18*). We estimated all model parameters (table S1) from BCI individual tree vital-rate data (*18*), except for the gap-generating disturbance rate, which was estimated from the central Amazon (*2*) and assumed to be responsible for half of the observed canopy mortality. The critical parameter of θ (1.28) was measured directly on BCI (*22*).

The resulting landscape-level size distribution matches the probability distribution of diameters on BCI well throughout the full range of the diameters (Fig. 4A). It captures the power function throughout intermediate diameters and the departures in both tails. Size-dependent demographic rates also compare well with this simple model (fig. S2). To understand the mechanisms that generate this goodness of fit, we turn to its mathematical approximation.

Consider the succession of a single patch of forest (size P), initiated by one cohort of seedlings after a patch-clearing disturbance. After the canopy closes, the number of canopy individuals (N_c) is a function of only their size (stem diameter d_c and crown area = ϕd_c^{θ})

$$N_c = \frac{P}{\phi d_c^{\theta}} \quad (1)$$

As trees grow, the number that can fit in the canopy decreases

$$\frac{dN_c}{dd_c} = \frac{-P\theta}{\phi d_c^{\theta+1}} \quad (2)$$

The decrease in canopy trees is achieved in two ways: random mortality (μ_c), which kills the trees, and overtopping, which moves canopy trees to the understory. Over the time period it takes for 1 mm of growth in stem diameter (G_c^{-1})

$$\frac{P\theta}{\phi d_c^{\theta+1}} = \text{new understory trees} + \frac{\mu_c}{G_c}\frac{P}{\phi d_c^{\theta}} \quad (3)$$

While d_c is small, new understory trees in Eq. 3 are approximately equal to $\frac{P\theta}{\phi d^{\theta+1}}$, which is a power law in d of scaling $-(\theta + 1)$ (Fig. 4B). Taking the approximation that the slow-growing understory trees do not grow at all (G_u = 0) (*23*, *24*) and have

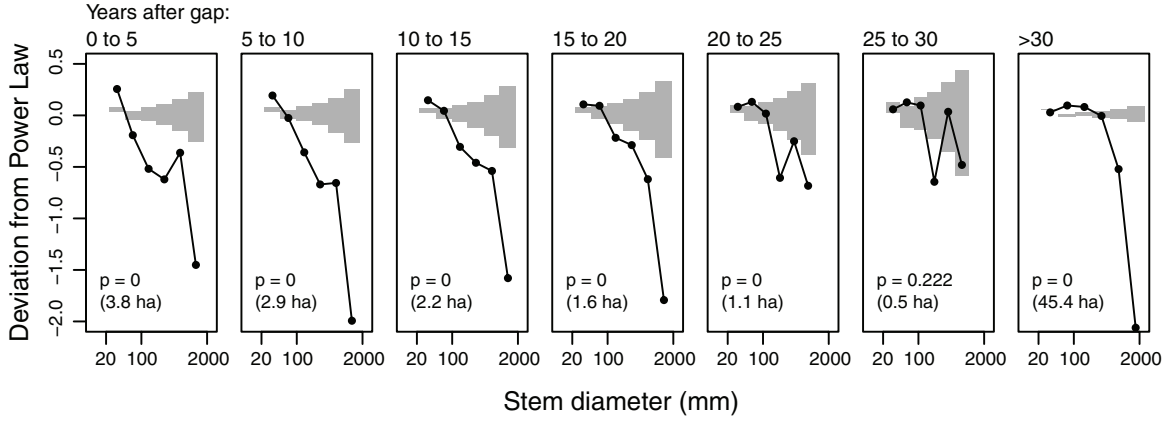

Fig. 2. Tree size distributions and time since local disturbance. Size distributions for combined 5 m by 5 m subplots at the same time in recovery (panel titles) from a gap (*18*). For clarity, deviations in log space from the power law are plotted (black, individuals mm^{-1} ha^{-1}). The area sampled is shown (in ha). Gray shows the expected range of deviation for the power law, given the area of data sampled (95% confidence interval). The P values are the proportion of synthetic distributions that fit worse than the data to the power law, using the Kolmogorov-Smirnov statistic as the metric of goodness of fit [P > 0.1 indicates a likely fit (*18*)].

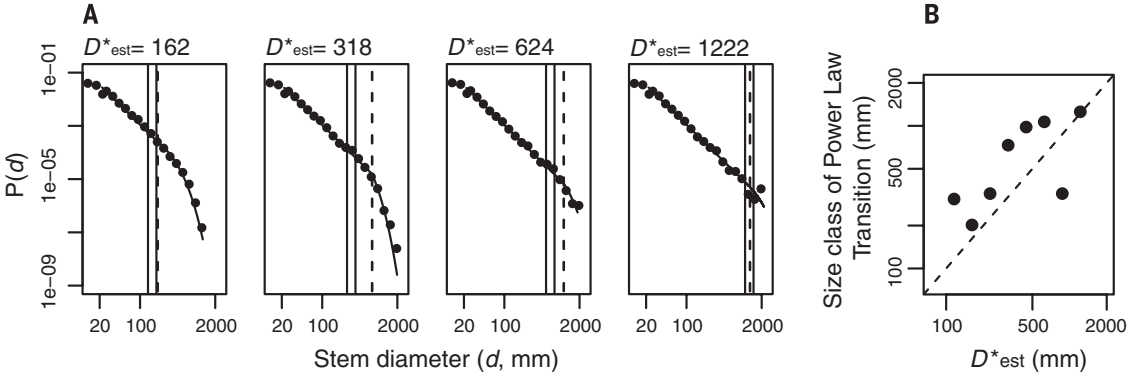

Fig. 3. Tree size distributions and forest size. (**A**) Size distributions for combined, circular, 20-m-diameter patches (points) grouped by estimated minimum diameter of canopy trees [D^*_{est} (*18*); solid vertical lines mark the range]. The power-law best fit to all data (Fig. 1) with the size class best fit for transition (dashed vertical lines) to an exponential tail is shown in black. (**B**) The full range of D^*_{est} and the size class of transition from power-law to exponential distribution.

a constant mortality rate (μ_u) the size distribution of understory trees at time t is (note: $d_c = G_c t$)

$$N_u(d,t) = \begin{cases} 0, t < \dfrac{d}{G_c} \\ \left(\dfrac{P\theta}{\phi d^{\theta+1}} - \dfrac{\mu_c}{G_c}\dfrac{P}{\phi d^{\theta}}\right) e^{-\mu_u\left(t-\frac{d}{G_c}\right)}, t \geq \dfrac{d}{G_c} \end{cases} \quad (4)$$

The expressions for N_c and N_u (Eqs. 1 and 4 and fig. S1) hold until the crown area lost by the mortality of canopy trees is greater than their increase from growth (until $t = \theta/\mu_c$). Assuming that the contribution of sites with $t > \theta/\mu_c$ is negligible, and a stochastic stand-clearing disturbance rate of μ, the landscape-level size distribution (for $d < G_c\theta/\mu_c$) is (*18*)

$$N(d) \approx \frac{P}{\phi d^{\theta}}\left(e^{-\mu\frac{d}{G_c}} - e^{-\mu\frac{d+1}{G_c}}\right) + \left(\frac{P\theta}{\phi d^{\theta+1}} - \frac{\mu_c}{G_c}\frac{P}{\phi d^{\theta}}\right)\frac{\mu}{\mu_u+\mu} e^{\frac{\mu_u d}{G_c}}\left(e^{-\frac{d}{G_c}(\mu_u+\mu)} - e^{-\frac{\theta}{\mu_c}(\mu_u+\mu)}\right) \quad (5)$$

Plotting Eq. 5 against the data and simulations (Fig. 4A, red) shows, despite simplifications, that the analytical model holds the mechanisms driving the power function shape of the size distribution. Here, the dominant power function is of the form $d^{-(\theta+1)}$ (in Eq. 5) (Fig. 4B), originating from the production of understory trees by overtopping (Eqs. 2 and 3).

In tropical forests, deviations from the power law occur at both tails, which are precisely the trees for which the overtopping process is not significant. Overtopping begins when the new seedlings are large enough to close the gap, and overtopping stops when crown area loss from canopy tree mortality catches up to gains from growth, setting, respectively, lower and upper limits on the power function.

Many terms of Eq. 5, including the upper diameter limit of applicability, may be important in forests that are unlike BCI, explaining the lack of power-law size structure in some temperate and dry tropical forests. For example, of the nine forests presented by Muller-Landau *et al.* (*5*, *10*), the two driest forests (Huai Kha Khaeng and Mudumalai) have the weakest power-law size structure. These two forests also lack evidence of the slow-growing overtopped trees that make up the power law in the model. In both the Huai Kha Khaeng and Mudumalai forests, growth rates remain high across the full range of diameters. Temperate forests also often lack power-law size structure (*25*–*27*). When parameterized with slow growth rates and infrequent stand-clearing disturbances, which are likely parameters for temperate forests (table S3), model simulations also produce a lack of power-law size structure (fig. S3).

The vital-rate scaling with size that drives the consistent power-law size structure of tropical forest trees is the scaling of the number of individuals by diameter that are experiencing the shift from fast growth in the sun to slow growth in the shade during the process of recovery from a gap disturbance (Eq. 2). In both the model and the data, the power-law size structure emerges after gap-generating disturbances (Fig. 2), and the overtopped (understory) individuals are those that follow the power law (Fig. 3). The scaling exponent of the underlying power law is dependent on only the allometric exponent of the crown area–to–diameter relationship (θ). Site-level average values of θ are consistent across diverse tropical forests (table S2), explaining the consistency of scaling of the power function.

Here, we have presented evidence that the consistency among tropical forest tree size distributions is driven by the unifying mechanisms of gap-generating disturbances and subsequent asymmetric competition for light. This explanation is in stark contrast to the energy equivalence prediction of metabolic scaling theory (*4*, *7*, *8*, *14*) and models based on demographic equilibrium (*5*, *10*, *12*, *13*), in which vital rates are constant with respect to tree size. Specifically, in order to mechanistically predict ecosystem services, including carbon storage, tropical forest models must incorporate canopy gaps [as in the Ecosystem Demography model (*28*)], the phototropic growth of individuals [as in the Perfect Plasticity Approximation model (*29*)], and the strong dependence of individual growth rates on light.

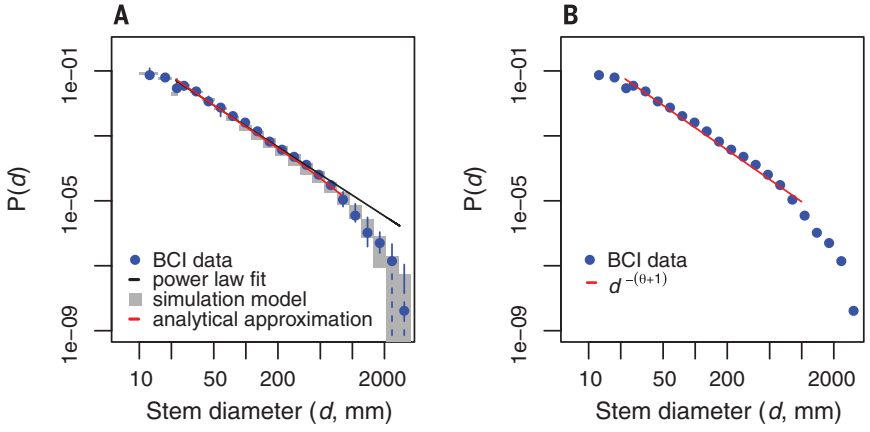

Fig. 4. Model and data comparison of tree size distributions. BCI forest dynamics plot data are shown in blue. (**A**) Data error is the 95% confidence interval for each size class from the plot cut into four subplots of 12.5 ha each (N = 28 patches). Gray boxes are simulation model results marking 95% confidence intervals for each size class (12.5 ha, N = 100 patches). The red curve shows the analytical approximation of the simulation model (Eq. 5). (**B**) BCI data (blue) compared with the dominant power-law scaling of the model ($\propto d^{-(\theta+1)}$ in Eq. 5, red).

REFERENCES AND NOTES

1. S. P. Hubbell, R. B. Foster, *Oikos* **63**, 48–61 (1992).
2. J. Q. Chambers *et al.*, *Proc. Natl. Acad. Sci. U.S.A.* **110**, 3949–3954 (2013).
3. D. C. Marvin *et al.*, *Proc. Natl. Acad. Sci. U.S.A.* **111**, E5224–E5232 (2014).
4. B. J. Enquist, K. J. Niklas, *Nature* **410**, 655–660 (2001).
5. H. C. Muller-Landau *et al.*, *Ecol. Lett.* **9**, 589–602 (2006).
6. M. P. H. Stumpf, M. A. Porter, *Science* **335**, 665–666 (2012).
7. B. J. Enquist, J. H. Brown, G. B. West, *Nature* **395**, 163–165 (1998).
8. G. B. West, J. H. Brown, B. J. Enquist, *Nature* **400**, 664–667 (1999).
9. H. Cyr, S. C. Walker, *Ecology* **85**, 1802–1804 (2004).
10. H. C. Muller-Landau *et al.*, *Ecol. Lett.* **9**, 575–588 (2006).
11. D. A. Coomes, R. B. Allen, *J. Ecol.* **95**, 1084–1097 (2007).
12. N. Rüger, R. Condit, *Funct. Ecol.* **26**, 759–765 (2012).
13. J. Lai *et al.*, *Oikos* **122**, 1636–1642 (2013).
14. B. J. Enquist, G. B. West, J. H. Brown, *Proc. Natl. Acad. Sci. U.S.A.* **106**, 7046–7051 (2009).
15. R. Condit, *Tropical Forest Census Plots* (Springer-Verlag, Berlin, Germany, and R. G. Landes Company, Georgetown, TX, 1998).
16. S. P. Hubbell *et al.*, *Science* **283**, 554–557 (1999).
17. S. P. Hubbell, R. Condit, R. B. Foster, http://ctfs.arnarb.harvard.edu/webatlas/datasets/bci (2005).
18. Materials and methods are available as supplementary materials on *Science* Online.
19. A. Clauset, C. R. Shalizi, M. E. J. Newman, *SIAM Rev.* **51**, 661–703 (2009).
20. K. Shinozaki, K. Yoda, K. Hozumi, T. Kira, *Jpn. J. Ecol.* **14**, 133–139 (1964).
21. G. B. West, B. J. Enquist, J. H. Brown, *Proc. Natl. Acad. Sci. U.S.A.* **106**, 7040–7045 (2009).
22. S. Bohlman, S. Pacala, *J. Ecol.* **100**, 508–518 (2012).
23. C. Uhl, K. Clark, N. Dezzeo, P. Maquirino, *Ecology* **69**, 751–763 (1988).
24. C. D. Canham, *Ecology* **69**, 786–795 (1988).
25. D. A. Coomes, R. P. Duncan, R. B. Allen, J. Truscott, *Ecol. Lett.* **6**, 980–989 (2003).
26. X. Wang *et al.*, *Oikos* **118**, 25–36 (2009).
27. L. I. Duncanson, R. O. Dubayah, B. J. Enquist, *Glob. Ecol. Biogeogr.* **24**, 1465–1475 (2015).
28. D. Medvigy, S. C. Wofsy, J. W. Munger, D. Y. Hollinger, P. R. Moorcroft, *J. Geophys. Res.* **114**, G01002 (2009).
29. D. W. Purves, J. W. Lichstein, N. Strigul, S. W. Pacala, *Proc. Natl. Acad. Sci. U.S.A.* **105**, 17018–17022 (2008).

ACKNOWLEDGMENTS

We thank J. Chave, H. C. Muller-Landau, and R. Chisholm for helpful discussion and L. Comita for sharing data. We gratefully acknowledge the support of the Carbon Mitigation Initiative of Princeton University and the National Institute for Mathematical and Biological Synthesis (NSF grant no. DBI-1300426, The University of Tennessee, Knoxville). The BCI forest dynamics research project was founded by S. P. Hubbell and R. B. Foster and is now managed by R. Condit, S. Lao, and R. Perez under the Center for Tropical Forest Science and Smithsonian Tropical Research in Panama. Numerous organizations have provided funding, principally in the United States. NSF and hundreds of field workers have contributed. The data are publicly available at http://ctfs.arnarb.harvard.edu/webatlas/datasets/bci.

SUPPLEMENTARY MATERIALS

www.sciencemag.org/content/351/6269/155/suppl/DC1
Materials and Methods
Supplementary Text
Figs. S1 to S3
Tables S1 to S3
Simulation Code
References (*30*–*38*)

20 August 2015; accepted 17 November 2015
10.1126/science.aad0592

MICROBIOME

Microbial community assembly and metabolic function during mammalian corpse decomposition

Jessica L. Metcalf,[1,2]* Zhenjiang Zech Xu,[2] Sophie Weiss,[3] Simon Lax,[4,5] Will Van Treuren,[6] Embriette R. Hyde,[2] Se Jin Song,[1,2] Amnon Amir,[2] Peter Larsen,[4,7] Naseer Sangwan,[4,7,8] Daniel Haarmann,[9] Greg C. Humphrey,[2] Gail Ackermann,[2] Luke R. Thompson,[2] Christian Lauber,[10] Alexander Bibat,[11] Catherine Nicholas,[11] Matthew J. Gebert,[11] Joseph F. Petrosino,[12] Sasha C. Reed,[13] Jack A. Gilbert,[4,5,7,8,14] Aaron M. Lynne,[9] Sibyl R. Bucheli,[9] David O. Carter,[15] Rob Knight[2,16]*

Vertebrate corpse decomposition provides an important stage in nutrient cycling in most terrestrial habitats, yet microbially mediated processes are poorly understood. Here we combine deep microbial community characterization, community-level metabolic reconstruction, and soil biogeochemical assessment to understand the principles governing microbial community assembly during decomposition of mouse and human corpses on different soil substrates. We find a suite of bacterial and fungal groups that contribute to nitrogen cycling and a reproducible network of decomposers that emerge on predictable time scales. Our results show that this decomposer community is derived primarily from bulk soil, but key decomposers are ubiquitous in low abundance. Soil type was not a dominant factor driving community development, and the process of decomposition is sufficiently reproducible to offer new opportunities for forensic investigations.

The process of decay and decomposition in mammalian and other vertebrate taxa is a key step in biological nutrient cycling. Without the action of vertebrate and invertebrate scavengers, bacteria, archaea, fungi, and protists, chemical decomposition of animal waste would proceed extremely slowly and lead to reservoirs of biochemical waste (*1*). The coevolution of microbial decomposers with the availability of vertebrate corpses over the past 400 million years is expected to result in conservation of key biochemical metabolic pathways and cross-kingdom ecological interactions for efficient recycling of nutrient reserves. Although mammalian corpses likely represent a relatively small component of the detritus pool (*2*, *3*) in most ecosystems, their role in nutrient cycling and community dynamics may be disproportionately large relative to input size, owing to the high nutrient content of corpses (*3*, *4*) and their rapid rates of decomposition [e.g., up to three orders of magnitude faster than plant litter (*2*)]. These qualities make corpses a distinct and potentially critical driver of terrestrial function (*5*, *6*).

When a mammalian body is decomposing, microbial and biochemical activity results in a series of decomposition stages (*5*) that are associated with a reproducible microbial succession across mice (*7*), swine (*8*), and human corpses (*9*). Yet the microbial metabolism and successional ecology underpinning decomposition are still poorly understood. At present, we do not fully comprehend (i) whether microbial taxa that drive decomposition are ubiquitous across environment, season, and host phylogeny; (ii) whether microbes that drive decomposition derive primarily from the host or from the environment; and (iii) whether the metabolic succession of microbial decomposition is conserved across the physicochemical context of decay and host phylogeny.

Several questions arise: Are microbial decomposer communities ubiquitous? What is the origin of the microbial decomposer community? How does mammalian decomposition affect the metabolic capacity of microbial communities? To answer these questions, we used mouse corpses in laboratory settings and human donors in outdoor settings (see supplementary materials and methods). We observed mouse decomposition on three different soil types under constant temperature and humidity, with insects excluded. We sampled microbial communities on the skin, abdominal cavity, and gravesoil (soils associated with decomposition) by destructively sampling five mice per soil type per time point every 3 days for the first 2 weeks and less frequently thereafter over 71 days of decomposition (fig. S1). Outdoor experiments on human corpses were conducted at the Sam Houston State University (SHSU) Southeast Texas Applied Forensic Science (STAFS) Facility (a willed-body donation facility), where human bodies were exposed to all natural elements, including invertebrate and vertebrate scavengers. We sampled the skin and gravesoil associated with four decomposing human bodies—two of which were placed in the winter and two in the spring—over 143 days and 82 days, respectively (fig. S1). Human donors were sampled either daily or every other day during the first month and less frequently thereafter. We used high-throughput amplicon-based sequencing of 16*S* ribosomal RNA (rRNA) genes (archaeal and bacterial community), 18*S* rRNA genes (microbial eukaryotic community), and internal transcribed spacer regions (fungal community) to characterize the full microbial diversity associated with decomposition (figs. S2 to S5).

A mammalian corpse is a disturbance habitat that selects for a specialized microbial community capable of decomposing a highly concentrated source of proteins and lipids, rather than the plant-derived polysaccharides from which most detritus is derived. Our results show that microbial communities change significantly during decomposition (tables S1 to S12) and become more similar to each other across body sites and gravesoils (supplementary materials). Although mice were decomposed on soils with different chemical properties (table S13), soil type was not a major driver of skin decomposer bacterial structure (Fig. 1A). A Random Forests regression model trained on our microbial data resulted in estimates of the postmortem interval (PMI) with errors ~2 to 3 days over first 2 weeks of decomposition (fig. S6). Additionally, estimates of PMI remained accurate when bacterial data associated with one soil type were used to train a regression model and predict PMI for samples associated with other soil types (fig. S7). In our human experiments, we also observed a reproducible succession of microbes across bodies within the same season (Fig. 1B and fig. S8), as well as accurate estimates of PMI across seasons and host species (Fig. 1C and fig. S9). We discovered that important features (i.e., microbes) in our experiment-specific regression models were similar across experiments (Fig. 1D). Together these results confirm that microbial succession was predictable across soil types, seasons, and host species.

The microbial decomposer community may emerge from multiple environments in which decomposer organisms are often rare (low abundance) before decomposition begins. For the mouse experiment, we used dynamic Bayesian inference neural information flow networks, which revealed that soil was significantly more likely to be a source of bacteria and archaea for

[1]Department of Ecology and Evolutionary Biology, University of Colorado, Boulder, CO 80309, USA. [2]Department of Pediatrics, University of California, San Diego, San Diego, CA 92037, USA. [3]Department of Chemical and Biological Engineering, University of Colorado, Boulder, CO 80303, USA. [4]Department of Ecology and Evolution, University of Chicago, 1101 East 57th Street, Chicago, IL 60637, USA. [5]Institute for Genomic and Systems Biology, University of Chicago, 900 East 57th Street, Chicago, IL 606037, USA. [6]Department of Microbiology and Immunology, Stanford University, Stanford, CA 94305, USA. [7]Biosciences Division, Argonne National Laboratory, South Cass Avenue, Argonne, IL 60439, USA. [8]Department of Surgery, University of Chicago, A27 South Maryland Avenue, Chicago, IL 60637, USA. [9]Department of Biological Sciences, Sam Houston State University, Huntsville, TX 77340, USA. [10]Nestlé Institute of Health Sciences, École Polytechnique Fédérale Lausanne, Bâtiment H, 1015 Lausanne, Switzerland. [11]BioFrontiers Institute, University of Colorado, Boulder, CO 80303, USA. [12]Alkek Center for Metagenomics and Microbiome Research, Department of Molecular Virology and Microbiology, Baylor College of Medicine, Houston, TX 77030, USA. [13]U.S. Geological Survey, Southwest Biological Science Center, Moab, UT 84532, USA. [14]Marine Biological Laboratory, 7 MBL St, Woods Hole, MA 02543, USA. [15]Laboratory of Forensic Taphonomy, Forensic Sciences Unit, Division of Natural Sciences and Mathematics, Chaminade University of Honolulu, Honolulu, HI 96816, USA. [16]Department of Computer Science and Engineering, University of California, San Diego, San Diego, CA 92037, USA.
*Corresponding author. E-mail: robknight@ucsd.edu (R.K.); jessica.metcalf@colorado.edu (J.L.M.)

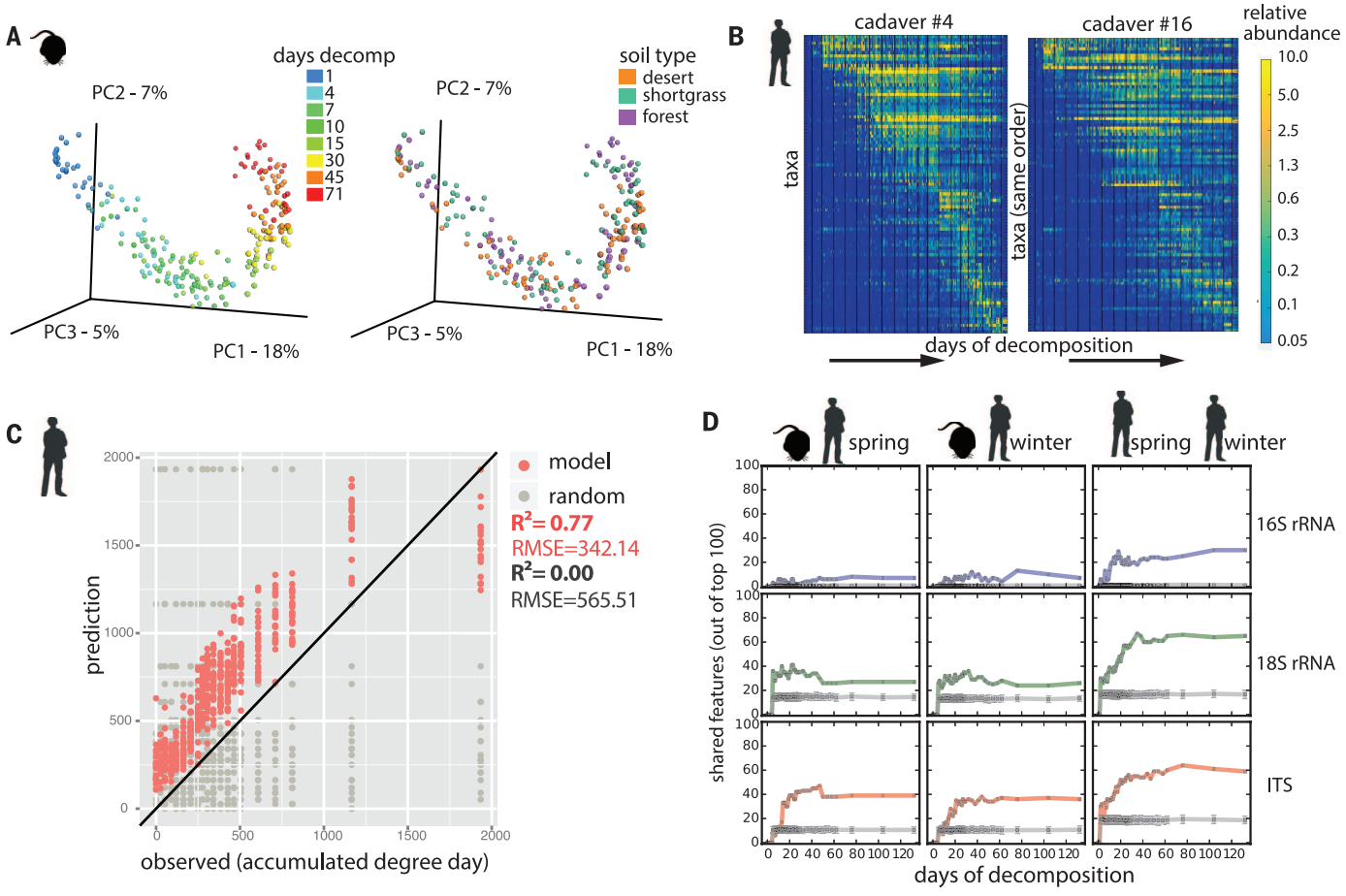

Fig. 1. Microbial decomposer communities are similar across environments. (**A**) Results of principal coordinates analysis (PCoA) based on unweighted UniFrac distances for mouse skin bacterial and archaeal communities. Samples are colored by days of decomposition (left) and soil type (right). (**B**) Log scale heat map of 16S rRNA operational taxonomic units (OTUs) colonizing the skin of human corpses. (**C**) A 16S rRNA–based Random Forests (RF) model using our winter-season skin-and-soil data set to train the model and predict the PMI of human bodies in the spring. Each point indicates a sample collected at a certain PMI, with RF-predicted PMIs shown in red and randomly guessed PMIs in gray. RMSE, root mean square error. (**D**) Percentage of top 100 PMI regression features from each environment that were shared (colored lines) versus number of shared features from randomly selected subsets of size 100 (gray lines). ITS, internal transcribed spacer.

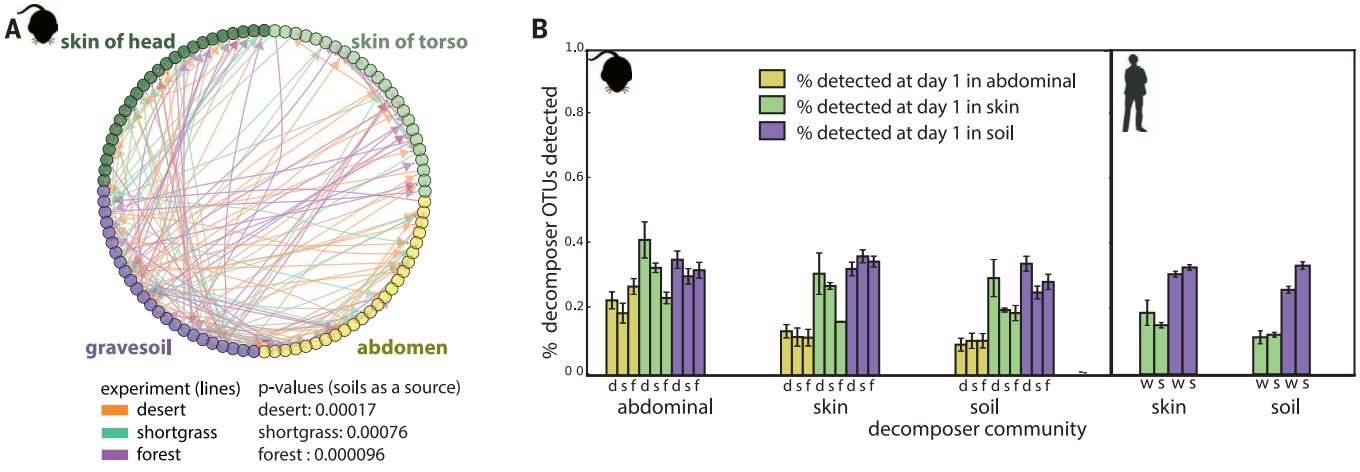

Fig. 2. Bacterial and archaeal decomposers emerge from multiple environments, but primarily from soil. (**A**) Dynamic Bayesian inference networks: A neural information flow network of microbial taxa during decomposition shows soils as the most common source of decomposers. (**B**) Results from deeply sequencing 16S rRNA amplicons from samples collected on the first day of each experiment. The *y* axis indicates the proportion of abdominal, skin, and soil decomposer OTUs (*x* axis) detected in each environment at the start of the experiment. Bars with standard error are ordered by soil type [desert (d), shortgrass (s), and forest (f)] (left) or season [winter (w) and spring (s)] (right). Decomposers were detected in soils more frequently than in the abdomen in every comparison (Mann-Whitney *U* test: $P < 0.05$).

the colonization of mice (Fig. 2A). To identify the potential sources of decomposer microbial communities, we deeply sequenced 16*S* rRNA amplicons from samples collected on the first day of each experiment. We searched these deeply sequenced data for decomposers, which we defined as microbes that differentially increased during decomposition, and found that ~40% of microbial decomposers were detected at very low relative abundances in soils at the start of experiments (supplementary text) (Fig. 2B). To understand the extent to which the blow fly, a common postmortem scavenger insect, may contribute to the microbial decomposer community, we also sequenced the bacterial and archaeal communities on 79 blow

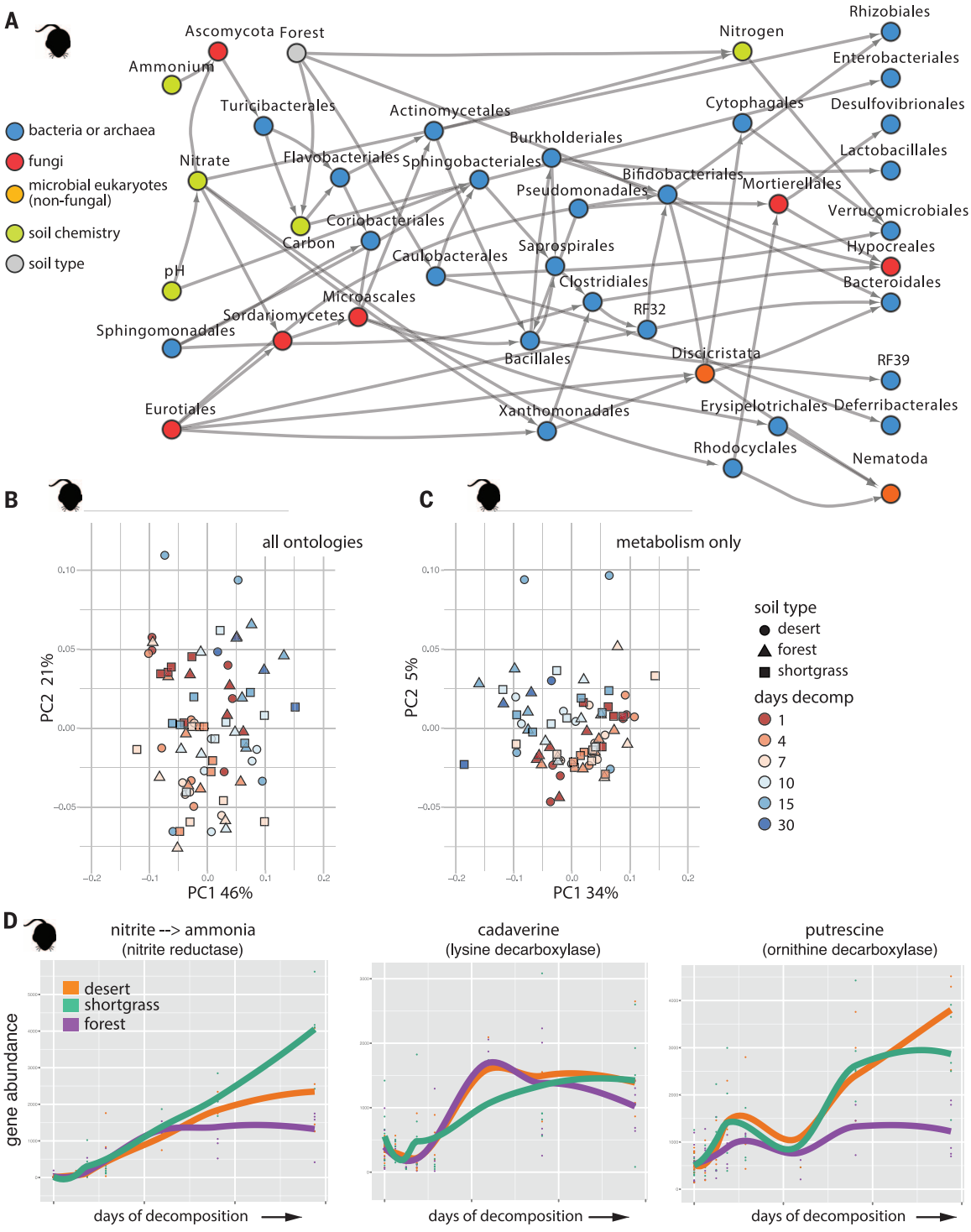

Fig. 3. Succession of decomposer communities in the abdominal cavity. (**A**) Dynamic Bayesian network of interactions between archaea, bacteria, microbial eukaryotes, and environmental abundance measurements during decomposition. Arrows indicate the direction of causality, and the network is arranged hierarchically so that it is a proxy for succession. (**B** and **C**) Results of PCoA of cecum, with all of the PICRUSt-predicted KEGG orthologies (KOs) (B) or KOs only classified as "metabolism" in KEGG functional hierarchies (C). (**D**) PICRUSt-predicted nitrite reductase, lysine decarboxylase, and ornithine decarboxylase enzyme-level genes in the mouse abdominal cavity during decomposition.

fly tarsi (supplementary materials) and discovered that they were a potential source for microbial decomposers, particularly in the human model experiment that occurred in the spring (fig. S10). Our results show that soil may be the main source of the microbial decomposer community, even though soil type is not important.

When a mammal dies, its immune system no longer functions and its internal temperatures change (*10*), radically altering the environment for microbial colonization and growth. Most endogenous mammalian microbes reside in the gastrointestinal tract, and postmortem changes in the gut microbial community lead to corpse bloating and, eventually, rupture (*5*). To investigate the microbial community dynamics of the abdominal cavity during decomposition, we used longitudinal data from the mouse abdomen samples to construct a dynamic Bayesian network of interactions between different taxa and several soil environmental factors (as a proxy for the abdominal environment). Nematodes are dependent on the actions of fungi and bacteria, with kinetoplastids (Discicristata) playing a key role in community succession (Fig. 3A). Fungi in the groups Eurotiales and Ascomycota are strong drivers of community structure, whereas fungi in Hypocreales appear to depend on the presence of bacteria for colonization of the abdomen. These shifts in microbial taxa are associated with large shifts in functional gene abundances, as predicted from 16*S* rRNA data analysis using the PICRUSt (phylogenetic investigation of communities by reconstruction of unobserved state) software (Fig. 3B) (*11*), particularly for Kyoto Encyclopedia of Genes and Genomes (KEGG) orthology group "metabolism" (Fig. 3C). We detected predicted increases in genes related to nitrogen cycling and amino acid degradation, including those required for the breakdown of lysine and arginine into the foul-smelling decomposition by-products cadaverine and putrescine (Fig. 3D).

After corpse rupture, ammonia-rich fluids permeate the soil, resulting in extreme and significant effects on the nitrogen concentration and pH of gravesoil (Fig. 4A, fig. S11, and table S13). This rich source of nutrients and the marked changes to soil chemistry initiate a clear ecological succession of soil microbial organisms with increased capacity for nitrogen cycling and tolerance for the altered soil chemical environment (Fig. 4B and fig. S12). Predicted functions of bacterial communities increased in relative abundance of genes for amino acid degradation and subsequent ammonia production (Fig. 4C). Surprisingly, although we observed increases in soil nitrate concentrations and processes that consume nitrate (figs. S13 and S14), we did not see genetic signs of increased nitrification rates (figs. S13 and S14). This suggests that nitrification pulses induced by vertebrate decomposition may occur on finer spatial or temporal scales or, alternatively, that the PICRUSt reference database lacks genomes from the vertebrate corpse microbial nitrifier community (e.g., fungal genomes). Taken together, analysis of the full community of predicted metabolism-related functional genes, in association with the PMI and soil chemistry data, revealed marked changes in functional potential during decomposition. The large and rapid taxonomic changes in microbial communities—as well as their subsequent effect on the predicted metabolic capacity of both the corpse (Fig. 3) and its surrounding environment (Fig. 4 and fig. S13) during decomposition—may be part of a microbial strategy to outcompete insects and scavengers for an ephemeral, nutrient-rich resource. The dramatic changes in community structure and function may also reflect the selective pressures applied by the biogeochemical hotspot formed during corpse decomposition (Fig. 4A) (*5*). As a consequence, microbial succession during decomposition appears to be a predictable process that has implications for biogeochemical cycling and forensic science.

These data are important in the context of ecosystem function. Decomposition is a fundamental

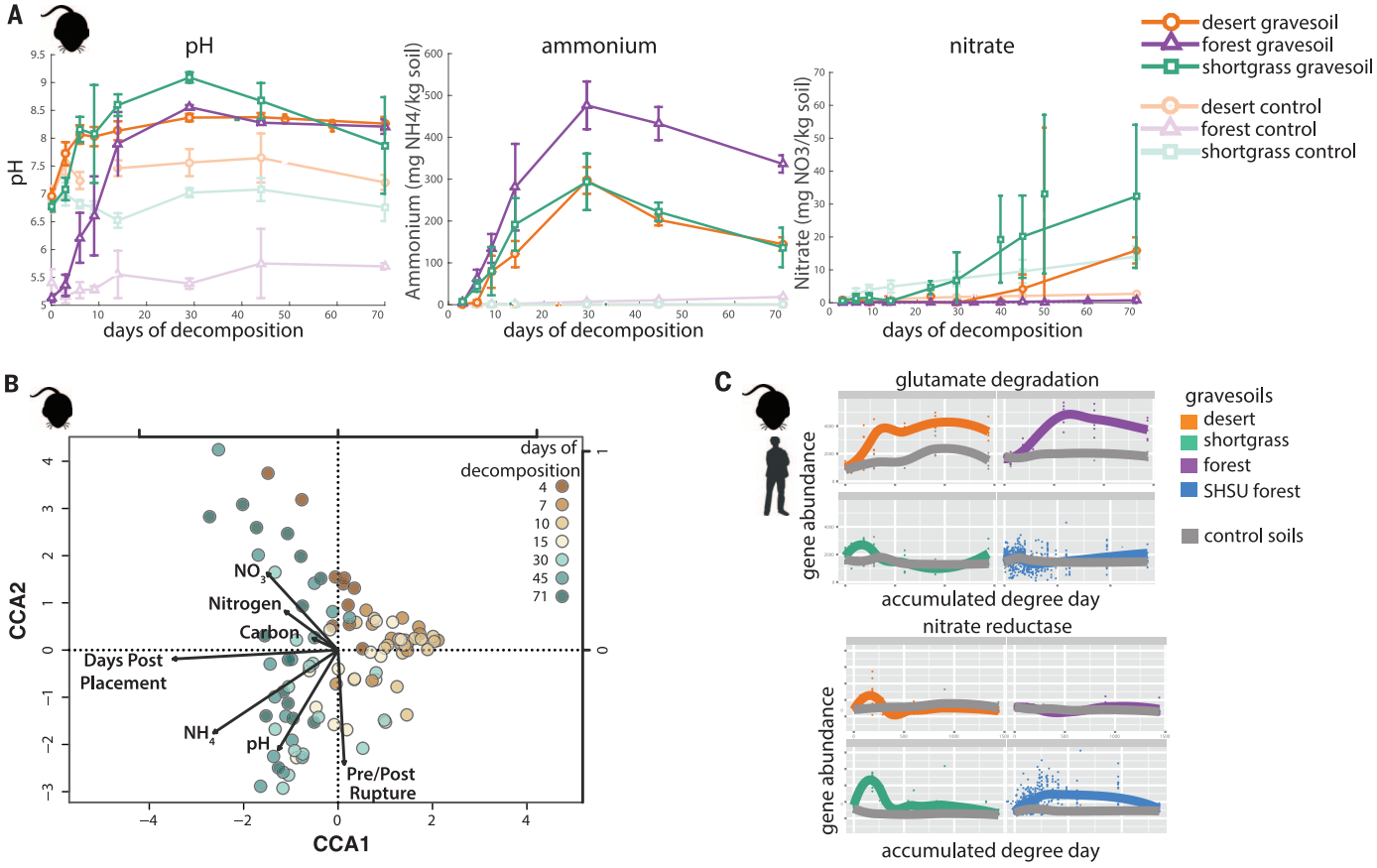

Fig. 4. Effect of mammalian decomposition on soils. (**A**) pH, ammonium, and nitrate concentrations in mouse gravesoils and control soils. Error bars indicate 1 SD from the mean of five sample measurements. (**B**) Canonical correspondence analysis (CCA) of gravesoil bacterial predicted gene ontologies during decomposition. PICRUSt-predicted function data are based on KOs, with only genes classified as "metabolism" included in this analysis. (**C**) Predicted gene abundances of glutamate dehydrogenase and nitrate reductase in soils during decomposition.

microbial function spanning terrestrial ecosystems, and though plant inputs are the dominant source of organic matter, vertebrate corpse inputs can be important resources (*5*, *6*). For example, one rain forest in Panama was estimated to receive 750 kg in mammal corpses annually per square kilometer (*12*). Although this represents less than 1% of the mass of plant litter received by another Panamanian rain forest (*13*), corpse nutrient sources can be an order of magnitude more concentrated than plant litter (*5*), and direct comparisons between plant and animal decomposition resources are rare (*14*). Thus, much is still unclear about the role of corpse inputs in larger-scale biogeochemical cycling (e.g., global carbon and nitrogen cycling) and in supporting specific communities and microbial diversity (*14*), and our results provide an important microbial perspective.

A societal impact of these results is the value of microbial data as physical evidence in medicolegal death investigation. We show that decomposer microbial communities could potentially serve as temporal (succession-based) and spatial (origin-based) (supplementary text) forms of physical evidence, such as the time elapsed since death (PMI) and the location of death. Our observation that postmortem microbial communities changed in a clock-like manner that provided an estimate of absolute PMI is similar to using the development of fly larvae to estimate PMI. However, the fly larvae PMI proxy is limited by corpse accessibility and season, resulting in PMI estimates in the range of weeks, months, and even years (*15*). Taken together, our findings demonstrate that postmortem microorganisms can provide both spatial and temporal insight into the events surrounding death.

REFERENCES AND NOTES

1. J. A. Gilbert, J. D. Neufeld, *PLOS Biol.* **12**, e1002020 (2014).
2. R. R. Parmenter, J. A. MacMahon, *Ecol. Monogr.* **79**, 637–661 (2009).
3. M. Swift, O. Heal, J. Anderson, *Decomposition in Terrestrial Ecosystems* (Blackwell Scientific, Oxford, 1979).
4. J. C. Moore *et al.*, *Ecol. Lett.* **7**, 584–600 (2004).
5. D. O. Carter, D. Yellowlees, M. Tibbett, *Naturwissenschaften* **94**, 12–24 (2007).
6. P. S. Barton, in *Carrion Ecology, Evolution, and Their Applications*, M. E. Benbow, J. K. Tomberlin, A. M. Tarone, Eds. (CRC Press, 2015), pp. 273–292.
7. J. L. Metcalf *et al.*, *eLife* **2**, e01104 (2013).
8. J. L. Pechal *et al.*, *Int. J. Legal Med.* **128**, 193–205 (2014).
9. E. R. Hyde, D. P. Haarmann, J. F. Petrosino, A. M. Lynne, S. R. Bucheli, *Int. J. Legal Med.* **129**, 661–671 (2015).
10. W. E. D. Evans, *The Chemistry of Death* (Charles C Thomas, Springfield, IL, 1963).
11. M. G. I. Langille *et al.*, *Nat. Biotechnol.* **31**, 814–821 (2013).
12. D. Houston, in *Neotropical Ornithology* (American Ornithologists' Union Monograph no. 36, Washington, DC, 1985), pp. 856–864.
13. M. Kaspari *et al.*, *Ecol. Lett.* **11**, 35–43 (2008).
14. P. S. Barton, S. A. Cunningham, D. B. Lindenmayer, A. D. Manning, *Oecologia* **171**, 761–772 (2013).
15. J. Amendt *et al.*, *Int. J. Legal Med.* **121**, 90–104 (2007).

ACKNOWLEDGMENTS

The data reported in this paper are available in the Qiita database (http://qiita.ucsd.edu/) (accession numbers 10141 to 10143 and 10321) and the European Bioinformatics Institute European Nucleotide Archive (www.ebi.ac.uk/ena) (accession numbers ERP012866, ERP012879, ERP012880, and ERP012894). We thank the donors and their families for their contribution to scientific research; the STAFS Facility at SHSU and the Molecular, Cellular, and Developmental Biology Transgenic Facility at the University of Colorado, Boulder, for providing the space and opportunity for this research; N. Fierer, J. Zelikova, and J. Leff for assistance with project logistics and data processing; and the Mountain Research Station and Shortgrass Steppe Long Term Ecological Research for permission to collect soils. Mice were euthanized humanely under approved protocol no. 08-04-ACK-01 (principal investigator G.A.). This research was funded by the Office of Justice Programs National Institute of Justice Awards NIJ-2011-DN-BX-K533 (J.L.M., D.O.C., R.K.) and NIJ-2012-DN-BX-K023 (S.R.B. and A.M.L.). Research capacity and infrastructure at Chaminade University of Honolulu is supported by NIH Building Research Infrastructure and Capacity Program P789097-876. W.V.T. and S.W. were supported by the National Human Genome Research Institute grant 3 R01 HG004872-03S2, and NIH grant 5 U01 HG004866-04. J.L.M. was partially supported by a Templeton Foundation grant (R.K. and V. McKenzie). Use of trade, product, or firm names is for informational purposes only and does not constitute an endorsement by the U.S. government. J.F.P. is Chief Scientific Officer and Founder of Diversigen; C.N. is an employee of miRagen Therapeutics; and R.K. is Chief Science Officer and employee of Biota Technology, a member of the Scientific Advisory Panel at Temasek Life Sciences Laboratory, and a speaker at Nestec, Nestle Research Center.

SUPPLEMENTARY MATERIALS

www.sciencemag.org/content/351/6269/158/suppl/DC1
Materials and Methods
Supplementary Text
Figs. S1 to S19
Tables S1 to S20
References (*16*–*29*)

19 August 2015; accepted 25 November 2015
Published online 10 December 2015
10.1126/science.aad2646

ANCIENT MICROBIOME

The 5300-year-old *Helicobacter pylori* genome of the Iceman

Frank Maixner,[1]*† Ben Krause-Kyora,[2]† Dmitrij Turaev,[3]† Alexander Herbig,[4,5]† Michael R. Hoopmann,[6] Janice L. Hallows,[6] Ulrike Kusebauch,[6] Eduard Egarter Vigl,[7] Peter Malfertheiner,[8] Francis Megraud,[9] Niall O'Sullivan,[1] Giovanna Cipollini,[1] Valentina Coia,[1] Marco Samadelli,[1] Lars Engstrand,[10] Bodo Linz,[11] Robert L. Moritz,[6] Rudolf Grimm,[12] Johannes Krause,[4,5]‡ Almut Nebel,[2]‡ Yoshan Moodley,[13,14]‡ Thomas Rattei,[3]‡ Albert Zink[1]*‡

The stomach bacterium *Helicobacter pylori* is one of the most prevalent human pathogens. It has dispersed globally with its human host, resulting in a distinct phylogeographic pattern that can be used to reconstruct both recent and ancient human migrations. The extant European population of *H. pylori* is known to be a hybrid between Asian and African bacteria, but there exist different hypotheses about when and where the hybridization took place, reflecting the complex demographic history of Europeans. Here, we present a 5300-year-old *H. pylori* genome from a European Copper Age glacier mummy. The "Iceman" *H. pylori* is a nearly pure representative of the bacterial population of Asian origin that existed in Europe before hybridization, suggesting that the African population arrived in Europe within the past few thousand years.

The highly recombinant pathogen *Helicobacter pylori* has evolved to live in the acidic environment of the human stomach (*1*). Today, this Gram-negative bacterium is found in approximately half the world's human population, but fewer than 10% of carriers develop disease that manifests as stomach ulcers or gastric carcinoma (*2*, *3*). Predominant intrafamilial transmission of *H. pylori* and the long-term association with humans has resulted in a phylogeographic distribution pattern of *H. pylori* that is shared with its host (*4*, *5*). This observation suggests that the pathogen not only accompanied modern humans out of Africa (*6*), but that it has also been associated with its host for at least 100,000 years (*7*). Thus, the bacterium has been used as a marker for tracing complex demographic events in human prehistory (*4*, *8*, *9*). Modern *H. pylori* strains have been assigned to distinct populations according to their geographic origin (hpEurope, hpSahul, hpEastAsia, hpAsia2, hpNEAfrica, hpAfrica1, and hpAfrica2) that are derived from at least six ancestral sources (*4*, *5*, *8*). The modern *H. pylori* strain found in most Europeans (hpEurope) putatively originated from recombination of the two ancestral populations Ancestral Europe 1 and 2 (AE1 and AE2) (*6*). It has been suggested that AE1 originated in Central Asia, where it evolved into hpAsia2, which is commonly found in South Asia. On the other hand, AE2 appears to have evolved in northeast Africa and hybridized with AE1 to become hpEurope (*4*). However, the precise hybridization zone of the parental populations and the true origin of hpEurope are controversial. Early studies observed a south-to-north cline in AE2/AE1 frequency in Europe (*4*, *6*). This finding has been attributed to independent peopling events that introduced these ancestral *H. pylori* components, which eventually recombined in Europe since the Neolithic period. More recently, it has been suggested that the AE1/AE2 admixture might have occurred in the Middle East or Western Asia between 10,000 and 52,000 years ago and that recombinant strains were introduced into Europe with the first human recolonizers after the last glacial maximum (*7*).

In this study, we screened 12 biopsy samples from the gastrointestinal tract of the Iceman, a 5300-year-old Copper Age mummy, for the presence of *H. pylori*. Stable isotope analyses showed that the Iceman originated and lived in Southern Europe, in the Eastern Italian Alps (*10*). Genetically, he most closely resembles early European farmers (*11*–*13*). The Iceman's stomach was discovered in a reappraisal of radiological data and contains the food he ingested shortly before his death (Fig. 1) (*14*). The study material included stomach content, mucosa tissue, and content of the small and large intestines (table S1). By using direct polymerase chain reaction (PCR), metagenomic diagnostics, and targeted genome capture (figs. S1 and S2), we determined the presence of *H. pylori* and reconstructed its complete genome.

Metagenomic analysis yielded endogenous ancient *H. pylori* DNA (15,350 reads) in all gastrointestinal tract contents (Fig. 1 and table S4). A control data set derived from Iceman's muscle tissue was negative. The distribution of the observed read counts throughout the Iceman's intestinal tract is similar to that in modern *H. pylori*–positive humans, with abundance decreasing from the stomach toward the lower intestinal tract (*15*, *16*). The retrieved unambiguous reads were aligned to a modern *H. pylori* reference genome (strain 26695) and showed damage patterns indicative of ancient DNA (fig. S7) (*17*). After DNA repair, the *H. pylori* DNA was enriched up to 216-fold by using in-solution hybridization capture (Agilent) (fig. S5). From this data set, 499,245 nonredundant reads mapped to 92.2% of the 1.6-Mb *H. pylori* reference genome with an 18.9-fold average coverage (Fig. 2). In comparison with the reference, the Iceman's ancient *H. pylori* genome had ~43,000 single-nucleotide polymorphisms (SNPs) and 39 deletions that range from 95 base pair (bp) to 17 kb and mainly comprise complete coding regions. Owing to deletions, the number of genomic variants is slightly below the range of what can be observed between modern *H. pylori* strains (table S13). The analysis of SNP allele frequencies does not indicate an infection by more than one strain (supplementary materials S6). In addition, as expected for this highly recombinant bacterium, we found evidence for gene insertions from *H. pylori* strains that differ from the reference genome (details about the InDels are provided in supplementary materials S8).

[1]Institute for Mummies and the Iceman, European Academy of Bozen/Bolzano (EURAC), Viale Druso 1, 39100 Bolzano, Italy. [2]Institute of Clinical Molecular Biology, Kiel University, Schittenhelmstrasse 12, 24105 Kiel, Germany. [3]CUBE–Division of Computational Systems Biology, Department of Microbiology and Ecosystem Science, University of Vienna, Althanstrasse 14, 1090 Vienna, Austria. [4]Institute for Archaeological Sciences, University of Tübingen, Rümelinstrasse 23, 72072 Tübingen, Germany. [5]Max Planck Institute for the Science of Human History, Kahlaische Strasse 10, 07745 Jena, Germany. [6]Institute for Systems Biology, 401 Terry Avenue North, Seattle, WA 98109, USA. [7]Scuola Superiore Sanitaria Provinciale "Claudiana," Via Lorenz Böhler 13, 39100 Bolzano, Italy. [8]Department of Gastroenterology, Hepatology, and Infectious Diseases, Otto-von-Guericke University, Leipziger Strasse 44, 39120 Magdeburg, Germany. [9]Université de Bordeaux, Centre National de Référence des Helicobacters et Campylobacters and INSERM U853, 146 rue Léo Saignat, 33076 Bordeaux, France. [10]Department of Microbiology, Tumor and Cell Biology, Karolinska Institutet, 141 83 Stockholm, Sweden. [11]Department of Veterinary and Biomedical Sciences, Pennsylvania State University, University Park, PA 16802, USA. [12]Robert Mondavi Institute for Food Science, University of California, Davis, CA 95616, USA. [13]Department of Zoology, University of Venda, Private Bag X5050, Thohoyandou 0950, Republic of South Africa. [14]Department of Integrative Biology and Evolution, Konrad Lorenz Institute for Ethology, University of Veterinary Medicine Vienna, Savoyenstrasse 1a, 1160 Vienna, Austria.
***Corresponding author. E-mail: frank.maixner@eurac.edu (F.M.); albert.zink@eurac.edu (A.Z.)** †These authors contributed equally to this work. ‡These authors contributed equally to this work.

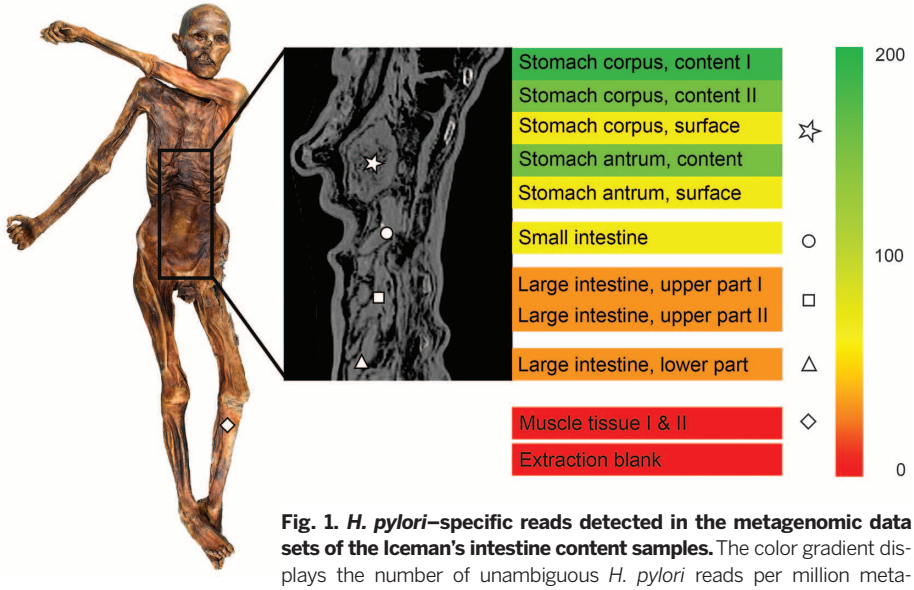

Fig. 1. *H. pylori*–specific reads detected in the metagenomic data sets of the Iceman's intestine content samples. The color gradient displays the number of unambiguous *H. pylori* reads per million metagenomic reads. Control metagenomic data sets of the Iceman's muscle tissue and of the extraction blank were included in the analysis. The different intestinal content sampling sites are marked in the radiographic image by the following symbols: asterisk, stomach content; circle, small intestine; square, upper large intestine; triangle, lower large intestine. The sampling site of the muscle control sample is highlighted in the Iceman overview picture (diamond).

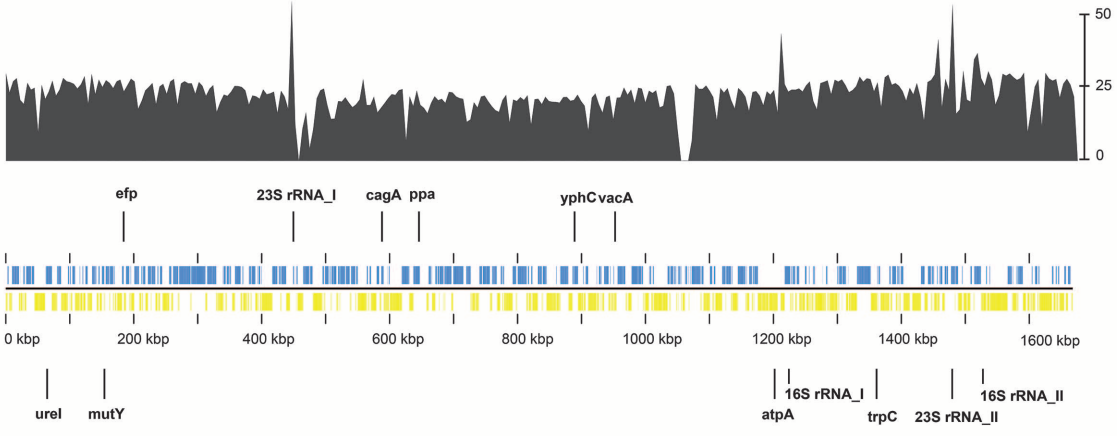

Fig. 2. Gene coverage and distribution of the enriched and validated Iceman *H. pylori* reads mapped onto the 1.6 Mb large reference genome *H. pylori* 26695. The coverage plot displayed in black is superimposed onto the genomic plot. The bar on the right-hand side indicates a coverage of up to 50×. The gene coding sequences are shown in blue (positive strand) and yellow (negative strand) bars in the genomic plot. The loci of the ribosomal RNA genes, of two virulence genes (*vacA* and *cagA*), and of seven genes used for MLST analysis are highlighted in the genome plot.

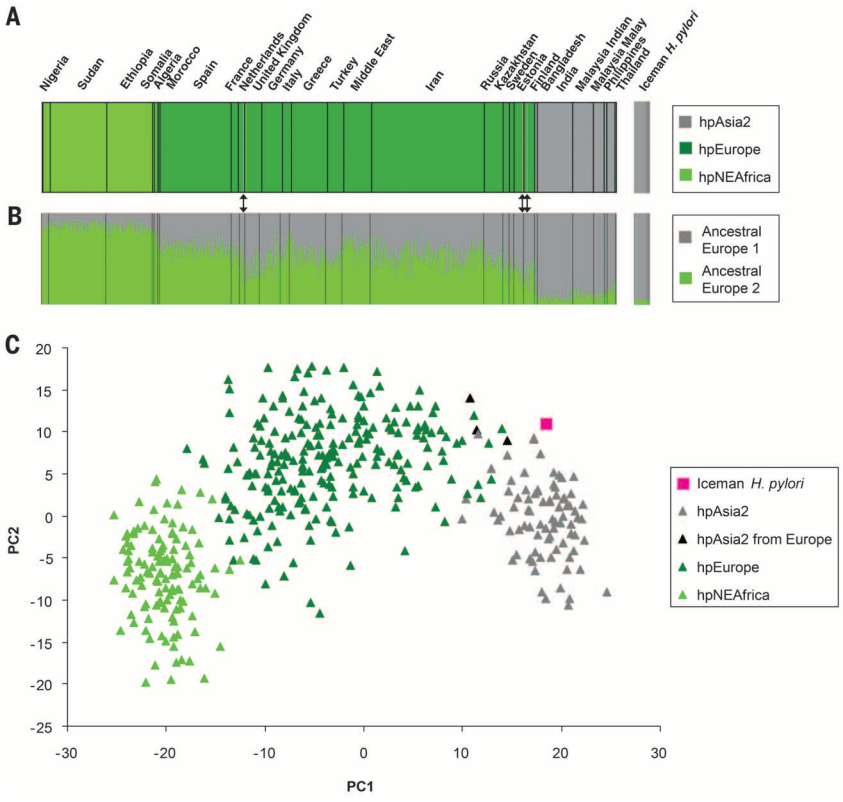

Fig. 3. Multilocus sequence analyses. (**A**) Bayesian cluster analysis performed in STRUCTURE displays the population partitioning of hpEurope, hpAsia2, and hpNEAfrica and the Iceman's *H. pylori* strain (details about the worldwide population partitioning of 1603 reference *H. pylori* strains are available in fig. S14). (**B**) STRUCTURE linkage model analysis showing the proportion of Ancestral Europe 1 (from Central Asia) and Ancestral Europe 2 (from northeast Africa) nucleotides among strains assigned to populations hpNEAfrica, hpEurope, and hpAsia2 and the Iceman's *H. pylori* strain on the extreme right. The black arrows indicate the position of the three extant European hpAsia2 strains. (**C**) Principal component analysis of contemporary hpNEAfrica, hpEurope, and hpAsia2 strains and the Iceman's *H. pylori* strain.

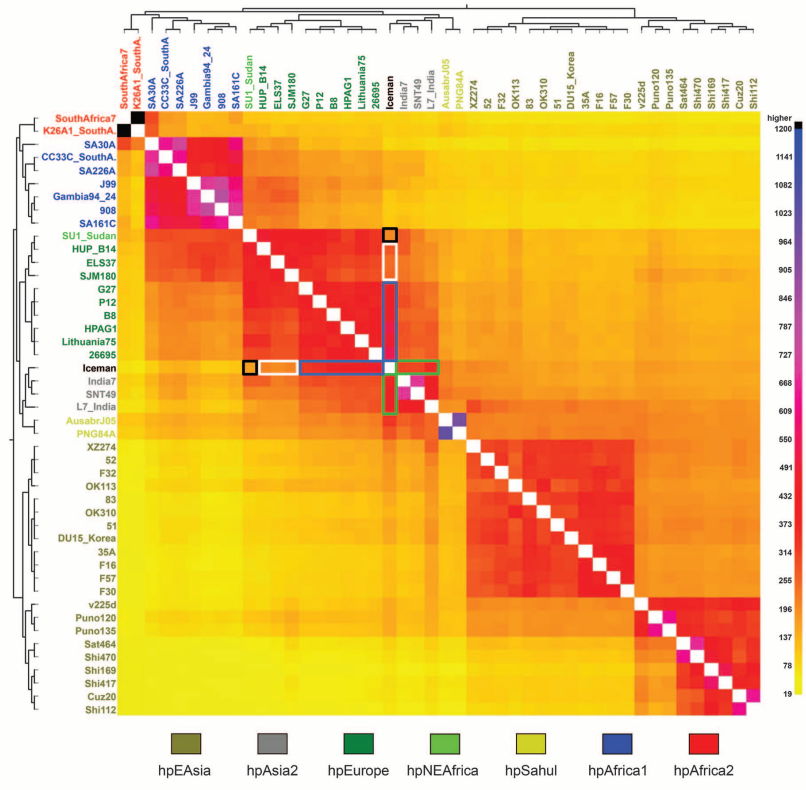

Fig. 4. Comparative whole-genome analysis. Co-ancestry matrix showing *H. pylori* population structure and genetic flux. The color in the heat map corresponds to the number of genomic motifs imported from a donor genome (column) to a recipient genome (row). The inferred tree and the *H. pylori* strain names are displayed on the top and left of the heat map. Strain names are colored according to the *H. pylori* population assignment provided in the legend below the heat map. Signs for population ancestry are highlighted in the heat map with green, blue, black, and white boxes.

Subsequent sequence analysis classified the ancient *H. pylori* as a *cagA*-positive *vacA* s1a/i1/m1 type strain that is now associated with inflammation of the gastric mucosa (fig. S11) (*18*). Using multistep solubilization and fractionation proteomics, we identified 115 human proteins in the stomach metaproteome, of which six were either highly expressed in the stomach mucosa (trefoil factor 2) (*19*) or present in the gastrointestinal tract and involved in digestion (supplementary materials S10). The majority of human proteins were enriched in extracellular matrix organizing proteins ($P = 3.35 \times 10^{-14}$) and proteins of immune processes ($P = 2 \times 10^{-3}$) (fig. S13). In total, 22 proteins observed in the Iceman stomach proteome are primarily expressed in neutrophils and are involved in the inflammatory host response. The two subunits S100A8 and S100A9 of calprotectin (CP) were detected with the highest number of distinct peptide hits in both analyzed samples. Inflamed gastric tissues of modern *H. pylori*–infected patients also show high levels of CP subunit S100A8 and S100A9 expression (*20*, *21*). Thus, the Iceman's stomach was colonized by a cytotoxic *H. pylori*–type strain that triggered CP release as a result of host inflammatory immune responses. However, whether the Iceman suffered from gastric disease cannot be determined from our analysis owing to the poor preservation of the stomach mucosa (fig. S3).

Comparative analysis of seven housekeeping gene fragments with a global multilocus sequence typing (MLST) database of 1603 *H. pylori* strains with the STRUCTURE (*22*) no-admixture model assigned the 5300-year-old bacterium to the modern population hpAsia2, commonly found in Central

and South Asia (Fig. 3A and fig. S14). The detection of an hpAsia2 strain in the Iceman's stomach is rather surprising because despite intensive sampling, only three hpAsia2 strains have ever been detected in modern Europeans. Stomachs of modern Europeans are predominantly colonized by recombinant hpEurope strains. Further analysis with the STRUCTURE linkage model (*23*), used to detect ancestral structure from admixture linkage disequilibrium, revealed that the ancient *H. pylori* strain contained only 6.5% [95% probability intervals (PI) 1.5 to 13.5%] of the northeast African (AE2) ancestral component of hpEurope (Fig. 3B). Among European strains, this low proportion of AE2 is distinct and has thus far only been observed in hpAsia2 strains from India and Southeast Asia. In contrast, the three European hpAsia2 strains (Fig. 3B, black arrows) contained considerably higher AE2 ancestries than that of the *H. pylori* strain of the Iceman (Finland 13.0%, PI 5.9 to 21.7; Estonia 13.2%, PI 6.2 to 22.3; and the Netherlands 20.8%, PI 11.5 to 31.7), although 95% probability intervals did overlap. A principal component analysis (PCA) of the MLST sequences of the hpAsia2, hpEurope, and hpNEAfrica populations revealed a continuum along PC1 that correlates with the proportion of AE2 ancestry versus AE1 ancestry of the isolates (Fig. 3C). The Iceman's ancient *H. pylori* was separated from modern hpEurope strains, and its position along PC1 was close to modern hpAsia2 strains from India, reflecting its almost pure AE1 and very low AE2 ancestry.

Comparative whole-genome analyses (neighbor joining, STRUCTURE, and principle component analyses) with publicly available genomes (n = 45) confirmed the MLST result by showing that the Iceman's ancient *H. pylori* genome has highest similarity to three hpAsia2 genomes from India (figs. S15 to S17). Although the Iceman's *H. pylori* strain appears genetically similar to the extant strains from northern India, slight differences were observed along PC2 in both MLST (Fig. 3C) and genome PCAs (fig. S17) and in the neighbor joining tree (fig. S15). To further study genomic-scale introgression, we performed a high-resolution analysis of ancestral motifs using fineSTRUCTURE (*24*). The resulting linked co-ancestry matrix (Fig. 4) showed that the ancient *H. pylori* genome shares high levels of ancestry with Indian hpAsia2 strains (Fig. 4, green boxes), but even higher co-ancestry with most European hpEurope strains (Fig. 4, blue boxes). In contrast, the Iceman's *H. pylori* shares low ancestry with the hpNEAfrica strain, a modern representative of AE2 (Fig. 4, black box), and with European strains originating from the Iberian Peninsula, where the proportion of AE2 ancestry is relatively high (Fig. 4, white box) (*4*). Our sample size (n = 1) does not allow further conclusions about the prevalence of AE1 in ancient Europe and the course or rate of AE2 introgression. However, the ancient *H. pylori* strain provides the first evidence that AE2 was already present in Central Europe during the Copper Age, albeit at a low level. If the Iceman *H. pylori* strain is representative of its time, the low level of AE2 admixture suggests that most of the AE2 ancestry observed in hpEurope today is a result of AE2 introgression into Europe after the Copper Age, which is later than previously proposed (*4*, *6*). Furthermore, our co-ancestry results indicate that the Iceman's strain belonged to a prehistoric European branch of hpAsia2 that is different from the modern hpAsia2 population from northern India. The high genetic similarity of the ancient strain to bacteria from Europe implies that much of the diversity present in Copper Age Europe is still retained within the extant hpEurope population, despite millennia of subsequent AE2 introgression.

REFERENCES AND NOTES

1. S. Suerbaum, C. Josenhans, *Nat. Rev. Microbiol.* **5**, 441–452 (2007).
2. P. Malfertheiner, F. K. Chan, K. E. McColl, *Lancet* **374**, 1449–1461 (2009).
3. R. M. Peek Jr., M. J. Blaser, *Nat. Rev. Cancer* **2**, 28–37 (2002).
4. D. Falush *et al.*, *Science* **299**, 1582–1585 (2003).
5. Y. Moodley, B. Linz, *Genome Dyn.* **6**, 62–74 (2009).
6. B. Linz *et al.*, *Nature* **445**, 915–918 (2007).
7. Y. Moodley *et al.*, *PLOS Pathog.* **8**, e1002693 (2012).
8. Y. Moodley *et al.*, *Science* **323**, 527–530 (2009).
9. T. Wirth *et al.*, *Proc. Natl. Acad. Sci. U.S.A.* **101**, 4746–4751 (2004).
10. W. Müller, H. Fricke, A. N. Halliday, M. T. McCulloch, J. A. Wartho, *Science* **302**, 862–866 (2003).
11. W. Haak *et al.*, *Nature* **522**, 207–211 (2015).
12. A. Keller *et al.*, *Nat. Commun.* **3**, 698 (2012).
13. I. Lazaridis *et al.*, *Nature* **513**, 409–413 (2014).
14. P. Gostner, P. Pernter, G. Bonatti, A. Graefen, A. R. Zink, *Arch. Sci.* **38**, 3425–3431 (2011).
15. A. F. Andersson *et al.*, *PLOS ONE* **3**, e2836 (2008).
16. N. Segata *et al.*, *Genome Biol.* **13**, R42 (2012).
17. S. Sawyer, J. Krause, K. Guschanski, V. Savolainen, S. Pääbo, *PLOS ONE* **7**, e34131 (2012).
18. K. R. Jones, J. M. Whitmire, D. S. Merrell, *Front. Microbiol.* **1**, 115 (2010).
19. M. Uhlén *et al.*, *Science* **347**, 1260419 (2015).
20. J. A. Gaddy *et al.*, *PLOS Pathog.* **10**, e1004450 (2014).
21. S. T. Leach, H. M. Mitchell, C. L. Geczy, P. M. Sherman, A. S. Day, *Can. J. Gastroenterol.* **22**, 461–464 (2008).
22. J. K. Pritchard, M. Stephens, P. Donnelly, *Genetics* **155**, 945–959 (2000).
23. D. Falush, M. Stephens, J. K. Pritchard, *Genetics* **164**, 1567–1587 (2003).
24. D. J. Lawson, G. Hellenthal, S. Myers, D. Falush, *PLOS Genet.* **8**, e1002453 (2012).

ACKNOWLEDGMENTS

We acknowledge the following funding sources: the South Tyrolean grant legge 14 (F.M., N.O.S., G.C., V.C., M.S., and A.Z.), the Ernst Ludwig Ehrlich Studienwerk, dissertation completion fellowship of the University of Vienna (D.T.), the Graduate School Human Development in Landscapes and the Excellence Cluster Inflammation at Interfaces (B.K. and A.N.), the European Research Council (ERC) starting grant APGREID (J.K. and A.H.), the National Institutes of Health from the National Institute of General Medical Sciences under grants R01 GM087221 (R.M.), S10 RR027584 (R.M.), and 2P50 GM076547/Center for Systems Biology (R.M). E. Leproust and O. Hardy are highly acknowledged for their help in the RNA bait design. We thank the sequencing team of the Institute of Clinical Molecular Biology at Kiel University for support and expertise. We are grateful to E. Hütten for proofreading of the main text. We are grateful to Olympus, Italy, for providing us with equipment for endoscopy. F.M. and A.Z. conceived the investigation. F.M., B.K., D.T., R.G., J.K., A.N., Y.M., T.R., and A.Z. designed experiments. P.M., L.E., E.E.V., M.S., F.M., and A.Z. were involved in the sampling campaign. F.M., B.K., M.R.H., J.H., U.K., and G.C. performed laboratory work. F.M., B.K., D.T., A.H., M.R.H., N.O.S., B.L., R.L.M., R.G., J.K., Y.M., and T.R. performed analyses. F.M. wrote the manuscript with contributions from B.K., D.T., A.H., M.R.H., U.K., N.O.S., V.C., B.L., R.L.M., R.G., J.K., Y.M., A.N., T.R., and A.Z. Data are available from the European Nucleotide Archive under accession no. ERP012908. The authors declare no competing interests.

SUPPLEMENTARY MATERIALS

www.sciencemag.org/content/351/6269/162/suppl/DC1
Materials and Methods
Figs. S1 to S17
Tables S1 to S13
References (*25*–*93*)

15 August 2015; accepted 20 November 2015
10.1126/science.aad2545

PALEOCLIMATE

Reconciliation of the Devils Hole climate record with orbital forcing

Gina E. Moseley,[1]* R. Lawrence Edwards,[2] Kathleen A. Wendt,[1,2] Hai Cheng,[2,3] Yuri Dublyansky,[1] Yanbin Lu,[2] Ronny Boch,[1]† Christoph Spötl[1]

The driving force behind Quaternary glacial-interglacial cycles and much associated climate change is widely considered to be orbital forcing. However, previous versions of the iconic Devils Hole (Nevada) subaqueous calcite record exhibit shifts to interglacial values ~10,000 years before orbitally forced ice age terminations, and interglacial durations ~10,000 years longer than other estimates. Our measurements from Devils Hole 2 replicate virtually all aspects of the past 204,000 years of earlier records, except for the timing during terminations, and they lower the age of the record near Termination II by ~8000 years, removing both ~10,000-year anomalies. The shift to interglacial values now broadly coincides with the rise in boreal summer insolation, the marine termination, and the rise in atmospheric CO_2, which is consistent with mechanisms ultimately tied to orbital forcing.

Changes to Earth's orbital configuration relative to the Sun, known as the Milankovitch hypothesis, astronomical theory, or orbital forcing, have long been considered the leading theory for the primary mechanism driving Quaternary glacial-interglacial cycles (*1*–*3*) and associated climate change. The hypothesis is supported by a huge array of evidence from paleoclimate records across the globe, which show that major shifts in

climate took place throughout the Quaternary on orbital time scales (*2*, *4*, *5*). One particular seminal paleoclimate record, however, the ~500-thousand-year (ky) Devils Hole record from Nevada (fig. S1) (36°25′N, 116°17′W; 719 m above sea level), has challenged this hypothesis for nearly three decades (*6*–*8*). Of note is the controversy (*4*, *9*–*11*) surrounding the timing of events at the end of the penultimate glacial period [Termination II (TII)]. At issue is whether TII preceded the rise in boreal insolation, in which case TII could not result directly from orbital forcing. The current Devils Hole chronology places the TII shift to interglacial values ~10 ky before the rise in boreal summer insolation (Fig. 1) and the duration of the last interglacial period to almost double its equivalent in other records, both of which are inconsistent with a straightforward explanation in terms of orbital forcing.

The controversial findings generated discussion on (i) dating accuracy (*12*–*16*) and resolution (*17*, *18*); (ii) the possibility that the record represents a regional hydrological signal (*19*–*21*); and (iii) phase leads and lags between proxy records (*7*, *18*, *22*). Deviation from an orbital pacing was highlighted in the original Devils Hole record (*6*), with a chronology based on alpha-counting ^{230}Th and ^{234}U/^{238}U dating of sample DH-2. This record was later replicated with higher-precision thermal ionization mass spectrometric ages on sample DH-11 and extended deeper in time (*7*, *8*). A mechanism was immediately suggested whereby water-sourced ^{230}Th incorporated during calcite growth could lead to artificially old ages (*12*, *14*). However, measurements on the outer surfaces of DH-11 and DH-2, both of which had been submerged for an extended period of time, showed that this process operated only at low efficiency, under the presumption that the adsorption of ^{230}Th was irreversible (*15*, *16*). Several years later, concordant ^{231}Pa and ^{230}Th ages were obtained on an ~80-ky-old subsample of DH-11 (*13*), consistent with an accurate chronology for this portion of the record. In the following two decades, the accuracy of the DH-11 chronology remained unchallenged.

More recently, marine cores off the west coast of the Americas recorded changes in temperature before marine δ^{18}O terminations (*21*). These observations were interpreted in terms of changing surface currents resulting in changing temperature. If Devils Hole recorded these early changes in regional temperature, the difference between the Devils Hole record and the marine δ^{18}O record would be explained.

The record was then extended to the Holocene, using samples DHC2-3 and DHC2-8 (*23*), both collected from Devils Hole 2 (*24*), a cave similar to Devils Hole and 200 m away from it. The portion near TI could also be explained in terms of changing surface currents in the eastern Pacific (*21*).

Despite the apparent resolution, the controversy has subsequently been revived. Great Basin dripstone (fig. S1) records exhibit shifts to interglacial values around the time of marine TII (*25*, *26*) and TI (*27*) and therefore replicate neither of the early shifts documented at Devils Hole (*7*, *8*, *23*). Thus, the controversy currently centers on major chronological discrepancies between the subaerially formed Great Basin dripstone and subaqueously formed Devils Hole records.

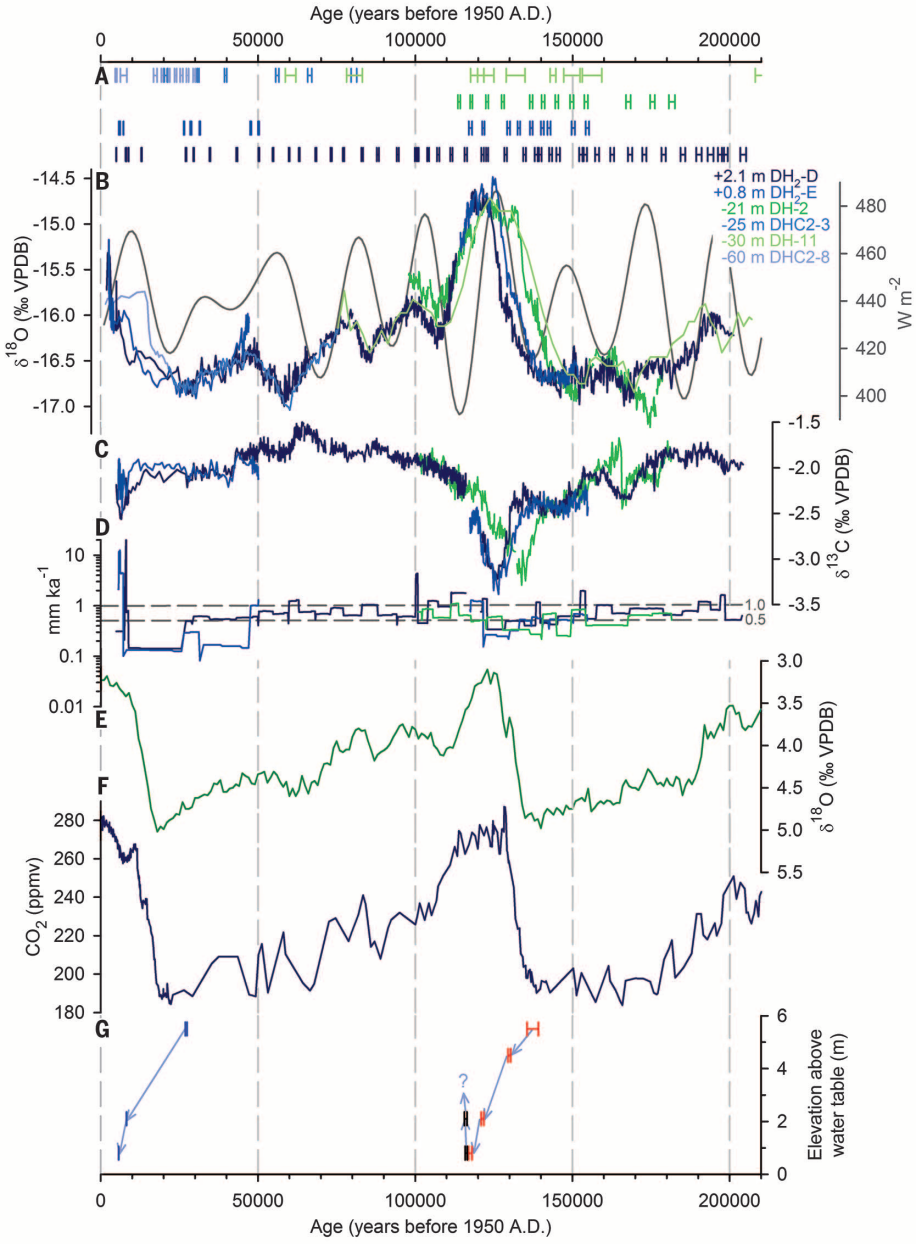

Fig. 1. Comparison of Devils Hole records with other paleoclimate archives. (**A**) ^{230}Th ages with 2σ uncertainties for DHC2-8 (light blue) (*23*), DHC2-3 (light-mid blue) (*23*), DH-11 (light green) (*7*, *8*, *23*), DH-2 (dark green) (this study), DH$_2$-E (mid-dark blue) (this study), and DH$_2$-D (dark blue) (this study). VPBD, Vienna Pee Dee belemnite standard. (**B**) δ^{18}O records for samples in (A) [same color codes and references as in (A)] and 65°N July insolation (dark gray) (*32*). (**C**) δ^{13}C records for DH-2, DH$_2$-E, and DH$_2$-D [same color codes as in (A)]. (**D**) Growth rate of samples from this study with [same color codes as in (A)]. (**E**) Stacked global benthic δ^{18}O records (*5*). (**F**) Antarctica CO$_2$ composite curve (*38*–*40*). (**G**) ^{230}Th ages on mammillary calcite with 2σ uncertainty (*24*). Pre-folia, red; post-folia, black; pre-growth hiatus, blue. Arrows indicate the direction of water-table change.

[1]Institute of Geology, University of Innsbruck, Innrain 52, 6020 Innsbruck, Austria. [2]Department of Earth Sciences, University of Minnesota, 310 Pillsbury Drive SE, Minneapolis, MN 55455, USA. [3]Institute of Global Environmental Change, Xi'an Jiaotong University, Xi'an 710049, China.
***Corresponding author. E-mail: gina.moseley@uibk.ac.at**
†Present address: Institute of Applied Geosciences, Graz University of Technology, Rechbauerstraße 12, 8010 Graz, Austria.

To address this controversy, we tested the reproducibility of the Devils Hole record by reanalyzing DH-2 (fig. S2) (*6*) from Devils Hole proper and by analysis of four newly drilled cores (fig. S2) from Devils Hole 2. The previously studied samples were all collected at substantial depth below the current water table (DH-2 = −21 m; DH-11 = −30 m; DHC2-3 = −25 m; DHC2-8 = −60 m), whereas the new cores from Devils Hole 2 were collected from above the water table (DH_2-D = +2.1 m; DH_2-E = +0.8 m; DH_2-G = +4.5 m; DH_2-J = +5.5 m) (fig. S3).

Considering our data, the results confirm the overwhelming majority of the features of the original studies (*6*–*8*, *23*), verifying the original analytical results and the reliability with which the groundwater system and the calcite precipitated from it record climate. Portions of the record have now been replicated four times with similar results. The general character and range of $\delta^{18}O$ variations, and the U isotopic compositions and concentration, are all similar to those in the original reports (*6*, *8*, *23*) (Fig. 1 and table S1). Further, large portions of our chronology replicate the original chronologies (*8*, *23*). Between 28 to 112 thousand years ago (ka), DH_2-D replicates at significantly higher resolution the timing of the previous chronology (*8*, *23*) (Fig. 1), while further adding support for the timing of the isotopic maximum that occurs at about the time of marine isotope stage 5a, with an age of 82.5 ± 0.7 ka, replicating the original ^{230}Th age of 80.6 ± 2.5 ka (*7*, *8*) and the ^{231}Pa age 82.5 ± 2.8 ka (*13*).

Considering our data sample by sample, starting with our deepest sample (DH-2: −21 m), we find that within quoted uncertainties, the newly analyzed portion of DH-2 replicates both the original DH-2 (*6*) and DH-11 records (*7*, *8*), thus verifying the original analytical results, including measurement of the U and Th isotopes used in calculating ages. The first hint of an age discrepancy occurs at about the time of TII, because the shift in $\delta^{18}O$ values in our DH-2 record is nominally later than the shift in DH-11 (*7*, *8*) (Figs. 1 and 2).

Moreover, comparison of our two highest-elevation $\delta^{18}O$ records (DH_2-D: +2.1; DH_2-E: +0.8 m) to those from deeper cores yields large discrepancies in chronology, well outside of analytical error (Figs. 1 and 3 and fig. S4). These discrepancies are largely confined to and clearly observed at times that correspond to each of the last two terminations, but are best resolved during TII because calcite deposition rates are higher than during TI (Fig. 1 and fig. S5). The ^{230}Th chronology of the shift to interglacial values is systematically younger for cores collected at higher elevation (Figs. 1 and 2), with the shallowest core recording a time of 132.2 ± 1.5 ka (*24*) for the midpoint of the shift to interglacial values, as compared with a value of 142 ± 3 ka (*18*) for the deepest sample for which TII data have been reported. The shift toward glacial values at the end of the last interglacial is similar in all records (Figs. 1 and 2). Therefore, the duration of the last interglacial $\delta^{18}O$ peak as recorded in the samples also shifts systematically with sample elevation, with a last interglacial duration of 16.1 ky (measured from the midpoint of rise to the midpoint of fall) recorded in DH_2-D as compared to a DH-11 duration of ~22 ky (table S2) (*7*, *8*, *18*). Considering just the portion of the peak that records the highest $\delta^{18}O$ values, DH_2-D records a 6-ky duration (from 127 to 121 ka), which is close to half the duration recorded in DH-11 (*7*, *8*, *18*). Thus, the shallowest core records the latest shift to interglacial conditions and the shortest duration for the last interglacial $\delta^{18}O$ peak (Figs. 1 and 2).

The explanation for the relationship between apparent age and sample elevation probably lies in ^{230}Th incorporated in the growing calcite from the water, as raised previously (*12*, *14*) and argued to be negligible (*15*, *16*). The discussion at that time assumed irreversible adsorption of ^{230}Th onto the walls (*12*, *14*–*16*). In light of our data and considering advanced understanding in the distribution of ^{230}Th in seawater (*28*, *29*), we consider irreversible exchange unlikely. Indeed, vertical profiles through the ocean water column show that both particulate and dissolved ^{230}Th increase in concentration with depth, indicating reversible exchange of ^{230}Th between water and particulate matter (*28*). Furthermore, sharp increases in dissolved ^{230}Th in the upper 200 m of the ocean have been demonstrated (*29*). The

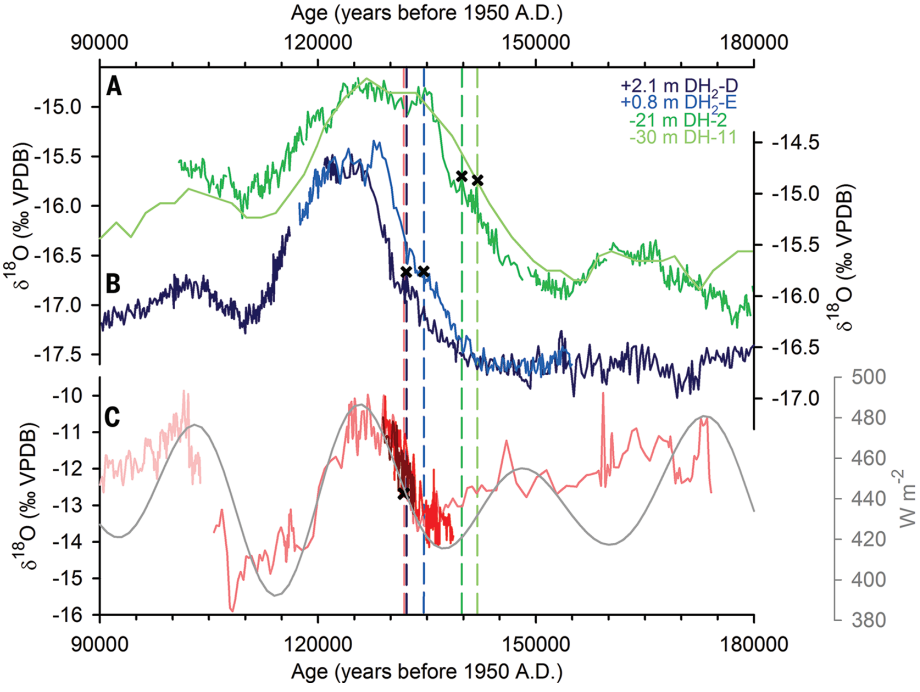

Fig. 2. Timing of TII and the last interglacial in speleothem records. (**A**) DH-2 (dark green) (this study) and DH-11 (light green) (*7*, *8*, *23*). (**B**) DH_2-D (dark blue) (this study) and DH_2-E (mid-blue) (this study). (**C**) Great Basin composite dripstone record ("Leviathan chronology," pink) (*30*); Lehman Cave (red) (*26*) (dark red) (*25*); and 65°N July insolation (gray) (*32*). The midpoints of transitions are indicated with x's and vertical dashed lines.

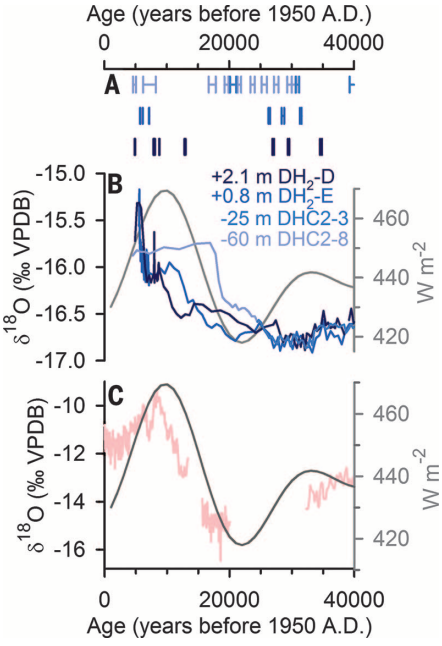

Fig. 3. TI in Devils Hole and Great Basin paleoclimate records. (**A**) ^{230}Th ages with 2σ uncertainties: DHC2-8 (light blue) (*23*), DHC2-3 (light-mid blue) (*23*), DH_2-E (mid blue) (this study), and DH_2-D (dark blue) (this study). (**B**) $\delta^{18}O$ records for samples in (A) with same color codes and 65°N July insolation (dark gray) (*32*). (**C**) $\delta^{18}O$ Great Basin composite dripstone record ("Leviathan chronology") (*30*) and 65°N July insolation (dark gray) (*32*).

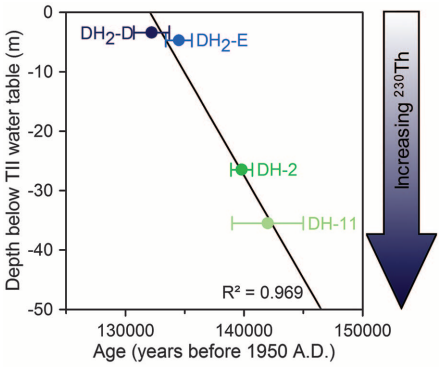

Fig. 4. The age of the TII $\delta^{18}O$ midpoint of –15.7 per mil versus depth below the water table [+5.5 m above present elevation (*24*)] for each sample. DH-11 (light green) (*7*, *8*, *23*), DH-2 (dark green) (this study), DH_2-E (mid blue) (this study), and DH_2-D (dark blue) (this study). Uncertainties are 2σ. R^2, coefficient of determination.

systematic increase of ^{230}Th ages with depth (Figs. 1, 2, and 4) in Devils Hole may thus be the result of increasing concentrations of ^{230}Th down the water column. The strong correlation (coefficient of determination, R^2 = 0.97) between the age of the TII midpoint in each sample versus depth (Fig. 4) (*24*) is consistent with a reversible exchange–generated increase of ^{230}Th with depth in the TII Devils Hole water column.

The appearance of age anomalies during terminations may result from several factors. First, the water table was higher than at present during both TI and TII, before it progressively declined during the respective following interglacials (Fig. 1), in agreement with progressively drier conditions during interglacials (*30*, *31*). One would therefore expect that for a given elevation, the water ^{230}Th concentration would have increased during the pluvial periods associated with terminations and then decreased over the course of the proceeding interglacial. Second, lower depositional rates during times of the anomalies (Fig. 1 and fig. S5) may play a role in the incorporation of excess ^{230}Th onto the calcite (*12*). Finally, wetter conditions associated with higher water tables could be associated with increased groundwater flow rates and ^{230}Th fluxes into the open fractures.

Regardless of the details of the mechanism, if progressively higher levels of ^{230}Th at depth are responsible for the anomalies, then the shallowest core, which records the youngest ages, has the most accurate chronology. Thus, we consider the chronology of the DH_2-D $\delta^{18}O$ record to be the closest to the true age. Because the DH_2-D record is in close agreement with the timing of $\delta^{18}O$ shifts in Great Basin dripstone records [Figs. 2 and 3; particularly considering an up to 2-ky groundwater transit time in the Devils Hole system (*23*)], we conclude that DH_2-D has negligible initial ^{230}Th and provides an accurate chronology.

In contrast to DH-11 (*7*, *8*), the timing of TII and the duration of the last interglacial $\delta^{18}O$ peak (either midpoint to midpoint or peak value duration) in the DH_2-D record are all consistent with orbital forcing. The DH_2-D $\delta^{18}O$ shift to interglacial values is broadly coincident with the rise in boreal summer insolation (*32*), the rise in atmospheric CO_2 (*33*), the marine termination (*34*), and the TII Weak Monsoon Interval (*4*). The mechanism for ^{18}O enrichment in precipitation could be increasing temperature (*6*–*8*, *21*, *23*), in which case the temperature rise could be caused by the rise in global atmospheric CO_2, which has been closely tied to orbital forcing (*4*). However, it is also likely that changes in the proportion of summer (high-$\delta^{18}O$ today) to winter (low-$\delta^{18}O$ today) meteoric precipitation (i.e., changes in seasonality) played a role. If so, the low $\delta^{18}O$ values before the glacial-interglacial transition could be partly explained by a larger proportion of low-$\delta^{18}O$ cool season rainfall associated with pluvial conditions. The pluvial conditions in turn, could be caused by the splitting of the jet stream (*35*) around the Laurentide Ice Sheet to the north. In this case, the proportion of (low-$\delta^{18}O$) winter season moisture would diminish as the ice sheet melted, as a result of increased boreal summer insolation. The rise in insolation could also trigger (high-$\delta^{18}O$ summer) North American monsoon-like rainfall in the region, increasing the mean annual $\delta^{18}O$ of precipitation. We conclude that some combination of these orbitally based processes contributed to the observed shift in $\delta^{18}O$. Temperature changes of Devils Hole water have been small (*36*), so that the temperature-dependent calcite-water fractionation would have had little effect on calcite $\delta^{18}O$. Also, the rainfall seasonality mechanisms do not directly relate to regional temperature and could plausibly explain the absence of a Devils Hole "lead" that is analogous to the lead in temperature observed in the marine cores (*21*).

Finally, in our (DH_2-D) chronology, the prominent low in $\delta^{13}C$ at the end of TII is shifted to younger values by about 7 ky (Fig. 1) relative to the DH-2 and DH-11 (*37*) records, thus coinciding with the boreal summer insolation peak. Because this could be a time of regional warmth and relatively high warm-season rainfall, our timing supports the idea (*37*) that such $\delta^{13}C$ lows are caused by more extensive vegetation cover and productivity in the source region for the aquifer.

Our chronologies from Devils Hole have demonstrated that there is a systematic offset in the age of calcite deposited at increasing depths in these open fractures across glacial terminations, thus helping to solve one of the great paleoclimate enigmas of the past three decades.

REFERENCES AND NOTES

1. C. Emiliani, *J. Geol.* **63**, 538–578 (1955).
2. J. D. Hays, J. Imbrie, N. J. Shackleton, *Science* **194**, 1121–1132 (1976).
3. J. Imbrie, *J. Geol. Soc. London* **142**, 417–432 (1985).
4. H. Cheng *et al.*, *Science* **326**, 248–252 (2009).
5. I. E. Lisiecki, M. E. Raymo, *Paleoceanography* **20**, 1–17 (2005).
6. I. J. Winograd, T. B. Coplen, B. J. Szabo, A. C. Riggs, *Science* **242**, 1275–1280 (1988).
7. I. J. Winograd *et al.*, *Science* **258**, 255–260 (1992).
8. K. R. Ludwig *et al.*, *Science* **258**, 284–287 (1992).
9. R. N. Drysdale *et al.*, *Science* **325**, 1527–1531 (2009).
10. A. L. Thomas *et al.*, *Science* **324**, 1186–1189 (2009).
11. G. Marino *et al.*, *Nature* **522**, 197–201 (2015).
12. R. L. Edwards, C. D. Gallup, *Science* **259**, 1626–1627 (1993).
13. R. L. Edwards, H. Cheng, M. T. Murrell, S. J. Goldstein, *Science* **276**, 782–786 (1997).
14. N. J. Shackleton, *Nature* **362**, 596 (1993).
15. K. R. Ludwig, K. R. Simmons, I. J. Winograd, B. J. Szabo, A. C. Riggs, *Science* **259**, 1626–1627 (1993).
16. K. R. Ludwig *et al.*, *Nature* **362**, 596 (1993).
17. C. D. Gallup, R. L. Edwards, R. G. Johnson, *Science* **263**, 796–800 (1994).
18. I. J. Winograd, J. M. Landwehr, K. R. Ludwig, T. B. Coplen, A. C. Riggs, *Quat. Res.* **48**, 141–154 (1997).
19. W. S. Broecker, *Nature* **359**, 779–780 (1992).
20. P. M. Grootes, in *Climatic Change in Continental Isotopic Records*, P. K. Swart *et al.*, Eds. (Geophysical Monograph 78, American Geophysical Union, 1993), pp. 37–46.
21. T. D. Herbert *et al.*, *Science* **293**, 71–76 (2001).
22. T. J. Crowley, K.-Y. Kim, *Science* **265**, 1566–1568 (1994).
23. I. J. Winograd *et al.*, *Quat. Res.* **66**, 202–212 (2006).
24. Materials and methods are available as supplementary materials on *Science* Online.
25. J. D. Shakun, S. J. Burns, P. U. Clark, H. Cheng, R. L. Edwards, *Geophys. Res. Lett.* **38**, L18701 (2011).
26. M. Cross *et al.*, *Quat. Sci. Rev.* **127**, 186–198 (2015).
27. E. Steponaitis *et al.*, *Quat. Sci. Rev.* **127**, 174–185 (2015).
28. M. P. Bacon, R. F. Anderson, *J. Geophys. Res.* **87**, 2045–2056 (1982).
29. S. B. Moran, M. A. Charette, J. A. Hoff, R. L. Edwards, W. M. Landing, *Earth Planet. Sci. Lett.* **150**, 151–160 (1997).
30. M. S. Lachniet, R. F. Denniston, Y. Asmerom, V. Polyak, *Nat. Commun.* **5**, 1–8 (2014).
31. J. S. Munroe, B. J. Laabs, *Geol. Soc. Am. Bull.* **125**, 322–342 (2013).
32. A. L. Berger, *J. Atmos. Sci.* **35**, 2362–2367 (1978).
33. J. R. Petit *et al.*, *Nature* **399**, 429–436 (1999).
34. J. F. McManus, D. W. Oppo, J. L. Cullen, *Science* **283**, 971–975 (1999).
35. COHMAP Members, *Science* **241**, 1043–1052 (1988).
36. T. Kluge, H. P. Affek, Y. Dublyansky, C. Spötl, *Earth Planet. Sci. Lett.* **400**, 251–260 (2014).
37. T. B. Coplen, I. J. Winograd, J. M. Landwehr, A. C. Riggs, *Science* **263**, 361–365 (1994).
38. D. Lüthi *et al.*, *Nature* **453**, 379–382 (2008).
39. L. Bazin *et al.*, *Clim. Past* **9**, 1715–1731 (2013).
40. D. Veres *et al.*, *Clim. Past* **9**, 1733–1748 (2013).

ACKNOWLEDGMENTS

This work was supported by the Austrian Science Fund (FWF) project no. FP263050 to C.S. and in part by NSF grants 1103403 to R.L.E. and H.C., 1103320 to R.L.E., and NSFC grant 41230524 to H.C. This research was conducted under research permit numbers DEVA-2010-SCI-0004 and DEVA-2015-SCI-0006 issued by Death Valley National Park. We thank I. J. Winograd for providing the study with sample DH-2, M. Wimmer for preparation and measurement of the stable isotopes, K. Wilson and R. Freeze for assistance in the field, and M. Cross for discussion of Great Basin paleoclimate. Data can be downloaded from the National Oceanic and Atmospheric Administration's National Centers for Environmental Information (www.ncdc.noaa.gov/paleo/paleo.html).

SUPPLEMENTARY MATERIALS

www.sciencemag.org/content/351/6269/165/suppl/DC1
Materials and Methods
Supplementary Text
Figs. S1 to S6
Tables S1 and S2
References (*41*–*59*)

10 September 2015; accepted 2 December 2015
10.1126/science.aad4132

CELL BIOLOGY

Accurate concentration control of mitochondria and nucleoids

Rishi Jajoo,[1]* Yoonseok Jung,[1] Dann Huh,[1]† Matheus P. Viana,[2] Susanne M. Rafelski,[2] Michael Springer,[1] Johan Paulsson[1]‡

All cellular materials are partitioned between daughters at cell division, but by various mechanisms and with different accuracy. In the yeast *Schizosaccharomyces pombe*, the mitochondria are pushed to the cell poles by the spindle. We found that mitochondria spatially reequilibrate just before division, and that the mitochondrial volume and DNA-containing nucleoids instead segregate in proportion to the cytoplasm inherited by each daughter. However, nucleoid partitioning errors are suppressed by control at two levels: Mitochondrial volume is actively distributed throughout a cell, and nucleoids are spaced out in semiregular arrays within mitochondria. During the cell cycle, both mitochondria and nucleoids appear to be produced without feedback, creating a net control of fluctuations that is just accurate enough to avoid substantial growth defects.

Mitochondria are cytoplasmic organelles present in most eukaryotes. They generate much of the chemical energy of cells and have key roles in signaling, apoptosis, and disease (*1*–*3*). However, little is known about how their abundances or their DNA-containing nucleoids are controlled during the cell cycle or at cell division (*4*–*6*).

To quantitatively investigate these processes in the symmetrically dividing fission yeast *Schizosaccharomyces pombe*, we developed methods to count nucleoids and measure the volume of mitochondria in single cells. Time-lapse imaging of mitochondrial matrix–targeted fluorescent mCherry protein confirmed previous observations that mitochondria are pushed to the cell poles by the mitotic spindle (*7*, *8*) before cell division (Fig. 1A) in roughly equal amounts, irrespective of where the cell eventually divides. This seemed to support theoretical predictions that mitochondria segregate by being pushed or pulled into each cell half, as observed for most other DNA molecules, from bacterial plasmids (*9*) to chromosomes. However, in the last 15% of the cell cycle—after chromosome segregation but before cytokinesis—the mitochondria escaped from the poles and spatially reequilibrated throughout the length of the cell, in virtually every cell observed both for wild-type (Fig. 1A) and asymmetrically dividing mutants (*pom1*Δ; Fig. 1, B and C, and fig. S1). Movement to the poles was independent of Mmb1p, and reequilibration of mitochondria occurred when mitochondria colocalized with the newly formed microtubule network (see supplementary text and figs. S2 and S3). Quantifying exact volumes of mitochondria via three-dimensional image analysis (*10*) showed that mitochondrial partitioning occurs by a qualitatively different principle, conserving concentrations rather than numbers when cell division is asymmetrical (Fig. 1D). These findings are consistent with the hypothesis that mitochondrial movement to the poles is used to facilitate proper spindle alignment (*8*).

Because the migration of the mitochondria to the poles has all the appearances of an active segregation mechanism and coincides with the segregation of nuclear DNA, we considered whether the nucleoids were still segregated by this mechanism—that is, whether nucleoids remained in the cell half in which they were originally placed by the spindle even after most of the mitochondrial volume reequilibrated. Counting mitochondrial nucleoids was not previously possible because of the interfering signal from nuclear DNA, and we therefore optimized existing staining procedures (*11*) using the dye Sybr Green I (SGI, Molecular Probes) and cross-validated the results with two other single-cell methods (figs. S4 to S6). SGI stains almost all nucleoids in the cell (~85%; fig. S7), but the necessary washing procedure perturbs their exact spatial positions. Simply counting copies within each newly divided cell revealed that the nucleoids segregated in proportion to the cytoplasmic volume in each daughter (Fig. 1D and fig. S8), just as with mitochondria.

Thus, the mitochondrial volume and nucleoids on average segregated in proportion to the available cytoplasmic volume (Fig. 1D), more like passively segregating RNAs and proteins than like actively segregating chromosomes. However, the nucleoids showed smaller deviations from the average trend than would be expected from passive mechanisms (Fig. 2 and figs. S9 to S11). Specifically, without active placement, low-abundance components should display at least binomial errors, and larger errors yet if spatial locations are randomized by upstream factors. The observed nucleoid errors were instead substantially sub-binomial.

These observations could be reconciled by a conceptually simple mechanism whereby nucleoids are regularly spaced within mitochondria and the mitochondrial volume is evenly distributed through cells (Fig. 3A), similar to how carboxysomes segregate in cyanobacteria (*12*). Semiregular spacing was in fact suggested for nucleoids in human and budding yeast cells (*13*–*15*) but had not been linked to segregation, because it was unclear whether the regularity was consistent throughout mitochondria and because nucleoid segregation further depends on how the mitochondrial volume segregates. Localization patterns can also change greatly at the time of division; for example, nucleoids could be moved to specific locations in cells or accurately sorted into clusters that then were actively placed in both daughter cells.

To test clustering and spacing models of nucleoid segregation (Fig. 3A), we disrupted the mitochondrial spatial patterns by means of an *mmb1*Δ mutant in which mitochondria cannot attach to microtubule filaments (*16*) and used our quantitative postmortem assay to count nucleoids and measure the cytoplasmic and mitochondrial volumes in newly divided cells. Both mitochondria and nucleoids segregated with large errors relative to the cytoplasmic volume, but the number of nucleoids on average tracked the mitochondrial volume. Given the fraction of mitochondrial volume in each individual daughter cell, the number of nucleoids still displayed sub-binomial errors (Fig. 3B and figs. S12 and S13). For example, if the two daughters received 30% and 70% of the mitochondrial volume, respectively, on average 30% of nucleoids went into the first daughter and 70% went into the other, but the statistical error was lower than expected from independent sorting with those probabilities. Mmb1-based control is thus required for accurate segregation of the mitochondrial volume (*16*), perhaps because mitochondria are too large and filamentous (*7*, *16*, *17*) to achieve spatial uniformity by free diffusion, whereas nucleoid segregation uses an additional level of control within the mitochondria.

These observations rule out many nucleoid sorting models. For example, if nucleoids were accurately sorted into clusters but the mitochondria were randomized, nucleoids would not display sub-binomial errors even after accounting for the randomized mitochondrial volume. However, the results are exactly as expected if nucleoids are regularly spaced out within mitochondria, in which case only the total amount of mitochondria in each cell matters.

To further test this model, we used the asymmetrically dividing *pom1*Δ mutant to measure the statistical partitioning errors versus the septum location. When cells divided asymmetrically, the error in nucleoid numbers was still sub-binomial with probabilities set by the relative cytoplasmic volumes (Fig. 3C and figs. S9 and S10). This is again as expected from the regular spacing model and rules out numerous alternatives (e.g., models in which filaments push or pull nucleoids into specific locations in opposite

[1]Department of Systems Biology, Harvard Medical School, Boston, MA 02115, USA. [2]Department of Developmental and Cell Biology, University of California, Irvine, CA 92697, USA. *Present address: Department of Biomedical Engineering, University of California, Irvine, CA 92697, USA. †Present address: Department of Molecular and Cellular Biology, Harvard University, Cambridge, MA 02138, USA. ‡Corresponding author. E-mail: johan_paulsson@harvard.edu

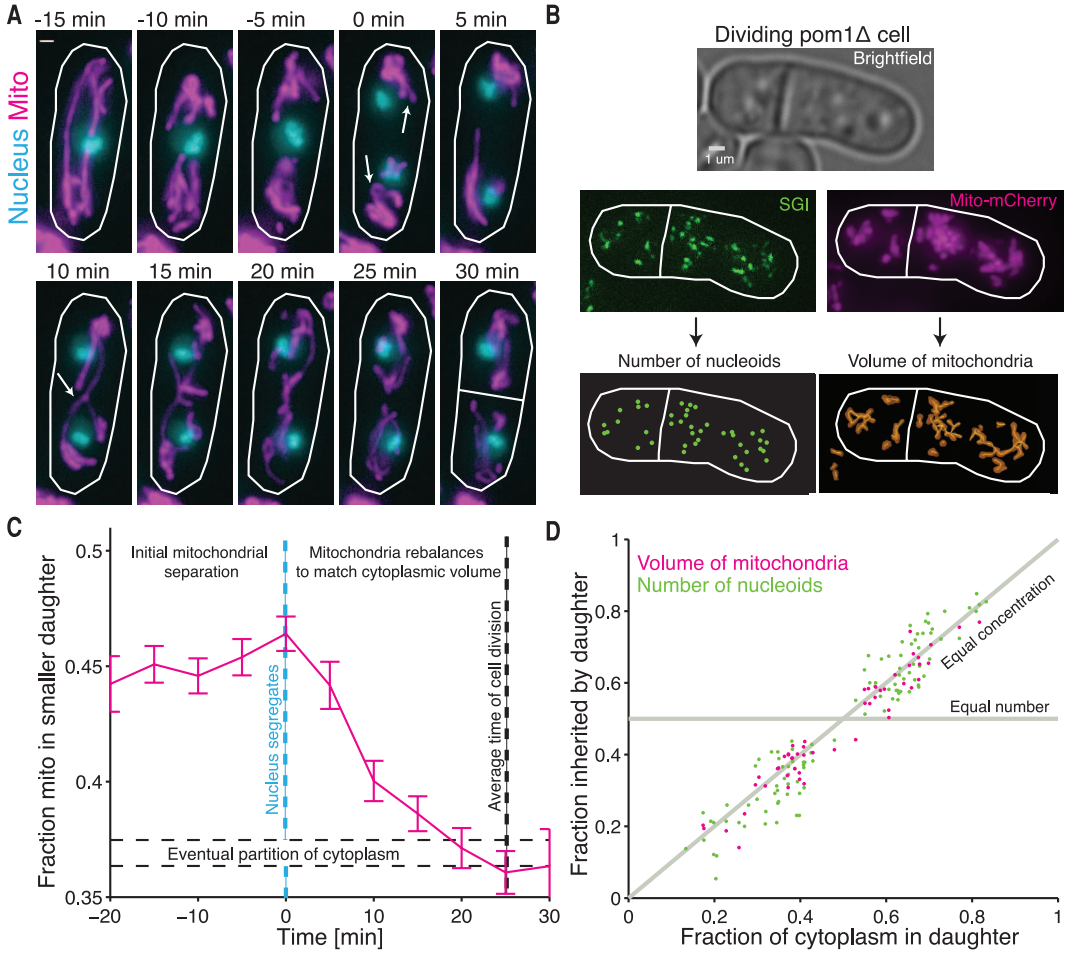

Fig. 1. Spatial reequilibration of mitochondria and nucleoids after nuclear segregation matches cytoplasmic division. (**A**) Time-lapse images of a dividing wild-type cell (RJP041) with mCherry-labeled mitochondria and GFP-labeled nuclei (magenta and cyan, respectively). Arrows at 0 min indicate initial separation of nuclei and further bunching of the mitochondria to the poles, followed by reformation of a continuous mitochondrial network at 10 min but before division at 30 min. (**B**) For individual dividing *pom1Δ* cells (RJP025), the number of nucleoids in each daughter cell was determined with semiautomated spot detection of SGI signal, and the mitochondrial volume in each cell half was determined using the surface-based volume reconstruction from the MitoGraph software package (*10*). Scale bars in (A) and (B), 1 μm. (**C**) Fraction of mitochondria in the part of the cell region that will eventually become the smaller daughter as a function of time for *pom1Δ* cells (RJP042). Images of cells as in (A) were taken every 5 min and aligned to when nuclei first separated (blue dashed line). Average cell division occurred 25 min after nuclear separation, with approximately 37% of cytoplasmic volume inherited by the smaller daughter (dashed horizontal lines). Error bars indicate SEM. Dashed horizontal lines represent the average partition of the cytoplasm ± SEM (n = 91 cells). (**D**) Fraction of nucleoids and of mitochondrial volume in each *pom1Δ* daughter cell as computed in (B), plotted as a function of the fraction of cytoplasmic volume in each daughter cell. The coefficient of determination between cytoplasmic volume and number of nucleoids is r^2 = 0.88 (102 cells); for cytoplasmic volume and mitochondrial volume, the coefficient is r^2 = 0.88 (52 cells).

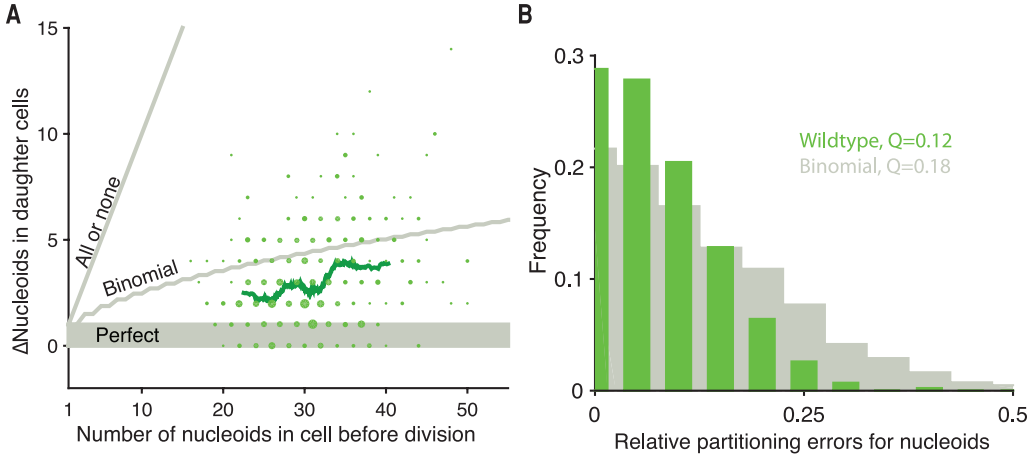

Fig. 2. Partitioning of mitochondria and nucleoids to daughter cells. (**A**) Absolute difference between the number of nucleoids segregated between wild-type sister cells, plotted against the total number of nucleoids (RJP005 and DH60). The areas of plotted points are proportional to the number of observations. The green line represents a running average of 80 points. Gray lines indicate models of perfect, binomial, and all-or-none segregation. We found that 76% of cells segregate better than binomial (including 28% that are perfect) and 24% segregate worse than binomial. Binomial predictions assumed that each nucleoid had the same chance of being inherited by either daughter (n = 420 cells). More spot overlap in daughters with higher numbers can also reduce the observed error slightly but appears to contribute marginally, because we observed even more strongly sub-binomial errors in cells where each daughter received as few as 10 copies. (**B**) The same data as in (A) plotted as a histogram of relative errors for nucleoid segregation compared to a binomial model. Q is defined as $Q = \sqrt{\langle (L-R)^2 \rangle / \langle (L+R)^2 \rangle}$, where L and R are the numbers of nucleoids that partition to the left and right daughter cells, respectively, and the angle brackets represent averages over all cells (*27*).

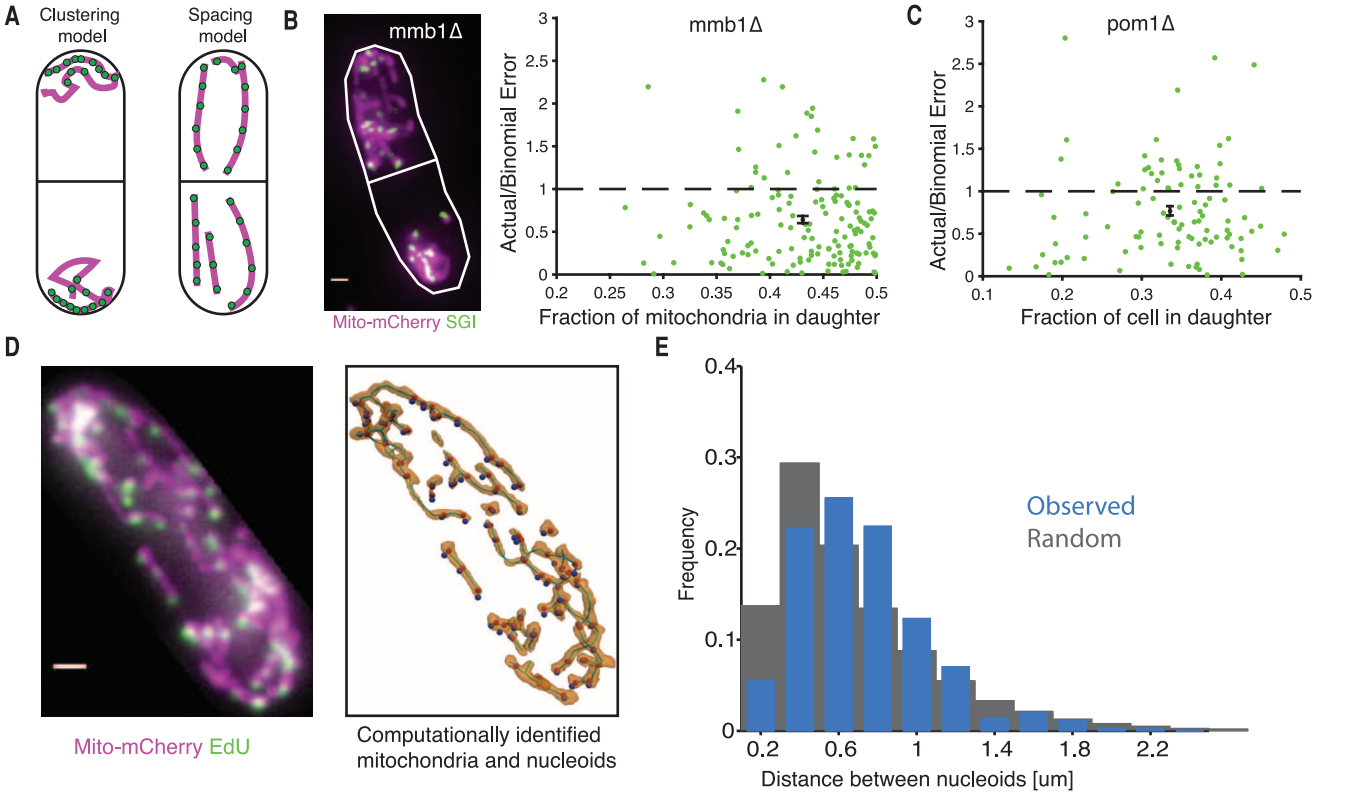

Fig. 3. Requirement of accurate mitochondrial segregation and regular spacing of nucleoids within mitochondria to produce accurate segregation of nucleoids. (**A**) Two models of how nucleoids could be segregated accurately to daughter cells: Measured and ordered clustering (left) or regular spacing within mitochondria that are themselves evenly partitioned between cells (right). (**B**) Left: image of *mmb1*Δ with mito-mCherry (magenta) and SGI (green). Scale bar, 1 μm. Right: Nucleoid segregation error normalized to the binomial model plotted against the degree of asymmetric mitochondrial division in *mmb1*Δ cells. (**C**) Nucleoid segregation error normalized to the binomial model plotted against the degree of asymmetric division in *pom1*Δ cells. The green points are individual cells, and the black point is their average. Error bars indicate SEM. (**D**) Left: A fixed cell (RJP028) with mCherry-labeled mitochondria (magenta) and EdU-labeled nucleoids (green). Right: The same cell analyzed with Mitograph (*10*) to identify mitochondria (gold) and nucleoids (blue dots). Nucleoids were then projected onto the nearest part of the mitochondrial network (red dots). Scale bar, 1 μm. (**E**) Histogram of the actual distances between neighbor nucleoids for 1871 nucleoids in 24 cells (blue) and randomly redistributed nucleoids within the mitochondrial network (gray). Redistributed nucleoids were restricted to be farther apart than the microscope resolution limit. This again shows that the sub-binomial errors do not reflect higher undercounting in the daughter with more copies.

cell halves) (Fig. 3A). To be consistent with these data, any putative mechanism for counting nucleoids into clusters—the main alternative to spacing—would not only need to place nucleoids in each daughter regardless of the septum position and reliably count copies, but also sense the relative position of the septum and adjust numbers accordingly. By contrast, the simplest spacing model predicts all observed phenotypes directly (Fig. 3A).

To directly observe spatial patterns of nucleoids, we then developed a method to visualize the native spatial locations of nucleoids within mitochondria. We used a strain of *S. pombe* that expressed a mitochondrial matrix–targeted mCherry and could incorporate 5-ethynyl-2´-deoxyuridine (EdU) into nucleoids (*18*), which can be visualized through ligation of a bright fluorophore (*19*). This method requires fixed, cell cycle–arrested cells, but unlike the SGI assay above, it allows us to visualize native mitochondrial morphology and nucleoid positions in interphase cells (see supplementary materials). It also sidesteps the problem that even the most monomeric fluorescent proteins (FPs) may not be monomeric enough (*20*) to faithfully report the localization of DNA in situations where many copies are in close proximity (*21*), as is the case for mitochondrial DNA copies in nucleoids. Mapping both the mitochondrial network and the position of nucleoids (Fig. 3D) showed that nucleoids were indeed semiregularly spaced within mitochondria (Fig. 3E), and this level of regularity can quantitatively explain the low nucleoid segregation errors (fig. S14). The molecular mechanisms underlying even spacing are not known, but we found that the sub-binomial partitioning is unchanged by the fission-inhibiting drug mdivi-1 (fig. S15).

To evaluate the control of nucleoid production, we compared the distribution of nucleoid numbers in cells at the beginning and end of the cell cycle (Fig. 4A). The difference was well described by a Poisson distribution (Fig. 4B), as expected if new nucleoids were added independently of the current number of nucleoids. It is possible that extrinsic noise sources or effects of self-replication cancel out against noise suppression mechanisms, but this seems unlikely because *mmb1*Δ, *pom1*Δ, and *wee1*Δ mutants were also well described by Poisson production despite having very different segregation errors (Fig. 4B). We further developed a microfluidic device that keeps growth conditions exceptionally constant over time (see supplementary materials) and tracked the abundance of several mitochondrial proteins fused to green fluorescent protein (GFP). The amount of protein produced during the cell cycle did not depend on the initial amount inherited: Similarly sized newborn cells expressed the same amount of the mitochondrial proteins, on average, regardless of the starting amount (Fig. 4C). Thus, neither nucleoids nor mitochondrial proteins appear to use feedback control for production; rather, they passively control errors by regressing to the mean with constant production, much like cell size control of bacteria (*22*). This makes sense in light of theoretical work showing that feedback-driven noise suppression is mechanistically challenging and energetically expensive (*23*, *24*).

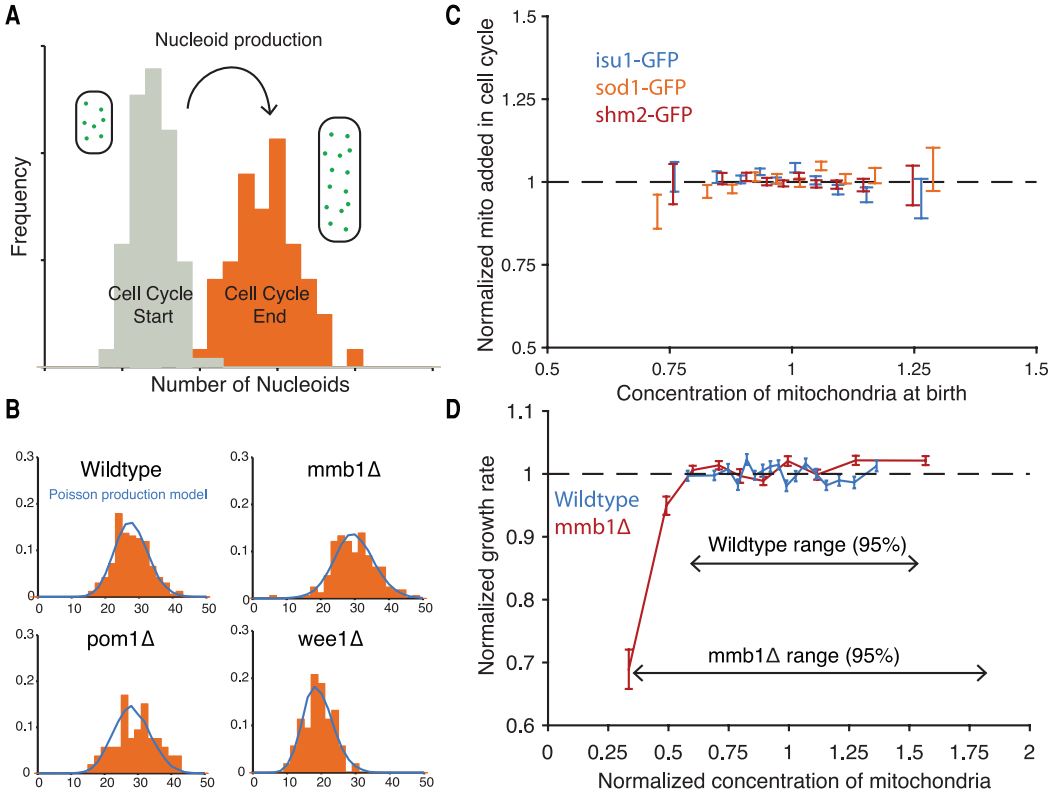

Fig. 4. Nucleoid and mitochondrial production is constant and cell growth depends on mitochondrial concentration. (**A**) Schematic of data used to infer nucleoid production. In dividing cells, the number of nucleoids was measured for both newborn daughter cells (gray) and just-divided mother cells (orange) and then normalized to the average volume of each population. (**B**) For modeling of nucleoid production without feedback control, a Poisson distribution based on the average number of nucleoids at the beginning of the cell cycle was added to the full distribution of nucleoids at the beginning of the cell cycle. The resulting distribution is plotted in blue against the actual data from the end of the cell cycle (orange) for each strain. On average over all data sets and strains, the standard deviation predicted by the Poisson model differed from the actual data by 15%. (**C**) Total mitochondria added during the cell cycle divided by the added cell volume, plotted against the concentration of mitochondria in newborn cells. Both are normalized by their respective averages. The fluorescence signals of mitochondrially localized GFP fusion proteins were used as a proxy for the amount of mitochondria in the cell. A running average of data is shown with error bars representing the SEM of the observations (isu1-GFP, n = 835 cells; sod1-GFP, n = 1167 cells; shm2-GFP, n = 2720 cells). (**D**) Normalized growth rate of cells plotted against the normalized concentration of mitochondria, for both wild-type cells (n = 3582) and *mmb1*Δ cells (n = 2056). Each point is an average of 200 cells; error bars denote SEM.

Our results show that the noise control of mitochondrial nucleoids in *S. pombe* is qualitatively different from the control of chromosomes or macromolecules. Chromosomes use substantial resources to ensure that each copy replicates once per cell cycle, with much less than Poisson noise, whereas mRNAs and proteins generally display super-Poisson noise in production because of expression bursts or variation in the gene expression machinery (*25*). Mitochondrial nucleoids show Poisson production, as if they use passive control but inherit no fluctuations from the production machinery or from self-replication. At cell division, chromosomes are allocated in equal numbers to daughter cells regardless of volume differences, whereas cytoplasmic mRNAs and proteins on average segregate in proportion to cytoplasmic volume but with at least binomial partitioning errors (*26*). Mitochondrial nucleoids instead use active control at two levels to ensure that they segregate in proportion to cytoplasmic volume but with sub-binomial errors due to semiregular spacing. This achieves relatively small noise in concentrations, despite low numbers of segregating units and random differences in cytoplasmic volume between daughter cells, and may reflect that mitochondria are a key source of metabolite, lipid, and energy production and therefore may be needed in proportion to the size of the individual cell. Indeed, we found that growth rates were very similar across the range of natural variation in mitochondrial concentrations, whereas cells with lower concentrations showed significant growth defects (Fig. 4D and fig. S16).

REFERENCES AND NOTES

1. Z. Liu, R. A. Butow, *Annu. Rev. Genet.* **40**, 159–185 (2006).
2. S. Hoppins, J. Nunnari, *Science* **337**, 1052–1054 (2012).
3. M. R. Duchen, *Mol. Aspects Med.* **25**, 365–451 (2004).
4. S. Mukherji, E. K. O'Shea, *eLife* **3**, e02678 (2014).
5. Y. H. M. Chan, W. F. Marshall, *Science* **337**, 1186–1189 (2012).
6. S. M. Rafelski *et al.*, *Science* **338**, 822–824 (2012).
7. M. P. Yaffe, N. Stuurman, R. D. Vale, *Proc. Natl. Acad. Sci. U.S.A.* **100**, 11424–11428 (2003).
8. N. Krüger, I. M. Tolić-Nørrelykke, *Curr. Biol.* **18**, R646–R647 (2008).
9. E. C. Garner, C. S. Campbell, D. B. Weibel, R. D. Mullins, *Science* **315**, 1270–1274 (2007).
10. M. P. Viana, S. Lim, S. M. Rafelski, *Methods Cell Biol.* **125**, 77–93 (2015).
11. C. Briggs, M. Jones, *Acta Histochem.* **107**, 301–312 (2005).
12. D. F. Savage, B. Afonso, A. H. Chen, P. A. Silver, *Science* **327**, 1258–1261 (2010).
13. J. Tauber *et al.*, *Int. J. Biochem. Cell Biol.* **45**, 593–603 (2013).
14. F. J. Iborra, H. Kimura, P. R. Cook, *BMC Biol.* **2**, 9 (2004).
15. C. Osman, T. R. Noriega, V. Okreglak, J. C. Fung, P. Walter, *Proc. Natl. Acad. Sci. U.S.A.* **112**, E947–E956 (2015).
16. C. Fu, D. Jain, J. Costa, G. Velve-Casquillas, P. T. Tran, *Curr. Biol.* **21**, 1431–1439 (2011).
17. M. P. Yaffe *et al.*, *Proc. Natl. Acad. Sci. U.S.A.* **93**, 11664–11668 (1996).
18. S. Sivakumar, M. Porter-Goff, P. K. Patel, K. Benoit, N. Rhind, *Methods* **33**, 213–219 (2004).
19. A. Salic, T. J. Mitchison, *Proc. Natl. Acad. Sci. U.S.A.* **105**, 2415–2420 (2008).
20. D. Landgraf, B. Okumus, P. Chien, T. A. Baker, J. Paulsson, *Nat. Methods* **9**, 480–482 (2012).
21. S. Tal, J. Paulsson, *Plasmid* **67**, 167–173 (2012).
22. S. Taheri-Araghi *et al.*, *Curr. Biol.* **25**, 385–391 (2015).
23. I. Lestas, G. Vinnicombe, J. Paulsson, *Nature* **467**, 174–178 (2010).
24. J. Paulsson, M. Ehrenberg, *Q. Rev. Biophys.* **34**, 1–59 (2001).
25. E. M. Ozbudak, M. Thattai, I. Kurtser, A. D. Grossman, A. van Oudenaarden, *Nat. Genet.* **31**, 69–73 (2002).
26. N. Rosenfeld, J. W. Young, U. Alon, P. S. Swain, M. B. Elowitz, *Science* **307**, 1962–1965 (2005).
27. D. Huh, J. Paulsson, *Proc. Natl. Acad. Sci. U.S.A.* **108**, 15004–15009 (2011).

ACKNOWLEDGMENTS

Supported by NIH grant GM095784 and NSF award 1137676 (J.P., R.J., and Y.J.), NIH training grant GM080177 (R.J.), a Samsung Scholarship (Y.J.), NSF grant MCB-1330451 (M.P.V. and S.M.R.), and the Ellison Medical Foundation (S.M.R.). We thank B. Ward, S. Reuveni, Z. Wunderlich, and S. Bakshi for helpful discussions and critical reading of the manuscript, and D. Landgraf, F. Winston, N. Rhind, B. Westermann, and T. Fox for gifts of strains and reagents.

SUPPLEMENTARY MATERIALS

www.sciencemag.org/content/351/6269/169/suppl/DC1
Materials and Methods
Supplementary Text
Figs. S1 to S16
Table S1
References (*28*–*38*)

15 February 2015; accepted 1 December 2015
10.1126/science.aaa8714

PROTEIN AGGREGATES

Cytoplasmic protein aggregates interfere with nucleocytoplasmic transport of protein and RNA

Andreas C. Woerner,[1] Frédéric Frottin,[1] Daniel Hornburg,[2] Li R. Feng,[1]* Felix Meissner,[2] Maria Patra,[3] Jörg Tatzelt,[3,4] Matthias Mann,[2,5] Konstanze F. Winklhofer,[3,5,6] F. Ulrich Hartl,[1,5]† Mark S. Hipp[1,5]†

Amyloid-like protein aggregation is associated with neurodegeneration and other pathologies. The nature of the toxic aggregate species and their mechanism of action remain elusive. Here, we analyzed the compartment specificity of aggregate toxicity using artificial β-sheet proteins, as well as fragments of mutant huntingtin and TAR DNA binding protein–43 (TDP-43). Aggregation in the cytoplasm interfered with nucleocytoplasmic protein and RNA transport. In contrast, the same proteins did not inhibit transport when forming inclusions in the nucleus at or around the nucleolus. Protein aggregation in the cytoplasm, but not the nucleus, caused the sequestration and mislocalization of proteins containing disordered and low-complexity sequences, including multiple factors of the nuclear import and export machinery. Thus, impairment of nucleocytoplasmic transport may contribute to the cellular pathology of various aggregate deposition diseases.

Cellular protein homeostasis (proteostasis) is controlled by a complex network of factors, including molecular chaperones, proteases, and their regulators (*1*, *2*). Misfolded proteins are recognized and either refolded, degraded, or sequestered to distinct cellular sites. However, when these proteostasis machineries become compromised, as is increasingly the case during aging (*1*, *3*), aberrant proteins tend to accumulate as toxic aggregate species. This process is associated with numerous neurodegenerative diseases and other disorders (*4*).

Intracellular protein aggregation in disease occurs predominantly in the cytoplasm and nucleus, with toxic effects possibly arising in both locations (*5*–*7*). Here, we investigated the basic mechanisms by which aggregates exert cytotoxicity in a compartment-specific manner. We used authentic disease proteins and artificial β-sheet proteins known to form prefibrillar and fibrillar aggregates (*8*, *9*). The artificial proteins are members of a combinatorial library designed to form β strands. They have no evolved biological function, and their mRNA does not contain tri- or hexanucleotide repeat regions (fig. S1, A to C), which may contribute to neurodegenerative pathology (*10*, *11*). We analyzed two of these proteins, β17 and β23, which vary in aggregation efficiency and toxicity. An artificial protein forming a soluble α-helical bundle (αS824) served as a nontoxic control (*8*, *9*).

β17 and β23 form aggregates in the cytoplasm and nucleus of human embryonic kidney 293T (HEK293T) cells (*9*). To identify the cellular compartment in which toxicity arises, we added a nuclear export sequence (NES) or nuclear localization sequence (NLS) to the proteins (fig. S1A). NES-β17 and NES-β23 formed large cytoplasmic inclusions that stained with the amyloid-specific dye NIAD-4 (Fig. 1A and fig. S2A), suggesting the presence of cross-β structure (*12*, *13*). NLS-β17 and NLS-β23 formed multiple nuclear inclusions in close proximity to the nucleolus (Fig. 1, A and B). These inclusions stained only weakly with NIAD-4 and displayed reduced detergent solubility compared to the cytoplasmic aggregates (Fig. 1C and fig. S2A). The β proteins in both cytoplasmic and nuclear inclusions were highly immobile, as measured with β17–green fluorescent protein (GFP) fusion proteins (fig. S2B).

The toxicity of the nuclear β proteins was significantly reduced compared to their cytoplasmic counterparts and the proteins lacking a localization signal (Fig. 1D and fig. S3, A and B). This reduced toxicity was not due to lower expression levels (Fig. 1C and fig. S3C) or the presence of an NLS. Point mutations in the NLS prevented nuclear targeting and increased toxicity (fig. S3, A and B). Thus, otherwise virtually identical proteins form biochemically distinct aggregate species in the cytoplasm and nucleus that differ markedly in toxicity.

The nuclear aggregates coimmunoprecipitated with the abundant, negatively charged nucleolar protein nucleophosmin-1 (NPM1) (Fig. 1E) (*14*). During mitosis, when the nuclear envelope breaks down and nucleoli are disassembled, NPM1 distributed diffusely throughout the cell, but maintained its apparent association with the aggregates, as shown for NLS-β17 (fig. S4). Thus, NPM1 may have a chaperone-like function in shielding the surfaces of potentially toxic aggregates (*15*), and this may have prevented access of the NIAD-4 dye. Notably, cells with cytoplasmic aggregates underwent mitosis only very rarely.

The expression of β proteins in the cytoplasm altered the distribution of nuclear pore complex (NPC) proteins and partially dislocated NPC proteins to the cytoplasmic inclusions of NES-β17 and NES-β23 (Fig. 1A). In contrast, expression of NLS-β17 and NLS-β23 had no visible effect on NPC integrity (Fig. 1A and fig. S3A). To test whether the cytoplasmic aggregates interfered with nuclear transport processes, we used a GFP reporter carrying NES and NLS signals (Shuttle-GFP or S-GFP). In control cells, S-GFP accumulated predominantly in the cytoplasm (Fig. 2, A and B). Expression of NLS-β17 did not alter the distribution of S-GFP. However, NES-β17 caused a significant retention of S-GFP in the nucleus (Fig. 2, A and B). This inhibition of nuclear export was even more pronounced in cells containing cytoplasmic inclusions of polyQ-expanded Htt exon 1 (Htt96Q) (Fig. 2, A and B). Upon addition of the exportin inhibitor leptomycin B (LMB) (*16*) to control cells, S-GFP accumulated in the nucleus within 15 min (Fig. 2, A and B), reflecting rapid nuclear import. Again, this import was significantly inhibited by cytoplasmic aggregates of NES-β17 and Htt96Q, but not by nuclear NLS-β17. Thus, the cytoplasmic aggregates analyzed interfere with both import and export of proteins through the nuclear pore.

We also analyzed the nuclear translocation of the endogenous protein nuclear factor κB (NF-κB) subunit p65 upon activation with the cytokine tumor necrosis factor–α (TNFα) (*17*). p65 readily translocated in control cells and in cells expressing nuclear β-sheet proteins. In contrast, cells containing cytoplasmic aggregates failed to support p65 transport (Fig. 2C), even though phosphorylation of p65 and degradation of inhibitor of nuclear factor κB (IκB) were not altered (fig. S5).

Next we tested whether cytoplasmic aggregates also affected the transport of RNA. In control cells, polyadenylate [poly(A)] RNA (mRNA) was distributed throughout the cytoplasm and was present in small nuclear ribonucleic particles (Fig. 3A) (*18*). Expression of the nuclear β proteins did not influence this pattern. However, we observed a substantial nuclear accumulation of mRNA in cells expressing either the cytoplasmic β proteins, Htt96Q, or a GFP-tagged C-terminal fragment of TAR DNA binding protein–43 (TDP-F4) (Fig. 3, A and B, and fig. S6A). Similar fragments of TDP-43 aggregate in the cytoplasm of neuronal cells in amyotrophic lateral sclerosis and frontotemporal dementia (*19*).

Impairment of mRNA export from the nucleus would explain the reported reduction in protein synthesis capacity of β-protein–expressing cells (*9*). Indeed, expression of the cytoplasmic β proteins, but not the nuclear β proteins, resulted in a significant reduction in protein biosynthesis (Fig. 3C

[1]Department of Cellular Biochemistry, Max Planck Institute of Biochemistry, Am Klopferspitz 18, D-82152 Martinsried, Germany. [2]Department of Proteomics and Signal Transduction, Max Planck Institute of Biochemistry, Am Klopferspitz 18, D-82152 Martinsried, Germany. [3]Neurobiochemistry, Adolf Butenandt Institute, Ludwig Maximilians University, Schillerstr. 44, D-80336 Munich, Germany. [4]Department of Biochemistry of Neurodegenerative Diseases, Institute of Biochemistry and Pathobiochemistry, Ruhr University Bochum, Universitätsstraße 150, D-44801 Bochum, Germany. [5]Munich Cluster for Systems Neurology (SyNergy), D-80336 Munich, Germany. [6]Department of Molecular Cell Biology, Institute of Biochemistry and Pathobiochemistry, Ruhr University Bochum, Universitätsstraße 150, D-44801 Bochum, Germany. *Present address: National Institutes of Health, Bethesda, MD 20892, USA. †Corresponding author. E-mail: hipp@biochem.mpg.de (M.S.H.); uhartl@biochem.mpg.de (F.U.H.)

and fig. S6B). Quantitative analysis of mRNA levels confirmed that the strong reduction in cytoplasmic mRNA content was due to inhibition of export from the nucleus and not to reduced RNA synthesis or increased turnover (fig. S6, C and D).

Inhibition of mRNA export by cytoplasmic aggregates was reproduced in neuroblastoma cells and primary neurons (figs. S7 and S8). Mutant Htt preferentially forms nuclear inclusions in primary neurons (*7*), and these did not interfere with mRNA export (fig. S8). However, in the striatum and cortex of the R6/2 mouse, which is transgenic for human polyQ-expanded Htt exon 1 (*20*), mutant Htt forms cytoplasmic and nuclear aggregates (*21*). We observed significant alterations in mRNA distribution in brain slices of 9-week-old R6/2 mice. More than 10% of the neurons analyzed showed either an accumulation of mRNA in the nucleus or an overall reduction in mRNA levels (Fig. 3, D and E, and fig. S9A).

Protein aggregates may exert toxicity through aberrant interactions with other proteins, resulting in their functional impairment and sequestration (*9*, *22*). Quantitative interactome analysis of the β proteins in HEK cells previously identified several proteins involved in nuclear transport, including importin subunit alpha-1/KPNA2 and THOC2 (*9*), a subunit of the THO (suppressor of the transcriptional defects of hpr1Δ by overexpression) complex involved in mRNA export (*23*, *24*). A similar interactome analysis in primary neurons expressing either β17-GFP or GFP alone identified the seven-subunit THO complex as a highly enriched β-protein interactor (Fig. 4A and tables S1 to 3). Indeed, expression of NES-β17 caused mislocalization and, in some cases, aggregation of THOC proteins in the cytoplasm, as shown with antibodies against THOC2 (Fig. 4B). Notably, the nuclear inclusions of NLS-β17 did not coaggregate with THOC2, although most of the THOC2 was present in the nucleus. Mislocalization of THOC2 to the cytoplasm also occurred in cells containing cytoplasmic Htt96Q or TDP-F4 aggregates (Fig. 4B), and in the brains of R6/2 mice (fig. S9B). THOC2 often formed separate inclusions

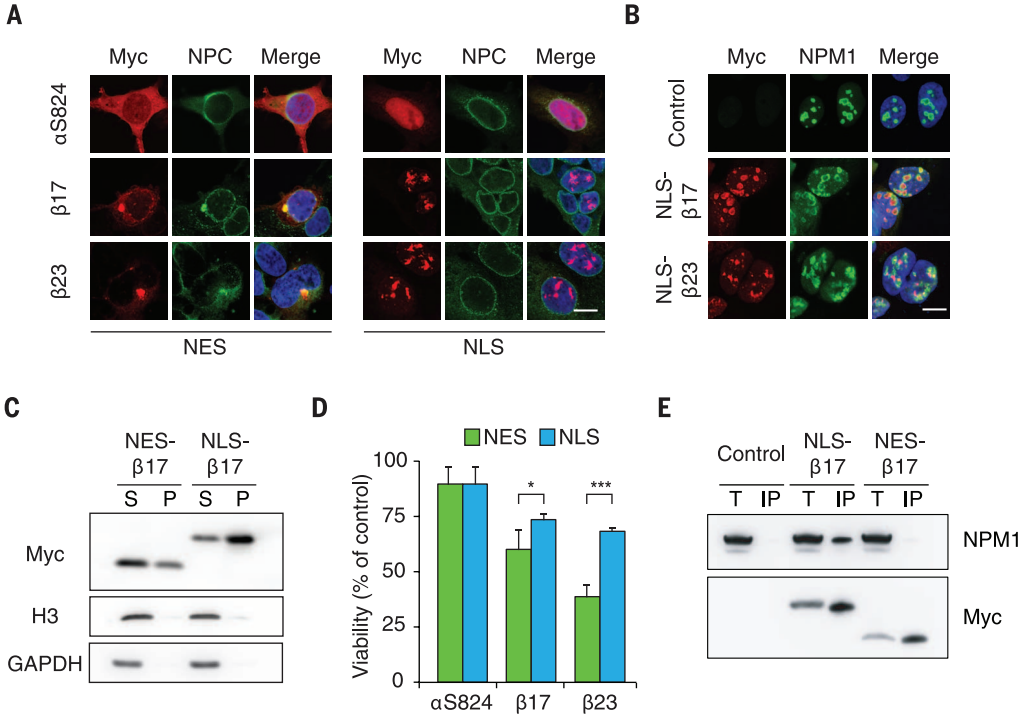

Fig. 1. Targeting aggregation-prone proteins to cytoplasm or nucleus modulates their properties. HEK293T cells 24 hours after transfection of the indicated NES- and NLS-proteins. (**A**) Anti-Myc (red), anti-NPC (nuclear pore complex) proteins (green), and DAPI (4′,6-diamidino-2-phenylindole) (blue). Scale bar, 10 μm. (**B**) Anti-Myc (red), nucleoli labeled with anti-NPM1 (green) and DAPI (blue). Scale bar, 10 μm. (**C**) Solubility of β proteins directed to cytoplasm and nucleus. S, soluble fraction; P, pellet fraction; H3, histone H3; GAPDH, glyceraldehyde-3-phosphate dehydrogenase. (**D**) Viability of HEK293T cells expressing αS824 and β proteins, as measured by MTT [3-(4,5-dimethylthiazol-2-yl)-2,5-diphenyltetrazolium bromide] assay. All values relative to untransfected control cells. Data are mean + SD, $n = 4$ independent experiments. $^{*}P \le 0.05$, $^{***}P \le 0.001$ by unpaired Student's t test. (**E**) HEK293T cells were transfected with the indicated constructs; after cell lysis, anti-Myc was used for immunoprecipitation (IP). T, total.

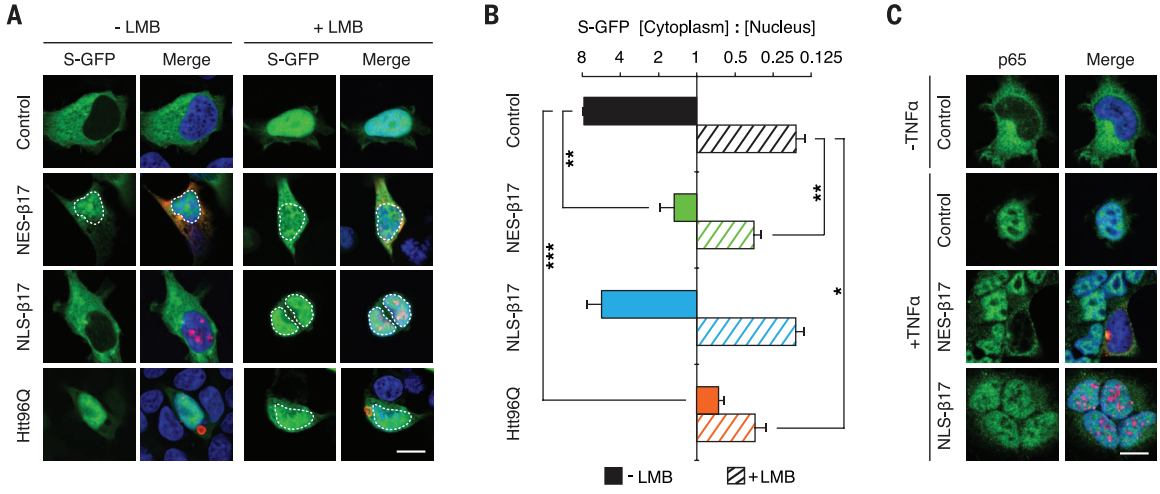

Fig. 2. Cytoplasmic aggregates interfere with nuclear protein transport. (**A**) HEK293T cells cotransfected with S-GFP (green) and either empty vector (Control), NES-β17, NLS-β17, or Htt96Q (red); DAPI (blue). Leptomycin B (LMB; 10 ng/ml) was added for 15 min where indicated. Scale bar, 10 μm. (**B**) Quantification of S-GFP distribution from data in (A). The x axis shows enrichment of S-GFP in the nucleus relative to the cytoplasm. Data are mean + SD, $n = 3$ independent experiments. $^{*}P \le 0.05$, $^{**}P \le 0.01$, $^{***}P \le 0.001$ from unpaired Student's t test. (**C**) HEK293T cells transfected with empty vector (Control), NES-β17, or NLS-β17 (red) were analyzed for NF-κB p65 localization (green) with and without TNFα treatment (30 min). Nuclear DNA (blue). Scale bar, 10 μm.

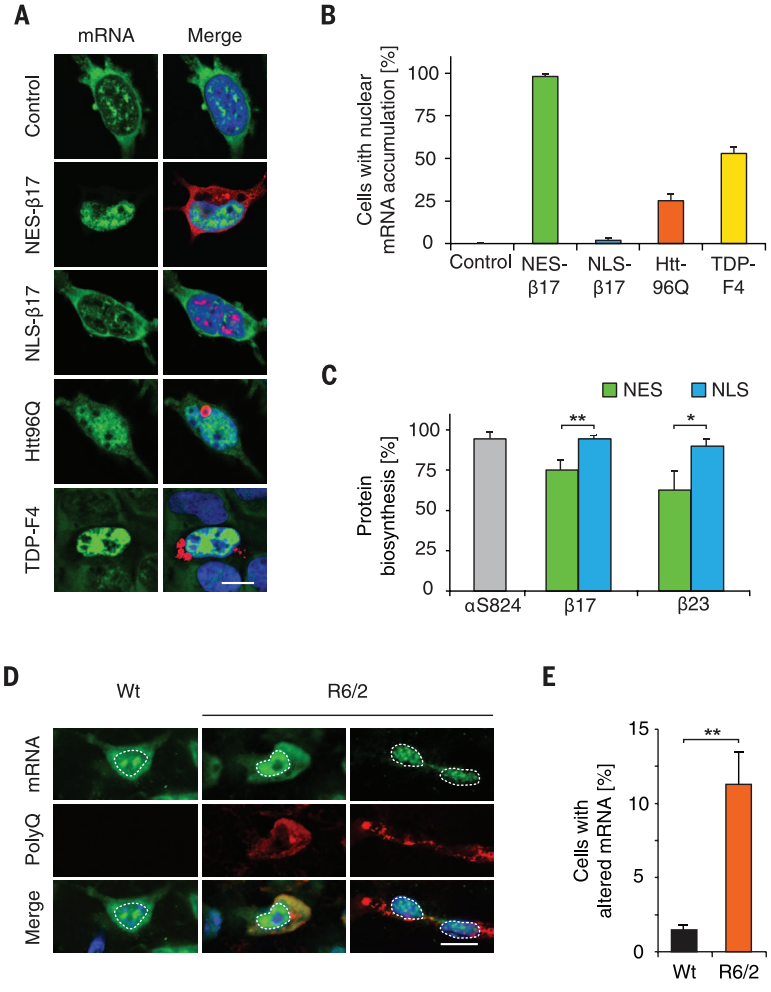

Fig. 3. Protein aggregates in the cytoplasm inhibit mRNA export. (**A**) HEK293T cells were analyzed for polyA RNA (green), NES-β17, NLS-β17, Htt96Q, or TDP-F4 (red); DAPI (blue). Scale bar, 10 μm. (**B**) Quantification of (A). Data are mean + SD, $n = 3$ independent experiments. (**C**) Quantification of protein biosynthesis from data in fig. S6B. ^{35}S-Met incorporation in control cells was set to 100%. Data are mean + SD, $n = 3$ independent experiments. $^{*}P \leq 0.05$, $^{**}P \leq 0.01$ from unpaired Student's t test. (**D**) Distribution of polyA RNA (green) in brain slices of 9-week-old wild-type (Wt) and R6/2 mice, transgenic for human polyQ-expanded Htt exon 1. PolyQ expanded Htt (red); nuclear DNA (blue). The middle panel shows an example of a cell with nuclear accumulation of mRNA and mRNA remaining in the cytoplasm. The right panel shows a cell with strongly reduced overall mRNA levels. (**E**) Quantification of fraction of cells from Wt and R6/2 mice with abnormal polyA RNA distribution from data in (D). At least 1000 cells were analyzed per animal. Data are mean + SD, $n = 3$ independent experiments. $^{**}P \leq 0.01$ from unpaired Student's t test.

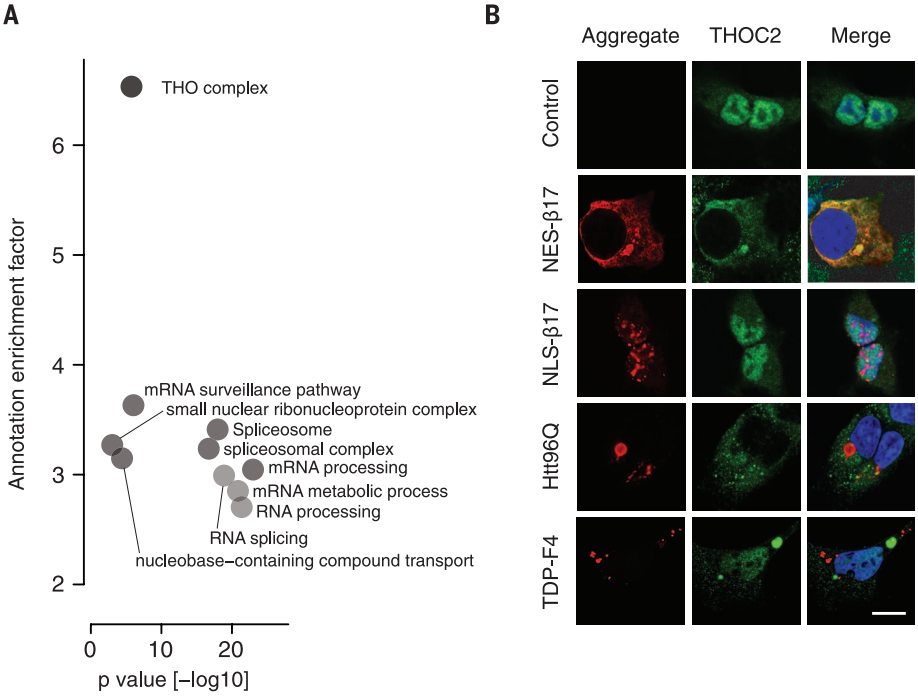

Fig. 4. Cytoplasmic aggregates cause mislocalization of nuclear transport factors. (**A**) The β17-GFP interactome was determined by anti-GFP pull-down and quantitative mass spectrometry, with cells expressing GFP alone as a control. Significant interactors were analyzed for highly enriched annotations. The y axis indicates the fold enrichment of annotations; the x axis depicts the significance of the respective enrichment. The THO complex was the most strongly enriched interactor of β17-GFP in primary neurons. (**B**) Immunofluorescence analysis of HEK293T cells transfected with empty vector (Control), NES-β17, NLS-β17, Htt96Q, or TDP-F4. THOC2 (green), protein aggregates (red), DAPI (blue). Scale bar, 10 μm.

that did not colocalize with these aggregates (Fig. 4B), consistent with the prion-like behavior described for certain RNA binding proteins when dislocated to the cytoplasm (*25*). Importin α-1 and importin α-3 were also mislocalized to cytoplasmic β-protein aggregates (fig. S10, A and B).

Besides THOC, the β-protein interactome in primary neurons contained splicing factors and several other RNA binding proteins (Fig. 4A and table S1), suggesting that the cytoplasmic aggregates affect not only mRNA export, but also nuclear mRNA processing. Indeed, cells containing cytoplasmic aggregates exhibited a more pronounced accumulation of mRNA in the nucleus than cells in which THOC2 was down-regulated (fig. S10C) (*26*).

Our findings provide insight into common mechanisms that are likely to contribute to aggregate toxicity in neurodegenerative diseases and other disorders. Cytoplasmic aggregates of artificial β-sheet proteins and authentic disease proteins caused a pronounced impairment of nucleocytoplasmic transport and a redistribution of nuclear shuttle factors to the cytosol. Several of these transport proteins, including THOC2 (fig. S11), contain disordered and low-complexity sequences that may render them vulnerable to interactions with the interactive surfaces of cytoplasmic aggregates (table S2). Thus, the inhibition of nuclear transport observed in this system can be assigned to proteotoxicity, rather than to aberrant interactions between RNA repeat sequences and RNA binding proteins (*10*). Such repeat RNAs occur in the coding region or in untranslated regions of disease genes and are associated with amyotrophic lateral sclerosis, frontotemporal dementia, and CAG repeat disorders (*11*). Their coexistence with protein aggregates has confounded the analysis of toxicity mechanisms (*10*, *27*, *28*).

Surprisingly, otherwise identical aggregation-prone proteins did not interfere with nucleocytoplasmic transport when directed to the nucleus. How the nuclear environment alters the interaction properties of the β proteins remains to be investigated in detail, but our findings suggest that the negatively charged, nucleolar protein NPM1 is involved in shielding interactive aggregate surfaces. Indeed, recent reports that misfolded cytoplasmic proteins are actively imported into the nucleus for degradation (*29*) support a protective role for the intranuclear sequestration of aberrant proteins (*7*). However, specific aggregation-prone proteins may escape recognition by the nuclear quality-control machinery. For example, nuclear aggregates of polyQ expansion proteins have been shown to interfere with transcriptional regulation by engaging transcription factors containing glutamine repeats (*30*). A better understanding of nuclear proteostasis may help in developing new strategies for the treatment of proteinopathies.

REFERENCES AND NOTES

1. E. T. Powers, R. I. Morimoto, A. Dillin, J. W. Kelly, W. E. Balch, *Annu. Rev. Biochem.* **78**, 959–991 (2009).
2. F. U. Hartl, A. Bracher, M. Hayer-Hartl, *Nature* **475**, 324–332 (2011).
3. R. C. Taylor, A. Dillin, *Cold Spring Harb. Perspect. Biol.* **3**, a004440 (2011).
4. T. P. Knowles, M. Vendruscolo, C. M. Dobson, *Nat. Rev. Mol. Cell Biol.* **15**, 384–396 (2014).
5. K. Y. Liu *et al.*, *Hum. Mol. Genet.* **24**, 1602–1616 (2015).
6. A. S. Hackam, R. Singaraja, T. Zhang, L. Gan, M. R. Hayden, *Hum. Mol. Genet.* **8**, 25–33 (1999).
7. F. Saudou, S. Finkbeiner, D. Devys, M. E. Greenberg, *Cell* **95**, 55–66 (1998).
8. M. W. West *et al.*, *Proc. Natl. Acad. Sci. U.S.A.* **96**, 11211–11216 (1999).
9. H. Olzscha *et al.*, *Cell* **144**, 67–78 (2011).
10. K. Zhang *et al.*, *Nature* **525**, 56–61 (2015).
11. R. Nalavade, N. Griesche, D. P. Ryan, S. Hildebrand, S. Krauss, *Cell Death Dis.* **4**, e752 (2013).
12. E. E. Nesterov *et al.*, *Angew. Chem. Int. Ed. Engl.* **44**, 5452–5456 (2005).
13. T. Jakhria *et al.*, *J. Biol. Chem.* **289**, 35781–35794 (2014).
14. W. Y. Chan *et al.*, *Biochemistry* **28**, 1033–1039 (1989).
15. A. Szebeni, M. O. Olson, *Protein Sci.* **8**, 905–912 (1999).
16. B. Wolff, J. J. Sanglier, Y. Wang, *Chem. Biol.* **4**, 139–147 (1997).
17. P. A. Baeuerle, D. Baltimore, *Cell* **53**, 211–217 (1988).
18. K. C. Carter, K. L. Taneja, J. B. Lawrence, *J. Cell Biol.* **115**, 1191–1202 (1991).
19. C. Yang *et al.*, *PLOS ONE* **5**, e15878 (2010).
20. L. Mangiarini *et al.*, *Cell* **87**, 493–506 (1996).
21. H. Li *et al.*, *Hum. Mol. Genet.* **8**, 1227–1236 (1999).
22. B. Bolognesi *et al.*, *ACS Chem. Biol.* **5**, 735–740 (2010).
23. N. Visa *et al.*, *Cell* **84**, 253–264 (1996).
24. H. Cheng *et al.*, *Cell* **127**, 1389–1400 (2006).
25. O. D. King, A. D. Gitler, J. Shorter, *Brain Res.* **1462**, 61–80 (2012).
26. B. Chi *et al.*, *Nucleic Acids Res.* **41**, 1294–1306 (2013).
27. B. D. Freibaum *et al.*, *Nature* **525**, 129–133 (2015).
28. A. Jovičić *et al.*, *Nat. Neurosci.* **18**, 1226–1229 (2015).
29. M. S. Hipp, S. H. Park, F. U. Hartl, *Trends Cell Biol.* **24**, 506–514 (2014).
30. K. L. Sugars, D. C. Rubinsztein, *Trends Genet.* **19**, 233–238 (2003).

ACKNOWLEDGMENTS

We thank R. Klein, K. Schulz-Trieglaff, and I. Dudanova from the Max Planck Institute of Neurobiology for help with the preparation of primary neurons and brain slices, and J. Cox, F. Hosp, and M. Duerrbaum for support with proteomic data analysis. We thank C. Klaips and D. Balchin for critically reading the manuscript. The research leading to these results has received funding from the European Commission under grant FP7 GA ERC-2012-SyG_318987–ToPAG (to A.C.W., D.H., M.M., F.U.H., and M.S.H.), the Munich Cluster for Systems Neurology (K.F.W, M.M, F.U.H. and M.S.H.), the German Research Foundation (J.T., K.F.W.), and the Hans and Ilse Breuer Foundation (M.P.). F.U.H has an advisory position with Proteostasis Therapeutics Inc.. Data from the mass spectrometry analysis described in this manuscript can be found in the supplementary materials.

SUPPLEMENTARY MATERIALS

www.sciencemag.org/content/351/6269/173/suppl/DC1
Materials and Methods
Figs. S1 to S11
Tables S1 to S3
References (*31*–*47*)

7 August 2015; accepted 11 November 2015
Published online 3 December 2015
10.1126/science.aad2033

STEM CELL NICHE

Fetal liver hematopoietic stem cell niches associate with portal vessels

Jalal A. Khan,[1,2,5] Avital Mendelson,[1,2] Yuya Kunisaki,[1,2]* Alexander Birbrair,[1,2] Yan Kou,[6] Anna Arnal-Estapé,[1,2]† Sandra Pinho,[1,2] Paul Ciero,[1] Fumio Nakahara,[1,2] Avi Ma'ayan,[6] Aviv Bergman,[4] Miriam Merad,[5] Paul S. Frenette[1,2,3]‡

Whereas the cellular basis of the hematopoietic stem cell (HSC) niche in the bone marrow has been characterized, the nature of the fetal liver niche is not yet elucidated. We show that Nestin$^+$NG2$^+$ pericytes associate with portal vessels, forming a niche promoting HSC expansion. Nestin$^+$NG2$^+$ cells and HSCs scale during development with the fractal branching patterns of portal vessels, tributaries of the umbilical vein. After closure of the umbilical inlet at birth, portal vessels undergo a transition from Neuropilin-1$^+$Ephrin-B2$^+$ artery to EphB4$^+$ vein phenotype, associated with a loss of periportal Nestin$^+$NG2$^+$ cells and emigration of HSCs away from portal vessels. These data support a model in which HSCs are titrated against a periportal vascular niche with a fractal-like organization enabled by placental circulation.

Hematopoietic stem cells (HSCs) are generated in the mouse fetus around embryonic day 10.5 (E10.5) from hemogenic endothelium of the dorsal aorta (*1*, *2*), then migrate to the placenta via the umbilical arteries (*3*) and return to the fetus via the umbilical vein (*4*). The umbilical vein delivers oxygenated blood to the fetus via the portal sinus, whose branches give rise to the portal vessels in the fetal liver (FL). In this organ, HSCs undergo marked expansion (*5*). The predictable growth curve of HSCs during development suggests that hitherto unknown determinants set the numbers of these cells.

Although FL HSCs are highly proliferative, a hallmark of adult bone marrow (BM) HSCs is their cell cycle quiescence (*6*). Perivascular cells expressing Nestin (*7*), CXCL12 (*8*), and the leptin receptor (*9*) contribute to HSC maintenance. Nestin$^+$NG2$^+$ arteriolar pericytes (*10*), as well as megakaryocytes (*11*, *12*), maintain quiescent HSCs

[1]Ruth L. and David S. Gottesman Institute for Stem Cell and Regenerative Medicine Research. Albert Einstein College of Medicine, Bronx, NY, USA. [2]Department of Cell Biology, Albert Einstein College of Medicine, Bronx, NY, USA. [3]Department of Medicine, Albert Einstein College of Medicine, Bronx, NY, USA. [4]Department of Systems and Computational Biology, Albert Einstein College of Medicine, Bronx, NY, USA. [5]Department of Oncological Sciences, Icahn School of Medicine at Mount Sinai, New York, NY, USA. [6]Department of Pharmacology and Systems Therapeutics, Icahn School of Medicine at Mount Sinai, New York, NY, USA.
*Present address: Department of Medicine and Biosystemic Science, Kyushu University, Fukuoka 812-8582, Japan. †Present address: Department of Pathology, Yale University School of Medicine, New Haven, CT 06510, USA. ‡**Corresponding author. E-mail: paul.frenette@einstein.yu.edu**

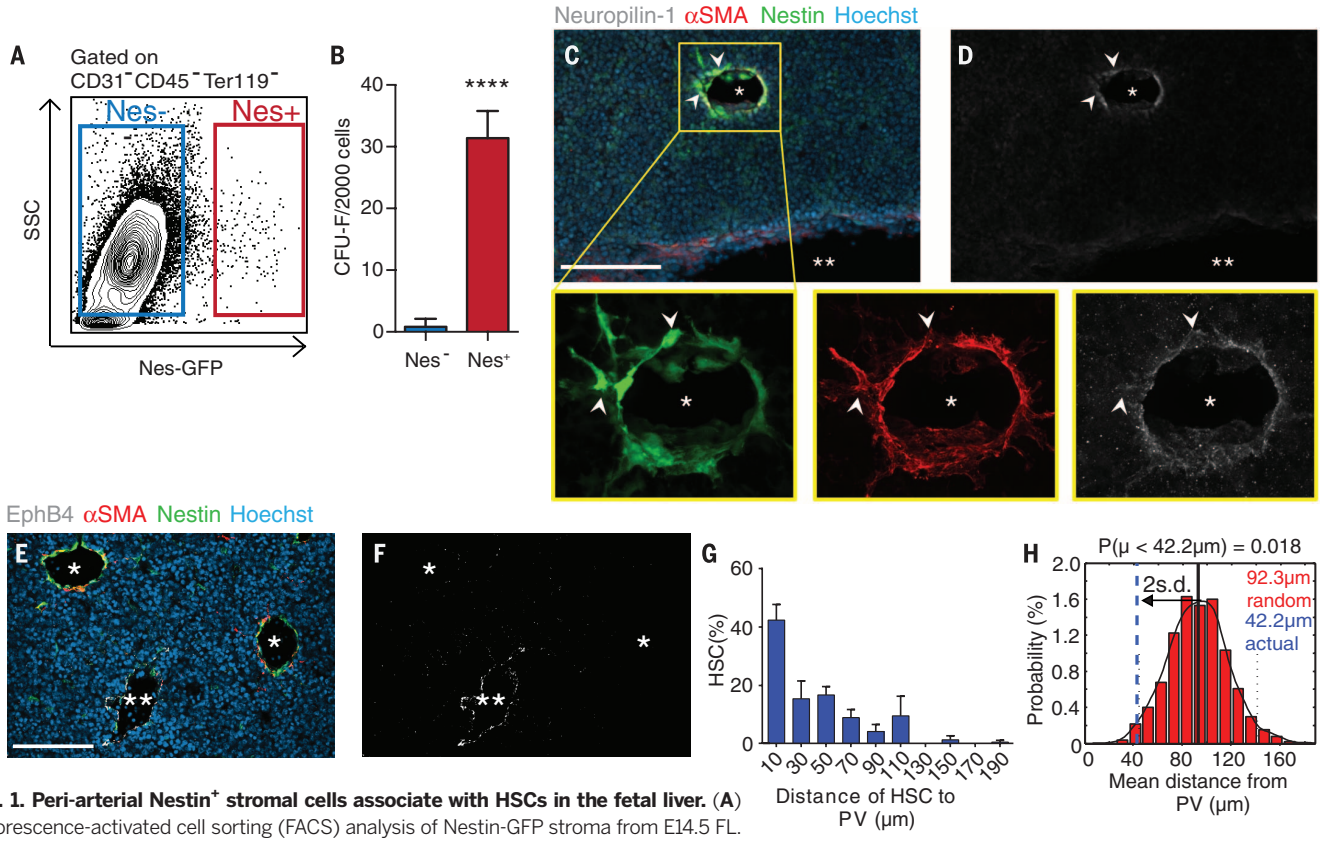

Fig. 1. Peri-arterial Nestin$^+$ stromal cells associate with HSCs in the fetal liver. (**A**) Fluorescence-activated cell sorting (FACS) analysis of Nestin-GFP stroma from E14.5 FL. (**B**) CFU-F from sorted FL cells; $n = 4$. (**C** to **F**) Immunofluorescence analyses of Nestin-GFP E14.5 FL cryosections stained for Neuropilin-1 [white, (C) and (D)] or EphB4 [white, (E) and (F)]. Colocalization of αSMA$^+$ and Nestin$^+$ pericytes around Neuropilin-1$^+$ portal vessels (*) but not EphB4$^+$ veins (**). Scale bar, 100 μm. (**G**) Distance distribution between CD150$^+$CD48$^-$CD41$^-$Lineage$^-$ HSCs and Nestin$^+$ cells from whole-mount stained Nestin-GFP FL ($n = 105$ from 12 E14.5 FLs), binned into 20-μm intervals. (**H**) Probability distribution of mean distances from simulations of randomly positioned HSCs in relation to Nestin$^+$ cells. Actual mean distance shown in relation to mean of simulations ± 2 SD. ****$P < 10^{-4}$.

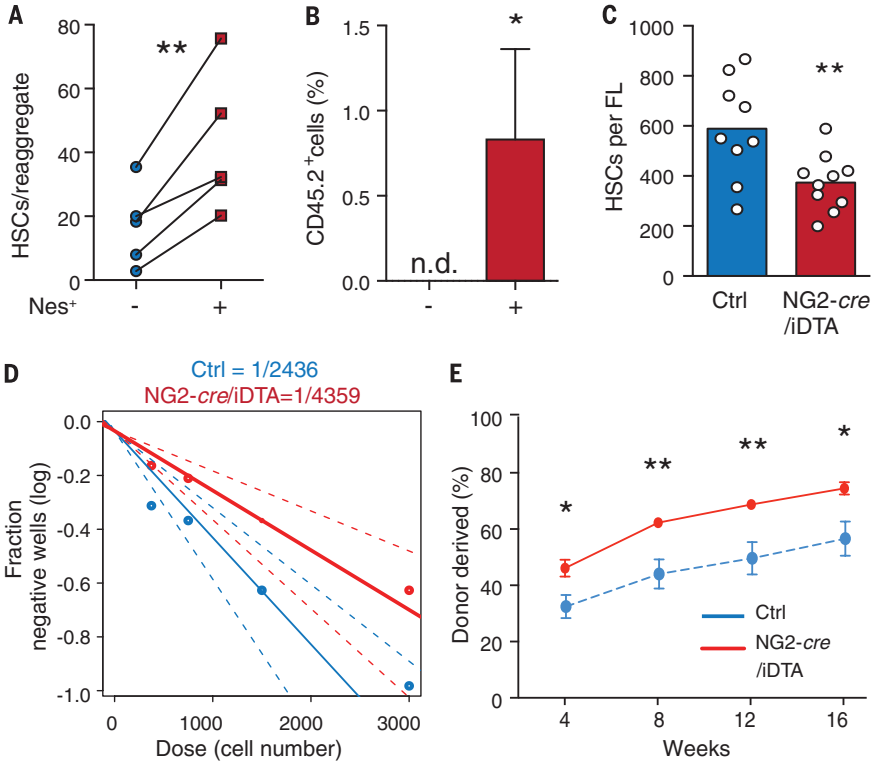

Fig. 2. Nestin$^+$ perivascular cells drive HSC expansion in vivo. (**A**) FACS quantification of CD150$^+$Sca1$^+$ CD45$^+$ CD48$^-$Lin$^-$ HSCs in reaggregates, with or without Nestin$^+$ cells. (**B**) Donor engraftment 16 weeks after transplantation of reaggregates together with congenic competitor cells. n.d., not detectable. $n = 6$ to 7 per group. (**C**) CD150$^+$CD48$^-$Sca1$^+$CD11b$^+$CD45$^+$CD41$^-$Lineage$^-$DAPI$^-$ HSC numbers in control and NG2-depleted littermates. (**D**) Limiting dilution analyses of LTC-ICs in Lineage$^-$ cells from NG2-depleted (red) and control (blue) littermate FLs. (**E**) Competitive repopulation assays of NG2-depleted and control FL. $n = 6$ and 7 mice per control and depleted littermates, respectively. *$P < 0.05$, **$P < 0.01$.

in the BM. Much less is known about the FL niche promoting HSC proliferation. FL-derived stromal cell lines support HSC expansion in vitro (*13*, *14*). However, a HSC niche in the liver has not been demonstrated in vivo.

Within the E14.5 FL of Nestin-GFP (green fluorescent protein) transgenic mice, endothelial cells and a rare population of stromal cells (Fig. 1A) (0.045% ± 0.007% of total nucleated cells) are marked by GFP. These stromal cells, hereafter termed Nestin$^+$ cells, are highly enriched in colony-forming unit–fibroblast activity (CFU-F) (Fig. 1B) and expressed mesenchymal lineage markers and DLK1, but neither the biliary marker EpCAM (*15*) nor hepatic genes (fig. S1, A and B). FL CFU-F colonies derived from Nestin$^+$ cells had trilineage mesenchymal lineage capacity when cultured in defined conditions (fig. S1, C to F). Nestin$^+$ cells expressed α-smooth muscle actin (αSMA) (fig. S1G), the pericyte marker NG2 (fig. S2, C and D), and colocalized with αSMA staining on portal vessels expressing the endothelial arterial markers Ephrin-B2 and Neuropilin-1 but not the venular marker EphB4 (fig. S1, H to J, and Fig. 1, C to F). Thus, Nestin$^+$ cells are pericytes abutting *Efnb2* and Neuropilin-1–expressing endothelia on portal vessels. Last, Nestin$^+$ cells were enriched for HSC niche and expansion factors (fig. S1, K and L), raising the potential for regulating FL HSCs.

To evaluate the spatial relationships between HSCs and Nestin$^+$ cells, we stained CD150$^+$CD48$^-$CD41$^-$Lineage$^-$ HSCs in whole-mount FLs and evaluated the significance of the associations by computational modeling (*10*). A large HSC fraction (>40%) was located within 20 μm of Nestin$^+$ cells on portal vessels (Fig. 1G). We then simulated nonpreferential HSC placement on images of whole-mount prepared FLs to define the distribution of randomly localized HSCs to portal vessels. The observed HSC mean distance to Nestin$^+$ cells (42.2 μm) was statistically different from that of randomly placed HSCs (92.3 μm, P = 0.018) (Fig. 1H). The close physical associations between HSCs and Nestin$^+$ periportal cells suggest that the portal vasculature may harbor a HSC niche.

We adapted the reaggregate organ culture assay in which selected populations are pelleted and cultured on the surface of a porous membrane (*16*). A FL cell mixture containing hematopoietic stem and progenitor cells (Lineage$^-$CD45$^+$), CD31$^+$ endothelial cells, and hepatic parenchymal/stromal cells (CD45$^-$Lineage$^-$) was separated by cell sorting and was reaggregated with or without Nestin$^+$ cells (ratio ~235/1) and cultured in the absence of exogenous cytokines or serum (fig. S2A). Significantly higher numbers of phenotypic HSCs (*17*) were maintained in the reaggregates containing Nestin$^+$ cells after 7 days in culture (Fig. 2A and fig. S2B), and these reaggregates contained detectable long-term repopulating FL HSC activity after transplantation, whereas the controls did not (Fig. 2B). These results suggest that factors produced by the FL Nestin$^+$ cells were sufficient to maintain HSCs in culture.

In contrast to Nestin-GFP, which also labels FL endothelial cells, NG2 expression was specific to Nestin$^+$ pericytes (~98% overlap) (fig. S2, C to G) and αSMA$^+$ portal vessels, as determined by NG2-*cre* transgenic mice (*18*) crossed with inducible TdTomato transgenic mice (fig. S2, H and I). We then crossed male NG2-*cre* mice with female Cre-inducible diphtheria toxin A (iDTA) mice to deplete NG2$^+$ cells by selective expression of DTA after NG2-*cre*–mediated excision of a floxed-STOP cassette (*19*). Embryos were staged in utero by crown-rump length (CRL) using ultrasound imaging (fig. S2J). NG2-*cre*/iDTA fetuses did not exhibit gross developmental defects compared with littermates (fig. S3A) and had similar CRL (fig. S3B). Although NG2-*cre* activity was detected in mural cells surrounding the midline dorsal aorta at E11 (fig. S3C), we found no difference in HSCs and LSKs in E12 to E12.5 FLs of NG2-*cre*/iDTA transgenic mice (fig. S3, D to G), suggesting that HSC specification and homing to FL were not significantly altered. At E14.5, however, HSCs were significantly reduced (by ~45%) (Fig. 2C and fig. S3H) in FLs from NG2-*cre*/iDTA fetuses compared with control littermates, whereas progenitors were unaffected (fig. S3, I and J). Limiting dilution analyses also revealed a 45% reduction of long-term culture–initiating colonies (LTC-IC) (*20*) in NG2-*cre*/iDTA FLs compared with control littermates (Fig. 2D). These data suggest that Nestin$^+$NG2$^+$ cells provide a niche in the FL.

HSCs from NG2-*cre*/iDTA mice FLs exhibited reductions (~43%) in bromodeoxyuridine uptake compared with littermate controls, suggesting that Nestin$^+$NG2$^+$ cells are required for HSC proliferation (fig. S3K). Consistent with previous reports suggesting a reduced capacity of S/G_2/M-phase HSCs to engraft irradiated recipient mice (*20*, *21*), we observed an increase in HSC engraftment in NG2-*cre*/iDTA FLs compared with control littermates (Fig. 2E and fig. S4A). Indeed, engraftment-competent G_0/G_1-phase HSCs were enriched in NG2-*cre*/iDTA mice compared with littermate controls, whereas the S/G_2/M-phase HSCs (DNA > 2n)

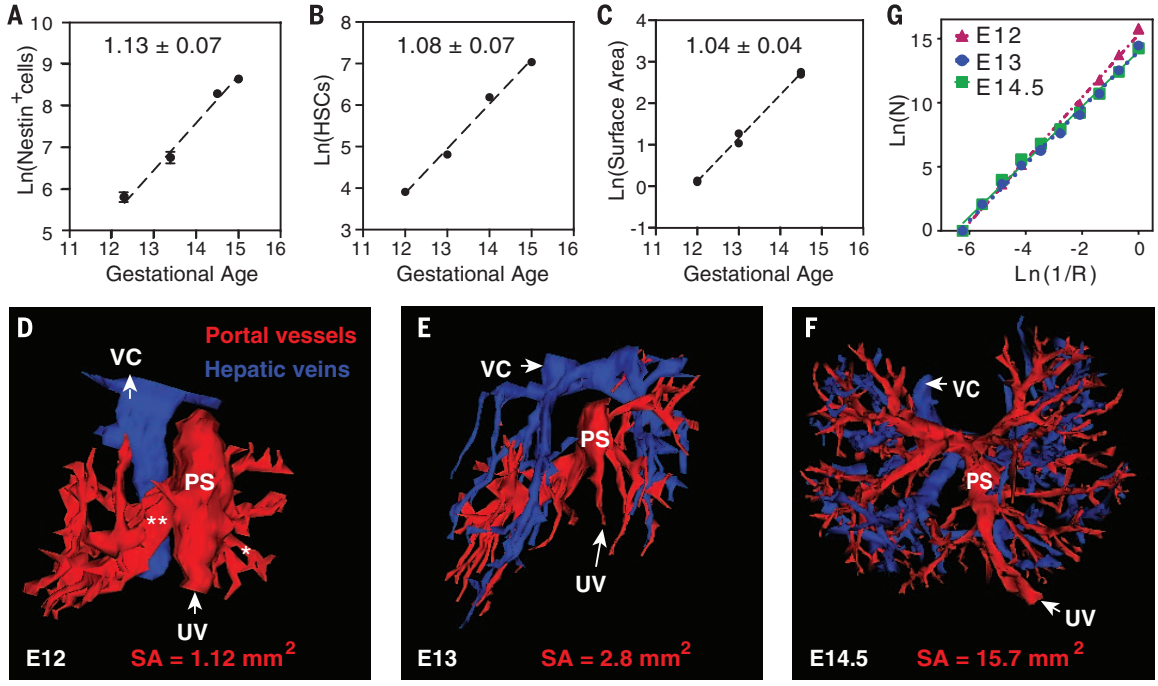

Fig. 3. Fractal geometry underlies HSC expansion. (**A**) Nestin$^+$ cells expand from E12 to E15 according to a power law (R^2 = 0.95). (**B**) HSC numbers relative to gestational age plotted from quantification of Ema *et al.* (*5*). (**C**) Portal vessel surface area from E12 to E14.5 scales according to a similar power law (R^2 = 0.99; n = 6). Slopes indicated in panels. (**D** to **F**) 3D reconstructions of afferent PVs (red) and efferent veins (blue) in E12 (D), E13 (E), and E14.5 (F) FLs. PS, portal sinus; VC, vena cava; SA, surface area. (**G**) Calculation of the scale-invariant fractal dimension of FL afferent vessels using box-counting.

were reduced (fig. S4, B to F). Together, these data indicate that Nestin$^+$ cells are required to drive fetal HSC expansion.

Because arteriole-associated Nestin$^+$NG2$^+$ cells promote HSC quiescence in adult BM (*10*) and analogous cells appear to exert opposite functions in the FL, we next sequenced cDNA libraries of Nestin$^+$NG2$^+$ cells sorted from BM and FL stroma from Nestin-GFP;NG2-DsRed double-transgenic mice (fig. S5). Most (95.6%) BM and FL Nestin$^+$NG2$^+$ cell transcripts were statistically indistinguishable, but FL transcripts accounted for the majority of differentially expressed (DE) genes (fig. S5, A and B), suggesting that these cells are highly similar. Indeed, BM and FL Nestin$^+$NG2$^+$ cells had similar expression of many HSC niche and pericyte genes (fig. S5, F and H). Accordingly, reaggregation of E14.5 FL cell mixtures with similar numbers of adult BM Nestin^{bright} cells (*10*) or FL Nestin$^+$ cells revealed a similar capacity to support HSCs (fig. S4G). In addition, *Scf*, *Angptl2*, and *Igf2* expression in Nestin$^+$ cells were similar at E12, E13, and E14.5, suggesting that Nestin$^+$ cells do not expand HSCs by increasing expression of these factors (fig. S4, H and I). FL DE genes were analyzed with the Enrichr gene-set enrichment analysis tool (*22*); genes involved in mitosis, metabolism, and growth—as well as knockout phenotypes including abnormal blood vessel development, blood circulation, and cell proliferation—were significantly enriched (fig. S5, C to E). Chromatin immunoprecipitation sequencing enrichment analyses (*23*) applied to identify upstream regulatory factors highly connected to FL DE genes pointed to key drivers of cell cycle progression (fig. S6, A to C). Accordingly, FL Nestin$^+$ cells differentially expressed cell cycle genes, including Ki67, and were actively proliferating (figs. S5I and S1M).

The enrichment of genes promoting cell cycle progression and vascular development supports the hypothesis—as implied by the niche concept—that the expansion of Nestin$^+$NG2$^+$ cells and portal vessels is synchronized with HSC expansion. The absolute numbers of Nestin$^+$ cells increased logarithmically over E12 to E14.5 (Fig. 3A). When compared with numbers of HSCs (Fig. 3B) (*5*), the rates of expansion were indistinguishable (Fig. 3, A and B) [$P = 0.69$, analysis of covariance (ANCOVA)]. We next mapped the vasculature by tracing vessels in consecutive cryosections of Nestin-GFP$^+$ FLs from E12 to E14.5 (fig. S7, A to C) to generate complete three-dimensional (3D) surface maps (Fig. 3, D to F). Portal vessels receiving blood from the umbilical vein (UV) were lined with Nestin$^+$ cells (fig. S7, A to C, and Fig. 3, D to F), in contrast to αSMA-negative hepatic veins that lacked Nestin$^+$ cell lining (fig. S7C). At E13 and E14.5, portal vessel branching became progressively more intricate (Fig. 3, E and F), and the surface area of these structures increased logarithmically. Nestin$^+$ cell numbers and portal vessels' surface area scaled over time with indistinguishable slopes ($P = 0.47$, ANCOVA) (Fig. 3, A and C), suggesting that the HSC niche expansion is also related to portal vessel surface area.

That Nestin$^+$ cell and portal vessel expansion fit a power law suggests that they follow a fractal-like

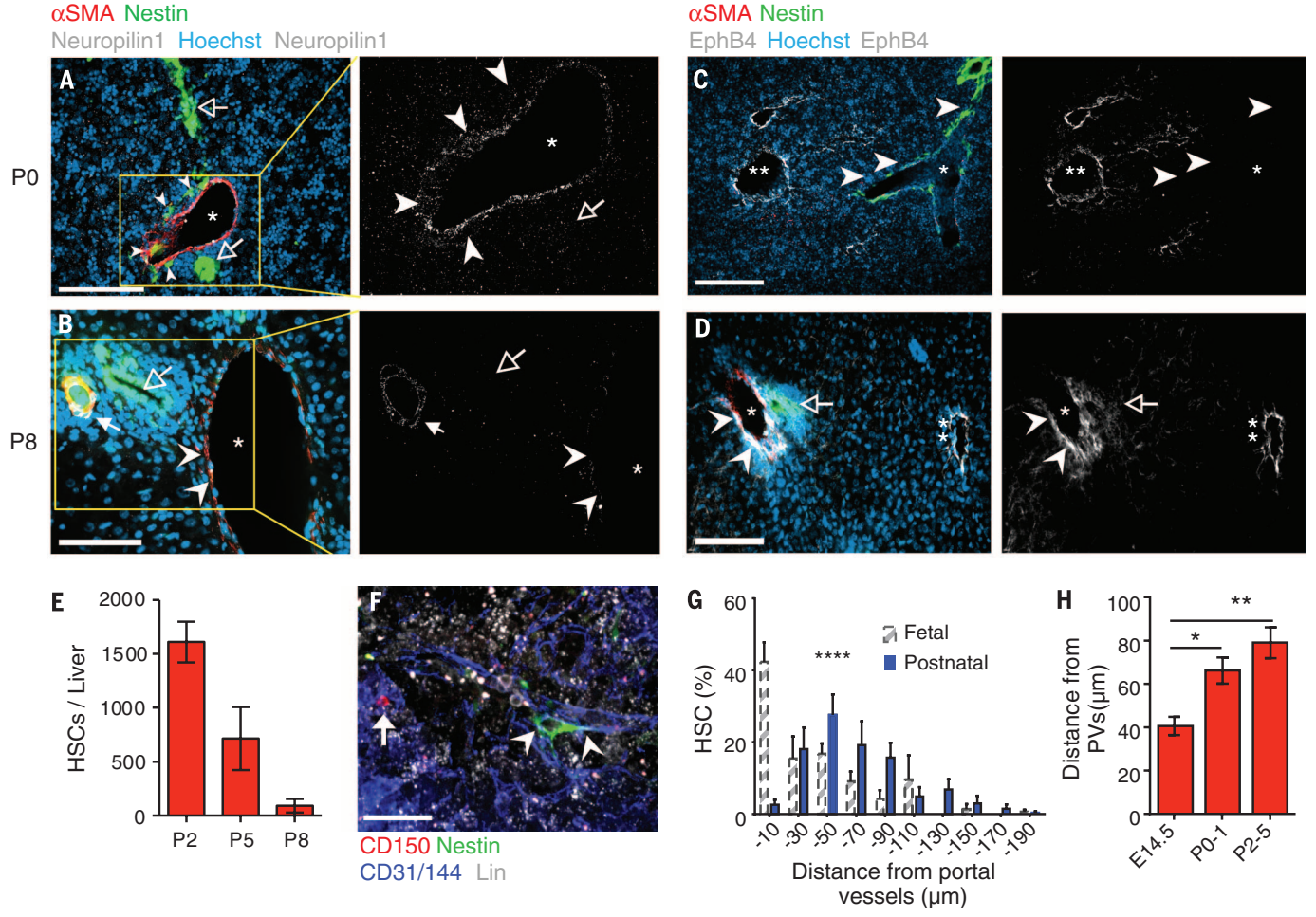

Fig. 4. Ligation of the umbilical vein inlet terminates the portal vessel HSC niche. (**A** to **D**) Immunofluorescence analyses of P0 [(A) and (C)] and P8 [(B) and (D)] liver cryosections stained for αSMA (red), Nestin-GFP (green), nuclear dye Hoechst (blue), and Neuropilin-1 or EphB4 (white). *, portal vessels; **, hepatic veins; arrowheads, Nestin$^+$ cells (P0) or outline of portal vessel; solid arrow, hepatic artery; open arrows, bile ducts. (**E**) FACS analysis showing decreasing numbers of CD150$^+$CD48$^-$Sca1$^+$CD11b$^+$CD45$^+$CD41$^-$Lineage$^-$DAPI$^-$ HSCs between P2 and P8. (**F**) Representative whole-mount immunofluorescence imaging of a CD150$^+$CD48$^-$Lin$^-$ HSC (arrow) in P3 fetal liver. Arrowheads, portal vessel. (**G**) Distance distribution of HSCs from portal vessels ($n = 77$ from 20 livers). FL HSC measurements from Fig. 1G (dashed-line bars) are shown for comparison. (**H**) HSC distances from portal vessels in fetal and postnatal livers showing increasing mean distances with age. Scale bars: (A) to (D), 100 μm; F, 20 μm. *$P < 0.05$, **$P < 0.01$, ****$P < 0.0001$.

organization. Fractals are geometries exhibiting self-similarity; the observed structures share characteristics across spatial levels (*24*). To characterize the multiscale behavior of portal vessels, we applied a 3D box-counting algorithm. This method consists of overlaying the object with a series of 3D grids of exponentially decreasing block sizes (R) and counting the number of boxes intersecting the object (N). By analyzing the slope of N plotted against R^{-1} on a bilogarithmic scale, the dimensionality of the object was determined. Box-counting analysis revealed that portal vessels were self-similar over three decades of scale. Furthermore, the dimensionality was relatively constant as portal vessels branched over E12 to E14.5 (2.15 to 2.35) (Fig. 3G). These findings suggest that the expansion of HSCs and Nestin$^+$ cells during fetal development is governed by fractal-like geometries of the portal vessel niche.

After birth, ligation of the umbilical inlet leads to dramatic hemodynamic changes in portal vessel flow (fig. S8, A to E). Whereas at postnatal day 0 (P0), portal vessels expressed the arterial markers Neuropilin-1 and Ephrin-B2 and were accompanied by Nestin$^+$ cells (Fig. 4A and fig. S8F), their expression levels were markedly reduced in P8 portal vessels, which were, by then, devoid of Nestin$^+$ cells (Fig. 4B and fig. S8G), in part due to Nestin$^+$ cell apoptosis as detected by terminal deoxynucleotidyl transferase–mediated deoxyuridine triphosphate nick end labeling staining (fig. S8, H and I). At this time, portal vessels expressed EphB4 (Fig. 4, C and D), suggesting that they transited into a vein phenotype.

These notable changes were associated with a marked reduction in liver HSC content at P8 (Fig. 4E). Perinatal HSCs were also rapidly established in the neonatal spleen (fig. S8J) and might also contribute to sustaining blood production until the BM becomes fully functional (*25*, *26*). Using whole-mount imaging, we found that, in contrast to the fetal liver, few HSCs (<3%) were located within 20 μm of postnatal portal vessels (P0 to P5) (Fig. 4, F and G), and mean HSC distances to portal vessels increased significantly (Fig. 4H). These results thus further underscore the critical role for the arterial portal vessels in forming a FL niche.

Our data support the concept that HSCs are titrated against a branching portal vessel network. Fractal geometries of vessel branching optimize the delivery of blood (*27*), with each division serving a smaller compartment within the organ. The availability of niche cells to sustain proliferating HSCs may thus be tied to the innate growth of the portal vascular tree. Our results also provide a biological explanation for the rapid loss of HSCs in the postnatal liver, where dramatic postnatal changes in portal vessels lead to a loss of niche cells and the migration of HSCs away from the portal niche. As HSCs emerge from the largest artery (aorta), expand around arterial portal vessels of the fetal liver, and are later maintained quiescent in the adult marrow near small arterioles (*10*, *11*), the arterial vasculature may provide an adaptive niche, serving hematopoiesis at multiple stages of mammalian life.

REFERENCES AND NOTES

1. A. Medvinsky, E. Dzierzak, *Cell* **86**, 897–906 (1996).
2. J. C. Boisset *et al.*, *Nature* **464**, 116–120 (2010).
3. M. F. de Bruijn, N. A. Speck, M. C. Peeters, E. Dzierzak, *EMBO J.* **19**, 2465–2474 (2000).
4. C. Gekas, F. Dieterlen-Lièvre, S. H. Orkin, H. K. A. Mikkola, *Dev. Cell* **8**, 365–375 (2005).
5. H. Ema, H. Nakauchi, *Blood* **95**, 2284–2288 (2000).
6. A. Wilson *et al.*, *Cell* **135**, 1118–1129 (2008).
7. S. Méndez-Ferrer *et al.*, *Nature* **466**, 829–834 (2010).
8. A. Greenbaum *et al.*, *Nature* **495**, 227–230 (2013).
9. L. Ding, T. L. Saunders, G. Enikolopov, S. J. Morrison, *Nature* **481**, 457–462 (2012).
10. Y. Kunisaki *et al.*, *Nature* **502**, 637–643 (2013).
11. I. Bruns *et al.*, *Nat. Med.* **20**, 1315–1320 (2014).
12. M. Zhao *et al.*, *Nat. Med.* **20**, 1321–1326 (2014).
13. K. A. Moore, B. Pytowski, L. Witte, D. Hicklin, I. R. Lemischka, *Proc. Natl. Acad. Sci. U.S.A.* **94**, 4011–4016 (1997).
14. S. Chou, H. F. Lodish, *Proc. Natl. Acad. Sci. U.S.A.* **107**, 7799–7804 (2010).
15. M. Tanaka *et al.*, *Mech. Dev.* **126**, 665–676 (2009).
16. J. M. Sheridan, S. Taoudi, A. Medvinsky, C. C. Blackburn, *Genesis* **47**, 346–351 (2009).
17. I. Kim, S. He, O. H. Yilmaz, M. J. Kiel, S. J. Morrison, *Blood* **108**, 737–744 (2006).
18. X. Zhu, D. E. Bergles, A. Nishiyama, *Development* **135**, 145–157 (2008).
19. D. Voehringer, H. E. Liang, R. M. Locksley, *J. Immunol.* **180**, 4742–4753 (2008).
20. M. B. Bowie, D. G. Kent, M. R. Copley, C. J. Eaves, *Blood* **109**, 5043–5048 (2007).
21. E. Passegué, A. J. Wagers, S. Giuriato, W. C. Anderson, I. L. Weissman, *J. Exp. Med.* **202**, 1599–1611 (2005).
22. E. Y. Chen *et al.*, *BMC Bioinformatics* **14**, 128 (2013).
23. A. Lachmann *et al.*, *Bioinformatics* **26**, 2438–2444 (2010).
24. A. L. Goldberger *et al.*, *Proc. Natl. Acad. Sci. U.S.A.* **99** (suppl. 1), 2466–2472 (2002).
25. J. L. Christensen, D. E. Wright, A. J. Wagers, I. L. Weissman, *PLOS Biol.* **2**, e75 (2004).
26. F. M. Wolber *et al.*, *Exp. Hematol.* **30**, 1010–1019 (2002).
27. H. K. Hahn, M. Georg, H.-O. Peitgen, in *Fractals in Biology and Medicine*, G. A. Losa, D. Merlini, T. F. Nonnenmacher, E. R. Weibel, Eds. (Birkhäuser, 2005), pp. 55–66.

ACKNOWLEDGMENTS

We are grateful to the National Institutes of Health (NIH) for support: Integrated Training in Pharmacological Science program (NIGMS T32 063754) and National Heart, Lung, and Blood Institute (NHLBI) Ruth L. Kirschstein National Research Service Award (NRSA) predoctoral M.D./Ph.D. fellowship (F30 943257) to J.A.K.; NHLBI Ruth L. Kirschstein NRSA postdoctoral fellowship F32 HL123224 to A.Me.; R01 grants HL097700, DK056638, and HL069438 to P.S.F.; and R01 grants CA164468 and DA033788 to A.Be. S.P. is a New York Stem Cell Foundation–Druckenmiller Fellow. A.Ma. is supported by U54HL127624, U54CA189201, and R01GM098316. We thank A. L. Kolodkin for providing antibody to Nrp1 and L. Silberstein for RNA-sequencing recommendations. We thank O. Uche and L. Tesfa for technical assistance with sorting and K. O'Connell for technical assistance with Vevo Ultrasound imaging technology. We are also grateful to the New York State Department of Health (NYSTEM Program) for shared facility (C029154) and research support (N13G-262). This work was funded by NIH grants R01 DK056638, R01 HL116340, R01 HL069438, and NYSTEM grants (C029154 and C029570). J.A.K. designed and analyzed experiments in this study. Y.Ku. performed transplantations. J.A.K. and Y.Ku. performed the in vivo experiments. J.A.K., Y.Ku., and A.Me. performed whole-mount experiments; J.A.K., A.A.-E., P.C., A.Me, and A.Bi. performed immunostaining. J.A.K. and S.P. performed the LTC-IC experiments; A.Me. and S.P. performed differentiation assays; J.A.K., F.N., and A.Me. performed expression analyses; J.A.K. performed the RNA-sequencing experiments; Y.Ko., A.Ma., and J.A.K. analyzed the RNA-sequencing data; J.A.K. and A.Be. performed computational modeling and statistical analysis of the data; and J.A.K. and P.S.F. wrote the manuscript. The authors declare no competing financial interests.

SUPPLEMENTARY MATERIALS

www.sciencemag.org/content/351/6269/176/suppl/DC1
Materials and Methods
Figs. S1 to S8
Table S1
References (*28*–*39*)

12 July 2015; accepted 15 September 2015
Published online 3 December 2015
10.1126/science.aad0084

PROTEIN STRUCTURE

The structure of the β-barrel assembly machinery complex

Jeremy Bakelar,[1] Susan K. Buchanan,[2] Nicholas Noinaj[1]*

β-Barrel outer membrane proteins (OMPs) are found in the outer membranes of Gram-negative bacteria and are essential for nutrient import, signaling, and adhesion. A 200-kilodalton five-component complex called the β-barrel assembly machinery (BAM) complex has been implicated in the biogenesis of OMPs. We report the structure of the BAM complex from *Escherichia coli*, revealing that binding of BamCDE modulates the conformation of BamA, the central component, which may serve to regulate the BAM complex. The periplasmic domain of BamA was in a closed state that prevents access to the barrel lumen, which indicates substrate OMPs may not be threaded through the barrel during biogenesis. Further, conformational shifts in the barrel domain lead to opening of the exit pore and rearrangement at the lateral gate.

Gram-negative bacteria contain both an inner membrane (IM) and an outer membrane (OM) that serve important roles in nutrient import, cell signaling, waste export, and protection. Integral membrane proteins in the IM all have an α-helical fold consisting of one or more α-helices. In the OM, however, integral membrane proteins have a β-barrel fold consisting of 8 to 26 antiparallel β-strands. In pathogenic strains of bacteria, some outer membrane proteins (OMPs) can also serve as

[1]Markey Center for Structural Biology, Department of Biological Sciences, Purdue University, West Lafayette, IN 47907, USA. [2]National Institute of Diabetes and Digestive and Kidney Diseases, National Institutes of Health, Bethesda, MD 20892, USA.
***Corresponding author. E-mail: nnoinaj@purdue.edu**

virulence factors that mediate infection. OMPs are only found in the OMs of Gram-negative bacteria, mitochondria, and chloroplasts (*1*, *2*).

The exact mechanism explaining how OMPs are folded and inserted into the OM remains unknown; however, studies have identified a general pathway and conserved machinery that is responsible for the biogenesis of OMPs (*3*–*5*). A majority of these advances have been made by working with Gram-negative bacteria (*3*, *6*, *7*). Here, the nascent OMPs are first synthesized in the cytoplasm with an N-terminal leader sequence that directs them to the Sec translocon for transport across the IM, into the periplasm (Fig. 1A). Chaperones, such as SurA and Skp, then further escort the nascent OMPs to a multicomponent complex called the β-barrel assembly machinery (BAM) complex, which is responsible

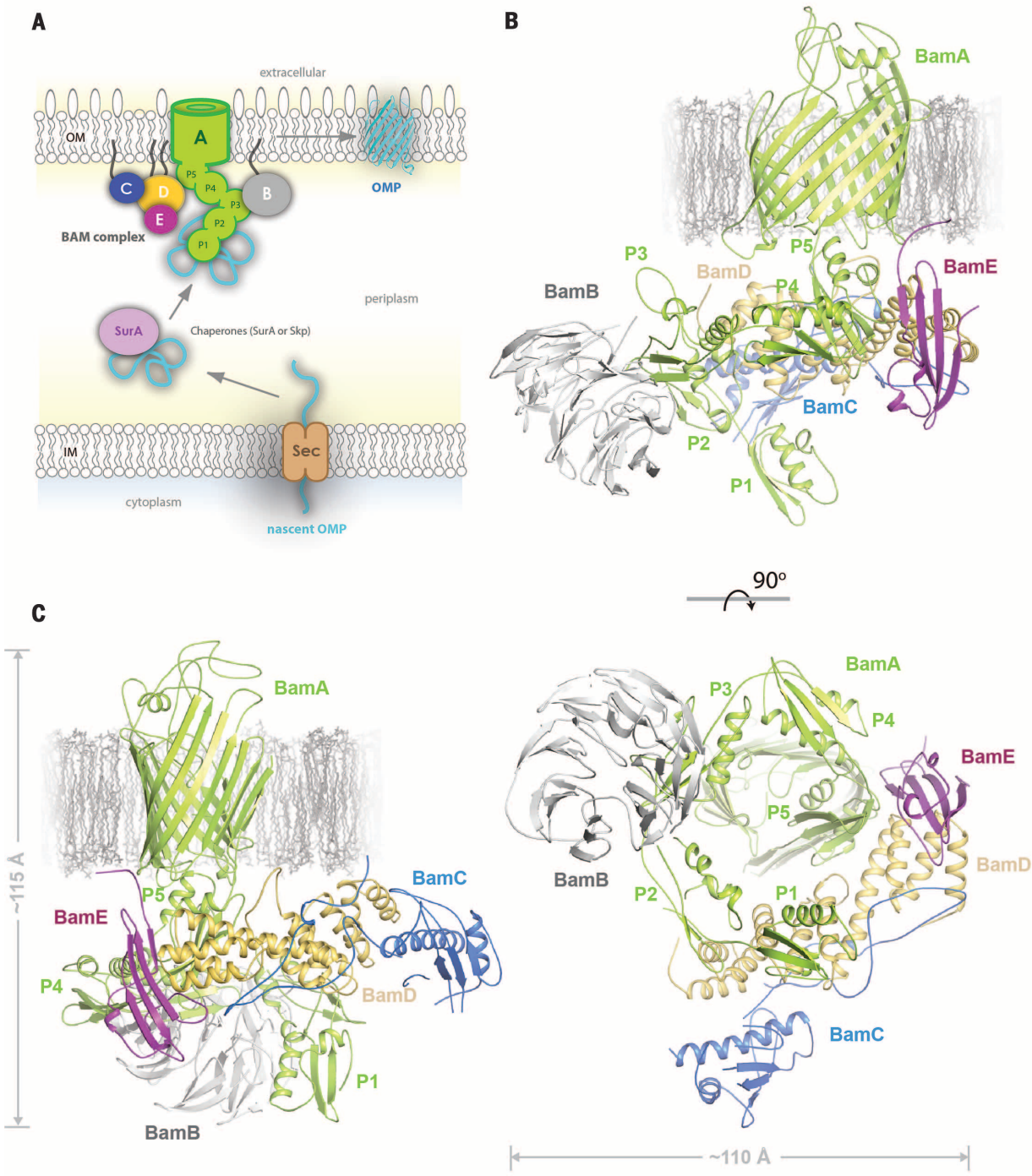

Fig. 1. The structure of the BAM complex. (**A**) The pathway for the biogenesis of β-barrel OMPs in Gram-negative bacteria. (**B**) A membrane view of the structure of the full BAM complex, formed from merging the crystal structures of BamACDE and BamAB (PDB ID 4PK1). The bottom panel shows the periplasmic view, rotated 90° along the *x* axis relative to the top panel. BamA is shown in green, BamB in gray, BamC in blue, BamD in gold, and BamE in purple. (**C**) The β-barrel domain of BamA undgoes a dramatic conformational change along strands β1 to β8, which can be seen here. This panel is rotated ~90° along the *y* axis relative to the top view of panel (B). The overall measurements of the BAM complex are ~115 by 115 by 115 Å.

for folding and inserting OMPs into the OM (*4*, *8*). In *Escherichia coli*, the BAM complex consists of five components, BamA, B, C, D, and E. BamA, a 16-stranded OMP, is the central component of the complex and is conserved both in mitochondria and chloroplasts, whereas BamB to BamE are all lipoproteins. BamA and BamD are essential for viability; however, all components are required for efficient OMP folding and insertion (*9*–*11*). BamB and BamD interact directly with BamA via nonoverlapping binding sites, whereas BamC and BamE interact directly with BamD to stabilize the complex (*9*, *12*).

Structures of all the Bam components have now been reported, including partial complexes of BamAB and BamCD (*7*, *13*–*23*). The full-length structure of BamA from *Neisseria gonorrhoeae* revealed a large periplasmic domain consisting of five polypeptide transport–associated (POTRA) domains and a C-terminal 16-stranded β-barrel domain. Subsequent studies showed that the barrel domain of BamA opens laterally in the membrane, possibly to allow insertion of the substrate OMPs into the OM (*16*, *18*, *24*). BamB may serve as a scaffold to assist in the handoff of nascent OMPs from SurA to BamA, whereas BamC, BamD, and BamE may serve to regulate the function of BamA (*14*, *17*, *25*). The structures have offered clues to how each component may function within the complex; however, the lack of structural information regarding the fully assembled complex has hindered progress toward exploring the mechanism further. We used x-ray crystallography to solve the structure of the BamACDE subcomplex to 3.4 Å resolution and used the previously reported partial structure of BamAB to form a model of the fully assembled BAM complex from *E. coli*. The periplasmic domain of BamA was found in a closed state, which prevented access to the barrel lumen from the periplasm. Binding of BamCDE to BamA causes conformational twisting of strands β1 to β8 and leads to opening of the exit pore and structural rearrangement of the lateral opening site. These structural changes suggest that the role of BamCDE may be to modulate the conformational states of BamA, which regulate the BAM complex.

The BAM complex from *E. coli* was expressed from a single plasmid and purified as previously described with some modifications (supplementary methods) (*11*). SDS–polyacrylamide gel electrophoresis (SDS-PAGE) analysis verified the presence of the full complex, which produced a monodisperse peak as seen with size-exclusion chromatography (fig. S1). We crystallized the complex in C_8E_4 and collected data at the SER-CAT ID22 beamline at the Advanced Photon Source. The crystal structure of the complex was then solved by molecular replacement (fig. S2 and table S1). On the basis of crystal-packing analysis, it was clear that BamB was absent rather than being disordered. This was possibly due to proteolytic degradation during incubation. This was verified by SDS-PAGE analysis of crystals and of the original protein sample, both of which lacked BamB after extended incubation or storage (fig. S1). The crystal structure contains full-length BamA, BamD, and BamE but only the N-terminal flexible domain and the first globular helix-grip domain of BamC, with the second helix-grip domain presumably being disordered. To model the fully assembled BAM complex, we used the previously reported structure of the partial BamAB complex [Protein DataBank (PDB) ID 4PK1] (*14*) to dock BamB into our crystal structure by aligning along POTRA3 of BamA (Fig. 1, B and C; movie S1; and model S1). For all accessory lipoproteins, the N-terminal residues are positioned in close proximity to where the OM would sit; however, no lipid anchors were observable in our crystal structure.

BamCD in our structure aligned well with the previously reported complex (PDB ID 3TGO), which has a root mean square deviation (RMSD) of 1.25 Å across both chains (Fig. 2, A and B). BamE interacts with the opposite side of BamD [buried surface area (BSA) ~800 $Å^2$] along the C-terminal end (Fig. 2A and tables S2 and S3). Although BamC and BamE interact with BamD via nonoverlapping binding sites, they make minimal contact with one another (BSA ~140 $Å^2$). Residues 215 to 344 of BamC, consisting of a linker and the second helix-grip domain, were disordered in our crystal structure. Previous studies have shown that the two helix-grip domains of BamC are found on the outside of the cell (*26*), which suggests that one or both may interact with the surface-exposed loops of BamA. No interaction was observed in our structure, which indicates that if the two helix-grip domains do indeed interact with BamA, a membrane bilayer and/or substrate may be required to release BamC from BamD so it can be presented on the surface.

The structure of BamD consists of five tetratricopeptide-repeat (TPR) motifs (*15*, *21*, *27*) and sits parallel to the membrane, with TPR4 and 5 forming the binding site for BamE, which is oriented perpendicular to the membrane (Fig. 2A). The binding interface agrees well with previously published work, where BamD was found to bind BamE along the interface containing residues R29, I32, F68, N71, T72, R78, and T92 (*23*, *28*). The extensive binding interface has numerous hydrogen bonds using both side-chain and backbone atoms, as well as a salt bridge between D66 of BamE and K233 of BamD (Fig. 2, C and D). The binding is further strengthened by interactions of M64 and F68 of BamE with hydrophobic pockets in BamD. The interaction between BamC and BamE is mediated primarily by hydrophobic interactions; the loop of BamC helps to form the large hydrophobic pocket where F68 of BamE binds BamD (table S4).

In agreement with previous studies (*29*), BamD binds BamA along POTRA5 almost exclusively through TPR3 and 4 (BSA ~1100 $Å^2$) (Fig. 3, A and B, and table S5). The extensive binding interface between BamD and POTRA5 of BamA is mediated by hydrogen bonds that use side-chain and backbone atoms and three salt bridges between residues H139, R197, and R188 of BamD and residues D358, E373, and D481 of BamA, respectively (Fig. 3, B and C). The salt bridge formed by R197 of BamD and E373 of BamA is central to this interaction and agrees with previous studies that implicate these residues in binding (*30*, *31*). The extended loop of BamD TPR3 (residues 123 to 130) interacts with periplasmic loop 1 of BamA (residues 449 to 452; BSA ~120 $Å^2$) (fig. S3). TPR1 and 2 of BamD also interact minimally with POTRA2 of BamA (BSA ~115 $Å^2$) (Fig. 3, B and D), which suggests that BamD may also participate in modulating the conformation of the POTRA domains of BamA during OMP biogenesis.

BamA interacts with BamD, and this is enhanced by the presence of BamE. However, no studies have shown that BamA also interacts with BamE (*9*, *12*). In our crystal structure though, we observe not only the interaction of BamE with BamD but also an extensive interaction of BamE with POTRA5 of BamA (BSA ~750 $Å^2$) (Fig. 3, B and E, and table S6). This binding interface is composed of numerous hydrogen bonds between side-chain and backbone atoms, as well as hydrophobic interactions primarily from W376 of BamA (BSA ~130 $Å^2$). Residue Y28 of BamE interacts with periplasmic loop 3 of BamA, forming hydrogen bonds with P518 and E521, which anchor the N terminus of BamE in close proximity to the barrel domain of BamA. This may serve to orient BamCDE optimally for interacting with BamA (Fig. 3, A and F). The observation that BamE bridges BamD and BamA agrees well with previous work indicating that BamE stabilizes the interaction of BamD with BamA (*12*). Previous studies identified BamE residues involved in BamD binding (*23*); however, not all of these residues mapped to that interface in our structure. Instead, residues Y37, L38, T61, and L63 lie along the interface with POTRA5 of BamA, which suggests that binding of BamD may lead to conformational changes in BamE that promote association with BamA. Also, the BamE residues identified to interact with phosphatidylglycerol (PG) (G60, T70, N71, V76, and F95) are located within the periplasm as far as 35 Å from the OM (*23*). Therefore, it is unlikely that the PG-binding role of BamE contributes directly to the role of the BAM complex; however, it is still possible that the recruitment of PG in proximity to the BAM complex increases the efficiency of OMP biogenesis.

No structure of full-length BamA from *E. coli* has been reported previously, although a structure containing the β-barrel domain and POTRA5 is available (*16*). In this structure, POTRA5 was oriented away from the barrel domain in an open conformation allowing access to the barrel lumen from the periplasm (fig. S4). However, in our structure, POTRA5 is in a closed conformation relative to the β-barrel domain, fully occluding access to the barrel lumen from the periplasm. Compared with the BamA structure from *N. gonorrhoeae* (*18*), the POTRA domains rotate ~90° along the plane of the membrane upon interaction with BamCDE. POTRA5 makes numerous contacts with periplasmic loops 1, 2, 3, 4, and 6, with the most extensive interactions through periplasmic loops 1, 2, and 4 (fig. S5). This conformation constitutes a ~45° hingelike conformational change of POTRA5 to the closed state (Fig. 4A). POTRA5 interacts most extensively

with periplasmic loop 4 (fig. S5 and movie S2), which is stabilized by a salt bridge between E396 (POTRA5) and R583 (periplasmic loop 4) and pi stacking between R421 (POTRA5) and Y585 (periplasmic loop 4). Conformational flexibility of the POTRA domains has been well documented (*29*, *32*, *33*). Therefore, it remains to be determined whether the association of BamCDE is solely responsible for the closed conformation.

Binding of BamCDE leads to a conformational twist of the β-barrel domain of BamA, with the most dramatic change emanating from strand β1 (~45°) and gradually diminishing until strand β9. This conformation is due to the strong interaction of POTRA5 with BamCDE and with periplasmic loop 4, which imposes mechanical strain on the first half of the barrel (Fig. 4, B, D, and E, and movie S2). This leads to a change in the angle of the first eight strands in the membrane, such that strands β1 and β16 no longer associate as a β-sheet, leading to opening of the exit pore along extracellular loops 1, 2, and 3. This agrees with recent studies that have shown that disulfide cross-linking the exit pore in a closed state renders the BAM complex nonfunctional (*24*). Aligning BamA from our complex structure with the previously reported *E. coli* BamA structure containing POTRA5 only (PDB ID 4C4V) yielded an RMSD of 1.07 Å for the entire β-barrel domain. However, the RMSD for strands β1 to β8 alone was 2.74 Å, whereas the RMSD for strands β9 to β16 was 0.67 Å, which highlighted the shift observed in our structure.

Although the conformational change of the barrel of BamA led to opening of extracellular loops 1, 2, and 3 along the exit pore, the remaining loops 4, 5, 6, 7, and 8 remained largely unchanged. The exception is that loop 4 undergoes a slight shift to stabilize loop 6 (Fig. 4, C and D). The rest of loop 6 was unchanged, including the conserved VRGF motif (fig. S6). Another consequence of the conformational twist is structural rearrangement at the lateral gate, such that strand β1 no longer interacts with strand β16 (last strand) to close the barrel, in contrast to what has been observed in all other OMPs with known structure (Fig. 4, F and G). Rather, most of strand β16 sits tucked inside the barrel lumen, whereas periplasmic loop 7 and strand β15 contact strand β1 at an offset angle of ~45° (Fig. 4, D to G). This agrees with studies that rendered the BAM complex nonfunctional by disulfide cross-linking the lateral gate closed (*24*).

Based on our crystal structure of BamACDE and the existing crystal structure of BamAB (*14*), we report the structure of the fully assembled

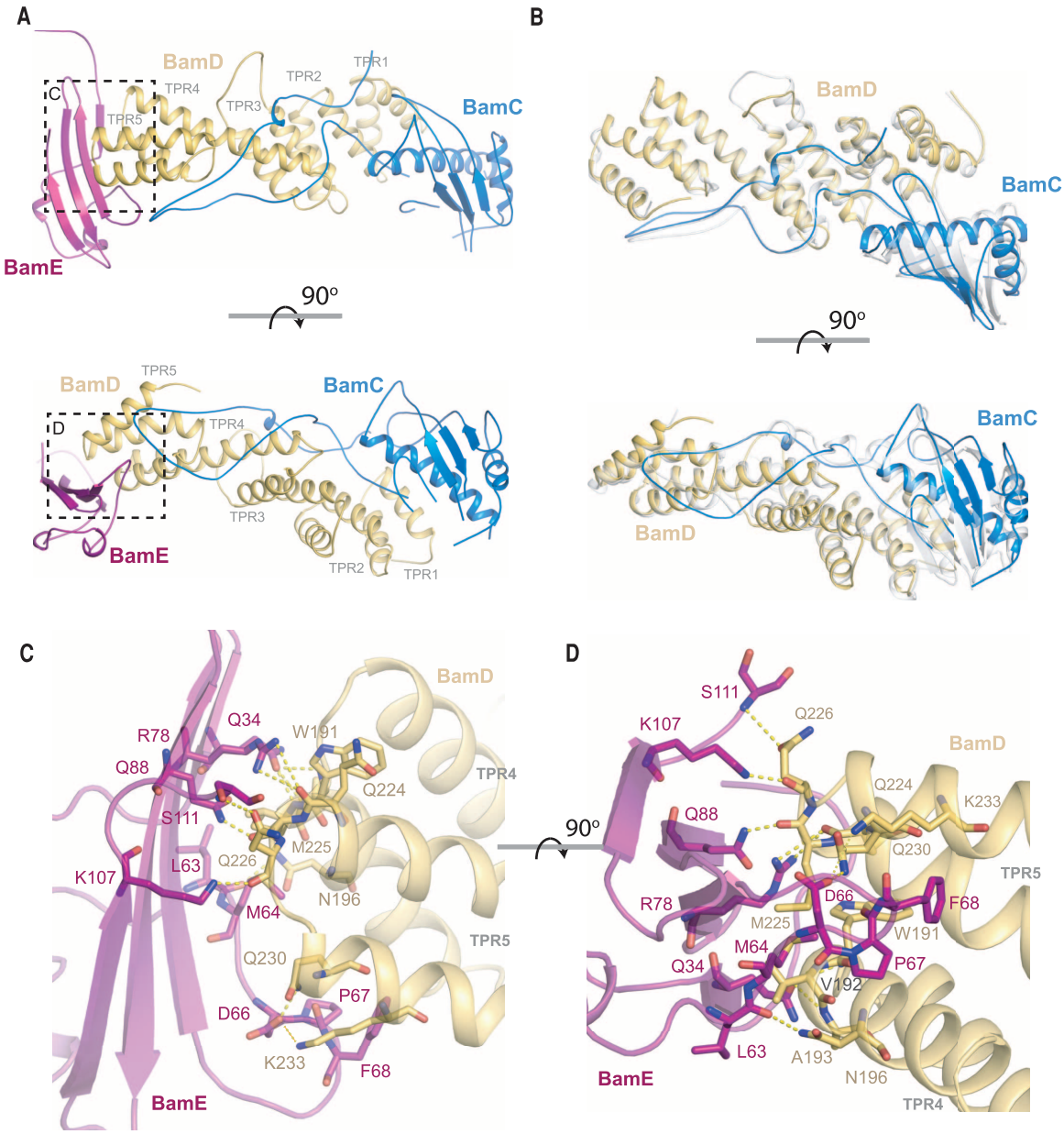

Fig. 2. Interactions of BamC and BamE with BamD. (**A**) The complex structure of BamCDE is shown here with BamD in gold, BamC in blue, and BamE in purple. The TPR domains of BamD are indicated. The bottom panel is rotated 90° along the *x* axis relative to the top. (**B**) The interactions between BamC and BamD are nearly the same as that observed in the previously reported crystal structure (PDB ID 3TGO) with an RMSD of 1.25 Å across both chains. The bottom panel is rotated 90° along the *x* axis relative to the top. (**C**) View showing the interactions of BamE with BamD TPR4 and 5 through an extensive interface with a buried surface area of ~800 Å^2, containing a mix of hydrogen bonds, salt bridges, and hydrophobic interactions. (**D**) A view from the top that is rotated 90° along the *x* axis to further illustrate the extensive binding interface.

BAM complex from *E. coli* (movies S1 and S2 and model S1). As further validation, our structure is in agreement with a model for the BAM complex that we recently reported that was based on all structural, functional, genetics, and biochemical studies to date (*34*). Our structure reveals that upon binding BamCDE, the barrel domain of BamA undergoes a conformational twist that dramatically changes the angle of the strands (shear) in the membrane, which leads to opening of the exit pore and rearrangement at the lateral gate. This suggests that binding of BamCDE

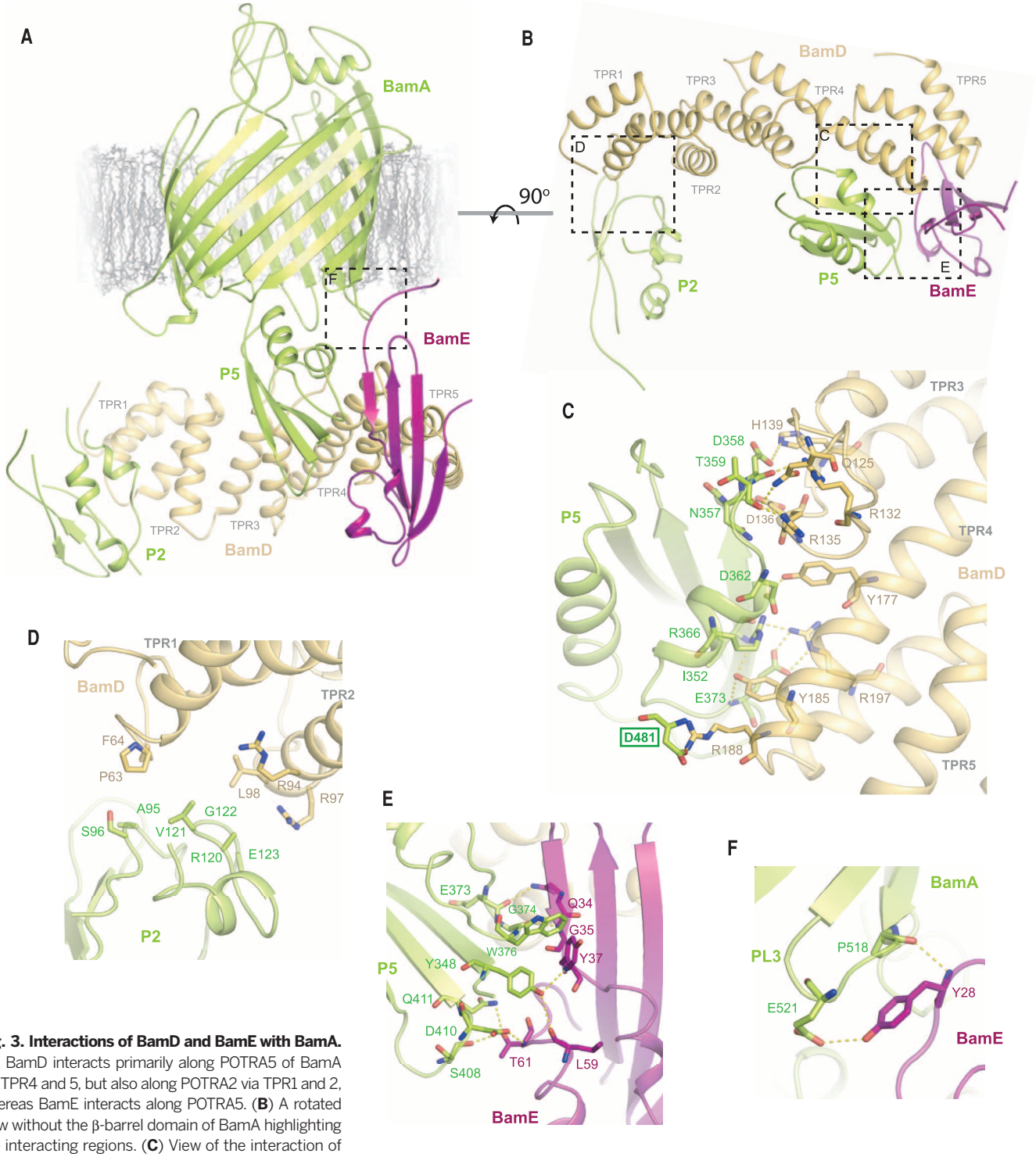

Fig. 3. Interactions of BamD and BamE with BamA. (**A**) BamD interacts primarily along POTRA5 of BamA via TPR4 and 5, but also along POTRA2 via TPR1 and 2, whereas BamE interacts along POTRA5. (**B**) A rotated view without the β-barrel domain of BamA highlighting the interacting regions. (**C**) View of the interaction of BamD with POTRA5 of BamA, showing an extensive binding interface with a buried surface area of ~1100 Å^2, containing a mix of hydrogen bonds, salt bridges, and hydrophobic interactions. Residue R197 of BamD clearly forms a salt bridge with E373 of BamA. Residue D481 (green box) is from periplasmic loop 2 of BamA. (**D**) View of the interactions between TPR1 and 2 of BamD with POTRA2 of BamA. Although these interactions are minimal here, they could assist in modulating the conformation of BamA. (**E**) View of the interactions of BamE with POTRA5 of BamA, an extensive interaction with a buried surface area of ~750 Å^2, containing a mix of hydrogen bonds, salt bridges, and hydrophobic interactions. (**F**) The N-terminal region of BamE was found anchored via hydrogen bonding interactions of residue Y28 to residues E521 and P518 of BamA periplasmic loop 3.

modulates the conformation of BamA, which may serve to regulate the BAM complex. This may also serve to "tune" the β-barrel domain of BamA to fold OMPs with differing shear numbers by adjusting the angle of the strands in the membrane to match that of the substrate OMPs or to further destabilize the local membrane, which would reduce the kinetic barrier for OMP insertion (*35*). Further, the lumen of the barrel of BamA is fully occluded from the periplasm. Therefore, OMPs are likely inserted into the membrane at the lateral gate rather than first

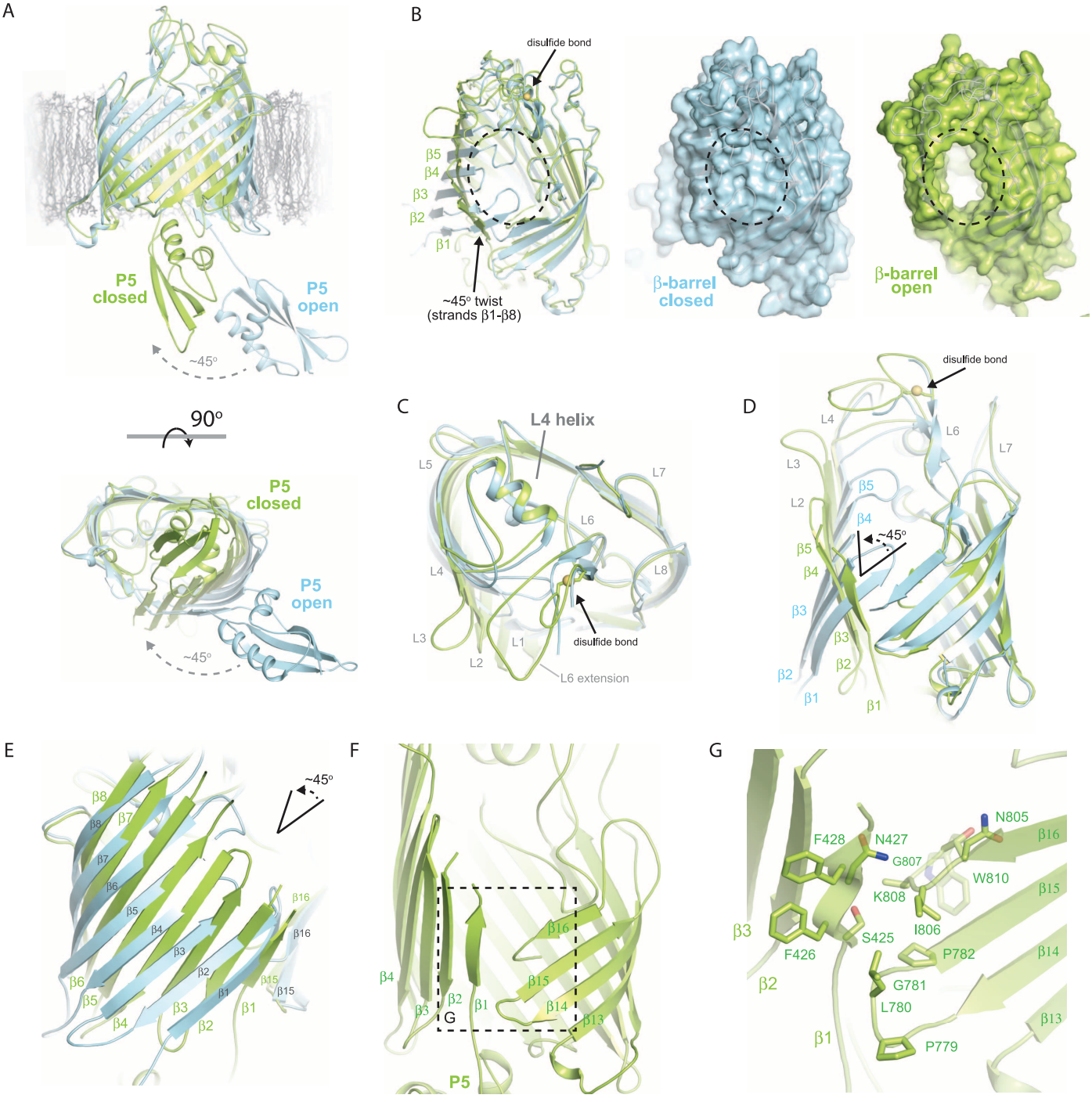

Fig. 4. Conformational changes in the barrel domain of BamA. (**A**) Superposition of BamA from our structure (green) with PDB ID 4C4V (cyan) reveals ~45° hingelike conformational change of the POTRA domains to a closed, periplasm occluded state. (**B**) Binding of BamCDE to BamA leads to an unprecedented twist of strands β1 to β8, with the most dramatic change emanating from strand β1 (~45°) and gradually diminishing until strand β9 (movie S2). This leads to opening of the exit pore (~15 Å by ~27 Å) and lateral gate. (**C**) In response to the shift of the barrel strands, an opening of surface loops 1, 2, and 3 was observed; however, surface loops 4, 5, 6, 7, and 8 were mostly unchanged. (**D**) Rotated view highlighting the strand shift along strands β1 to β8 of the barrel domain of BamA. (**E**) View of the strand shift along strands β1 to β8 rotated ~90° relative to (D), illustrating a twist of the strands rather than just a simple rotation. (**F**) View of the lateral gate in BamA, where strand β1 and β16 no longer form a β-sheet interaction to close the barrel; rather, strands β15 and β16 are situated at ~45° angle relative to strand β1. (**G**) View showing residues along the lateral gate, with β16 sitting tucked inside the barrel and periplasmic loop 7 interacting with strand β1.

being threaded through the barrel domain. The lateral gate is positioned central to the BAM complex and would be directly accessible for substrate handoff by the accessory lipoproteins or by the POTRA domains of BamA.

REFERENCES AND NOTES

1. C. T. Webb, E. Heinz, T. Lithgow, *Trends Microbiol.* **20**, 612–620 (2012).
2. E. Schleiff, J. Soll, *EMBO Rep.* **6**, 1023–1027 (2005).
3. T. J. Knowles, A. Scott-Tucker, M. Overduin, I. R. Henderson, *Nat. Rev. Microbiol.* **7**, 206–214 (2009).
4. C. L. Hagan, T. J. Silhavy, D. Kahne, *Annu. Rev. Biochem.* **80**, 189–210 (2011).
5. R. Voulhoux, M. P. Bos, J. Geurtsen, M. Mols, J. Tommassen, *Science* **299**, 262–265 (2003).
6. N. Noinaj, S. E. Rollauer, S. K. Buchanan, *Curr. Opin. Struct. Biol.* **31**, 35–42 (2015).
7. K. H. Kim, S. Aulakh, M. Paetzel, *Protein Sci.* **21**, 751–768 (2012).
8. D. P. Ricci, T. J. Silhavy, *Biochim. Biophys. Acta* **1818**, 1067–1084 (2012).
9. J. C. Malinverni *et al.*, *Mol. Microbiol.* **61**, 151–164 (2006).
10. C. L. Hagan, S. Kim, D. Kahne, *Science* **328**, 890–892 (2010).
11. G. Roman-Hernandez, J. H. Peterson, H. D. Bernstein, *eLife* **3**, e04234 (2014).
12. J. G. Sklar *et al.*, *Proc. Natl. Acad. Sci. U.S.A.* **104**, 6400–6405 (2007).
13. K. H. Kim, S. Aulakh, M. Paetzel, *J. Biol. Chem.* **286**, 39116–39121 (2011).
14. K. B. Jansen, S. L. Baker, M. C. Sousa, *J. Biol. Chem.* **290**, 2126–2136 (2015).
15. R. Albrecht, K. Zeth, *J. Biol. Chem.* **286**, 27792–27803 (2011).
16. R. Albrecht *et al.*, *Acta Crystallogr. D Biol. Crystallogr.* **70**, 1779–1789 (2014).
17. N. Noinaj, J. W. Fairman, S. K. Buchanan, *J. Mol. Biol.* **407**, 248–260 (2011).
18. N. Noinaj *et al.*, *Nature* **501**, 385–390 (2013).
19. A. Heuck, A. Schleiffer, T. Clausen, *J. Mol. Biol.* **406**, 659–666 (2011).
20. K. H. Kim, M. Paetzel, *J. Mol. Biol.* **406**, 667–678 (2011).
21. C. Dong, H. F. Hou, X. Yang, Y. Q. Shen, Y. H. Dong, *Acta Crystallogr. D Biol. Crystallogr.* **68**, 95–101 (2012).
22. D. Ni *et al.*, *FASEB J.* **28**, 2677–2685 (2014).
23. T. J. Knowles *et al.*, *EMBO Rep.* **12**, 123–128 (2011).
24. N. Noinaj, A. J. Kuszak, C. Balusek, J. C. Gumbart, S. K. Buchanan, *Structure* **22**, 1055–1062 (2014).
25. K. B. Jansen, S. L. Baker, M. C. Sousa, *PLOS ONE* **7**, e49749 (2012).
26. C. T. Webb *et al.*, *J. Mol. Biol.* **422**, 545–555 (2012).
27. C. M. Sandoval, S. L. Baker, K. Jansen, S. I. Metzner, M. C. Sousa, *J. Mol. Biol.* **409**, 348–357 (2011).
28. Single-letter abbreviations for the amino acid residues are as follows: A, Ala; C, Cys; D, Asp; E, Glu; F, Phe; G, Gly; H, His; I, Ile; K, Lys; L, Leu; M, Met; N, Asn; P, Pro; Q, Gln; R, Arg; S, Ser; T, Thr; V, Val; W, Trp; and Y, Tyr.
29. S. Kim *et al.*, *Science* **317**, 961–964 (2007).
30. D. P. Ricci, C. L. Hagan, D. Kahne, T. J. Silhavy, *Proc. Natl. Acad. Sci. U.S.A.* **109**, 3487–3491 (2012).
31. N. W. Rigel, D. P. Ricci, T. J. Silhavy, *Proc. Natl. Acad. Sci. U.S.A.* **110**, 5151–5156 (2013).
32. P. Z. Gatzeva-Topalova, T. A. Walton, M. C. Sousa, *Structure* **16**, 1873–1881 (2008).
33. P. Z. Gatzeva-Topalova, L. R. Warner, A. Pardi, M. C. Sousa, *Structure* **18**, 1492–1501 (2010).
34. P. K. O'Neil, S. E. Rollauer, N. Noinaj, S. K. Buchanan, *Biochemistry* **54**, 6303–6311 (2015).
35. D. Gessmann *et al.*, *Proc. Natl. Acad. Sci. U.S.A.* **111**, 5878–5883 (2014).

ACKNOWLEDGMENTS

We thank H. Bernstein for providing the pJH114 plasmid. J.B. and N.N. are supported by the Department of Biological Sciences at Purdue University and by the National Institute of Allergy and Infectious Diseases (1K22AI113078-01). S.K.B. is supported by the Intramural Research Program of the NIH, National Institute of Diabetes and Digestive and Kidney Diseases. We thank the staff at the Southeast Regional Collaborative Access Team (SER-CAT) beamline at the Advanced Photon Source, Argonne National Laboratory, for their assistance during data collection. Use of the Advanced Photon Source was supported by the Office of Basic Energy Sciences, Office of Science, U.S. Department of Energy, under contract no. W-31-109-Eng-38 (SER-CAT). Coordinates and structure factors for the BamACDE complex have been deposited into the PDB with PDB ID 5EKQ.

SUPPLEMENTARY MATERIALS

www.sciencemag.org/content/351/6269/180/suppl/DC1
Materials and Methods
Figs. S1 to S6
Tables S1 to S6
Movies S1 and S2
References (*36*–*41*)

31 August 2015; accepted 20 November 2015
10.1126/science.aad3460

CHEMOTAXIS

Polysialylation controls dendritic cell trafficking by regulating chemokine recognition

Eva Kiermaier,[1]*† Christine Moussion,[1]† Christopher T. Veldkamp,[2,3] Rita Gerardy-Schahn,[4] Ingrid de Vries,[1] Larry G. Williams,[2] Gary R. Chaffee,[2] Andrew J. Phillips,[2] Friedrich Freiberger,[4] Richard Imre,[5] Deni Taleski,[6] Richard J. Payne,[6] Asolina Braun,[7] Reinhold Förster,[7] Karl Mechtler,[5] Martina Mühlenhoff,[4] Brian F. Volkman,[3] Michael Sixt[1]*†

The addition of polysialic acid to N- and/or O-linked glycans, referred to as polysialylation, is a rare posttranslational modification that is mainly known to control the developmental plasticity of the nervous system. Here we show that CCR7, the central chemokine receptor controlling immune cell trafficking to secondary lymphatic organs, carries polysialic acid. This modification is essential for the recognition of the CCR7 ligand CCL21. As a consequence, dendritic cell trafficking is abrogated in polysialyltransferase-deficient mice, manifesting as disturbed lymph node homeostasis and unresponsiveness to inflammatory stimuli. Structure-function analysis of chemokine-receptor interactions reveals that CCL21 adopts an autoinhibited conformation, which is released upon interaction with polysialic acid. Thus, we describe a glycosylation-mediated immune cell trafficking disorder and its mechanistic basis.

Polysialylation is a rare posttranslational modification executed by the two enzymes ST8Sia II and ST8Sia IV (*1*). These polysialyltransferases generate long α2,8-linked linear homopolymers of sialic acid, which are attached to N- and/or O-linked glycans (*2*). Polysialylation is mainly known to control the developmental plasticity of the vertebrate nervous system by modulating cell-cell and cell-matrix adhesions (*3*). Polysialic acid (polySia) further promotes cancer growth and metastasis through largely unknown mechanisms (*4*, *5*) and, as such, is pursued as a therapeutic target (*6*). Recent evidence also suggests various functional implications during immune responses (*7*–*10*).

We immunologically characterized mice lacking ST8Sia IV (*11*), the polysialyltransferase expressed in hematopoietic cells. Under steady-state conditions, mutant animals showed severely reduced cellularity of peripheral lymph nodes (LNs) (Fig. 1A) and frequently lacked small popliteal LNs (10 LNs missing out of 16 expected). Infliction of inflammatory stimuli in mutant and control mice failed to trigger LN swelling in the former (Fig. 1B). In contrast, cellularity of the spleen did not differ significantly between control and mutant mice (Fig. 1A), which might indicate specific defects in lymphocyte homing to LNs. However, we could not detect polySia on the surface of T and B cells, and we did not observe any cell-autonomous trafficking defects in the lymphocyte compartment (fig. S1, A and B). In contrast, polySia was readily detectable on the surface of dendritic cells (DCs) during steady-state conditions (Fig. 1C, upper panel, and fig. S1C), and it was additionally elevated upon inflammatory stimulation (Fig. 1C, lower panel). LNs of *St8sia4*-deficient mice contained reduced amounts of DC subsets known to migrate from peripheral tissues into the LNs (Fig. 1D). Although

[1]Institute of Science and Technology Austria (IST Austria), Am Campus 1, 3400 Klosterneuburg, Austria. [2]Department of Chemistry, University of Wisconsin–Whitewater, 800 West Main Street, Whitewater, WI 53190, USA. [3]Department of Biochemistry, Medical College of Wisconsin, 8701 Watertown Plank Road, Milwaukee, WI 53226, USA. [4]Institute for Cellular Chemistry, Hannover Medical School [Medizinische Hochschule Hannover (MHH)], Carl-Neuberg-Strasse 1, 30625 Hannover, Germany. [5]Research Institute of Molecular Pathology, Vienna Biocenter, Dr. Bohr Gasse 7, 1030 Vienna, Austria. [6]School of Chemistry, The University of Sydney, Sydney, New South Wales 2006, Australia. [7]Institute of Immunology, Hannover Medical School (MHH), Carl-Neuberg-Strasse 1, 30625 Hannover, Germany.
***Corresponding author. E-mail: eva.kiermaier@ist.ac.at (E.K.); sixt@ist.ac.at (M.S.)** †These authors contributed equally to this work.

DCs constitute only ~1% of cells in the LNs, they control LN size by instructing stromal cells to recruit lymphocytes and maintain their homeostasis (*12*, *13*). Hence, a reduced size of the DC compartment might provide a potential explanation for reduced overall LN size. To test whether defective migration from the periphery was responsible for reduced DC numbers in LNs, we performed skin-painting experiments, in which endogenous DCs of the skin are mobilized and subsequently migrate, via the afferent lymphatic vessels, into the draining LN (*14*). In *St8sia4*-deficient mice, migration of DCs into draining LNs was almost completely abrogated (Fig. 1E).

We next used an in vitro reconstituted system to measure the migratory potential of polySia-deficient DCs. To this end, we generated DCs in vitro from bone marrow precursors. We confirmed that control cells up-regulate polySia upon inflammatory stimulation, whereas *St8sia4*-deficient cells differentiated normally but completely lacked polySia (fig. S1D). When we co-injected control and *St8sia4*-deficient DCs into the footpads of wild-type recipient mice, polySia-deficient DCs were completely unable to enter the LNs (Fig. 2A), formally showing that polySia dependency is cell-autonomous. We next incorporated the in vitro–generated DCs into three-dimensional (3D) collagen gels and exposed them to gradients of the chemokines CCL19 and CCL21 (Fig. 2B). By binding to CCR7, these chemokines guide DCs into the draining LN (*15*). Whereas the migratory response toward gradients of CCL19 was equally efficient for control and knockout cells, polySia-deficient DCs were completely refractory to CCL21 (Fig. 2B). Similarly, signaling, as measured by Akt and extracellular signal–regulated kinase (ERK) phosphorylation, was largely abolished in response to CCL21, whereas the CCL19-triggered signal was comparable to that in control cells (fig. S2). Hence, polySia-deficient DCs were capable of differentiating and migrating regularly but were selectively unresponsive toward CCL21.

En route from the periphery into the LN, CCL21 mediates two key steps: (i) directed interstitial migration toward the dermal lymphatic vessel and (ii) migration from the LN's subcapsular sinus into the deep T cell area. To exclude any confounding effects of CCL19, we probed DC migration in *Ccl19*-deficient hosts. To bypass the skin and directly measure migration within the LN, we injected DCs into the afferent lymphatic vessel (fig. S3A) (*16*). Within the LN,

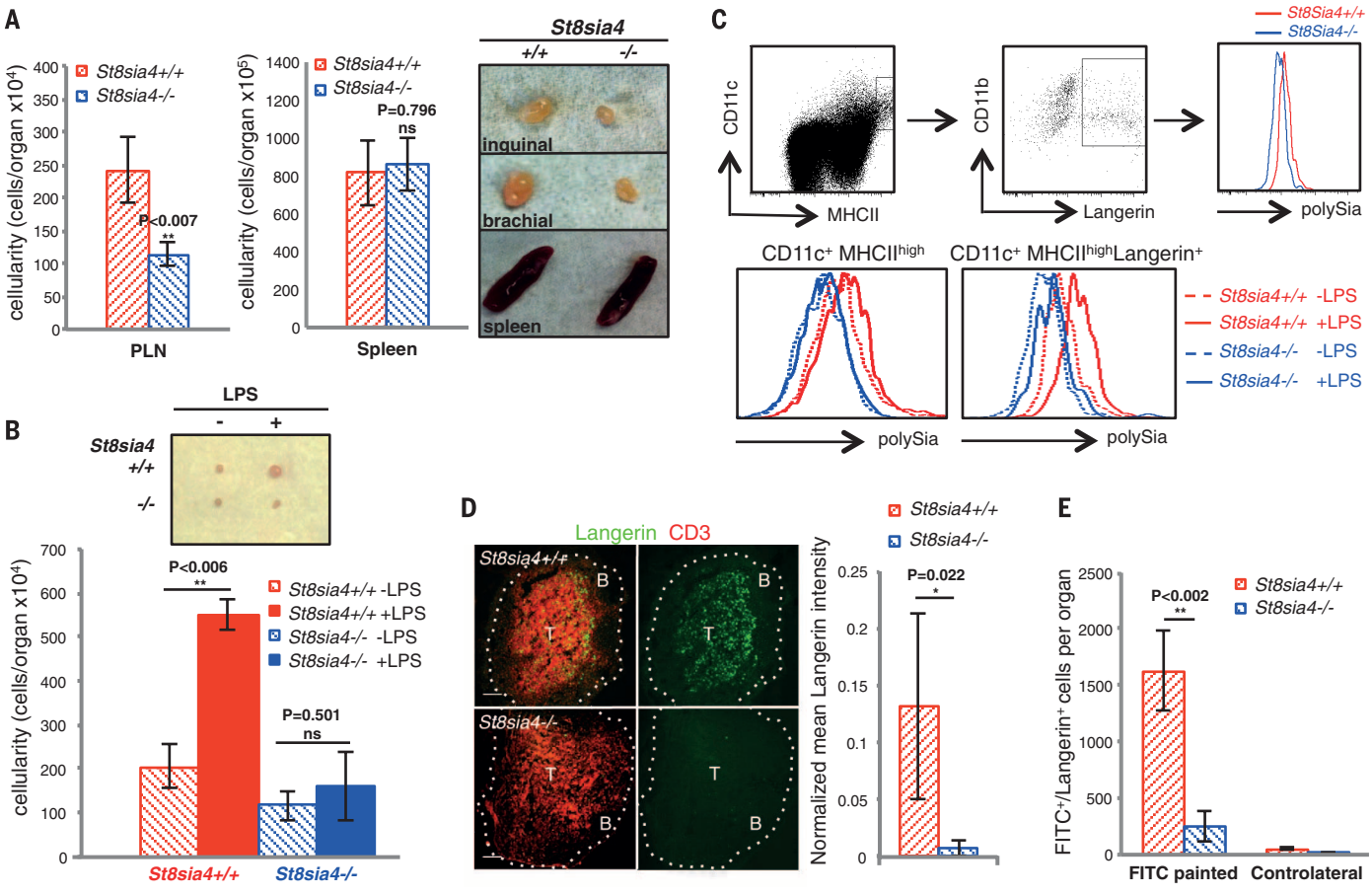

Fig. 1. PolySia on DCs is required for regular LN homeostasis and regulates inflammatory responses. (**A**) Cellularity of secondary lymphoid organs in *St8sia4*-deficient (*St8sia4*$^{-/-}$) and control mice (left). The graphs show the total leukocyte numbers of single organs. Brachial and inguinal LNs have been pooled as peripheral LNs (PLNs). The results shown are averages of three independent experiments with six different age-matched mice per genotype, ± SD. On the right is a representative image of secondary lymphoid organs from *St8sia4*$^{-/-}$ and control mice. (**B**) Lipopolysaccharide (+LPS) or phosphate-buffered saline only (–LPS) was injected into the hind footpads of *St8sia4*$^{-/-}$ and control mice, and popliteal LNs were analyzed 48 hours after injection. The image shows representative popliteal LNs from *St8sia4*$^{-/-}$ and control animals. The graph shows average cellularity ± SD of three independent experiments with seven animals analyzed per genotype. (**C**) Flow cytometry of polySia levels on leukocytes isolated from popliteal LNs from *St8sia4*$^{-/-}$ and control mice in a steady state (upper right panel) and after LPS injection (lower panels). Migratory DCs are defined as CD11c^{+} MHCII^{high} and further classified by Langerin staining. In the upper left panels, dots indicate single cell events. Gates are shown. (**D**) Immunohistology of inguinal LNs from *St8sia4*$^{-/-}$ and control mice (left). B and T cell areas are indicated. Scale bar, 150 μm. The graph on the right shows the quantification of Langerin intensities. Bars represent normalized mean Langerin intensities (± SD) of PLNs of three different mice per genotype. (**E**) Fluorescein isothiocyanate (FITC) painting of *St8sia4*$^{-/-}$ and control mice. The graph shows averages ± SD of the total numbers of FITC^{+} and Langerin^{+} cells per organ from five different mice per genotype. Controls are derived from non-painted ears (controlateral). For all bar graphs, differences between *St8sia4*$^{-/-}$ and control mice were examined by two-tailed unpaired Student's *t* tests.

polySia-deficient DCs behaved like control cells and entered the deep T cell parenchyma, whereas *Ccr7*-deficient DCs were unable to leave the subcapsular sinus, as previously shown (Fig. 2C) (*16*). Next, we selectively probed migration within the skin and co-incubated skin explants with polySia-deficient and control DCs. We found that only control cells entered the dermal lymphatic vessels, whereas polySia-deficient DCs did not even infiltrate the dermal interstitium (Fig. 2D), therefore precisely phenocopying *Ccr7*-deficient DCs (*17*). Similarly, in cultured ear explants of *St8sia4*-deficient mice, DCs remained in the interstitium and failed to enter the lumen of lymphatic vessels, in contrast to DCs in control tissue (fig. S3B). Hence, DCs require polySia to sense dermal CCL21, whereas sensing of LN CCL21 is independent of polySia. Tissue context–specific presentation of CCL21 might explain why T cells, which do not express polySia, are able to home into LNs of *Ccl19*-deficient mice (*18*), although they only responded to CCL19 and not to CCL21, when exposed to soluble chemokine (fig. S3C). This prompted us to study the molecular mechanism underlying polySia-dependent CCL21 sensing.

Although the chemokine domain of CCL21 is structurally similar to that of CCL19 (*19*, *20*), CCL21 carries a positively charged C-terminal extension, which mediates binding to glycans, particularly heparan sulfate residues (*21*). It has been suggested that, via these residues, CCL21 might also interact with negatively charged polySia (*9*). Consequently, cell surface polySia might act as a co-receptor and increase the local availability of CCL21 for CCR7 (*22*). Of the seven proteins that were described as polySia carriers (*2*), only neuropilin-2 was expressed on mature DCs (*7*, *23*). However, in vivo and in vitro migration assays with neuropilin-2–deficient DCs did not show any perturbed migratory responses (fig. S4, A and B). Because neuropilin-2–deficient DCs still carried polySia, we immunoprecipitated polySia from lysates of mature DCs and used mass spectrometry to identify the underlying protein scaffold(s). This unbiased approach revealed three previously unknown putative polySia carriers, including CCR7 (fig. S4C and table S1). CCR7 and neuropilin-2 emerged as the only candidate molecules exposed on the cell surface.

This suggests that, apart from neuropilin-2, CCR7 is a second polySia carrier on the surface of mature DCs. To further investigate CCR7 as a direct target of polysialylation, we used a human embryonic kidney (HEK) 293 cell system. When green fluorescent protein (GFP) was immunoprecipitated from lysates of cells coexpressing a CCR7-GFP fusion protein and ST8Sia IV, polySia

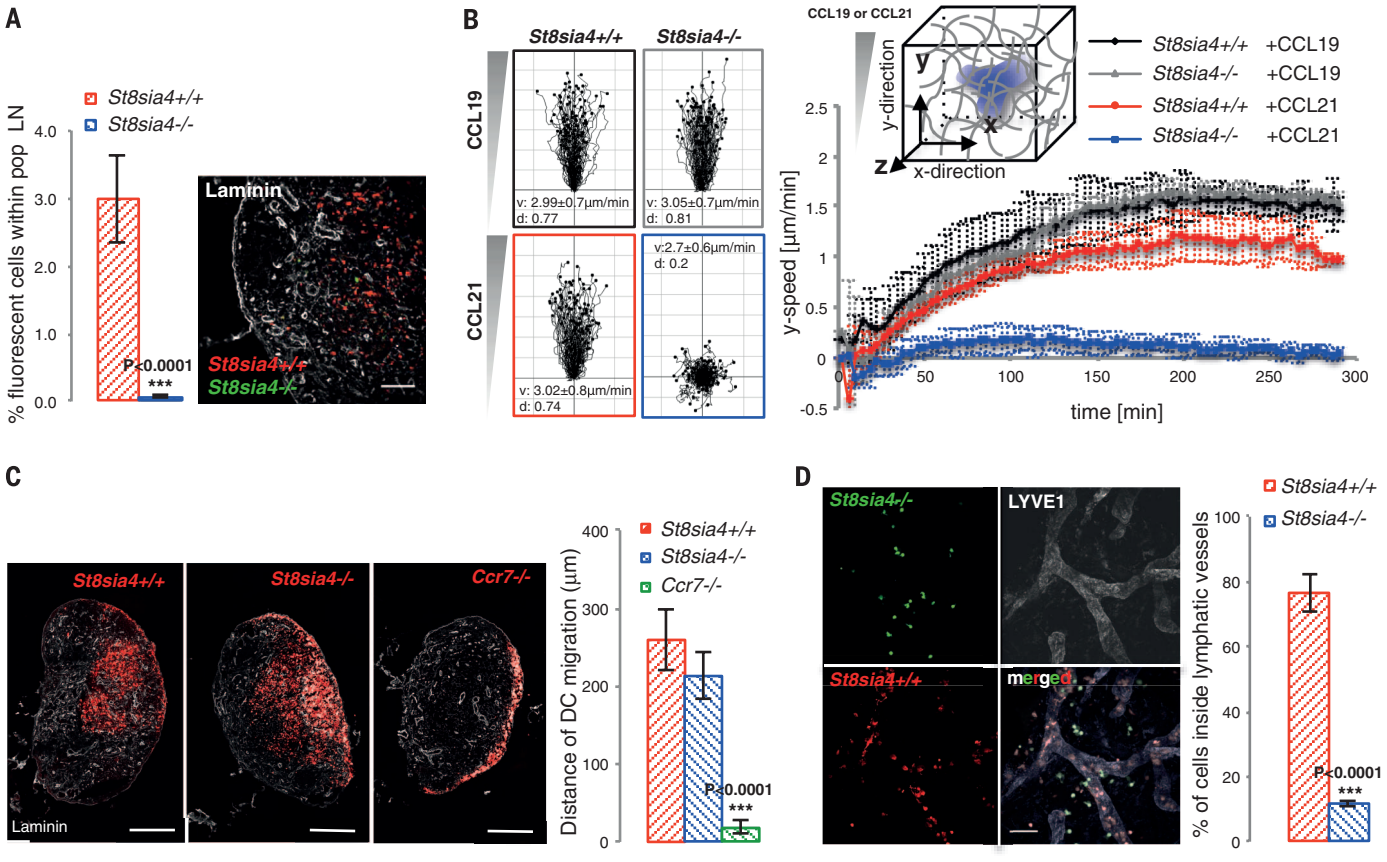

Fig. 2. PolySia affects CCL21 sensing in peripheral tissues. (**A**) Footpad injection of TAMRA (tetramethylrhodamine azide)– and CFSE (carboxyfluorescein diacetate succinimidyl ester)–labeled *St8sia4*$^{-/-}$ and control bone marrow DCs into wild-type recipient mice. Mice were euthanized 48 hours after injection and analyzed by flow cytometry (left) and immunohistochemistry (right). Cryosections of popliteal (pop) LNs were stained against laminin. Scale bar, 100 µm. (**B**) The left panels show single cell tracks of *St8sia4*$^{-/-}$ and control bone marrow DCs migrating within 3D collagen matrices toward CCL19 and CCL21 gradients (indicated by gray wedges; 0.33 µM per gel). Average velocities (v) ± SD and directionality (d) are indicated for each genotype and condition. On the right is an automated analysis of *y*-directed velocities of DC migration in 3D collagen gels. The curves show average speeds in the *y* direction over time ± SD from eight independent experiments with cells isolated from at least three different mice. The inset illustrates the experimental setup. (**C**) Intralymphatic injection of TAMRA-labeled *St8sia4*$^{-/-}$, control, or *Ccr7*$^{-/-}$ bone marrow DCs into *Ccl19*$^{-/-}$ recipient mice. Ten hours after injection, popliteal LNs were stained against laminin to visualize LN architecture (parenchyma and cortical sinus). The graph on the right shows average migratory distances ± SD of TAMRA^{+} DCs from the LN edge to the parenchyma (at least five mice per group). Scale bar, 250 µm. (**D**) On the left are *z*-stack projections of wild-type ear sheets incubated with *St8sia4*$^{-/-}$ and control bone marrow DCs and stained against LYVE1. Quantification of cells inside lymphatic vessels is shown in the graph on the right. Bars indicate average values ± SD of five different fields per view of three independent experiments. Scale bar, 100 µm. For all bar graphs, differences between groups were examined by two-tailed Student's *t* tests [(A) and (D), unpaired; (C), paired].

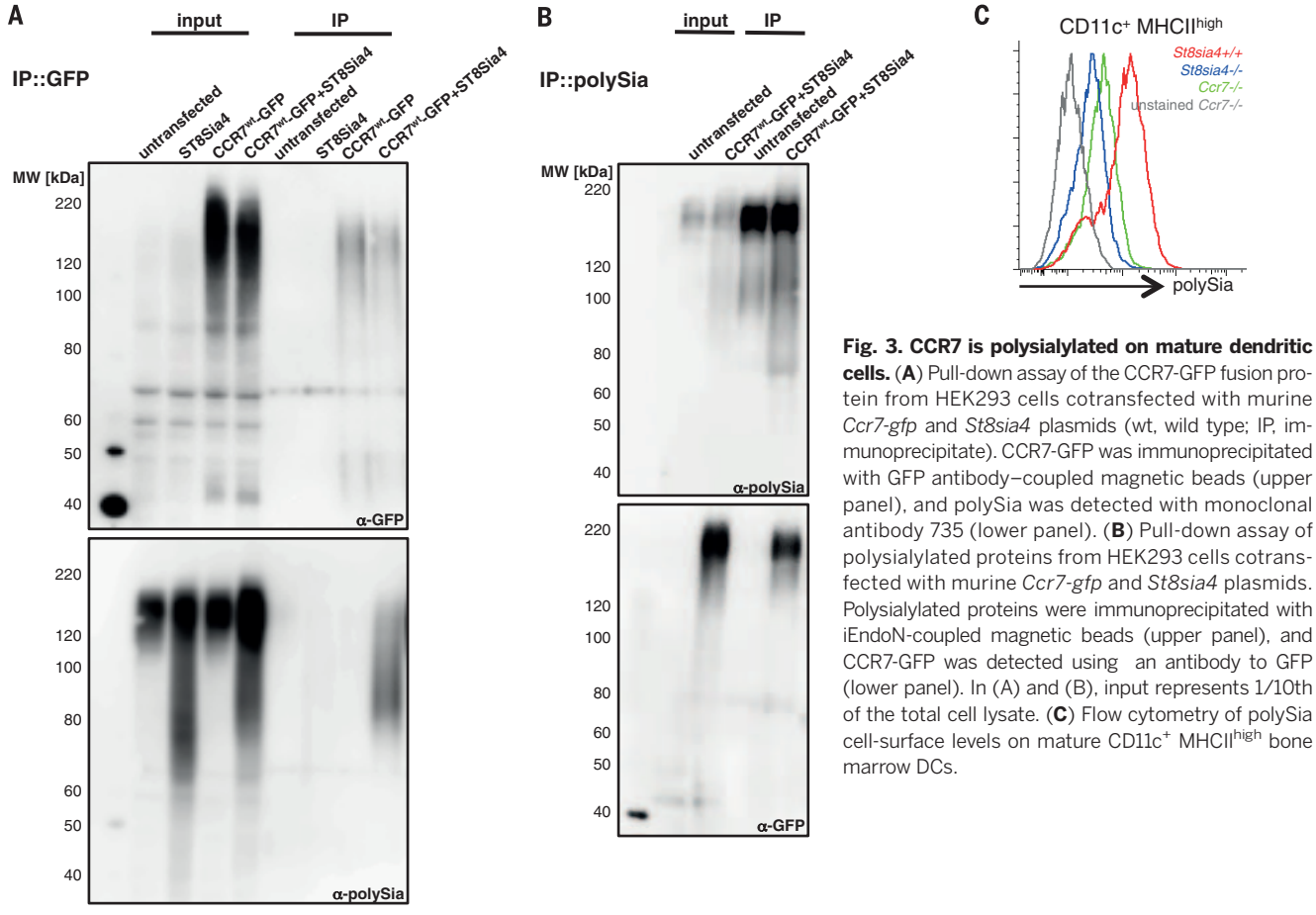

Fig. 3. CCR7 is polysialylated on mature dendritic cells. (**A**) Pull-down assay of the CCR7-GFP fusion protein from HEK293 cells cotransfected with murine *Ccr7-gfp* and *St8sia4* plasmids (wt, wild type; IP, immunoprecipitate). CCR7-GFP was immunoprecipitated with GFP antibody–coupled magnetic beads (upper panel), and polySia was detected with monoclonal antibody 735 (lower panel). (**B**) Pull-down assay of polysialylated proteins from HEK293 cells cotransfected with murine *Ccr7-gfp* and *St8sia4* plasmids. Polysialylated proteins were immunoprecipitated with iEndoN-coupled magnetic beads (upper panel), and CCR7-GFP was detected using an antibody to GFP (lower panel). In (A) and (B), input represents 1/10th of the total cell lysate. (**C**) Flow cytometry of polySia cell-surface levels on mature CD11c^{+} MHCII^{high} bone marrow DCs.

could be detected in the precipitate, whereas it was absent in precipitates of both single transfectants (Fig. 3A). Vice versa, precipitation of polySia revealed CCR7-GFP specifically in the double transfectants (Fig. 3B). Further biochemical and mutational analysis in HEK293 cells indicated that polySia was attached to both the N- and O-linked glycans of CCR7, because inhibition of either N- or O-glycosylation did not fully abrogate polysialylation of CCR7 (fig. S4, D and E). To substantiate that CCR7 is polysialylated in DCs, we used flow cytometry to analyze cell-surface levels of polySia in *Ccr7*-deficient and control DCs and found reduced polySia on *Ccr7*-deficient cells (Fig. 3C). This further suggests that, apart from neuropilin-2, CCR7 is a second carrier of polySia on the surface of mature DCs.

A co-receptor model would predict that polySia on CCR7 might bind CCL21's C terminus, thereby effectively increasing receptor-to-ligand affinity. To test this idea, we C-terminally truncated CCL21 and performed chemotaxis assays. At odds with a co-receptor model, the responsiveness of polySia-deficient DCs to CCL21 was restored when the chemokine was C-terminally truncated (Fig. 4A). This finding indicated that, rather than enhancing CCR7 binding to CCL21, the polySia-CCL21 interaction might promote signaling by releasing CCL21 from an otherwise inactive state. This would be consistent with an autoinhibition model, in which the C terminus of CCL21 induces structural alterations within the chemokine domain that prevent signaling but that can be reversed upon polySia binding.

CCL21's C terminus is unstructured and does not adopt a stable fold (*20*). We therefore performed nuclear magnetic resonance spectroscopy to detect chemical shifts that might distinguish the chemokine domain conformation of full-length CCL21 from that of C-terminally truncated CCL21. As expected, truncation caused chemical shift changes in residues with immediate proximity to the truncation site (fig. S5A). However, additional chemical shifts localized to the α-helix of the chemokine domain (residues 63, 64, 66, 67, 69, and 70) and to additional residues (26, 31, 41, 47, and 54; Fig. 4B and fig. S5A). These shift perturbations distal to the site of truncation suggest that CCL21's C terminus transiently interacts with the chemokine domain of CCL21, thereby providing a putative structural correlate of functional autoinhibition. When polySia was titrated to full-length CCL21, residues belonging to the putative autoinhibition signature shifted to positions similar to those observed in the spectra of truncated CCL21 (Fig. 4C and fig. S5B). Hence, in the presence of polySia, the chemokine domain of full-length CCL21 adopts a similar conformation as that of C-terminally truncated CCL21. PolySia binding to truncated CCL21 was considerably weaker than to full-length CCL21, confirming that interactions mainly take place via the C terminus (fig. S5C). Together, these data suggest that CCL21's C terminus structurally alters its chemokine domain, probably by transient binding, and that this structural alteration is abrogated by polySia binding to CCL21's C-terminal extension.

To functionally challenge the autoinhibition model, we took advantage of the fact that the polySia-insensitive chemokine CCL19 naturally lacks a C-terminal extension and produced a recombinant chemokine with CCL21's C terminus transplanted to CCL19 (Fig. 4D, right panel). Chemotaxis assays revealed that control DCs responded to the chimeric chemokine with kinetics that were more similar to those observed for CCL21 than for CCL19 (Fig. 4D, left panel). The maximal directed response of wild-type DCs toward the chimera was slightly diminished in comparison with the response toward CCL19. Most relevantly, transplantation of CCL21's C terminus to CCL19 conferred polySia sensitivity, because the response of polySia-deficient DCs to the chimeric chemokine was largely abrogated. These data corroborate a model in which polySia releases CCL21 from an autoinhibited state by interacting with CCL21's C terminus.

We have described here a glycosylation-dependent immune cell trafficking defect and its underlying molecular mode of action. The polySia-dependent release of CCL21 autoinhibition is a mechanism of chemokine regulation that is likely to be relevant for other chemokines that have

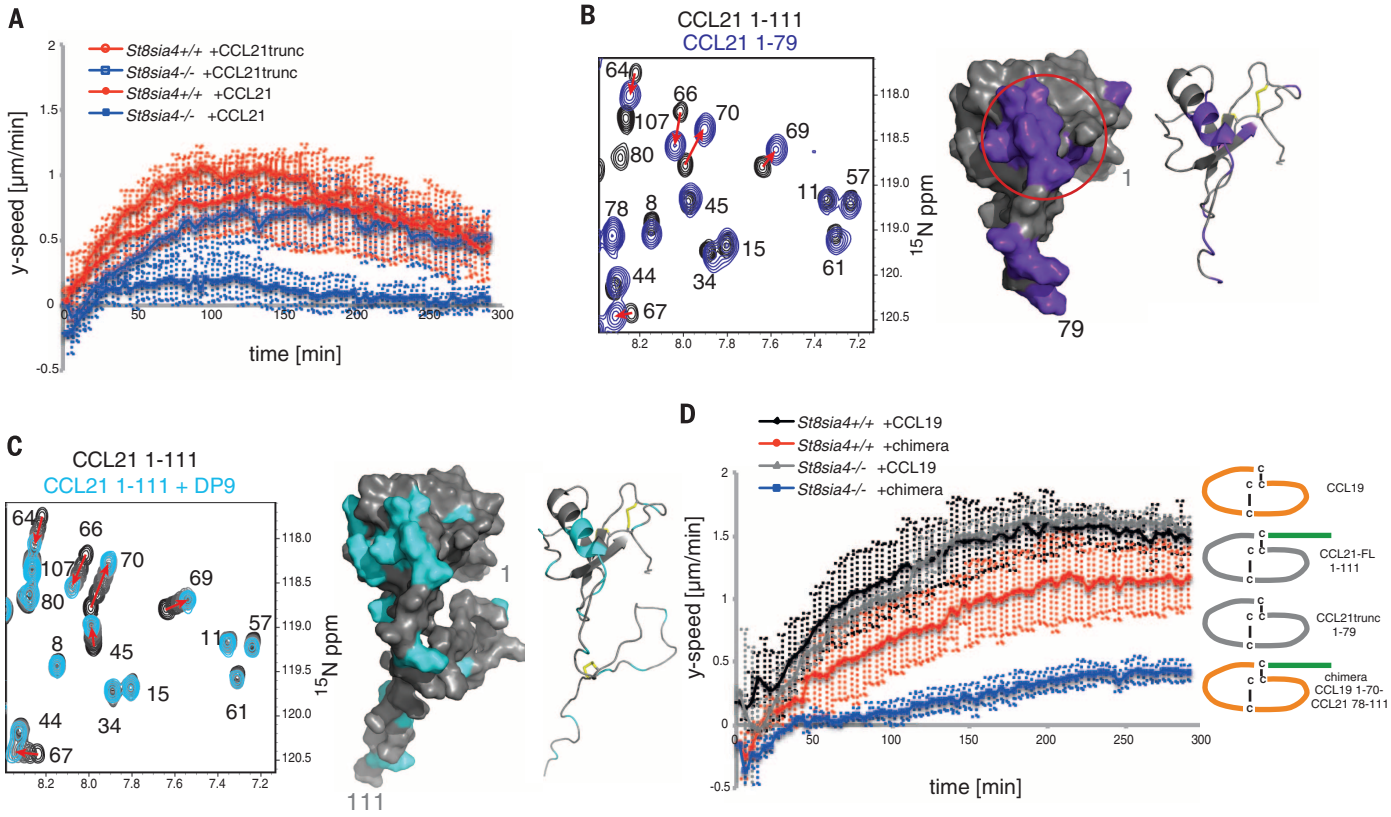

Fig. 4. Identification of an autoinhibitory interaction site within CCL21. (**A**) Migration of mature bone marrow DCs within 3D collagen gels toward truncated CCL21 (CCL21trunc). Shown are average speeds in the *y* direction over time ± SD from eight independent experiments with cells generated from at least three different mice. (**B**) The left panel shows overlays of a portion of the ^{15}N-^{1}H HSQC (heteronuclear single-quantum coherence) spectra of full-length CCL21 (CCL21-FL) residues 1 to 111 (black) and CCL21trunc residues 1 to 79 (purple) (ppm, parts per million). Red arrows indicate chemical shifts of the respective residue. On the right, the first 79 amino acids of the CCL21-FL structure are depicted with residues (purple) that showed significant changes in chemical shift perturbations upon truncation. The red circle indicates a putative autoinhibitory site. (**C**) The left panel shows overlays of a portion of the ^{15}N-^{1}H HSQC spectra of CCL21-FL 1 to 111 (black) and CCL21-FL titrated with increasing concentrations of polySia DP9 (grays to cyan; DP, degree of polymerization). On the right, residues within CCL21-FL with significant polySia-induced chemical shift perturbations are colored cyan. (**D**) Migration of mature bone marrow DCs toward the chimeric chemokine (left) and schematic representations of chemokines used for in vitro migration assays (right).

similar C-terminal extensions. The finding that polySia dependency is restricted to the skin suggests that, depending on the molecular context, CCL21 can either be present in the autoinhibited or the active form. The mechanism that we describe also illuminates how glycosylation of a G protein–coupled receptor allows discrimination between two alternative ligands. Apart from being the key coordinator of adaptive immune cell trafficking, the CCR7 axis is also centrally involved in the spread of metastatic tumors, suggesting that our findings may be therapeutically relevant.

REFERENCES AND NOTES

1. U. Rutishauser, *Nat. Rev. Neurosci.* **9**, 26–35 (2008).
2. M. Mühlenhoff, M. Rollenhagen, S. Werneburg, R. Gerardy-Schahn, H. Hildebrandt, *Neurochem. Res.* **38**, 1134–1143 (2013).
3. R. L. Schnaar, R. Gerardy-Schahn, H. Hildebrandt, *Physiol. Rev.* **94**, 461–518 (2014).
4. R. A. Falconer, R. J. Errington, S. D. Shnyder, P. J. Smith, L. H. Patterson, *Curr. Cancer Drug Targets* **12**, 925–939 (2012).
5. A. Harduin-Lepers *et al.*, *Front. Biosci. (Elite Ed.)* **4**, 499–515 (2012).
6. Y. M. J. Al-Sarareh *et al.*, *PLOS ONE* **8**, e73366 (2013).
7. S. Curreli, Z. Arany, R. Gerardy-Schahn, D. Mann, N. M. Stamatos, *J. Biol. Chem.* **282**, 30346–30356 (2007).
8. A. Rey-Gallardo *et al.*, *Glycobiology* **20**, 1139–1146 (2010).
9. M. Bax, S. J. van Vliet, M. Litjens, J. J. García-Vallejo, Y. van Kooyk, *PLOS ONE* **4**, e6987 (2009).
10. P. M. Drake *et al.*, *J. Immunol.* **181**, 6850–6858 (2008).
11. M. Eckhardt *et al.*, *J. Neurosci.* **20**, 5234–5244 (2000).
12. C. Moussion, J.-P. Girard, *Nature* **479**, 542–546 (2011).
13. M. Wendland *et al.*, *Immunity* **35**, 945–957 (2011).
14. S. E. Macatonia, S. C. Knight, A. J. Edwards, S. Griffiths, P. Fryer, *J. Exp. Med.* **166**, 1654–1667 (1987).
15. R. Förster *et al.*, *Cell* **99**, 23–33 (1999).
16. A. Braun *et al.*, *Nat. Immunol.* **12**, 879–887 (2011).
17. M. Weber *et al.*, *Science* **339**, 328–332 (2013).
18. A. Link *et al.*, *Nat. Immunol.* **8**, 1255–1265 (2007).
19. C. T. Veldkamp *et al.*, *Biochemistry* **54**, 4163–4166 (2015).
20. M. Love *et al.*, *Biochemistry* **51**, 733–735 (2012).
21. J. Hirose, H. Kawashima, O. Yoshie, K. Tashiro, M. Miyasaka, *J. Biol. Chem.* **276**, 5228–5234 (2001).
22. A. Rey-Gallardo, C. Delgado-Martín, R. Gerardy-Schahn, J. L. Rodríguez-Fernández, M. A. Vega, *Glycobiology* **21**, 655–662 (2011).
23. M. Rollenhagen *et al.*, *J. Biol. Chem.* **288**, 22880–22892 (2013).

ACKNOWLEDGMENTS

We thank S. Schüchner and E. Ogris for kindly providing the antibody to GFP, M. Helmbrecht and A. Huber for providing *Nrp2*$^{-/-}$ mice, the IST Scientific Support Facilities for excellent services, and J. Renkawitz and K. Vaahtomeri for critically reading the manuscript. The data described in this manuscript are tabulated in the main paper and in the supplementary materials. This work was supported by the European Research Council (grants ERC GA 281556 to M.S. and ERC GA 322645 to R.F.), funding from the STROMA (Stromal Cell–Immune Cell Interactions in Health and Disease) Initial Training Network of the European Commission Framework Programme, a START award from the Austrian Science Foundation (FWF) to M.S., grant FWF TRP 308-N15 to K.M., and U.S. NIH grants 1R15CA159202-01 to C.T.V. and R01AI058072 and R01GM09738 to B.F.V.

SUPPLEMENTARY MATERIALS

www.sciencemag.org/content/351/6269/186/suppl/DC1
Materials and Methods
Figs. S1 to S5
Table S1
References (*24*–*35*)

21 July 2015; accepted 1 December 2015
Published online 10 December 2015
10.1126/science.aad0512

AAAS 2016 ANNUAL MEETING | WASHINGTON, DC FEBRUARY 11–15

Global Science Engagement

Advance registration rates are available through January 19, 2016. AAAS members are eligible for further discounts.

Browse the program and register online now.

aaas.org/meetings

AAAS, publisher of *Science*, thanks the sponsors and supporters of the 2016 Annual Meeting

European Commission

SUBARU

RESEARCH COUNCILS UK

HELMHOLTZ ASSOCIATION

THE KAVLI FOUNDATION

for its generous support of the Science Journalism Awards

NANYANG TECHNOLOGICAL UNIVERSITY

As of December 21, 2015

CALL FOR PAPERS! MANUSCRIPTS DUE MAY 1, 2016.

WE'VE GOT A **MATERIAL INTEREST** IN YOU

Time sequence of buckling silicon microwires.

Publish in our Special Series, Materials By Design. We'll waive all APCs. Use code: ADVSSMBD

Science Advances, the new, open-access journal from AAAS, is publishing interdisciplinary research that advances the frontiers of science and technology. We're now preparing an exciting Special Series, Materials By Design, showcasing important work in material science and engineering with potential global impact.

You're invited to submit your research to the series, and if our guest editors select your manuscript for publication, we'll waive all APCs. *Science Advances* offers expert editing, rapid publication, and all the marketing clout you'd expect from the publisher of *Science*.

Submit your research at ScienceAdvances.org

ScienceAdvances | AAAS
SIGNIFICANT RESEARCH, GLOBAL IMPACT

Rotary Evaporator

The advanced RC 600 Rotary Evaporator is an efficient, robust instrument designed for intensive day-to-day use in a wide range of laboratories. Its well-planned ergonomic design and intuitive control interface ensure ease of use, allowing rapid user familiarity and straightforward operation. For maximum operator safety, a simple flask exchange mechanism and an easy-to-pour heating bath are incorporated, and there is minimal exposed tubing. The SCC 950 offers precise, cost-effective vacuum control of two separate processes concurrently, and is perfect for simultaneous operation of two RC 600 Rotary Evaporators. For laboratories with an uncontrolled vacuum source, the VC 900 is ideal. It allows existing pumps from KNF and other manufacturers—as well as central vacuum sources—to be upgraded, enabling accurate control of vacuum processes. The N 920 G diaphragm vacuum pump features an integrated gas ballast valve for superior handling of aggressive gases and vapors.

KNF Neuberger
For info: 609-890-8600
www.knfusa.com

Gold Nanoparticles

A highly monodisperse, premium line of Gold NanoSpheres specially designed for use in lateral flow assays is available in a range of different sizes for improved assay performance. The particles offer a combination of high cherry red contrast and optimal surface area (to minimize wasted targeting biomolecules) for effective and efficient analyte testing. Thorough characterization data and lot-specific transendothelial migration (TEM) images are included with every product. The gold nanoparticles can be synthesized at 10–25X higher concentrations as compared to traditional protocols to boost assay sensitivity. Scale-up to larger volumes is offered without any compromise on particle monodispersity and quality. The monodispersity in shape and size along with minimal batch-to-batch variations ensure data quality and consistency for assay developers, dramatically enhancing lateral flow assay sensitivity and reliability. Custom conjugation of antibodies, aptamers, and proteins on the particle surface and personalized tech support for assay development are also available.

NanoHybrids
For info: 512-270-8469
www.nanohybrids.net

Centrifuge

The Hi Cen GR is a large-volume, floor-standing refrigerated centrifuge, which has a maximum capacity of 4 × 1,000 ml and can be used with swing-out or angle rotors. Its speed of up to 18,000 rpm and g-force of 36.223 × g puts this model at the high end of performance levels. It is also possible to centrifuge small volumes at high speed in a fixed-angle rotor [10 ml tubes at 17,500 rpm (33.554 × g)]. Centrifugation of high volumes, such as 4 × 1000 ml in a swing-out rotor or 4 × 750 ml in a swing-out rotor with windshield, is also possible with this very versatile machine. Nineteen different swing-out and fixed-angle rotors are available. As is typical with many of the centrifuges, this microprocessor controlled model has a number of standard features including a maintenance free, brushless induction drive, stainless-steel chamber with additional inner guard ring, overspeed detection, imbalance detection, and cutoff.

Herolab
For info: +44-(0)-1223-515440
www.herolab.de

Gene Expression Assay

The QuantiGene Singleplex assay is designed for polymerase chain reaction (PCR)-free gene expression measurement and now includes a 384-well format that is easily automatable for high-throughput (HT) compound screening. The easy-to-use, high-sensitivity assay measures gene expression with minimal sample preparation, using branched DNA for signal amplification. A key feature of the assay is that it does not require RNA or DNA purification, reverse transcription, or PCR amplification, so biases and sample losses resulting from these preparation steps are eliminated. This robust assay, also available in a 96-well format, can directly detect gene expression changes as small as 10 percent. The Z-factors of the QuantiGene Singleplex HT assay are consistently higher than those of other assay types such as quantitative PCR. Ideal applications for the QuantiGene Singleplex HT assay include compound screening in drug discovery, biomarker validation, and small interfering RNA (siRNA) knockdown studies. The assay accommodates a range of sample types, including heavily degraded and cross-linked RNA in formalin-fixed paraffin-embedded (FFPE) samples and RNA in blood.

Affymetrix
For info: 888-999-1371
www.affymetrix.com

Cloning Kit

The Vivantis Flex-C Cloning kit is a highly efficient, rapid, and easy-to-use polymerase chain reaction (PCR) cloning kit. The Flex-C Enzyme allows direct cloning of any PCR fragments to any linearized expression vector at any site in a single 20-minute reaction. The application protocol is simple. The PCR fragments can be generated by PCR polymerases with primers that are designed to have at least 10 bases of homology at their linear ends. No additional treatment of the PCR fragment is required. The linearized vector can be generated by PCR or restriction enzymes. The Flex-C Enzyme joins PCR fragments and linearized vectors accurately and efficiently by recognizing the 10 base pair (bp) overlap at their ends. This method allows cloning multiple fragments into a single vector in a single reaction without subcloning. The kit is highly efficient, with a 95% insert rate. It also includes Vivantis Taq DNA Polymerase and reaction buffers as well as deoxynucleotide triphosphate (dNTP) for subsequent PCR screening of clones.

Vivantis Technologies
For info: +44-(0)-1223-515440
www.vivantechnologies.com

Electronically submit your new product description or product literature information! Go to www.sciencemag.org/products/newproducts.dtl for more information.

Newly offered instrumentation, apparatus, and laboratory materials of interest to researchers in all disciplines in academic, industrial, and governmental organizations are featured in this space. Emphasis is given to purpose, chief characteristics, and availability of products and materials. Endorsement by *Science* or AAAS of any products or materials mentioned is not implied. Additional information may be obtained from the manufacturer or supplier.

Join AAAS. Get instant access to *Science*. Support all of the sciences.

When you subscribe to *Science*, you become part of the American Association for the Advancement of Science (AAAS), a nonprofit community of more than 100,000 members worldwide who believe in the power of science to make the world a better place. AAAS is hard at work promoting science in government, schools, and in the public commons around the globe.

AAAS's award-winning journal *Science* offers the top peer-reviewed research across multiple disciplines. With your subscription, you'll get:

- 51 weeks of home delivery of *Science*
- Instant online retrieval of every *Science* article ever published, dating back to 1880
- Full access to the *Science* mobile site and apps
- Career advice, webinars, blogs and fascinating features exclusively for AAAS members
- Members-only newsletters, and much more

With increasing public skepticism about science–and public funding for research more uncertain than ever–our work has never been more important. Join hands with us today!

Visit promo.aaas.org/joinaaas. Together, we can make a difference.

Science
AAAS

R&D SYSTEMS
a bio-techne brand

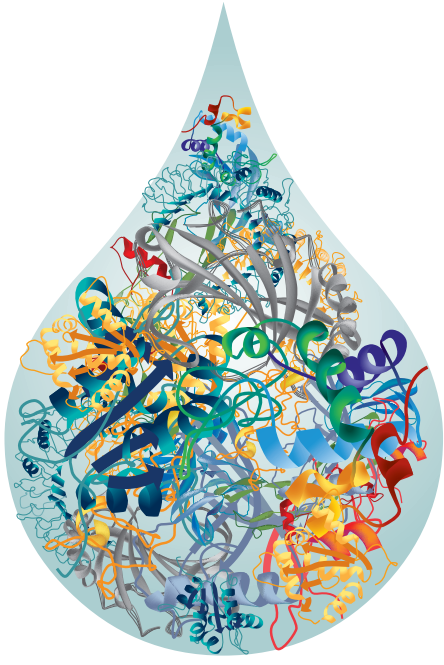

What's in Your Sample?

Find Your Answers!

rndsystems.com/
Immunoassays

Science Careers Advertising

For full advertising details, go to ScienceCareers.org and click For Employers, or call one of our representatives.

Tracy Holmes
Worldwide Associate Director
Science Careers
Phone: +44 (0) 1223 326525

THE AMERICAS

E-mail: advertise@sciencecareers.org

Fax: +1 (202) 289 6742

Tina Burks
Phone: +1 (202) 326 6577

Nancy Toema
Phone: +1 (202) 326 6578

Online Job Posting Questions
Phone: +1 (202) 312 6375

EUROPE / INDIA / AUSTRALIA / NEW ZEALAND / REST OF WORLD

E-mail: ads@science-int.co.uk

Fax: +44 (0) 1223 326532

Sarah Lelarge
Phone: +44 (0) 1223 326527

Kelly Grace
Phone: +44 (0) 1223 326528

Online Job Posting Questions
Phone: +44 (0) 1223 326528

JAPAN

Katsuyoshi Fukamizu (Tokyo)
E-mail: kfukamizu@aaas.org
Phone: +81 3 3219 5777

Hiroyuki Mashiki (Kyoto)
E-mail: hmashiki@aaas.org
Phone: +81 75 823 1109

CHINA / KOREA / SINGAPORE / TAIWAN / THAILAND

Ruolei Wu
Phone: +86 186 0082 9345
E-mail: rwu@aaas.org

All ads submitted for publication must comply with applicable U.S. and non-U.S. laws. *Science* reserves the right to refuse any advertisement at its sole discretion for any reason, including without limitation for offensive language or inappropriate content, and all advertising is subject to publisher approval. *Science* encourages our readers to alert us to any ads that they feel may be discriminatory or offensive.

ScienceCareers
FROM THE JOURNAL SCIENCE AAAS

ScienceCareers.org

PRESIDENT /CEO

Okinawa Institute of Science and Technology Graduate University

The Okinawa Institute of Science and Technology Graduate University (OIST) has initiated an international search for the President/Chief Executive Officer.

OIST (**www.oist.jp**) is an international, doctoral-level graduate university of science and technology established in 2011 by the Government of Japan. It is located in Okinawa, a semitropical island at the southernmost extreme of Japan. The mission of OIST is to carry out world-class graduate education and research in the natural sciences, and to stimulate the sustainable economic development of Okinawa. English is the language of instruction and more than half of the faculty, students and research staff are international. The first stage of growth of the university has been completed, with 50 independent faculty research units, over 100 doctoral students in the Graduate School, 750 research and administrative staff, and extensive support facilities located in three well-equipped research laboratories and a central administration building. There are no academic departments, the research units cover a broad range of life and physical sciences and are highly interdisciplinary, and faculty and students come from more than 50 countries (see “Peer Review 2015 Report” at **https://www.oist.jp/oist-publications-reports**).

The President of OIST Graduate University serves as the CEO of the OIST School Corporation and is responsible for the overall leadership and management of the University, in close cooperation with the Board of Governors. The President will lead the next stage of expansion of the University, aimed at doubling the size by the year 2023. The President is expected to support technology transfer of OIST intellectual property and to encourage R&D-based economic development in Okinawa.

Candidates are expected to have outstanding scientific credentials, preferably with at least five years’ experience in high-level, international research and academic administration. Proficiency in spoken and written English is necessary; knowledge of Japanese is not required. The appointment is full-time, and the term of office is five years and renewable. The starting date is negotiable.

All applications, nominations, and inquiries should be submitted by email to **president-search@oist.jp**. A detailed position description and application process can be found at **http://www.oist.jp/presidential-search**. The first review of applications will start around **March 1, 2016**. Applications will continue to be accepted until the position is filled.

Declaration: OIST Graduate University is an Equal Opportunity Educator and Employer committed to increasing the diversity of its executives, faculty, students and staff by having proactive policies in place. Applications from women and other underrepresented groups are strongly encouraged.

Science Careers online @sciencecareers.org

ScienceCareers online @sciencecareers.org

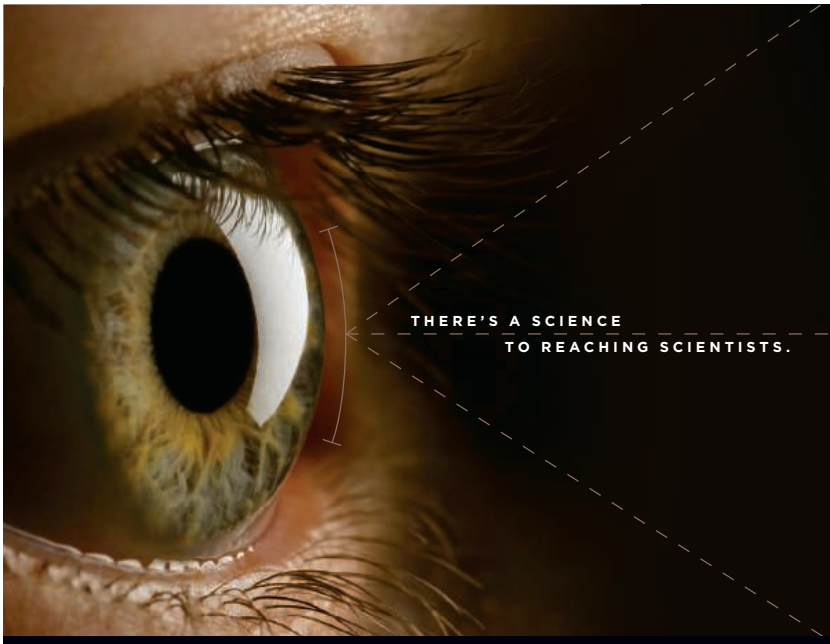

Save these Dates!

Faculty Careers

January 29, 2016

Reserve ads by January 12 to guarantee space.

Postdoc Careers

March 25, 2016

Reserve ads by March 8 to guarantee space.

For recruitment in science, there's only one Science

Two Fantastic Recruiting Opportunities!

FACULTY CAREERS | January 29, 2016

Gear up to recruit for the faculty positions at your university with this much anticipated issue that reaches thousands of Ph.D. scientists looking for positions in academia.

Reserve ads by January 12 to guarantee space.

POSTDOC CAREERS | March 25, 2016

Be sure to promote your openings to the thousands of scientists who will be reading *Science* to find out about the latest postdoc opportunities.

Reserve ads by March 8 to guarantee space.

Produced by the *Science*/AAAS Custom Publishing Office.

SCIENCECAREERS.ORG

ScienceCareers
FROM THE JOURNAL SCIENCE AAAS

To book your ad: **advertise@sciencecareers.org**

The Americas
202-326-6577

Europe/RoW
+44 (0) 1223-326500

Japan
+81-3-3219-5777

China/Korea/Singapore/Taiwan
+86-186-0082-9345

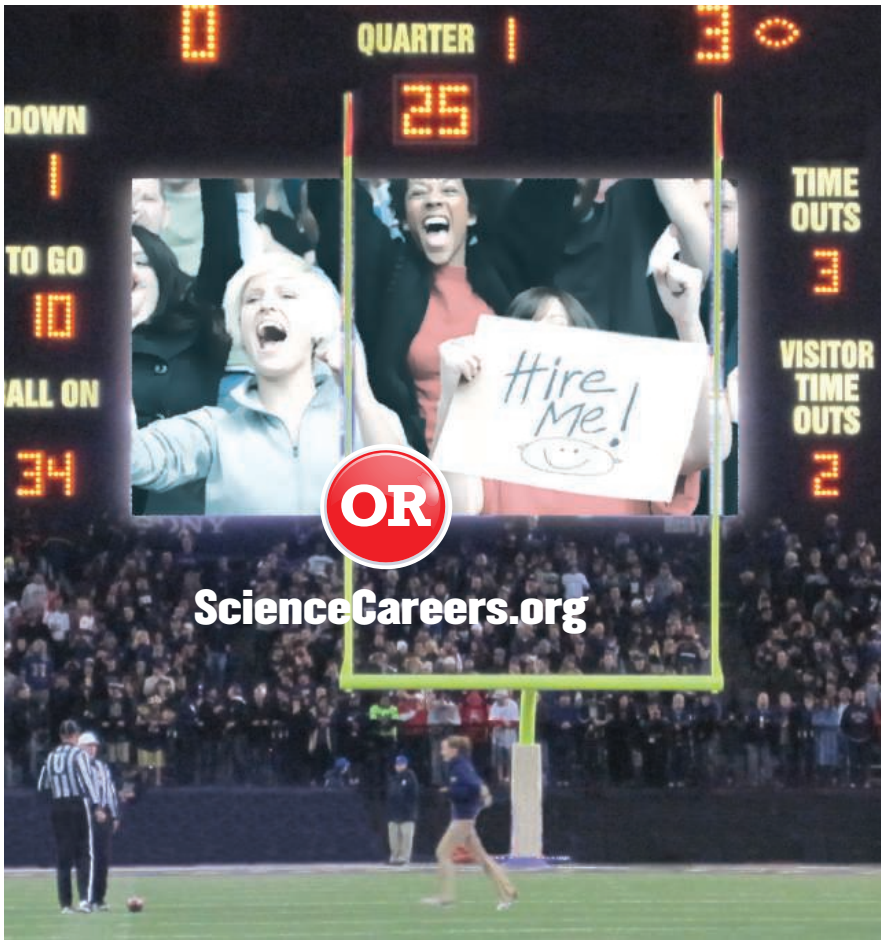

Learn more and keep your job search out of the cheap seats.

- Search thousands of job postings
- Create job alerts based on your criteria
- Get career advice from our Career Forum experts
- Download career advice articles and webinars
- Complete an individual development plan at "myIDP"

Target your job search using relevant resources on **ScienceCareers.org**.

ScienceCareers
FROM THE JOURNAL SCIENCE AAAS

Join Germany's international research community

© DAAD/Volker Lannert

Discover the opportunities that Germany offers:

- First-class doctoral training
- Excellent career opportunities in research and industry
- Attractive funding programmes for international researchers

Visit us at the
European Career Fair 2016
Johnson Athletic Center, MIT
Cambridge, USA
6 February 2016, 9 am – 4 pm
Booth numbers: G1–11; F1–10

Find us on Facebook:
facebook.com/
Research.in.Germany

Follow us on Twitter:
twitter.com/
ResearchGermany

AN INITIATIVE OF THE
Federal Ministry of Education and Research

Research in Germany
Land of Ideas
www.research-in-germany.org

ScienceCareers online @sciencecareers.org

myIDP: A career plan customized for you, by you.

For your career in science, there's only one Science

my IDP ScienceCareers

Recommended by leading professional societies and the NIH

Features in myIDP include:

- Exercises to help you examine your skills, interests, and values.
- A list of 20 scientific career paths with a prediction of which ones best fit your skills and interests.
- A tool for setting strategic goals for the coming year, with optional reminders to keep you on track.
- Articles and resources to guide you through the process.
- Options to save materials online and print them for further review and discussion.
- Ability to select which portion of your IDP you wish to share with advisors, mentors, or others.
- A certificate of completion for users that finish myIDP.

Visit the website and start planning today!
myIDP.sciencecareers.org

ScienceCareers In partnership with:

advancing the life sciences 1912-2012 FASEB Federation of American Societies for Experimental Biology

UCSF University of California San Francisco

Medical College of Wisconsin

Burroughs Wellcome Fund

Join the Conversation!

Twitter is a great way to connect with AAAS members and staff about the issues that matter to you most. Be a part of the discussion while staying up-to-date on the latest news and information about your personal member benefits.

Follow us @AAASmember and join the conversation with #AAAS

AAAS MemberCentral

MemberCentral.aaas.org

MEETINGS

JGI JOINT GENOME INSTITUTE
A DOE OFFICE OF SCIENCE USER FACILITY

Microbial and Plant Systems Modulated by Secondary Metabolites Meeting

May 2–4, 2016 • Walnut Creek, CA

This meeting, hosted by the U.S. Department of Energy Joint Genome Institute, will bring together those interested in the role of secondary metabolites in plant-microbe and microbe-microbe interactions to discuss approaches for studying and manipulating the impact of secondary metabolites on environmental systems. Participants will also learn about JGI capabilities—large-scale DNA sequencing, synthesis and data mining—available to them.

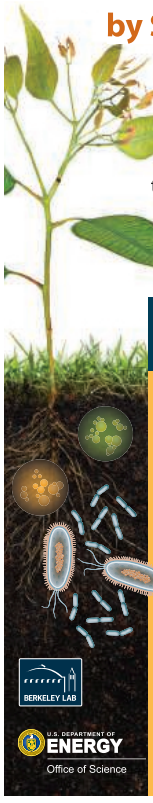

Registration is limited to 90 participants. Register here:
http://bit.ly/JGI-Metabolites

Confirmed speakers include:

Emily Balskus, *Harvard*
Gabriele Berg, *Graz University of Technology*
Clint Chapple, *Purdue University*
Jeff Dangl, *University of North Carolina, Chapel Hill*
Lars Dietrich, *Columbia University*
Monica Höfte, *Ghent University*
Ikhlas Khan, *National Center for Natural Products Research*
Mark Lange, *Washington State University*
Joyce Loper, *USDA-ARS, Oregon State University*
Bradley Moor, *Scripps Institution of Oceanography*
Sarah O'Connor, *John Innes Centre, UK*
Anne Osbourn, *John Innes Centre, UK*
Reuben Peters, *Iowa State University*
Jos Raaijmakers, *NIOO Wageningen*
Mohammad Seyedsayamdost, *Princeton University*
Lloyd Sumner, *The Samuel Roberts Noble Foundation*
Dorothea Tholl, *Virginia Tech University*
Julia Vorholt, *ETH Zurich*

BERKELEY LAB
U.S. DEPARTMENT OF ENERGY
Office of Science

16-JGI-2383

Download the *Science* Careers jobs app from Science

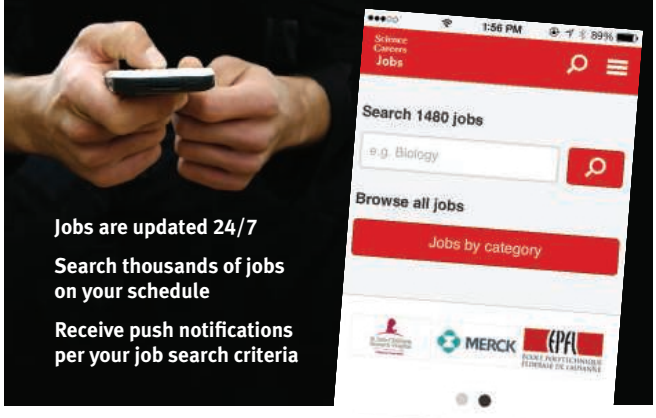

Jobs are updated 24/7

Search thousands of jobs on your schedule

Receive push notifications per your job search criteria

Get a job on the go.
Search worldwide for thousands of scientific jobs in academia, industry, and government. The application process is seamless, linking you directly to job postings from your customized push notifications.

Scan this code to download app or visit **apps.sciencemag.org** for information.

ScienceCareers | AAAS
FROM THE JOURNAL SCIENCE

ScienceCareers.org

By **Roger S. Day**

Want a letter? You write it for me

A few years back, I asked two colleagues for letters of support for my grant proposal. One colleague drafted a letter personally. The other, citing heavy time pressures, asked me to draft the letter myself. I was sympathetic, but I felt queasy pretending to be someone else as I described my own work. To appease my conscience, I wrote as myself: "I" meant me and "you" meant my colleague. This was risky. If the colleague simply signed and sent the letter, neglecting the required pronoun switcheroo, the letter would instantly reveal its true originator. I am grateful that the colleague saved me that embarrassment, and even added authentic language to the letter.

Later, at a workshop on winning grant-writing strategies, I asked the instructor about this practice, describing my discomfort. The response was, "Get over it." The practice is common, after all. A letter from an established senior person—a VIP for short—can strengthen an application for school admission, a job, or a grant. To write an informed, original letter from scratch, however, would require more knowledge of the candidate and the project than the VIP has time to acquire. It would be a poor professional investment, with the VIP's own duties, articles, and grant proposals clamoring for attention. Furthermore, as a salary comparison would show, the VIP's time is far more precious than the applicant's. (But how valid is this? Who knows what the applicant might achieve years hence? What was an hour of young Einstein's time worth?)

"This is an injustice to both the applicant and the responsible VIP."

So the VIP says, "Sure! Glad to help! Of course, I'm a busy person. Draft it for me." The applicant may be startled. How awkward, trying to write words of praise about oneself while pretending that they are someone else's. How much flattery is too much, or too little? Besides, isn't this a deception that betrays academia's dedication to truth?

In fact, a reviewer can often detect words that originated with the applicant. The discovery correctly devalues the letter, harming the applicant's chances. When the VIP does write an original and well-informed letter, the reviewer may still assume that its authorship, like that of so many other letters, is partly misrepresented. This is an injustice to both the applicant and the responsible VIP.

Pity the applicant receiving two such requests, feeling doubly queasy trying to draft two different letters for the same committee. Facing time pressure, the applicant may give both VIPs similar drafts, hoping they will make the extra effort to customize their letters enough to disguise the common origin. On a committee reviewing one such applicant, I read two letters that were virtually identical. The applicant took the fall, but the fault lies with the two VIPs, whose indifference doomed the application.

The worst consequence of this practice is the message imprinted on a young applicant's mind: "Everybody does it." Apparently, minor frauds like this are not just condoned but expected by academic leaders. Apparently, people rise in the system by offloading work to the less powerful. Apparently, the words of the more prestigious are not golden; sometimes they are not even their own. Perhaps around the corner a slightly larger fraud is acceptable, including those too-common courtesy authorships for the highly placed. Then that leads to larger ones: covering up data problems and, ultimately, falsifying data. Thus do we introduce young people to our system. Several students I know lost some respect for VIPs who had students writing letters that they should be writing themselves.

You can help fix this. If you are a VIP asked to write a letter of support and you write it yourself, just add a notation: "The content of this letter is original with the undersigned author." Applicant, go ahead and encourage your VIP to add it. The readers will know to exempt the letter from the usual degraded valuation. If this practice catches on, our scientific culture may swing back toward reverence for integrity. ■

Roger S. Day is an associate professor of biomedical informatics and biostatistics at the University of Pittsburgh in Pennsylvania. Send your story to SciCareerEditor@aaas.org.

ILLUSTRATION: ROBERT NEUBECKER

Published by AAAS